Book of Abstracts

20th International Symposium on Flow Visualization

Delft, the Netherlands

TU Delft

Technical Sessions

ISFV20 Sponsors and Exhibitors

LaVision
FOCUS ON IMAGING

DANTEC DYNAMICS

Photron
High Speed Cameras

MicroVec

E·R·C·O·F·T·A·C

LASER 2000

IOP Publishing

V.S.J.

Day 1

TECHNICAL SESSION 1
AERODYNAMICS

Chaired by Markus Raffel

Evolution mechanisms of a suboff propeller wake

Gaetano Micci[1,*] and Mario Felli[2]
1: Dept. of Aerospace Engineering, University of "Roma Tre", Italy
2: National Research Council of Italy, Italy
* Correspondent author: gaelucamicci@gmail.com

Keywords: Tip vortices, wake instability, PIV, unsteady forces

ABSTRACT The performance of naval propellers is strongly affected by the inflow characteristics, which can alter their propulsive efficiency as well as their structural response and acoustic performance. For example, the unsteady inflow generated by the ship hull and appendages along with the turbulence ingested by the propeller, produce unsteady responses of the propeller that might increase the overall radiated noise (see Cumpsty & Lowrie 1974; Robison & Peake 2014) and fatigue stresses on the blades and the shaft (see Carlton 2012). Furthermore, environmental effects such as waves or currents, and vehicle maneuvering can lead to increased unsteady loading conditions accompanied by massive flow separation and a significant lateral flow which can cause propeller over-torque/over-thrust and lateral forces. Therefore, enhanced understanding of the mechanism underlying the interaction between the upstream flow, the propeller and the dynamics of the coherent turbulent structures detached from the blades is critical to successful design of propellers and of the ship's aft-body.

Most previous studies on the wake dynamics of propellers and rotor systems have dealt with uniform inflow conditions focusing on the propeller wake evolution, instability and breakdown (see e.g. Okulov & Sorensen, 2007; Felli et al., 2011, Felli & Falchi, 2020). These studies have shown that propeller wake instability is driven by the mutual inductance instability mode (Widnall 1972) which leads adjacent vortex filaments to pair analogously to the leapfrogging motion of two inviscid vortex rings (e.g. Okulov, 2004; Felli et al., 2011). The pairing phenomenon occurs in a row of equidistant identical vortices, whereby amplifications of small perturbations cause the vortices to oscillate in such a way that neighboring vortices approach each other and start to group in pairs. Felli et al. (2011) showed that the mutual-inductance mode is manifested through a multi-step grouping process that depends on the blade number.

In spite of the recent findings from the propeller wake instability research, little attention has been paid to the study of the propeller performance and wake dynamics when propeller operates in behind conditions including off-design. More in general, the relation among the ship operational scenario, the propeller loading, the dynamics of the subsequent vortex system, the characteristics of the inflow, the resulting coherent turbulence structures in the wake and the dynamic response of the ship is a complex and challenging problem of hydrodynamic research, closely related to the improvement of performance, efficiency, safety, acoustic signature and to the reduction of stresses on the hull, on its appendages and on the transmission mechanisms. In response to the need to insight into the fundamental underlying mechanisms of propeller wake evolution in realistic ship/propeller operational scenarios and to provide reliable and archival quality experimental data for the validation of advanced CFD methods for the analysis of the propeller flow, the present paper reports the results of a parametric survey of the propeller wake flow in different operative conditions for the case of a 7-bladed propeller in behind conditions.

The survey was conducted in the Large Free Surface Cavitation Channel at CNR-INM (i.e. 10m length x 3.6m width x 2.25m depth test section) on a reference Suboff-propeller system consisting of a notional submarine hull, i.e. the DARPA Suboff (see e.g. Crook, 1990; Chase, 2012) and a 7-bladed propeller, i.e. the INSEAN E1658. A sketch of the model installation in the facility is shown in the left of Figure 1. The study was based on propeller and suboff force and moment measurements, flow visualizations, wave elevation measurements and phase-locked detailed 2D-PIV flow measurements.

PIV measurements were performed using a system of three synchronous cameras (i.e. 16 bits, 2560 pixel x 2160 pixel, 6.5 µm pixel size, 50 frames/s maximum frame rate), illuminated by a 200 mJ/pulse Nd-YAG laser. The three cameras were arranged side by side in the longitudinal direction with the optical axes perpendicular to the laser sheet (see right of Figure 1). This configuration allowed the full coverage of the region of interest. The phase-locked statistical analysis was performed over a population of 500 image pairs, recorded for 28 even-spaced propeller positions. The measurement campaign covered an extensive set of propeller conditions in terms of advance coefficient, propeller depth, Froude number and yaw angle.

Figures 2 and 3 show some exemplifying results of the propeller wake evolution for two different depths of the propeller/suboff (i.e. z=D and z= 1.5D, where z is the depth at the propeller axis and D is the propeller diameter). Contour plots refer to the phase-locked averaged (Figure 2) and instantaneous (Figure 3) fields of the azimuthal component of the vorticity.

At the shallowest shaft depth (z/D=1) the interaction between the propeller-hull and the free surface is strongest and involves an upward displacement of the propeller wake streamtube and a substantial distortion of the propeller tip vortices in the rotational upper region. As the propeller depth increases, free surface-effects become considerably weaker, the propeller tip vortices in the rotational upper region tend to be more stable and the topologies of the vorticity field in the top and bottom regions of the propeller wake appear more similar. A substantial effect is produced on the hub vortex that is involved in a rapid destabilization

and in a pronounced oscillation when the propeller operates at the shallowest depth, as proved by the widely diffused vorticity trace in the left of Figure 3.

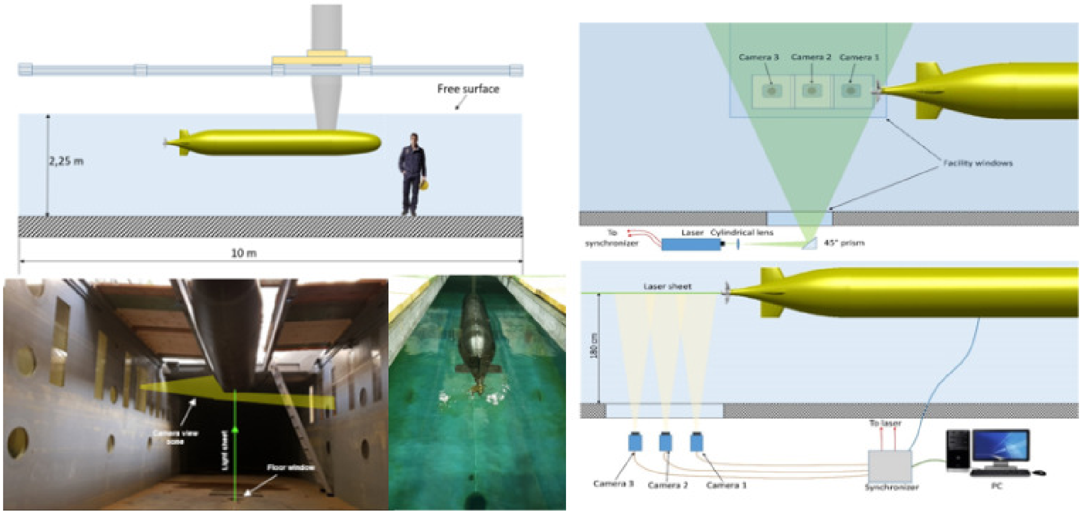

Figure 1. Experimental set up. Test section of the facility (top-left), picture of the model installation in the test section (bottom-left). Experimental set up of the PIV measurements (right).

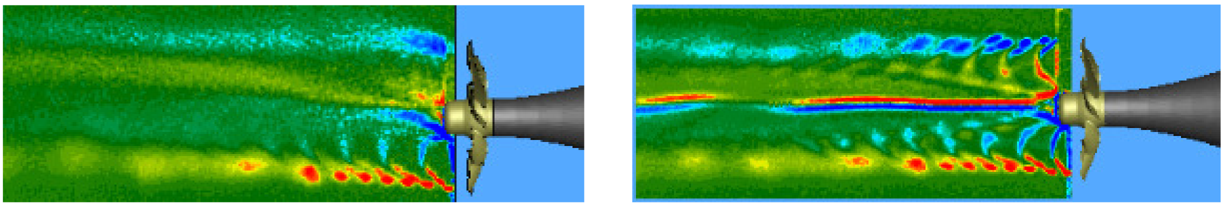

Figure 2. Phase locked averaged fields of the out-of-plane vorticity component for two different propeller depths (left: z/D=1, right: z/D=2). Propeller operating at J=0.82

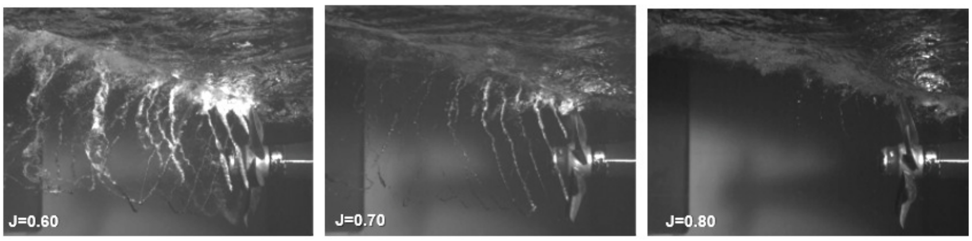

Figure 4. Snapshots of the ventilated propeller vortices for the shallowest shaft depths. Pictures refer to different propeller loading conditions.

1 REFERENCES

- Carlton, J., (2012). ‘Marine propellers and propulsion’. Elsevier, ISBN 9780080971230.
- Chase, N., & Carrica, P. M. (2013). ‘CFD simulations of a submarine propeller and application to self-propulsion of a submarine’. Ocean Engineering, 60, 68-80.
- Cumpsty, N. A. & Lowrie, B. W., (1974). ‘The cause of tone generation by aeroengine fans at high subsonic speeds and the effect of forward speed’. J. Engine Power 96 (3), 228–234.
- Felli, M., & Falchi, M. (2020). ‘Propeller tip and hub vortex dynamics from the near to the very far field by time-resolved PIV measurements’. Proc of 33rd Symposium on Naval Hydrodynamics, Osaka, Japan.
- Felli, M., Camussi, R., & Di Felice, F. (2011). ‘Mechanisms of evolution of the propeller wake in the transition and far fields’. Journal of Fluid Mechanics, 682, 5-53.
- Ivanell, S., Mikkelsen, R., Sørensen, J. N. & Henningson, D. S. (2010), ‘Stability analysis of the tip vortices of a wind turbine’. Wind Energy 13 (8), 705–715.
- Okulov, V. L. & Sørensen, J. N. Stability of helical tip vortices in rotor far wake. J. Fluid Mech. 576, 1–25, 2007.
- Widnall, S. E. The stability of helical vortex filament. J. Fluid Mech. 54, 641–663, 1972.

Near-wall investigation of laminar separation bubbles using the temperature sensitive single-shot lifetime method

Tudor V. Venenciuc[1,*], Christian Klein[2], Christian J. Kähler[1]

1:Institute of Fluid Mechanics and Aerodynamics, University of the Bundeswehr Munich, Neubiberg 85577, Germany

2: Institute of Aerodynamics and Flow Technology, German Aerospace Center (DLR), Bunsenstrasse 10, Göttingen, 37073 , Lower Saxony, Germany

* Correspondent author: tudor-victor.venenciuc@unibw.de

Keywords: laminar separation bubble, footprint, TSP, single-shot lifetime

Laminar separation bubbles (LSB) develop at aerodynamically low Reynolds numbers, at which unmanned aerial vehicles, gliders and wind turbine blades operate and are thus of great scientific interest. They form when a laminar flow separates due to an adverse pressure gradient and transition to a turbulent flow, which enhances the wall normal momentum exchange, which can result in a reattachment. Its formation on the suction side of airfoils leads to drastic variations in drag, pitch moments and lift. During flight, a maneuverable aircraft experiences a wide range of free-stream conditions and it is therefore impervious to research the aerodynamical behavior in facilities that can produce a wide range of scenarios. As the separation bubble is usually quite thin, its analysis becomes challenging and the extraction of near wall flow features is often higly uncertain. The focus of this project is to assess if the footprints of the flow structures on the surface can be spatially and temporally resolved using the single-shot temperature sensitive lifetime method in an environment in which the less flexible intensity method cannot be employed. If the reliable measurement of the footprints becomes possible, this technique could provide many details which are hardly accessible to other experimental methods.

To perform the measurements, an SD-7003 hydrofoil is equipped with a heating element and installed in the towing tank of the University of the Bundeswehr in Munich. Europium based temperature sensitive paint is sprayed on the suction side and six UV-LEDs provide the excitation light necessary for the phosphorescent coating. Because of the open surface of the tank, water waves and variable levels of impurities cause drastic variations in the illumination patterns, which render the intensity method obsolete. The surface temperature must therefore be acquired using the single-shot lifetime method.

Tow tests conducted at constant velocities corresponding to $Re_C = 6 \cdot 10^4$ and angles of attack ranging from 2° to 8°, display the expected time and span-wise averaged thermal profiles. Different heating powers, ranging from approx. 660 W/m^2 to 2000 W/m^2 , are employed and the influence of the heat flux on the occurrence of the LSB is assessed. The low levels of free-stream turbulence, as well as the harmonic global velocity fluctuations produced by the towing rig, create clear footprints of vortical structures with high levels of span-wise coherence, coinciding with the observations of Michelis et al. (2018). This allows the averaging of the thermal signal over the span of the heating element, which compensates for the relatively low signal-noise ratio, and still visualise the propagation of the Kelvin-Helmholtz instabilities downstream (see right hand side of figure 1). The results show a highly periodic vortex shedding starting in the vicinity of the time-averaged reattachment line. Furthermore, it could be shown that the shedding frequency matches the slight velocity oscillations of the wing model (see figure 2). This implies the receptivity of the vortex shedding to external disturbances. Since at higher angles of attack the frequency with the highest growth rate increases, the amplitude of the harmonics of the tow velocity fluctuation attains greater magnitudes. The measurements are not straight forward and within the conference paper we will outline how to make such measurements possible. Furthermore we would like to present flow details which could not be resolved before.

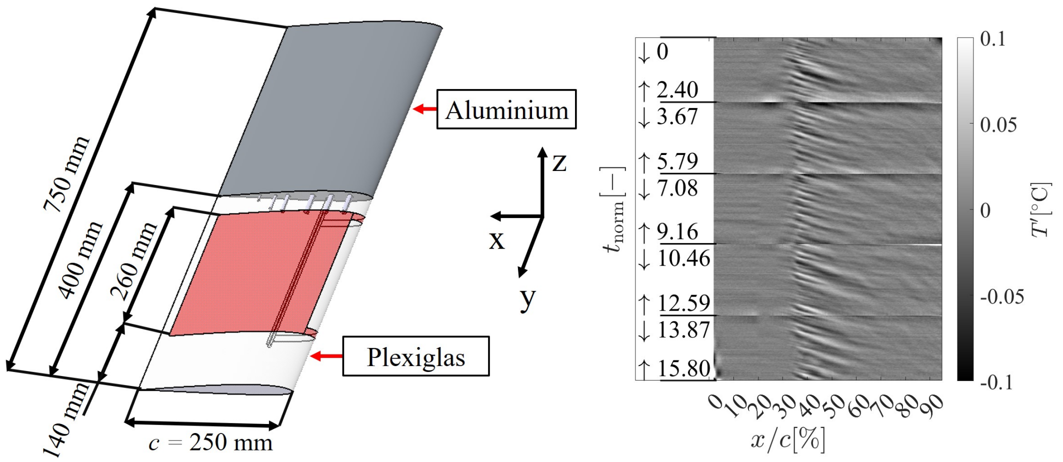

Figure 1. Left: CAD model of the SD-7003 foil equipped with the heating element (red region). Right: high-pass filtered thermal signal averaged over the span of the heating element at α = 6° and $Re_c = 6 \cdot 10^4$

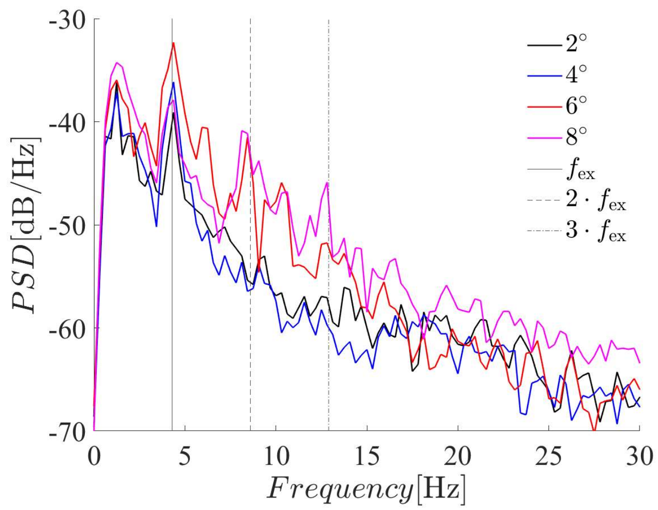

Figure 2. Spectral content in the vicinity of the time-averaged reattachment location. The high-pass filtered signal is processed after span-wise averaging the thermal values. f_{ex} is the frequency at the highest velocity oscillation amplitude of the towing system.

Michelis T, Kotsonis M, Yarusevych S (2018) Spanwise flow development within a laminar separation bubble under natural and forced transition. Experimental Thermal and Fluid Science 96:169–179.

Flow Field Measurements around an Over-The-Wing Propeller at Incidence

Hasse N.J. Dekker[1,2,*], Woutijn J. Baars[1], Fulvio Scarano[1], Daniele Ragni[1] and Marthijn Tuinstra[2]
1: Faculty of Aerospace Engineering, Delft University of Technology, The Netherlands
2: Vertical Flight and Aeroacoustics, Royal Netherlands Aerospace Centre, The Netherlands
* Correspondent author: h.n.j.dekker-1@tudelft.nl

Keywords: PIV, Aerodynamics, Propulsion, Over-The-Wing, eVTOL

ABSTRACT The flow field around an over-the-wing propeller along eVTOL flight conditions has been experimentally investigated using stereoscopic particle image velocimetry and pressure orifices. At high angles of attack, the results show an increase in spanwise variations of the pressure coefficient during inclination and a reduction of the stream tube contraction. During the early stages of stall, the propeller's suction cannot prevent the boundary layer to separate at the wing's leading edge. Instead, the separated region is accelerated, resulting in a velocity pattern which represents the ingestion of ground vortices.

1 INTRODUCTION

Urban Air Mobility (UAM) aims at a transportation system that will shorten travel times in metropolitan areas, by enabling air-linked destinations in closer proximity to one another than regular airports. This is achieved by leveraging eVTOL (electric Vertical Take-Off and Landing) configurations, to deploy highly versatile and maneuverable disruptive aircraft systems. Making use of the great scalability characteristics of electric motors, allows for increased design freedom for the propulsion system. Hence, disruptive solutions are discovered, resulting in unexplored aerodynamic and aeroacoustic installation effects. A promising configuration is known as the "Over-The-Wing (OTW) Propeller" or "OTW-DEP", in which the propulsors are mounted over the suction side of the wing, with its' axes alling with the wing's chord line. By this orientation, the propeller noise is shielded by the wing, which can be used to reduce fly-over noise. Additionally, the propulsors induce flow over the wing leading to improved aerodynamic characteristics of the wing (Muller *et al.*, 2014). Previous studies considered the OTW propeller system either in cruise conditions (Perry *et al.*, 2021), or with a detached flap for STOL purposes (de Vries *et al.*, 2021). Along the flight path of an eVTOL aircraft, the propulsors provide a large amount of thrust and angles of attack that are close to, or over the stall angle are encountered (Chauhan & Martins, 2020). This greatly changes the aerodynamic interactions between propeller and wing system, leading to complex and highly three-dimensional flow fields. To understand these installations effects, the flow around an over-The-Wing propeller is characterized by means of pressure orifices and stereoscopic Particle Image Velocimetry (PIV).

2 EXPERIMENTAL SETUP

The experiments were performed in the Aeroacoustic Wind Tunnel (AWT) Facility at the Netherlands Aerospace Centre in Marknesse. A wing model was mounted vertically on a turntable in the floor of the 95x95cm^2 closed test section, see Figure 1. The chord c of the wing comprises 240 mm and the boundary layer was tripped at 10% chord on both sides.

Figure 1 (left) Exterior of the AWT, (middle) wing and propeller setup in the test section and (right) stereoscopic-PIV setup

At the mid span position of the wing, a propeller is mounted (radius of 63.5 mm) and operated at a shaft frequency of 383 *Hz*. The flow measurements include pressure orifices in the center span position of the wing, where 59 static pressure taps are fitted. At the same spanwise position, stereoscopic Particle Image Velocimetry (PIV) is employed to characterize the flow at the inflow of the propeller, using the setup as illustrated on the right side of Figure 1. The flow is seeded with DEHS tracer particles particles ($\tau = 2$ µs) which are illuminated by an evergreen laser (200 mJ/pulse) in a sheet of 3mm thickness, at a repetition rate of 15 Hz. Recording is performed by two sCMOS cameras (*Imager sCMOS CLHS*), equiped with an objective of focal length $f = 50$ mm, set at numerical aperture $f_{\#} = 8$. The resulting field of view spans 19 x 25 cm^2 (3 *R* x 4 *R*). The propeller position is varied in spanwise direction in steps of 10mm along the measurement plane, to obtain time-averaged surface pressures contours and the volumetric flow field around the propeller. Each measurement comprises of at least 300 recordings for a time duration of 20 s.

3 RESULTS

The aerodynamic interactions between the propeller and wing are investigated for three levels of inlination for a constant advance ratio; a zero angle of attack, an angle of attack of 8º, which positions the propeller in a strong adverse pressure gradient, and the early onset of stall at $\alpha = 12$º. The results are presented in Figure 2 by the wing's surface pressure contours and normalized velocity magnitude contours and streamlines for $z/c = 0.2$.

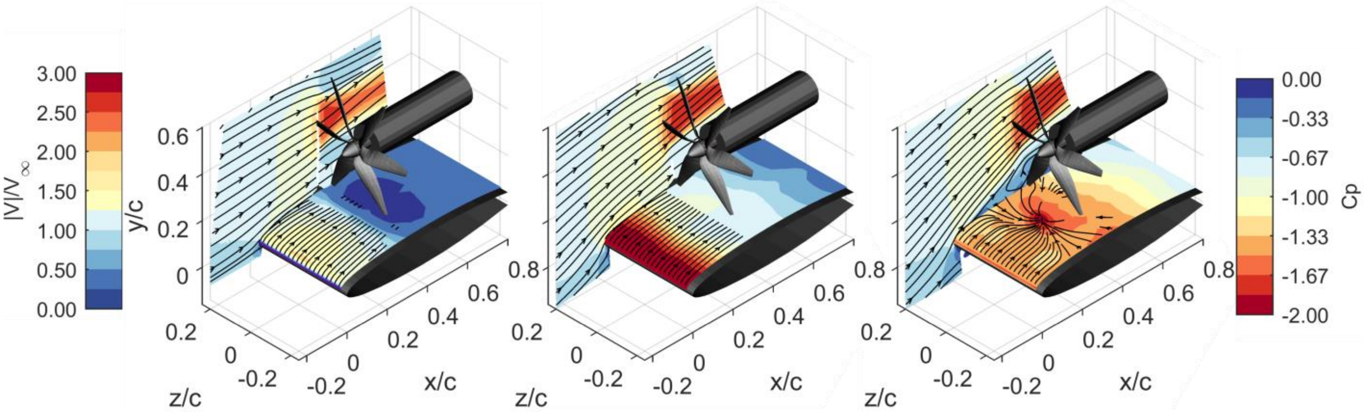

Figure 2 Pressure coefficient C_p contours over wing surface in (x,z)-plane and projected streamlines extracted at $dy = 0.025c$, and normalized velocity magnitude $|V|/V_\infty$ and 2D velocity streamlines in (x,y)-plane for $\alpha = 0$º (left) $\alpha = 8$º (middle) and $\alpha = 12$º (right) for $x_p/c = 0.3$ and $J = 0.3$.

The results for $\alpha = 0$º, in the left of Figure 2, show a low pressure region upstream of the propeller. The pressure jump at the propeller disk leads to higher pressures downstream, which is projected on the wing. A symmetric pressure distribution is present, where the absolute value of pressure is 25% higher in the mid span position, compared to the edges of the domain. The contraction of the propeller stream tube is visible by the streamlines both on the wing's surface and the extracted velocity field slice. By inclination of the system to $\alpha = 8$º, the pressures of the wing are reduced by its circulation. Notable are also spanwise variations visible downstream of the disk. The increase in flow velocity by circulation, leads to a reduction in thrust provided by the propeller, as is visible by the less pronounced contraction of the streamlines. In the early onset of stall, for $\alpha = 12$º, the propeller's suction is not able to delay the boundary layer separation. Instead, flow is induced inside the separated boundary layer from spanwise and axial directions, which represents a flow pattern similar to the ingestion of ground vortices.

4 CONCLUSIONS

The flow around an OTW propeller at incidence is investigated using stereoscopic PIV and pressure offrices. The results highlight different flow regimes as the angle of attack of the system is increased. Hence, the results are valueable to the understanding of the aerodynamic installation effects of this propulsion system layout for eVTOL aircraft.

5 REFERENCES

- Chauhan, S. S., & Martins, J. R. (2020). Tilt-wing eVTOL takeoff trajectory optimization. Journal of aircraft, 57(1), 93-112.
- Müller, L., Heinze, W., Kožulović, D., Hepperle, M., & Radespiel, R. (2014). Aerodynamic installation effects of an over-the-wing propeller on a high-lift configuration. Journal of Aircraft, 51(1), 249-258.
- Perry, A. T., Bretl, T., & Ansell, P. J. (2021). Aeropropulsive Coupling Effects on a General-Aviation Aircraft with Distributed Electric Propulsion. Journal of Aircraft, 58(6), 1351-1363.
- de Vries, R., van Arnhem, N., Avallone, F., Ragni, D., Vos, R., Eitelberg, G., & Veldhuis, L. L. (2021). Experimental Investigation of Over-the-Wing Propeller–Boundary-Layer Interaction. AIAA Journal, 59(6), 2169-2182.

An experimental study of the 3D unsteady aerodynamics of a surging airfoil

Guanqun Xu[1,*] , Sowmya Iyer[1,2], Wei Yu[1], Andrea Sciacchitano[1] and Carlos Ferreira[1]
1: Dept. of Flow Physics and Technology, Delft University of Technology, The Netherlands
2: Dept. of Wind Energy, Technical University of Denmark, Denmark
* Correspondent author: g.xu-1@tudelft.nl

Keywords: Stereo PIV, Surging, Airfoil, Vortex shedding, Lock-in

1 BACKGROUND

When a wind turbine is at standstill, the blade is often pitched by a large angle of attack (AOA) to cut out of the wind. In this situation, enormous vorticity could occur at both the trailing and leading edge along the blade. The vortex shedding frequency will lock on the structural frequency when these two values get close, and this phenomenon is known as the lock-in effect. Then, vortex-induced vibration (VIV) will occur which has a high potential to increase the fatigue load of the wind turbine. As it is pretty challenging to analyse the result when aerodynamics is coupled with the structural response, it is reasonable to first look into airfoils with pre-defined motions. Previous numerical research has focused on the wake structure of a plunging two-dimensional NACA0012 airfoil, examining the combined effects of oscillation frequency and amplitude (Young & Lai, 2004).
Experimental study has also been conducted on a pitching and surging airfoil, specifically examining the dynamic separation process at the leading edge area (Dunne & McKeon, 2015). Studies have also been conducted on plunging and surging airfoils at low Reynolds numbers, but the unsteady aerodynamics at larger AOAs (greater than 20°) remain unknown (Choi et al., 2015). It is worth noting that in most predefined motion studies, the amplitude of motion is typically kept small for stability reasons.

2 EXPERIMENTAL SETUP

The primary objective of this research is to investigate the unsteady vortex shedding of a plunging airfoil at a 90° angle of attack (AOA), with large motion amplitudes designed to replicate the standstill AOA. The experimental campaign was conducted at the Open Jet Facility of Delft University of Technology in February 2023, as illustrated in Figure 1. The airfoil model NACA0021 was tested under pre-defined sinusoidal surging motion. After getting the static vortex shedding frequency, fst, from steady measurement, the frequency of the motion is designed to be 5 Hz and 2.5 Hz so as to investigate the motion effect. The motion amplitude was fixed at 1 chord (7.5 cm). Phased-averaged Particle Image Velocimetry (PIV) measurements were performed to capture the flow field in the upstream, near-wake, and far-wake regions at different spanwise locations. Fog droplets (1μm diameter) from a SAFEX smoke generator were used as seeding particles. The flow was illuminated by a Quantel Evergreen Nd: Yag laser (200 mJ pulse energy, 15 Hz maximum repetition rate, 532 nm wavelength). Flow field imaging was captured using two LaVision's Imager sCMOS cameras (2560 × 2160 pixels, 16 bit, 6.5 × 6.5 μm pixel size) with 105 mm Nikon lenses.

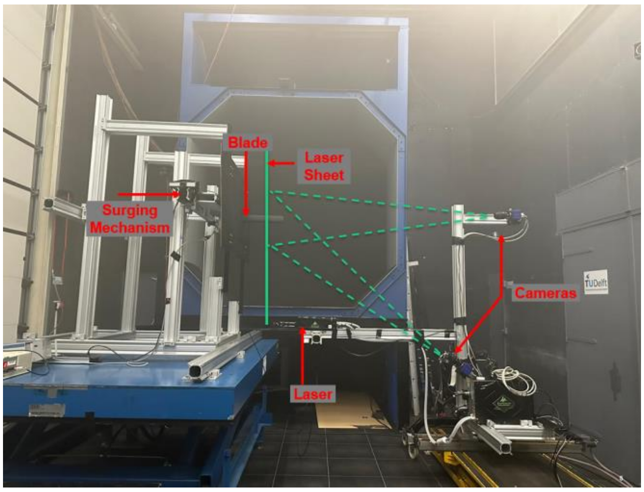

Figure 1. Experimental setup.

3 RESULT

In Figure 2, the vorticity field around the surging airfoil is depicted, specifically at 3 chords inboard from the tip, with a moving frequency of 5Hz. As the airfoil moves upstream (from 0° to 90° in phase), vorticity gradually accumulates, and the wavelength of the vorticity reaches its maximum at 90°. Subsequently, as the airfoil moves back (from 90° to 270° in phase), starting vortex slowly builds up at the front, and the wake vortex sheds completely at 270°. Afterward, a new wake vortex is generated as the airfoil moves against the wind (from 270° to 315° in phase). This entire cycle illustrates a specific vortex-shedding process, where the frequency of vortex shedding coincides with the moving frequency, resulting in a lock-in effect.

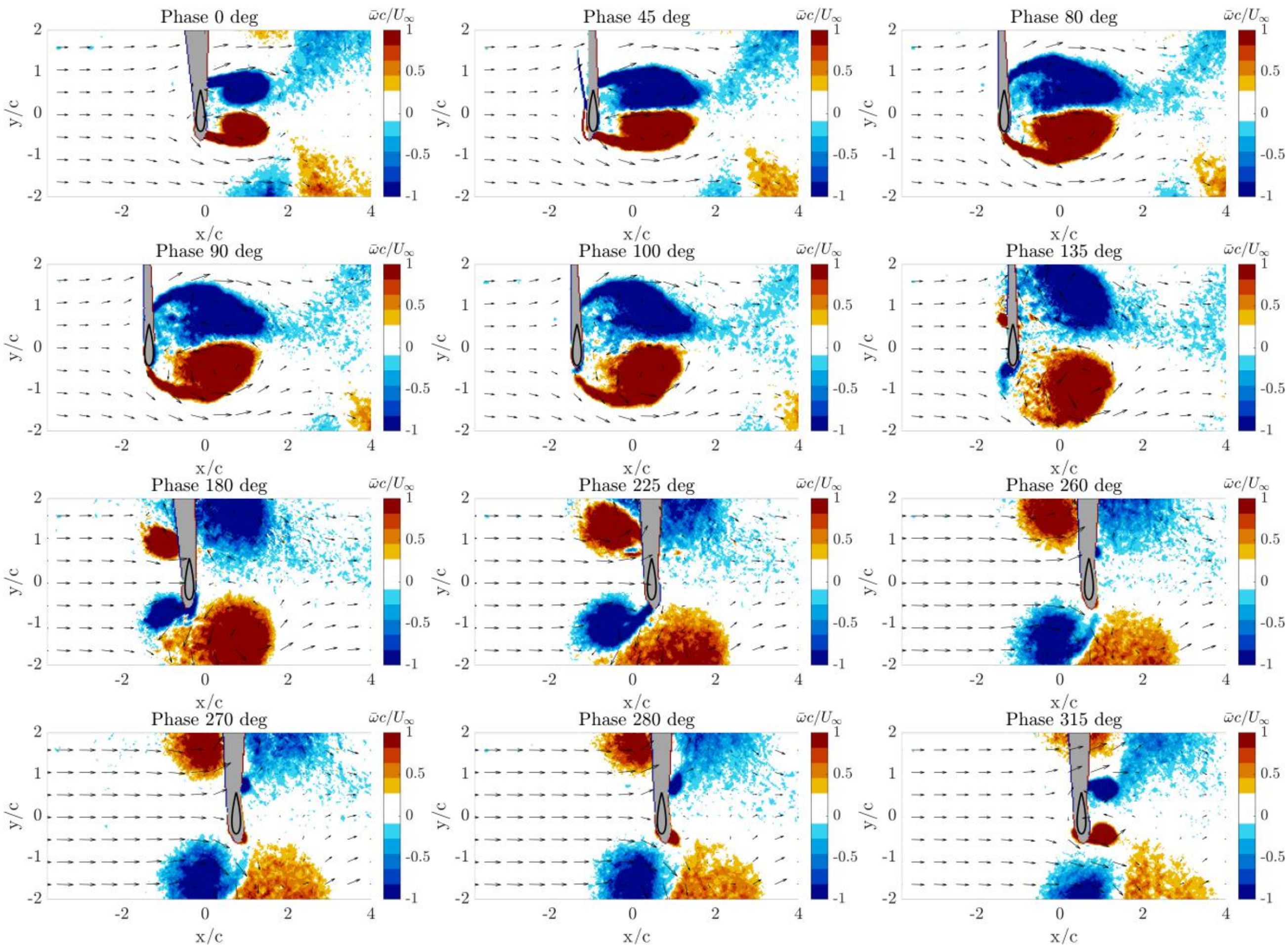

Figure 2. Vorticity around a surging airfoil at 5Hz, 3 chords inboard from the tip with the freestream velocity coming from the left.

4 REFERENCES

Choi, J., Colonius, T., & Williams, D. R. (2015). Surging and plunging oscillations of an airfoil at low Reynolds number. *Journal of Fluid Mechanics*, *763*, 237-253.

Dunne, R., & McKeon, B. J. (2015). Dynamic stall on a pitching and surging airfoil. *Experiments in Fluids*, *56*(8), 157.

Young, J., & Lai, J. C. (2004). Oscillation frequency and amplitude effects on the wake of a plunging airfoil. *AIAA journal*, *42*(10), 2042-2052.

Experimental study on drag coefficient of circular plate with holes

Kazuki Namba[1,*] and Yoshihiro Kubota[2]
1: Course of Advanced Mechatronics Systems, Toyo University, Japan
2: Dept. of Mechanical Engineering, Toyo University, Japan
* Correspondent author: s36a02200145@toyo.jp

Keywords: **Drag coefficient, Circular plate with holes, Shear layer, visualization**

ABSTRACT The aim of this study is to investigate the mechanism of the drag coefficient increasing in hole-opened circular plate. Visualization and measurement of drag coefficient of circular plate with multiple holes were carried out using towing experiment. Visualization around the holed model showed shear layer between jet ejected from holes and separated flow. Circular plate models with holes opened in parameter of numbers and aperture ratio increased drag coefficient. Total hole circumference of holes and drag coefficient showed proportional relationship and that is considered to be related to maximum total hole area.

1 INTRODUCTION

Existing of holes in the bluff body gives an influence that changes drag. C_D, drag coefficient of circular plate with a hole is greater than that of circular plate as an example (JSME, 2007). Furthermore, C_D is increased by the increase of hole size. In the case of porous plate, formation of shear layer due to flow passed through the hole and circumvented flow has already discussed and was described the difference of recirculation region between non-hole circular plate and holed one (Steiros & Hultmark, 2018). In this study, we focused not only the relation between just number of holes, size and drag coefficient but geometrical characteristics of circular plate with multiple holes. Physical modeling of drag coefficient included the bound of hole has possibility to be applied new control ways of drag in existing shape.

2 EXPERIMENTAL METHODS

Hole opened circular plate models was created with parameters of the number of holes (3, 4, 6) and aperture ratio (0.1, 0.2, 0.3) decided by ratio of total hole area and reference circular plate with the diameter of 80mm. Table 1 shows the experimental models. Visualization and drag coefficient measurement of them were carried out with towing. Figure 1 shows the sketch of experimental setup. Circular model is moved 3m in the water by belt driving rail running with constant velocity of 0.2m/s. The rail runs through acceleration of 0.1m/s^2 and deceleration of 0.1m/s^2. Shooting photograph of flow around the models was taken by camera on the rail. Water in the tank is visualized by micro bubbles and laser sheet strikes in the center of the plate. Shutter speed is 1/60 seconds. Drag is measured by pressure sensor (sampling frequency: 1.2kHz) attached behind the model and drag coefficient calculated by the equation of $C_D=2D/\rho u^2A$. Here, D is drag, ρ is density of water, u is velocity, A is projected area. Analyzed data is used 2seconds just before deceleration model considering the vibration of rail acceleration phase.

Table 1. Experimental models.

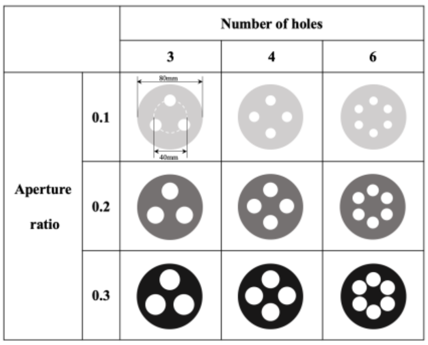

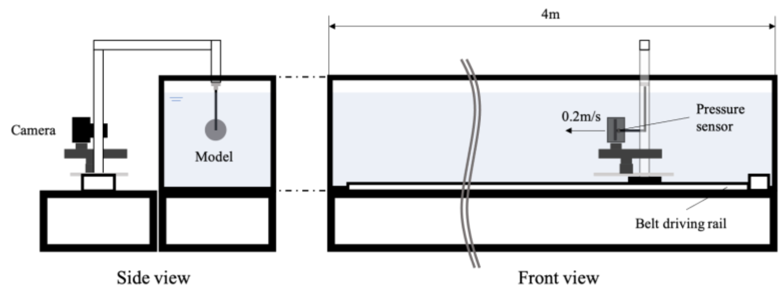

Figure 1. Experimental setup of towing.

3 RESULTS AND DISCUSSION

Visualization photograph in Figure 2 showed flow passed in the hole and that circumvented around the plate. These flows make shear layer that is considered to be related to the increasing of drag. In order to discuss the factor evaluates the increase of drag coefficient, relationship between hole and drag coefficient was showed in Figures. Figure 3 shows the relation between number of holes and drag coefficient. It is increased with difference of aperture ratio showed by color brightness of points in the same number of holes. As the integration parameter, total hole circumference of holes was added to evaluate drag coefficient of models as shown in Figure 4. Drag coefficient was increased by the total circumference of holes and the maximum value is around 1.3. It is considered shear flow behind the model insisted previously and friction happens when flow passed each hole increase drag coefficient. The transition of drag coefficient is considered converging at any constant value. It is resulted from the relation with maximum number and size of individual holes opened in the plate. Holes are opened on the half diameter of the circular plate as a model condition in this study. Total circumference of holes is written in an equation with square root of aperture ratio.

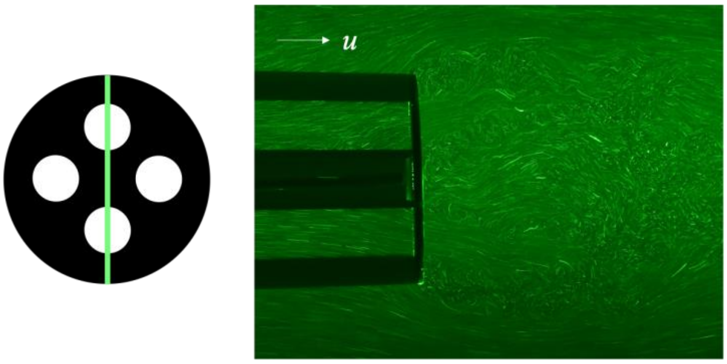

Figure 2. Flow around the experiment model with 4 holes and 0.2 aperture ratio.
Green line on the model view: the part laser sheet stlikes.

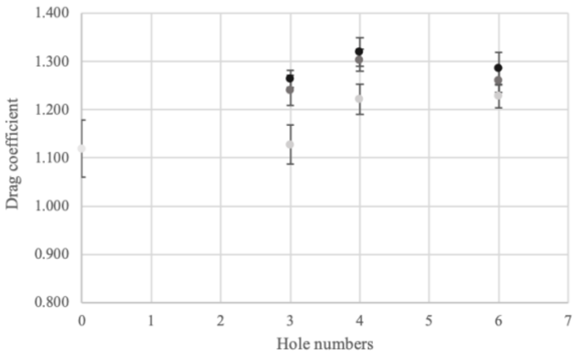

Figure 3. Relation of Drag coefficient and number of holes

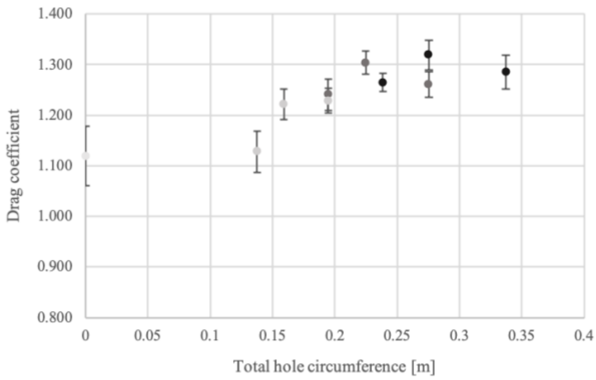

Figure 4. Relation of Drag coefficient and total hole circumference

4 CONCLUSION

Circular plate with multiple holes was estimated experimentally by visualization and drag coefficient measurement. As a result, relation of drag coefficient and hole circumference was found and that is expressed to be determined by the condition for opening holes. This geometrical rules and shear flow effect the increasing of drag coefficient by holes.

5 REFERENCES

- Japan Society of Mechanical Engineering. (2007). Flow in the pipe and force that works objects in the flow. Mechanical Engineers' Handbook Fundamentals (pp. α4-85).
- Steiros, K., & Hultmark, M. (2018). Drag on flat plates of arbitrary porosity. Journal of Fluid Mechanics, 853(R3), 1-11.

TECHNICAL SESSION 2
PARTICLE IMAGE VELOCIMETRY

Chaired by Christian Kähler

Improvement of Tomo-PIV Analyses in the Nasal Cavities

Sandra Melina Tauwald[1,2,*], Florian Erzinger[2], Maurizio Quadrio[3],
Markus Rütten[4], Christian Stemmer[5], and Lars Krenkel[1,2]
1: Regensburg Center of Health Sciences and Technology (RCHST), Germany
2: Dept. of Biofluidmechanics, Regensburg University of Applied Sciences (OTH), Germany
3: Dept. of Aerospace Science and Technology, Politecnico Milano, Italy
4: Institute of Aerodynamics and Flow Technology, German Aerospace Center (DLR), Germany
5: Chair of Aerodynamics and Fluid Mechanics, Technical University of Munich (TUM), Germany
* Correspondent author: melina.tauwald@oth-regensburg.de

Keywords: Tomo-PIV, Biomedical Flow, Non-Free-of-Sight, Breathing Cycle, Refractive Index Matching

The nasal cavities act as the main gateway to the entire respiratory system and thus play a pivotal role in respiratory homeostasis. The primary physiological function is for humidifying, warming, and particle filtering (Zubair et al., 2011). Indispensable for the physiological function is the sufficient contact of the respiratory air with the mucosa, the lining epithelium of the airways (Mlynski, 2013). Otorhinolaryngologists need detailed information of the flow regime in the patient-specific geometry in order to make a suitable diagnosis, preoperative planning, and thus achieve a successful surgery result. While the complex morphological structure of the nasal passageways is limited in access, the interaction of its anatomical form and its function requires investigations through either computational fluid dynamics (CFD) or in-vitro experiments (Doorly et al., 2008). The literature reveals investigations comprising CFD and/or experimental studies (Cozzi et al., 2017; Hörschler et al., 2006; Lintermann & Schröder, 2019). Nevertheless, the suitability of these investigations for the implementation to the medical field needs careful consideration. Emerging problems range from simplified geometries, neglecting the effects of cyclic respiratory flow, to the application of a suitable computational model (Zubair et al., 2011). These problems represent major challenges, and might be overcome by the hereinafter described tomo-PIV setup and investigations.

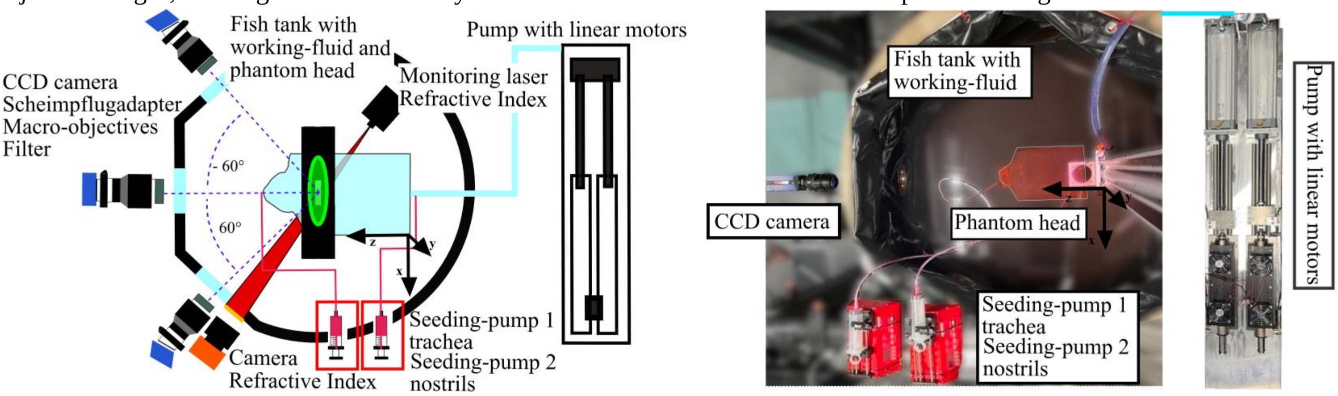

Figure 1. Experimental setup (sketch left, photograph right) in a top view including the RIM, the tomo-PIV setup and the flow inducing pump system.

A silicone model of the upper respiratory tract, based on a computer tomographic (CT) scan (ethical approved) of a person's head has been manufactured. The experimental setup (figure 1) includes the model placed in a fish tank filled with working-fluid (WF) attached to a traversing unit. Three aspects have to be highlighted: the refractive index (RI) matching (RIM), the tomo-PIV setup, and the flow inducing part. The RIM monitoring contains a line laser placed vis-à-vis the 60° angled porthole. After passing the Region of Interest (RoI), the light sheet exiting the fish tank is visualized on a scaled paper and captured by a camera. Thereby, a kinked laser line on the scaled paper indicates a non sufficient matching of the RIs of the geometry and the WF. The tomo-PIV setup contains three CCD-cameras (1600x1200) equipped with macro objectives, Scheimpflug adapters, and cut-off filters. The tracer particles (20-50 μm) are seeded by two syringe pumps, either via the trachea or via the nostrils, depending on the cycle state, and illuminated by a double-pulsed laser. The initial plate calibration of the cameras is refined in each RoI by a Volume Self Calibration (VSC). The volumetric reconstruction and vector calculation is done with a final window size of 40 voxels and a maximum expected displacement of 24 voxels. Images are captured by several inter double-frame rates (PIV-dts) depending on the cycle state and the geometry's shape. Whithin the flow inducing part, comprising a linear motor driven piston pump, the induced flow rate is based on test persons data adjusted by Reynolds and Womersley similarity, leading to a cycle period of 24.8 seconds, including the expiration part of 11.72 seconds. Thereby, peak flow rates are achieved at 6.0 seconds (0.370 l/s) for expiration and 17.7 seconds (-0.372 l/s) for inspiration. All components are centrally controlled by a programmable logic controller. The in-place RIM monitoring shows the best results whithin a RI of 1.4139. The final achieved RoI reaches a size of 34 mm x 34 mm x 6 mm with a scale factor of 29 pix/mm.

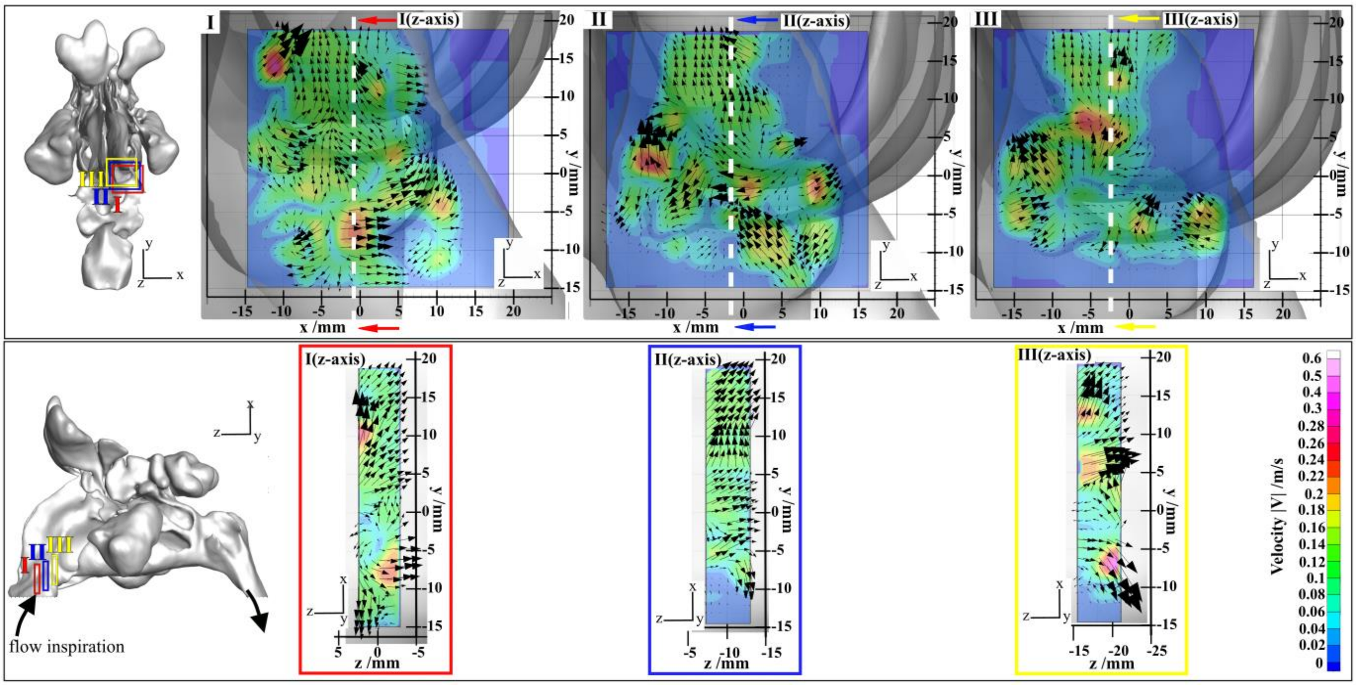

Figure 2. Examplary velocity distributions in three different RoIs. The left part indicates the positions in the geometry. The right part shows the velocity magnitudes, colour-coded, in a coronal section (upper part) and in a sagittal section (lower part).

While non-free-of-sight tomo-PIV investigations are sensitive to optical distortions, a precise RIM is necessary to achieve a successfull calibration. The in-place RIM monitoring provides a precise RI control, leading to VSC-errors lower than 0.1 pixel. The defined seeding strategy of this study, adapted to the respective cycle phase enables a nearly homogenous tracer particle seeding and a sufficient seeding density. The marker particles in the geometry and a defined coordinate system of the geometry-moving traversing unit allows a matching of the small investigated RoIs into the micro CT-scan (STL-data, 11 mio faces) of the silicone head. Figure 2 shows velocity fields in three RoIs during inspiration at 15.9 seconds in the cycle, comprising a flow rate of -0.303 l/s and analyzed by a PIV-dt of 7 ms. The RoIs are located at the right nostril, ascending in direction of the conchae (boxes in figure 2 left). The exemplary xy-slices (I-III) show the coronal cross section perpendicular to the main direction of the flow (figure 2 upper part) and the yz-slices (I(z-axis)-III(z-axis)) show the sagittal section, indicated by the white dashed line. The colour-coded velocity magnitudes |V| reach up to 0.3 m/s. The vector field shows a main flow in direction of the upper region of the main nasal cavities. However, this changes, visible at the yz-slices, the closer the RoI is to the conchae. Additionally, also in respect to the comparison of repeating cycles, unsteady peaks in the velocity magnitudes are visible. The described project provides high-spatial resolved flow data in several RoIs of a test person's nasopharynx considering different breathing cycle states. The combination with the micro-CT scan of the geometry will provide an experimental validation base for numerical investigations. The highly complex geometry combined with a cyclic flow requires investigation of PIV-parameters, like PIV-dt and seeding strategies, in each RoI. The experimental setup enables a high spatial resolution investigation comprising detailed information of the flow regime in several RoIs in the nasopharynx whithin different cycle states. Furthermore, the precise time-control of the setup's components combined with repeated measurements provides analyses of unsteady flow phenomena.

Cozzi, F., Felisati, G., & Quadrio, M. (2017). Velocity measurements in nasal cavities by means of stereoscopic PIV - preliminary tests. *J. Phys. Conf. Ser.* Advance online publication. https://doi.org/10.1088/1742-6596/882/1/012010

Doorly, D., Taylor, D. J., Franke, P., & Schroter, R. C. (2008). Experimental investigation of nasal airflow. *Proc Inst Mech Eng H*(222), 439–453. https://doi.org/10.1243/09544119JEIM330

Hörschler, I., Brücker, C., Schröder, W., & Meinke, M. (2006). Investigation of the impact of the geometry on the nose flow. *Eur. J. Mech.*(25), 471–490. https://doi.org/10.1016/j.euromechflu.2005.11.006

Lintermann, A., & Schröder, W. (2019). A Hierarchical Numerical Journey Trough the Nasal Cavity: From Nose-Like Models to Real Anatomies. *Flow Turbulence Combust.*(102), 89–116. https://doi.org/10.1007/s10494-017-9876-0

Mlynski, G. H. (Ed.). (2013). *Nasal Physiology and Pathophysiology of Nasal Disorders: Physiology and Pathophysiology of Nasal Breathing*. Springer. https://doi.org/10.1007/978-3-642-37250-6_20

Zubair, M., Abdullah, M. Z., Ismail, R., Shuaib, I. L., Hamid, S. A., & Ahmad, K. A. (2011). Review: A Critical Overview of Limitations of CFD Modeling in Nasal Airflow. *J Med Biol Eng.*(32), 77–84. https://doi.org/10.5405/jmbe.948

Experimental Validation of Scanning PIV system via Investigating flow past a circular cylinder

Mitanjali[1,*], Jun Chen[2] and Vaibhav K Arghode[1]
1: Dept. of Aerospace Engineering, Indian Institute of Technology Kanpur, India
2: Dept. of Mechanical Engineering, Purdue University, USA
* Correspondent author: mits@iitk.ac.in

Keywords: Scanning PIV, Dual Color, Velocity Field Measurement

ABSTRACT

Scanning PIV system consists of two CW DPSS lasers of different wavelengths (green and blue in the present investigation), which sweep through the region of interest to provide appropriate illumination. The illuminated region is captured by a conventional DSLR color camera. Synchronization of the camera and laser sweep is achieved through a microcontroller board. A well studied problem of flow past a circular cylinder is used for experimental validation of the system. The wake structure past a circular cylinder could be captured for a range of Re number in laminar and initial transition region. All the equipment used in this system are simple and cheap which makes the system cost effective and portable.

1 INTRODUCTION

Particle Image Velocimetry (PIV) is an optical technique to measure the velocity field in a 2D plane [1]. The technique facilitates non-intrusive spatial velocity measurement [2], as compared to the point wise intrusive techniques, such as hot wire anemometer. This method has been successfully implemented on a wide range of flows. Though the technique is very simple, it consists of heavy equipment such as dual cavity Nd-YAG laser, CCD camera and synchronizer. It makes the system complex and costly.

With the objective of cost reduction and field deployment a dual-color scanning-based PIV system has been proposed in our previous study [3] and a mathematical model has been developed. The model was tested on a few theoretical fluid flow problems such as uniform parallel flow, rigid body vortex flow. The study of flow over a circular cylinder was also considered along with the CFD simulation and results the results compared well with the computational data. In the present investigation, the system is experimentally demonstrated via. investigating the flow over a circular cylinder at low Reynolds number.

2 METHODOLOGY

In this system the illumination is achieved by two different wavelength CW lasers. The two beams (green and blue in this case) scan through the test section simultaneously with a small angular difference between them. The scan time depends on the frequency of scanning and sets exposure time for the camera. The camera shutter speed is set accordingly and a single-color image is captured. The captured image consists of particle images from both illuminations unlike in conventional PIV where the two illuminations are captured on two separate frames. The captured image is separated in two frames based on the color and subsequently the displacement and the velocity field is obtained. A schematic of the system is shown in Figure 1.

3 EXPERIMENTAL VALIDATION AND PRELIMINARY RESULTS

The scanning PIV system is demonstrated experimentally via. investigating flow past a circular cylinder. Experimental facility is developed with an arrangement of aluminum cylinder travelling vertically at a certain speed through steady water within a small acrylic water tank. As the cylinder starts moving through the flow, vortices form and shed periodically behind it due to flow separation if the Re number is above a critical value ~42. Image is captured when the cylinder reaches the extreme end of the test section. Flow at four different Re in the range of 70-300 has been investigated by varying the speed of the cylinder. Results for Re = 204 are shown in the Figure 2. The wake structure of the cylinder could be captured.

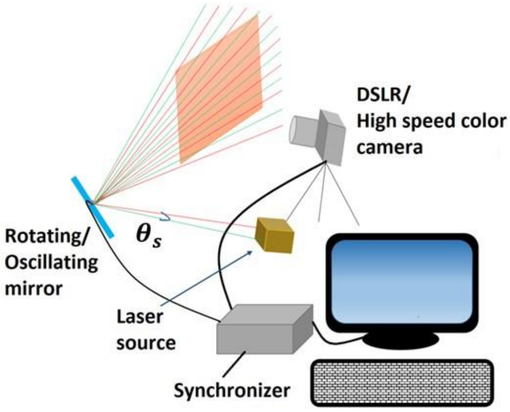

Figure 1. Schematic of the scanning PIV system.

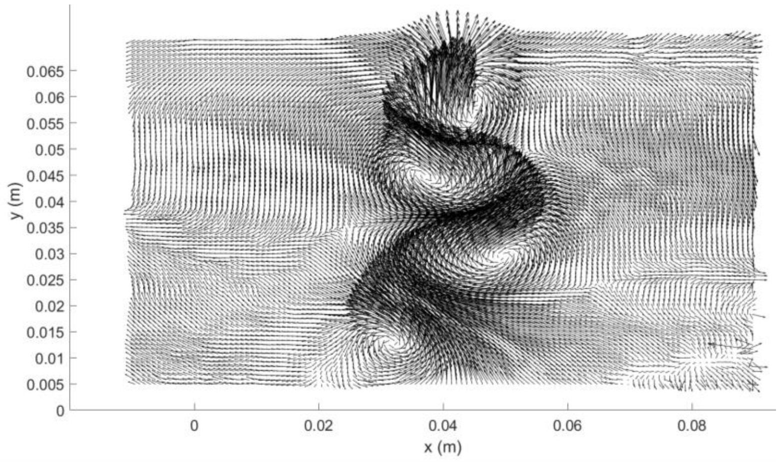

(a) Vector field

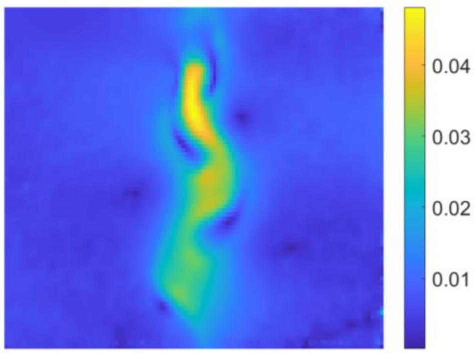

(b) Velocity Contour

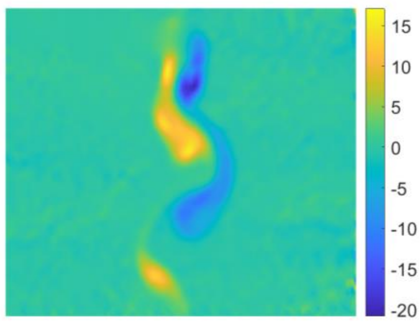

(c) Vorticity Contour

4 CONCLUSION

Dual-color, scanning-based PIV system has been developed. The system is easy to handle and cost effective due to the use of conventional DPSS lasers for illumination, DSLR camera to record the flow and Arduino for synchronization of lasers and camera. Flow past a circular cylinder in the laminar region and initial transition region is investigated. Periodic shedding of the vortices could be captured for the Re numbers in the laminar region as well as the onset of instability was observed for higher Re cases.

5 REFERENCES

- Raffel, M., Willert, C. E., Wereley, S. T. and Kompenhans, J., (2007). Particle Image Velocimetry, Springer.
- Adrian, R. J., Westerweel, J., (2011). Particle Image Velocimetry. Cambridge University Press.
- Mitanjali, Arghode, V. K. (2022). Investigation of Dual Color Angular Beam Scanning (DCABS) PIV system. Optics and Lasers in Engineering, 151, 106916.

Particle Image Based Simultaneous Velocity and Concentration Measurement

Abhilash Sankaran[1,*] Rainer Hain[1],
and Christian J. Kähler[1]
1: Universität der Bundeswehr München,
Institute of Fluid Mechanics and Aerodynamics
* Correspondent author: abhilash.sankaran@unibw.de

Keywords: Stereoscopic PIV, Particle concentration, Voronoi cells

A non-intrusive, image based particle concentration measurement technique is presented. The method applies a stereoscopic PIV measurement system in combination with an optical particle counter for calibration. The technique presented hence can be utilized for combined measurement of the velocity and the concentration field in the intended area. The calibration function is determined as a function of both space and concentration such that the variation of the image particle density due to the laser profile and camera viewing are considered within the calibration. Further, image analysis for different ways to measure the concentration field would be discussed in the full paper. A simple technique applying moving average procedure to obtain the particle concentration is applied which utilizes a fixed length scale. This method leads to suboptimal results when there are large concentration differences within the field of view. A significant scenario of interest is a highly non-uniform distribution of the particles that can occur in different flow fields of practical importance like concentrated jet issuing to ambient. The method based on Voronoi cells (Delaunay triangulation) for the determination of the concentration will be presented. The advantage with Voronoi tessellations is that the cells are sized appropriately depending on the number of points/local concentration. Effectively, the length scale is chosen appropriately by the cells rather than manual selection of the length scale. The technique can also be applied where the interface determination is important.

Particle concentration measurement techniques typically rely on particle counting methods at point locations to determine the average of the number of particles entering the system. This gives the quantitative information based on the absolute number of particles entering the system at the measurement point. In many fluid mechanical systems, the concentrations of the species are time or space dependent or both. For the space dependent case one can get information from multiple points averaged for reasonable long times to derive the average concentration profiles. However, for other cases the particle counter method by itself lacks the necessary information. Concentration field measurements are useful to understand the spatial distribution of the concentration in various scenarios including detection of boundaries of the species or mixing effectiveness, to name a few. Here, a method of directly detecting the particle images and calculation based on the particle images and calibration with particle counter is proposed.

An experimental example flow case of a turbulent puff is considered. The air is nebulized with DEHS particles of average diameter ≈ 0.4 µm. A stereoscopic PIV system is setup with the cameras in forward scattering mode. The forward scattering mode is necessary to obtain a high signal-to-noise ratio of the particle images. This allows the clear detection of particle images for the concentration determination. The data analysis was carried out using DaVis software from LaVision and MATLAB. The velocity field information was obtained from the stereoscopic velocity measurement. The obtained velocity magnitude distribution for two instances of the turbulent puff is shown in Fig. 1.

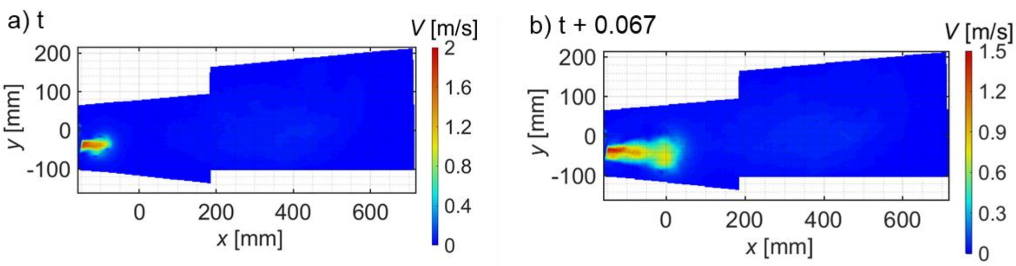

Figure 1. Average velocity magnitude contour (30 cycles averaged) at two instances of the turbulent puff. The total volume expelled is 1000 mL with a frequency of 16 cycles/min and the air was preheated to 37°C. *t* is the time instance normalized by the cycle time (3.75 s).

Further, the focus of the current work is the determination of the concentration field utilizing the same data from the stereoscopic particle images. To do this, one needs the calibration of the particle image data to the physical concentration. For calibration, separate sets of particle images are taken with uniform concentration in the room and simultaneous measurement using the particle counter as reference. The measured contour of the particle concentration in the image CI as particles per pixel (ppp) is derived with smoothing the particle points with a sliding average of 16 pixel. The obtained contour for one of the physical concentration is shown in Fig. 2a. The similar procedure is done for nine different physical concentrations spanning the concentration levels of interest. A smoothing spline fit is obtained for all points in the *x*-*y*-plane as a function of concentration as shown in Fig. 2b. The instantaneous concentration derived using the calibration function described above is presented in Fig. 3. Further, a technique based on Voronoi cells (Delaunay triangulation) could be applied for natural selection of the cells based on local concentration. Such a method has been utilized for astronomical observation, see Schaap and Van De Weygaert (2000). A preliminary analysis with the construction of Voronoi cells around the experimental particle distribution is shown in Fig. 4. The technique would be developed and presented in the full paper.

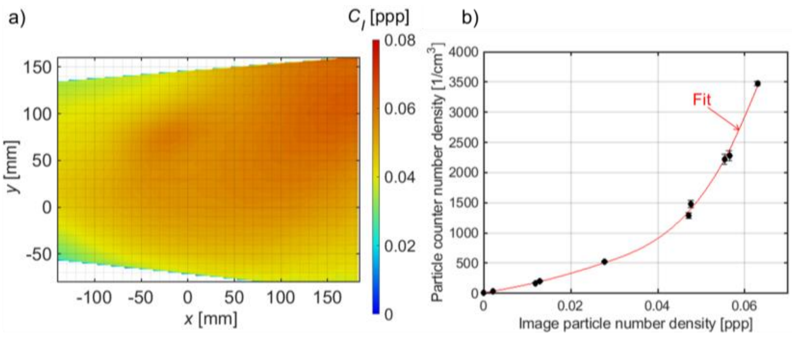

Figure 2. a) Contour of the measured variation of C_I (ppp) at the physical particle concentration of 1283 1/cm^3. (b) The experimental points of C_I at different physical particle concentration and the calibration function obtained at point (-100, 49) as a smoothing spline fit.

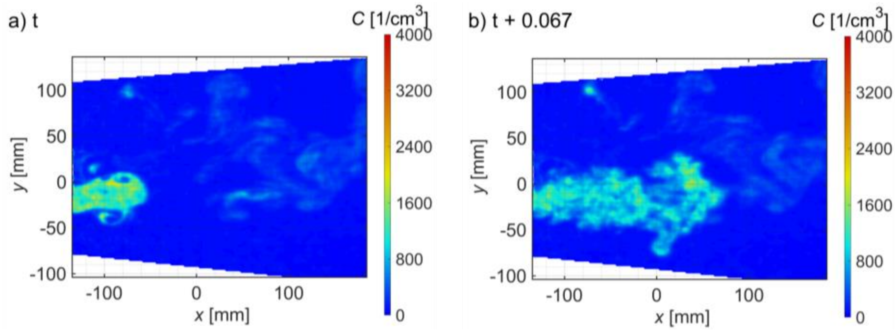

Figure 3. Instantaneous particle concentration contour at two instances of the turbulent puff.
The total volume expelled is 1000 mL with a frequency of 16 cycles/min and the air was preheated to 37°C.
t is the time instance normalized by the cycle time (3.75 s).

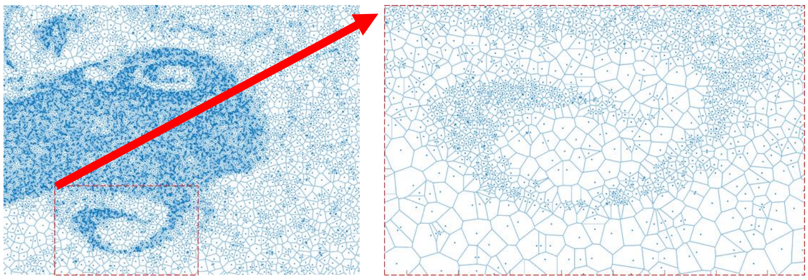

Figure 4. Voronoi cells around the particle positions at time instance *t* (instance shown in Fig. 3a).

ACKNOWLEDGEMENTS

This research is funded by dtec.bw – Digitalization and Technology Research Center of the Bundeswehr which we gratefully acknowledge. dtec.bw is funded by the European Union – NextGenerationEU.

REFERENCES

Schaap W., & Van De Weygaert, R. (2000) Continuous fields and discrete samples: reconstruction through delaunay tessellations. arXiv preprint astro-ph/0011007

Analysis of Sound Generation in the Human Voice based on PIV Measurements

Stefan Becker[1], Christoph Näger[1,*],
Alexander Lodermeyer[2] and Stefan Kniesburges[3]
1: Institute of Fluid Mechanics, Friedrich-Alexander-Universität Erlangen-Nürnberg, Germany
2: Institute of Process Machinery and Fluid System Dynamics, Friedrich-Alexander-Universität Erlangen-Nürnberg, Germany
3: Division of Phoniatrics and Pediatric Audiology at the Department of Otorhinolaryngology, Head and Neck Surgery, University Hospital Erlangen, Medical School at Friedrich-Alexander-Universität Erlangen-Nürnberg, Germany
* Correspondent author: christoph.naeger@fau.de

Keywords: particle image velocimetry, acoustics, human phonation, dynamic mode decomposition

1 Introduction

The human voice is generated in a complex interplay of fluid flow, structural vibration and acoustics. In this process, the vocal folds are stimulated to vibrate by a flow of air $\dot{V}$ from the lungs. This oscillation in turn leads to a modulation of the air flow, resulting in a pulsating jet flow in the vocal tract. The sound that constitutes thereby is mainly generated aeroacoustically from the turbulent pulsating jet flow. This sound is filtered through the vocal tract and radiated through the mouth, resulting in the voice. A detailed investigation of this process in vivo is often hindered due to limited access to the flow field in the larynx and trachea. Therefore, clinicians often rely on measurements of the vocal fold vibration for the diagnosis of speech impairments.

In an academical setting, these limitations are often circumvented by investigating the phonation process on excised human or animal larynges or artificial vocal folds. This allows for a better access of the regions of interest and more in-depth analysis of the underlying physics. For performing detailed flow analysis in and above the glottis, particle image velocimetry (PIV) has been proven as a useful tool in the past. Classical planar PIV measurements allowed to study the basic features of the supra- and intraglottal aerodynamics (see e.g. Oren et al. (2014), Lodermeyer et al. (2015)). Also tomographic PIV measurements have been applied in voice research recently, allowing to study volumetric quantities such as the maximum flow declination rate (de Luzan et al. (2020)).

However, especially high-speed PIV has emerged as a valuable method for connecting supraglottal aerodynamics and the resulting acoustics of the voice (Lodermeyer et al. (2018), Lodermeyer et al. (2021)). Therefore, in this work we use high-speed PIV measurements to investigate the human phonation process on a synthetic larynx model. For a better understanding of the connection between the flow field and its corresponding acoustic sources, we additionally apply dynamic mode decomposition (DMD, Schmid (2010)) to the measured flow fields, which enables us to gain insight into coherent flow structures at for the phonation process relevant frequencies.

2 Methods

Synthetic vocal folds were cast from a single layer of silicone. Their shape was based on the M5 model by Scherer et al. (2001). The experimental setup is depicted in figure 1. A vocal tract of rectangular cross section with a length of 180mm was added downstream of the vocal folds. A silencer was added upstream to attenuate emerging sound in the inflow hose. The vocal tract wall was made of glass to allow for optical access for the high-speed camera. PIV measurements were conducted with a measurement frequency of 2x5 kHz and a pulse distance of 4µs. The measured velocity fields were then used in combination with a Poisson solver to obtain pressure fields as well. This allowed us to use different aeroacoustic source term formulations e.g. PCWE (Perturbed Convecrive Wave Equation), Lighthill and AWE (Acoustic Wave Equation) on the PIV-grid. These could be interpolated onto a finite element grid, which enabled us to do acoustic radiation simulations based on our PIV measurements.

3 Results and Discussion

The aerodynamics in the VT were shown to be dominated by a fundamental oscillation frequency and its corresponding higher harmonics. The DMD analysis revealed that the basic oscillation frequency of the vocal folds is the dominant cause for the oscillation of the jet. The higher harmonic frequencies on the other hand are characterized by periodically shedding vortex pairs of decreasing size with increasing frequency. These vortex pairs lead to strong aeroacoustic sources. A fourier transformation of the source terms revealed, that the main source region for the base frequency was located just downstream of the glottis. For the higher harmonics, the source regions moved slightly further downstream in the channel.

The acoustic radiation simulations showed a good agreement with experimental microphone measurements in their broadband level. Also the peak locations at the oscillation frequency and its higher harmonics are captured well. There exist however some differences in the peak levels between the measurement and the simulations (see Fig 2).

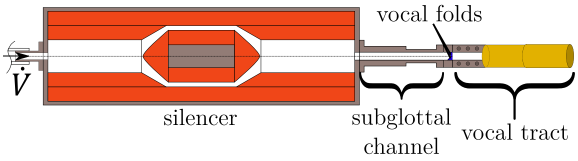

Figure 1. The experimental setup. The vocal fold position is indicated between the vocal tract and the subglottal channel. A silcencer is placed upstream to attenuate emerging sound in the inflow hose.

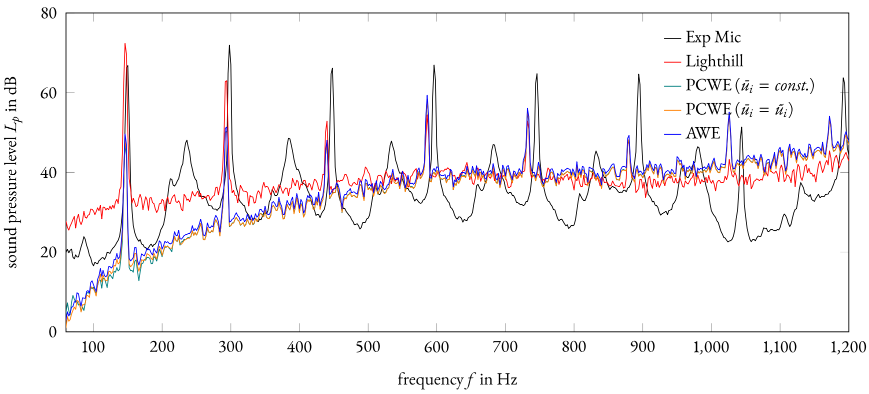

Figure 2. Comparison of the the sound pressure level L_p for the acoustic analogies based on a perturbation ansatz PCWE, and AWE compared to the experimental microphone measurement (black) and the simulation based on Lighthills´s formulation (red)

4 Conclusion

The described measurement procedure enabled us to perform detailed investigations in analyzing the human phonation process. The DMD analysis revealed vortex pairs shedding at the glottis that can be used to explain the resulting aeroacoustic source terms. An interesting direction to extend this approach is the investigation of two-way fluid-acoustic-interaction. Titze (2007) described, that the acoustic standing waves in the vocal tract can under certain circumstances influence the (sub-)glottal flow field as well as on the vocal fold vibration. This phenomenon will be analyzed with the developed approach in future works.

5 REFERENCES

- de Luzan, C.F., Oren, L., Maddox, A., Gutmark, E., Khosla, S.M. (2020). Volume velocity in a canine larynx model using time-resolved tomographic particle image velocimetry. Experiments in Fluids, 61, 63.

- Lodermeyer, A., Becker, S., Döllinger, M., Kniesburges, S. (2015). Phase-locked flow field analysis in a synthetic human larynx model. Experiments in Fluids, 59, 77.

- Lodermeyer, A., Tautz, M., Becker, S., Döllinger, M., Birk, V., Kniesburges, S. (2018). Aeroacoustic analysis of the human phonation process based on a hybrid acoustic PIV approach. Experiments in Fluids, 59, 13.

- Lodermeyer, A., Bagheri, E., Kniesburges, S., Näger, C., Probst, J., Döllinger, M., Becker, S. (2021). The mechanisms of harmonic sound generation during phonation: A multi-modal measurement-based approach. The Journal of the Acoustical Society of America, 150, 3485-3499.

- Oren, L., Khosla, S., Gutmark, E. (2014). Intraglottal geometry and velocity measurements in canine larynges. The Journal of the Acoustical Society of America, 135, 380-388.

- Scherer, R.C., Shinwari, D., Witt, K.J.D., Zhang, C., Kucinschi, B.R., Afjeh, A.A. (2001). Intraglottal pressure profiles for a symmetric and oblique glottis with a divergence angle of 10 degrees. The Journal of the Acoustical Society of America, 109, 1616-1630.

- Schmid, P.J. (2010). Dynamic mode decomposition of numerical and experimental data. Journal of Fluid Mechanics, 656, 5-28.

Spanwise stall-cell organisation of an aerofoil with leading-edge tubercles

Mogeng Li[1, *] and Fulvio Scarano[1]
1: Faculty of Aerospace Engineering, TU Delft, The Netherlands
* Correspondent author: mogeng.li@tudelft.nl

Keywords: unsteady aerodynamics, stall cells, PTV, STB

ABSTRACT The stall of a NACA0021 aerofoil with leading-edge tubercles is investigated experimentally in this work. Time resolved three-dimensional flow field on the suction side of the aerofoil is captured using shake-the-box (STB) particle tracking velocimetry (PTV). Pairs of counter-rotating streamwise vortices generated at each tubercle enhances the mixing of the low-speed fluid at the wall and high-speed fluid in the free stream. At 15° angle-of-attack (AoA), stable stall-cell structures are observed to originate from the trough between tubercles, spanning approximately 4 tubercle wavelengths (equivalently 1 mean chord length). For AoAs larger than 20°, the stall cells are not fixed at certain troughs, but wander along the spanwise direction.

1 INTRODUCTION

The sinusoidal leading-edge modification to a wing or blade is inspired by the tubercle structures on the pectoral flippers of humpback whales. These structures are believed to enhance their swimming, featuring highly dynamic manoeuvres. Leading edge tubercles have been shown to increase the post-stall lift force by up to 50% with little drag penalty (Johari *et al.*, 2007). This favourable effect is attributed to the enhanced mixing facilitated by the streamwise vortex pairs produced by the tubercles (Hansen *et al*., 2011; Cai *et al.*, 2017). The structure of these vortex pairs has been relatively well characterised at small angles-of-attack (AoAs). At near- and post-stall AoAs, larger aperiodic structures spanning several wavelengths (involving multiple vortex pairs) have been observed (Cai *et al.*, 2017), but the formation mechanism of such aperiodicity is less well understood. In this work, we aim to further elucidate the flow structures around the stall angle with the aid of 3D time resolved PTV. The results will shed light on the mechanism of stall-cell modulation by spanwise wavelengths, which can eventually be utilised in separation control and lift hysteresis reduction for engineering applications.

2 EXPERIMENTAL SETUP

A symmetric NACA0021 aerofoil is selected as the baseline geometry, which is a generic representation of the cross section of turbine blades. The leading-edge of the tubercled aerofoil model can be described as

$$x_{LE} = A \sin\left(\frac{2\pi y}{\lambda}\right), \tag{1}$$

where A and λ denote the amplitude and wavelength of the tubercles, respectively, and y is the distance along the spanwise direction. The baseline aerofoil is then stretched between the leading edge and 30% mean chord length ($0.3c$, where the maximum thickness is reached), while preserving the leading-edge radius of the baseline profile and a smooth joint with the section aft the maximum thickness point (Wei, New & Cui, 2015). In other words, the section $x > 0.3c$ of a tubercled aerofoil is identical to that of the baseline model. A sketch of the tubercled aerofoil is shown in figure 1.

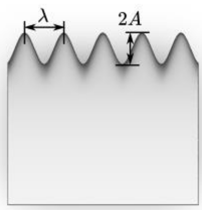

Figure 1 – Geometry of the aerofoil with tubercles at the leading edge.

The experiments are conducted in the W-Tunnel in the Aerodynamics Laboratory at TU Delft, which is a low-speed open return facility with a 1.2 m long cross-section area of 0.6 × 0.6 m^2. The measurements are performed at a free-stream velocity $U_\infty =$ 5 m/s with a turbulence level rated to approximately 1%. Three full-span aerofoil models with tubercle amplitudes $A =$ $\{0, 0.05, 0.1\}\, c$ are designed in SolidWorks and manufactured using stereolithography by Materialise HQ. The mean chord length of all models is chosen as $c = 0.1$ m, leading to an aspect ratio of 6 and a Reynolds number $\mathrm{Re} = 3.3 \times 10^4$ based on the chord length and free-stream velocity, and the tubercle wavelength is fixed at $\lambda = 0.25c$. The models are referred to as the *baseline*, *A05L25* and *A10L25*. The model is installed vertically at 0.9 m from the tunnel inlet on the centreline of the working section, fixed by two pins located at the quarter-chord point. For each aerofoil model, the AoA is varied from 0° to 30° with a step of 5°.

The velocity field on the suction side of the aerofoil is measured using a 3D time resolved PTV system. A schematic of the setup is shown in figure 2. The flow is seeded with neutrally buoyant helium-filled soap bubbles (HSFB) (Faleiros *et al*., 2019) with a nominal diameter of approximately 300 μm introduced in the settling chamber and illuminated with a LaVision LED light source. Three Photron SA1.1 high-speed cameras (1024 × 1024 pixels, 5400 fps, pixel pitch 20 μm). The region-of-interest is 768 × 1024 pixels and subtend an angle of 45 degrees. The cameras are equipped with Nikon 60 mm ($f_{\#}$ = 11) lenses and arranged at approximately 1 m from the model. The measurement volume spans 0.22 × 0.29 × 0.10 m^3. Synchronisation of illumination and imaging systems is realised through a LaVision programmable timing unit (PTU) controlled from a computer with the DaVis10 software. A sequence of 7276 images is recorded at 2000 Hz (approximately 3.6 s sampling time) at each AoA for all models, and the images are processed using the shake-the-box algorithm (Schanz, Gesemann & Schröder, 2016) in DaVis10.

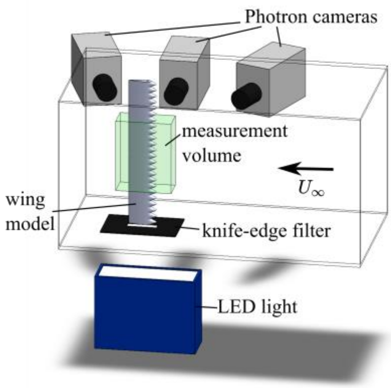

Figure 3 – Experimental arrangement in the W-Tunnel and 3D PTV system layout.

3 RESULTS

Iso-surfaces of the time-averaged streamwise vorticity field are shown in figure 3, for three values of the AoA for the model A10L25. An array of equal-spaced counter-rotating streamwise vortices is generated at the tubercles, with the negative-signed (clockwise, blue) vortex on the left and the positive-signed (counter-clockwise, green) vortex on the right of each tip. After developing in the first portion of the airfoil (x/c < 0.3) the two vortices tend to move apart from each other and eventually meet the opposite-signed vortex produced by the adjacent tubercle, and extend into the wake region at AoA = 5°. The scenario is profoundly altered at AoA = 15°, where stall-cell like structures spanning approximately 4λ (equivalent to one mean chord length) appear, in agreement with the observations of Cai *et al.* (2017). When the AoA is increased to 30°, the large stall-cell structures wander along the span of the wing, and no clear structures are observed beyond half chord length from the leading edge in the time-averaged field.

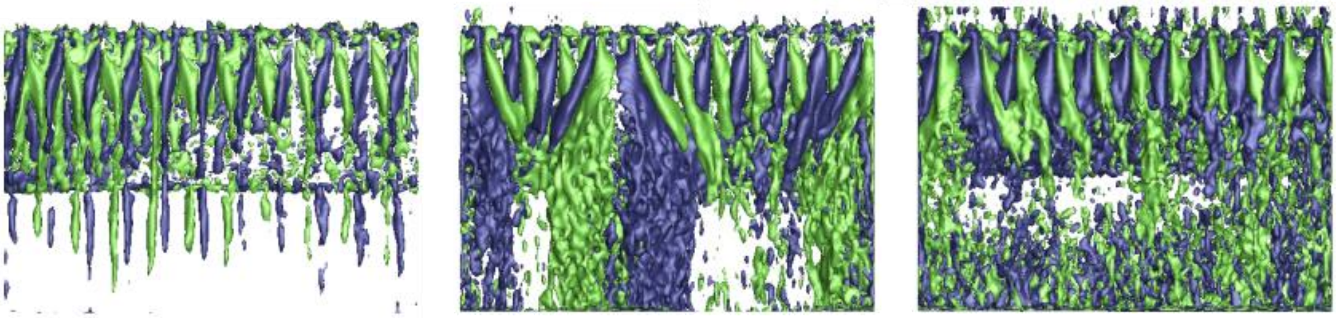

Figure 4. Time-averaged streamwise vorticity distribution by at AoA = 5° (left), 15° (middle) and 30° (right) of model *A10L25* (suction side). Blue iso-surface is at $\omega_x = -50\mathrm{s}^{-1}$ and green $\omega_x = 50\mathrm{s}^{-1}$. Air flows from top to bottom.

REFERENCES

- Cai, C., Zuo, Z., Maeda, T., Kamada, Y., Li, Q. A., Shimamoto, K., & Liu, S. (2017). Periodic and aperiodic flow patterns around an airfoil with leading-edge protuberances. Physics of fluids, 29(11), 115110.
- Faleiros, D. E., Tuinstra, M., Sciacchitano, A., & Scarano, F. (2019). Generation and control of helium-filled soap bubbles for PIV. Experiments in Fluids, 60, 40.
- Johari, H., Henoch, C., Custodio, D., & Levshin, A. (2007). Effects of leading-edge protuberances on airfoil performance. AIAA Journal, 45(11), 2634-2642.
- Hansen, K. L., Kelso, R. M., & Dally, B. B. (2011). Performance variations of leading-edge tubercles for distinct airfoil profiles. AIAA Journal, 49(1), 185-194.
- Wei, Z., New, T. H. & Cui, Y. D. (2015). An experimental study on flow separation control of hydrofoils with leading-edge tubercles at low Reynolds number. Ocean Engineering, 108, 336-349.
- Schanz, D., Gesemann, S., & Schröder, A. (2016). Shake-The-Box: Lagrangian particle tracking at high particle image densities. Experiments in Fluids, 57, 1-27.

Analysis of Corona Wind in Cross-cut Finned Channel Using PIV

Sunuk Kim[1,*] Dong Kee Sohn[1] and Han Seo Ko[1,2,*]
1: School of Mechanical engineering, Sungkyunkwan University, Republic of Korea
2: Dept. of Smart Fab Technology, Sungkyunkwan University, Republic of Korea
* Correspondent author: hanseoko@skku.edu

Keywords: PIV, Cross-cut fin, Corona wind, Heat transfer

ABSTRACT An efficient heat exchanger should have high heat transfer performance with low pressure drop. The heat transfer is proportional to the airflow rate, however, the improvement in airflow rate is restricted by an increase of pressure drop. To overcome the issue, this study presents a method to accelerate the flow of local regions around the surface of a heat exchanger by installing a wire electrode on the cross-cut fins to generate corona wind flow. Then, the pressure drop is suppressed to enhance the heat transfer performance by accelerating and controlling the flow of the corona wind. Parametric study on the velocity and temperature of the corona wind from the wire to the cross-cut fins with various design parameters in the channel was performed. In addition, the flow behavior of the accelerated corona wind was analyzed using Particle Image Velocimetry (PIV) processing. As a result, the local maximum velocity of 2 m/s was obtained near the wall with the applied voltage of 12 kV. And in the case of the cross-cut fins, the mean stream was induced through the channel owing to the acceleration of fluids by the corona wind in the downstream direction.

1 Introduction

In recent decades, there has been significant growth in the application of high-power electronic systems, resulting in a need for effective cooling methods to dissipate large amounts of heat. To address this need, research has been actively conducted on active cooling methods such as fan cooling, and more recently, on the application of corona wind to regulate pressure drop between fins during forced convection (Khattak & Ali, 2019). Corona wind, also known as ionic wind, refers to an electrohydrodynamic (EHD) flow in an atmospheric environment that enhances heat transfer by inducing motion of molecules or particles through the interplay of electric and flow fields (Saadatmand et al., 2022). Unlike conventional fans, EHD devices do not have any moving parts and can directly convert electric energy into fluid kinetic energy, making them advantageous due to their low power consumption and absence of noise or vibration. It has been observed that the application of corona wind between fins can prevent pressure drop by accelerating the flow near the wall, and can also enhance the heat transfer coefficient at local surfaces (Tian et al., 2021), making it essential in micro cooling.

2 Experiemental setup

In the experimental setup as shown in Figure 1, a channel made of polycarbonate with dimensions of 24 × 70 × 170 mm³ was used to conduct the PIV test. Three cross-cut fin channels were installed in the channel walls to induce the corona wind. Each cross-cut fin channel had one tungsten wire and two aluminum conductive tape electrodes installed on both walls. A high voltage supply was connected in parallel to each wire, while each aluminum tape was connected to a multimeter to measure current and ground. A diode laser (MGL N-532 A) with a power of 10 W was utilized to produce a laser sheet with the aid of a cylindrical lens in the visualization plane. The high-speed camera (FASTCAM mini AX100) was used to capture the movement of particles at a frame rate between 1000 and 2500 fps, with respect to the Reynolds number. The particles for the PIV were sourced from di-ethylhexyl-sebacate (DEHS) and had a diameter between 0.2 and 0.3 µm. The seeding generator was used to spray the particles. The ambient conditions were maintained at a fixed temperature of 25°C and relative humidity of 25 % in an external chamber with the size of 600 × 600 × 1000 mm³.

3 Experimental results

Figure 2 displays the velocity patterns in the channel for two types of fins: cross-cut fins in a steady state (a) and plain fins (b). With cross-cut fins, the corona wind caused fluid acceleration in the downstream direction, inducing a mean stream through the channel. On the other hand, with plain fins, the corona wind generated a simultaneous flow in both upstream and downstream directions. When cross-cut fins were used, the corona wind directed towards the repeated edges accelerated the surface flow on the downstream edges, resulting in a decrease of the pressure drop through the passage. The electric field intensity was found to be relatively higher at the beginning of the repeated edges because the wire was closer to the downstream edge than that of the upstream edge of the fins. As a result of this imbalance in electric field strength, the corona wind flowed in the direction where the electric field intensity was increasing. Conversely, plain fins lacked cutting edges as they were continuously formed, making it impossible to concentrate the electric field strength at a specific point. Therefore, the corona wind flowed towards both up and downstream walls. As predicted, the collision of reversed flow with the mean stream caused vortex formation in the central area due to the corona wind, resulting in an increase of static pressure inside the channel. This effect is demonstrated in Figure 2. The recirculation zone was eventually formed in the central area, preventing the entry of the mean stream (along with particles) into the channel.

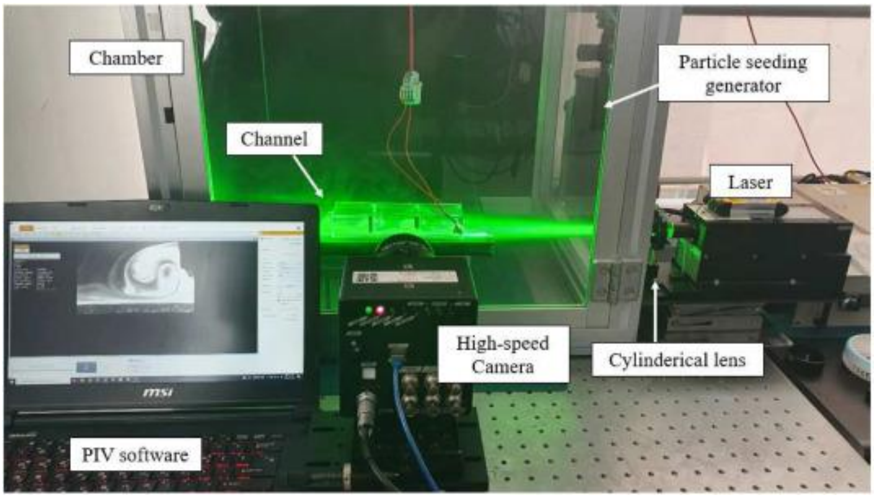

Figure 1. Experimental setup for PIV processing.

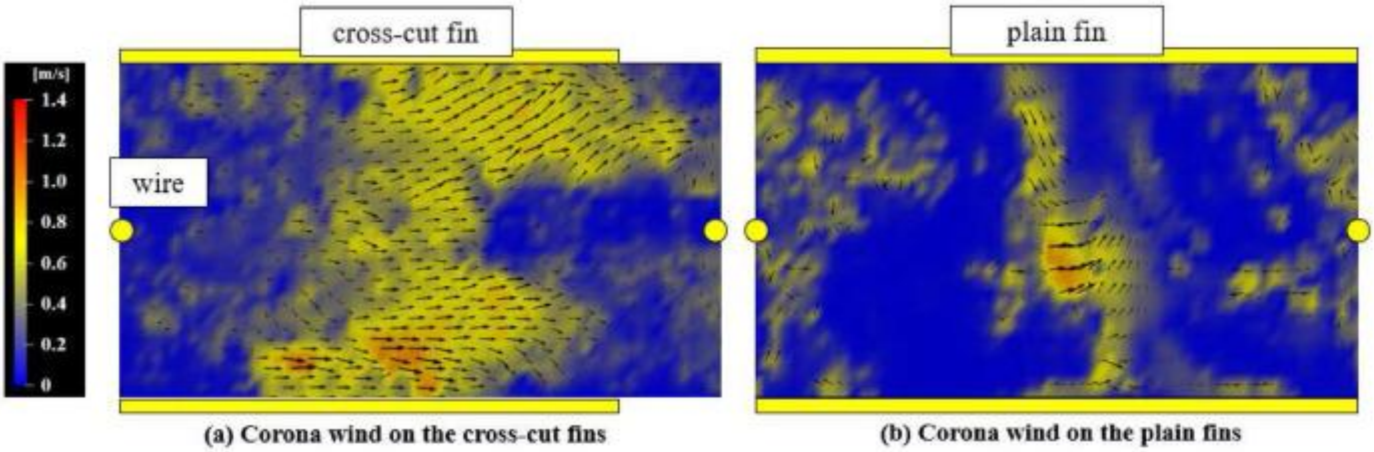

Figure 2. Velocity fields of corona wind with (a) Cross-cut fin and (b) Plain fin.

4 Conclusion

This study analyzed the velocity and temperature characteristics of the corona wind with cross-cut fins using PIV and conducted the parametric investigation of those fins by varying the electrode interval and the number of fins. The results of the PIV showed that the cross-cut fins were suitable geometries for accelerating the flow near the wall with lower pressure drops. For the 12-kV applied voltage and 24-mm electrode interval, the local velocity near the wall exceeded 2 m/s. Compared to general fins without the corona wind, the local velocity on the wall improved by 72 % with the corona wind on the cross-cut fins. The optimal geometric dimensions for the ratio of cross-cut fin length to space was 16, which improved the heat transfer coefficient by 36 % compared to that of normal fins. Therefore, the cross-cut fin arrangement proved to be the optimal geometry for implementing the corona wind in this application.

5 REFERENCES

- Khattak, Z., & Ali, H. M. (2019). Air cooled heat sink geometries subjected to forced flow: A critical review. International Journal of Heat and Mass Transfer, 130, 141–161
- Saadatmand, A., Goharkhah, M., & Nejad, A. M. (2022). Heat transfer enhancement in mini channel heat sinks utilizing corona wind: A numerical study. International Journal of Heat and Mass Transfer, 182, 121970
- Tian, S., Ren, X., Yang, Q., Shao, S., Sun, Z., & Liu, S. (2021). Development of a miniature ionic wind blower for active cooling in different scale: Embedded electrode and modularized design. International Journal of Thermal Sciences, 170(July), 107188

TECHNICAL SESSION 3
HEAT AND COMBUSTION

Chaired by Satoshi Someya

Flow Visualization of Heat Pipe with Annular Wick Structure

Joseph Seo[1,*], Hansol Kim[2], and Yassin Hassan[1,2]
1: Dept. of Nuclear Engineering, Texas A&M University, United States
2: J. Mike Walker '66 Department of Mechanical Engineering
* Correspondent author: reynolds@cambridge.org

Keywords: Heat pipe, annular gap, confocal chromatic sensor, phase change

ABSTRACT An annular wick-type heat pipe's interior and gap are visualized. The experimental setup includes a heating and cooling system, a measurement system, and high-speed cameras to observe heat pipe flow. The narrow gap between the wick structure and the pipe causes large-scale pulsating and a boiling frequency of 0.5 to 2.0 Hz. Gravity also affects the heat pipe's performance, causing different temperature spike trends at the operating limit.

1 INTRODUCTION

A variety of hydrodynamic and heat transfer phenomena can occur inside a heat pipe. Some of the most common flow phenomena inside a heat pipe include the interaction of the heat pipe's wick with the working fluid. The wick absorbs the working fluid and distributes it evenly, draws the fluid to the evaporator section, vaporizes the working fluid through heat, and in the condenser, the evaporated working fluid liquefies and is absorbed by the wick surface and returned to the evaporator. This heat transfer through the internal working fluid makes the heat pipe a powerful heat transfer device. However, despite these complex internal flow phenomena, heat pipes have typically been used as a conductance model, or black box model, through the external temperature. Since the heat transfer phenomena are caused by the hydrodynamic phenomena of the internal flow of the heat pipe, visualizing and analyzing the internal phenomena as well as the external temperature of the heat pipe can provide a deeper understanding of the operating limits of the heat pipe. It also provides researchers with a deeper understanding of the flow phenomena of the working fluid in the heat pipe and how it affects the heat transfer performance. In addition, measuring and analyzing the temperature and velocity inside and outside the heat pipe, while simultaneously analyzing the flow phenomena visually, can provide insight into the performance and behavior of the heat pipe. This knowledge can be used to design and optimize heat pipe systems.

2 EXPERIMENTAL SETUP

This study is focusing on visualizing the inside and gap region of the annular wick-type heat pipe. To fabricate the wick structure, mesh screens were wrapped around a 1.2 m long rod with a diameter of 17 mm. Spot welds retained the cylindrical shape of the wick structure along the axial direction with 1.5 ~ 2.0 mm intervals. After removing the rod, the wick structure was inserted into a 1.2 m borosilicate seamless glass tube pipe with an outer and inner diameter of 25.4 mm and 19.9 mm, respectively. The dimensions of the manufactured wick are 18.8 mm of inner diameter, 0.49 mm of thickness, and 19.29 mm of outer diameter. Heat pipe fabrication consists of cleaning, vacuuming, fluid filling, and sealing processes. The inside of the glass tube pipe and wick structure was cleaned using ethanol. Each end of the pipe was closed using compression fittings. One side of the pipe was connected to the vacuum pump and working fluid insertion system. After -90 kPa of vacuum pressure was achieved by the vacuum pump, 240 mL of DI water was inserted into the pipe as a working fluid. Then, the pipe was sealed by a locking ball valve connected to the vacuum pump. As a final step of the fabrication, leakage was checked to verify the condition inside the heat pipe. Figure 1 presents the heat pipe visualization experimental setup. The experimental setup consists of three parts, the heat pipe, the heating & cooling system, and the measurement system. The experimental setup can be inclined with the four gas pressure springs so that the entire device can be set angle from 0 to 90 degrees. A transparent heater, the evaporator section of the heat pipe, is connected to a direct current power supplier with a maximum output of 3 kW. A water jacket with a variable flow rate was installed at the condensing region of the heat pipe to remove the heat transferred by the heat pipe. The inlet temperature of the cooling fluid inside the water jacket was controlled by a Merilin M33 chiller from the Neslab company. The visualization of the flow inside the heat pipe was performed by high-speed cameras. Confocal chromatic sensors were used to measure the liquid film thickness near the inner wall, while an infrared camera was installed at the bottom to monitor the temperature change of the heater.

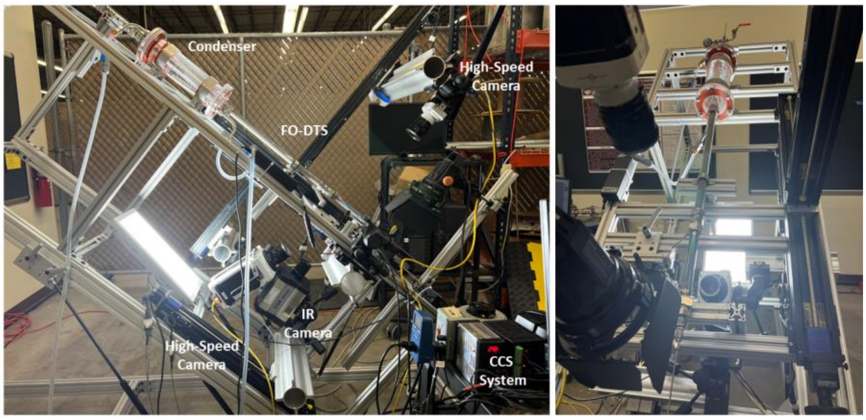

Figure 1. A windmill in a winter landscape near Delft.

3 RESULTS AND DISCUSSION

Multiple sets of high-speed images of fluids inside the evaporator and condenser were obtained with varying boundary conditions. One of the interesting found from this visualization study is that a large-scale pulsating occurs in the evaporator and the generated steam pushes the liquid up to the condenser region. This is mainly because of the narrow gap between the wick structure and the pipe. Since this large and rapid boiling shows periodical characteristics, a frequency analysis was performed as shown in Figure 2. The results show the frequency of the boiling ranged from 0.5 ~ 2.0 Hz and varies according to the heating power.

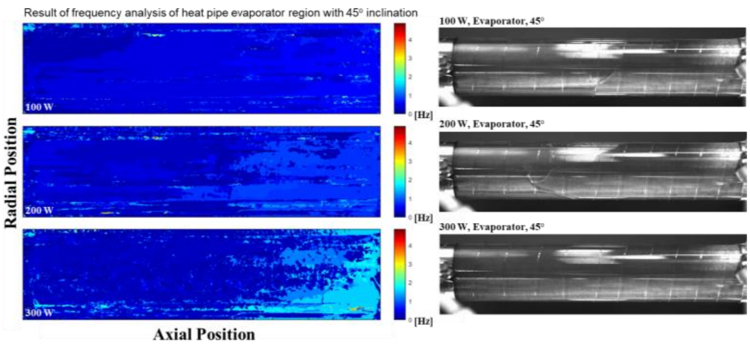

Figure 2. The results from frequency analysis of the boiling pattern.

The effect of gravity on the heat pipe is also tested. As an example, the temperature changing during the development of the operating limits of the heat pipe with multiple inclination angles is checked with an IR camera. The result shown in Figure 3 reveals that gravity not only affects the performance of the heat pipe but also results in the different trends of temperature shoot-up during the operating limit.

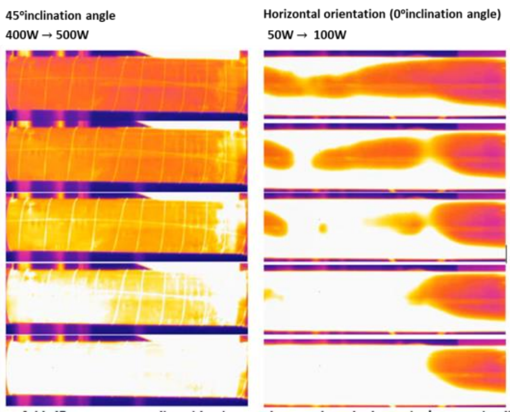

Figure 3. The IR camera image at the onset of the operating limitation with varying inclination angles.

Simultaneous visualization of the particle cloud and flame in dust explosions

Stefan Puttinger[1,*], Christoph Spijker[2] and Simon Schneiderbauer[1]

1: Dept. of Particulate Flow Modelling, Johannes Kepler University Linz, Austria
2: Chair of Thermal Processing Technology, Montanuniversität Leoben, Austria
* Correspondent author: stefan.puttinger@jku.at

Keywords: Dust deflagration, Flow visualization, Flame propagation, K-means clustering, Optical flow

ABSTRACT Dust deflagration remains a severe safety hazard in process industries. From a modelling perspective there is still long way to go to capture all aspects of dust explosions correctly. CFD Modelling activities in this field of research triggered the need for in-house high-fidelity validation data. A common approach to obtain experimental data on dust deflagration is to use high-speed cameras at sufficient frame rates. This usually leads to a trade-off in camera shutter settings so that either the dust cloud remains underexposed and is hardly visible, or the flame is too bright and saturates the pixels. In the present paper we propose a setup that uses a laser light sheet to illuminate the particle cloud while, at the same time, the camera settings can be chosen in way that pixel saturation can be kept on a low level in the flame area. The recordings are done with a color high-speed camera then processed in the YCbCr color space. Beside macroscopic values like the vertical dust cloud and flame propagation velocities we also obtain spatially resolved velocity data by using optical flow algorithms.

1 INTRODUCTION

Dust deflagration can happen any time when manipulating fine powders of combustible materials. Two major parameters describing the security hazard of a certain material are the minimum ignition energy (MIE) and the so-called K_{ST} value, which is the maximum pressure gradient after ignition normalized by the cubic root of the volume of the test vessel. The K_{ST} value is commonly measured in the 20 liter SIWEK apparatus and the MIE can be tested in a Hartman tube device (Dorsett, 1960). While the former has limited optical access, the latter represents a strongly wall-bounded flow. Hence, these standardized devices are not the optimal choice to obtain validation data for CFD model developments. The setup discussed in section 2 provides flow conditions under low wall influence and is fully optically accessible.

2 EXPERIMENTAL APPARATUS

The test rig shown in Fig. 1a consists of two separate chambers. The lower part serves to disperse the dust particles. A pressurized air pulse from a mushroom shaped nozzle raises the particles from a cup. The cup is removable and can be filled with particles outside the box and weighted on a balance. A second air valve provides additional purge air to shift the particle cloud from the dispersion box to the observation chamber. The observation chamber consists of four Perspex walls and has a square cross section of 400 x 400 mm. The two compartments are connected with a hole of 80 mm. Right above this orifice two electrodes ignite the dust cloud at a certain Δt to the initial pressure pulse. A 532 nm continuous wave (cw) laser is used to illuminate the center plane of the compartment. A color high-speed camera (Chronos 2.1) is placed at a 90° angle to the laser plane and set to a frame rate of 1000 Hz. A more detailed description of the test setup can be found in Puttinger et al. (2023).

3 IMAGE PROCESSING AND RESULTS

Figure 1b shows an example image series of a dust deflagration event of 4g of maize starch. The image sequence covers approximately 1 s of real time and clearly demonstrates the advantage of the presented test setup. The laser light sheet provides a proper illumination of the dust particles before ignition and even during the deflagration event. We also see unburnt particles in the decaying phase of the flame. At the same time the flame structure is clearly visible and does not drive the camera into saturation.

To obtain validation data for CFD model testing we need to extract quantitative data from the videos. This is done on two levels - first we obtain macroscopic data like the vertical expansion velocities of the dust cloud and the flame as well as the occupied areas and second, we calculate spatially resolved velocity fields by applying a neural network (NN) based optical flow algorithm. As a first step in the processing pipeline the images are transformed to the YCbCr color space since it allows a more robust separation of the dust cloud and the flame than the RGB color space. During the burning phase the red channel shows strong background reflections that result in a changing background intensity over the image series. Furthermore, the color of the flame changes slightly with the amount of mass. Using the luminosity channel Y for further processing of the dust cloud and subtracting the inverse image of the chrominance channel Cr from Y for processing of the flame proved to be a robust solution (Fig. 1c).

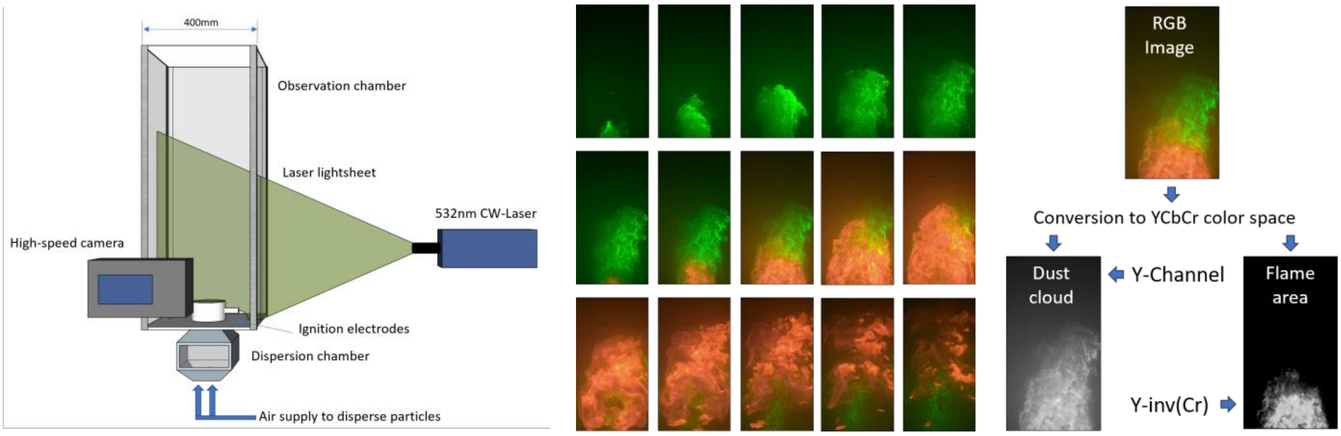

(a) (b) (c)

Figure 1. (a) Sketch of the experimental setup, (b) image sequence of a deflagration experiment with 4g of maize starch, (c) conversion of the original RGB image to the YCbCr color space and separation into the dust cloud and the flame area.

Identifying the outer boundaries of the dust cloud and the flame leads to a classic threshold problem. The gray-level histograms of the separated color channels do not show a clear binary distribution. Hence, Otsu's method is not suitable to separate the dust cloud ant the flame from its background. Using a k-means algorithm to cluster the gray-level values can provide more accurate results (Fig. 2). Three or four clusters are best suited for the present video data. To obtain smooth edges for the boundaries of the particle cloud and flame, the images were blurred with a Gaussian filter kernel before clustering. The consecutive frames were then processed by the DeepFlow method (Weinzaepfel et al., 2013) to calculate the spatially resolved velocity fields. For the dust cloud the results have been compared to PIV and found to be very reliable, for the flame area the calculated velocities show higher uncertainties due to the lack of texture in the central flame area and the overlay of the flame and the laser sheet.

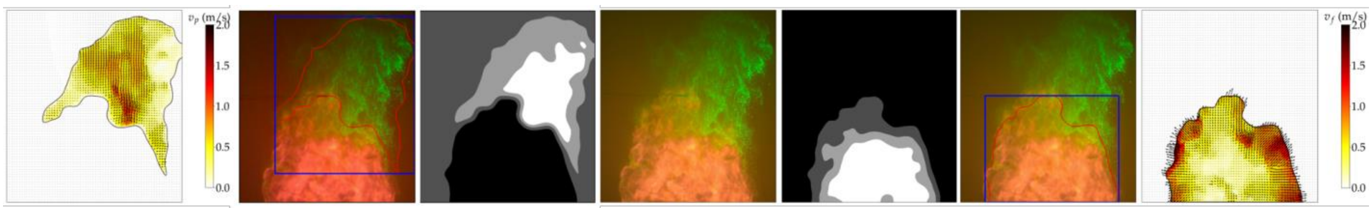

(a) (b) (c)

Figure 2. Example of the image processing from the original image (center) for the dust cloud (left) and the flame (right). The images in between demonstrate the extraction of the boundaries (red) and bounding box (blue) via k-means clustering.

4 CONCLUSION AND OUTLOOK

The proposed test setup allows to visualize the dust cloud and the flame with one camera during the same deflagration experiment. A machine learning based post processing allows to accurately identify the boundaries of the dust cloud and the flame and can also provide spatially resolved velocities. Up to now only organic dusts were used for the experiments. Ongoing research includes the extension of the test rig and the post processing method for metallic dusts.

5 ACKNOWLEDGEMENT

The authors would like to express their gratitude to HOERBIGER Safety Solutions (IEP Technologies) for initiating and funding this research cooperation. This HOERBIGER initiative promotes the advancement of science in the combustion sector.

6 REFERENCES

Dorsett, H. G. (1960). Laboratory equipment and test procedures for evaluating explosibility of dusts. U.S. Department of the Interior, Bureau of Mines.

Puttinger, S., Spijker, Ch., Schneiderbauer, S., Pirker, S., Meyer, G., Buchner, C., & Kerbl, A. (2023). Dust cloud evolution and flame propagation of organic dust deflagration under low wall influence. Journal of Loss Prevention in the Process Industries, accepted for publication.

Weinzaepfel, P., Revaud, J., Harchaoui, Z., & Schmid, C. (2013). DeepFlow: Large Displacement Optical Flow with Deep Matching. 2013 IEEE International Conference on Computer Vision, 1385–1392. https://doi.org/10.1109/ICCV.2013.175

Experimental Measurement of Boundary Conditions for Conjugate Heat Transfer in a Hemispherical Upper Plenum

Blake R. Maher[1,*] Noah Sutton[1], and Yassin Hassan[2]
1: Dept. of Mechanical Engineering, Texas A&M University, United States
2: Dept. of Mechanical Engineering & Dept. of Nuclear Engineering, Texas A&M University, United States
* Correspondent author: brmaher27@tamu.edu

Keywords: PIV, LIF, Optical fiber, Conjugate heat transfer

The hemispherical upper plenum is a geometry which features heavily in advanced nuclear reactor design concepts. High temperature gas cooled reactor (HTGR) designs and liquid metal fast reactor designs are primarily associated with this geometry. Under typical operating conditions, HTGRs flow coolant from the upper plenum downward through the core. During a loss of flow (LOF) accident condition, this flow is reversed and is driven by natural convection. The result is a rapidly flowing upward plume of hot coolant which impinges on the upper surface of the hemispherical plenum. Another flow regime of great concern in fast reactor designs is the thermally stratified condition in which hot fluid becomes trapped at the top of the plenum with a relatively cool jet flowing into the plenum but failing to adequately penetrate and mix the fluid in the plenum. This results in a axially delineated separation of hot and cold regions in the plenum. The height of maximum temperature differential within the plenum and its interfacing region with the solid material comprising the plenum wall represents a point of extreme heat flux gradient between the fluid and solid. Accurately predicting the location and degree of this gradient is a key aspect of useful conjugate heat transfer simulations in these reactor concepts. Important characteristics in addition to this include the fluid flow parameters in the near wall region, the fluid temperature, and the surface temperature of the plenum wall both internally and externally. Experiments were conducted to provide this data set for both the natural convection and thermally stratified cases. The data gathered is intended to be used as a validation library for simulations accounting for the conjugate heat transfer between the coolant, plenum, and surrounding environment. The experimental facility employed in these experiments is comprised of a borosilicate glass hemisphere mounted to an aluminum structure containing a single inlet jet and annular outlet path positioned at the plenum wall. This test section sits within a borosilicate glass correction box which is used to minimize optical distortion on the plenum surface by reducing the incident angle of the view of the camera and laser to the glass wall. In the natural convection case, flow is driven by two heaters with a combined output capacity of 3250 Watts. In the stratified case, flow is motivated by use of a pump. Flow rate is monitored using an electromagnetic flow meter. Temperature within the plumbing and correction box is monitored by thermocouples. Temperature within the plenum is monitored and measured using a combination of thermocouples, distributed temperature sensing optical fiber, and planar laser induced fluorescence (P-LIF). LIF is a temperature measurement technique which has been discussed greatly across a wide range of geometries and flow regimes. LIF is based on the measurement of fluorescent light intensity from a temperature sensitive dye in a fluid. In this experiment, Rhodamine-b was used as the dye with a green light filter employed on the camera lens during temperature measurements to remove light reflection from the laser and seed particles. Distributed temperature sensing was conducted using a Luna Technologies ODiSI-B single channel system with a single, unsheathed optical fiber. An unsheathed fiber was selected in order to remove the effects of the sheath on heat transfer to the fiber and thus time constant and spatial resolution of the measurement. Flow velocity measurements are carried out using particle image velocimetry (PIV) employing a 20-Watt continuous laser, high speed camera, and silver coated glass microsphere seeding particles. The two-dimensional two component PIV measurement technique is a well developed and greatly discussed method in flow visualization based on the principle of seed particle tracking across an array of time steps and conversion of the correlated displacement profile to velocity. The software employed to carry out data processing for PIV includes a combination of in-house and commercially available codes. The average of all images is first subtracted in order to remove the background from the image and leave only the seeded particles. Masking is performed to reduce the effective area required to be processed. A three-pass algorithm was selected using 64x64 and 32x32 pixel interrogation windows with 50% overlap between passes along with a gaussian fit peak and correlation map to validate calculated vectors. Spurious vectors were eliminated and interpolated using surrounding results. Spatial calibration was carried out using two targets of known size at the focal plane of the camera. This combined with the known frame rate, the pixel per frame displacement was converted to meters per second. These measurements can be employed for a wide range of physics studies and validation exercises but this work seeks to focus on the presentation of data for validation of conjugate heat transfer studies. The key aspect of this study is on the thermal aspects of measurement and near wall flow behavior. In the natural convection case, the optical fiber surface temperature measurements indicated that maximum heat transfer occurred near the top of the plenum in the region of greatest vorticity along the wall. This behavior is consistent with established norms and intuition. The transition from high to low heat transfer was relatively smooth along the wall, gradually decreasing to the minimum value near the plenum floor. The correction box was held at an ice bath condition during the natural convection tests in order to maximize the temperature differential across the glass wall and the measured temperature differential along the plenum floor was negligible, as would be expected of the natural convection condition during steady state. In the stratified case, the temperature gradient was inverted with the correction box being heated by a combination heater-circulator unit while a relatively cold (still above room temperature) jet was injected to the plenum at the same Reynolds number (Re) as the natural convection case (Re ~ 1100). The observed temperature gradient across the glass was maximum at the plenum floor and minimum at the top of the plenum as would be expected in a plenum with hot fluid trapped in the upper region and cold fluid unable to penetrate. Of greater note was the existence of a sharp increase in temperature gradient through the plenum wall at an axial height equivalent to the maximum height of jet penetration as indicated by time averaged velocity profiles. This test was repeated at several other Re and the height of maximum thermal gradient continued to match well. It should be acknowledged that this does not indicate a conclusive correlation between these features but does suggest further work to establish a potential correlation and the variables which affect the link between jet penetration and axial height of maximum temperature gradient. It was also found that this height matched well in the LIF measured temperature profile. What was of particular interest was the jet reversal behavior. Rather than the jet impinging on the hot fluid layer and spreading immediately outward, the jet immediately reversed and moved downward in an annular geometry outside the jet core. This resulted in very low velocity along the plenum wall. This is in great contrast to the natural convection case which has a relatively high wall velocity. This difference in wall velocity must be accounted for in the calculation of an effective heat transfer coefficient between the fluid in the plenum and the wall. The presentation of the data discussed will allow for the pairing of flow visualization measurements as well as temperature measurements carried out using a variety of methods of measurement in order to maximize the usefulness of the data for simulation validation. The combination of temperature and flow data presented offers a unique and comprehensive package of data which can be used to validate simulation and contribute to the available data for development of modelling techniques and correlations to better understand the behavior within the non-isothermal upper plenum in a range of flow regimes.

- Adrian, R. J. (2005). Twenty years of particle image velocimetry. *Experiments in fluids, 39*, 159-169.
- Alwafi, A., Nguyen, T., Hassan, Y., & Anand, N. K. (2022). Experimental analysis of a non-isothermal confined impinging single plume using time-resolved particle image velocimetry and planar laser induced fluorescence measurements. *International Journal of Heat and Mass Transfer*, *193*, 122952.
- Conder, T. E., Skifton, R. S., & Budwig, R. S. (2012, November). Particle Image Velocimetry Measurements in a Representative Gas-Cooled Prismatic Reactor Core Model: Flow in the Coolant Channels and Interstitial Bypass Gaps. In *ASME International Mechanical Engineering Congress and Exposition* (Vol. 45226, pp. 1291-1299). American Society of Mechanical Engineers.
- Crimaldi, J. P. (2008). Planar laser induced fluorescence in aqueous flows. *Experiments in fluids*, *44*, 851-863.
- Lu, C., Hiscox, B. D., Terrani, K. A., & Brown, N. R. (2018). Fully ceramic microencapsulated fuel in prismatic high temperature gas-cooled reactors: analysis of reactor performance and safety characteristics. *Annals of Nuclear Energy*, *114*, 277-287.
- Holler, D., Vaghetto, R., & Hassan, Y. (2019). High-resolution wall temperature measurements with distributed fiber optic sensors. *International Journal of Thermal Sciences*, *145*, 106042.
- Nguyen, T., Muyshondt, R., Hassan, Y. A., & Anand, N. K. (2019). Experimental investigation of cross flow mixing in a randomly packed bed and streamwise vortex characteristics using particle image velocimetry and proper orthogonal decomposition analysis. *Physics of Fluids*, *31*(2), 025101.
- Schultz, R. R., Gougar, H., Vegendla, P., Obabko, A., & Thomas, J. (2017). *Identification and characterization of thermal fluid phenomena associated with selected operating/accident scenarios in modular high temperature gas-cooled reactors* (No. INL/EXT-17-43218). Idaho National Lab.(INL), Idaho Falls, ID (United States).
- Vegendla, P., Hu, R., & Zou, L. (2020, May). CFD Model Validation for a Benchmark Data of Texas A&M 1/16th Scaled VHTR Upper Plenum. In *Verification and Validation* (Vol. 83594, p. V001T01A001). American Society of Mechanical Engineers.
- Wang, M., Chen, J., Zhang, D., Zhang, J., Tian, W., Su, G. H., & Qiu, S. (2020). Numerical study on the thermal stratification characteristics in the upper plenum of sodium-cooled fast reactor (SFR). *Annals of Nuclear Energy*, *138*, 107222.
- Westerweel, J. (1994). Efficient detection of spurious vectors in particle image velocimetry data. *Experiments in fluids*, *16*(3-4), 236-247.

Optimization on nanoparticle injection strategy for magnetic hyperthermia treatment

Qian Jiang, Hui Tang*
Department of Mechanical Engineering, The Hong Kong Polytechnic University, Hong Kong, China
* Correspondent author: h.tang@polyu.edu.hk

Keywords: Heat transfer, Magnetic hyperthermia, Optimization, Nanoparticle distribution

ABSTRACT Magnetic hyperthermia is a newly developed cancer therapy. During the treatment, magnetic nanoparticles (MNPs) are firstly injected into a tumor, and then subjected to an external high-frequency alternating magnetic field to elevate the temperature of the tumor to slightly above 43℃ (Chang et al., 2018). Although having been demonstrated to be effective, how to impose fatal thermal damage to cancerous tissues while minimizing the damage to surrounding healthy tissues is still a great challenge. Since the amount of heat generated in the therapy highly depends on the distribution of MNPs, their injection location and distribution pattern in the tissue are critical to treatment efficacy. As an extension of our previous work (Jiang et al., 2022), in this study we developed a three-dimensional Lattice Boltzmann method (LBM) and particle-swarm-optimization (PSO) based framework to search for the best nanoparticles injection strategy for magnetic hyperthermia treatment. Both regular spherical and irregular tumors are considered. The tumor is located at the center of a cubic healthy tissue. A constant temperature (37℃) is applied at outer boundaries of the tissue block.

The temperature distribution is defined by the Pennes bio-heat transfer equation (Pennes, 1948) as

$$(\rho c)_{nf}\frac{\partial T}{\partial t} = k_{nf}\left(\frac{\partial^2 T}{\partial^2 x} + \frac{\partial^2 T}{\partial^2 y} + \frac{\partial^2 T}{\partial^2 z}\right) + \dot{m}_b c_b (T_b - T) + Q \tag{1}$$

which is solved with the D3Q7 MRT-LBM scheme. The subscript nf means the properties of nanofluid. $\dot{m}_b$ denotes the density flow rate of temperature-dependent perfusing blood. Q means the amount of heat generated by MNPs, defined as the Rosensweig model $Q = \pi\phi\mu_0\chi_0 H_0^2 f \frac{2\pi f\tau_R}{1+(2\pi f\tau_R)^2}$ (Rosensweig, 2002). ϕ is the local volume fraction of MNP, and at the given location (x, y, z) is the superposition of each injection in Gaussian shape

$$\phi_i(x,y,z) = \phi_{i0}\exp\left[-\frac{(x-x_i)^2 + (y-y_i)^2 + (z-z_i)^2}{2\sigma_i^2}\right] \tag{2}$$

$$\phi(x,y,z) = \sum_{i=1}^{n}\phi_i(x,y,z) \tag{3}$$

The best distribution of MNP is searched by the PSO algorithm, including the volume fraction amplitude ϕ_{i0}, the standard deviation σ_i, and the locations of each injection site (x_i, y_i, z_i). ϕ_{i0} and σ_i are set the same at all injection sites in the spherical tumor, whereas they are allowed to be different in the irregular tumor. The temperature being between 43℃ and 46℃ in the tumor, lower than 43℃ in the healthy tissue, and close to 43℃ at the interface are the criteria for evaluating the performance of magnetic hyperthermia. Moreover, the dose of MNP should be as low as possible. The optimization will generate a set of optima, with which the best waiting time t_{opt}, the best volume of MNPs V_{opt} and the best locations of injection sites $(x_{opt}, y_{opt}, z_{opt})$ can be determined.

Our results show that this framework performs well in three-dimensional MNP injection strategy searching. For the spherical tumor, four cases are considered, namely 1-site, 4-site, 6-site and 8-site injections. The single-site injection fails because of a large volume of overheated zone appearing in tumor. The multi-site injection strategies surpass the single-site injection. The more the injection sites, the better the performance (see Figure 1). In addition, the increase of injection sites diminishes the MNP volume required, makes the injection locations closer to the tumer center, and reduces the waiting time after the injection, as listed in Table 1. More cases and details will be revealed and presented in our talk.

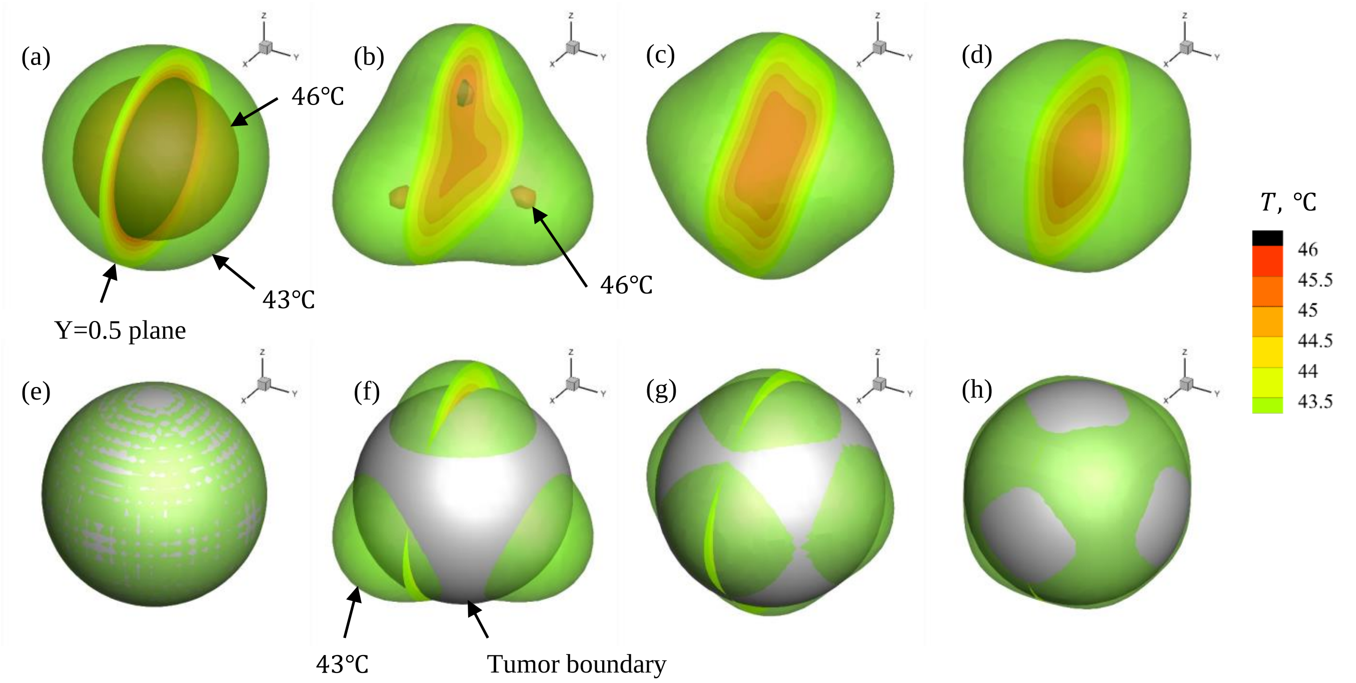

Figure 1 Optimal spatial temperature distribution around a spherical tumor. (a) ~ (d) show the temperature profile that above 43℃ for the one-, four-, six, and eight-site injection cases; (e) ~ (h) highlight the temperature distribution at tumor boundary. The outer transparent green surface denotes the isotherm of 43℃, while the inner transparent red surface denotes the isotherm of 46℃. The gray ball defines the tumor boundary.

Table 1 Optimization results in spherical tumor cases

Inject strategy	d, mm	T_{max}, ℃	V, $m^3 \cdot 10^{-9}$	t, min
1-site	0	56.60	1.60	19.92
4-site	4.36	46.15	1.94	20.00
6-site	4.08	46.00	1.86	19.99
8-site	4.00	46.00	1.79	19.27

ACKNOWLEDGMENTS

This study was financially supported by the Research Grants Council of Hong Kong under General Research Fund (Project No. 15214418).

REFERENCES

- Chang, D., Lim, M., Goos, J., et al. (2018). Review: Biologically Targeted Magnetic Hyperthermia: Potential and Limitations. Front Pharmacol, 9, 831.
- Jiang, Q., Ren, F., Wang, C., et al. (2022). On the magnetic nanoparticle injection strategy for hyperthermia treatment. International Journal of Mechanical Sciences, 235, 107707.
- Pennes, H. H. (1948). Analysis of tissue and arterial blood temperatures in the resting human forearm. Journal of applied physiology, 1(2), 93-122.
- Rosensweig, R. E. (2002). Heating magnetic fluid with alternating magnetic field. Journal of Magnetism and Magnetic Materials, 252, 370-374.

Hydrogen enrichment effects on swirl stabilized CH4 flames

Sarah Link[1*] , Francesca de Domenico[1] , Georg Eitelberg[1] , Arvind Gangoli Rao[1]
1: Dept. of Flow Physics and Technology, Delft University of Technology, The Netherlands
* Correspondent author: S.J.Link@tudelft.nl

Keywords: Hydrogen enriched combustion, PIV, OH* Chemiluminescence

1 Background

Hydrogen is the most promising fuel to accelerate the energy transition due to its carbon-free combustion. However, hydrogen has significantly different combustion characteristics compared to fossil fuels, including higher flame speeds and lower chemical time scales. This causes challenges such as higher risks of flashbacks and a higher tendency to emit NO_x when operating hydrogen in conventional swirl-stabilized aero-engine and gas turbine combustion chambers. To avoid flashback, modifications of the burner geometry, for example, the introduction of a non-rotating air jet on the center line of the swirling flow (Burmberger et al. 2011) are required to guarantee a safe operation with hydrogen. It has been shown that this axial air injection (AAI) reduces the flashback propensity for H_2 flames (Terhaar et al. 2015). However, it also decreases the effective swirl number which influences the flow field in the combustion chamber and the mixing quality of fuel and air. This is especially marked for fuels like CH_4 which have a much lower diffusivity than H_2. A worse mixing quality usually results in an increase in local temperatures and consequently in higher NO_x. Additionally, a decrease in the swirl number decreases the lower blowoff limit, since fewer hot products are recirculated back into the reaction zone. It is, therefore, necessary to evaluate the effect of AAI on the combustor performance, including the flow field and the emissions of the flame.

2 Experimental set-up

Experiments were performed in a lab-scale swirl stabilized combustor (geometric swirl numbers Sw 0.7 and 1.1) operating at a power of P_{th} = 11kW and at CH_4/H_2 fuel mixtures ranging from 0% H_2 to 100% H_2 in mole fractions (resulting in an overall equivalence ratio from $\varphi = 0.7$ to $\varphi = 0.58$). The percentage of AAI indicates how much of the total airflow gets injected in the axial direction (see Figure 1). For the PIV measurements in non-reacting and reacting conditions, the CH_4 stream was seeded with TiO_2 particles. The particles were illuminated with a dual pulsed Nd:YAG laser (EverGreen, Pulse energy 200mJ at 532 nm) at 15 Hz. The flow fields were recorded with two sCMOS cameras in the center plane (LaVision, 2560 x 2160 pixels), resulting in a 14.4 pix/mm resolution. A proper orthogonal decomposition (POD) of the flow field has been performed, to identify the coherent structures in the flow field.

The OH* signal of the flame was captured with an sCMOS camera (Tucson, 5472 x 3648 pixels). An OH* bandpass filter (bandwidth 50nm and centered at 325 nm) was mounted in front of the camera. The intensity of the OH* radical can be used as a reference for heat release distribution in time-averaged or phase-averaged images (Meng et al. 2021). Each image is first normalized by the maximum pixel value of the image. An Abel deconvolution is then applied to transform the line of sight signal into a trace of the signal in the axial plane of the burner (Simons et al. 1995).

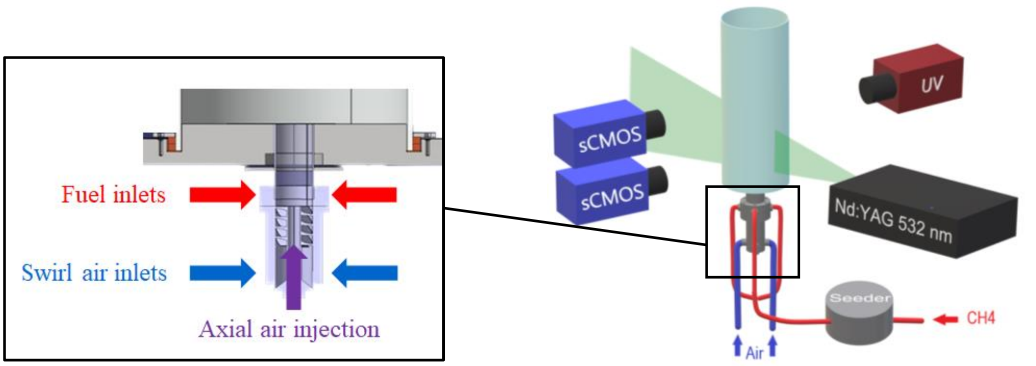

Figure 1. Schematic of the experimental set-up

3 Results

Figure 2 shows the reacting average flow field (S_w = 0.7, CH_4 = 100%) of the streamwise velocity component for different percentages of AAI. Introducing AAI significantly influences the shape and size of the center recirculation zone. Above a critical value of AAI (and consequently below a critical swirl number), the inner recirculation zone gets destroyed and the flow field resembles more the one of a jet. Results from the POD showed, that for 0% AAI the coherent structures in the flowfield feature the ones of a precessing vortex core (PVC), a single, helical structure commonly found in swirling flows. The PVC increases the level of turbulent kinetic energy close to the injector and is therefore favorable for the mixing of fuel and air. No PVC is present for 10% AAI and 20% AAI for the shown flow fields. This is again expected to be related to the decrease of swirl numbers below a critical level. In agreement with this, higher NO_x emissions were measured for high percentages of AAI. However, the results also show that AAI significantly increases the operational range of the combustor and enables flashback-free operation for fuels with high H_2 content.

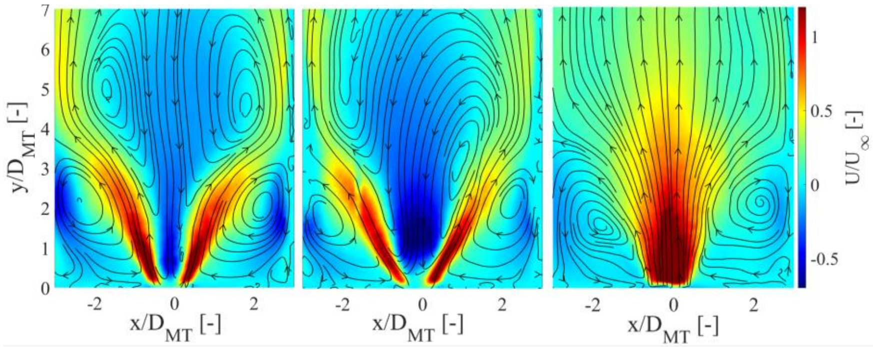

Figure 2. Average streamwise velocity field for S_w = 0.7 at different percentages of AAI

Figure 3 shows the effect of hydrogen enrichment on the Abel-deconvoluted OH* emissions of the flame. Up to 80% in H_2 content, an increase in hydrogen content results in a more compact flame moving closer to the mixing tube outlet in the axial direction. Furthermore, the intensity for the OH* signal increases with increasing H_2 content, which is expected to result from the more compact flames, which consequently have a higher heat release per area. For higher heat release also higher NO_x emissions are measured. Interestingly, the 100% H_2 has a much lower OH* signal compared to H_2-enriched cases, despite higher NO_x emissions (not shown here). This might be because of the missing OH formation path of CH + O_2 and the lower equivalence ratio φ, resulting in a lower flame temperature. However, this will be verified in future 1D flamelet simulations and controlled experiments.

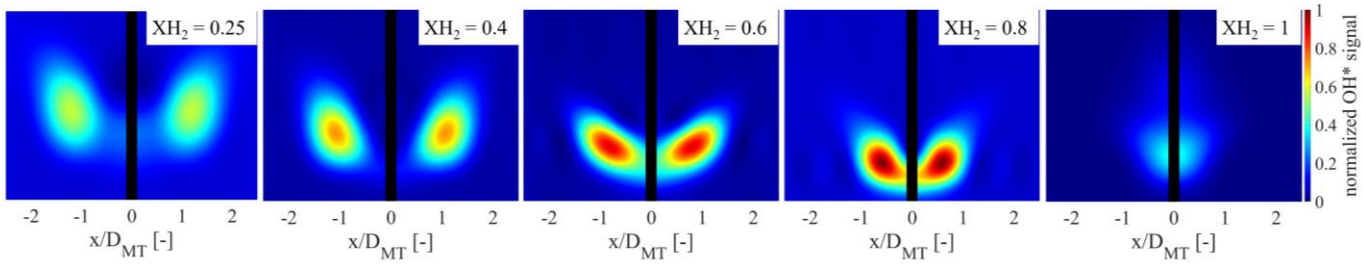

Figure 3. Abel deconvoluted and normalized OH* images for Sw = 0.7, AAI 10% at different %H_2

4 References

- Burmberger, S., & Sattelmayer, T. (2011). Optimization of the aerodynamic flame stabilization for fuel flexible gas turbine premix burners. Journal of Engineering for gas turbines and Power, 133(10).
- Meng, S., Wu, S., & Zhang, M. (2021). Numerical and experimental study of flow structure and heat release distribution in a stratified swirl flame with high-speed PIV and OH* measurements. AIP Advances, 11(7), 075311.
- Reichel, T. G., Terhaar, S., & Paschereit, O. (2015). Increasing flashback resistance in lean premixed swirl-stabilized hydrogen combustion by axial air injection. Journal of Engineering for Gas Turbines and Power, 137(7), 071503.
- Simons, S. N., & Yuan, Z. G. (2003, March). The filtered Abel transform and its application in combustion diagnostics. In 1995 Fall Meeting, Western States Section (No. E-13773).

Identification of ignition kernels from Chemiluminescence imaging in a Flameless Combustor

Rishikesh Sampat[1,*], Ferry Schrijer[1] and Arvind Gangoli Rao[1]
1: Dept. of Flow Physics and Technology, TU Delft, The Netherlands
* Correspondent author: r.p.sampat@tudelft.nl

Keywords: Chemiluminescence, Hydrogen Combustion, Ignition kernels

1 Introduction

Flameless Combustion is a regime that has potential for very low NO_x emissions while maintaining high levels of combustion efficiency(Perpignan, Gangoli, and Roekaerts 2018). This regime is known to stabilize through autoignition kernels produced spontaneously due to high temperature of reactants as opposed to conventional premixed flames that rely on back diffusion of heat and radical species(Gordon et al. 2007). Chemiluminescence is a commonly used technique to image combustion flows using spontaneously emitted light from the combustion process. In the present work, a methodology to identify ignition kernels from chemiluminescence images is developed followed by extraction of statistical information based on observed fluctuation feature topology which is used to classify events as autoignition or flame propagation.

2 Methodology

A jet stabilised combustor was operated with varying fuel blends of CH_4 and H_2. The burner head consists of 12 nozzles which inject a homogeneous air-fuel mixture in the chamber. As the nozzles are located radially away from the centerline and the fact that the flow is confined by the chamber, the resulting jets undergo internal recirculation such that hot combustion products are recicirculated back to mix with the fresh reactants. This generates the hot-vitiated conditions required for Flameless Combusiton. A Nikon D7500 DSLR camera was used to image the reaction zone. The images were first processed to extract the "blue" component which has a peak around 455nm and a FWHM of 100nm. This captures the CH* (431 nm) for flames with CH_4, however, a significant blue spectrum is also seen for H_2 enriched flames up to 100%. The occurrence of a visible H_2 flame is explained by Schefer et al. 2009, wherein the spectrum is attributed to emission by water and a blue continuum. The mean images are tabulated in Fig1, varying with equivalence ratio(Φ) and hydrogen percentage.

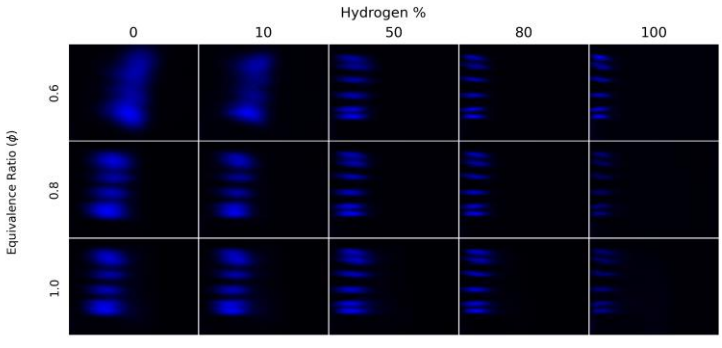

Figure 1: Averaged chemiluminescence images, Φ vs H_2%

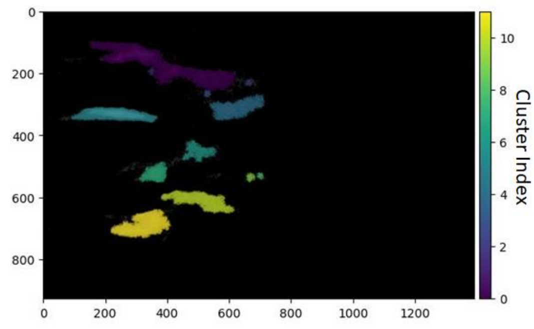

Figure 2: Example of clusters detected in instantaneous image.

Further the instantaneous fluctuation images are analysed for statistics of the flame structures. These structures are identified and grouped in clusters based on the density of distribution and space between the structures, using the DBSCAN (Density Based Spatial clustering of applications with noise) algorithm(Schubert et al. 2017). This is used directly from the scikit-learn python library. The main parameters were eps and minPts for the algorithm, where a point is considered a core point if at least minPts points are within distance eps of it. In addition, the clustering operation was done on images from which relevant points were selected based on a threshold criteria. The blue component of images were chosen, converted to grayscale and then normalised and rescaled to 0-255(8 bit scale). The resultant images were downscaled using a pyramid algorithm in OpenCV to reduce the size of the image used while retaining the main features. Of these downscaled images, only pixels having a value greater than a certain threshold value were used for clustering. Further, the information of each cluster is used to construct pdfs of parameters such as aspect ratio of clusters, characteristic length scale (L_{xx}) and x location of center of mass (X_{COM}).

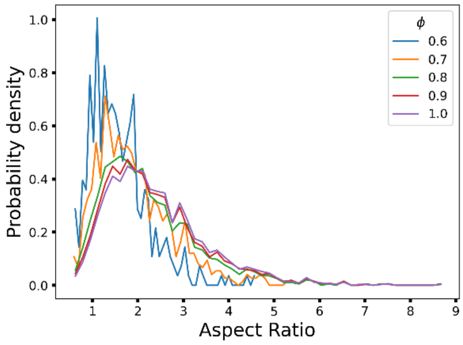

Figure 3: PDF of aspect ratio for CH_4=100%, H_2=0%

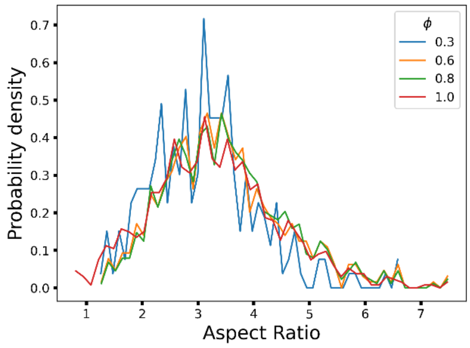

Figure 4: PDF of aspect ratio for H_2=100%

3 Result

An example image with detected clusters is shown in Fig2. The aspect ratio pdf seems to have a peak around 1-1.5 for the 0% H_2 cases(Fig3), while this shifts to a value of 3-3.5 for 100% H_2 cases(Fig4). This indicates that H_2 addition leads to longer, flatter flame kernels. If one correlates this to the phenomenon of autoignition, one can view the system as having an "igniter", i.e. the recirculating hot products and the fresh reactant jet stream. They interact at the interface which would be a turbulent-turbulent interface. If the gases from the two streams mix completely before igniting, it leads to formation of an autoignition kernel that would evolve evenly in all directions, thereby leading to a low aspect ratio(almost 1). On the other hand, if the mixture ignites before complete mixing, the ignition occurs by diffusion of heat and radicals across the interface, i,e flame propagation, leading to a flame kernel that would align with the interface,leading to longer, larger aspect ratio kernels. Thus, although not a sufficient condition, larger aspect ratio flame kernels indicate a higher probability of flame propagation while lower aspect ratio kernels hint at autoignition stabilization. This is explained schematicallly in Fig5. Thus H_2 addition shifts the CH_4 flame from distributed and autoignitive to concentrated, flame propagation stabilised.

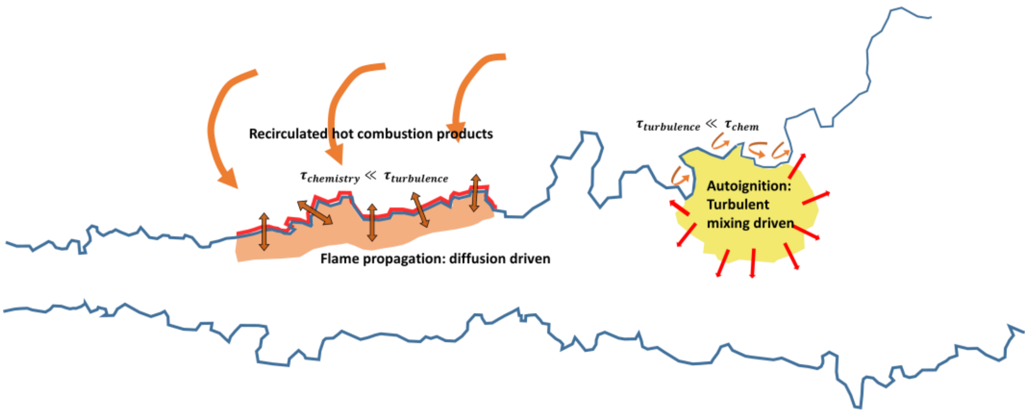

Figure 5: Schematic indicating structure of flame propagation vs Autoignition events.

4 REFERENCES

- Gordon, R. L., A. R. Masri, S. B. Pope, and G. M. Goldin. 2007. “A Numerical Study of Auto-Ignition in Turbulent Lifted Flames Issuing into a Vitiated Co-Flow.” *Combustion Theory and Modelling* 11(3): 351–76.
- Perpignan, A V, Arvind Gangoli, and Dirk J E M Roekaerts. 2018. “Flameless Combustion and Its Potential towards Gas Turbines.” 69.
- Schefer, R. W., W. D. Kulatilaka, B. D. Patterson, and T. B. Settersten. 2009. “Visible Emission of Hydrogen Flames.” *Combustion and Flame* 156(6): 1234–41. http://dx.doi.org/10.1016/j.combustflame.2009.01.011.
- Schubert, Erich et al. 2017. “DBSCAN Revisited, Revisited: Why and How You Should (Still) Use DBSCAN.” *ACM Transactions on Database Systems* 42(3).

TECHNICAL SESSION 4
TURBULENT BOUNDARY LAYERS

Chaired by Gerrit Elsinga

Capturing Inner Layer Dynamics With Zero Mean Velocity

Sedat Tokgoz[1,2,*], Jerry Westerweel[2] and Gerrit E. Elsinga[2]
1: Dept. of Aeronautical Eng., Gebze Technical University, Turkey
2: Laboratory for Aero & Hydrodynamics, Delft University of Technology, The Netherlands
* Correspondent author: sedattokgoz@gtu.edu.tr

Keywords: Tomographic PIV, Taylor-Couette, Turbulence, Boundary Layer, Time-Resolved

ABSTRACT

Taylor-Couette flow, i.e. the flow between two concentric cylinders, allows access to a wide variety of flow regimes by controlling the rotation rates of the cylinders (Andereck et al., 1986). Additionally, the turbulent drag can be accurately measured, because the flow is confined. Due to these advantages, Taylor-Couette flow is widely used in turbulence studies. Here, it is used as a model for the inner layer of a turbulent boundary layer, and we measure the dynamics of the near-wall coherent structures using time-resolved tomographic particle image velocimetry.

The measurements were performed in our Taylor-Couette facility with a $d = 10\,mm$ gap between the cylinders (Ravelet et al., 2010). The shear rate in the gap between the cylinders was adjusted to yield shear Reynolds numbers of $Re_s = 2000$ and 3000, while the rotation rate in the gap was zero. Furthermore, the gap width was small compared to the cylinder radius ($< 10\%$), so that wall curvature effects can be neglected. At these conditions, the Reynolds number based on the friction velocity and the gap width, Re_τ, is between 44 and 64. These values are commonly associated with the inner layer. However, the mean velocity in the gap is approximately zero, which means that the flow structures remain within the measurement volume for relatively long times. This is advantageous, because the near-wall cycle is slow with a period of the order of 300 wall units of time (Hamilton et al., 1995; Jiménez & Simens, 2001). In traditional boundary layer measurements, the observation time is much less due to advection (e.g.Jodai & Elsinga, 2016). Our experiments are akin to the numerical studies on inner layer dynamics by Jiménez & Pinelli (1999) , Jiménez & Simens (2001) and Hamilton et al. (1995), in which the effect of outer layer turbulence is suppressed by a filter or a wall (as in our case).

The time-resolved tomographic PIV measurements covered the full gap between the cylinders (Figure 1). The size of the measurement volume was approximately $4.7d \times 2.5d \times d$, corresponding to approximately $208 \times 110 \times 44$ in wall units in the axial, azimuthal and radial directions, respectively. Time-series of 10000 images were recorded at recording frequency of 300 Hz for $Re_s = 2000$, which equals to time resolution of 0.0626 in wall units of time. Total observation time is $T^+ = 625$, where the superscript + indicates a normalization in wall units. The final interrogation window size is $40 \times 40 \times 40\,voxels$, corresponding to $5.68 \times 5.68 \times 5.68$ in wall units, which means that the small-scale flow structures are well resolved.

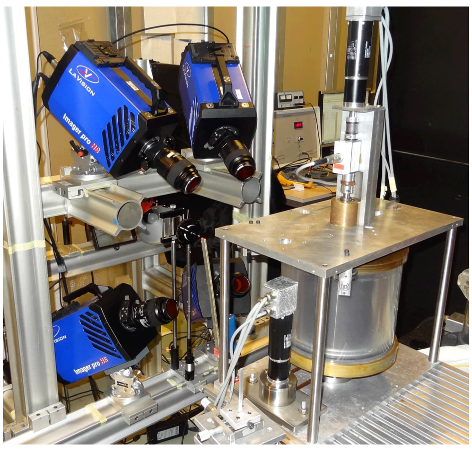

Figure 1. Experimental setup with high-speed cameras.

The results reveal the various kinds of vortical structures, such as the well-known streamwise vortices and hairpins (Adrian, 2007). Also, we observe the merging and splitting of near-wall low-speed streaks. The Figure 2 below shows a dynamic sequence of events in which a streamwise vortex stretches, splits and eventually decays. Note that the time scale associated with this event is approximately two orders of magnitude shorter than that of the full near-wall cycle. In our talk, we will examine the dynamic events surrounding the vortical structures in more detail.

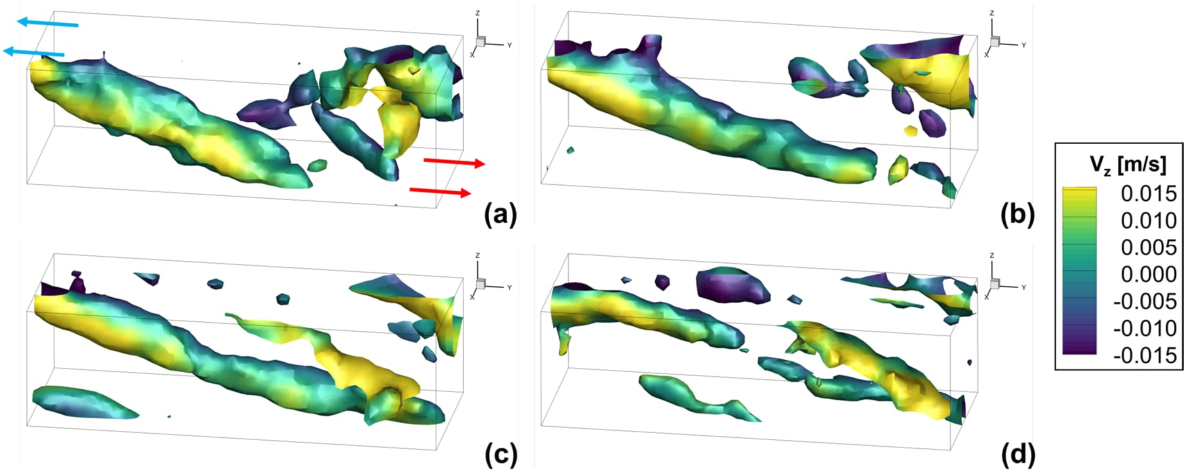

Figure 2. Example of stretch and break-up at (a) $\Delta t^+ = 0$, (b) $\Delta t^+ = 1.58$, (c) $\Delta t^+ = 3.16$, and (d) $\Delta t^+ = 4.74$. Isosurfaces are $Q^+ = 0.34$, and the radial velocity is color coded. Intermediate steps are skipped for better visibility. The red and blue arrows indicate the rotation direction of the inner and outer cylinders, respectively.

REFERENCES

Adrian, R. J. (2007). Hairpin vortex organization in wall turbulence. *Physics of Fluids*, *19*(4), 041301. https://doi.org/10.1063/1.2717527

Andereck, C. D., Liu, S. S., & Swinney, H. L. (1986). Flow regimes in a circular Couette system with independently rotating cylinders. *Journal of Fluid Mechanics*, *164*, 155–183.

Hamilton, J. M., Kim, J., & Waleffe, F. (1995). Regeneration mechanisms of near-wall turbulence structures. *Journal of Fluid Mechanics*, *287*, 317–348. https://doi.org/10.1017/S0022112095000978

Jiménez, J., & Pinelli, A. (1999). The autonomous cycle of near-wall turbulence. *Journal of Fluid Mechanics*, *389*, 335–359. https://doi.org/10.1017/S0022112099005066

Jiménez, J., & Simens, M. P. (2001). Low-dimensional dynamics of a turbulent wall flow. *Journal of Fluid Mechanics*, *435*, 81–91. https://doi.org/10.1017/S0022112001004050

Jodai, Y., & Elsinga, G. E. (2016). Experimental observation of hairpin auto-generation events in a turbulent boundary layer. *Journal of Fluid Mechanics*, *795*, 611–633. https://doi.org/10.1017/jfm.2016.153

Ravelet, F., Delfos, R., & Westerweel, J. (2010). Influence of global rotation and Reynolds number on the large-scale features of a turbulent Taylor-Couette flow. *Physics of Fluids*, *22*(5), 1–8. https://doi.org/10.1063/1.3392773

Estimation of coherent structures in wall-bounded turbulence through non-intrusive sensing of wall heat-transfer fluctuations

Firoozeh Foroozan[1,*] Andrea Ianiro[1], Stefano Discetti[1] and Woutijn J. Baars[2]
1: Dept. of Aerospace Engineering, Universidad Carlos III de Madrid, Spain
2: Faculty of Aerospace Engineering, Delft University of Technology, The Netherlands
* Corresponding author: firoozeh.foroozan@uc3m.es

Keywords: PIV processing, Heat transfer, Turbulent Boundary Layer

ABSTRACT

Turbulent Boundary Layers (TBLs) have been the focus of research in aerodynamics for decades, mainly due to their significant contribution to wall friction drag in a large variety of industrial and aeronautical applications. The importance of wall-attached coherent structures populating TBLs, which are responsible for carrying approximately 60% of the tangential Reynolds stress in wall turbulence, has inspired the quest for non-intrusive wall-based measurement methods to capture their footprint at the wall. For instance, based on sensing of such a footprint, stochastic estimation can be used for predicting the velocity field of turbulent channel flow, solely from wall-based observations [1]. Results revealed that the velocity field in the near-wall region can be estimated with reasonable accuracy from the wall-based input field. An experimental sensor system that measures a flow-quantity at the wall---thus eliminating any form of drag of the system itself---is particularly valuable for realizing real-time, wall-based flow control methodologies that are aimed at, e.g., heat transfer enhancement or turbulent drag reduction [2]. In tandem to the proof-of-concept of such a sensor, the estimation schemes for the off-the-wall velocity field (with the sensor field as input) needs investigation and will demonstrate its applicability for control-sensing.

This work reports an experimental arrangement, consisting of a non-intrusive film-based sensor embedded within the wall below a TBL flow, and synchronized flow-field measurements using PIV. The experimental campaign was carried out in an open-loop wind tunnel at the Delft University of Technology, comprising a cross-sectional area of $60 \times 60 cm^2$. A TBL was generated downstream of an initial trip (P40-grit sandpaper) applied on all four walls and developed under ZPG conditions with the aid of a curved ceiling. Nominal free-stream velocity settings of $5\, m/s$ and $10\, m/s$ were selected, which correspond to friction Reynolds numbers of 990 and 1800, respectively, at the primary measurement location.

The convective heat-transfer fluctuations on the wall beneath the TBL were measured using high-repetition-rate Infrared (IR) thermography. For this purpose, a non-intrusive heated-thin-foil sensor [3] was designed, manufactured, and flush-mounted within the bottom wall at the mid-span position. The sensor comprised a thin stainless-steel foil of $10\ \mu m$ thickness that was heated by a direct current, uniformly applied across the leading- and trailing-edge sides of the foil. The IR snapshots are acquired from the backside of the sensor at a high frequency to read the foil temperature T_W. Having data of the input heat flux $\dot{q}_{in}$ (due to the Joule heating) and T_W, the convective heat-transfer coefficient between the foil and the flow was estimated through an energy balance on the foil [4]. Results are presented in terms of the Nusselt number, $Nu \equiv hl/k$, and a sample of an instantaneous distribution of *Nu* is presented in figure 1(a), for the case of $Re_\tau = 990$.

Velocity fields above the foil-sensor were measured using planar PIV, in a wall-parallel plane at the start of the logarithmic region around $y^+ = 80$. An instantaneous fluctuating velocity field is shown in figure 1(b). Data of the IR camera and PIV system were acquired in a synchronized manner, using a function generator, so that a sub-set of the Nusselt number fields were synchronized with the lower frame-rate PIV measurements. The synchronized data enables an assessment of the correlation between the stream-wise velocity fluctuations and the heat transfer fluctuations at the wall. With the identification of coherence comes the ability to stochastically estimate turbulent flow structures, solely based on an unconditional input of the convective heat flux distribution.

A similar, previous study in the water tunnel of Universidad Carlos III de Madrid successfully applied the described technique with a water fluid medium. In the current work it is thus demonstrated that this measurement technique can be applied in aerodynamics applications. The time-resolved heat transfer measurements captured the instantaneous convective heat transfer coefficient at the wall, thereby capturing a footprint of the large-scale wall-attached flow structures.

ACKNOWLEDGEMENT

- F. Foroozan, S. Discetti and A. Ianiro have been supported by the project ARTURO, funded by the Spanish State Research Agency. ref. PID2019-109717RBI00/AEI/10.13039/501100011033.
- F.Foroozan has been supported by the mobility grant provided by Universidad Carlos III de Madrid.

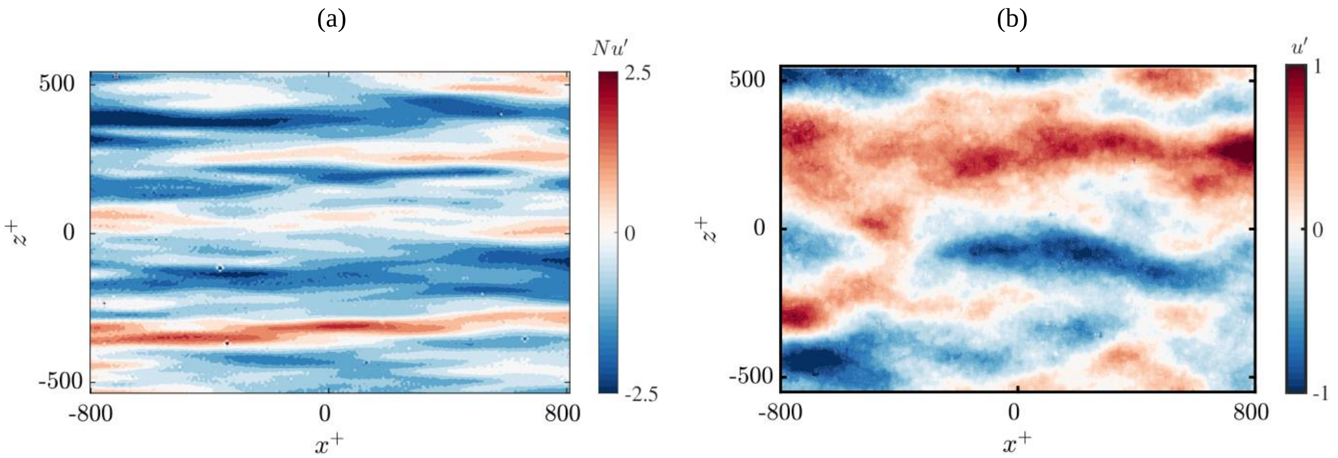

Figure 1. (a) An instantaneous fluctuation Nu field captured at the wall. (b) The stream-wise velocity fluctuation field u' at $y^+ = 80$ captured at the same time instant. Coordinates x^+ and z^+ resemble the stream-wise and span-wise directions in viscous units, and the flow is from left to right.

REFERENCES

[1] Encinar, M. P., and Jimenez, J., (2019): Logarithmic-layer turbulence: A view from the wall, Phys. Rev. Fluids, 4, 114603.

[2] Jimenez, J., (2018): Coherent structures in wall-bounded turbulence, J. Fluid Mech., 842, P1.

[3] Carlomagno G. M., and Cardone G., (2010): Infrared thermography for convective heat transfer measurements, Exp. Fluids, 49, pp. 1187–1218.

[4] Nakamura, H., (2009): Frequency response and spatial resolution of a thin foil for heat transfer measurements using infrared thermography, Int. J. Heat Mass Transf., 52, pp. 5040–5045.

Boundary Layer Measurements of the Flow along a Streamwise Oriented Cylinder using PTV

Christoph Näger[1,*], Florian Wachter[1] and Stefan Becker[1]
1: Institute of Fluid Mechanics, Friedrich-Alexander-Universität Erlangen-Nürnberg, Germany
* Correspondent author: christoph.naeger@fau.de

Keywords: Particle tracking velocimetry, axisymmetric turbulent boundary layer, axial cylinder flow, towed array sonar

1 Introduction

Turbulent flows along surfaces with curvature normal or transversal to the mean flow direction are common in engineering applications. However, it is only for strong curvatures that the curvature effects become noticeable (Neves et al. (1994)). Strong effects of transverse curvature on the turbulent flow may occur when fluid flows parallel to a cylindrical surface and a turbulent boundary layer (TBL) develops, the thickness of which considerably exceeds the curvature radius of the surface. The simplest case in which such conditions are present is the flow over a long circular which is oriented in streamwise direction. In such a case, a turbulent boundary layer develops around the cylinder that is commonly called axisymmetric turbulent boundary layer (ATBL). The most prominent application examples where ATBLs develop are the flows around marine seismic streamers or towed array sonars when they are dragged underwater behind a ship (Woods (2006)).

In contrast to planar TBLs, ATBLs are not well understood up to now and the body of experimental and numerical data is rather limited. Furthermore, unlike planar TBLs, the existence of a streamwise infinitely continuous growth of the ATBL thickness δ around a long cylinder in axial flow is controversial among researchers. Jordan (2011) states that there is experimental evidence that the ATBLs around long slender cylinders reach a maximum δ and only fluctuate around that thickness further downstream. In contrast, based on numerical simulations, Neves (1992) expects a steady growth of the ATBL in streamwise direction for a real axial flow along a cylinder.

Another difference to planar TBLs is that the velocity profile of ATBLs does not follow the logarithmic law of the wall. Instead, ATBLs show a trend that the slope of the velocity profile in the logarithmic region decreases, becomes negatively curved and drops below the planar log law (see e.g. Neves et al. (1994) and Jordan (2011)). This phenomenon is referred to as negative wake.

Since the data on ATBL is rather limited, the aim of the experimental study in this work was to gain more information on the turbulent flow around a long circular cylinder that is oriented in streamwise direction. For this, we investigated the flow around an axially oriented cylinder with a radius of 11mm in three different free stream velocities (0.5m/s, 1m/s and 2m/s). The goal was to gather information on the mean flow characteristics, the turbulence intensity and Reynolds stress profiles. To minimize the influence on the flow, a non-intrusive measurement approach was preferred. Therefore, particle tracking velocimetry (PTV) was applied, which allowed to extract velocity information close to the cylinder wall.

2 Methods

The PTV measurements were carried out in the large-scale water tunnel of the Institute of Fluid Mechanics at the Friedrich-Alexander-University Erlangen-Nuremberg. It has a rectangular cross section with dimensions of 1 x 0.8m² and a test section length of 8.8m. In the center of the test section, a cylinder was mounted in axial flow direction spanning through the whole length of the water tunnel. The cylinder had a diameter of 0.022m, which is a typical size of thin towed array sonars. It was built from 2m long sections of hollow aluminum pipes. The cylinder was designed to be neutrally buoyant in water to avoid sagging (downwards due to gravity or upwards due to buoyancy). It was mounted on both turning vanes of the water tunnel located in the settling chamber and the return section.

To capture the details of the boundary layer developing around the cylinder a 2D planar PTV approach was chosen. Compared to particle image velocimetry this has the advantage that no bias errors due to strong gradients in the flow and low seeding densities occur, which is often the case in flows close to walls (Kähler et al. (2012)). The laser head used for illumination of the seeding particles and the high-speed camera were mounted to a single traverse that was able to move along the water tunnel's test section in axial direction. This made it possible to change the measurement position without the need of recalibration and realignment of camera and laser light sheet. Three measurement positions were chosen at distances of 1.3m, 3.7m and 8.5m downstream from the start of the test section. At each position, two different measurements were performed: to evaluate the boundary layer thickness a magnification factor of 1:15 was chosen, where the image spanned 30 x 30 cm². For studying detailed velocity profiles in proximity to the cylinder wall, the image size in the second measurement was chosen at approximately 4 x 4 cm² resulting in a magnification factor of 1:2. Three different velocities were investigated to study the influence of different free stream velocities on the ATBL. The measurement frequency was chosen to be 1 kHz for all configurations.

3 Results and Discussion

All measurements show a rather full velocity profile, indicated by the shape factor approaching unity, which explains a relative high wall shear stress and friction coefficients in comparison to planar TBLs. The mean velocity profiles show a negative wake with the profiles lying below the planar logarithmic law of the wall. The measured mean velocity profiles are in good agreement with the alternative law of the wall for ATBLs developed by Lueptow (1990). Furthermore, they also show a very similar behavior to the mean velocity profile in a numerical study by Wachter et al. (2021), where they used a similar configuration of cylinder radius and free stream velocity. The measurements at $U_\infty = 1\ \mathrm{m/s}$ and at different positions along the cylinder reveal that the thickness of the ATBL is not continuously growing in downstream direction. The boundary layer thickness instead increases from the front to the mid position, while slightly decreasing from mid to rear position. This behavior supports the findings and theories of several researchers claiming that the δ of ATBLs reach a maximum at a certain position and only fluctuate around that thickness further downstream.
Concerning the turbulence intensity and Reynolds stress profiles, the measurement data shows a qualitatively similar behavior to the data from Wachter et al. (2021) and Jordan (2011). Especially the root-mean-squared velocity fluctuations in streamwise and wall-normal direction show a good agreement with the data in the literature in peak location as well as peak height. The axial-radial Reynolds stress of our measurements also shows a similar peak location compared to Wachter et al. (2021) and Jordan (2011); however, the peak height is significantly lower in our data than the reported values from the literature.

4 Conclusion

Our results regarding the limited growth of the boundary layer thickness support the theories and experimental findings of researchers in the literature. However, in our present study this could also be influenced by the TBL developing around the water tunnel walls. There is a region of approximately 0.2 m between the ATBL of the cylinder and the TBL of the tunnel walls. To verify if this distance is enough to neglect the influence of the TBL on the ATBL, further investigations will have to be carried out in the future. Moreover, the difference in the peak height of the axial-radial Reynolds stress has to be analyzed in more detail in the future. As there is a rather limited body of comparable data available in the literature, further studies could help explaining the differences between the already published numerical data (Wachter et al. (2021) and Jordan (2011)) and the present experimental findings.

5 REFERENCES

- Jordan, S.A. (2011). Axisymmetric turbulent statistics of long slender circular cylinders. Physics of Fluids 23(7), 075-105.
- Kähler, C.J., Scharnowski, S., Cierpka, C. (2012). On the uncertainty of digital PIV and PTV near walls. Experiments in Fluids 52(6), 1641-1656.
- Lueptow, R.M. (1990). Turbulent boundary layer on a cylinder in axial flow. AIAA Journal 28(10), 1705-1706.
- Neves, J.C. (1992). Numerical study of axial turbulent flow over long cylinders. PhD thesis, Mechanical Engineering, Stanford University.
- Neves, J.C., Parvis, M., & Moser, R.D. (1994). Effects of convex transverse curvature on wall-bounded turbulence. part 1. The velocity and vorticity. Journal of Fluid Mechanics, 272, 349-382.
- Wachter, F., Metelkin, A., Jovanovic, J., Praß, J., Becker, S. (2021). Numerical investigation of the effect of convex transverse curvature and concave grooves on the turbulent boundary layer along a cylinder in axial flow.
- Woods, M.J. (2006). Computation of axial and near-axial flow over a long circular cylinder. PhD thesis, Mechanical Engineering School, University Adelaide, Australia.

Turbulent Boundary Layer over Acoustic Liners

Haris Shahzad[1,*], Jean M. Favre[2], Stefan Hickel[1] and Davide Modesti[1]
1: Faculty of Aerospace Engineering, Technical University of Delft, The Netherlands
2: Swiss National Supercomputing Center, Lugano, Switzerland
* Correspondent author: h.shahzad@tudelft.nl

Keywords: Turbulence, Rough-wall flows, Direct Numerical Simulation, Permeable surfaces,

ABSTRACT

INTRODUCTION

Aircraft engines are the primary source of noise during take-off and landing. In order to reduce noise, engine nacelles are equipped with noise control devices called acoustic liners. Acoustic liners consist of a porous facesheet and a solid backplate with a honeycomb core in between the two. The perforations and honeycomb core resemble Helmholtz resonators. Acoustic liners exhibit a resonance frequency that can be tuned to the dominant frequency of the engine fan for noise reduction. Due to the passive nature of these devices and their efficacy, acoustic liners are widely used and represent the state of the art in engine noise reduction. However, they behave like roughness and tend to increase aircraft drag. The increase in drag was accepted as a necessary compromise as the need to reduce noise emissions took precedence and acoustic liners have primarily been studied and optimised from an acoustic perspective (Sivian, 1935, Ingard and Labate, 1950). An in-depth understanding of how acoustic liners impact engine aerodynamics and how they modulate the turbulent boundary layer is necessary to be able to optimise them both acoustically and aerodynamically.

METHODOLOGY

We perform DNS of a turbulent boundary layer over acoustic liners using the solver STREAmS (Bernandini *et al.,* 2023). The simulation is performed in a rectangular box of size $L_x \times L_y \times L_z = 115\delta_0 \times (15 + k)\delta_0 \times 5\,\delta_0$, where δ_0 is the inflow boundary layer thickness, and k is the depth of the acoustic liner. Freestream Mach number is $M = u_\infty/c_\infty = 0.3$, where u_∞ is the freestream velocity and c_∞ is the speed of sound based on freestream conditions, and the friction Reynolds number is $Re_\tau \approx 800 - 2400$. The domain consists of an initial smooth wall region of length $L_{x,s} = 45\delta_0$, followed by an acoustic liner array that extends from $x/\delta_0 = 45$ to the end of the domain, $x/\delta_0 = 115$. The equations are discretized on a Cartesian grid with a mesh size $N_x \times N_y \times N_z = 21504 \times 448 \times 1120$. A liner with porosity $\sigma = 0.322$ is used. An instantaneous flow visualistaion is shown in Figure 1, where structures are visualised using the Q criterion and the orifice configuration is also shown.

RESULTS

Compared to the smooth wall, the rough wall leads to very high wall-normal velocity near the surface of the facesheet. High velocity magnitudes tend to be concentrated around the orifices, so much so that the position of the orifices is clearly visible in the velocity contours. Wall-normal velocity fluctuations have been previously been proposed as the mechanism that leads to the drag increase over acoustic liners by Wilkinson (1983) and Shahzad *et al.* (2022). Similar observations can be made for the streamwise velocity. High-speed and low-speed streaks, typical of near-wall turbulence, are perturbed by the significant wall-normal velocity fluctuations at the wall and, thus, break down over the liner. Immediately after the smooth-to-rough transition, there exists a small region where we observe spanwise coherent structures that are probably the footprint of Kelvin-Helmholtz like structures, which disappear further downstream.

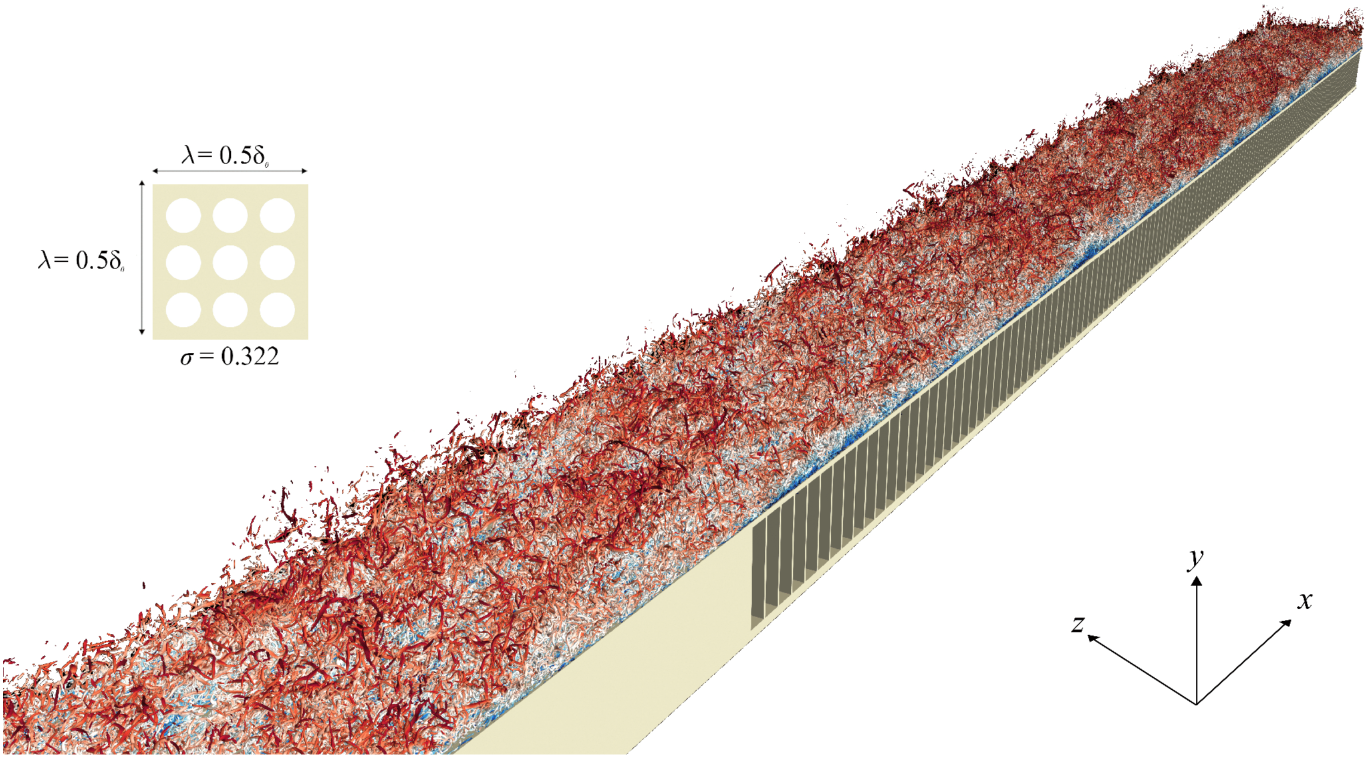

Figure 1. Instantaneous flow field of the boundary layer simulation. Orifice configurations within a single cavity are also shown at the top left. Vortical structures are visualised using the Q-Criterion, coloured by the streamwise velocity.

REFERENCES

- Journal article: Sivian, L. J., "Acoustic impedance of small orifices," J. Acoust. Soc, Vol. 7, No. 2, 1935, pp. 94–101. https://doi.org/10.1121/1.1915795.
- Journal: Acoustic circulation effects and the nonlinear impedance of orifices," J. Acoust. Soc. Am., Vol. 22, No. 2, 1950, pp. 211–218. https://doi.org/10.1121/1.1906591.
- Journal: Bernardini, M., Modesti, D., Salvadore, F., Sathyanarayana, S., Della Posta, G., and Pirozzoli, S., "STREAmS-2.0: Supersonic turbulent accelerated Navier-Stokes solver version 2.0," Comput. Phys. Commun., Vol. 285, 2023, p.108644. https://doi.org/https://doi.org/10.1016/j.cpc.2022.108644.
- Journal: Shahzad, H., Hickel, S., and Modesti, D., "Turbulence and added drag over acoustic liners," arXiv:2210.17354 - physics, 2022.
- Journal: Wilkinson, S. 1983 Influence of wall permeability on turbulent boundary-layer properties. In AIAA paper 1983-294.

TECHNICAL SESSION 5

BACKGROUND-ORIENTED SCHLIEREN

Chaired by Chris Willert

Some exemplary optical flow measurement techniques - Results obtained and work in progress

Markus Raffel
DLR-Institute of Aerodynamics and Flow Technology
37073 Göttingen, Germany
* Markus.Raffel@dlr.de

Keywords: DIT, BOS, PIV, optical set-up, image processing,

ABSTRACT

The major breakthrough at qualitative flow visualization was made in the late 20th century, early 21st century, when it became possible to illuminate flow features with high power lasers or LEDs and to store and process images of flow features digitally. The proposed article will describe some principles that lead to progress in Particle Image Velocimetry, Background Oriented Schlieren and Differential Infrared Thermography techniques from the author's personal viewpoint. Following this line, more recent tests and developments of PIV recording and evaluation techniques will be presented, which take advantage of forward scattering of tracer particles by in-line recording set ups. Various techniques for recording and dedicated subsequent evaluation have been tested of which one will shortly be described in the following abstract.

1 EXEMPLARY PROCEDURES USED IN PIV, DIT AND BOS

During the 80s and 90s of the last century, when Particle Image Velocimetry (PIV) was being performed by autocorrelation of doubly exposed images, it was hampered by the directional ambiguity of the measured velocity vectors. This was eventually solved by an increase of image complexity resulting from a second source of particle image displacement - the so-called image shifting - introduced by a synchronized recording via a rotating mirror.

The Background Oriented Schlieren Technique (BOS) - after its introduction in 1999 - could not be used with moving cameras for flight tests until the well-defined reference had been replaced by a second measurement image. This resulted in a higher complexity of cross-correlation results, but allowed to obtain valuable results of compressible flows during flight testing with airborne cameras.

The relatively slow heating (and cooling) of airfoils by the surrounding boundary layer flow made the application of infrared thermography for unsteady boundary layer transition detection impractical for decades. Measurements of dynamically varying transition locations and dynamic stall - for example on rapidly pitching airfoils - with thermographic cameras, could only be achieved once a second measurement image had been subtracted instead of a well-defined reference image. This first increased the result's ambiguity and therefore required more complex evaluation schemes, but eventually lead to success.

2 WORK IN PROGRESS – IN-LINE PIV: RECORDING

The following figure depicts an example of an in-line PIV set-up. The light of a small intense light source is focused by an illuminating lens into a light trap, which is located in front of a distant imaging lens. With the exception of smaller quantities due to lens imperfections and pollutions the majority of the emitted light is therefore hindered from reaching the imaging sensor. When tracer particles enter the illuminating beam, their forward scattered light will increase the intensity of the imaging sensor. In contrast to the residual light caused by lens imperfections, lens pollutions and out-of-focus tracer particle, the light scattered by particles, which are in the depth of field of the imaging lens, will be well concentrated onto just a few pixels. However, unlike in conventional PIV illumination, the image will not only consist of bright sharp particle images on a more or less dark background, but of bright ambient light with an additional small amount of sharp particle images.

The setup shown in the following, demonstrated the feasibility of the proposed image recording described above. The light source - shown on the left-hand side - was the LED of an ordinary flash lamp. The illuminating lens, as well as the imaging lens - shown on the right-hand side - were commercially available 400m Nikon objective lenses. The camera had a 4000 x 6000 pixel sensor. The tracer particles we used had a nominal size of appr. 1-2 microns.

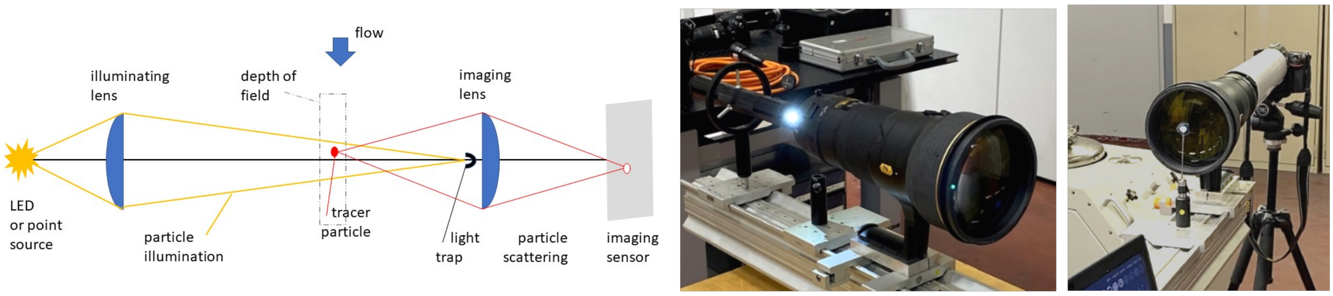

Figure 1. Set-up for in-line PIV recording

3 IN-LINE PIV: EVALUATION

The following figure depicts a typical result of an in-line PIV recording obtained with the aforementioned set up. It can be seen that the image is dominated by the residual light caused by lens imperfections and lens pollutions as well as the light scattered by out-of-focus particles.

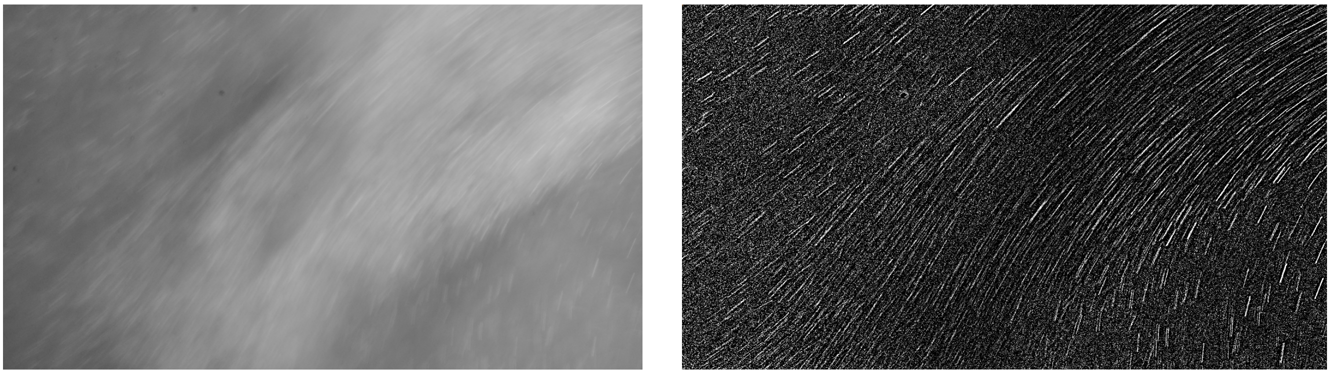

Figure 2. Raw image (left) and high-pass filtered image of an in-line PIV recording (right)

After the application of a digital high-pass filter the background intensity has been reduced and the traces of the in-focus particle illumination becomes clearly visible.

Similar to the exemplary recording schemes for autocorrelation PIV, BOS and DIT, the chosen in-line PIV set-up complicates the evaluation of the obtained images. However, once the right evaluation schemes and digital filters were found, we obtained flow field data from very small tracer particles illuminated with an ordinary flashlamp.

The full paper will describe further recording and evaluation procedures, which have been applied and analyzed in more detail.

REFERENCES

- Book: M. Raffel, C. Willert, F. Scarano, C. Kähler, S. Wereley, J. Kompenhans, Particle Image Velocimetry, 3rd edition, ISBN 9783319688527, Springer-Verlag, 669 pages, 2018
- Journal article: Raffel, M., Kompenhans, J.: Theoretical and experimental aspects of image-shifting by means of a rotating mirror system for particle image velocimetry. Meas. Sci. Technol. 6(6), 795 (1995). DOI 10.1088/0957-0233/6/6/016. URL http://stacks.iop.org/0957-0233/6/i=6/a=016
- Journal article: Raffel, M.: Background-oriented schlieren (BOS) techniques. Exp. Fluids 56(3), 1–17 (2015). DOI 10.1007/s00348-015-1927-5. URL https://doi.org/10.1007/s00348-015-1927-5
- Journal article: M. Raffel and C. B. Merz, “Differential Infrared Thermography for Unsteady BoundaryLayer Transition Measurements,” AIAA Journal, vol. 52, no. 9, 2014. DOI: 10.2514/1. J053235.

Wave field measurements of regular wave-monopile interaction using Free-Surface Synthetic Schlieren

Gosse Oldenziel[1,2,*] , Antonio Moreno-Rodenas[1], Niek Bruinsma[1], and Wout Bakker[1,3]
1: Deltares, Delft, The Netherlands
2: Laboratory for Aero- and Hydrodynamics, faculty of 3Me, Delft University of Technology, Delft, The Netherlands
3: Department of Hydraulic Engineering, Faculty of Civil Engineering and Geosciences, Delft University of Technology, Delft, The Netherlands
* Correspondent author: gosse.oldenziel@deltares.nl

Keywords: wave field measurement, optical measurement techniques, background oriented schlieren, free-surface synthetic schlieren, wave scattering, wave monopile interaction

ABSTRACT Spatio-temporal wave patterns due to wave field-structure interaction can be very complex to measure and analyze when using (intrusive) point probes. Free surface field measurements can offer much needed insight in this domain. Nevertheless, to the best of the authors' knowledge, these methods are rarely used in experimental offshore engineering and research. In these fields, typical domain sizes are at least in the order of several m^2, whereas (optical) free surface field measurements are often not performed in domains with dimensions larger than roughly 0.5×0.5 m^2. In the current work, the optical free-surface measurement technique named Free-Surface Synthetic Schlieren (FS-SS), is applied to measure the interaction between an incident wave field and a surface piercing cylinder, or monopile, in a domain of several m^2, for the first time. The FS-SS method is validated for wave fields with wavelengths $\lambda \ll L$ to $\lambda \gg L$, where L is the domain size in the direction of wave propagation. In the present abstract, wave field-monopile interaction measurements are presented for $D/\lambda = 0.2$, where D is the monopile diameter. For this case, the interaction wave field is analyzed by subtracting the measured wave field in absence of a structure from the measured interaction wave fields. The measured difference wave field reveals many interaction phenomena, such as locations of amplification, both near the monopile and further away, a wake that has certain similarities with a Kelvin wake, and a circular small wavelength diffraction pattern. It is concluded that the FS-SS method, including the proposed improvement using additional sensor data, is a useful addition to the toolbox of hydraulic engineers and researchers, and that especially the measured locations of wave amplification in the far field will not be easily detected using (arrays of) point probes.

1 INTRODUCTION

Despite the signifcant progress in recent years in (optical) techniques to measure water wave fields (Settles et al. 2017; Moisy et al. 2009; Gomit et al. 2022), it is remarkable how rarely these techniques are applied in experimental work for ofshore engineering applications. Specifically for the quantifcation of complex wave fields, free-surface field measurements can help in the identifcation of spatio-temporal patterns of relevance which point probes alone often do not resolve. Examples are the wave fields that occur due to wave–structure interaction, for example wave generation due to calving ice bergs (Heller et al. 2019) or the interaction of a wave with a surface piercing cylinder, or monopile. The interaction between an incident wave field and a monopile is currently one of the most practically relevant and fundamental wave fields. The diffraction of waves on a monopile has often been modeled, in many cases however, poor agreement has been found between measurements and first- and second order diffraction solutions (Stansberg and Kristiansen 2005). Phenomena arising from certain nonlinear interactions are suspected to have led to damage on several Gravity-Based Structures (GBS) in the North Sea (Sheikh and Swan 2005; Swan and Sheikh 2015). Although extreme waves themselves are not in the current scope, the ability to measure wave fields in a synoptical manner in the laboratory, including nonlinear interactions, is important for the further development of the understanding of all aspects of wave field–structure interaction, including quantification of the wave facility behavior itself. For the measurement of wave fields in laboratory setups, there are several optical techniques available to the experimentalist. In the present work the optical limitations of the location of the relevant basin, being in a generally accessible hydraulic hall and not in an optical laboratory, lead to the application of the robust refraction-based Free-Surface Synthetic Schlieren (FS-SS) method as presented by Moisy et al. (2009).

2 EXPERIMENTAL SETUP AND METHOD

A sketch of the experimental setup is shown in Figure 1. The setup consists of a camera located above the rectangular measurement domain (4×3 m^2), which has a random dot pattern at the bottom. The final field of view in direction of wave propagation is L = 3.37 m. Four intrusive wave height meters along the right side of the domain (in wave propagation direction) are used to compare the FS-SS measurement with. A monopile with diameter D = 0.200 m is placed in the domain to quantify the wave-monopile interaction. Images are aquired at a framing rate of 25 Hz.

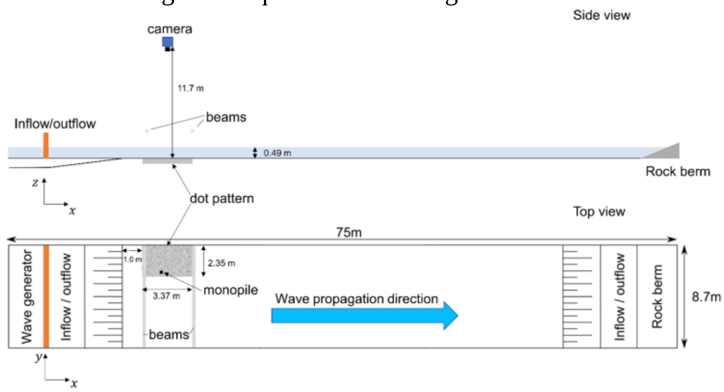

Figure 1: Top: sketch of experimental setup (side view). Bottom: sketch of experimental setup (top view).

A geometric mask and a min–max flter are applied to the raw images after which the multi pass image correlation is performed with the frst pass at a window size of 64×64 pixels with 50% overlap and the fnal two passes at a window size of 16×16 pixels with 50% overlap (Adrian, R. J., & Westerweel, J. 2011). This leads to a vector spacing of 14.3 mm. From the measured displacement fields the free surface gradient field is calculated as:

$$\nabla h_f = \frac{-\delta \boldsymbol{r}}{h^*} \tag{1}$$

See (Moisy et al. 2009), where **r** denotes the apparent displacement and h^* denotes a constant. The free-surface gradient field is subsequentially integrated to yield the free surface field using the PIVMAT MATLAB library supplied by (Moisy et al. 2009). Note that in this method, only the free-surface gradient is quantified, so additional assumptions are needed to estimate the mean water level.

3 VALIDATION OF FS-SS METHOD FOR REGULAR WAVES

The FS-SS method is validated for eleven regular wave conditions, consisting of waves at four different wavelengths, all generated at one or multiple amplitudes. The wave height is defined as:

$$H = \eta_{max} - \eta_{min} \tag{2}$$

where η is the free surface elevation relative to the mean water level, and η_{min} and η_{max} denote the minimum and maximum wave height for each individual wave period. The still water level is denoted as h and is equal to 0.489 m. In Figure 2 the difference in wave height between the FS-SS measurement and the intrusive point probes is indicated for all conditions versus the wavelength λ. The left subplot indicates the relative difference upon assuming that the mean free surface, as measured using FS-SS, is at the mean water level h, and in the right subplot the relative difference is shown upon using the point probe signal of the centrally located wave height meter to determine the free-surface elevation at the relevant location (x/L = 0.5). This technique is here referred to as 'data fusion'. It is found that for small wavelengths ($\lambda/L < 0.5$) the assumption that the mean elevation is zero leads to (very) small differences between FS-SS and the point probes (< 5%), whereas for large wavelengths ($\lambda/L > 0.5$) the additional point probe measurement leads to differences between the intrusive probes and FS-SS of < 15% except for one outlying case.

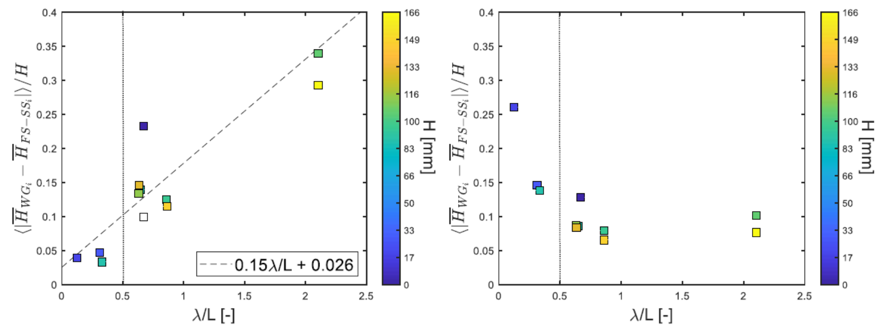

Figure 2: mean difference in measured wave height between wave gauge data and FS-SS reconstruction relative to wave height H, at x/L = 0.01, x/L = 0.14 and x/L = 0.27 and x/L = 0.51 versus relative wavelength. In both subfigures the dotted vertical line indicates the wavelength above which the data fusion improves the agreement between FS-SS and wave gauge data. Left subfigure: conventional implementation of FS-SS. The dashed line indicates a linear fit to the data.

4 RESULTS FOR REGULAR WAVE INTERACTION WITH A MONOPILE

In Figure 3, difference fields are presented of measured wave fields where a monopile is present minus wave fields without a monopile. The fields are presented for wave condition D/λ = 0.20 in the presence of a monopile. In the fields it can be observed that a circular wave pattern is generated that is centered in the monopile and that is superposed on the plane wave. Next to this, locations of wave amplification due to interaction of incoming waves with reflected waves can be observed. In Figure 3 the circular wave that is centered in the monopile has not yet reached the boundary of the basin, so no boundary reflections are present. An asymmetry in the diffraction around the monopile causes the short wavelength diffraction waves to interlock near the edge of the wake, as is indicated in the right subfigure in Figure 3. These waves thus form a wake structure with certain similarities to a Kelvin wave pattern, such as having a clearly discernible angle, as is indicated in Figure 3.

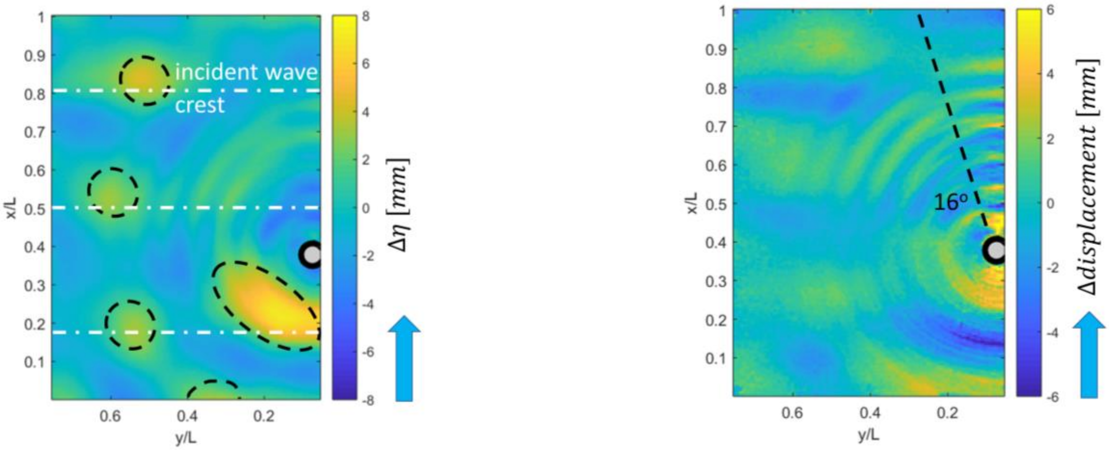

Figure 3: Interaction between wave and monopile for case D/λ = 0.20. Left: elevation difference field of typical wave-monopile interaction pattern. T = 11.76 s. Right: measured displacement difference field with wake at time t = 11.76 s. Incident waves are propagating in the direction of positive x values.

5 CONCLUSIONS

The FS-SS method is applied at large scale in a hydraulic laboratory to measure wave fields due to interaction of a regular wave and a monopile. It is found that for small wavelengths ($\lambda/L < 0.5$) the assumption that the mean elevation is zero leads to (very) small differences between FS-SS and the point probes (< 5%). Additionally, it is found that the incorporation of a water level measurement using a point probe improves the agreement between intrusive wave height meters and the FS-SS measurement for large wavelengths ($\lambda/L > 0.5$) as compared to assuming a zero-mean free-surface. Wave field-monopile interaction measurements are presented for $D/\lambda = 0.2$, where D is the monopile diameter. For this case, the interaction wave field is analyzed by subtracting the measured wave field in absence of a structure from the measured interaction wave fields. The measured difference wave field reveals many interaction phenomena such as locations of amplification, both near the monopile and further away, a wake that has certain similarities with a Kelvin wake, and a circular small wavelength diffraction pattern. It is concluded that the FS-SS method, including the proposed improvement using additional sensor data, is a useful addition to the toolbox of hydraulic engineers and researchers, and that especially the measured locations of wave amplification in the far field will not be easily detected using (arrays of) point probes.

6 REFERENCES

- Adrian, R. J., & Westerweel, J. (2011). *Particle image velocimetry* (No. 30). Cambridge university press.
- Gomit, G., Chatellier, L., & David, L. (2022). Free-surface flow measurements by non-intrusive methods: a survey. *Experiments in Fluids*, *63*(6), 94.
- Heller, V., Chen, F., Brühl, M., Gabl, R., Chen, X., Wolters, G., & Fuchs, H. (2019). Large-scale experiments into the tsunamigenic potential of different iceberg calving mechanisms. *Scientific Reports*, *9*(1), 1-10.
- Moisy, F., Rabaud, M., & Salsac, K. (2009). A synthetic Schlieren method for the measurement of the topography of a liquid interface. *Experiments in Fluids*, *46*(6), 1021-1036.
- Settles, G. S., & Hargather, M. J. (2017). A review of recent developments in schlieren and shadowgraph techniques. *Measurement Science and Technology*, *28*(4), 042001.
- Sheikh, R., & Swan, C. (2005). The interaction between steep waves and a vertical, surface-piercing column. *J. Offshore Mech. Arct. Eng.*, *127*(1), 31-38.
- Stansberg, C. T., & Kristiansen, T. (2005). Non-linear scattering of steep surface waves around vertical columns. *Applied ocean research*, *27*(2), 65-80.
- Swan, C., & Sheikh, R. (2015). The interaction between steep waves and a surface-piercing column. *Philosophical Transactions of the Royal Society A: Mathematical, Physical and Engineering Sciences*, *373*(2033), 20140114.

Density Measurement around the Model Surface by Background Oriented Schlieren using Digital Projectors

Masanori Ota[1*], Masato Yamagishi[1], Hiroki Nagai[2]
1: Graduate School of Engineering, Chiba University, Japan
2: Institute of Fluid Science, Tohoku University, Japan
* Correspondent author: ota@faculty.chiba-u.jp

Keywords: BOS technique, Background projection,

ABSTRACT The Background Oriented Schlieren (BOS) technique has been applied to various measurements due to its simplicity and robustness. However, the measured flow field must contain the image blur, and it is unavoidable in the conventional BOS setup. In order to overcome this drawback and achieve adequate sensitivity, a digital projector is introduced in the BOS setup in this paper. The sensitivity and magnitude of BOS measurement can be controlled flexibly in the proposed technique.

1 PURPOSE

The BOS (Background Oriented Schlieren) technique proposed by Meier [1] enables quantitative density measurement of a flow fields together with computer-aided image analysis with very simple setup. The application range of this technique is very wide because of its robustness and advantages. However, the conventional BOS technique has drawbacks, such as a lower sensitivity and image blur due to diverging light observation. In general, a camera has to focus on the background image placed behind the measurement target, therefore this image blur at the measurement position is unavoidable. The relation between sensitivity and blurring is in trade-off. To overcome this problem a digital projector is installed in the BOS measurement in this paper. The background projection approach was firstly introduced by Leopold et al. [2] to keep the background pattern and test model in the wind tunnel within the depth of field of camera lens. In this paper a digital projector and telecentric optical system [3] are newly introduced to adjust sensitivity and magnitude of the BOS measurement flexibly.

2 METHOD

Figure 1 shows the schematic diagram of the BOS setup using a digital projector. From left side, the background pattern is projected parallel through the telecentric optical system consists of projector lens, Lens 1, and an aperture. The background pattern is focused on the position shown as 'projected background' in the figure. At camera side, optical setup is also telecentric one consists of Lens 2 and camera lens. Projected light ray is bent due to the density gradient in the medium, then captured at the image sensor with displacement Δh as shown in a solid line. Displacement Δh is obtained as telecentric BOS setup expressed as Eq. (1) [3] where l_b is distance between density gradient and projected background, f_{camera} and f_{Lens2} are focal length of camera lens and Lens 2 respectively. Please note that the displacement obtained with this setup is opposite to that of the conventional BOS measurement. The focal position of the background can be adjusted at any position.

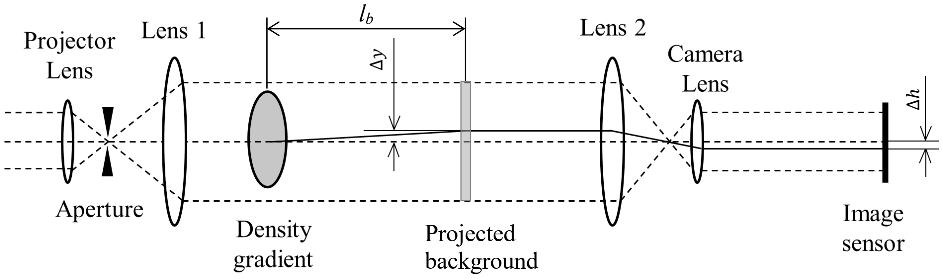

Figure 1. BOS setup with background projection

$$\Delta h = -\frac{l_b f_{\text{camera}}}{f_{\text{Lens 2}}}\frac{1}{n_0}\int \frac{\partial n}{\partial r(x,y)}dl \qquad (1)$$

3 RESULT

Examples of resultant images are shown in figure 2. A cone model with semi apex angle was 20º is installed in supersonic wind tunnel and flow Mach number was set to 2.0 in this case. Left figure is obtained with conventional BOS setup and it is clearly shown that the test model is blurred, and shock wave is also captured thick because camera has to focus on the background behind the flow field. On the other hand, the test model and shock wave generated from the tip of cone model clearly captured in right figure obtained with the proposed technique. The sensitivity and magnitude of BOS measurement can be controlled by adjusting projected-background position and aperture size with the proposed setup.

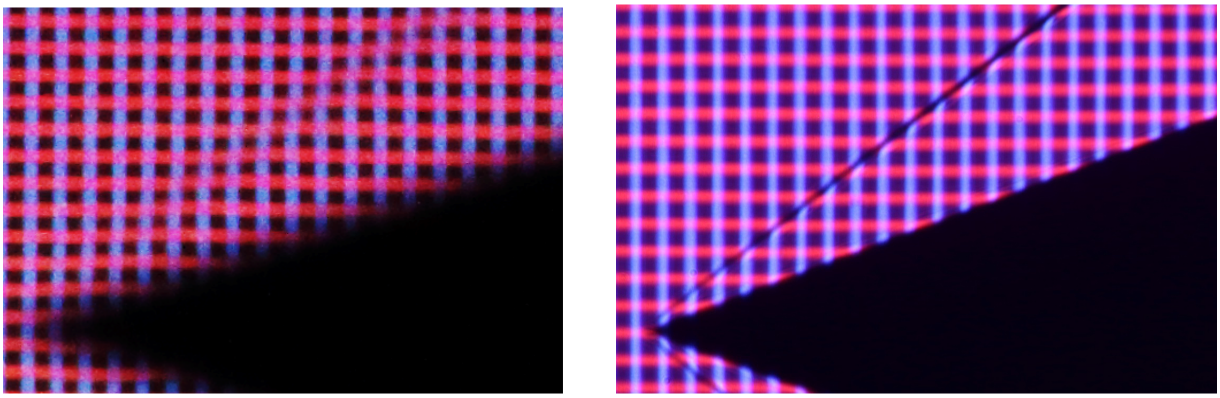

Figure 2. Example of BOS image (Left: conventional BOS, Right: BOS with background projection)

4. CONCLUSION

To overcome the drawback of the conventional BOS, a digital projector and telecentric optical system are introduced in BOS measurement. The test model and flow field can be captured very sharp while the background pattern is also sharp. By using a digital projector, high brightness photography can be achieved with low cost and it is advantageous to the measurement of unsteady phenomena together with high-speed camera.

5. REFERENCES

[1] G. E. A. Meier (2002). Computerized background-oriented schlieren. Experiments in Fluids, 33, 181-187.

[2] Leopold F, Jagusinski F, Demeautis C, Ota M, Klatt D. (2012). Increase of accuracy for CBOS by background projection. *Proc. 15th ISFV*, Minsk Belarus, ISFV15–087, 1-8.

[3] Ota M, Leopold F, Noda R, Maeno K (2015). Improvement in spatial resolution of background-oriented schlieren technique by introducing a telecentric optical system and its application to supersonic flow. Experiments in Fluids, 56(48) 1-10.

Jet Flow Visualization Using Smartphone BOS

Giray Oguzman[1,2*] and Sedat Tokgoz[2]
1: Dept. of Aeronautical Eng., Istanbul Technical University, Turkey
2: Dept. of Aeronautical Eng., Gebze Technical University, Turkey
* Correspondent author: oguzman@gtu.edu.tr

Keywords: Background-Oriented Schlieren (BOS), Smartphone, Jet, Concentration

ABSTRACT
Smartphones have a variety of sensors built-in, such as accelerometers, gyroscopes, GPS, magnetometers, and cameras, which can be used to collect data for scientific research. They have the potential to revolutionize scientific research by enabling large-scale data collection at a relatively low cost. Experimental studies using smartphones have been conducted in various fields, from medicine to natural sciences, including flow visualization (Cierpka et al., 2016; Settles, 2018). Background Oriented Schlieren (BOS) is a quantitative measurement technique, where a camera and a background target with random patterns are placed on opposite sides of the test section. Any changes in the refraction index along the optical path can be detected as the displacements on the recorded image of the background target (Meier, 2002). These changes in the refraction index might be due to changes in density, temperature, pressure, or concentration. It was already shown that (Settles, 2018; Hayasaka & Tagawa, 2019) smartphones can be used for BOS measurements (smartphone BOS). In this study, we aim to parametrically investigate the capabilities of quantitative smartphone BOS measurements, and reveal the actual accuracy of the technique.

The measurements are performed inside a water-filled aquarium with dimensions of $485\ x\ 290\ x\ 190\ mm$, in the horizontal, vertical, and depth directions. The flow is provided by a circular jet with a diameter of $5\ mm$, which is immersed in water, and driven by gravitational force only. The distances from the background target to the jet center, and from the jet center to the smartphone are $1\ m$, each (Figure 1). In order to impose a change in the refraction index, a sugar-water mixture is used as the jet fluid. Sugar-water mixture has the advantages of being highly refractive and diffusing slowly into water (Peters et al., 1992). Another advantage is the easiness of controlling the refractive index parametrically by changing the sugar concentration. The smartphone used in this study is *Samsung Note 20*, which has a resolution of $4032\ x\ 3024\ pixels$. Images are recorded via *Open Camera* application that is freely available on Android store. Despite the preinstalled default camera application, *Open Camera* app allows advanced controlling of smartphone's camera. Lighting is a regular LED light that is used for general purposes, and consists of 96 LEDs. Displacements of the background target are computed using *PIVlab* tool for Matlab (Thielicke & Sonntag, 2021). The background target is a synthetic particle image velocimetry (PIV) image generated by the *PIVlab* tool printed on a A0-sized paper. The diameters of the particles on the recorded images are approximately $5\ pixels$. In order to avoid moving or vibrating the phone during image recording, stylus pen that comes with the phone was used for triggering the image recording via Bluetooth.

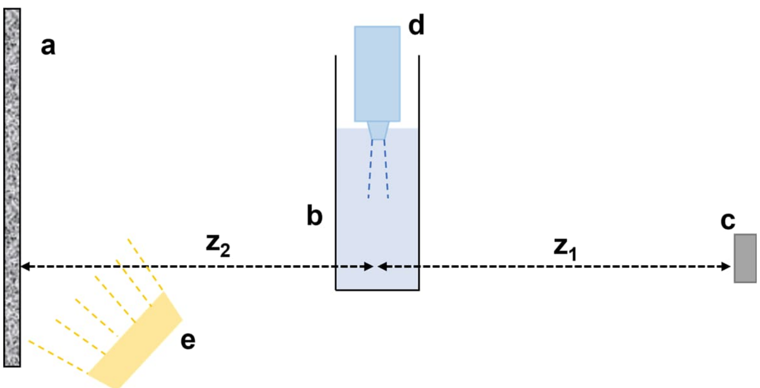

Figure 1. Sketch of the experimental setup; (a) background target, (b) aquarium, (c) smartphone, (d) sugar-water mixture tank and jet, (e) LED light source. The distances are $z_1=z_2=1\ m$.

Three different sugar-water mixtures with concentrations of 0.3%, 0.5%, and 1.0% are investigated in this study. Apparent displacements of the jet with concentrations of 0.3% and 0.5% are shown in Figure 2. As expected, higher concentration causes a stronger change in the refractive index, therefore results in a stronger apparent displacement. This is more obvious for the measurements taken at 1.0% concentration (Figure 3). However, characteristic features of the jet were captured for all cases, even for the lowest concentration. We will parametrically examine the capability of smartphone BOS in more detail.

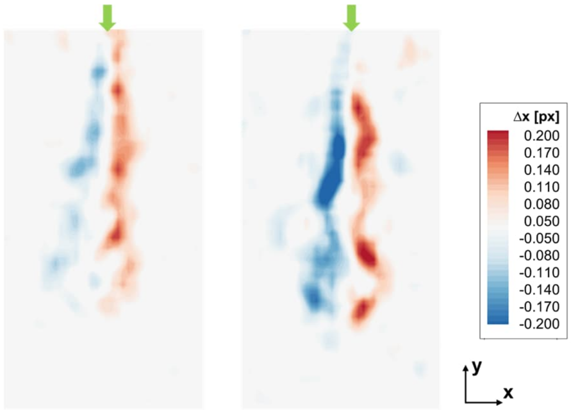

Figure 2. Instantaneous measurements of the jet flow with sugar-water concentration of (left) 0.3%, and (right) 0.5%. Apparent displacements due to concentration gradients in the x-direction are color coded. Green arrows indicate the centers of the circular jets.

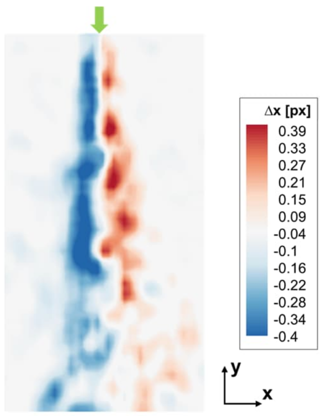

Figure 3. Instantaneous measurement of the jet flow with a sugar-water concentration of 1.0%. Apparent displacements due to concentration gradients in the x-direction are color coded. Green arrow indicates the center of the circular jet.

REFERENCES

Cierpka, C., Hain, R., & Buchmann, N. A. (2016). Flow visualization by mobile phone cameras. *Experiments in Fluids*, *57*(6), 108. https://doi.org/10.1007/s00348-016-2192-y

Hayasaka, K., & Tagawa, Y. (2019). Mobile visualization of density fields using smartphone background-oriented schlieren. *Experiments in Fluids*, *60*(11), 171. https://doi.org/10.1007/s00348-019-2817-z

Meier, G. E. A. (2002). Computerized background-oriented schlieren. *Experiments in Fluids*, *33*(1), 181–187. https://doi.org/10.1007/s00348-002-0450-7

Peters, F., Kuralt, T., & Schniderjan, J. (1992). Visualization of water flow by sugar schlieren. *Experiments in Fluids*, *12–12*(4–5), 351–352. https://doi.org/10.1007/BF00187313

Settles, G. S. (2018). Smartphone schlieren and shadowgraph imaging. *Optics and Lasers in Engineering*, *104*, 9–21. https://doi.org/10.1016/j.optlaseng.2017.07.002

Thielicke, W., & Sonntag, R. (2021). Particle Image Velocimetry for MATLAB: Accuracy and enhanced algorithms in PIVlab. *Journal of Open Research Software*, *9*(1), 12. https://doi.org/10.5334/jors.334

Response of optical flow based background oriented schlieren to random dot patterns

Bora O. Cakir[1,2*], Sergio Lavagnoli[1], Bayindir Saracoglu[1] and Christer Fureby[2]
1: Dept. of Turbomachinery and Propulsion, von Karman Institute for Fluid Dynamics, Belgium
2: Dept. of Energy Sciences, Lund University, Sweden
* Correspondent author: bora.orcun.cakir@vki.ac.be

Keywords: Density varying flows, Schlieren, BOS, Optical flow, Speckle patterns

ABSTRACT The degraded resolution and sensitivity characteristics of BOS can be recovered by means of utilizing an optical flow based image processing scheme for the displacement detection stage. However, the background patterns conventionally employed in BOS setups suit the needs of the cross-correlation approach, whereas optical flow is associated with a completely different mathematical background. Thus, in order to characterize the resolution and sensitivity response of optical flow based BOS to the background generation configurations a parametric study comprising synthetic and experimental assessments is performed.

1 INTRODUCTION

The conventional background patterns in background oriented schlieren (BOS) are adjusted to suit the needs of the cross-correlation approach, have a high SNR in correlation maps, which yields random dot patterns based on the optical configuration of the measurement system (Adrian, 2011).Alternatively, in line with the sequential downsampling of images following a coarse-to-fine resolution layout, multi-scale procedural noise patterns can be used as the background image (Atcheson et al., 2009). Even though synthetic assessments performed in a controlled environment attributed the greatest accuracy to optical flow (OF) application with procedural background patterns, unavoidable experimental uncertainties of illumination and printing artifacts make random dot patterns to be the most robust option as multi-scale patterns are vulnerable against the noise (Cakir et al., 2022). Nevertheless, due to the scarcity of quantitative assessments on the use of optical flow for PIV and BOS applications, a proper characterization of the influence of background generation parameters yielding a speckle pattern does not exist. This prevents the reaching the full potential of optical flow especially in BOS where a considerably high level of control over the light intensity features is available in comparison to PIV. Therefore, this study aims to perform a quantitative characterization of the sensitivity and resolution limits of optical flow based BOS in response to the computer generated speckle pattern configurations where two synthetic investigations utilizing a 1D shock tube scenario and high resolution DNS datasets (Livescu, 2008) as well as an experimental assessment by means of a heated air jet are conducted to demonstrate the theoretical and practical considerations associated with their employment.

2 SYNTHETIC ASSESSMENT

Firstly, an immediate improvement in reconstruction accuracy is observed when speckle size is increased from the conventional value of d_P =1 pix which yields imaged speckles of 2~3 pixels. This situation relaxes the demand on sensitivity whereas the localization of displacement vectors with a chaotic spatial distribution requires a less sparse coefficient matrix for the optical flow to converge to a higher accuracy reconstruction which is satisfied with d_P >1 pix. It is also observed that beyond d_P >1 pix a certain threshold of sparsity is exceeded which is a limiting factor for d_P =1 pix to achieve low AEPE values, since beyond d_P >2 pix, the change in AEPE values is small. Similarly, for constant dot size (d_P), raising concentration of particles allows the reconstruction accuracy to increase. Nonetheless, reduction in AEPE stops when the particle concentration exceeds a certain limit which varies based on the particle size (Fig.1, left). As this limit is not reached in case of speckles with d_P >2 pix, the trend of reduction of AEPE value with increasing N_I is maintained. This is attributed to the reduction in the rank of the coefficient matrix by the overpopulation of the background which is only possible for the small sizes of speckles as increasing particle size defined in circular shapes yields larger gaps between the speckles allowing larger illumination intensity gradients to be computed in comparison to the overpopulated small speckles. Overall, the best combination of these parameters is achieved with d_P =2 pix and N_I =0.039 ppp which yields a pattern that is densely populated to with high-contrast illumination intensity gradients to enable best displacement capturing capability.

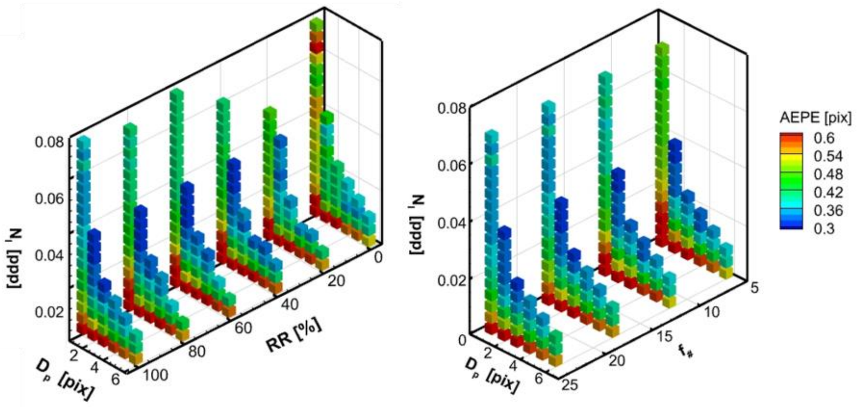

Figure 1. Average end-point error values for varying particle concentration N_I, particle size d_P and particle distribution randomness ratio RR for constant (left) and varying (right) aperture ($f_\#$).

3 EXPERIMENTAL ASSESSMENT

The experimental setup employed in this work is implemented around Steinel HL 1610 S heat gun. It has two operation modes ejecting heated air at temperatures of 575 K and 783 K with speeds of 4.7 m/s and 8.2 m/s respectively from an nozzle diameter of 0.033 m. The corresponding nozzle diameter based Reynolds numbers of the operation modes are Re_D = 3200 and Re_D =3400. Configuration of the BOS setup is composed of a Hamamatsu ORCA-Flash4.0 V3 Digital CMOS camera, a f = 100 mm Nikkor lens, four Chazon 100W 10x10 LED arrays as the light source and backgrounds laser printed on 240 g/m^2 paper (Fig.2).

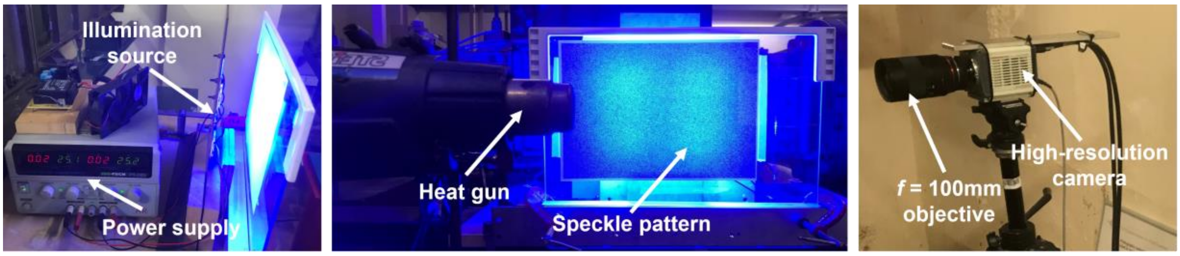

Figure 2. Experimental setup of the background oriented schlieren system with the illumination configuration (left), heat gun and the illuminated speckle pattern (middle) and image acquisition system (right).

4 OUTLOOK TO THE FULL PAPER

The use of an optical flow (OF) based image processing allows to recover high fidelity density field variations at the deflection detection stage of background oriented schlieren (BOS). However, the background patterns conventionally employed in BOS setups suit the needs of the cross-correlation approach whereas optical flow is associated with a completely different mathematical background in comparison its block matching counterparts. Thus, in order to characterize the resolution and sensitivity response of optical flow based BOS to the background generation configurations, a parametric study comprising a theoretical assessment utilizing a 1D shocktube problem and a numerical assessment using a high-fidelity DNS simulation are performed. Additionally, the practical applicability of the speckle pattern configurations is investigated via an experimental assessment employing a heat gun, results of which will be included in the full paper.

5 REFERENCES

- Adrian, R., & Westerweel, J. (2011). Particle image velocimetry. Cambridge University Press
- Atcheson, B. Heidrich, W. & Ihrke, I. (2009) An evaluation of optical flow algorithms for background oriented schlieren imaging, Experiments in Fluids 46 (3) 467–476.
- Cakir, B.O., Lavagnoli, S., Saracoglu, B.H. & Fureby, C. (2023). Assessment and application of optical flow in background-oriented schlieren for compressible flows. Exp Fluids 64(11).
- Livescu, D. & Ristorcelli, J. R. (2008) Variable-density mixing in buoyancy-driven turbulence, Journal of Fluid Mechanics 605, 145–180.

TECHNICAL SESSION 6
MULTIPHASE FLOWS

Chaired by Francisco Pereira

Concentration measurements of evaporating multiple-binary mixture droplets using surface plasmon resonance imaging

Hyung Ju Lee[1] Chang Kyoung Choi[1,2], and Seong Hyuk Lee[1,*]
1: School of Mechanical Engineering, Chung-Ang University, Republic of Korea
2: Mechanical Engineering-Engineering Mechanics, Michigan Technological University, USA
* Correspondent author: shlee89@cau.ac.kr

Keywords: Surface Plasmon Resonance, Droplet evaporation, Multiple-binary mixture droplets, Concentration

ABSTRACT

Droplet evaporation is applied to surface coating methods manufacturing printed electronics (Bromberg, Ma, & Singler, 2013). Particle deposition patterns using droplet evaporation strongly depend on the liquid compositions generating the coffee-ring, uniform, and multi-ring patterns (Wang, Orejon, Takata, & Sefiane, 2022). Also, the binary mixture droplets (BMDs) have distinctive characteristics in which more volatile components evaporate preferentially, called selective evaporation (Jeong, Lee, Choi, & Lee, 2021). Hence the contact-line motions and internal flow fields are quite different from the single-component droplets. Practically, multiple droplets are deposited on the substrate for mass production. For the multiple droplets, the vapor is overlapped with the vapor evaporated from the neighboring droplet, which causes vapor accumulations. The vapor accumulation suppresses the local evaporation flux of the droplets, inducing the concentration gradient for the BMDs. Therefore, the present study investigates the evaporation characteristics of multiple-binary mixture droplets (M-BMDs), visualizing liquid concentrations. Droplet-to-droplet distances and initial ethanol concentrations are considered to examine the local interaction of the multiple droplets.

Surface plasmon resonance imaging (SPRi) is used to measure the time-varying liquid concentration of the M-BMDs to compare the surface tension gradient along the contact line region affecting the internal flow motions. Simultaneously, the shadowgraph method visualizes the droplet shape from the side. Figure 1 presents the experimental setup to measure the liquid concentration with the bottom view and to capture the droplet shape with the side view. The optical array converts the white light to parallel and monochromatic p-polarized light to obtain the surface plasmon resonance signal. Three droplets with a volume of 60 nl are subsequently deposited on the gold substrate using the nanoliter dispenser. The liquid concentration is calculated using the correlation between the ethanol concentration and the surface plasmon resonance signal. Also, vapor distributions and local evaporation flux of each component are obtained through three-dimensional numerical simulations.

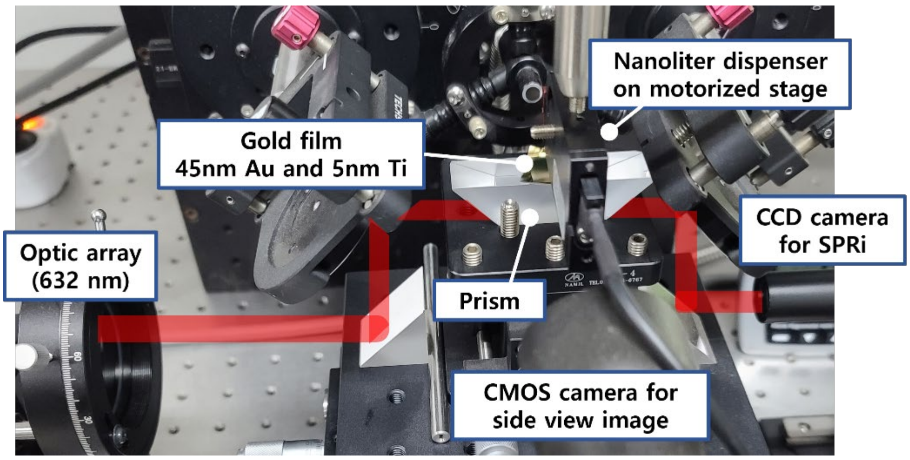

Figure 1. Experimental setup of SPRi for concentration measurement and shadowgraph method for the droplet shape.

The evaporation time was delayed for the M-BMDs compared to that of the single droplet due to the vapor accumulation. Also, the contact-line motions of the binary mixture droplets showed the three stages I) a spreading stage, II) a rapid sliding stage, and III) a moderate sliding stage regardless of single- and multiple droplets. The single droplet showed a decrease in the ethanol concentration with uniform distributions during evaporation due to selective evaporation, in which more volatile components preferentially evaporated. On the other hand, the M-BMDs revealed the local ethanol concentration gradient along the contact line regions, as shown in Fig. 2. The side droplets showed a lower ethanol concentration far away from the center droplet and a higher concentration near the adjacent droplet region. When the M-BMDs evaporated, the vapor of each component accumulated near the adjacent droplet region, which suppressed the local evaporation flux of the droplets; this is called the vapor shielding effect. Also, the ethanol component with higher volatility preferentially evaporated far away from the adjacent droplet. The vapor accumulation and suppression of the evaporation flux in the adjacent region were confirmed by the numerical simulations of the M-BMDs. Therefore, the local ethanol concentration difference appeared during the evaporations, which induced the surface tension gradient along the liquid-air interface. The surface tension gradients of the droplets were also compared, showing the directionality of solutal Marangoni stresses depending on the location of the droplets. Moreover, the scaled lifetime, which is the ratio of evaporation time between single- and multiple droplets, showed good agreement with the previously reported experiments and theoretical models (Chen et al., 2022).

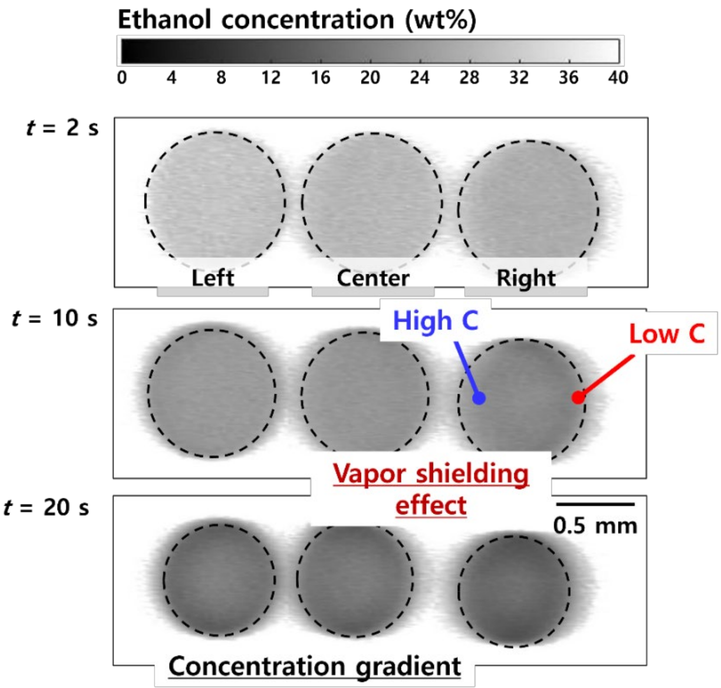

Figure 2. Time-varying ethanol concentration distributions of M-BMDs.

REFERENCES

- Bromberg, V., Ma, S. Y., & Singler, T. J. (2013). High-resolution inkjet printing of electrically conducting lines of silver nanoparticles by edge-enhanced twin-line deposition. Applied Physics Letters, 102(21), 214101.
- Chen, H., An, Q. R., Zhang, H. Y., Li, C. S., Fang, H. S., & Yin, Z. P. (2022). Predicting the lifetimes of evaporating droplets in ordered arrays. Physics of Fluids, 34(8), 082010.
- Jeong, C. H., Lee, H. J., Choi, C. K., & Lee, S. H. (2021). Selective evaporation rate modeling of volatile binary mixture droplets. International Journal of Heat and Mass Transfer, 178, 121584.
- Wang, Z., Orejon, D., Takata, Y., & Sefiane, K. (2022). Wetting and evaporation of multicomponent droplets. Physics Reports, 960, 1-37.

ACKNOWLEDGEMENTS

This work was supported by the National Research Foundation of Korea (NRF) grant funded by the Korea government (MSIT) (NRF-2021R1A2C3014510)

Characterization of air lubrication regimes using imaging and PIV

Lina Nikolaidou[1,*], Angeliki Laskari[1], Tom van Terwisga[2,3], Christian Poelma[1]
1: Dept. of Process & Energy, Delft University of Technology, Netherlands
2: Dept. of Maritime and Transport Technology, Delft University of Technology, Netherlands
3: Maritime Research Institute of the Netherlands (MARIN), Netherlands
* Correspondent author: M.Nikolaidou@tudelft.nl

Keywords: air cavity, air layer, planar PIV, multiphase flow, interface detection

Air lubrication techniques have been proposed and investigated over the past years, as methods to reduce the friction drag (e.g. below the hull of a ship). In order to investigate the multiphase phenomena at play, an air layer is created by controlled air injection within a spatially developing liquid turbulent boundary layer (TBL) over a flat plate. Past studies (Elbing et al. 2008) indicated that depending on the liquid freestream velocity and the air flow rate, three different air phase regimes are observed: a bubbly regime, a transitional regime and an air layer regime, with the latter one being the most desirable for drag reduction. According to their definitions, once a drag reduction of 20% is achieved the transitional regime is reached, while a drag reduction larger than 80% marks the onset of the air layer regime. In the present study, rather than using the drag reduction to characterize each regime we aim to investigate the morphological characteristics of each regime and classify them accordingly. Then we will focus on the air layer regime and more specifically on the air layer thickness, a parameter that has hardly been looked at in literature, possibly due to the difficulties that such a measurement entails. The method to acquire the thickness will also be explained.
In order to capture the different air phase regimes, an imaging camera was used in a down-up configuration. Four different liquid freestream velocities ($Re_x \approx 2.8 - 3.8 \times 10^6$) were tested along with different air flow rates (Q_{air} varied from 2.5 l/min to 52 l/min) resulting in images of different air phase regimes. A LaVision Imager sCMOS CLHS camera fitted with a 24 mm lens was used to image the air phase regimes in a streamwise-spanwise plane. An LED panel provided background illumination. The image frame rate was 2 Hz, allowing acquisition of independent snapshots. The field of view was approximately 700 x 600 mm^2 and the magnification approximately 3.6 px/mm in both directions. Based on the results, a regime map can be determined (Figure 1). For a low Q_{air}, dispersed bubbles are present in the flow. Increasing the air flow rate results in the formation of air patches of various sizes and shapes. Further increasing the air flow rate results in the air layer regime. In this regime a clear air cavity separates the solid wall from the liquid phase with the air layer having a thickness of several millimeters.

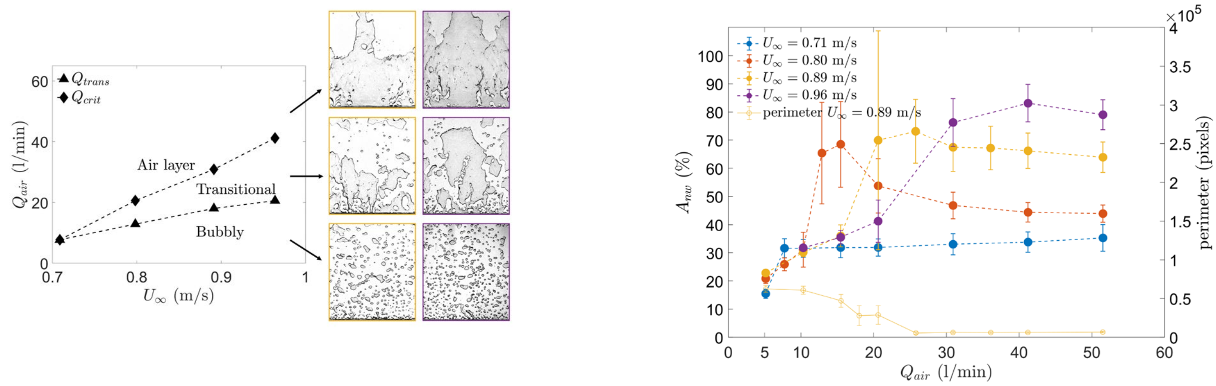

Figure 1. Left: Air phase diagram along with characteristic images of each regime. Images with yellow and purple outline correspond to $U_\infty = 0.89$ m/s and $U_\infty = 0.96$ m/s liquid velocities respectively (see also right figure). Flow is from down up. Right: The non-wetted area versus air flow rate for various liquid freestream velocities. In the case of $U_\infty = 0.89$ m/s also the perimeter is shown.

In order to quantify the air phase in each condition, the percentage of non-wetted area A_{nw} is defined as:

$$A_{nw} = \frac{A_{air}}{A_{total}} \times 100 \tag{1}$$

where A_{air} is the plate area covered by air and A_{total} is the total plate area. To calculate the A_{nw}, the grayscale images are binarized based on an intensity threshold. Small structures are removed and morphological closing (dilation followed by an erosion) is performed and the remaining bubbles/air patches are filled. An initial increase of Q_{air} results in an increase of A_{nw}: a steeper increase and a large standard deviation for A_{nw} is observed for the transitional regime indicating the highly dynamic character of the air phase in this regime. Once the air layer regime is reached, further increasing the air flow rate has no effect and A_{nw} remains unchanged.
For the case of an air layer regime, imaging of the air phase was coupled with snapshot planar PIV (2D-2C) of the incoming TBL as well as the flow around the air layer in a streamwise-wall normal plane. Two high-resolution LaVision LX pro (16 MegaPixel), 12-bit cameras were used. The acquisition frequency was 0.7 Hz and 1600 - 2500 statistically independent images were recorded for each FOV. In the absence of seeding particles in the air phase, a noticeable decrease of the correlation value R of the particle image pairs was evident. The thickness $t_{air}$was then determined from the time averaged correlation value R of the particle image pairs (Figure 2). Subsequent appropriate thresholding using Otsu's method (Otsu 1979) and image processing of the mean correlation map allowed the determination of the mean air water interface and its maximum thickness (at the apex of the concave interface, see also insert in Figure 2) for all conditions. In Figure 2 also the mean streamwise velocity around the air layer is shown and the air layer shape is acquired from the mean correlation map. The air layer thickness was found to be 15 ± 1 mm.

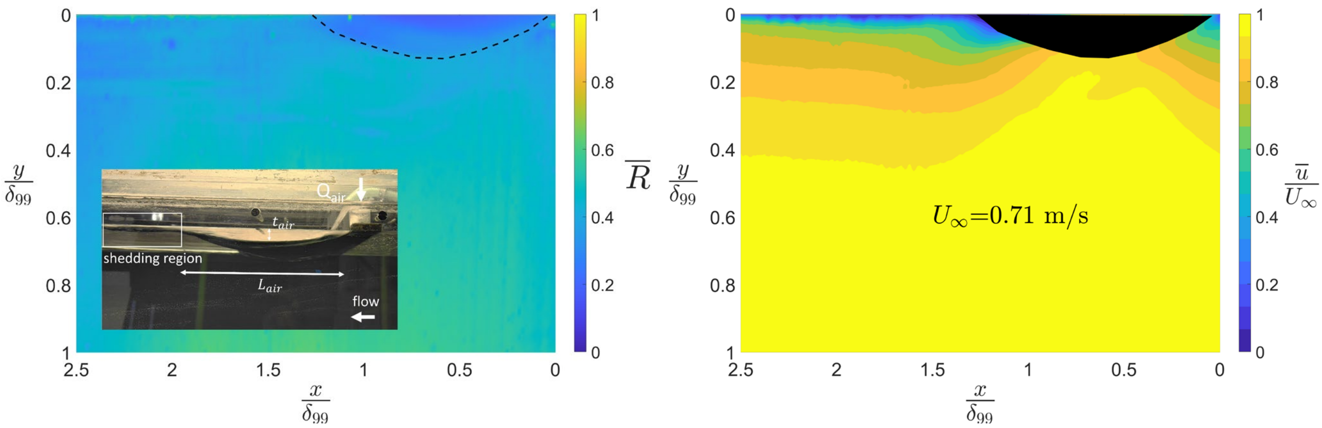

Figure 2. Left: Mean correlation map used to extract the air layer thickness. Dashed line indicates the edge of the air layer. Right: Contour plot of the mean streamwise velocity around the air layer. Flow is from right to left.

To conclude, three different air phase regimes are detected for different liquid freestream velocities and air flow rates, which can be characterized by the resulting non-wetted area. Once the air layer regime is reached the thickness of the air layer can be calculated from the mean correlation map of the particle image pairs. On one hand, the spatial resolution of the PIV (2 mm based on the final interrogation size) was sufficient to provide a value for t_{air}, on the other hand the uncertainty due to the method and the reflections at the air water interface make it difficult to determine a trend of t_{air} with the different liquid freestream velocities.

REFERENCES

Elbing, B. R., Winkel, E. S., Lay, K. A., Ceccio, S. L., Dowling, D. R., & Perlin, M. (2008). Bubble-induced skin-friction drag reduction and the abrupt transition to air-layer drag reduction. Journal of Fluid Mechanics, 612, 201-236.

Otsu, N. (1979). A threshold selection method from gray-level histograms. IEEE transactions on systems, man, and cybernetics, 9(1), 62-66.

Tomographic PIV Investigation on the Dynamics of Cavitating Tip Vortex

Qingqing Ye[1,*] , Yuwei Wang[1] and Xueming Shao[1]
1: Dept. of Mechanics, Zhejiang University, P.R. China
* Correspondent author: qingqing_ye@zju.edu.cn

Keywords: Tomographic PIV, Tip vortex cavitation, Three dimensional vortical structures, Vortex instability

ABSTRACT In present work, unsteady three-dimensional flow field of tip vortex generated by a NACA 662-415 hydrofoil is investigated under cavitating condition using time-resolved tomographic-PIV. Two main cavitation modes are identified, namely breathing and double-helical mode. The time-averaged flow consists a system of two streamwise vortices for all three conditions, originated from the tip and the hydrofoil trailing edge, respectively. The shape of the tip vortex resembles to that of the cavity oscillation mode. The instantaneous flow organization indicates spanwise interaction between tip vortex and flow separation over the hydrofoil, contribute to wiggling motion over the cylindrical-shaped vortices for both breathing and double-helical cavitation modes and induces perturbation growth. The cavitation modes enhance the wandering motion of the tip vortex and change the vortex trajectory. POD analysis will be performed, revealing the spatial distribution of the unsteady flow features.

1 INTRODUCTION

Tip vortex cavitation is the first type of cavitation emerges in marine propellers, the generation of which is related to the low pressure at the vortex center [1]. The emergence of tip vortex cavitation usually accompanies by a significant increase in noise radiation and large pressure fluctuations of the ship hulls, which influences on the comfort level of passenger liners and the health of marine animals. The tip vortex is highly three-dimensional in nature near the tip, due to the strong interaction with the boundary layer and neighboring vortical structures[2]. Smaller scale flow structures are also produced around the tip vortex due to mutual interaction between the multiple streamwise vortices and flow separation. As a result, even in the wetted flows, it is challenging to predict the shape, strength and trajectory of the tip vortex. More detailed quantitative experimental evidence is essential to further understand the unsteady vortex dynamics induced by cavitation.

The present study focuses on the effect of cavitation on the tip vortex generated by NACA662-415 elliptic hydrofoil. Three-dimensional flow organization is captured by using time-resolved tomographic PIV. The experiments under different cavitation number are conducted to obtain various cavitation modes, and to establish the connection between the cavity morphology and unstable vortical structures. The streamwise vortex system and axial velocity distribution are analyzed by time-averaged flow topology. The influence of cavitation on unsteady flow features and vortex wandering is analyzed by the instantaneous flow organization. The POD analysis is performed to obtain the dominant unstable spatial mode of the vortex, shedding light on the instability mechanisms contributed by cavity surface oscillation.

2 EXPERIMENTAL SETUP AND FLOW CONDITIONS

The experiments were conducted in the cavitation tunnel at Institute of Fluid Engineering, Zhejiang University. The cross section of the tunnel is 200.5 × 200.5 mm^2 with a total length of 1020 mm. The maximum velocity is 10 m/s. The tip vortex cavitation was produced by a NACA 66$_2$-415 elliptic hydrofoil, mounted along the symmetry plane of the side wall of the test section, as shown in Figure 1. The maximum chord (c) and span (s) of the model were 83.7 mm and 100.1 mm, respectively. The free stream velocity U_∞ was set to 5.0 m/s for all the test cases. For the static pressure at atmospheric condition, the cavitation number σ is 7.8. The angle of attack was set to 9° to anticipate vortex cavitation. The tomographic PIV system features four high-speed cameras (two Photron FASTCAM Mini AX100 and two Photron FASTCAM SA4, 1024×1024 pixels) arranged in a cross-like configuration with a maximum aperture angle of 40° to obtain good reconstruction quality, as shown in Figure 1. In order to eliminate the influence of laser reflection caused by the cavity interface, the flow is seeded with fluorescent particles (poly particles, Rhodamine B dye, 35μm average diameter). The tracer particles were illuminated by a Nd:YLF high speed laser (Vlite-Hi-527–50, 50 mJ per pulse at 1 kHz). The camera lens were equipped with long-pass filters. As a result, only the light emitted by the fluorescence particles was received. The fields of view were both 53.4×28.6×15 (x×y×z) mm^3. The resultant digital image resolution is 24.6 pixel/mm. The ensemble size of the dataset is 500 snapshots, acquired at 3200 Hz.

3 PRELIMINARY RESULT

The dynamics of the tip vortex cavity are captured by high-speed image. Strong tip vortex cavitation incepts at the cavitation number of σ = 4.1, featuring a stationary double helix, as shown in Figure 2(a) referred to as 'double helical cavitation'. The cavity showed a twisted structure in space and the cross section at the largest diameter presented an elliptical shape. Arndt, Arakeri & Higuchi [3] suggested that such deformation may be associated with the initial twisting from the tip region.

In the time-averaged flow field (Figure 2(b)), the tip vortex features a helical shape until the most downstream region, which does not diffuse into the circular cylinder pattern. The wavelength of the helical structure is identical to that of the cavity, indicating a strongly influenced by the cavitaty. The cross-sectional shape of the vortex varies in the streamwise direction, yielding a vortex radius of 1.5 times of that of the wetted flow condition. Lower vorticity magnitude and faster decaying process are observed compared with the other conditions. The spanwise location of the tip vortex moves closer to the hydrofoil root.

The instantaneous flow features reveals a significant distortion of the tip vortex, indicating contribution of cavity vibration on the unsteadiness of the vortical structures. Stronger vortex shedding phenomenon is produced. The separated vortices are entrained into tip vortex, leading to more intense interaction and vortex stretching. Small-scale structures emerge over and around the tip vortex. The secondary structure is further distorted into smaller discrete fragments. The deformation of both the primary and secondary vortex implies faster growth of elliptical instability in the cavitation flow. Although small-scale vortex structures becomes more populated and rather dominant, the twisted shape corresponding to that of the cavity can still be identified. The onset of vortex instability will be further elaborated by extracting the fluctuating component of streamwise vortex.

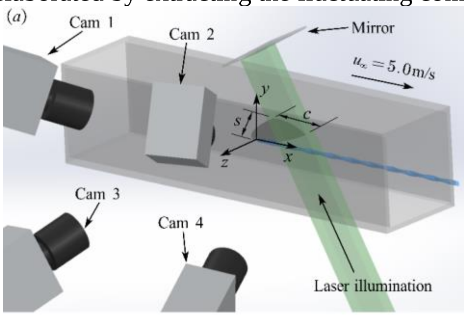

Figure 1. Conceptual sketch of tomographic PIV setup.

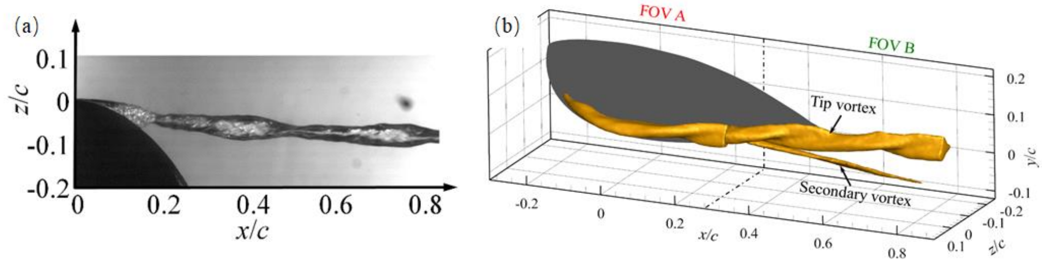

Figure 2. (a) Flow visualization of tip vortex cavity; (b)Iso-surfacee of time-averaged streamwise vorticity .

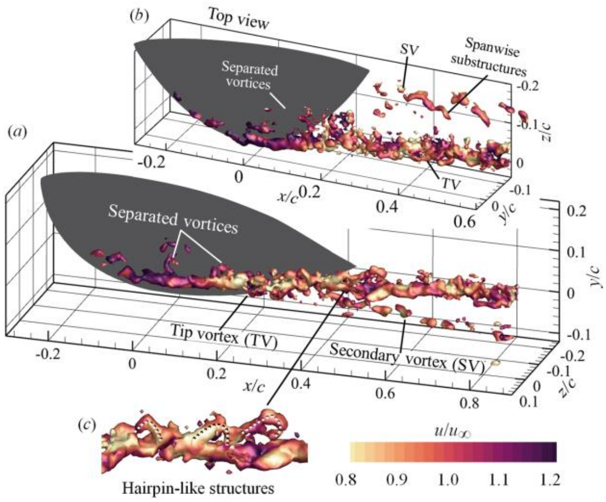

Figure 3. Instantaneous flow organization of double helical cavitation .

4 REFERENCES

- Arndt, R.E.A., (2002). Cavitation in vortical flows. Annual Review of Fluid Mechanics, **34**(1): p. 143-175.
- Asnaghi, A., Svennberg, U., & Bensow, R.E. (2020). Large eddy simulations of cavitating tip vortex flows, Ocean engineering, **195**: p. 106703
- Arndt, R.E.A., Arakeri, V.H., & Higuchi, H. (1991) Some observations of tip-vortex cavitation, Journal of Fluid Mechanics, 1991, 229: p.269-289.

The Viscous Effect on the Droplet–Liquid Pool Impact

Guilherme M. Bessa[1] and David S. Nobes[1*]
1: Dept. of Mechanical Engineering, University of Alberta, Canada
* Correspondent author: dnobes@ualberta.ca

Keywords: Droplet Impact, Interfacial Flows, Vortex Ring, Rayleigh Jets, PIV

ABSTRACT This investigation focuses on the impact of droplets on a deep liquid pool. Despite over a century of research, the dynamics and variables governing the problem during early and late impact regimes remain poorly understood. To shed light on this intriguing phenomenon, time-resolved particle image velocimetry is used to probe deeper into the flow field within the liquid domain. The primary parameters varied in the present study are the droplet size, impact height, and fluid rheology.

1 INTRODUCTION

A present concern in several *ex-vivo* medical devices is a leakage leading to blood dripping, which may be resulting in damage to the blood cells, known as hemolysis. Despite decades of hemolysis-related research, seminal questions remain about how different types of fluid stresses result in red blood cell (RBC) membrane disruption. To address this hypothesis, the present work aims to investigate the stress distributions over the entire time domain of a drop impact on a liquid surface under a comprehensive range of Froude and Weber numbers. For such, an experimental setup was designed to allow flow measurements with Particle Image Velocimetry (PIV). As blood is a shear-thinning fluid, non-Newtonian solutions, similar to blood, are used to consider nonlinear rheological effects. Newtonian solutions with different water and glycerol concentrations and pure water are used for comparison. From a fluid mechanics point of view, while the study of drop impact kinematics has been well explored over the last few decades thanks to high-speed imaging techniques and numerical analysis, research on drop impact dynamics has only gained momentum in the last 10 years and is still requiring further efforts. Quantitative measurements of the stress distributions underneath impacting drops are highly demanding and are important not only for verifying the key assumptions made here but mainly to understand the phenomenon as a whole. All in all, as it is known that extensional flow causes the deformation of a fluid particle, and consequently deforms the RBC membrane *a priori*, the present study will focus on measuring the spatiotemporal features of the stress distributions from early- to late-impact regimes.

2 METHODOLOGY

An experimental setup was designed to enable optical access to the flow field below the drop impact point on a liquid surface. An acrylic container is used to hold the liquid pool seeded with tracer particles. To investigate the role of viscous effects in the transient event resulting from droplet impact, two non-Newtonian blood-type solutions are prepared with 40% w/w water-glycerol, one with 200 ppm of xanthan gum and the other with 400 ppm. Furthermore, for comparison purposes, pure water and two other Newtonian solutions are also included in the study: aqueous-glycerol mixtures at 20% and 40% w/w. The droplet is impinged on the liquid surface by using a syringe featured with different-sized needles to generate droplets of approximately 2.5, 4.0, and 5.5 mm. A syringe pump drives the syringe for dispensing drops in a controlled manner. The impingement height is varied by using a vertical traverse system. A single high-speed camera (Phantom v611, Vision Research, Inc., USA) is used to capture both, the drop impact velocity and the flow field below the liquid surface. The experiment is performed using a continuous-wavelength DPSS laser (LRS-0532 Series, LaserGlow Technologies).

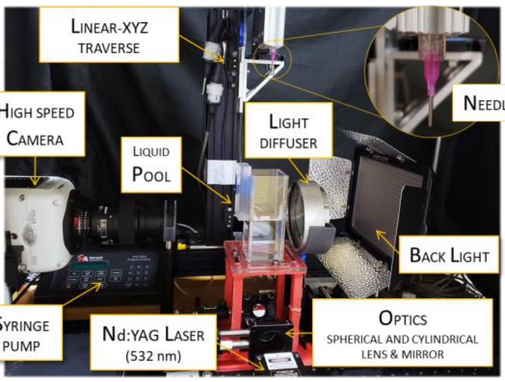

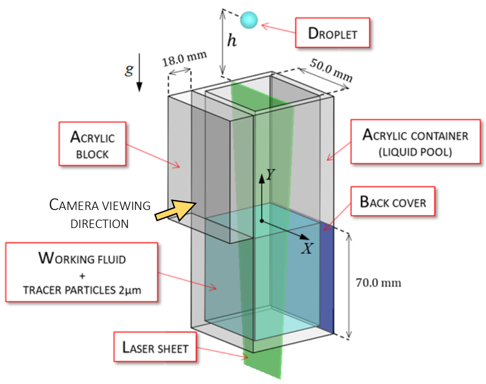

Figure 1. On the left-hand side, a photo of the experimental apparatus shows the main setup components. On the right side, is a 3D schematic representation of the square acrylic container used as a liquid pool.

3 RESULTS

The experimental results of the impact behavior of droplets of two different fluids, pure water, and water-glycerol 40% w/w, are presented below. The experiments were conducted under similar initial conditions (Froude ~ 50) to provide a comparative analysis of the droplet impact dynamics. Figure 2(a) shows a sequence of snapshots that depict the key moments of the water droplet impact process. Immediately after impact, a hemispherical cavity is formed in the quiescent liquid. The size of the cavity increases, and a wave swell forms on its periphery and propagates radially outwards. The streamlines indicate that during the collapse stage of the cavity, a vortex ring is formed at the cavity apex (t = 33.4 ms) and moves downwards while an inertia-driven central jet emerges (t = 39.8 ms) above the liquid surface. Due to Rayleigh-Plateau instabilities, the jet releases a drop (t = 64.8 ms) that, upon coalescing with the liquid pool (t = 143.9 ms), forms a second vortex ring (t = 215.6 ms) that carries away part of the energy of the impinging drop. A comprehensive description of the events underlying the impact of a water droplet can be found in Leng (2001). Figure 2(b) shows the sequential snapshots of the glycerol-water drop impact case. In this scenario, the size of the cavity increases, and its form changes. Eventually, it takes on a conical shape with a small cylindrical dimple at its bottom, as indicated in Figure 2(c). When the cavity begins to recede, the dimple is quickly pinched, and a liquid jet, narrower and faster than the jet seen in the case of water, is ejected out of the cavity. A small droplet with a diameter of approximately 0.3 mm, indicated by a black arrow in the frame at t = 30.5 ms, precedes the jet tip. It has been suggested that at a given flow regime the liquid viscosity dampens the smaller capillary waves created at impact while enabling the larger ones to travel deeper into the cavity (Michon *et al.* 2017). In this way, the cavity collapse process maintains its self-similar behavior for a prolonged period, leading to the formation of a high-pressure stagnation point where the cavity closes, ejecting a small droplet before the jet emerges. In this case, the vortex ring barely forms (t = 30.5 ms) and soon breaks down due to the higher viscous dissipation rate of the water-glycerol solution. The criteria for the generation of the vortex ring, which require a balance between inertia, capillary, and viscous forces, have been quantified in terms of Weber and Ohnesorge numbers. It is observed that there is a critical threshold for both dimensionless numbers below which a vortex ring is formed, as pointed out by Behera *et al.* 2019.

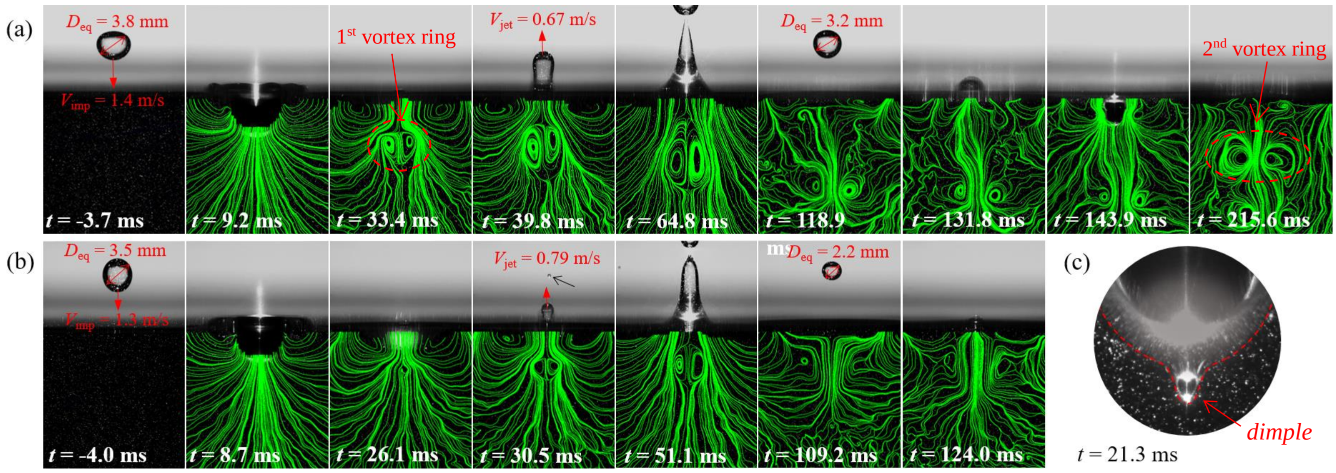

Figure 2. The sequence of snapshots of the impact process of water and water-glycerol droplets showing the streamlines superimposed onto it. (a) Water case: Fr = 55, We = 105, Re = 5189, and Oh = 0.0020. (b) Water-glycerol 40% w/w case: Fr = 50, We = 95, Re = 1396, and Oh = 0.0070. (c) A snapshot of the moment a dimple is formed at the bottom of the cavity opened due to the impact of the water-glycerol droplet.

4 CONCLUSIONS

The cascading events following the impact of a drop in a deep liquid pool are discussed. It is shown that different jets can emerge based on the Froude, Weber, and Reynolds numbers, which are utilized to characterize the impact parameters, and that viscosity is an important variable for describing cavity retraction and subsequent jet dynamics. The occurrence of vortices in the flow domain is also investigated and characterized quantitatively using the dimensionless Ohnesorge and Weber numbers. The present study will focus on measuring the spatiotemporal features of the shear-stress distributions from early- to late-impact regimes to evaluate whether the fluid stresses arising from the drop impact reach levels that can translate into red blood cell membrane failure. The presentation will discuss the experimental setup and review preliminary results.

5 REFERENCES

- Behera, M. R., Dasgupta, A., & Chakraborty, S. (2019). On the generation of vorticity and hydrodynamics of vortex ring during liquid drop impingement. *Physics of Fluids*, 31(8), 082108.
- Leng, L. J. (2001). Splash formation by spherical drops. *Journal of Fluid Mechanics*, 427, 73-105.
- Michon, G. J., Josserand, C., & Séon, T. (2017). Jet dynamics post drop impact on a deep pool. *Physical Review Fluids*, 2(2), 023601.

X-ray densitometry of ventilated cavities in the wake of a bluff body

Udhav U. Gawandalkar*[1] Nicholas Lucido[2], Prachet Jain[2]
Christian Poelma[1] Steven Ceccio[2,3], Harish Ganesh[2]
1: Process and Energy, Mechanical Engineering, Delft University of Technology, The Netherlands
2: Department of Naval Architecture and Marine Engineering, University of Michigan, Ann Arbor, USA
3: Department of Mechanical Engineering, University of Michigan, Ann Arbor, USA
* Correspondent author: u.u.gawandalkar@tudelft.nl

Keywords: ventilated cavities, super cavity, x-ray densitometry, void fraction fields

ABSTRACT Natural cavitation refers to the formation of unstable vapour cavities when the flow pressure drops below the vapour pressure. Ventilated cavities (VC), on the other hand, can be created *artificially* at fairly high pressure by injecting non-condensable gas behind a flow separating body called `cavitator'. This approach has gained significant attention due to its potential application in drag reduction in underwater transport. Further, VCs also find application in hydraulic engineering and process industries to mitigate the deleterious effects of natural cavitation such as wear, erosion, and vibrations.

For such applications, stable ventilated cavities are desired. Thus, flow conditions favouring stable cavities is of interest. The stability of the cavity depends on the rate of gas ejection out of the cavity which in turn is a function of the way cavity `seals-off', i.e. cavity closure [1]. Moreover, it is necessary to know a priori the volume of gas required for the ventilation to decipher the gas-ventilation demands. Therefore, it is critical to understand the physical mechanism responsible for gas-entrainment and leakage to optimise the benefits of ventilated cavities. Currently, the gas entrainment behind a 2-D bluff body as a cavitator remains unexplored, as most of the current studies deal with axisymmetric[1] [2], or wall-bounded cavitator [3]. Ventilated cavity flows are inherently turbulent, frothy and optically-opaque, all of which adds to the complexity of the flow. Thus, conventional light-based measurement techniques cannot provide any meaningful experimental observations of the internal flow in the cavity. Further, the liquid-gas interface and frothy cavity closure (critical for understanding entrainment-leakage physics) remains inaccessible. Consequently, we employ time-resolved X-ray densitometry to study the entrainment of gas in the wake of 2-D wedge. Moreover, the unique void fraction dataset can be used to validate the relevant numerical models.

The experiments are performed in University of Michigan 9-inch recirculating water tunnel with a test-section having a square cross-section of 76 × 76 mm^2. The ventilated cavities are generated behind a 2-D wedge having a height (H) of 19 mm, width (W) of 76 mm, and an angle of 15° (see figure 1a) . The wedge has an internal bore leading to multiple 1mm holes ventilation as shown in figure 1a. The non-condensable gas is injected through these holes in the wake of the wedge via a flow controller which maintains a precise gas mass flow rate ($\dot{Q}$). The gas mass flow rate is expressed as ventilation coefficient (C_{qs}), while the flow velocity (U_∞) is expressed as Fr. Each experiment is performed by fixing U_∞ (Fr), while ramping up the ventilation rate from no injection to the desired $\dot{Q}$, where it plateaus for 10 secs. The table summarises the range of flow parameters used.

U_∞[ms^{-1}] : {0.84 - 6.2}	$Fr = \frac{U_\infty}{\sqrt{gH}}$: {2 - 14.7}	$\dot{Q}$[SLPM] : {0 – 50}	$C_{qs} = \frac{\dot{Q}}{U_\infty WH}$: {0.01 - 0.12}

The qualitative observation of ventilated cavities is performed via high-speed imaging. Further, projected (y-averaged) void fraction fields are measured using time-resolved x-ray densitometry system elaborated in [4]. The current and the voltage of the x-ray source are set to 140 mA and 60 kV respectively, leading to measurement time of 1.6 s. The FOV corresponding to X- ray densitometry spans ($8.2H \times 4H$) in the $x{-}z$ plane. The final void fraction fields are evaluated with a spatial resolution of 0.16 mm ($0.0084H$) and a temporal resolution of 0.001 s.

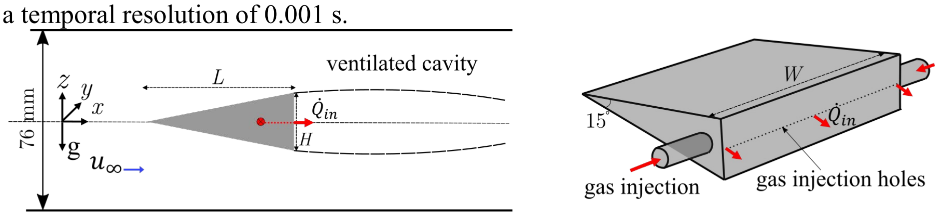

Figure 1. A schematic of the experimental setup (red arrows show the gas ventilation direction)

The ventilated cavities behind the wedge exhibit four different modes as a function of the ventilated coefficient (C_{qs}) and Fr as illustrated in the regime map (figure 2a). At low ventilation coefficient (red region in figure 2a), the *open* foamy cavity (FC) is seen which is marked by injected gas entrainment in the shear layer in the wake of wedge. The entrained gas is ejected periodically via Von Kármán vortex street as shown in figure 2b. At low Fr (<5), as C_{qs} is increased, dispersed gas bubbles coalesce to form a supercavity, having a mild re-entrant flow at its closure and two prominent branches near the walls. Consequently, they are termed as twin branched cavities (TBC) (green region in figure 2a). The cavity cambers up due to the buoyancy of the entrained gas (see figure 2c). Further, the gas is ejected via two routes: (i) the narrow mid-tail where a mild re-entrant flow ejects gas, (ii) the gas is also ejected periodically in chunks at the two branches via a growing instability.

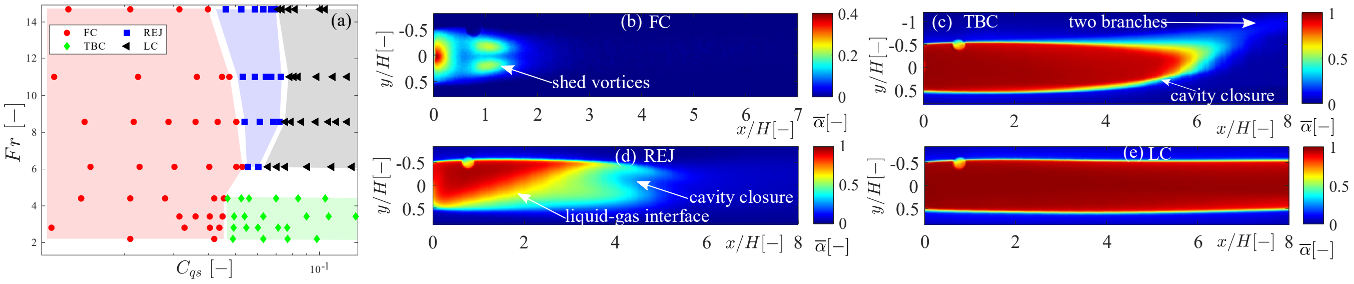

Figure 2. (a) The regime map (Fr-C_{qs}) showing different modes of ventilated cavities behind the wedge. The average void fractions corresponding to (b) Fr=14.8, C_{qs}=0.023 (c) Fr=2.2, C_{qs}=0.059, (d) Fr=6.27, C_{qs}=0.059 (e) Fr=11, C_{qs}=0.098.

At the higher Fr (> 6), open FC-type cavities exists at low C_{qs}. At intermediate C_{qs} , a supercavity is formed with a strong re-entrant flow (REJ) at the cavity closure (see blue region figure 2a). The cavity closure is marked by a stagnation point, which in combination with a strong adverse pressure gradient drives a significant liquid *into* the cavity (see figure 2d and figure 3b) (U_{REJ} ~ 1.8 ms^{-1}). The gas gets accumulated at the top due to the gravity. Further, the gas is ejected out periodically from the upper and lower half of the cavity (see figure 3b, c). Moreover, when the REJ front (red arrow in figure 3) impinges on the wedge, a larger gas ejection takes places from the bottom half as shown in figure 3f. Thus, the gas ejection is multimodal.

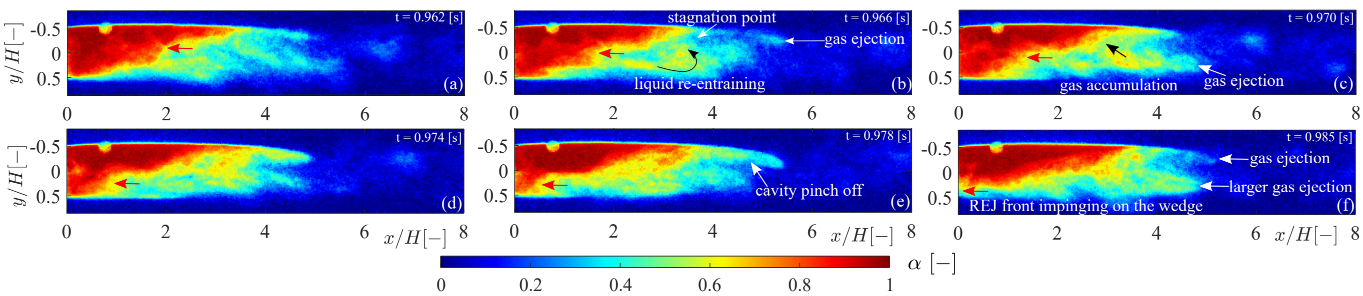

Figure 3. The dynamics of REJ cavity at Fr = 6.27, C_{qs} = 0.059. The red arrow shows the re-entrant jet front moving upstream.

With further increases in C_{qs}, the re-entrant jet recedes away from the wedge as the ventilated cavity grows as shown by a black arrow in figure 4. The cavity grows longer than 12H and are referred to as long cavities (LC) (see figure 2e). The internal flow in the cavity is not significant and the gas is ejected out in chunks by a growing instability at the cavity closure. In summary, X-ray densitometry has revealed critical features of the ventilated cavities such as cavity internal flow and cavity closure, generally inaccessible to the conventional measurement technique. The ventilated cavities are currently being studied more quantitatively (gas ejection frequency, gas ejection rate, and REJ velocity) to decipher scaling laws.

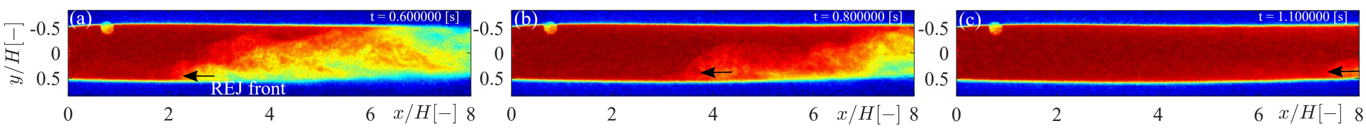

Figure 4. The formation of long cavities (LC) cavity at Fr = 11, C_{qs} = 0.098. The black arrow shows re-entrant flow front.

REFERENCES

[1] Vladimir N. Semenenko, "Artificial Supercavitation. Physics and Calculation," Kyiv, Ukraine, 2001.

[2] A. Karn, R. E. A. Arndt, and J. Hong, "An experimental investigation into supercavity closure mechanisms," *J. Fluid Mech.*, vol. 789, pp. 259–284, 2016, doi: 10.1017/jfm.2015.680.

[3] S. Qin, Y. Wu, D. Wu, and J. Hong, "Experimental investigation of ventilated partial cavitation," *Int. J. Multiph. Flow*, vol. 113, pp. 153–164, 2019, doi: 10.1016/j.ijmultiphaseflow.2019.01.007.

[4] S. A. Mäkiharju, C. Gabillet, B. G. Paik, N. A. Chang, M. Perlin, and S. L. Ceccio, "Time-resolved two-dimensional X-ray densitometry of a two-phase flow downstream of a ventilated cavity," *Exp. Fluids*, vol. 54, no. 7, 2013, doi: 10.1007/s00348-013-1561-z.

Day 2

PLENARY LECTURE
by Yassin Hassan

Chaired by Andrea Sciacchitano

Flow Visualization and Measurements in Complex Geometries of Nuclear Reactor Applications

Yassin A. Hassan[1,*]
1: Dept. of Nuclear Engineering, Texas A&M University, College Station, USA.
J. Mike Walker Dept. of Mechanical Engineering, Texas A&M University, College Station, USA.
* Correspondent author: y-hassan@tamu.edu

Keywords: Particle Image Velocimetry (PIV), Matched Index of Refraction (MIR), Nuclear Reactors, Rod Bundles.

ABSTRACT Fluid dynamics investigations in nuclear reactor cores are important to characterize thermal hydraulic responses in nuclear fuel assemblies. Nuclear reactor assemblies often consist of complex geometries where the opacity of the fuel elements pose limitations to investigate internal velocimetry characteristics. The implementation of flow visualizations using the matched-index-of-refraction (MIR) based particle image velocimetry (PIV) allows a quantification of several fluidics parameters overcoming the complexities – critical toward the safety and optimization of nuclear reactor designs.

The next generation of nuclear reactor designs, Generation IV, consist of several innovative nuclear reactor designs such as the Liquid Metal Fast Reactor (LMFR), Gas-cooled Fast Reactor (GFR), Pebble Bed Reactor (PBR), etc. The core of a nuclear fuel assembly usually consist of complex rod bundle arrangements or randomly packed spherical nuclear fuel elements [1]. To overcome this critical limitation, the MIR method (illustrated in Fig. 1 (b)), using two materials with the same optical indices of refraction allow for non-intrusive quantification of fluid dynamics behavior using PIV. Experimental PIV measurements were successfully performed in a randomly packed spherical bed used in PBRs (Fig. 1 (a)), to evaluate accident condition behavior in a 61-pin wire-wrapped LMFR fuel assembly due to blockages (Fig. 1 (c)), as well as to obtain an understanding of the core fluid dynamics behavior in the newest 127-pin LMFR core designs (Fig. 1 (d)).

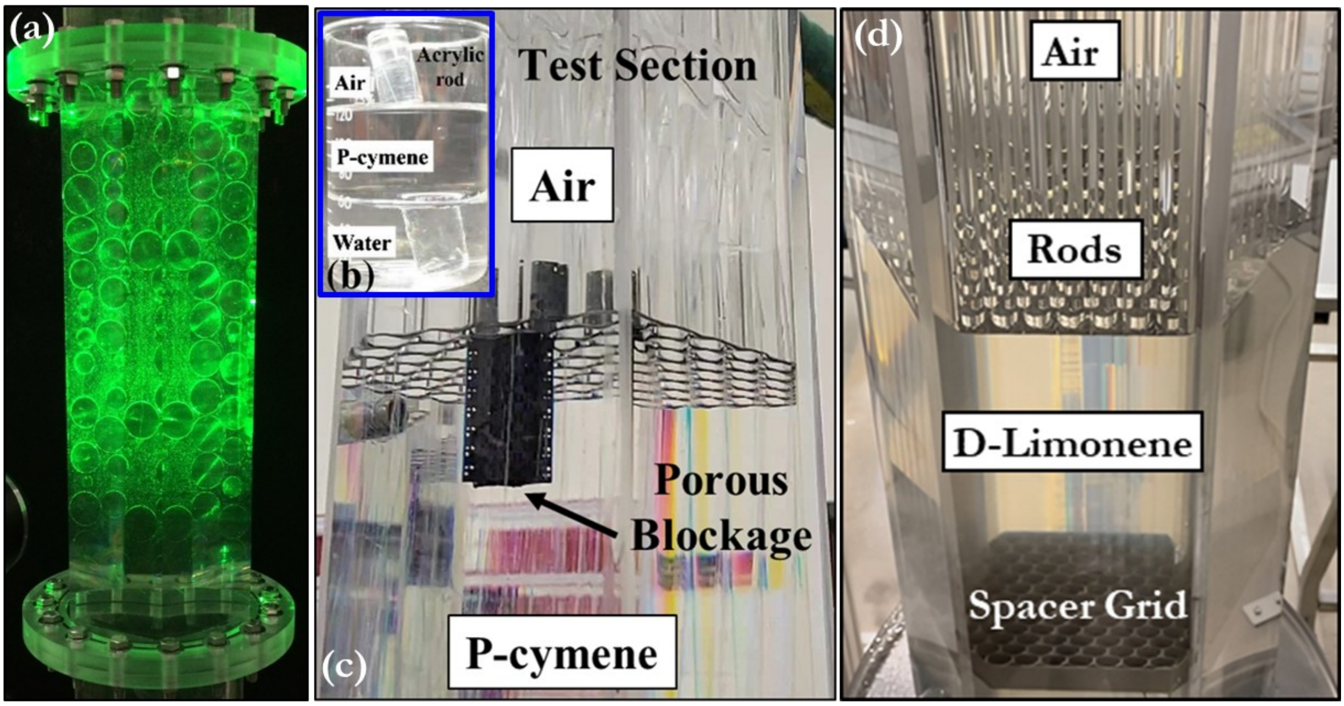

Figure 1. (a) The applications of PIV to nuclear reactor geometries facilitate the study of fluid dynamics in complex geometrical arrangements such as randomly packed spherical bed arrangements for PBR applications. (b) Demonstration of the MIR method with an acrylic rod submerged in water, p-cymene and air. (c) PIV experiments for accident condition

investigations due to porous blockages in a 61-pin wire-wrapped LMFR fuel assembly. (d) MIR demonstration for PIV tests in the largest experimental 127-pin LMFR fuel assembly in the world.

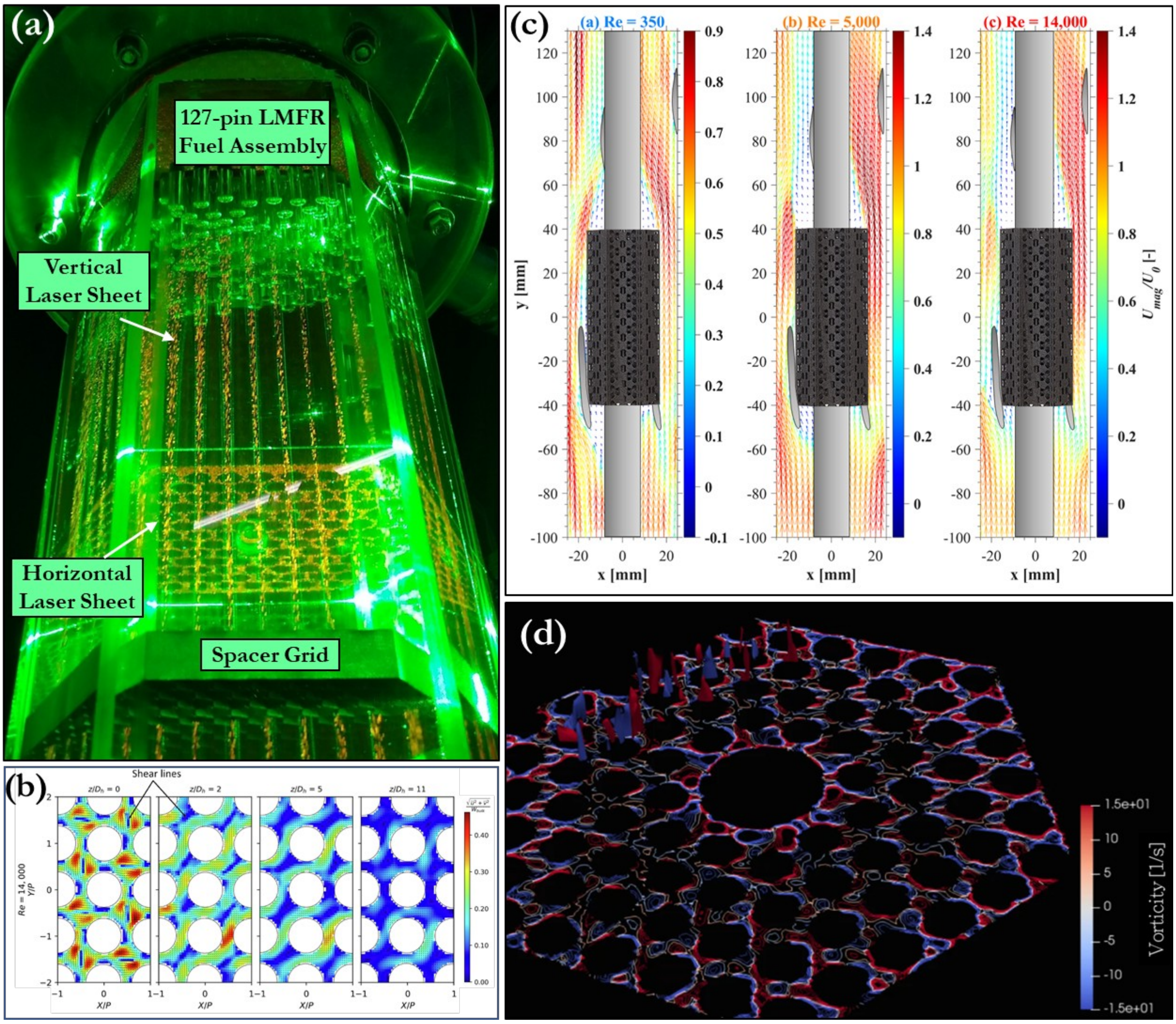

Figure 2. (a) TR-PIV tests for simulataneous vertical and horizontal planar measurements in the 127-pin prototypical LMFR fuel assembly. (b) Velocity magnitude for accident conditions due to a porous blockage in a 61-pin wire-wrapped LMFR fuel assembly. (c) Cross-flow studies showing velocity magnitudes emerging due to a mixing vane spacer grid in a 5x5 PWR fuel assembly. (d) Vorticity isosurfaces at the near-wall plane from PIV for a 84-pin GFR fuel assembly.

The successful implementation of PIV using MIR in complex fuel assemblies (an example seen in Fig. 2 (a)), allows the quantification of velocimetry parameters which are critical to understand flow responses in systems such as sensitive nuclear core fuel bundles. Characteristics such as wake regions, recirculation regions, flow attachment lengths, shear layers can be easily identified in critical regions to study the nominal nuclear reactor flow behavior (Fig. 2 (b)) or accident conditions (Fig. 2 (c)) – enabling the enhancement of the safety of such systems [2]. Turbulence studies in the wake regions of nuclear fuel spacer elements can be further investigated to optimize their designs (Fig. 2 (d)). The high-fidelity PIV data for such nuclear fuel assemblies significantly assist in the development and validation of computational fluid dynamics models [3].

1 REFERENCES

- Hassan, Y. (2019). High-fidelity experimental measurements for modeling and simulation of nuclear engineering applications. Nuclear Engineering and Design, 354, 110181.
- Menezes, C., Melsheimer, T., Pyle, D. W., Kinsky, M., & Hassan, Y. A. (2023). Flow characteristics within an interior subchannel of a 61-pin wire-wrapped hexagonal rod bundle with a porous blockage. Physics of Fluids, 35(2), 027106.

- Matozinhos, C. F., Tomaz, G. C., Nguyen, T., & Hassan, Y. (2021). Experimental investigation of turbulent flow characteristics in cross-flow planes of a 5× 5 rod bundle with a spacer grid. International Journal of Heat and Fluid Flow, 87, 108757.

TECHNICAL SESSION 7
UNSTEADY FLOWS

Chaired by Chuangxin He

Enhancement of Vortex Ring Circulation via Leapfrogging

Rigoberto Ortega[1,*] Lian Gan[1], and Phillip Gaskell[1]
1: Dept. of Engineering, Durham University, United Kingdom
* Correspondent author: rigoberto.ortega-chavez@durham.ac.uk

Keywords: vortex ring, leapfrogging, early time evolution, PIV,

ABSTRACT The formation of a pair of vortex rings and their early time evolution, resulting from the controlled discharge of an incompressible, Newtonian fluid into a stationary equivalent fluid bulk, is explored using two-dimensional particle image velocimetry (PIV) for a combination of different parameters, namely the stroke ratio (L/D_o), that describes the size of the ring, and the time difference between discharges. The experiments were performed in a tank of dimensions 900×800×2400 mm; a piston driven by a stepper motor was used to generate the vortex rings. The water displaced was supplied to the piston via two hoses connected to a secondary pipe mounted at the centre of one of the tank's side walls and extending into the tank a distance of approximately 200 mm, where an orifice plate with an orifice diameter, D_o, of 32 mm was located. This secondary pipe houses an inner pipe which could be rotated using a stepper motor connected to the inner pipe through a nozzle containing a series of surface holes, allowing water to enter it. This arrangement facilitates the addition of swirl to the resulting vortex ring flow. For all of the cases explored the Reynold number (U_oD_o/ν) is 2000. A Photron WX100 camera was located next to the water tank to obtain a field of view (FOV) of 10Do×5D_o, running at a frame rate of 250 Hz. A continuous 5W laser was employed for the PIV system. The cross-correlation interrogation window size applied is 16×16 pixels and 50% overlap giving a spatial resolution of 0.86 mm based on vector spacing.

Leapfrogging of two vortex rings consists of an increase in the radius of the leading ring and corresponding decrease of the radius of the following ring due to the interaction of their velocity fields. In turn, the propagation velocity of the leading ring decays whilst that of the following one is enhanced so that the latter catches up with and passes the leading ring. Previous research has observed that ring radius variation is strongly related to the kinetic energy of the ring, and by association, the formation number, defined by Gharib et al. (1998) as the maximum stroke ratio required to form a vortex ring without a trailing jet. The present work aims to define the best combination of parameters (L/D_o and time between discharge) using Leapfrogging to find the optimum following ring radius behaviour leading to an increase in its circulation.

Figure 1 shows three cases (A, B, C) where the time between discharges is a minimum for A, increasing by 60% for C, the leading and following ring has an L/D_o of 2.5 and 4, respectively. Each contour plot represents two-second intervals in the formation of the following vortex ring. The results reveal that reducing the time between discharges decreases the growth of the following ring radius over time, destabilising the vortex core. In figure 2 the following ring's radius and circulation over time is presented for case A, B and C; shown for comparison purposes is the case for an isolated ring. For case B and C, reduction of the following ring's radius increases the ring circulation in agreement with the results obtained by Dabiri & Gharib (2005); in their experiment they manipulated the nozzle diameter during the ring formation process, reducing the growth of its radius and increasing its formation number, and thus its circulation. At later times this effect is lost because the instabilities in the vortex core generated by the leading ring accelerate the vortex breakdown of the following ring. The lower levels of circulation with time for Case A, compared to the other cases, can be explained as being due to vorticity cancelation between the cores promoted by a higher reduction of radial growth when compared with the other cases, suggesting the existence of a critical following ring radius.

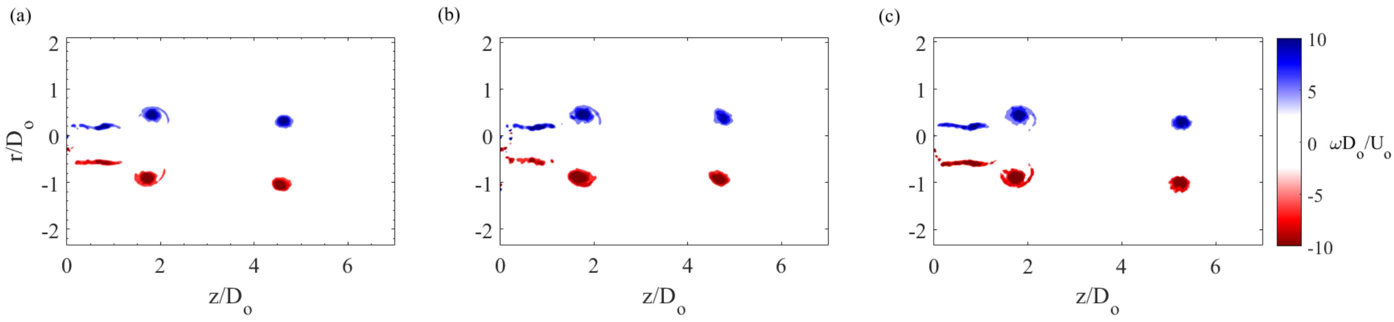

Figure 1. (a-c) Contour plot of vorticity magnitude for different times between discharges. From left to right, cases A at $T^*(tU_o/D_o)$=8.2, B at T^*=8.6 and C at T^*=9.4 respectively.

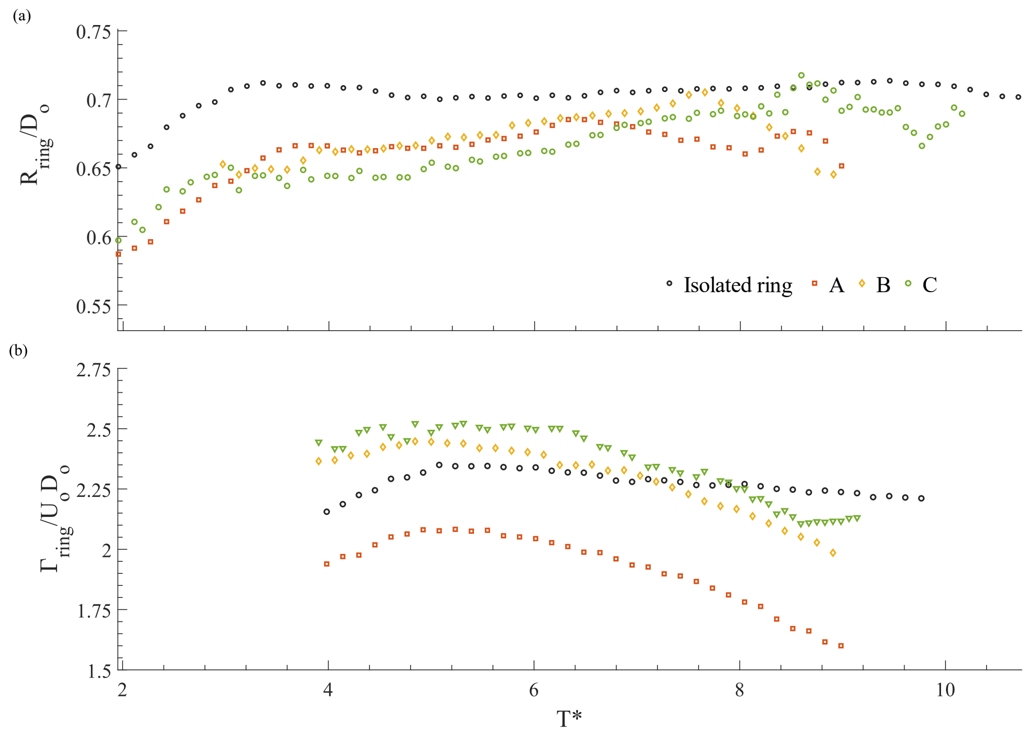

Figure 2. Evolution of the following ring's radius (a) and circulation (b) with time, for the different discharge times A, B, and C; shown also is the case for an equivalent following isolated ring in the absence of a leading ring.

REFERENCES

- Gharib, M., Rambod, E. & Shariff, K. 1998 A universal time scale for vortex ring formation. J. Fluid Mech. 360, 121–140.
- Dabiri, J. O & Gharib, M. 2005 Starting flow through nozzles with temporally variable exit diameter. J. Fluid Mech. 538, 111–136.

How similar is the starting vortex in a repeated experiment?

Jesse Reijtenbagh[1,*], Willem van de Water[1] and Jerry Westerweel[1]
1: Laboratory for Aero & Hydrodynamics, Delft University of Technology, the Netherlands
* Correspondent author: j.reijtenbagh@tudelft.nl

Keywords: Turbulence, PIV, Coherent structures, Vortex Dynamics

Every measurement contains uncertainty. In order to obtain relevant statistics and reproducible data an experiment should be repeated to reduce this uncertainty. However, velocity measurements in a starting flow will vary slightly between different realizations of the same experiment due to minor variations in initial conditions. The question is how to visualize the variation in repeated experiments. The differences in repeated experiments reveal instability mechanisms and the pathway to turbulence. To demonstrate these instability mechanisms, we study an unsteady flow behind an accelerated plate, an experiment that is repeated 42 times with robotic precision. The wake behind the plate evolves from coherent vortices to turbulence.
How vortices form behind a starting plate was already analyzed by Prandtl [1904], and is described by many researchers during the last century, for example Koumoutsakos and Shiels [1996] and Lucini and Tognaccini [2002]. These researches mainly focus on the formation of the starting vortex ring behind the plate, and therefore the distance the plate has travelled during this research is rather short and a turbulent wake has not been formed yet. The present research considers a larger distance to the point where the wake becomes turbulent.

In our experiments we measure the flow field around a 1:2 aspect ratio rectangular plate with a frontal area A = 0.020 m^2, that is uniformly accelerated with a = 0.82 m/s^2 to its final velocity U = 0.4 m/s, which corresponds to a Reynolds number of 40×10^3. The experiments were carried out in a $2.0\times2.0\times0.5\ m^3$ water-filled tank, where an industrial gantry robot was used to accelerate the plates. Planar PIV measurements were done to measure the instantaneous velocity field and circulation. We repeated this experiment 42 times. Further details on the setup can be found in Grift et al. [2019].

Given that the gantry robot replicates the movement very precisely, the measured velocity and vorticity fields are almost identical for different realizations during the starting motion and lose this similarity as the wake becomes more turbulent. Figure 1 shows the ensemble averaged vorticity field at different locations of the plate. Since this is averaged over 42 repetitions of the experiment, the fluctuations between the different repetitions are averaged out and the large scale structure remains. The question is how to visualize and quantify the similarities and differences between different repetitions of the experiment.

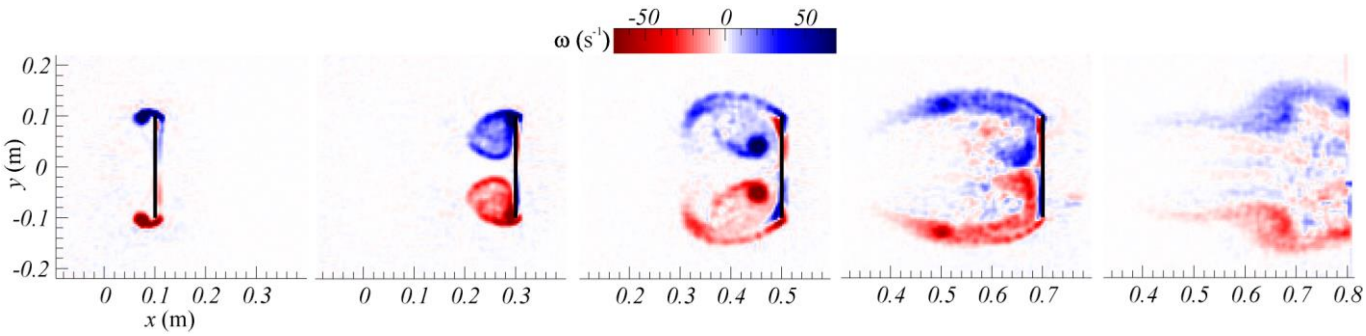

Figure 1. Ensemble averaged vorticity at travelled plate distances x = 0.1 m, 0.3 m, 0.5 m, 0.7 m, 0.82 m. The plate leaves the field of view at x = 0.814 m.

As an intuitive way to directly compare repetitions of the experiment we defined a difference field to describe the variation in the wake of the plate. In this difference field we consider 2 fluid parcels that start at the same location and time in different experiments, and track their distance d_T after time T. Since we have 42 repetitions of the same experiment, we can determine this difference field for 861 distinct pairs of different experiments. Figure 2(a) shows the average difference field over the 861 pairs for multiple plate locations.

Another method to characterize the wake behind the plate is the Finite-time Lyapunov exponent (FTLE), see Shadden et al. [2005] and Haller [2015]. The FTLE field Λ_T is based on the largest eigenvalue of the local Cauchy-Green strain tensor and

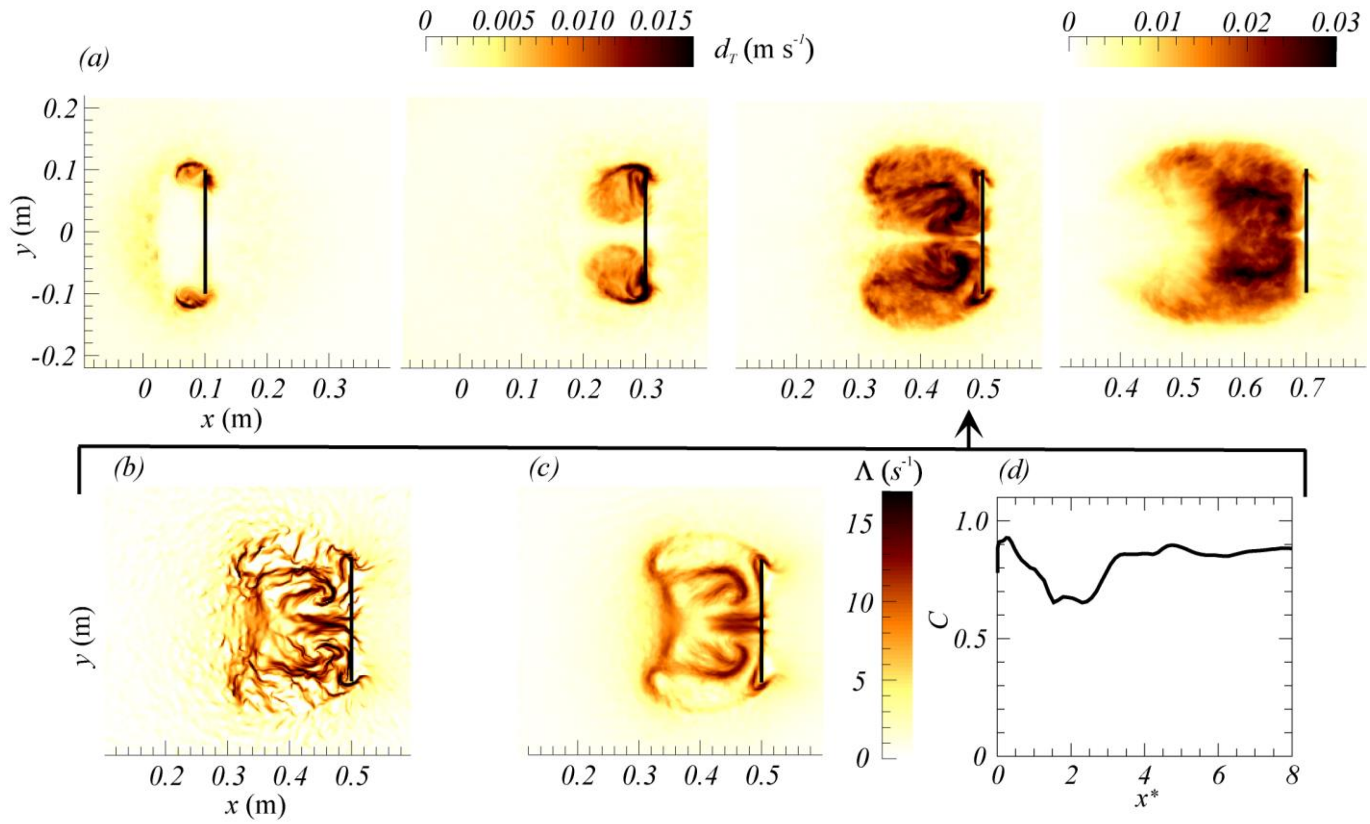

Figure 2. Difference and FTLE fields. (a) Average difference field at x = 0.1 m, 0.3 m, 0.5 m, 0.7 m, averaged over all 861 distinct pairs of the ensemble. Notice the change of scale at x = 0.7 m. (b) The FTLE field of a single realisation of the experiment at travelled distances x = 0.5 m. (c) Average FTLE-field at x = 0.5 m over 42 realisations. (d) Normalized correlation between the averaged FTLE field and the difference field over the full length of the experiment. Note x* is the travel distance of the plate made dimensionless with the plate height, i.e. x* = x/0.1.

indicates the exponential separation over a given time T of two infinitely close fluid parcels during a single experiment. Figure 2(b) shows the FTLE-field in a snapshot from one experiment, Figure 2(c) shows the average FTLE field for a single location from 42 different experiments. The average shows lines of local maxima at approximately the same locations as the FTLE field from a single experiment, however the average field contains less explicit lines. This shows again that the structure of different experiments is very similar, and only has small fluctuations on smaller scales. The average FTLE field shows a remarkable resemblance with the average difference field. This is supported by Figure 2(d), which shows the correlation between the FTLE-field and the difference field for the full length the experiment.

From Figure 2 we conclude that these experiments show some form of ergodicity. For turbulent flows this means the statistical properties of an ensemble are the same as those obtained from the time average of a single ensemble member, see Frisch [1995] and Galanti and Tsinober [2004] . Here we see that the temporal dynamics of a single ensemble member (shown by FTLE) predicts the variability between experiments (shown by the difference field).

REFERENCES

Frisch, U. (1995). Turbulence: the legacy of A. N. Kolmogorov. Cambridge University Press, Cambridge.

Galanti, B. and Tsinober, A. (2004). Is turbulence ergodic? Phys. Lett. A, 330:173–180.

Grift, E. J., Vijayaragavan, N. B., Tummers, M. J., and Westerweel, J. (2019). Drag force on an accelerated submerged plate. J. Fluid Mech., 866:369–398.

Haller, G. (2015). Lagrangian coherent structures. Annu. Rev. Fluid Mech., 47:137–62.

Koumoutsakos, P. and Shiels, D. (1996). Simulations of the viscous flow normal to an impulsively started and uniformly accelerated flat plate. J. Fluid Mech., 328:177.

Lucini, P. and Tognaccini, R. (2002). The start-up vortex issuing from a semi-infinite flat plate. J. Fluid Mech., 455:175–193.

Prandtl, L. (1904). ˙Uber Fl¨ussigkeitsbewegung bei sehr kleiner Reibung. In Verhandlungen des III. Internationalen Mathematiker- Kongresses, volume 904, pages 484–491. Leipzig: B. G. Teubner 1905.

Shadden, S. C., Lekien, F., and Marsden, J. E. (2005). Definition and properties of Lagrangian co-herent structures from finite-time Lyapunov exponents in two-dimensional aperiodic flows. Physica D: Nonlinear Phenomena, 212(3):271 – 304.

Visualization of Aerodynamic Performance of FIV-based Energy Harvesting System

Aref Afsharfard[1], Amirreza Shahsavari[1], and Kyung Chun KIM[1,*]
1: Pusan National University, School. of Mechanical Engineering, Eco-Friendly Smart Ship Parts Technology Innovation Center, Busan 46241, Republic of Korea
* Correspondent author: kckim@pusan.ac.kr

Keywords: PIV, Flow-Induced Vibration, Oscillating cylinder, Visualization, Energy Harvesting

ABSTRACT With the world's population growing and more and more developing countries becoming industrialized, it will need more energy than ever before. Regarding this issue, over the past three decades, researchers have made great strides in developing various types of energy harvesters. This is an important area of research for the world's needs. However, like any other resource, energy harvesters have their issues. The main challenges of the energy harvester are that generated power is low, although even this low-produced electricity is enough for low-powered technologies and devices such as wireless sensors to data loggers, transmitters, and other small-scale electronics. In order to overcome this difficulty, this study proposes a modified Flow-Induced Vibration (FIV) based energy harvester. Also, in this study, a nature-inspired FIV-based energy harvester is complemented by using a second bluff body, and its effect will be investigated. In order to reach the mentioned goal, this research considers multidisciplinary perspectives while studying the following topics:

I. Experimentally studying the approaches to increase the amplitude of FIV.
II. Utilizing the enhanced vibrations to extract energy.

To amplify the oscillation amplitude of the bluff body and, as a result, boost energy harvesting, a comprehensive examination of the near-wake flow using Particle Image Velocimetry (PIV) is conducted. Subsequently, the electromechanical equation of motion for the vibration-based energy harvester utilizing piezoelectricity is derived.
In addition, a series of wind tunnel experiments are conducted to prove the usefulness of the downstream rectangular plate and how it positively or negatively affects the harvester's efficacy.

INTRODUCTION

Having access to clean energy is an inevitable need for millions of people around the world. Wind energy is one of the well-known sources of energy. Flow-induced vibration-based energy harvesting is one of the interesting subjects that is extensively studied by many researchers. In the case of vibration-based energy harvesting, more attention is paid to piezoelectric devices because of their application for a wide range of frequencies. To investigate the effect of bluff bodies on the interaction of vortices, PIV is a well-known quantitative technique. Moreover, several studies have been done to understand the effect of the circular cylinder on the downstream flow parameters and its correlation with aerodynamic acting forces caused by alternate-shed vortices. A statistical study using LDV measurement on the wake parameters was done by Norberg. A comprehensive investigation of the correlation between aerodynamic forces and the near wake recirculation zone parameters, utilizing LDA, LIF, and DPIV, was conducted by Lam et al.

EXPERIMENTAL STUDY

The PIV technique is utilized to explain the reason for the FIV enhancement of the proposed system. Therefore, a low-speed wind tunnel with the square test section of 30 cm × 30 cm was employed, as shown in part (A) of Figure 1, with the main components of an electric inverter as the inlet velocity controlling system, air blower, motor, three mesh screens, and a honeycomb. To the similarity of nondimensionalized results, the experiment was carried out for the upstream velocity of 0.88 m/s, which corresponds to the Reynolds of 1670. The Phantom VEO 410 CCD camera and 105 mm Micro Nikon lens were used to capture 9000 consecutive snapshots with a resolution of 1200×800. A combination of optical lenses and a continuous wave laser (532 nm, 5W) made the illumination system. The image sampling rate was chosen as 2200 to gain particle displacement in the range of 3-5 pix/frame, and the results were post-processed by using PIV Lab with the interrogation sizes of the passes 64×64 pixels and 32×32 pixels. Finally, the bluff bodies were made by 3D-Printing, shown in part (B) of Figure 1.

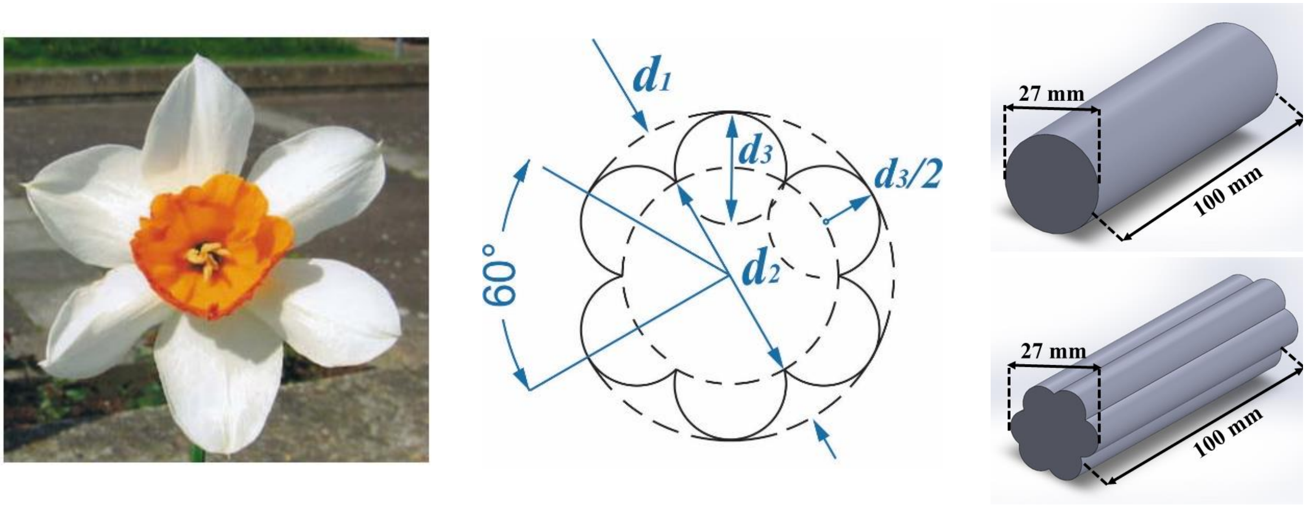

(a) (b) (c)

Figure 1. Amaryllis flower (a)); cross-section of the so-called petals cylinder (b); and 3D view of the bluff bodies (c)

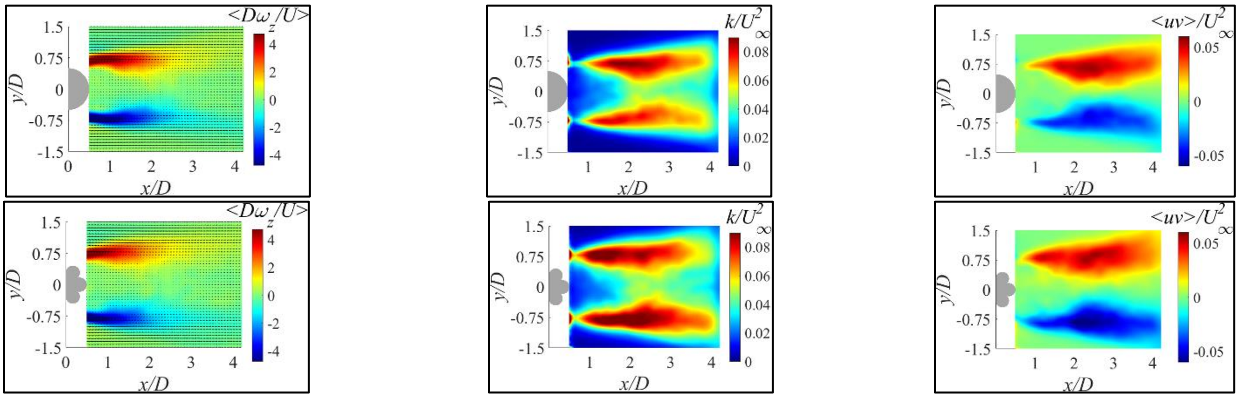

(a) (b) (c)

Figure 2. Comparison of: ensemble-averaged vorticity field (a), Normalized Turbulent Kinetic Energy (b), and Normalized Reynolds Shear Stress (c)

ACKNOWLEDGEMENTS

This work was supported by Brain Pool Program through the National Research Foundation of Korea (NRF), funded by the Ministry of Science and ICT (No. 2022H1D3A2A01081886). This work was also supported by the National Research Foundation of Korea (NRF) grant, which is funded by the Korean government (MSIT) (No. 2020R1A5A8018822)

REFERENCES

- Wang, J. et al., (2022). Wake galloping energy harvesting in heat exchange systems under the influence of ash deposition. Energy, Vol. 253, pp. 124175.
- Sobhanirad, S. & Afsharfard, A., (2019). Improving application of galloping-based energy harvesters in realistic condition. Archive of Applied Mechanics, Vol. 89, pp. 313–328.
- Nabavi, S. F., Farshidianfar, A., Afsharfard, A. & Khodaparast, H. H., (2019). An ocean wave-based piezoelectric energy harvesting system using breaking wave force. International Journal of Mechanical Sciences, Vol. 151, pp. 498–507.
- Kim, M., Kim, M., Hosseini, S., Jeong, J. & Kim, K. C., (2022). PIV measurement of turbulent flow characteristics inside an open-cell metal foam replica. Optics and Lasers in Engineering, Vol. 158, pp. 107143.
- Norberg, C., (1998). LDV-measurements in the near wake of a circular cylinder. ASME Paper No. FEDSM98-521 41–45

Simultaneous Fluorescent and Mie-scattering PIV in Gas Flow

Agastya Parikh[1,*], Mizuki Okada[2], Sergio Lavagnoli[2], Christian J. Kähler[1]

1: Institute of Fluid Mechanics and Aerodynamics, Universität der Bundeswehr München, Germany
2: Turbomachinery and Propultion Department, Von Kármán Institute, Sint-Genesius-Rode, Belgium
*Correspondent author: agastya.parikh@unibw.de

Keywords: PIV, Fluorescence, Entrainment, Flow Mixing, Boundary Layers

Introduction

Turbulent flows are a near-ubiquitous feature of life in the natural and engineered world. The flow mixing that is a defining feature of turbulence plays a crucial role in many natural and engineered processes that are of interest to scientists and engineers. As such, there has been significant scientific effort put into investigating the nature of turbulent mixing, particularly as it pertains to the case of entrainment at fluidic interfaces. Classical examples are turbulent jets and boundary-layer edge flows, where transport is said to occur across the turbulent-non turbulent interface (TNTI).

Early experiments focussed on a phenomenological approach, with techniques such as dye visualisation and laser-induced-fluorescence (LIF) being applied to qualitatively describe transport from non-turbulent quiescent flow into turbulent regions (Dahm and Dimotakis, 1987). To quantitatively investigate entrainment-based transport processes, some inventive solutions such as the use of pH-sensitive LIF with a basic turbulent jet in an acidic ambient flow, have been successfully demonstrated (Dahm and Dimotakis, 1987). However, these do not yield a direct measurement of the velocity field, which is crucial to the study of transport in fluid physics. With the advent of digital imaging, particle image velocimetry (PIV) has become established as a standard feature of the fluid mechanician's analytical toolbox for non-intrusive velocity measurements (McKeon et al., 2007; Raffel et al., 2018). Furthermore, with improvements in imaging and laser technology, spatially- and temporally-resolved PIV measurements are now widely applied to experiments in turbulent flows.

It is possible to use PIV to investigate the TNTI (Chauhan et al., 2014; Reuther and Kähler, 2018); for a globally-seeded (GS) flow, thresholding of higher-order derived quantities such as vorticity or turbulence kinetic energy is used to detect the interface (Reuther and Kähler, 2018). However, these often require a very high spatial resolution to accurately resolve the TNTI. This, in turn, tends to imply a reduction in the size of the field of view (FOV) being investigated. Furthermore, there is an element of uncertainty added by the choice of threshold used to distinguish turbulent and non-turbulent regions. In a systematic analysis of different PIV-based TNTI detection methods, a concentration-based approach was studied by Reuther and Kähler (2018). Here, the use of local seeding (LS) in the boundary layer boosted particle density in the turbulent portion of the flow to enable analysis analogously to a flow with a passive scalar (such as dye) without eliminating the ability to extract velocity field information. A still-remaining limitation in these experimental techniques is the ability to track the transfer of fluid across the interface directly. This represents a significant gap in experimental studies of entrainment and detraiment in free-shear flows.

Fluorescent Seeding

PIV is predicated upon the concept of using tracer particles which can accurately approximate the path of the flow (Scharnowski and Kähler, 2020, Raffel et al., 2018). In "classical" PIV, tracers are illuminated using a laser light sheet, and scatter the incident light towards the cameras to produce the particle images that are actually recorded. Over the years, tracer particles themselves have been modified for various purposes; the use of fluorescent particles has often been pursued to reduce the influence of reflections, particularly in liquids (Pedocchi et al., 2008). Perhaps more interestingly, fluorescence has also been used in two-phase flows for simultaneous (but independent) measurement of mixing sprays by Towers et al. (1999), effectively working as a form of flow tagging. Here, the mixing of two crossed nebulisers was studied by doping the water fed to one of them with Rhodamine 640, which fluoresces at a longer wavelength than the Mie scattering produced by un-doped particles. It was possible, despite the restrictions in processing technology at the time, to decouple the measurements by imaging the flow with a pair of cameras, one of which was equipped with a long-pass filter to isolate the fluorescent spray. This appears to be a promising conceptual starting point, whereby one could try to investigate entrainment around the TNTI.

Unfortunately, within the context of high-Reynolds number studies of turbulent shear flows, this becomes complicated for a number of reasons. In liquid flows, cost quickly becomes an issue, as dye-coated particles used are often very expensive (Pedocchi et al., 2008). Furthermore, the ability to separate portions of the flow from each other based on local introduction of tagged particles self-evidently gets diluted over time as more particles enter the facility. Furthermore, many studies of the TNTI are performed at high Reynolds numbers that are most easily studied in gas flows using large wind tunnels. Here again, cost becomes a major issue, as the particles are best used in open-return facilities. Recent work conducted by Okada et al. (2022) introduced the use of Pyrromethene 567 (P567) dissolved in Di-Ethyl-Hexyl-Sebacate (DEHS) as a relatively low-cost solution to the problem of performing fluorescent PIV in gas flows. Notably, the solubility of P567 in DEHS makes it very simple and practical to introduce without changes to seeding equipment. Furthermore, the size (and thus dynamics) of tracer particles are unaffected.

Proof-of-Concept

With the precedent for simultaneous PIV measurements using Mie scattering and fluorescence set in Towers et al. (1999) and the fluorescing DEHS solution developed by Okada et al. (2022), a new technique for analysing entrainment in gas flows is proposed. Namely, the ambient flow is (globally) seeded with regular DEHS particles, while the high-momentum flow is seeded locally using fluorescent particles generated from a solution of P567 in DEHS. This can then be simultaneously imaged using one camera sensitised *only* to fluorescent emission with an optical filter and a second camera that is sensitive to all light.

In order to conduct a proof-of-concept experiment and explore the feasibility of the proposed technique, the boundary layer developing along the floor of the Atmospheric Wind Tunnel Munich (AWM) at the Universität der Bundeswehr was imaged

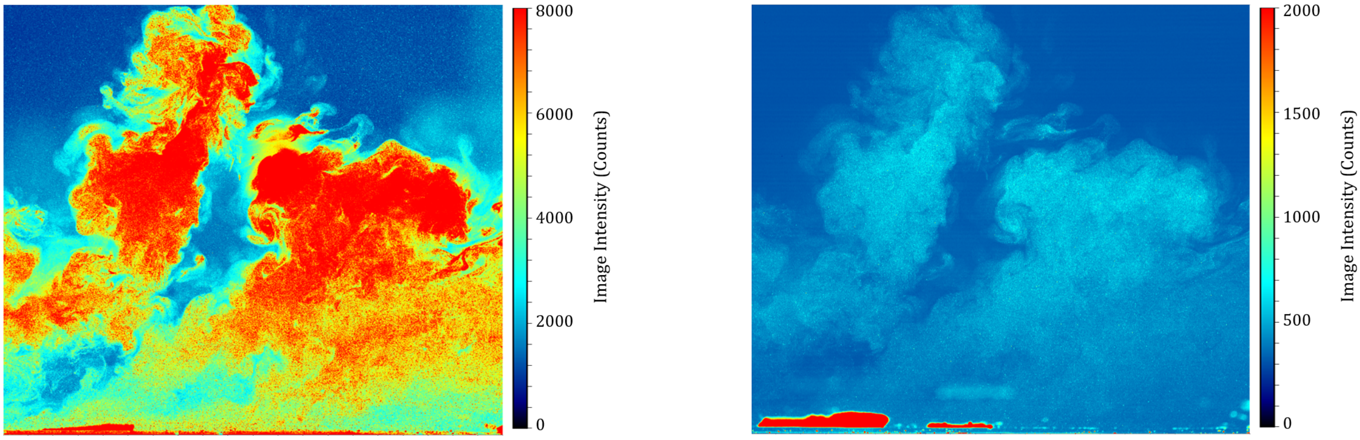

(a) (b)

Figure 1: A Mie scattering PIV image (a), alongside a fluorescence-only PIV image (b) in a streamwise wall-normal plane observing the AWM boundary layer. The fluorescent local seeding is isolated from the global + local seeding visible in the Mie scattering image. Note the significantly differing magnitudes of particle image intensity; the fluorescent emission is significantly weaker than Mie scattering.

downstream of the inflow contraction. The mean flow was seeded with (non-fluorescing) DEHS particles at the inlet tower of the AWM. A $1.60\,\mathrm{g\,l^{-1}}$ solution of P567 in DEHS was used with a small seeding generator at low pressure for local seeding near the start of the test section. A pair of Imager sCMOS cameras with Zeiss Makro-Planar f =100 mm lenses were used for imaging, one of which was fitted with a 532 nm band-stop filter to be sensitive only to fluorescent emission. The boundary layer was imaged in a streamwise, wall-normal plane along the centreline of the tunnel ~2 m downstream of the inlet. The FOV measures approximately 200 mm×170 mm and was imaged from opposing sides of the tunnel, allowing for good alignment of the images captured using both cameras. Two (corresponding) representative images from this early experiment are shown in Figure 1, where the ability to distinguish tagged particles in a realistic experimental scenario has been confirmed.

Future Steps

The preliminary results shown indicate that a dual GS-LS approach with the use of fluorescent DEHS for local seeding can be used to isolate the locally-seeded regions of the flow. Using a pair of cameras to observe an identical FOV allows for a near one-to-one comparison of the particle images obtained from Mie scattering and fluorescence. Here, the main challenge to be resolved is accurately matching the particle images in a manner such that the fluorescent local seeding can be "subtracted" from the unfiltered particle images. Misalignment of the particle images is practically impossible to eliminate on a pixel scale, but the use of cross-correlation as a pre-processing step is a possible solution to this issue. This is somewhat complicated by the far lower intensity of the particle images produced by the fluorescent particles, but a careful normalisation of intensity may help. A detailed description of the fluorescent DEHS, experimental process, and post-processing steps will be discussed in the conference paper. It is hoped that further development of the technique will make interesting new observations about the transport of momentum across the TNTI possible.

References

Chauhan, K., Philip, J., de Silva, C. M., Hutchins, N., & Marusic, I. (2014). The turbulent/non-turbulent interface and entrainment in a boundary layer. *Journal of Fluid Mechanics*, *742*, 119–151. https://doi.org/10.1017/jfm.2013.641

Dahm, W. J. A., & Dimotakis, P. E. (1987). Measurements of entrainment and mixing in turbulent jets. *AIAA Journal*, *25*(9), 1216–1223. https://doi.org/10.2514/3.9770

McKeon, B. J., Comté-Bellot, G., Foss, J. F., Westerveel, J., Scarano, F., Tropea, C., Meyers, J. F., Lee, J. W., Cavone, A. A., Schodl, R., Koochesfahani, M. M., Nocera, D. G., Andreopoulos, Y., Dahm, W. J., Mullin, J. A., Wallace, J. M., Vukoslavčević, P. V., Morris, S. C., Pardyjak, E. R., & Cuerva, A. (2007, July). Velocity, Vorticity, and Mach Number. In C. Tropea (Ed.). A. Yarin (Ed.). J. F. Foss (Ed.), *Springer Handbook of Experimental Fluid Mechanics* (pp. 215–472). Springer.

Okada, M., Pinho, J., & Lavagnoli, S. (2022). Fluorescent Tracer Particles for PIV Measurement in Gas Flows. *Proceedings of the 20th International Symposium on Application of Laser and Imaging Techniques to Fluid Mechanics*, *20*.

Pedocchi, F., Martin, J. E., & García, M. H. (2008). Inexpensive fluorescent particles for large-scale experiments using particle image velocimetry. *Experiments in Fluids*, *45*(1). https://doi.org/10.1007/s00348-008-0516-2

Raffel, M., Willert, C. E., Scarano, F., Kähler, C. J., Werely, S. T., & Kompenhans, J. (2018). *Particle Image Velocimetry: A Practical Guide* (3rd ed.). Springer. https://doi.org/10.1007/978-3-319-68852-7

Reuther, N., & Kähler, C. J. (2018). Evaluation of large-scale turbulent/non-turbulent interface detection methods for wall-bounded flows. *Experiments in Fluids*, *59*. https://doi.org/10.1007/s00348-018-2576-2

Scharnowski, S., & Kähler, C. J. (2020). Particle image velocimetry - Classical operating rules from today's perspective. *Optics and Lasers in Engineering*, *135*, 106185. https://doi.org/10.1016/j.optlaseng.2020.106185

Towers, D. P., Towers, C. E., Buckberry, C. H., & Reeves, M. (1999). A colour PIV system employing fluorescent particles for two-phase flow measurements. *Measurement Science and Technology*, *10*(9). https://doi.org/10.1088/0957-0233/10/9/309

Visualization Study on the Effect of Dynamic Vibration Absorber in Rotating Radar Antenna

Amirreza Shahsavari[1], Aref Afsharfard[1] and Kyung Chun KIM[1,*]

1: Pusan National University, School. of Mechanical Engineering, Eco-Friendly Smart Ship Parts Technology Innovation Center, Busan 46241, Republic of Korea

* Correspondent author: kckim@pusan.ac.kr

Keywords: PIV processing, Dynamic Vibration Absorber (DVA), Vibrations, Visualization

ABSTRACT Current research endeavors to improve the features and reduce the uninvited lateral oscillations of the rotary beam, widely used in industry and energy production, such as a blade of wind turbines, by employing a Dynamic Vibration Absorber (DVA). The vibration control of rotating beams like wind turbine blades or climate radar in the past few years has been studied by many researchers, and different types of vibration control devices have been proposed to decrease the vibration of the blades. Among these devices, aerodynamic control devices are usually small devices that are distributed along the span of the blade to affect the flow dynamically and consequently decrease the aerodynamic loads on the blades.

In order to achieve this goal, an analytical model based on the Euler-Bernoulli formulation was employed to examine the influence of the DVA on the vibratory behavior of the rotating beam, taking into account lateral excitation. In this regard, DVA's dynamic effect was considered an external force, and its application for decreasing lateral vibration is studied. Furthermore, PIV and visualization tests were conducted to analyze the aerodynamic influence of affixing the DVA to the rotating beam. The experiments were conducted in a wind tunnel with a velocity of 1.1 m/s on two models of the antenna, with and without DVA applied to the surface of the rotating beam. Flow visualization results were employed to analyze and compare variations in flow over the rotating beam and the wake region.

The first mode of vibration was studied to assess the efficacy of the DVA utilizing three different masses, which results demonstrate its capacity to suppress the undesired vibration of the model. Experimental results showed that the length of the vortex formation and consequent wake were extended beyond what was seen in a static beam without a DVA, as well as an increase in the width of the wake region. However, the amplitude of oscillation that is generated within the model at the far wake region is reduced when the DVA is included.

Therefore, using the DVA has the proper ability to improve the behavior of the system, and as a result, using the presented DVA on the climate antenna, this system can be designed longer, more flexible, and lighter, which results in decreasing its price.

EXPERIMENTAL STUDY

In this research, experiments were done in the open Circuit horizontal wind tunnel, in which the test section was rectangular with dimensions of 30*30 cm^2. The wind tunnel which was used in this study involved different parts such as a motor with the power of 7.5 Kw, an electric inverter, an air blower, an air inlet duct, a three-mesh screen, and a honeycomb mesh in order to uniform the flow. An inverter was used to change the flow velocity.

In the flow visualization test, a 200-mW diode laser with green color was used. A Canon 6D camera with a capacity of 20 megapixels in full HD was used for photography. The camera has an intelligent processor and the ability to adjust the light sensitivity. The camera shutter speed can be adjusted from 30 to 1.4000 seconds. A Canon 100mm macro lens was used on the camera to capture and record the results. An adjustable tripod equipped with a level was used to hold the camera steady during shooting to capture the photos better. To create an illuminated screen, a thin lens was mounted on the laser output that turns the laser output light into a triangular screen.

Particle Image Velocimetry is utilized to explain the reason for the VIV enhancement of the proposed system. As the similarity of nondimensionalized results, the experiment carried out for the upstream velocity of 1.1 m/s corresponds to the Reynolds of 1466. Phantom VEO 410 CCD camera and 105 mm Micro Nikon lens are used to capture 9000 consecutive snapshots with a resolution of 1200×800. A combination of optical lenses and a continuous wave laser (532 nm, 5W) made the illumination system. The image sampling rate was chosen as 5200 to gain particle displacement in the range of 3-5 pix/frame, and the results were post-processed by the use of PIV Lab with the interrogation sizes of the passes 64×64 pixels and 32×32 pixels. The models were made by 3D-Printing shown in part (B) of Figure 1.

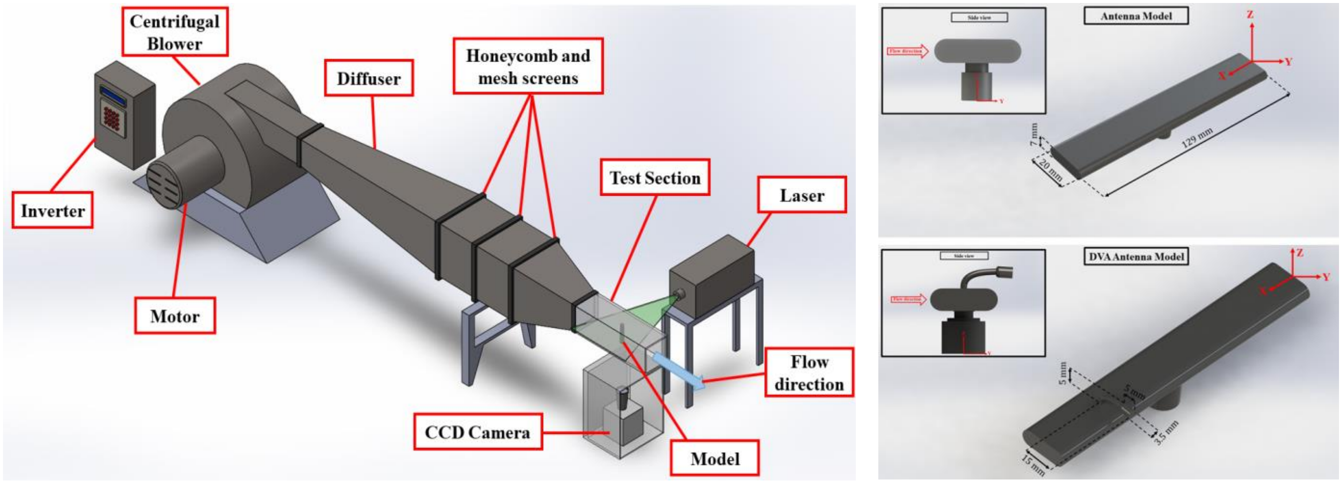

(a) (b)

Figure 1. Schematic of the test setup (a); and 3D view of the models (b)

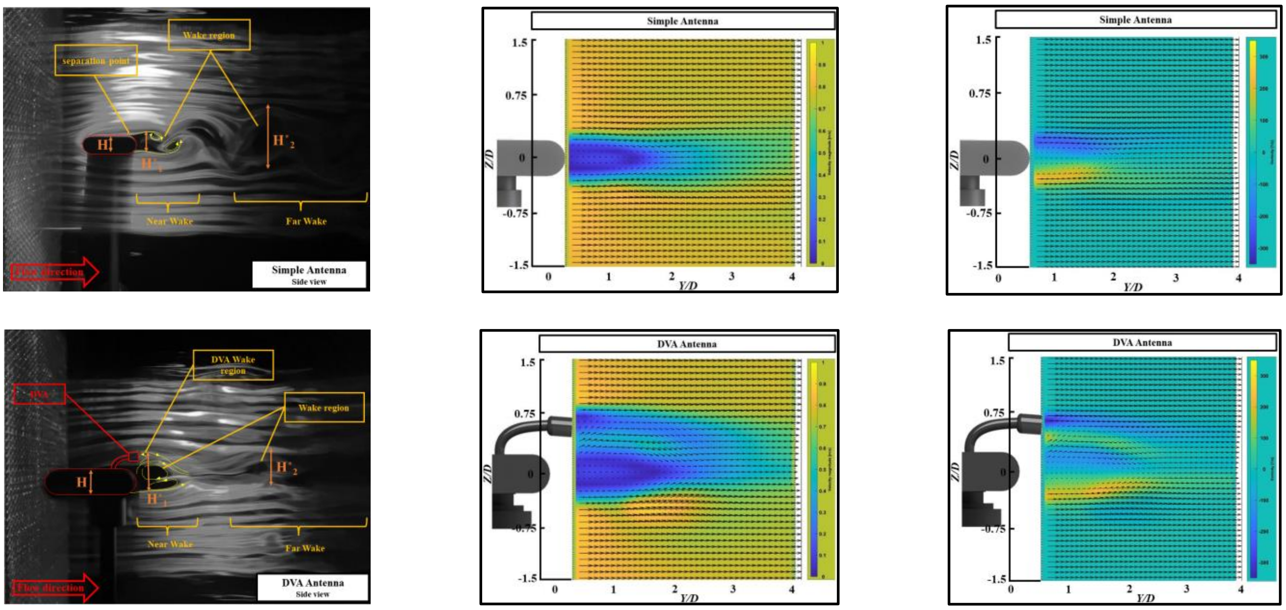

(a) (b) (c)

Figure 2. Flow visualization results for Simple climate radar and equipped climate radar with DVA (a), Contours of velocity magnitude (b), and Contours of vorticity (c) for the simple and DVA antenna.

ACKNOWLEDGEMENTS

This work was supported by Brain Pool Program through the National Research Foundation of Korea (NRF), funded by the Ministry of Science and ICT (No. 2022H1D3A2A01081886). This work was also supported by the National Research Foundation of Korea (NRF) grant, which is funded by the Korean government (MSIT) (No. 2020R1A5A8018822)

REFERENCES

- Zhang, Z., Nielsen, S. R. K., Basu, B. & Li, J. (2015). Nonlinear modeling of tuned liquid dampers (TLDs) in rotating wind turbine blades for damping edgewise vibrations. Journal of Fluids and Structures 59, 252–269.
- Basu, B., Zhang, Z. & Nielsen, S. R. K. (2016). Damping of edgewise vibration in wind turbine blades by means of circular liquid dampers. Wind Energy 19, 213–226.
- Richiedei, D., Tamellin, I. & Trevisani, A. (2021). Beyond the tuned mass damper: a comparative study of passive approaches to vibration absorption through antiresonance assignment. Archives of Computational Methods in Engineering 1–26.

Coherent Structures and Dynamics of Turbulent High-Speed Jets Investigated via Dual-PIV Coupled with Dynamic Mode Decomposition

Alexis Duddridge, Vishal Chaugule*, Callum Atkinson and Julio Soria
Laboratory for Turbulence Research in Aerospace & Combustion
Department of Mechanical and Aerospace Engineering
Monash University (Clayton Campus), VIC 3800, Australia
* Correspondent author: vishal.chaugule@monash.edu

Keywords: Turbulent jet, Particle image velocimetry, Dynamic mode decomposition, Coherent structures

ABSTRACT The large-scale coherent structures and their motions in turbulent high-speed jets have considerable influence on the application of these jets in propulsion systems and their role in aerodynamic noise generation. Experimental characterization of these structures and their evolution is of significant interest as it provides deeper understanding of the underlying flow instability mechanisms that affect mixing, combustion and aeroacoustics. This depends on the spatial and temporal resolution of the measurements, which need to be highly resolved in both these dimensions simultaneously for a fundamental characterization. However, the standard particle image velocimetry (PIV) technique, which is widely used for experimental fluid mechanics studies, is limited by the current technology of image acquisition sensors that allows high resolution measurements to be acquired in only one dimension and at the expense of the resolution in the other.

This study adopts a novel method to address the aforementioned challenge through the use of *Dual-PIV* velocity measurements coupled with their exact dynamic mode decomposition (*Exact DMD*) analysis. The *Dual-PIV* system comprises two independent, but synchronized, PIV systems illuminating and recording the same field-of-view with cross-talk minimized using polarization-based image separation. The timing interval between these two PIV systems can be made sufficiently small to resolve down to the smallest dynamically significant temporal scale, yielding two time-resolved velocity fields at sufficiently high-spatial resolution. An *Exact DMD* analysis (Tu et al., 2014) of these pairs of flow-field data vectors then yields the best linear approximation to the mapping matrix between them and allows the extraction of the frequencies of interest and the corresponding spatial modes. These methods are used together to study the coherent structure topology and dynamics of turbulent round high-speed subsonic and supersonic free-jet flows. The subsonic jet has a Reynolds number Re_d = 10,000 based on the jet orifice diameter d = 15 mm and the average velocity across the jet-exit U_j = 9.69 m/s. The supersonic jet is an under-expanded free-jet with the same jet diameter but at a nozzle pressure ratio of 3.4 and a maximum Mach number of 1.42. The description of the *Dual-PIV* system and the results of the high-speed subsonic free-jet are presented below.

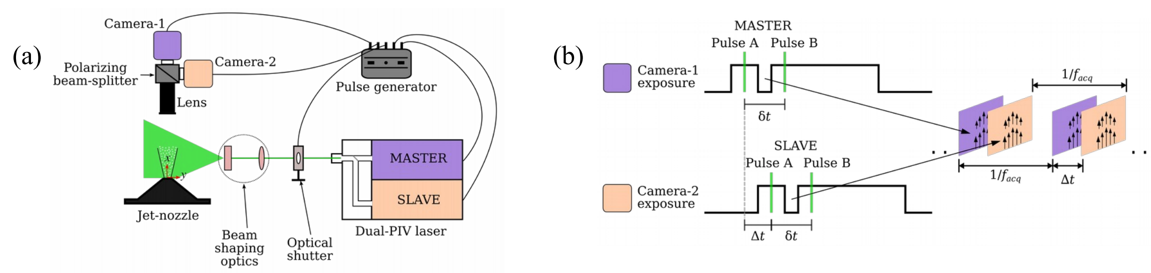

Figure 1: Schematics: (a) *Dual-PIV* system; (b) timing diagram and pairwise time-resolved velocity snapshots.

A schematic of the *Dual-PIV* set-up is shown in Figure 1(a), wherein an *Innolas SpitLight DPSS EVO IV* laser is used for 2C–2D PIV measurements. This is an optically and electronically integrated system of two orthogonally polarized PIV lasers in which each laser produces collinear pulsed laser light. The polarization difference between the two lasers is leveraged to enable *Dual-PIV* measurements by utilizing twin-cameras arranged around a polarizing beam-splitter with a single imaging lens mounted in front. *Camera-1* records the single-exposed image pair of the flow-field illuminated only by the *MASTER* laser, while *Camera-2* records the single-exposed image pair illuminated only by the *SLAVE* laser (Chaugule et al., 2023). The spatial resolution of the recorded images of both PIV image acquisition systems is 15.8±0.35 μm/px at a PIV velocity field acquisition rate of f_{acq} = 1 Hz.

A schematic of the *Dual-PIV* timing configuration is illustrated in Figure 1(b). The time between two pulses of the *MASTER* laser was set to δt = 12 μs, which was also used for the *SLAVE* laser. The time shift between the *MASTER* and SLAVE lasers was set to Δt = 8 μs, with pulse A of the *MASTER* laser taken as the reference. As the twin-camera exposure times were synchronized to this shift, the time between the sequential velocity fields (snapshots) obtained from *Camera-1* and *Camera-2* is equal to Δt. The time between the velocity snapshot pairs is, however, equal to the reciprocal of the image acquisition rate ($1/f_{acq}$). Analysis of the PIV images was performed using multi-grid/multi-pass cross-correlation digital particle image velocimetry (MCCDPIV) introduced by Soria (1996).

An *Exact DMD* analysis of the pair-wise sequential snapshots was performed where the linear map $\mathbf{A}$ optimally describes the flow evolution over the small temporal separation Δt and is given in matrix form as $\mathbf{X}_{t+\Delta t} = \mathbf{A}\mathbf{X}_t$. $\mathbf{X}_t$ and $\mathbf{X}_{t+\Delta t}$ are the matrices that contain both the streamwise and transverse fluctuating components of the velocity fields obtained from the PIV images recorded from *Camera-1* and *Camera-2*, respectively. 3000 velocity snapshots were used for the analysis.

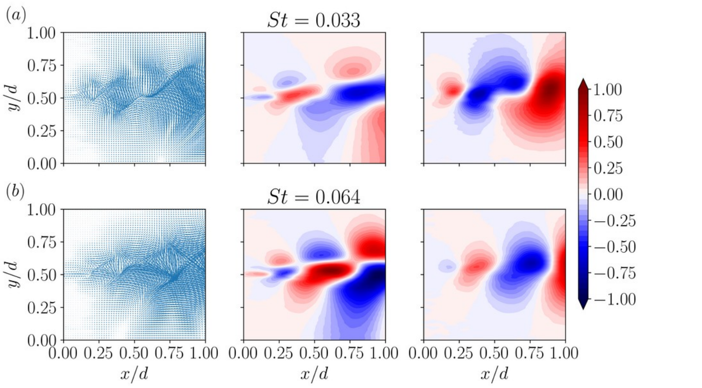

Figure 2: DMD modes visualised by the real part of the fluctuating velocity vectors (left column) and contours of their streamwise (middle column) and transverse (right column) components.

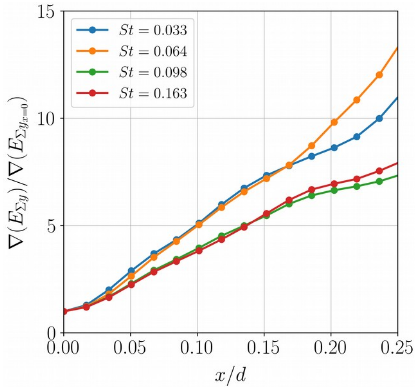

Figure 3: Streamwise variation of the gradient of the DMD modes energies.

The spatial structures of two of the four DMD modes, normalized by their corresponding maximum quantities, are shown in Figure 2. The Strouhal number is defined as $St = f\theta/U_j$, where $\theta = 0.046d$ is the momentum boundary-layer thickness at the jet nozzle-exit. The fundamental coherent dynamic mode is characterized by large-scale vortical structures with approximately one oscillatory period over the streamwise extent of the displayed near-field region, whereas the second harmonic mode has similar spatial features but with one and a half streamwise oscillatory periods. The energy of each DMD mode is given by its L^2 -norm of the complex streamwise and transverse components of the DMD velocity modes which is integrated along the cross-stream or transverse direction. The streamwise variation of the gradient of this energy (amplification), normalised by that at the jet-exit, is shown in Figure 3. The amplification of all the DMD modes is linear in the region $0.03 \leq x/d \leq 0.18$, with the amplification of the second harmonic DMD mode approximately equal to that of the fundamental mode.

The results demonstrate that the chosen low-dimensional linear system can extract coherent structures and their dynamic behaviour that accurately describe the underlying characteristics of the turbulent high-speed jet flow. This is affirmed by the fundamental DMD mode corresponding to St = 0.033 which matches the St of the most spatially amplified wave as predicted by classical linear stability theory (Michalke and Hermann, 1982). Overall, the coupled experimental and data decomposition methodology presented here is a robust technique to characterise the coherent structure dynamics in high-speed turbulent shear flows using non-sequential temporally resolved pairs of velocity flow fields with high-spatial resolution.

REFERENCES

Chaugule, V., Duddridge, A., Sikroria, T., Atkinson, C., & Soria, J. (2023) Investigating the Linear Dynamics of the Near-Field of a Turbulent High-Speed Jet Using Dual-Particle Image Velocimetry (PIV) and Dynamic Mode Decomposition (DMD). Fluids, 8, 73.

Michalke, A., & Hermann, G. (1982) On the inviscid instability of a circular jet with external flow. Journal of Fluid Mechanics 114:343–359

Soria, J. (1996) An investigation of the near wake of a circular cylinder using a video-based digital cross-correlation particle image velocimetry technique. Experimental Thermal and Fluid Science 12:221–233

Tu, J.H., Rowley, C.W., Luchtenburg, D.M., Brunton, S.L., & Kutz, J.N. (2014) On dynamic mode decomposition: Theory and applications. Journal of Computational Dynamics 1

TECHNICAL SESSION 8
DATA DRIVEN TECHNIQUES

Chaired by Miguel Mendez

Semi-Supervised Machine Learning in Data-Driven Flow Measurement

Junwei Chen* , Stefano Discetti and Marco Raiola[1]
1: Dept. of Aerospace Engineering, Universidad Carlos III de Madrid, Spain
* Correspondent author: junwei.chen@uc3m.es

Keywords: PIV processing, Machine learning, Data driven, POD

ABSTRACT In the previous work of Chen el at. (2022a), data-driven techniques demonstrated to be able to enrich snapshot PIV (Particle Image Velocimetry) with the time resolution of fast probe data. In this paper, a semi-supervised machine learning method is introduced, which allows to train not only on probe data labeled with simutaneous PIV outputs but also on unlabeled data from probe-only measurements. Then the new machine learning method is compared with EPOD and MLP, shows it's prevailence both in the accuracy and reducing the computation cost.

1 INTRODUCTION

Time-resolved PIV (TR-PIV) provides both spatial and temporal information, which is a powerful tool in locating the evolution of coherent structures, identifying physical phenomena and allows computing pressure fields from integration of the Navier-Stokes equations. However, it is not always achievable due to the budget and the restriction of laser and camera repetition rate. A good surrogate of TR-PIV can be obtained by combining snapshot PIV (no need in temporal resolution) and fast probe measurement. This has been recently applied in Chen el at. (2022a) using the EPOD (Extended Proper Orthogonal Decomposition) and Chen el at. (2022b) using the classical multilayer perceptron (MLP), aiming to pressure field reconstruction. Benefited from the capability to map nonlinear relations, the MLP outperforms the EPOD. In detail, the flow field $\boldsymbol{U}$ can be temporal-spatial decoupled via POD,

$$\boldsymbol{U}(\boldsymbol{x},t)=\sum_i \sigma_i a_i(t)\boldsymbol{\phi}_i(\boldsymbol{x}), \tag{1}$$

where the $\boldsymbol{x}$ and t stands for position and time, σ_i is the weight of the i$^{\text{th}}$ mode, and a_i is the coefficient for normalized orthogonal spatial basis $\boldsymbol{\phi}_i(\boldsymbol{x})$. The MLP regresses the relationship f between the probe data $\boldsymbol{p}$ and the coefficients $\boldsymbol{a}$,

$$\hat{\boldsymbol{a}}(t)=f(\boldsymbol{p}(t)), \tag{2}$$

where $\hat{\boldsymbol{a}}$ is the coefficient predicted via the model f, and the task is to find the optimal model,

$$\underset{f}{\operatorname{argmin}}\,|\boldsymbol{a}-f(\boldsymbol{p})|. \tag{3}$$

Despite the advancements in machine learning, the prediction accuracy of MLP still exhibits noticeable deviations from the ground truth, particularly when the POD spectrum lacks compactness. One approach to further enhance the mapping capability of the MLP is using semi-supervised techniques (Chapelle et al., 2006).

It must be remarked that the operative cost of recording $\boldsymbol{a}$ and $\boldsymbol{p}$ is different. The coefficients $\boldsymbol{a}$ are obtained by PIV field, which requires storage and processing recourses far superior than point probes $\boldsymbol{p}$. This limits the amount of simultaneous $\boldsymbol{p}$ and $\boldsymbol{a}$ available for supervised machine learning (i.e. fulfilling Eq. 3). However, if the model f confirms the assumption of translation invariance, which means when the model is trained well at time t_j, $\left|\boldsymbol{a}(t_j)-f\left(\boldsymbol{p}(t_j)\right)\right|\to 0$, it should work well also at time t_{j+k}, $\left|\boldsymbol{a}(t_{j+k})-f\left(\boldsymbol{p}(t_{j+k})\right)\right|\to 0$, where $k=0,\pm1,\pm2,\ldots$ This can be fulfilled by introducing another model g on the time derivative of $\boldsymbol{a}$,

$$\hat{\boldsymbol{a}}_t(t)=g(\boldsymbol{p}(t)), \tag{5}$$

and the optimization of f and g does not require to be supervised with the coefficient $\boldsymbol{a}_j$,

$$\underset{f,g}{\operatorname{argmin}}\left|\frac{f\left(\boldsymbol{p}(t_{j+1})\right)-f\left(\boldsymbol{p}(t_{j-1})\right)}{t_{j+1}-t_{j-1}}-g\left(\boldsymbol{p}(t_j)\right)\right|_j. \tag{6}$$

The training session includes 3 steps, and the current f and g are two MLP models,
(1) training f as a starter, which is actually the single MLP,
(2) training g using the model f in (1),
(3) training f and g together.
The training is supervised for f in step (1) and partially in step (3), while unsupervised for g and for partially f in step (3). This allows enriching the training by adquiring additional sequences of $\boldsymbol{p}$ without corresponding PIV measurements. In addition, the supervised machine learning for data-driven measurement is only trained in several individual snapshots without knowing the

evolution of the flow, but the unsupervised part can be trained in series of frames and tracking the variation of $\boldsymbol{a}$ in adjacent frames, thus suppressing unphysical temporal fluctuations.

2 VALIDATION

The semi-supervised machine learning was tested in different data sets including synthetic and experimental ones. In this abstract the same experiment on the wake of a wing already tested in Chen el at. (2022a) is included. The snapshot PIV is down sampled from the time-resolved one, and probe data are extract in several points of the PIV field to simulate probe data. Finally the pressure integrated from the velocity estimation of EPOD, MLP and the semi-supervised machine learning are compared to that from time-resolved PIV. An example of reconstructed pressure field is reported below.

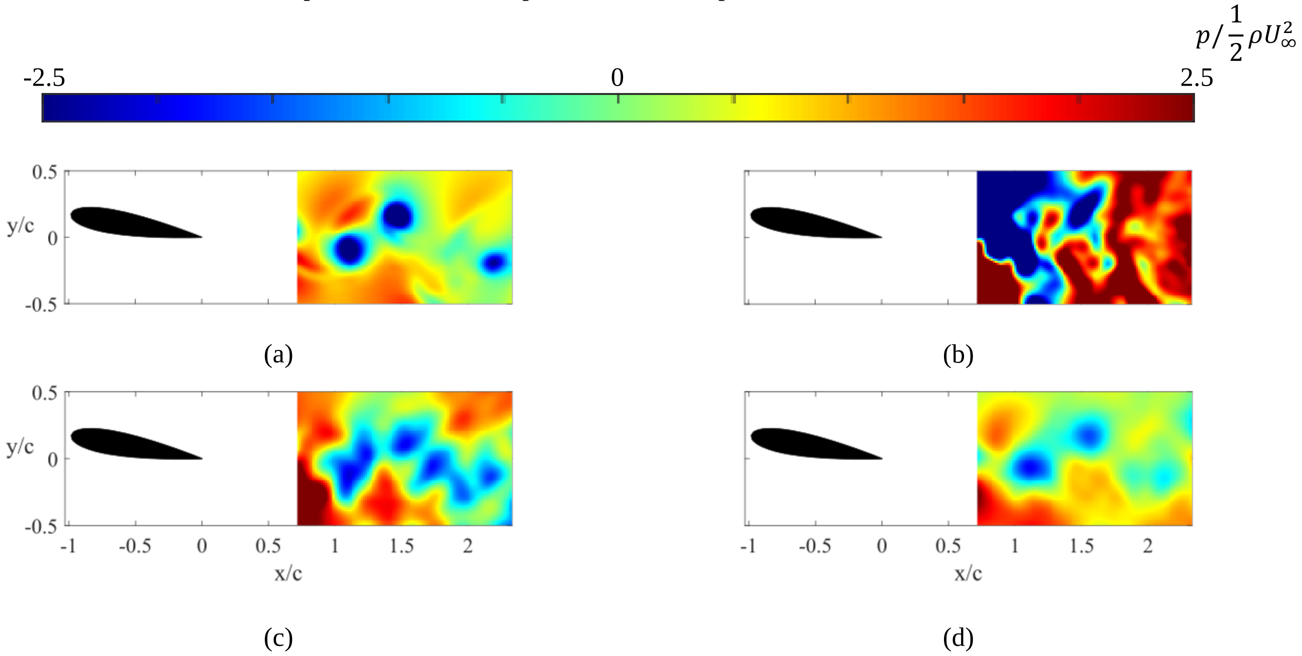

Figure 1. The pressure integrated from (a) time-resolved PIV field, (b) EPOD, (c), MLP and (d) semi-supervised machine learning.

Figure 1 shows the semi-supervised machine learning depicts high and low pressure areas more accurate to the MLP and EPOD. The MLP reduced the root-mean-square error of the domain shown in the figure and over 1000 frames by 50% and 73% comparing to the EPOD in velocity and pressure field reconstruction, and the semi-supervised machine learning gives a further reduction by 6% and 10%.

3 ACKNOWLEDGEMENT

This project has received funding from the European Research Council (ERC) under the European Union’s Horizon 2020 research and innovation programme (grant agreement No 949085).

4 REFERENCES

- Chapelle, O., Schölkopf, B., & Zien, A. (2006). A discussion of semi-supervised learning and transduction. In Semi-supervised learning (pp. 473-478). MIT Press.
- Chen, J., Raiola, M., & Discetti, S. (2022a). Pressure from data-driven estimation of velocity fields using snapshot PIV and fast probes. Experimental Thermal and Fluid Science, 136, 110647.
- Chen, J., Raiola, M., & Discetti, S. (2022b). Data-driven estimated velocity and pressure fields using snapshot PIV and fast probes. 20th International Symposium on Application of Laser and Imaging Techniques to Fluid Mechanics.

Two-phase Flow Regime Identification using Machine Learning Techniques

Shuichiro Miwa[1,*], Kohei Eguchi[2]
1: Nuclear Professional School, The University of Tokyo, Japan
2: Division of Applied Quantum Science and Engineering, Hokkaido University, Sapporo, Japan
* Correspondent author: miwa@n.u-tokyo.ac.jp

Keywords: Two-phase flow, Bubbly flow, Flow regime identification, CNN, Deep learning,

ABSTRACT A convolutional neural network (CNN)-based image analysis method was developed to identify the flow regime of gas-liquid two-phase flows rising vertically in a pipe. First, two-phase flow images were captured under a total of 377 inlet conditions, ranging from bubbly to annular flows. Based on the Mishima-Ishii flow regime map and the void fraction time series data obtained from the instrumentations, 37 flow conditions were selected as representative flow regime datasets suitable for the network training. Using these images, a new two-phase flow image identification model was developed by training a relatively simple CNN. Flow regime classification was then performed on the images for all flow conditions using the trained model, and it was confirmed that typical bubbly, slug, and annular flows could be classified under good accuracy.

1 INTRODUCTIOn

Gas-liquid two-phase flows are known to change into several flow modes depending on the flow rate of the gas-liquid phase due to the interaction that occurs at the gas-liquid interface. Since the flow pattern changes affect the flow and heat transfer characteristics of the two-phase flow, their accurate identification contributes to the safe and efficient operation of nuclear power plants and various other types of equipment. However, it is difficult to establish a unified view on flow pattern identification in the transition region, and objective flow pattern identification has been difficult in the past.

Various methods for flow pattern identification have been proposed in previous studies, and flow pattern diagrams such as the Mishima-Ishii flow regime map are widely used, but quantitative knowledge of the transition region near the boundary line remains scarce. Another long-established method of identification from the shape of the established density distribution obtained from the void fraction signal has also been used. In this method, impedance sensors (IMPS) and wire mesh sensors (WMS) are used to measure the time variation of void fraction from electrical signals using the electrical conductivity difference between gas and liquid. However, these devices require installation processing to embed the sensor in the flow path, and depending on the shape of the sensor, it may come into direct contact with the two-phase flow, which could undeniably affect the flow state.

On the other hand, identification by images taken from outside the transparent channel has also been proposed. In particular, studies incorporating deep learning, which has been applied to image analysis in various fields in recent years, into flow pattern identification have been reported. Shibata et al. combined videos of high-pressure gas-liquid two-phase flows into a single image using the time-strip method and trained a convolutional neural network (CNN) model to perform discrimination in the transition region between bubble and slug flows, and conducted a quantitative evaluation of the transition phenomena. However, the targeted flow modes were limited to bubble and slag flows, and accuracy verification including churn and annular flows was not conducted.

Based on the above, the two objectives of this study were (1) to construct a model that shows high discrimination accuracy under flow conditions that can be clearly classified into each flow pattern from bubbly flow to annular flow, and (2) to quantitatively evaluate the flow pattern transition phenomena. In the experiments and model building, images were acquired under a wide range of flow conditions, from bubbly flow to annular flow, and flow pattern identification was performed using a model built by training a CNN.

2 FLOW REGIME IDENTIFICATION USING CNN

Image and electrical signal data acquisition were performed on an experimental apparatus that generates gas-liquid two-phase flow by mixing air and water. The vertical ascending section of the two-phase flow loop was transparent acrylic piping with an inner diameter of 29 mm. An acrylic water jacket was installed around the piping in the imaging section. It was visually confirmed that this jacket mitigates the phenomenon that the gas-liquid phase passing near the pipe wall is obscured in the image due to light refraction. In this experiment, a high-speed camera was installed outside the water jacket and took images at 100~200 FPS for 20 seconds per flow condition. IMPS and WMS were installed in the flow channel near the filming area to acquire void fraction signal data and to measure the volumetric flow rates of water and air, respectively. Four sets of data acquisition were performed (Exp1 ~ Exp4) with various gas-liquid flow conditions, and data were acquired under 80 to 99 conditions per set, for a total of 377 conditions.

The data obtained from IMPS and WMS were computationally processed to obtain information on the time variation of the cross-sectional mean void fraction measured in each, the probability density distribution of the cross-sectional mean void fraction, and the time variation of the local void fraction measured in WMS. Examples of the time variation of the cross-sectional mean void fraction and probability density distribution for bubble flow and slag flow are shown in Fig. 1. While the three typical patterns, "bubble flow," "slag flow," and "churn or annular flow," were relatively easy to distinguish, no clear pattern differences were found between churn and annular flow. The 37 conditions with typical characteristics of each flow pattern were selected for the training and validation data of the CNN model.

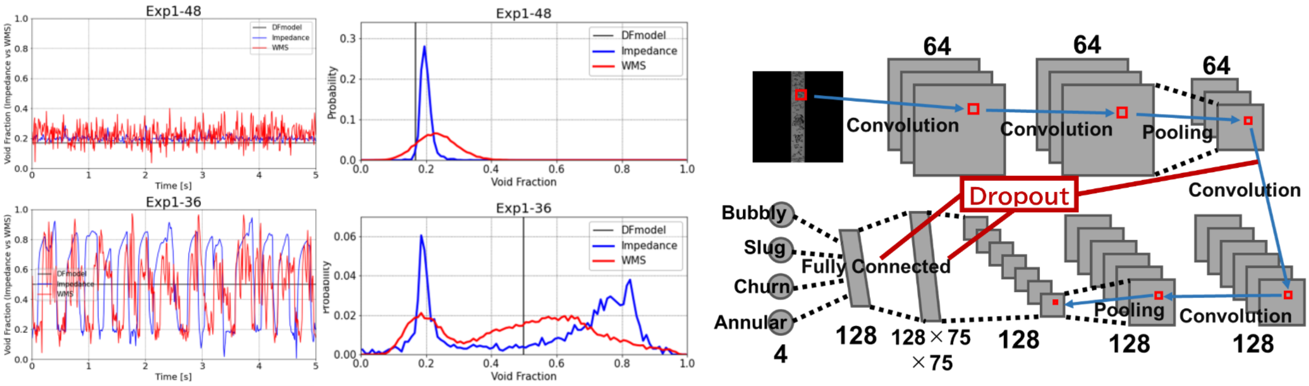

Figure 1. (Left) Area averaged void fraction signals obtained from IMPS and WMS, (Right) constructed CNN model

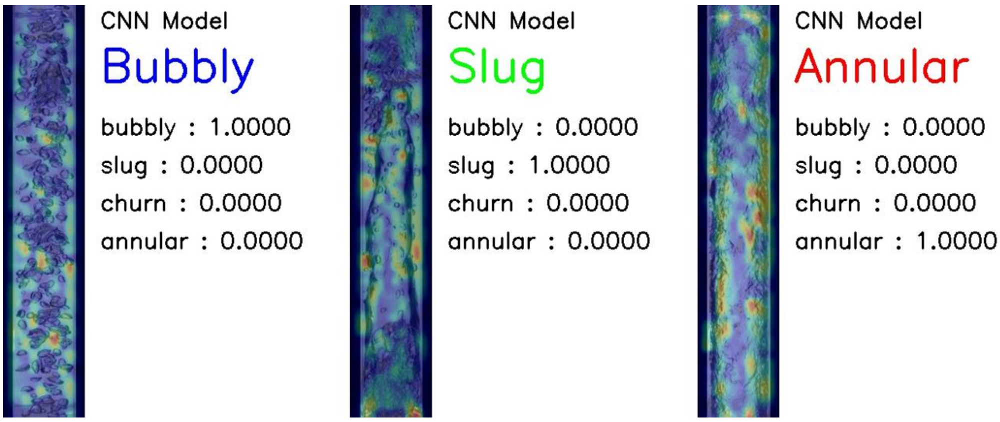

Figure 2. Identified two-phase flow high-speed images using the CNN model

In applying deep learning models to two-phase flow image identification, it is useful to know what features of the gas-liquid distribution in the image the model focuses on for identification. The output of the intermediate layer is shown in a heat map and merged with the original image to visualize the points of interest by the deep learning model in the image. The output of the second (downstream) pooling layer of the simple CNN model was used for visualization. 128 feature maps of size 75 × 75 were obtained for one image, and the average of the 128 maps was converted into a heat map (Figure 2). In the bubbly flow, there was a tendency to focus on the liquid phase rather than the bubbles, and the feature maps showed larger values at the periphery of bubbles of larger sizes and bubble aggregates. In the slug flow, the values were larger at the tip of the Taylor bubble and at the liquid film in the gap between the Taylor bubble and the pipe wall. Except for the Taylor bubble tip, both high and low values of interest were observed, but the liquid slug area with dense fine bubbles tended to have low values of interest in most cases.

3 SUMMARY

The flow regime identification using the CNN model showed that it was capable to identify the pattern with sufficiently high accuracy under clearly identifiable flow conditions. In the flow pattern transition region, the model predicted probabilities for the two flow patterns tended to vary significantly with time, and the time-averaged predicted probabilities for each flow pattern gradually increased or decreased with changes in gas phase flow rate, which is consistent with the transient nature of the flow pattern transition phenomenon. The transition from bubbly flow to slug flow was found to be more likely to occur at smaller voiding rates in flow conditions with lower gas phase flow rates. The visualization of feature maps verified the image features that CNN models focus on, and it was confirmed that different types of models generally focus on similar gas-liquid distribution shapes.

Physics-constrained and meshless data assimilation of three-dimensional particle tracking velocimetry

Manuel Ratz[1,*], Alessia Simonini[1] and Miguel A. Mendez[1]
1: von Karman Institute for Fluid Dynamics, Sint-Genesius-Rode, Belgium
* Correspondent author: manuel.ratz@vki.ac.be

Keywords: Data assimilation, Tomographic PTV, Radial basis function

Over the past decade, the measurement techniques providing the three-dimensional velocity field in all three dimensions (3D3C) have become state-of-the-art in many applications.

This includes particle image velocimetry (PIV) and particle tracking velocimetry (PTV), which produce velocity measurements in gridded and scattered data, respectively. In the case of scattered data, the post-processing to compute derived quantities such as vorticity or pressure is usually based on interpolation onto regular, possibly fine, grids (Schneiders & Scarano, 2016; Agarwal et al., 2021). Alternative methods consist in reconstructing individual particle tracks enforcing physical constraints (Gesemann et al., 2016) or using penalized Eulerian formulations with physics-informed neural networks (Cai et al., 2021). However, both methods require dense vector seeding and are computationally demanding because they require the solution of a nonlinear optimization problem.

Recently, a meshless formulation using Radial Basis Functions (RBF) has been proposed by Sperotto et al., 2022a. This approach approximates any functions (velocity or pressure fields) as a weighted sum of RBFs and thus provides an analytic expression that allows for fast and accurate computation of derivatives. Moreover, the RBF assimilation framework allows for imposing differential physical constraints and yields a set of quadratic optimization problems. The RBF framework was applied to laminar steady flow fields (Sperotto et al., 2022a) and more recently to turbulent flows in a Reynolds-averaged Navier-Stokes (RANS) framework (Sperotto et al., 2022b). However, both were applied only to synthetic data, with a numerical implementation that posed significant memory demands for three-dimensional flow fields. This work presents an implementation of the RBF-constrained assimilation framework to 3D particle tracking measurements and introduces several novelties to improve its numerical implementation.

The experimental test case consists of an underwater jet with a diameter of 15 mm and a maximum velocity of 0.45 m/s resulting in a Reynolds number of Re = 6750. The experimental setup is shown in Fig. 1(a). The tomographic imaging system consisted of 4 Speedsense M310 cameras with a resolution of 1280×800 px and objectives with a focal length of 100 mm. Dynamic studio was used to acquire 2000 snapshots with a frequency of 1000 Hz and post-process the PTV using the four-frame particle tracking algorithm (Kitzhofer et al. 2009). The reconstructed voxel volume spans a domain of 70×40×25 mm and achieves a scaling factor of 16 voxels/mm with a vector seeding of 4500 to 7000 vectors at each time step. An instantaneous velocity field is shown in Fig. 1(b).

In terms of numerical implementation, we explore three main paths to speed up the assimilation of physics-constrained mean and Reynolds stresses fields from 3D PTV. First, we use Wendland compact support functions instead of Gaussians. This produces sparse systems, which can be stored more efficiently. Second, we combine direct and iterative methods to solve the constrained regression at a reduced computational cost. Finally, we present an approach to compute Reynolds stresses without solving the assimilation at each time step. Instead, we use the RBFs as weights to compute local correlations in time directly on the scattered data.

The super-resolution fields of mean and Reynolds stress will be compared with well-known Reynolds average and self-similar formulations of the round jet flow for different jet velocities. The results open the paths to computing analytically differentiable time-averaged pressure fields from experimental data.

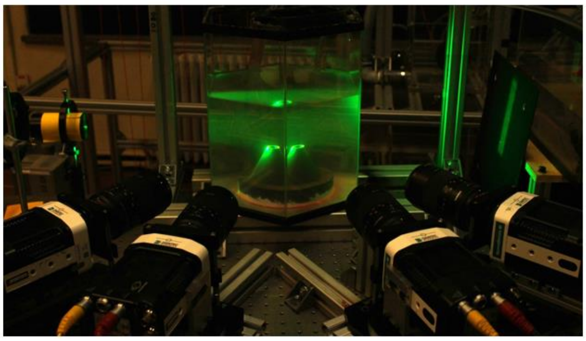

(a)

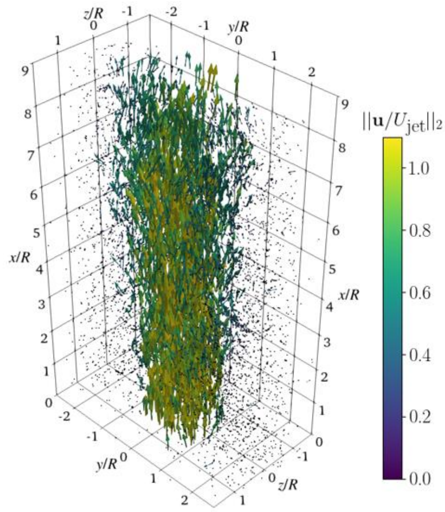

(b)

Figure 1. Experimental jet facility with the tomographic imaging system (a). Instantaneous 3D3C velocity field obtained with 3D PTV (b).

REFERENCES

The list of references should be alphabetized by the last names of the first author of each, using the APA formatting. Examples:

- Agarwal, K., Ram, O., Wang, J., Lu, Y., & Katz, J. (2021). Reconstructing velocity and pressure from noisy sparse particle tracks using constrained cost minimization. Experiments in Fluids, 62(4), (pp. 75).
- Cai, S., Wang, Z., Fuest, F., Jeon, Y., Gray, C., & Karniadakis, G. (2021). Flow over an espresso cup: Inferring 3-D velocity and pressure fields from tomographic background oriented Schlieren via physics-informed neural networks. Journal of Fluid Mechanics, 915.
- Gesemann, S., Huhn, F., Schanz, D. & Schröder, A. (2016). From Noisy Particle Tracks to Velocity, Acceleration and Pressure Fields using B-splines and Penalties. 18th International Symposium on Applications of Laser and Imaging Techniques to Fluid Mechanics.
- Kitzhofer, J., Kirmse, C. & Brücker, C. (2009). High Density, Long-Term 3D PTV Using 3D Scanning Illumination and Telecentric Imaging. In Imaging Measurement Methods for Flow Analysis (pp. 125–134).
- Schneiders, J. F. G. & Scarano, F. (2016). Dense velocity reconstruction from tomographic PTV with material derivatives. Experiments in Fluids 75(9).
- Sperotto, P., Pieraccini, S. & Mendez, M. A. (2022a). Meshless Method to Compute Pressure Fields from Image Velocimetry. Measurement Science and Technology 33(9), 094005.
- Sperotto, P., Pieraccini, S. & Mendez, M. A. (2022b). A RANS approach to the Meshless Computation of Pressure Fields From Image Velocimetry. 20th International Symposium on Applications of Laser and Imaging Techniques to Fluid Mechanics.

Experimental dataset investigation of deep recurrent optical flow learning for particle image velocimetry

Yuvarajendra Anjaneya Reddy[1,*], Joel Wahl[1], Mikael Sjödahl[1]
1: Department of Fluid and Experimental Mechanics, Luleå University of Technology, Sweden
* yuvarajendra.anjaneya.reddy@ltu.se

Keywords: Particle Image Velocimetry, Experimental dataset, Image pre-processing, Neural network, Optical flow

ABSTRACT

The main motto for deep learning alternatives in particle image velocimetry (PIV) is to develop an end-to-end manner neural network for estimating dense fluid motion by leveraging real-life experimental measurement data. Currently available supervised learning networks based on optical flow estimation have been successful in learning fluid displacements from time-resolved particle images. Note that these networks are trained on datasets that majorly comprise synthetic data and synthetically modified data to match real-world measurements. This is advantageous because it allows for greater control and variation than what can be easily achieved using real-world data for supervised learning. Real-world data would also require the estimation of flow fields (ground truths) for training purposes using conventional or other PIV methods, which could invite systematic errors to be mimicked by neural networks. However, it is important to ensure that the training dataset accurately reflects real-world PIV images so that users can have confidence in the end result. Improving the performance and generalization of a neural network requires a deeper understanding of how the neural networks respond to various image-processing steps and also gaining insights into if and at what level of image processing can be leveraged to improve the network's performance on real-world datasets.

In this study, we investigate the influence of input image preprocessing using the experimental data from PIV. Experiments for two-dimensional flow over a circular cylinder at various Reynolds numbers were carried out at different lighting conditions, and the setup is presented in Figure 1. The current state-of-the-art optical flow learning architecture, based on recurrent all-pair field transforms, (RAFT-PIV) will be used for testing [1]. The dataset generated from the experiments has image properties such as particle diameter (D_p) of 3 pixels, particle seeding density (N_{ppp}) of 0.01 particles per pixel with a maximum displacement (Δ_{max}) of 3 pixels between each time step. These image characteristics fall within the synthetic dataset regime used for training RAFT-PIV [2]. The image preprocessing steps used in this study will also aim to emulate physical dependencies or constraints encountered during experimental data accumulation. To validate the experimental dataset, the adaptive PIV technique implemented in Dantec DynamicStudio software, and the results from RAFT-PIV will be utilized. The quality of input particle images can significantly dictate the performance and learning strategy of these neural networks, as the optical flow estimation is close to per-pixel resolution. As an example, a visual comparison of results from RAFT-PIV upon feeding the inputs, the raw image pair (left), the high contrast image pair (middle), and the de-noised image pair (right) are shown in Figure 2. Through this investigation, we aim to contribute to the development of more effective deep learning models in optical flow learning for real-world particle image velocimetry applications.

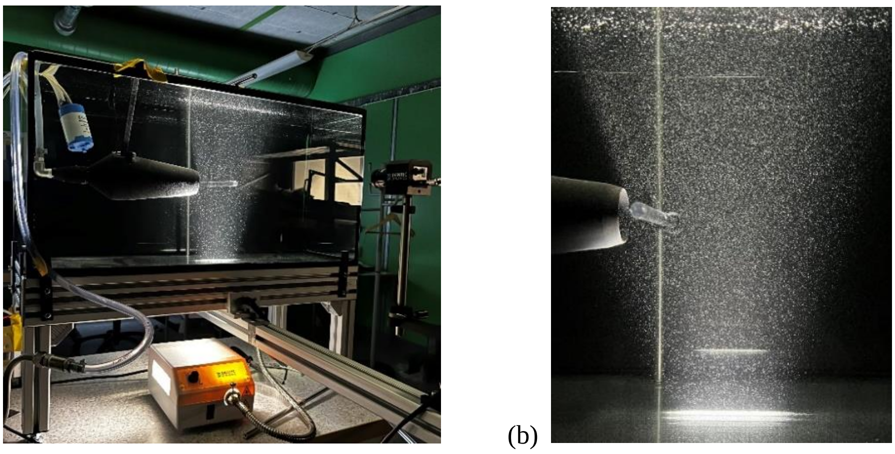

(a) (b)

Figure 1. Experimental setup: (a) Dantec Dynamics EduPIV setup with LED illumination. (b) Circular cylinder of 12[mm] diameter, with an inlet nozzle of 50[mm], for a range of Reynold numbers (Re), $500 \leq Re \leq 4500$

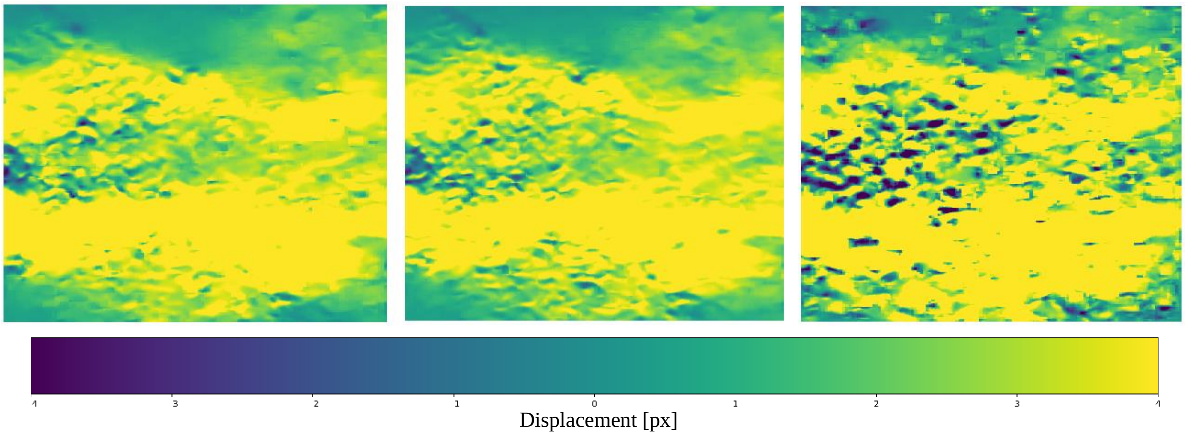

Figure 2. Comparison of streamwise displacement field results from RAFT-PIV upon feeding different pairs of input particle images. Result of raw input image pair without any image processing (left), high-contrast (Contrast Limited Adaptive Histogram Equalization) input image pair result (middle), and de-noised (Non-local Means Denoising algorithm) input image pair result (right).

REFERENCES

[1]. Lagemann, C., Lagemann, K., Mukherjee, S. & Schröder, W. (2021). Deep recurrent optical flow learning for particle image velocimetry data. Nature Machine Intelligence. 3. 641-651. 10.1038/s42256-021-00369-0.

[2]. Lagemann, C., Lagemann, K., Mukherjee, S. & Schröder, W. (2022). Generalization of deep recurrent optical flow estimation for particle-image velocimetry data. Measurement Science and Technology. 33. 10.1088/1361-6501/ac73db.

Fusing Tomo-PIV with Numerical Simulation: Data Assimilation for Multi-Physics Field Reconstruction

Chuangxin He*, Xin Zeng and Yingzheng Liu

School of Mechanical Engineering, Shanghai Jiao Tong University, China
* Correspondent author: chuangxin.he@sjtu.edu.cn

Keywords: Tomo-PIV, data assimilation, adjoint formulation, multi-physics

ABSTRACT Tomography particle image velocimetry (Tomo-PIV) has become the most widely used three-dimensional flow field measurement technique nowadays, with the reconstruction of the voxel gray field from particle images captured by different cameras, followed by the classical cross-correlation to determine the velocity vectors. However, Tomo-PIV is subject to various errors including the effect of the ghost particles induced by the multiplicative algebraic reconstruction technique (MART) algorithm and the cross-correlation using a specific interrogation window in shear flows; the spatial resolution is also greatly reduced using the cross-correlation algorithm. Such shortcomings can be surmounted by the state-of-art 4D-PTV, represented by 'Shake-The-Box (STB)' technique. Different from the conventional PTVs which use only two instants for the velocity vector identification, 4D-PTV relies on the successive tracking of the individual particles at different instants to form long trajectories. Discrete velocity vectors can then be determined on the trajectories with high resolution and accuracy, followed by the physcal-constraint interpolation schemes to reconstruct the velocity fields on the Euler grid. The long trajectory tracking is beneficial for the elimination of the ghost particle effects, while high frequency of the camera imaging, i.e., small displancements of the particles during two sucessive sampling instants, is requisite to identify the same particles in the image sequence (particle pairing). These give rise to the limitation of the present 4D-PTV technique which applicable only in the flows with speed less than 10 m/s using the current hardware devices. Data assimilation (DA) is a technique that fuses experimental measurements with numerical simulations to gather observations (measurement data) at a given time or given locations and use flow dynamic equations to estimate future states or global fields. The present presentation gives a detail introduction to the latest progress of our research group in adjoint-based data assimilation for Tomo-PIV measurements, including the flow data enhancement and pressure field determination. Particular attention is paid to increasing the dynamical range of 4D-PTV by a potential particle tracking capability using four-dimensional variation (4DVar) data assimilation scheme.

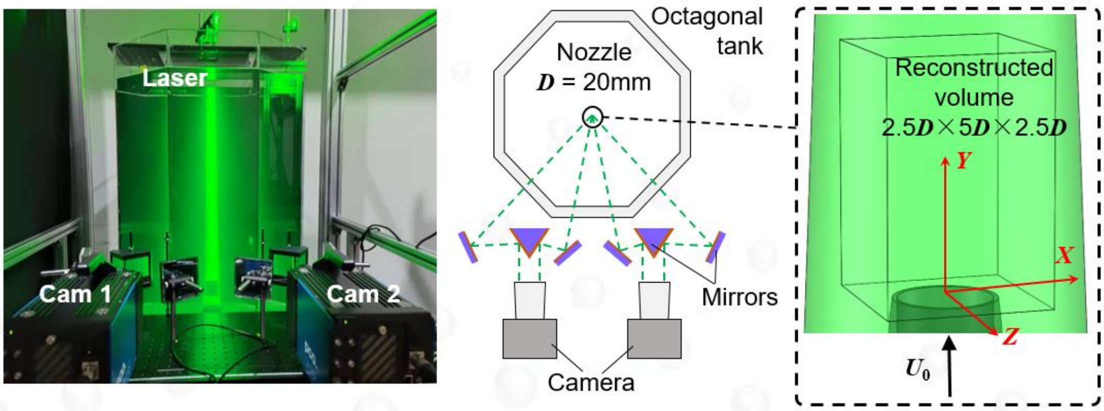

Figure 1.Experimental setup of the Tomo-PIV measurement.

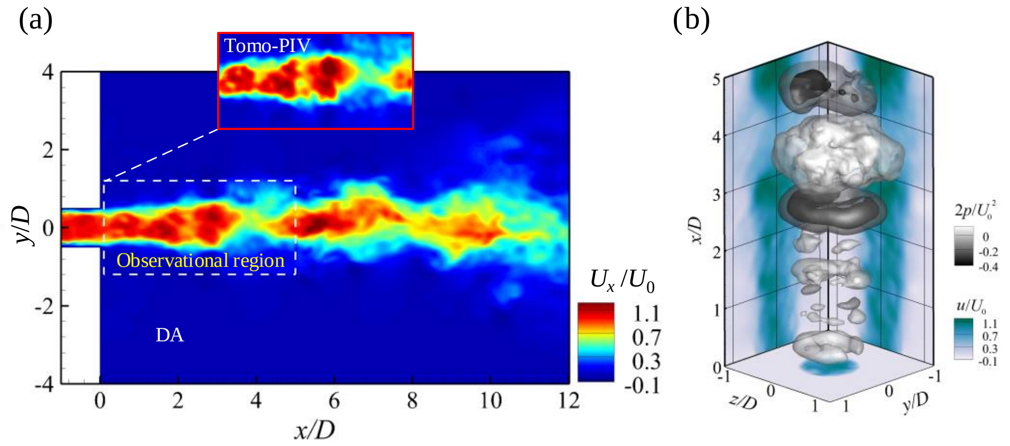

Figure 2. Data assimilation of the global flow fields (a) and pressure determination (b) in the turbulent jet.

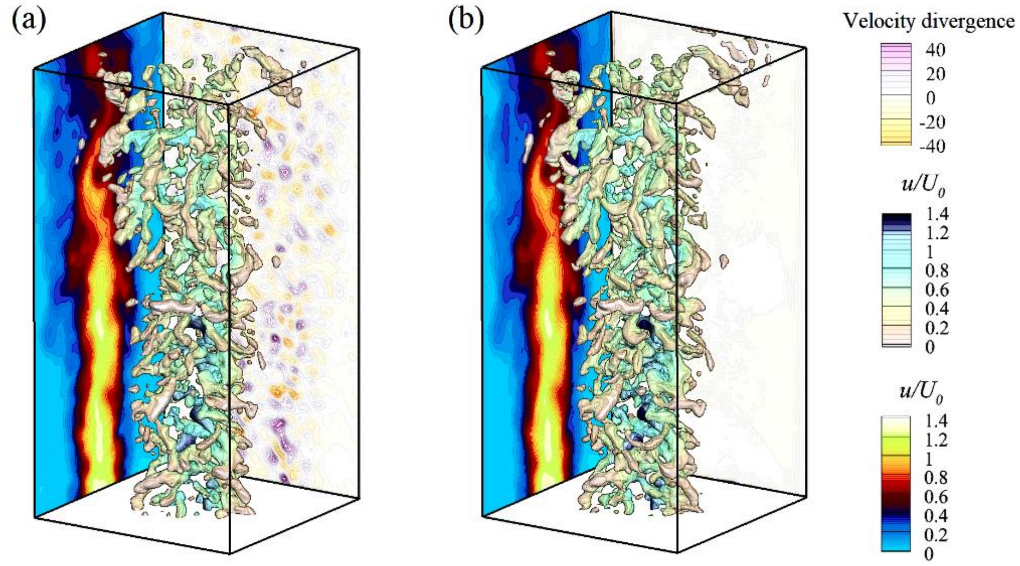

Figure 3. Vortical structures of the flow field at an observational instance. (a) original Tomo-PIV measurement, (b) 4DVar reconstruction. Divergence error is substantially reduced.

REFERENCES

[1] ZENG, X., HE, C., LIU, Y. (2022). GPU-accelerated MART and concurrent cross-correlation for tomographic PIV". Experiments in Fluids. Experiments in Fluids 63,91.

[2] HE, C., WANG, P., LIU, Y. (2022). Flow enhancement of tomographic particle image velocimetry measurements using sequential data assimilation". Physics of Fluids. 34: 035101

[3] Elsinga, GE., Scarano, F., Wieneke, B., Oudheusden, B. (2006). Tomographic particle image velocimetry. Experiments in Fluids 41:933-947.

[4] Schanz, D., Gesemann, S., Schrder, A. (2016). Shake-The-Box: Lagrangian particle tracking at high particle image densities. Experiments in Fluids 57:70.

A combination of KNN-PTV and physics-constrained RBFs for super-resolution in image velocimetry

Iacopo Tirelli[1,*], Miguel Alfonso Mendez[2] , Andrea Ianiro[1] and Stefano Discetti[1]
1: Universidad Carlos III de Madrid, Aerospace Engineering Research Group, Madrid, Spain
2: von Karman Institute for Fluid Dynamics, Environmental and Applied Fluid Dynamics, Sint-Genesius-Rode, Belgium
* Correspondent author: iacopo.tirelli@uc3m.es

Keywords: PIV, PTV, cRBFs, Resolution-enhancement

ABSTRACT This paper presents a novel super-resolution approach for image velocimetry, which combines K-Nearest-Neighbours Particle Tracking Velocimetry (Tirelli et al., 2023a, KNN-PTV) with constrained Radial Basis Functions (Sperotto et al., 2022, c-RBFs) regression. KNN-PTV improves the spatial resolution of a vector field by leveraging data coherence in space and time, while c-RBF enables the computation of an analytical vector field that adheres to physical constraints such as no-slip conditions at walls or the divergence-free for incompressible flows. We investigate the potential of the KNN-RBF combination in 2D and 3D applications, which are challenging for traditional methods due to sparser particle distributions. This extension is the focus of our ongoing research and will be discussed in detail in our upcoming conference contribution.

1 INTRODUCTION

The methodology presented in this paper aims to improve the spatial resolution of Particle Image Velocimetry (PIV) or Particle Tracking Velocimetry (PTV) by combining the ensemble approach of KNN-PTV (Tirelli et al., 2023a) with constrained regression using Radial Basis Functions (cRBFs), as proposed in Sperotto et al. (2022). KNN-PTV identifies similar flow structures at different time instants using a large ensemble of statistically independent snapshots, allowing for the enhancement of spatial resolution by merging particle vectors from different snapshots. The algorithm splits the measurement domain into subdomains to enforce similarity on a local scale and then uses an unsupervised KNN search in the space of significant flow features obtained through Proper Orthogonal Decomposition (POD) of the original data obtained via cross-correlation in PIV or binning in PTV. The enhanced fields obtained by KNN-PTV are then fed into the cRBFs regression to achieve super-resolution. This algorithm approximates the velocity field as a linear combination of RBFs, which is constrained to respect priors such as compliance with the boundary conditions or physical constraints (e.g. solenoidal velocity field in incompressible flow, etc.). The analytical approximating functions can be evaluated (and differentiated) on any grid a posteriori, making this approach to all effects "meshless".

The goal of this combination is to leverage the complementary strengths of KNN-PTV and c-RBFs to achieve physically constrained super-resolution by exploiting the space-time coherency of the data. In the preliminary combination presented in this work, the cRBF is fed with fields whose local density is increased via KNN-PTV.

2 VALIDATION AND PRELIMINARY RESULTS

The algorithm proposed was tested using synthetic PTV data derived from a direct numerical simulation (DNS) of a turbulent channel flow obtained from the Johns Hopkins Turbulence Database (http://turbulence.pha.jhu.edu/). The dimensions of the channel consist of 2 half-channel-heights h from wall to wall, $3\pi h$ in the span-wise direction and $8\pi h$ in the streamwise direction. For all simulation settings, please refer to Li et al. (2008). In this simulated experiment, subdomains of $2h \times h$ are extracted in the streamwise and wall-normal directions, respectively. The resolution is set at 512 pixels$/h$ and the particle image density is 0.01 particles per pixel. To reduce the correlation between different samples, the snapshots are generated with a time separation of 1 convective time. A large number of snapshots are extracted by exploiting flow homogeneity in the streamwise and spanwise directions. The subdomains are separated by $2h$ in the streamwise and $0.25h$ in the spanwise direction, resulting in a total of 11856 generated snapshots. The exact particles position fed the KNN-PTV to avoid errors from blending snapshots of other sources due to the image pairing process. The performance of the algorithm was evaluated using the normalized root mean square error δ_{RMS} as a metric, defined in Equation 7 of Tirelli et al. (2023a).

The contours of the instantaneous stream-wise velocity field estimated by standard PIV with an interrogation window of 32x32 pixels, KNN-PTV and KNN-PTV combined with RBF, along with the reference field from the original DNS, are shown in Figure 1. Table 1 shows the spatial average of the root mean square error δ_{RMS} evaluated for all the above-mentioned application.

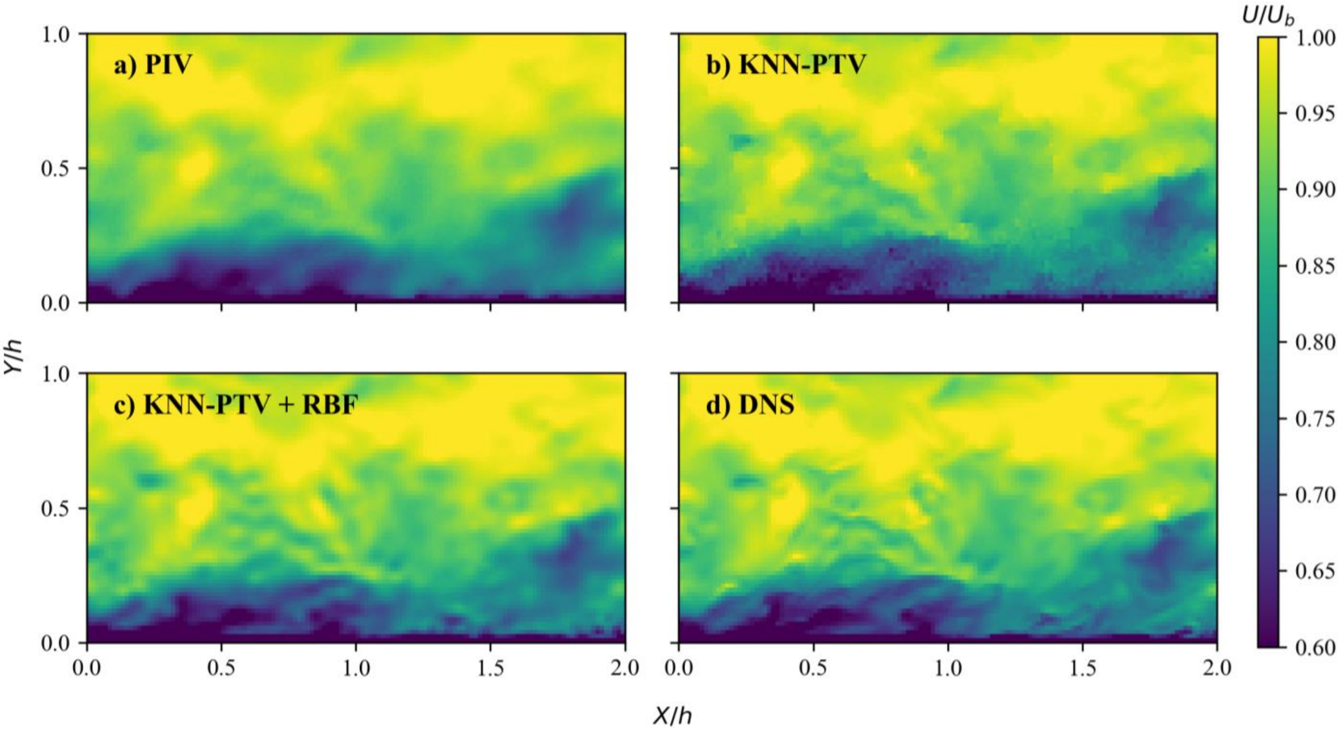

Figure 1. Instantaneous stream-wise velocity field contours estimated with: (a) standard PIV with interrogation window of 32×32 pixels, (b) KNN-PTV, (c) KNNPTV + RBF. The reference field from the original DNS is included for comparison (d) . The parameter used for dimensionless measurements of the stramwise velocity component U is the bulk velocity U_b = 7.5 pixels.

PIV IW = 32	KNN-PTV	KNN-PTV + RBF
0.0222	0.0196	0.0173

Table 1. Spatial average of the root mean square error $\langle \delta_{RMS} \rangle$ evaluated for PIV with interrogation window of 32 pixels, KNN-PTV and KNN-PTV with the help of RBF.

The benchmarking was performed against standard PIV with an interrogation window of 32 pixels, simulated by filtering the data with a moving average and down-sampling the result, and the stand-alone implementation of the KNN-PTV. From both the methodologies the bias error due to modulation effect on the mean flow has been removed as explained in Tirelli et al.(2023b). The c-RBF regression was constrained to have no-slip conditions at walls. Additionally, this condition was applied also as a penalty. The domain contained 3104 collocation points following the clustering approach explained in Sperotto et al. (2022). The preliminary results of the new methodology demonstrate promising accuracy in reconstruction.
The validation of the method on experimental test cases is currently ongoing. Furthermore, the authors are working on the extension to 3D. The combination of KNN-PTV and RBF methodologies is expected to be particularly well-suited for 3D flow analysis, as the enforcement of physical constraints should be able to compensate for the larger interparticle spacing. The results of this extension and its application to more complex flows will be presented in the final conference contribution.

3 REFERENCES

- Li, Y., Perlman, E., Wan, M., Yang, Y., Meneveau, C., Burns, R., ... & Eyink, G. (2008). A public turbulence database cluster and applications to study Lagrangian evolution of velocity increments in turbulence. Journal of Turbulence, (9), N31.
- Sperotto, P., Pieraccini, S., & Mendez, M. A. (2022). A meshless method to compute pressure fields from image velocimetry. Measurement Science and Technology, 33(9), 094005.
- Tirelli, I., Ianiro, A., & Discetti, S. (2023a). An end-to-end KNN-based PTV approach for high-resolution measurements and uncertainty quantification. Experimental Thermal and Fluid Science, 140, 110756.
- Tirelli, I., Ianiro, A., & Discetti, S. (2023b). A simple trick to improve the accuracy of PIV/PTV data. Experimental Thermal and Fluid Science, 110872.

4 ACKNOWLEDGEMENT

This project has received funding from the European Research Council (ERC) under the European Union’s Horizon 2020 research and innovation programme (grant agreement No 949085, NEXTFLOW ERC StG).

TECHNICAL SESSION 9
INDUSTRIAL FLOWS

Chaired by Yassin Hassan

Turbulent Flow Visualization in a 61-pin Wire-Wrapped Hexagonal Rod Bundle with a Porous Blockage

Craig Menezes[1,*] and Yassin Hassan[1,2]
1: Dept. of Nuclear Engineering, Texas A&M University, USA.
2: Dept. of Mechanical Engineering, Texas A&M University, USA.
* Correspondent author: craigmenezes@tamu.edu

Keywords: Particle Image Velocimetry, Matched Index of Refraction, Rod Bundle, Wire Wrapped, Porous Blockage.

ABSTRACT Characterization of flow phenomena within nuclear reactor cores is critical to identify important local thermal hydraulic phenomena. Liquid metal fast reactors (LMFRs) are an important subset of the upcoming generation-IV nuclear reactor designs, which require extensive fluid dynamics investigations. To study accident condition flow responses in such LMFR wire-wrapped rod bundles with complex geometries, time-resolved particle image velocimetry (TR-PIV) at a turbulent Reynolds number (Re) of 14,000 were performed using the matched-index-of-refraction (MIR) method – to obtain non-intrusive flow measurements in the interior subchannels of a 61-pin wire-wrapped rod bundle with a porous blockage installed. Proper Orthogonal Decomposition (POD) of the vorticity fields provided an energy-based classification of coherent structure formations caused by the presence of the porous blockage medium. These unique data sets are imperative toward the enhancement of operational safety in wire-wrapped rod bundles, as well as for computational fluid dynamics (CFD) model validations.

1 TR-PIV MEASUREMENTS USING MIR IN THE VICINITY OF THE POROUS BLOCKAGE

LMFR nuclear fuel bundles typically employ rods arranged in a tightly packed triangular lattice with a thin wire helically wrapped around an individual rod. The wire functions as a spacing mechanism for adjacent rods which prevent direct contact and simultaneously enhance mixing by inducing turbulence. The bundle lattice structure and the presence of the wires introduce geometrical complexities for local flow measurements. Blockages in such wire-wrapped rod bundles (due to possible debris aggregation or accumulation of corrosion products) are imperative to be studied, which additionally contribute to the aforementioned visualization complexity. To overcome these limitations, the MIR method using two materials possessing the same optical indices of refraction were used to obtain TR-PIV measurements in a 61-pin wire-wrapped rod bundle prototype. A porous blockage ($\varepsilon \approx 34.8\%$) was installed to emulate accident conditions. A dual-laser setup eliminated shadows due to the opacity of the porous blockage. Figures 1 (a)-(b) illustrates the two-dimension two-component (2D2C) TR-PIV setup along with demonstrations of the MIR method for flow field measurements (Fig. 1 (c)-(d)) at a turbulent Re condition of 14,000.

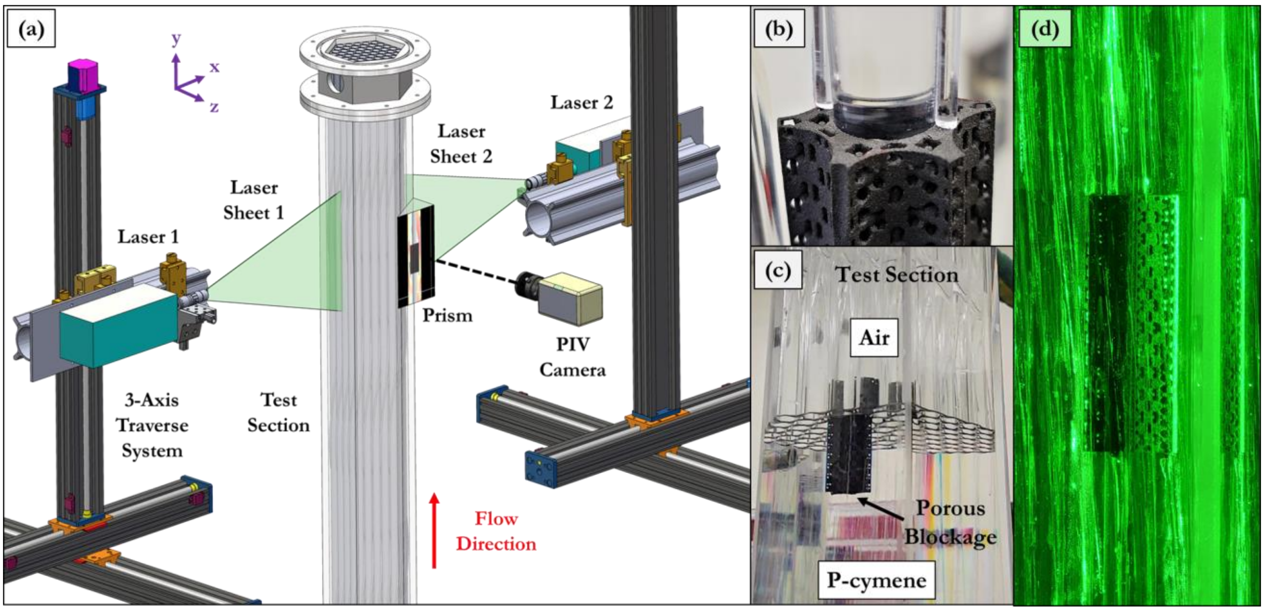

Figure 1. (a) Experimental setup for TR-PIV measurements in the 61-pin wire-wrapped rod bundle. (b) Installed porous blockage ($\varepsilon \approx 34.8\%$)on a wire-wrapped rod highlighting wire continuity. (c) Demonstration of the MIR method showing the optically clear region of the test section partially filled with the working fluid. (d) Example of a TR-PIV test with the operational dual-laser setup to obtain an unobstructed view of the blocked subchannels.

2 TR-PIV RESULTS AND POD ANALYSIS

To study flow effects in the vicinity of the porous blockage, 8,500 TR-PIV snapshots were obtained at a frame rate of 1,600 frames per second and were processed to obtain 2D2C velocity fields. The normalized velocity magnitude (U_{mag}/U_0; U_0 = 1.799 m/s) fields shown in Fig. 2 (a) highlighted important flow phenomena such as stagnation regions in the periphery of the blockage, as well as flow acceleration regions due to flow volume constriction in the blocked subchannels. Flow reattachment was observed on the blockage rod and wire turbulence effects were captured. Additionally, Proper Orthogonal Decomposition (POD) analysis was used to identify statistically dominant large-scale coherent flow structures for the vorticity fields. Figure 2 (b) shows the POD eigenvalue spectra which yields the turbulence kinetic energy (TKE) contained in each mode. The cumulative TKE spectra (Fig. 2 (b)) can be used to reconstruct vorticity fields up to a required TKE based on the decomposed modes.

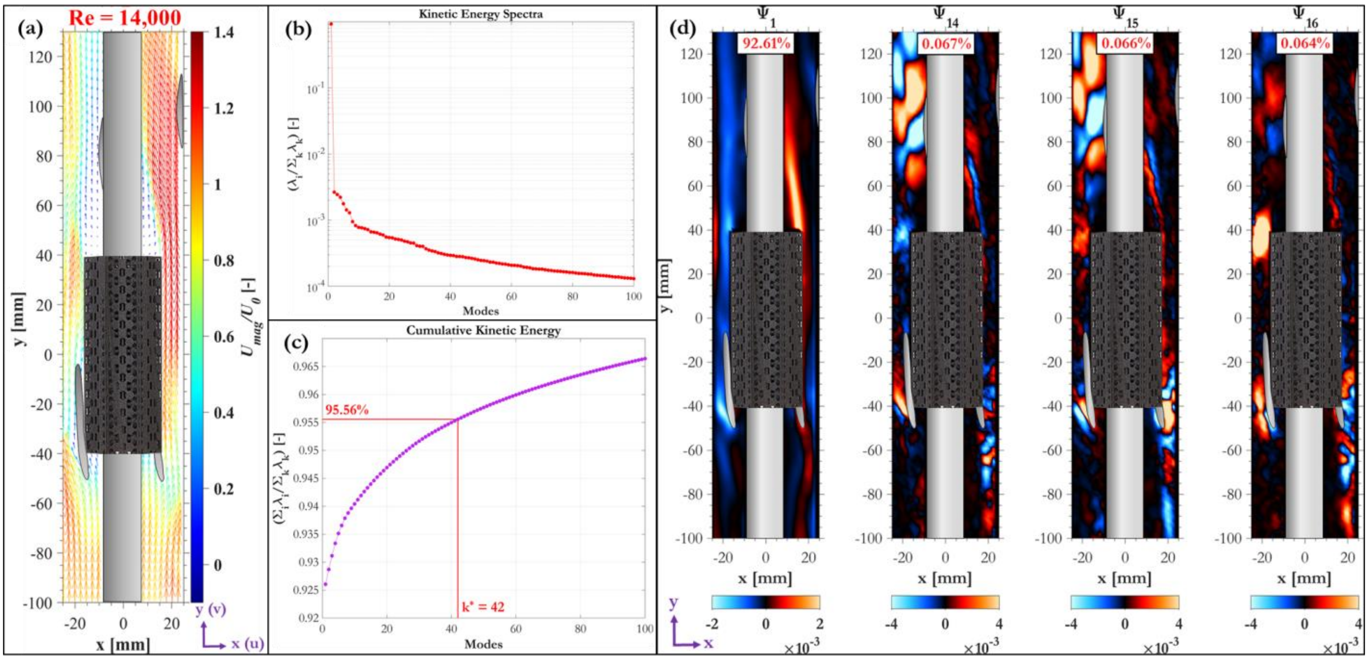

Figure 2. (a) Normalized velocity magnitude (U_{mag}/U_0) at Re = 14,000. (b) POD kinetic energy spectra. (c) POD cumulative kinetic energy spectra useful for the identification of cumulative kinetic energy contained in the decomposed modes. (d) Low-order POD spatial modes for vorticity ($\Psi_{1,14-16}$) with their TKE annotated highlighting important flow phenomena in the vicinity of the porous blockage in the interior subchannels of the 61-pin wire-wrapped rod bundle.

The low-order POD spatial modes ($\Psi_{1,14,15}$) in Fig. 2 (d) show the coherent structure formations in the blocked interior subchannels. Ψ_1 was observed to show strong similarity to the mean vorticity field due to 92.61% of the TKE contained in this mode. Subsequent spatial modes (Ψ_{2-13}) demonstrated a localization of turbulence in the leading edge regions of the helically wrapped wires (at $y \approx 50$ mm). Vortex street formations were captured in spatial modes Ψ_{14-16} indicating a lower overall contribution of such structures compared to turbulent structures generated in the vicinity of the wires. Such spatial decompositions are critical to identify mechanisms of turbulence and momentum transport – to characterize accident condition flow phenomena in partially blocked subchannels of a wire-wrapped rod bundle. The results and the analyses present unique data for the validation of CFD models and the development of reduced order flow models. The high-fidelity experimental data sets are imperative for the design optimization of wire-wrapped hexagonal rod bundles toward operational safety enhancements for LMFRs during nominal flow and accident conditions.

3 REFERENCES

- Nguyen, T., Vaghetto, R., & Hassan, Y. (2020). Experimental investigation of turbulent wake flows in a helically wrapped rod bundle in presence of localized blockages. Physics of Fluids, 32(7), 075113.
- Pacio, J., Chen, S. K., Chen, Y. M., & Todreas, N. E. (2022). Analysis of pressure losses and flow distribution in wire-wrapped hexagonal rod bundles for licensing. Part I: The Pacio-Chen-Todreas Detailed model (PCTD). Nuclear Engineering and Design, 388, 111607.
- Bovati, O., & Hassan, Y. (2022). Analysis of the turbulent flow in a partially blocked wire-wrapped rod bundle using LES with wall functions. International Journal of Heat and Fluid Flow, 97, 109041.
- Menezes, C., Melsheimer, T., Pyle, D. W., Kinsky, M., & Hassan, Y. A. (2023). Flow characteristics within an interior subchannel of a 61-pin wire-wrapped hexagonal rod bundle with a porous blockage. Physics of Fluids, 35(2), 027106.

Experimental analysis of dynamic menisci in dip coating

Damien Rigutto[1*], Jean-Marie Buchlin[1], Miguel A. Mendez[1]
1: Environmental and Applied Fluid Dynamics, von Karman Institute, Rhode-Saint-Genese, Belgium
* Correspondent author: damien.rigutto@vki.ac.be

Keywords: Advancing contact line, Dynamic contact angle, Interface detection, PTV

Dynamic wetting is fundamental in many coating processes. In static conditions, when a liquid is in contact with a solid wall, a meniscus is produced. The intersection between the gas-liquid interface and the solid surface occurs at a specific angle known as a static contact angle. When the solid and the interface are in relative motion, the angle is known as dynamic. Most of the theoretical and experimental efforts in its characterization have been focused on highly viscous fluids, for which inertia has a negligible effect.

A fundamental contribution is the empirical correlation proposed by Hoffman (1975), which links the dynamic contact angle to the Capillary number $Ca = \mu U/\sigma$ where μ is the liquid viscosity, σ is the gas-liquid surface tension, and U is the substrate velocity. This correlation was derived at the limit of Ca <<1, but many industrial configurations are characterized by large Ca. The dynamics of the contact angle influences the shape of the meniscus and its ability to remain attached to the solid even in the presence of surface defects. Moreover, the meniscus dynamic is also influenced by the velocity field underneath it. The flow field in the proximity of the contact line is characterized by large gradients required to allow for the velocity to be zero at the wall despite a relative motion between the contact line and the surface (see the triple point paradox (Huh and Scriven, 1970)).

This work investigates the meniscus dynamics on a moving surface and the flow fields underneath it. The configuration of interest is sketched in Figure 1a: the dynamic meniscus is formed as a gas-liquid interface is in contact with a tilted flat plate entering a bath with an angle θ_e and velocity U_p. This configuration is relevant to hot dip galvanization and was reproduced in a facility developed at the von Karman Institute (VKI). The facility consists of a large rotating cylinder partially immersed in a water bath, as sketched in Figure 1b. The cylinder (1) is made of stainless steel and has a diameter of 60 cm and 20 cm in width. It can reach tangential velocities up to 2 m/s. The rotation is driven by a DC motor (2) equipped with a PID controller. The liquid level can be adjusted to modify the entering angle. The measurement section is in the entering zone (3), while wipers are used on the other side (4), together with an air jet (5), to dry the cylinder before the submersion. The facility allows lateral, front, top, and bottom optical access to the entering zone. The range of possible operating conditions, in terms of the aforementioned Ca number and the Weber number $We = \rho U^2 l_c/\sigma$, with $l_c = \sqrt{\sigma/(\Delta\rho\ g)}$ the capillary length are illustrated in Figure 1c. The large velocities and the possibility of altering the water properties by changing the bath temperature allow for covering a wide range of conditions.

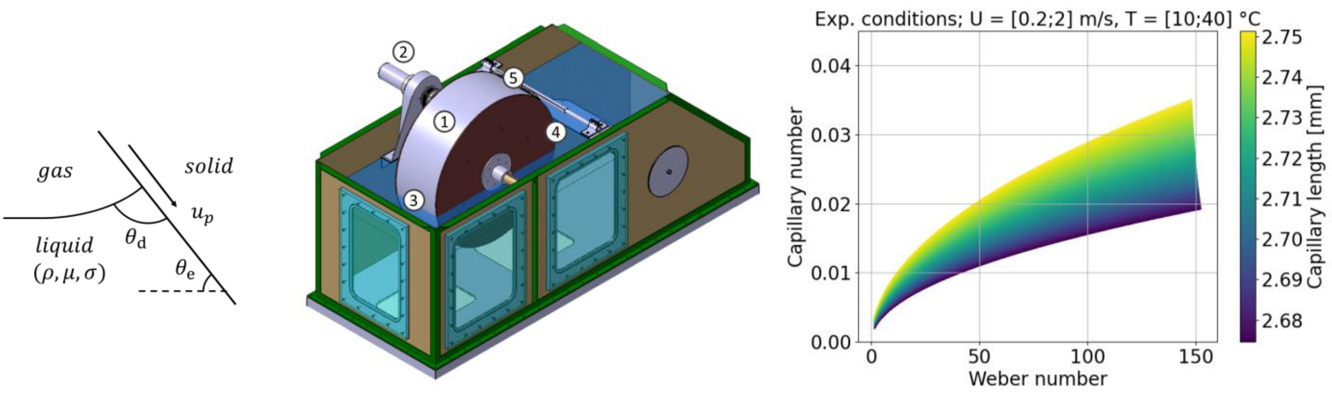

(a) (b) (c)

Figure 1. (a) Schematic of the investigated configuration and main parameters. (b) View of the VKI facility reproducing the dynamic wetting as in hot dip galvanizing. (c) Regions of possible operating conditions in terms of Capillary and Weber number

The facility is instrumented with (1) a device for Laser-Induced Fluorescence (LIF) visualization and detection of the meniscus interface and (2) image velocimetry. Figure 2 illustrates the measurement chain for the LIF-based interface detection of the meniscus. A high-speed camera (Figure 2a) on the side of the tank is used to acquire LIF images. As shown in Figure 2b, the liquid is seeded with Rhodamine B (CI-45170), and the meniscus is illuminated by a laser sheet (LSR-PS-II laser) to obtain images as in Figure 2c. These are post-processed using standard image processing routines to retrieve the meniscus interface and contact angle.

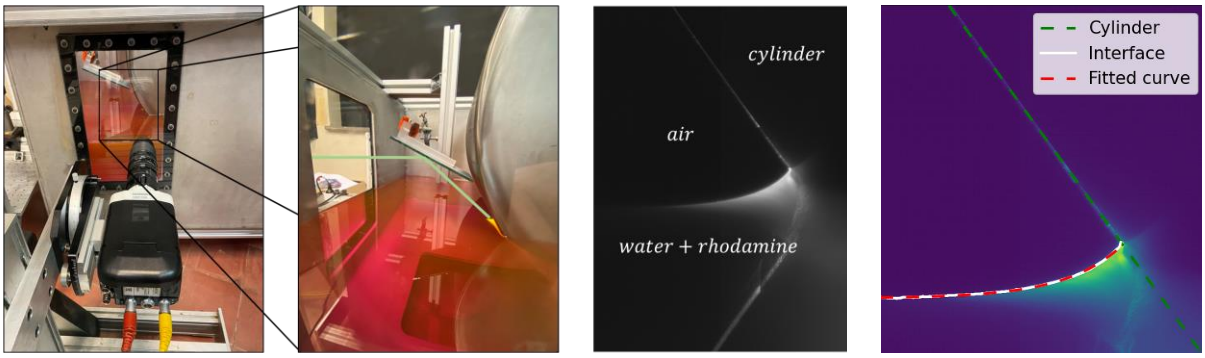

(a) (b) (c) (d)

Figure 2. Figures (a) and (b) show pictures of the high-speed camera installation and laser sheet illumination of the meniscus for the LIF-based visualizations. Figure (c) shows an example snapshot from the acquisition. Figure (d) shows the result of the image processing to detect the meniscus.

Concerning the image velocimetry, Figure 3 shows a picture of the measurement setup (a) and a preliminary measurement (b). In Figure 3a, the meniscus (see cylinder (1)) is illuminated from the side. The laser illumination is produced by a *QUANTRONIX DARWIN DUO* (2) and shaped into a sheet with the optical setup (3) before entering the bath (4). The image acquisition is carried out by the camera (5), which focuses on the flow below the interface. The liquid is seeded with *UVPMS-BR* particles, and the images were processed using the open-source PTV code TracTrac. From the resulting field in Figure 3b, the flow field reveals various relevant flow features, including the growth of the boundary layer on the cylinder wall and the large curvature of the streamlines near the immersion point.

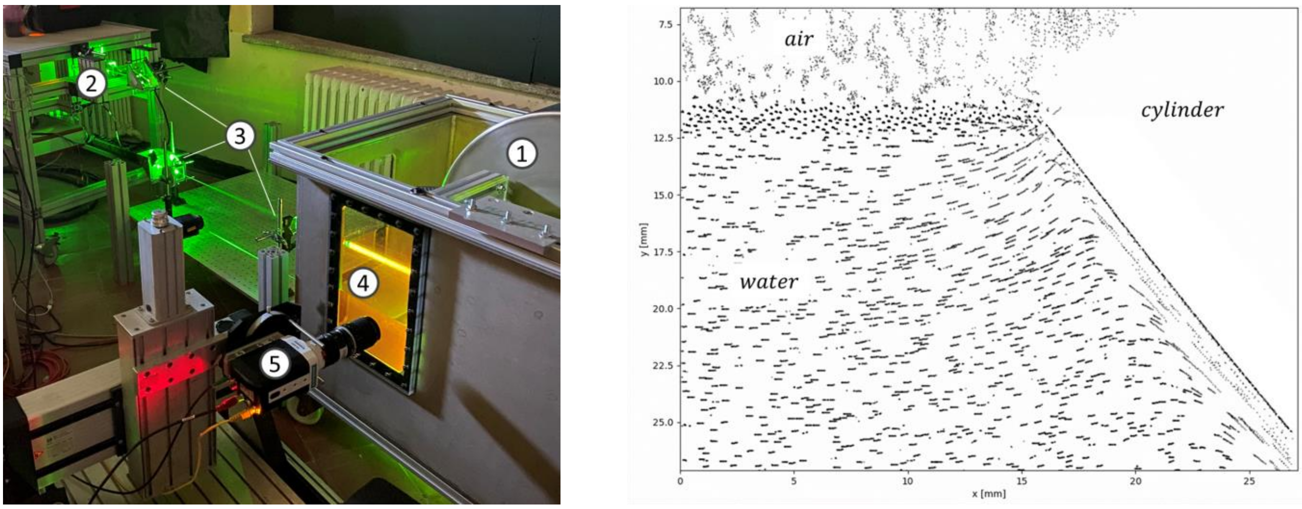

(a) (b)

Figure 3. Figure (a) shows a picture of the image velocimetry setup. Figure (b) shows an example of PTV measurement.

Combining the two measurement techniques, the full paper will present the impact of the operating parameter on the meniscus shape and the flow field near the contact line region.

- Journal article: Hoffman L. Richard, A Study of the Advancing Interface I. Interface Shape in Liquid-Gas Systems, Journal of Colloid and Interface Science 50, 228 (1975).
- Journal article: Huh CHUN and Scriven L. E., Hydrodynamic Model of Steady Movement of a Solid / Liquid / Fluid Contact Line, Journal of Colloid and Interface Science 35, 85 (1970).
- Website: TracTrac PTV software https://perso.univ-rennes1.fr/joris.heyman/trac.html

Flow Visualization Around a Cavitating Tip Vortex

Ozge Baskan Percin[1,*], Daniele Fiscaletti[2], Gerrit Elsinga[3] and Tom van Terwisga[2]
1: Dept. of Aerospace Engineering, Middle East Technical University, Türkiye
2: Dept. of Maritime & Transport Technology, Delft University of Technology, The Netherlands
3: Dept. of Process & Energy, Delft University of Technology, The Netherlands
* Correspondent author: obaskan@metu.edu.tr

Keywords: Flow visualization, Tomographic Particle Image Velocimetry, Tip Vortex, Cavitation

ABSTRACT In this study, the flow field around a cavitating tip vortex is visualized using time-resolved tomographic particle image velocimetry (Tomo-PIV). The experiments are performed in the cavitation tunnel at the Delft University of Technology. A right-handed two-blade marine propeller is used as the experimental model. Time-resolved three-dimensional flow in the wake of the propeller is visualized by seeding the flow with hollow glass particles and illuminating the measurement volume with a high-speed laser. The preliminary results reveal secondary vortices in the flow field and show that the unsteadiness in the flow decreases as the cavitation number increases.

1 INTRODUCTION

Cavitation, the formation of vapor-filled cavities, occurs in liquids when local pressure drops below vapor pressure. It causes degradation in efficiency in engineering systems such as pumps, valves, propellers, and pipes. In addition, the cavitation dynamics lead to noise - which can be harmful to the system and the environment enclosing it – and to physical damage in the system by eroding and destroying the solid surfaces in the flow. Therefore, understanding the physics of cavitation and developing tools that predict cavitation in the design phase is vital.

Marine propellers are one of the engineering systems, the performance of which is highly affected by cavitation. Cavitation on these propellers onsets at the tip of the propeller as a sheet cavity, which then transforms into a tip vortex cavity in the wake of the propeller. Visualizing the flow around cavities is challenging due to the cavitation bubbles blocking camera views. In this respect, particle image velocimetry (PIV) measurements performed around tip vortices were limited to planar measurement configurations or non-cavitating conditions in the literature. For example, Pennings et al.(2015) conducted stereoscopic PIV measurements to obtain flow fields around the cavitating tip vortex of a hydrofoil. Felli et al. (2015) used the tomographic-PIV technique to acquire three-dimensional phase-averaged marine propeller wake flow in non-cavitating conditions.

Therefore, the main objective of this study is to acquire time-resolved three-dimensional flow fields in the wake of a marine propeller using the tomographic-PIV technique. This first study explores the applicability of the measurement technique in cavitation conditions and allows for the analysis of acoustic sources and pressure fields using time-resolved three-dimensional velocity fields.

2 METHOD

2.1 Experimental Setup

The experiments are performed in the cavitation tunnel at the Delft University of Technology (Pennings. 2015). The tunnel has a test section with cross-section dimensions of 0.30×0.30 m^2 at the inlet and 0.30×0.32 m^2 at the outlet to ensure a near-zero streamwise pressure gradient throughout the test section. A right-handed two-blade marine propeller which is designed and provided by the Maritime Research Institute Netherlands (MARIN), is used as the experimental model. The model has a diameter D of 0.15 m and a chord length c of 0.054 m (at 70% radius location). As a result of the specific design of the blade, the leading-edge sheet cavity forming on the suction side of the propeller blade transforms into a tip vortex cavity.

2.2 Tomographic particle image velocimetry

The tomographic-PIV setup consists of four high-speed cameras (LaVision Imager Pro LX 16M) placed on the left and right sides of the test section (two cameras for each side). The cameras are equipped with 105 mm Nikon objectives with a numerical aperture $f_{\#} = 11$. The measurement volume of $100 \times 100 \times 10$ mm^3 (width×height×depth) is illuminated by a high-speed Nd: YLF laser, where the laser enters the test section vertically upward through its bottom wall made of acrylic. The digital resolution is 20 pixels/mm and the corresponding magnification factor is 0.22. The flow is seeded with 10 μm hollow glass particles (Sphericells). The average particle image density is approximately 0.04 particles per pixel (ppp). Tomographic PIV images are captured at an image recording frequency of 640 Hz (double-frame, full resolution) and 4.3 kHz by cropping the recordings and reducing the measurement volume size (single-frame). Image acquisition, image preprocessing, volume calibration, self-calibration, reconstruction, and three-dimensional cross-correlation-based interrogation are performed in LaVision DaVis 8.4. An automated image preprocessing sequence is built to mask the cavitating bubbles. Particle images are interrogated using windows of final size $40 \times 40 \times 40$ voxels (for full-resolution cases) and $32 \times 32 \times 32$ voxels (for cropped cases) with an overlap factor of 75%, resulting in a vector spacing of 0.5 mm and 0.4 mm, respectively, in each direction.

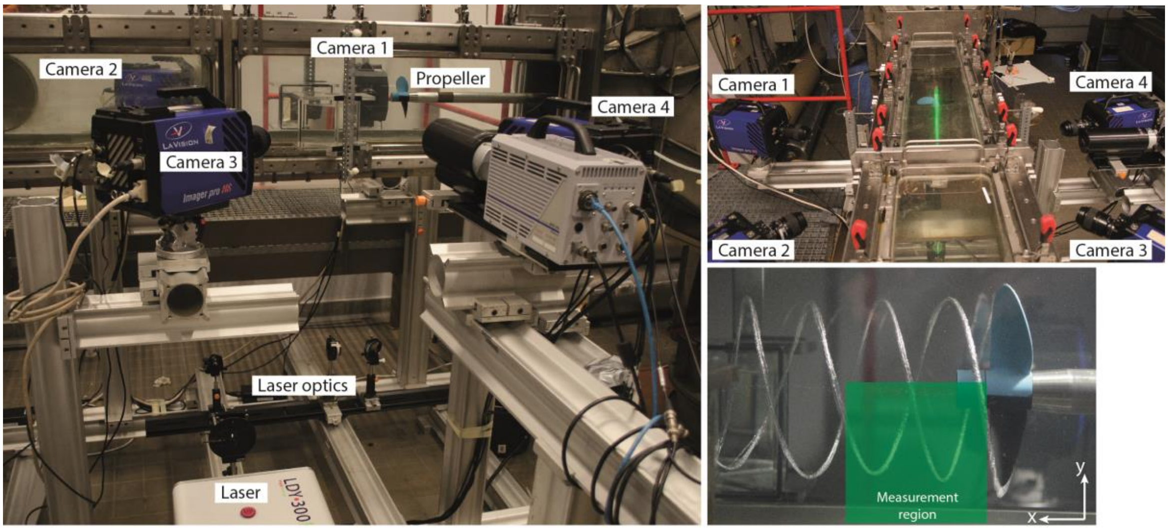

Figure 1. Overview of the experimental setup for the tomographic-PIV measurements. The setup comprises a marine propeller, four cameras, a high-speed laser, and laser optics (left). The cameras are positioned on either side of the test section (top right). The measurement region is illuminated by a high-speed Nd: YLF laser (bottom right).

3 RESULTS

Preliminary results for two different cases are shown in Figure 2. Isosurfaces of the Q criterion (Jeong and Hussain, 1995) are used to visualize the three-dimensional tip vortex and the secondary structures around it. In the first case (Figure 2-left), a significant cavitation bubble forms in the core of the tip vortex, whereas in the other case, no cavitation occurs (Figure 2-right). There is also a secondary vortical structure around the tip vortex for the case with strong cavitation. A detailed analysis of the vortical structures and the velocity fields in the vicinity of the cavitation bubble for the presented and additional cases with different cavitation numbers will be presented at the conference and in the final version of the paper. Their time evolution will be shown as well.

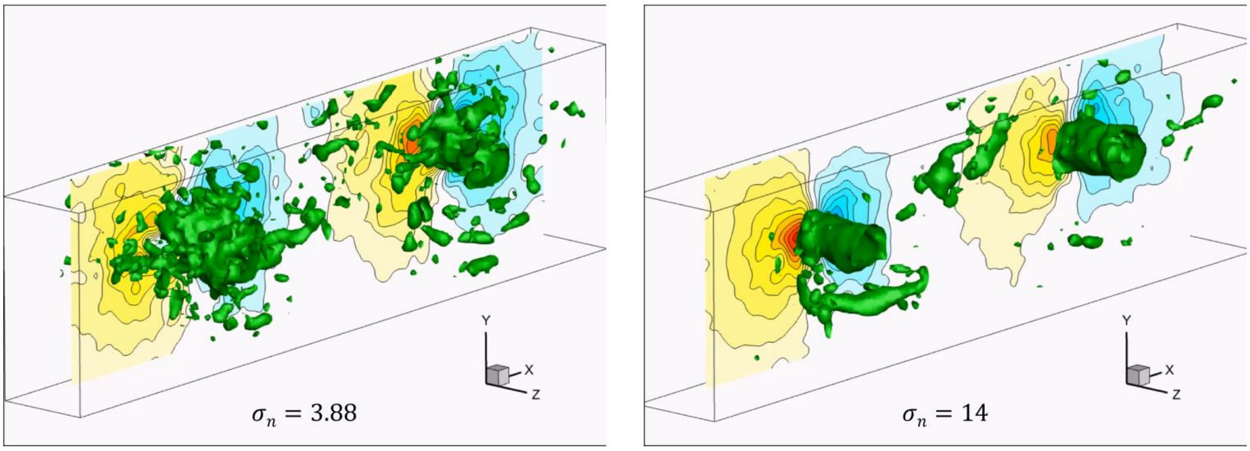

Figure 2. Isosurfaces of Q criterion together with the contours of vertical velocity component (y-velocity) in z = 0 plane for two cases (flow is from left to right): $\sigma_n = 3.88$ (cavitating, left) and $\sigma_n = 14$ (non-cavitating, right).

4 REFERENCES

- Pennings, P. C., Westerweel, J., & Van Terwisga, T. J. C. (2015). Flow field measurement around vortex cavitation. Experiments in Fluids, 56, 1-13.
- Felli, M., Falchi, M., & Dubbioso, G. (2015). Tomographic-PIV survey of the near-field hydrodynamic and hydroacoustic characteristics of a marine propeller. Journal of Ship Research, 59(04), 201-208.
- Jeong, J., & Hussain, F. (1995). On the identification of a vortex. Journal of Fluid Mechanics, 285, 69-94.

Schlieren and x-ray imaging of laser-particle interactions in metal additive manufacturing

Ioannis Bitharas[1*], Kyle Perkins[1], Tao Sun[2], Anthony D. Rollett[3], Andrew J. Moore[1]
1: Institute of Photonics and Quantum Sciences, Heriot-Watt University, UK
2: X-ray Science Division, Argonne National Laboratory, USA
3: Department of Materials Science and Engineering, Carnegie Mellon University, USA.
* Corresponding author: i.bitharas@hw.ac.uk

Keywords: Schlieren imaging, X-ray imaging, Laser-material interactions, 3D printing

ABSTRACT In laser powder bed fusion (LPBF), the most widely adopted additive manufacturing (AM) technique for metallic parts, the multiphase flow dynamics of the laser-material interactions strongly influence the quality of printed parts. Coaxial, high-speed synchrotron x-ray combined with schlieren imaging can therefore give deeper insight into the physics of such flows, by enabling simultaneous visualisation of all phases of matter present. In this work, atmospheric fluid and particle dynamics of Ti-6Al-4V and SS316 alloys are characterised under varying laser energy input, which can drastically change the morphology and stability of the liquid-vapour interface, as well as the intensity of the vapour jet. Characteristic laser-particle interactions that can affect mass transfer and defect formation are showcased. Data fusion and image analysis aid in relating our observations to process stability.

1 INTRODUCTION

During LPBF, a set of operating parameters (mainly laser power, scan speed and focused spot diameter) must be chosen to achieve stable melting of powder particles and substrate over several hours of printing. However, the interactions between the liquid metal pool, vapour jet and powder particles within the inert atmosphere can generate complex dynamics, which may lead to unfavourable flow regimes or high defect rates in printed parts (Bidare et al., 2018). Composite x-ray/visible light images (Figure 1b) allow us to probe into these dynamics, which are integral to the evolution of heat and mass transfer during laser processing. Further, we demonstrated how schlieren imaging alone can be used for process characterisation (and optimal parameter selection), based on the identified flow regimes (Bitharas et al., 2022). We use a high magnification, focusing schlieren setup (Figure 1a); pickoff mirrors M1, M2 allowed near-parallel folding of the optical path relative to the x-ray beam, thus enabling coaxial imaging.

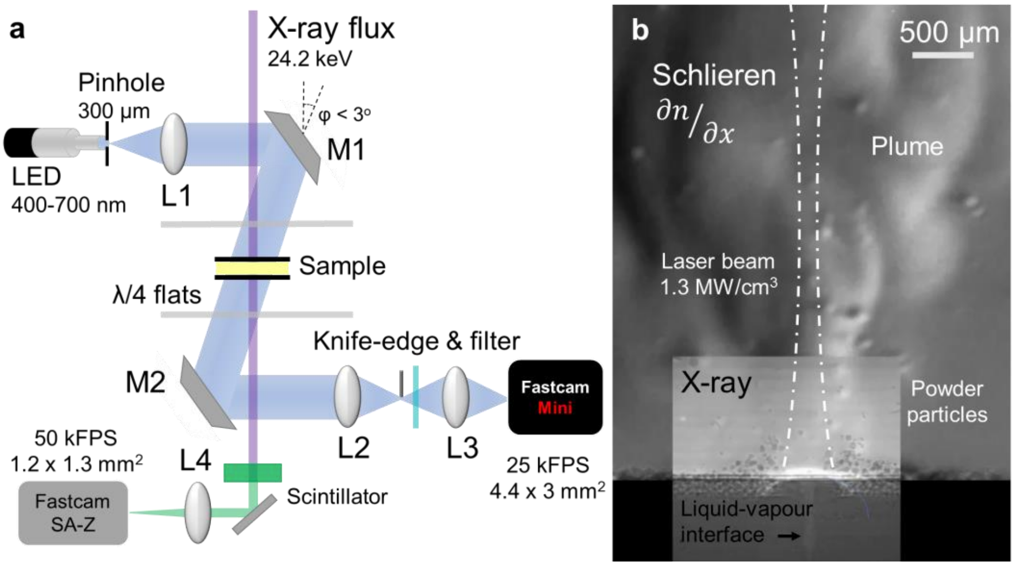

Figure 1. a) Combined lens-based focusing schlieren and synchrotron x-ray imaging setups. b) Composite image reveals multiphase flow dynamics as the laser beam melts and evaporates the metal plate and particles. (Bitharas et al., 2022)

2 COMBINED X-RAY AND SCHLIEREN VISUALISATION

In this set of new experiments, a stationary laser beam of diameter D ~100 μm is incident on the Ti-6Al-4V substrate, with a small number of Ti-6Al-4V particles, sized 120 ± 30μm. Interacting only with 2-3 particles at a time allowed for a more controlled set of initial conditions, which is ideal for validation of multiphysics models, but also provides a clearer view of the underlying physics, as shown in Figure 2. More cases are to be examined in this section, analysing the interesting melt pool/vapour jet dynamics that can develop when molten particles consolidate and fuse with the substrate.

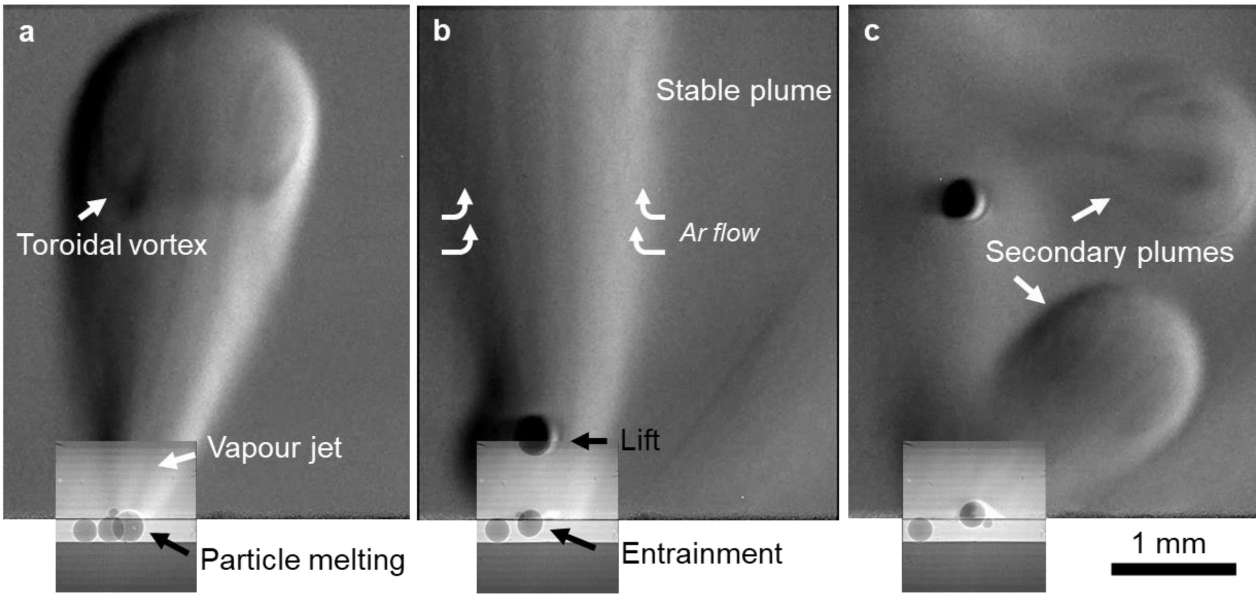

Figure 2. Dynamics of laser beam interacting with particles. a) A vapour depression is formed on a melting particle. The internal, toroidal vortex structure of the plume's convection front is revealed by the presence of evaporated Ti and Al nanoparticles. b) The molten particle is lifted upwards by the vapour flow, whilst a nearby particle is entrained in the plume by the inwards flow induced in the Ar atmosphere. c) Particle trajectories intersect the beam, resulting in the formation of vapour jets in new directions.

3 PROCESSING STABILITY CHARACTERISATION

Our combined x-ray/visible imaging has clearly shown that the state of the melt pool can be inferred by using schlieren alone, as a transition from stable to chaotic flow in the plume was observed during unstable, 'keyhole mode' melting. In this section, we will present results from a large set of schlieren imaging experiments on Ti-6Al-4V and SS316, quantifying the instability levels through standard image processing techniques. Metallography and surface profilometry of the solidified tracks determine the scaling of geometrical features of the melt pool with input energy density and allow us to relate atmospheric dynamics with unfavourable processing regimes.

4 DISCUSSION AND CONCLUSIONS

This latest set of visualisations showed that particles directly interacting with the laser beam melt and fuse with the substrate, or agglomerate with other particles. The interlinked dynamics of the jet of evaporated metallic species and recoil pressure forces on the liquid surface drive the stability of this process, as well as the bead geometry after solidification. It was shown that incomplete laser exposure or high particle mass can result in airborne particles, incomplete melting, or instability. The study of atmospheric fluid dynamics can elucidate stochastic events that lead to the formation of defects during printing, aiding us in selecting parameters that minimise their likelihood of occurrence. We demonstrate that stable processing maps for any material/machine can be derived (or enhanced) through atmospheric monitoring, which aids in maximising productivity whilst maintaining low porosity levels in printed parts.

5 REFERENCES

Bidare, P., Bitharas, I., Ward, R. M., Attallah, M. M. and Moore, A. J., Fluid and Particle Dynamics in Laser Powder Bed Fusion, *Acta Materialia*, vol. **142**, pp. 107–20, January 1, 2018.

Bitharas, I., Parab, N., Zhao, C., Sun, T., Rollett, A. D. and Moore, A. J., The Interplay between Vapour, Liquid, and Solid Phases in Laser Powder Bed Fusion, *Nature Communications*, vol. **13**, no. 1, p. 2959, May 26, 2022.

Flow field investigation of a diffuser blade using endoscopic PIV

Muhsin Can Akkurt[1, 2*], Kevin M. Van Geem[2], Delphine Laboureur[1]
1: The von Karman Institute for Fluid Dynamics, Belgium
2: Ghent University, Laboratory for Chemical Technology, Belgium
* Correspondent author: muhsin.can.akkurt@vki.ac.be

Keywords: particle image velocimetry, endoscopic PIV, steam cracking reactor, diffuser, subsonic flow

ABSTRACT

Steam cracking of hydrocarbons has been widely used in the chemical industry to produce light olefins such as ethylene, propylene, and butadiene [1]. The conventional steam cracking process is a highly energy-intensive operation in the petrochemical industry, where temperatures up to 1100°C are required due to endothermic chemical processes [2]. This step alone accounts for roughly 8% of this industry's total energy consumption and about 30% of the global industry's carbon dioxide emissions [3].

In traditional steam cracking reactors, the hydrocarbon and high-pressure steam mixture is heated by the combustion of fuel in the furnaces [4]. The primary drawback of utilizing furnaces for heat transfer is the fact that the heat transfer walls, instead of the working fluid, are the hottest section of the system. In many cases, the walls can be over 30% hotter than the internal gas.

In contrast, novel concept designs propose a turbomachine to replace the furnaces, where the mechanical energy of the rotor shaft can be transmitted directly to the working fluid, making the fluid the hottest element of the reactor [4]. Our design, which uses standard turbomachinery components, including a stator (IGV), rotor, and a diffuser, has the potential to significantly reduce CO_2 emissions by up to 90% compared to conventional steam crackers. As a result, this innovative technology could potentially serve as a viable replacement for traditional steam-cracking furnaces.

The main objective of our study is to provide experimental validation data for the CFD simulations in this type of reactor design process. In the present study, the diffuser vane has been selected to be experimentally investigated through Particle Image Velocimetry (PIV) measurements. The reason for this is twofold. On the one hand, the diffuser blade row converts the gas kinetic energy -which is increased by the rotor- into an entropy increase resulting in a high level of mixing downstream of this blade row. Secondly, the diffuser reduces the flow velocity which generates stationary shockwaves across which the flow decelerates from supersonic to subsonic speeds over a very small length. Hence, velocity is traded for enthalpy which results in very short heating times. Both reasons clearly stress the importance of the diffusers and thus the choice to experimentally investigate this blade.

This study focused on the subsonic investigation of the flow around the diffuser vane of our design. The planar e-PIV measurements are conducted at the low-speed cascade C-1 facility at the von Karman Institute, designed for the development of axial blade profiles and the investigation of primary and secondary flows in stationary compressor and turbine cascades.

To facilitate the PIV investigation 24 diffuser blades were mounted into the test section to ensure flow periodicity. To provide sufficient optical access into the investigation area, a plexiglass window was installed on one of the end-wall. Additionally, the opposite end wall surface was painted black to increase contrast in the PIV images and reduce laser reflections.

A custom-designed laser endoscope, with an outer diameter of 9mm and fitted with a cylindrical lens and an ND-YAG prism, was used to form and adjust the laser sheet. This endoscope allowed for precise positioning and adjustment of the laser sheet relative to the chord of the diffuser profile. The probe adapter enabled the adjustment of the produced light sheet to investigate the flow in the desired blade span positions.

Seeding particles (oil particles with diameter of about 1μm) were introduced into the flow using a seeding rake. To ensure uniform distribution, the rake contained four copper probes with evenly spaced holes along their length.

The inlet total and static pressures (P_1, P_{01}) were measured by a NACA probe placed upstream of the investigation area, at a distance of four axial chords.

In the flow investigation, an inlet chord-based Reynolds number (Re) of 183,000 was chosen to match the original design. Measurements were taken at multiple blade heights, including 8%, 15%, 23%, 31%, and 39% from the window. To illuminate the entire passage, three endoscope positions were evaluated due to the cambered shape of the diffuser blades, which blocked

the laser sheet. The combined observation areas of the three endoscope positions were used for the mid-span investigation at Re=183,000.

To expand the validation case for CFD simulations, inlet flow regimes between Re=96000 and Re=265000 were also examined for mid-span.

The average absolute velocity fields (Figure 1) at midspan height indicated that the mean velocity throughout the entire passage varies with the inlet Reynolds number and the vortical turbulent flow structures are being generated behind the trailing edge. It was observed that the inlet velocity within the range of Re=90000-280000 does not impact the flow structures across and downstream the passage, as represented by the streamlines.

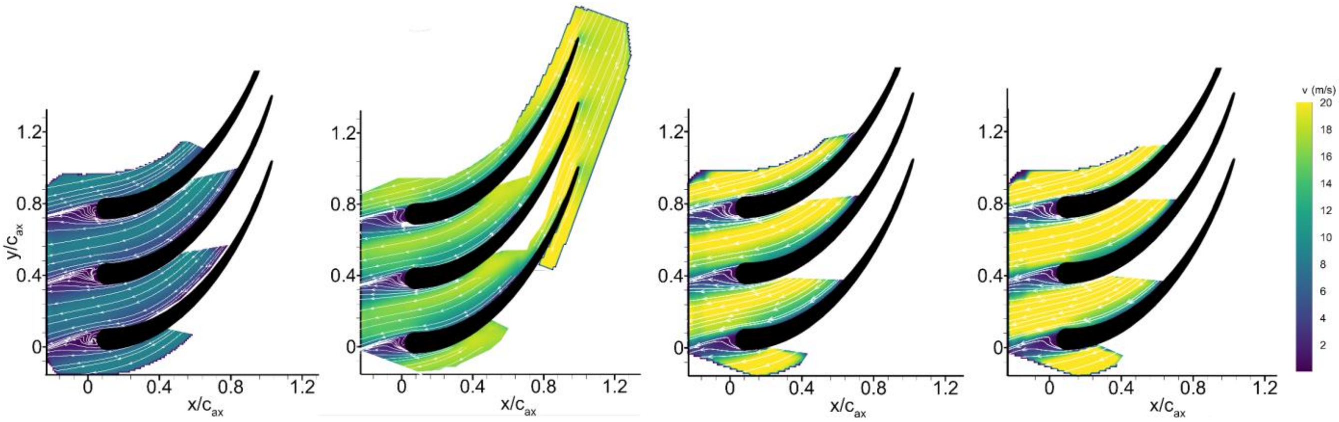

(a) **(b)** **(c)** **(d)**

Figure 1 The mean velocity fields at the flow regimes of Re=96000, Re=183000, Re=225000 and Re=265000

Moreover, analyzing results at various blade heights highlighted the influence of the boundary layer occurring within the passage. It was clearly observed that secondary flows along with bigger vortical structures contributing to more losses, are taking place as the cross-section approaches the wall from the midspan.

In conclusion, this study successfully utilized the planar PIV technique to investigate the flow within the diffuser passage under a range of operating conditions. Six span levels, including midspan, were examined at the inlet Reynolds number of the original design. The cambered profile of the blade required combining vector fields from three laser endoscope positions. The subsonic overview on these turbulence structures, responsible for converting the kinetic energy into losses, offered valuable insights into the flow field. The PIV methodology was confirmed to be used as a reference for future supersonic investigations, and the established PIV database can validate CFD calculations before supersonic evaluation of the diffuser.

REFERENCES

[1] Dedeyne J., Geerts M., Reyniers P., Wery F., Van Geem K., Marin G. B. (2020). Computational fluid dynamics based optimization of dimpled steam cracking reactors for reduced CO2 emissions, AIChE Journal, 66. doi:10.1002/aic.16255.
[2] Rubini D. (2020). A Novel Turbomachine for Hydrocarbon Cracking, University of Oxford.
[3] Neelis M., Patel M., Blok K., Haije W., Bach P. (2007). Approximation of theoretical energy-saving potentials for the petrochemical industry using energy balances for 68 key processes, Energy, 32, 1104–1123. doi:10.1016/j.energy.2006.08.005.
[4] Rubini, D., Karefyllidis, N., Xu, L., Rosic, B., Johannesdahl, H. (2022). A new robust regenerative turbo-reactor concept for clean hydrocarbon cracking. Journal of the Global Power and Propulsion Society, 6, 135-150. https://doi.org/10.33737/jgpps/150550

TECHNICAL SESSION 10

PARTICLE TRACKING VELOCIMETRY
LAGRANGIAN PARTICLE TRACKING

Chaired by Andreas Schröder

Near-wall Lagrangian particle tracking velocimetry using event-based imaging

Christian Willert[1*], Joachim Klinner[1]
1: German Aerospace Center (DLR), Institute of Propulsion Technology, 51170 Köln, Germany
* Correspondent author: chris.willert@dlr.de

Keywords: Event-based vision, Lagrangian particle tracking, wall shear stress.

ABSTRACT We describe the implementation of a particle tracking velocimetry (PTV) system based on event-based vision (EBV) and demonstrate its application for the characterization of a turbulent boundary layer (TBL) in air. One configuration uses a single event-camera to image a narrow light sheet extending wall-normal from the wall to obtain the time-resolved velocity profile. In the other configuration a thin light sheet grazes the surface of a glass window illuminating only the viscous sublayer of the turbulent boundary layer. The data simultaneously captured by three synchronized event-cameras is used to reconstruct the 3d particle tracks within a few 100 µm of the wall. Particle movement within the viscous sub-layer permit the estimation of the local, instantaneous wall shear stress under the assumption of linearity between particle velocity and wall shear stress. Thereby 2d distributions of the instantaneous wall shear stress are obtained. PTV tracking algorithms that are orders magnitude faster than correlation-based schemes provide data quality on par with currently used, considerably more expensive, high-speed PIV hardware.

Event-based imaging and its application in particle imaging velocimetry

EBV, dynamic vision sensing (DVS) or neuromorphic imaging describe a rather new sub-field within computer vision, differing considerably from classical frame-based imaging (Gallego et al., 2022). Rather than providing rectangular arrays of exposed sensor pixels, i.e. images, event-cameras provide an asynchronous stream of *events* consisting of pixel coordinates, time stamp and a binary contrast change signal. In this sense, event cameras only record contrast changes on the pixel level, either going from dark to bright (positive event) or bright-to-dark (negative event). Static areas in the scene provide no information. In the context of particle imaging, narrow event streaks are produced in the 2d-space-time domain and can be processed to provide 3D-3C PTV data in either real-time (Rusch and Rösgen, 2021, 2022) or offline (Borer et al., 2017; Drazen et al., 2011; Howell et al., 2020). The recently introduced event-based imaging velocimetry (EBIV) technique combines EBV and light sheet illumination to provide time-resolved, planar (2D-2C) velocity fields (Willert and Klinner, 2022; Willert, 2023). In the proposed contribution, we first introduce the use of event-based imaging to obtain profiles of turbulent quantities in analogy to profile-PIV technique (Willert, 2015), hereafter referred to as *event-based profile imaging velocimetry* or just *profile-EBIV*. The second part is devoted to the extension of EBIV to 3D-3C PTV to capture the particle motion within the viscous sublayer.

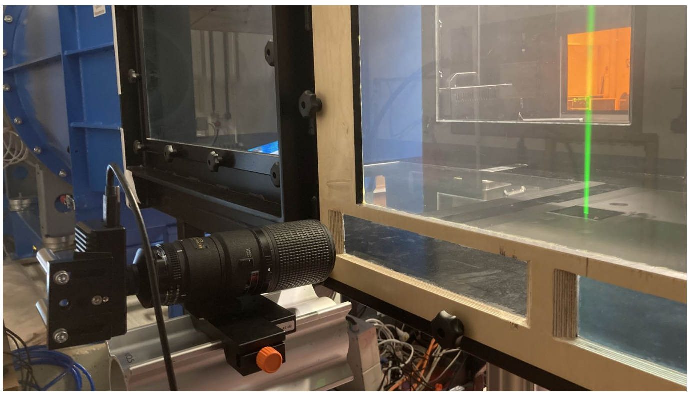

(a)

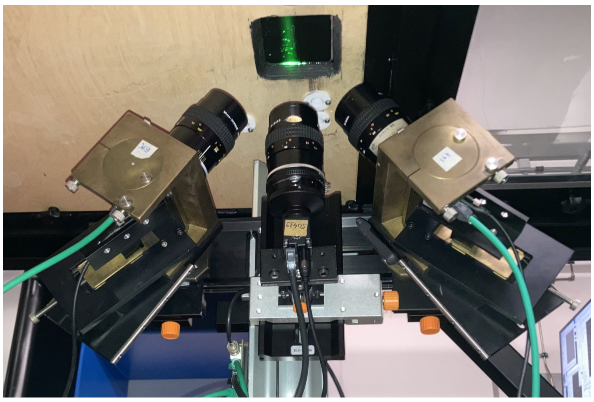

(b)

Figure 1: *(a): velocity profile measurement setup using a single event-camera at the 1 m wind tunnel of DLR in Göttingen; (b): triple event-camera setup for particle tracking in the viscous sublayer of a TBL.*

Profile-EBIV on a turbulent boundary layer

The profile-PIV technique as introduced by Willert (2015) has been extensively used to obtain both detailed velocity statistics as well as time-resolved data of turbulent flows in a variety of applications Cuvier et al. (2017); Willert et al. (2017, 2018, 2021). For *profile-EBIV* an event-camera is used in place of the high-speed camera and images a narrow field of view in the wall-normal direction (Fig. 1(a)). Seeding is equivalent to the 1 µm aerosol tracers used for conventional PIV in air. Measurements are performed in the 1 m windtunnel of DLR in Göttingen at free stream velocities of $U_\infty = 5-10\,\mathrm{m/s}$. Figure 2 provides exemplary velocity profile statistics obtained through the analysis of event recordings of 10 s duration and a laser pulsing rate of 10 kHz. The data shown in the left column is obtained by a multi-frame, pyramid-based cross-correlation scheme originally designed for PIV data processing. Preliminary results obtained using a pure particle tracking scheme are provided in the right column. Each data point represents bin-average statistics with a bin-size of $\Delta y = 50\,\mu\mathrm{m}$ ($\approx 0.8^+$). Both data sets show near perfect agreement with both corresponding DNS data as well as conventional PIV measurement data (not shown here), thereby documenting the viability of the proposed measurement technique.

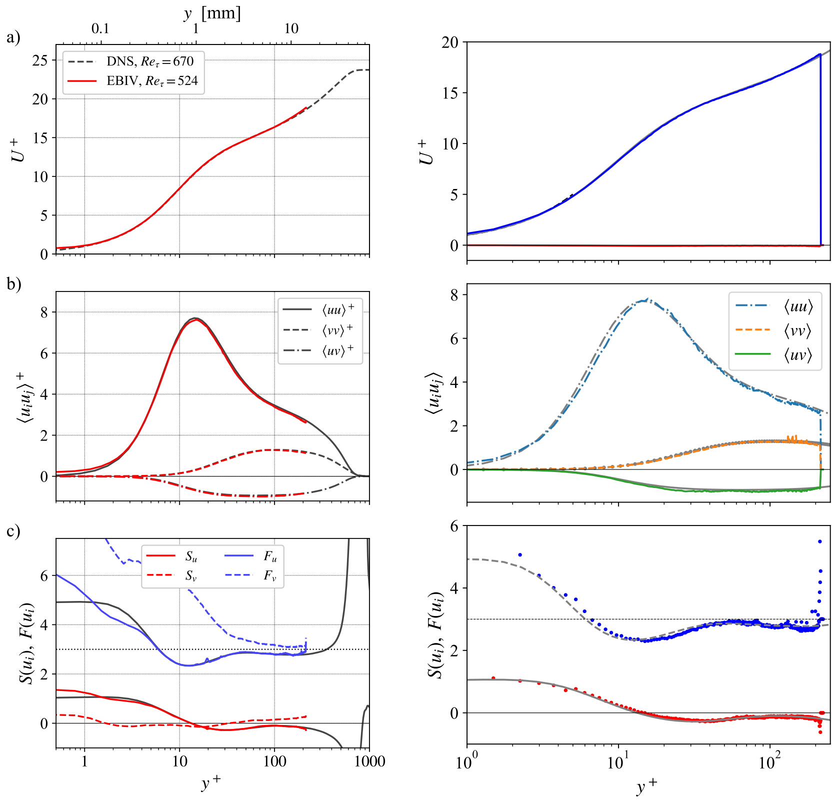

Figure 2: Exemplary velocity profiles in viscous scaling obtained with profile-EBIV records of 10 s duration for $\mathrm{Re}_\tau = 585$ using multi-frame correlation processing (left column) and 2d particle tracking (right column), both compared to DNS from Schlatter and Örlü (2010). PTV statistics are based on bin-averaging using bin a size of $\Delta y = 50\,\mu\mathrm{m}$.

Event-based particle tracking of the viscous sublayer

A second EBIV configuration captures the flow in the viscous sublayer of a TBL using a thin, wall-parallel light sheet of <0.5 mm thickness that is imaged by three synchronized event-cameras (see Fig. 1(b)). The dynamics of the near wall flow can already be visualized in the raw event data for which two examples are given in Fig. 3, although the static imagery can only partially reveal the true particle motion. Extreme events such as high-speed sweeps, strong spanwise motions or reverse-flow areas can be readily observed in a simple manner by scrolling through the recordings. After careful camera calibration using a y-translated target, 3D particle tracks can be reconstructed from the three event streams. With both the particle's wall-distance Δy and velocity $\mathbf{u}$ known, the corresponding wall shear stress can be estimated from $\tau_w = \mu \frac{du}{dy} \approx \mu \frac{\mathbf{u}}{\Delta y}$ with the assumption that the particle is located in the viscous sublayer (i.e. $y \lessapprox 4^+$). Two examples of preliminary (unfiltered) wall shear stress distributions are provided in Fig. 4, and, for instance, show the footprint streamwise streaks. The proposed contribution will provide details on the procedure for reconstruction of the 3D particle tracks from the event data records. Time-resolved 2d maps of both components of the wall shear stress are obtained from records of up to 1 minute duration, which, to best of the authors' knowledge, is not possible with currently available conventional imaging.

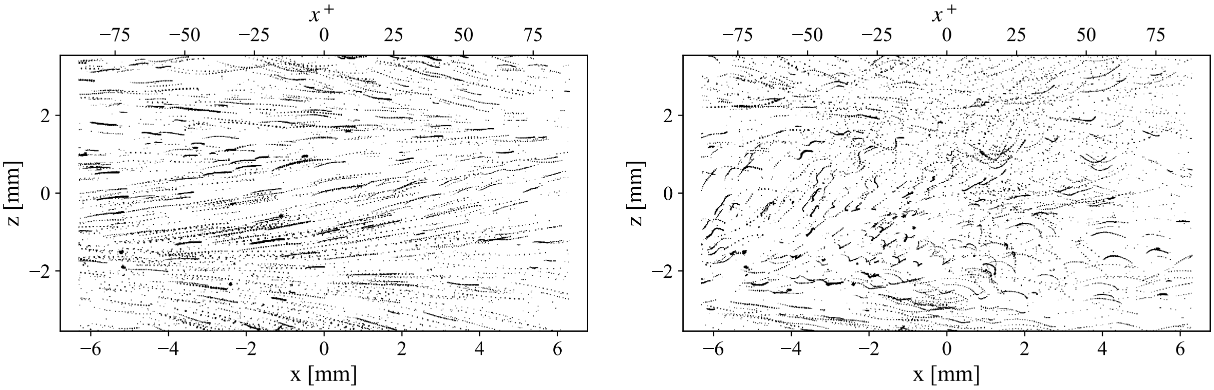

Figure 3: *Visualizations of the near wall flow ($y^+ < 8$) with mean flow left-to-right; (a) sweep event at $z = -2$ mm, (b) streaklines produced by a reverse flow event near the lower center (particles briefly moving upstream, best observed if animated).*

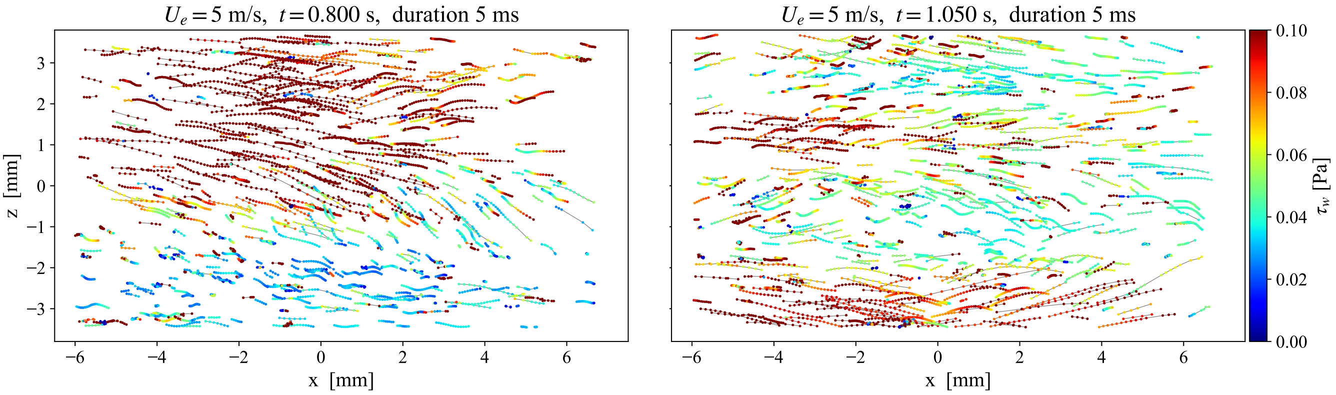

Figure 4: *Preliminary distributions of the wall shear stress magnitude obtained by estimating the velocity gradient experienced by particles moving within the viscous shear layer. The mean flow is from left to right.*

References

Borer D, Delbruck T, and Rösgen T (2017) Three-dimensional particle tracking velocimetry using dynamic vision sensors. *Experiments in Fluids* 58

Cuvier C, Srinath S, Stanislas M, Foucaut JM, Laval JP, Kähler CJ, Hain R, Scharnowski S, Schröder A, Geisler R, Agocs J, Röse A, Willert C, Klinner J, Amili O, Atkinson C, and Soria J (2017) Extensive characterisation of a high Reynolds number decelerating boundary layer using advanced optical metrology. *Journal of Turbulence* 18:929–972

Drazen D, Lichtsteiner P, Haefliger P, Delbruck T, and Jensen A (2011) Toward real-time particle tracking using an event-based dynamic vision sensor. *Experiments in Fluids* 51:1465–1469

Gallego G, Delbrück T, Orchard G, Bartolozzi C, Taba B, Censi A, Leutenegger S, Davison AJ, Conradt J, Daniilidis K, and Scaramuzza D (2022) Event-based vision: A survey. *IEEE Transactions on Pattern Analysis and Machine Intelligence* 44:154–180

Howell J, Hammarton TC, Altmann Y, and Jimenez M (2020) High-speed particle detection and tracking in microfluidic devices using event-based sensing. *Lab Chip* 20:3024–3035

Rusch A and Rösgen T (2021) TrackAER: Real-time event-based particle tracking. in *14th International Symposium on Particle Image Velocimetry (ISPIV 2021)*. page 176. Illinois Institute of Technology, Chicago, IL

Rusch A and Rösgen T (2022) Online event-based insights into unsteady flows with TrackAER. in *20th International Symposium on Application of Laser and Imaging Techniques to Fluid Mechanics*. Lisbon, Portugal

Schlatter P and Örlü R (2010) Assessment of direct numerical simulation data of turbulent boundary layers. *Journal of Fluid Mechanics* 659:116–126

Willert C (2015) High-speed particle image velocimetry for the efficient measurement of turbulence statistics. *Experiments in Fluids* 56:17

Willert C (2023) Event-based imaging velocimetry using pulsed illumination. *Experiments in Fluids* (under review)

Willert C, Cuvier C, Foucaut J, Klinner J, Stanislas M, Laval J, Srinath S, Soria J, Amili O, Atkinson C, Kähler C, Scharnowski S, Hain R, Schröder A, Geisler R, Agocs J, and Röse A (2018) Experimental evidence of near-wall reverse flow events in a zero pressure gradient turbulent boundary layer. *Experimental Thermal and Fluid Science* 91:320 – 328

Willert C and Klinner J (2022) Event-based imaging velocimetry: An assessment of event-based cameras for the measurement of fluid flows. *Experiments in Fluids* 63:101

Willert C, Schanz D, Novara M, Geisler R, Schroll M, Ribergard S, and Schröder A (2021) Multi-resolution, time-resolved piv measurements of a decelerating turbulent boundary layer near separation. in *14th International Symposium on Particle Image Velocimetry (ISPIV 2021)*

Willert C, Soria J, Stanislas M, Klinner J, Amili O, Eisfelder M, Cuvier C, Bellani G, Fiorini T, and Talamelli A (2017) Near-wall statistics of a turbulent pipe flow at shear Reynolds numbers up to 40 000. *Journal of Fluid Mechanics* 826

Meshless Track Assimilation (MTA) of 3D PTV data

Pietro Sperotto[1*], Bo Watz[1] and David Hess[1].
1: Dantec Dynamics A/S, Denmark.
* Correspondent author: pietro.sperotto@dantecdynamics.com

Keywords: 3D PTV, Data Assimilation, Meshless methods, Pressure from PIV/PTV, LPT.

ABSTRACT
The Meshless Track Assimilation (MTA) method is presented to compute the pressure field and enhance the data. The approach relies on Radial Basis Functions (RBFs) to enforce Navier-Stokes equations into the data. The method can handle highly noisy data giving an output of clean and smooth velocities vector and pressure fields. The work deals with the numerical methodology which for the abstract is briefly discussed. Then, the test case and its relative results are proposed. Finally, some conclusive thoughts and outlooks are given.

1 NUMERICAL METHODOLOGY

We seek an approximation of our flow field $\boldsymbol{u}$ and p as a linear combination of RBFs, typically this is achieved by interpolating or by least squares approaches. However, the latter methodology can be further enriched by the Navier-Stokes equations or derivates such as the Poisson equation of the pressure. Therefore, a corrected flow field or even a super-sampling of the data is achievable. The cost function is minimized by using a Limited-memory Broyden–Fletcher–Goldfarb–Shanno algorithm (L-BFGS), the gradient for the BFGS routine can be found analytically without involving any numerical tools such as finite difference.

The idea of super-sampling or correcting the data by imposing Navier-Stokes equations is not new, as many groups already showed, i.e. VIC+ and Flowfit. Nevertheless, the MTA exploits analytical differentiation making the method completely meshless and suitable for force estimation over objects.

2 TEST CASE

The method is applied on a 3D Particle Tracking Velocimetry (PTV) test case resulting from a water jet a nozzle diameter of $10.7mm$ and a flow rate of $Q = 75\ l/h$. The outlet velocity is $U_0 \simeq 0.23m/s$ and $Re_D = U_0 D/\nu \simeq 2500$, the flow is generated inside a volume of ~ 125l the water quantity inside the tank is kept constant by using a pump and a mass flow meter. Four SpeedSense M310 cameras running at 1200 fps, were used with 100mm Makro lenses with an aperture of f11. A Dual-Power 30-1000 laser illuminates 50µm PSP particles. The beam is widened through a telescope lens arrangement to illuminate a cylindrical volume, aligned with the jet axis, and a diameter of approximately 28mm.

For the velocity analysis, a TOMO-PTV routine in Dynamic Studio 8.0 is applied to 99 images with a seeding density of approximately 0.01ppp. The final tracks consist on average, of 4500 particles per time step and an average track length of 68 time steps, without further post-processing to test the filter capabilities of the method (see Figure 1). The shortest accepted tracks cover at least 6 consecutive snapshots. These tracks represent a problem as it is not possible to low pass filter them by a classic means.

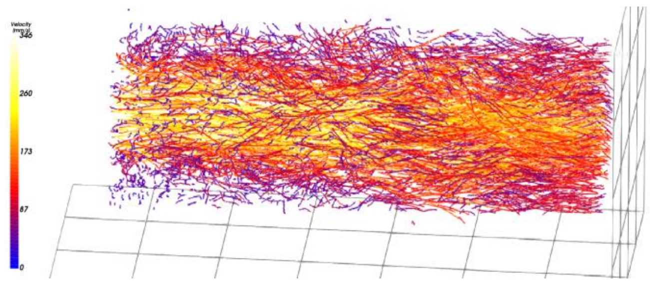

Figure 1: 3D PTV raw result from the jet flow used as input for MTA. Nozzles exit on the left hand side of the image

3 RESULTS

The raw tracks are directly fed to the optimization routine. The RBFs were used at any given snapshot to represent all quantity of the field distributed into a regular grid of size $12 \times 37 \times 12$ over the measurement volume for a total of 5328.

Figure 2 shows the reconstruction at frame 20, for the RBF based (left) and for a linear interpolation (right). RBF functions can reconstruct the toroidal structures of the flow field, here shown by iso-contours of the vorticity which are colour coded by the velocity. In strong contrast to the linear approach, where the structures are only small patches, and the typical toroidal shapes are impossible to recognize.

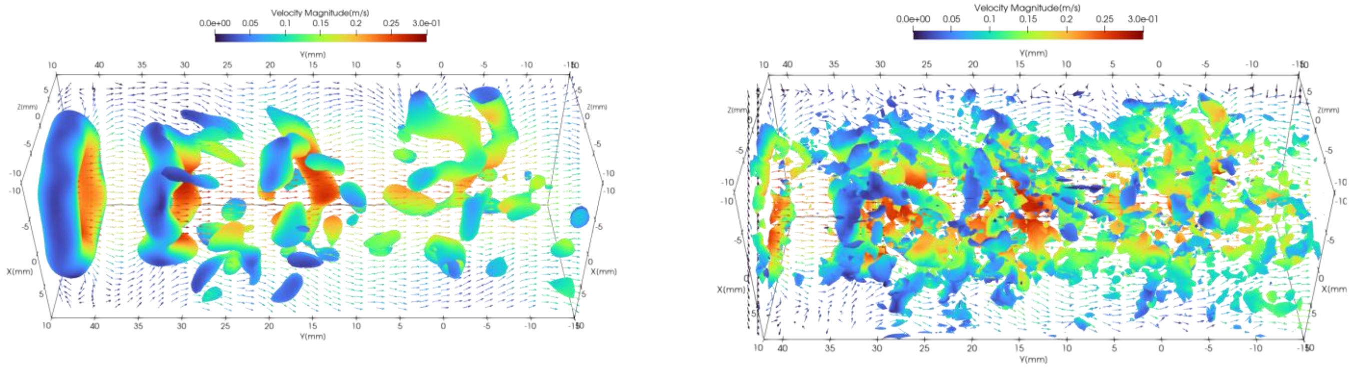

Figure 2: RBF(left) and linear (right) reconstruction of the flowfield of the iso surface of Q-criterion = $700Hz^2$ and velocity vector map coloured with the $||u||_2$

As a subproduct of MTA the pressure is retrieved and shown in Figure 3. Again, rings of high vorticity can be spotted at the exit of the nozzle in the form of low-pressure areas. Moreover, a high pressure zone is present between the toroids, probably due to caged fluid between the two structures. Then, going streamwise into the y direction the structures are broken into smaller ones blending the lower and higher pressure zone.

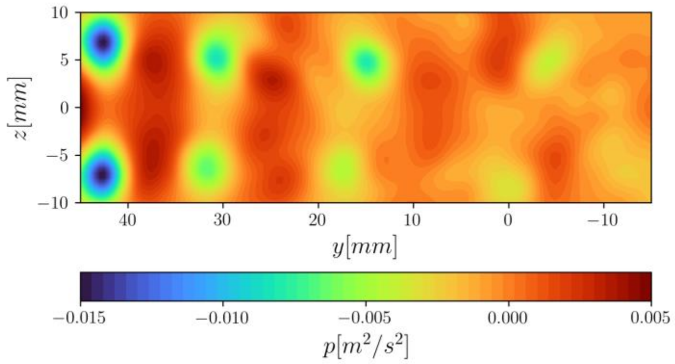

Figure 3: Pressure reconstruction in the middle x plane, the nozzle exit is on the left side

4 CONCLUSION

The method proposed demonstrates a strong capability to deal with noisy raw PTV data. However, it would be of great interest to show the capability of the approach to increase or transport the resolution of the original scattered data into a regular grid. The best tactic to tackle this aspect is to exploit a synthetic dataset. A synthetic database involving the John Hopkins Turbulence Database is currently under investigation to test the method for super resolution.

Moreover, an experimental investigation on the flow around a rigid body could be interesting to exploit properly the meshless feature of the approach. Finally, this kind of experimental investigation may support the combination of PTV with Digital Image Correaltion to study fluid structure interactions.

REFERENCES

- Huhn, F., Schanz, D., Manovski, P., Gesemann, S., & Schröder, A. (2018). Time-resolved large-scale volumetric pressure fields of an impinging jet from dense Lagrangian particle tracking. Experiments in Fluids, 59, 1-16.
- Schneiders, J. F., & Scarano, F. (2016). Dense velocity reconstruction from tomographic PTV with material derivatives. Experiments in fluids, 57, 1-22.
- Wendland, H. (1995). Piecewise polynomial, positive definite and compactly supported radial functions of minimal degree. Advances in computational Mathematics, 4, 389-396.
- Zhu, C., Byrd, R. H., Lu, P., & Nocedal, J. (1997). Algorithm 778: L-BFGS-B. ACM Transactions on Mathematical Software, 23(4), 550–560. https://doi.org/10.1145/279232.279236

Volumetric Lagrangian particle velocity and temperature measurements with Thermochromic Liquid Crystals

T. Käufer[1*], **C. Cierpka**[1]
1: Technische Universität Ilmenau, Institute of Thermodynamics and Fluid Mechanics, 98693 Ilmenau, Germany
* theo.kaeufer@tu-ilmenau.de

Keywords: Lagrangian particle tracking, particle image thermometry, Rayleigh-Bénard convection, temperature, velocity

ABSTRACT Temperature-driven flows are ubiquitous in our surroundings and are driving factors in many natural phenomena and engineering applications. Therefore, an understanding of the underlying flow physics and the convective heat transfer is essential. Since the specific configuration can only hardly be modeled, often a simpler, canonical model is studied instead. Such a model is Rayleigh-Bénard convection (Chillà and Schumacher, 2012). In the classical setup, it consists of a fluid confined by adiabatic side walls and isothermal heating and cooling plates at the bottom and top, respectively. If a critical temperature difference between the heating and cooling plate is applied, fluid motion sets in. The convection is governed by two dimensionless numbers, the Rayleigh number Ra $=\beta g \Delta T H^3/\nu\kappa$ and the Prandtl number Pr $= \nu/\kappa$. In the definition of these numbers, β, g, ΔT, and H are the thermal expansion coefficient, the acceleration due to gravity, the domain height and the temperature difference between the heating and cooling plate. Those represent the flow-driving forces. The kinematic viscosity ν and the thermal diffusivity κ act inhibiting the flow. Temporally and spatially resolved temperature and velocity data are crucial for a better understanding of the underlying physics and the direct determination of the heat transfer (Moller et al., 2022). One way to obtain this data is the experimental investigation of the flow phenomenon by volumetric temperature and velocity measurement techniques, as outlined in this abstract.
The present experimental arrangement was designed to allow for a combination of Particle Image Thermometry (PIT) (Dabiri, 2009)

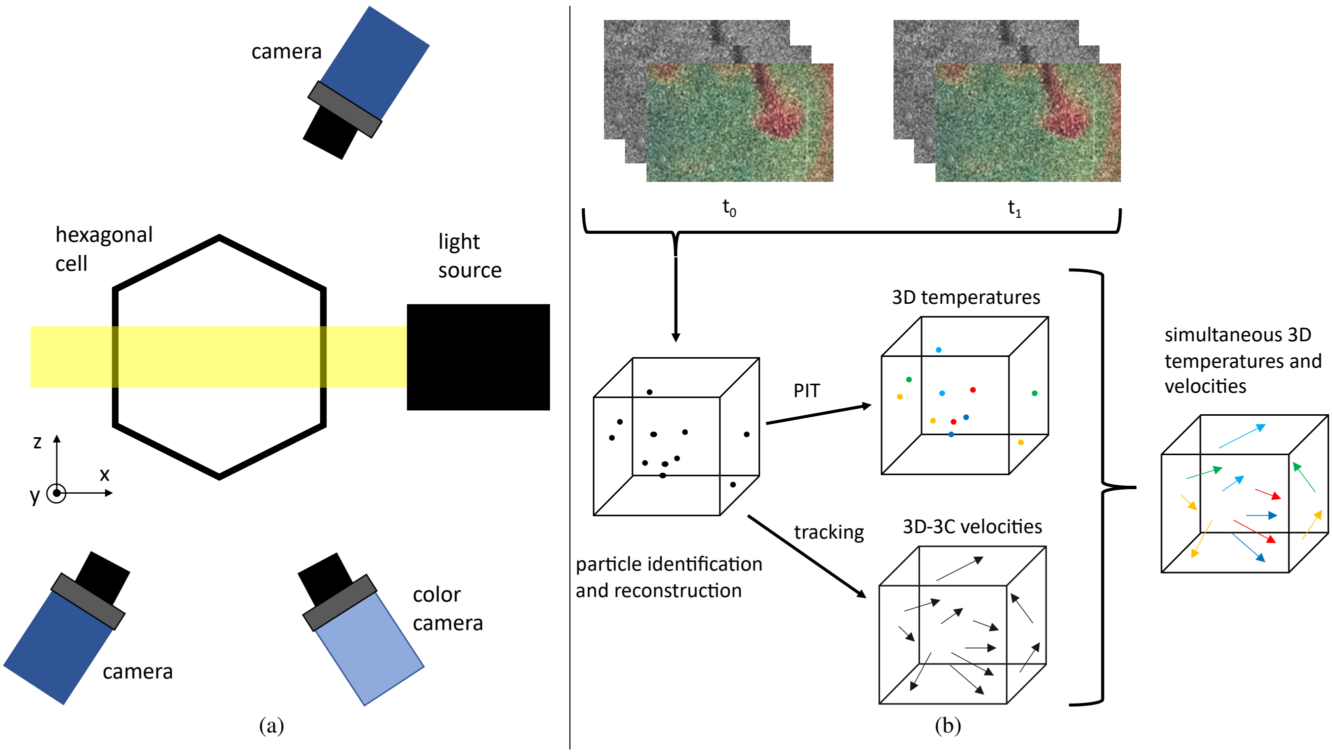

Figure 1: (a) Sketch of the experimental setup (b) and the processing scheme.

and Particle Tracking Velocimetry (PTV) (Malik et al., 1993) measurements to simultaneously estimate the particles' temperature and velocity, as shown in Figure 1 (a). PIT leverages temperature-sensitive Thermochromic Liquid Crystals (TLCs) particles to indicate the fluid's temperature. The color of the light reflected by these particles, when illuminated by polychromatic light, depends – among other factors, e.g., the observation angle – on their temperature (Moller et al., 2019).

The experiment, schematically shown in Figure 1 (b), is composed of a hexagonal cell made from glass with a width $W = 120$ mm along the diagonals. The bottom and top plates of the cell, whose temperatures can be precisely controlled, are made from aluminum to resemble almost perfect isothermal boundary conditions. The aspect ratio $\Gamma = W/H$ can be varied by adjusting the height H of the glass hexagon. A vertical section of thickness $d = 10$mm covering the whole height of the cell illuminated by collimated, polychromatic light of a custom-made LED light source with integrated optics. Two monochrome cameras and a Bayer pattern color camera are directed onto the illuminated section. The hexagonal shape of the convection cell allows observing the illuminated section under oblique viewing angles while maintaining an optical path perpendicular to the sidewall. Thereby chromatic and astigmatic optical aberrations are minimized, which is advantageous for both the velocity and the temperature measurements. The TLC particles used as seeding have a diameter of 60 - 100 μm. Since the density of the particles is slightly large than the density of water, a glycerin-water mixture with a volume ratio of approximately 15:85 is used as the fluid.

To obtain the functional relation between particle color and temperature, a neural network is trained on particle images extracted from calibration images at different temperatures similar to (Moller et al., 2020). The pixel coordinates of each particle image are also fed into the network, which thereby also learns the dependence of the color on the particle image position. After training, the neural network is then used to infer the temperature from the particle image and the particle image coordinates. The particle velocity and positions in space are obtained from the Shake-the-Box processing (LaVison GmbH). The individual results of the temperature and velocity processing are then joined together. Thereby the simultaneous temperature and velocity are obtained individually for each particle.

Figure 2 shows the temperature T (a) and the velocity magnitude $|V|$ (b) scatter plot of particles of 100 subsequent snapshots

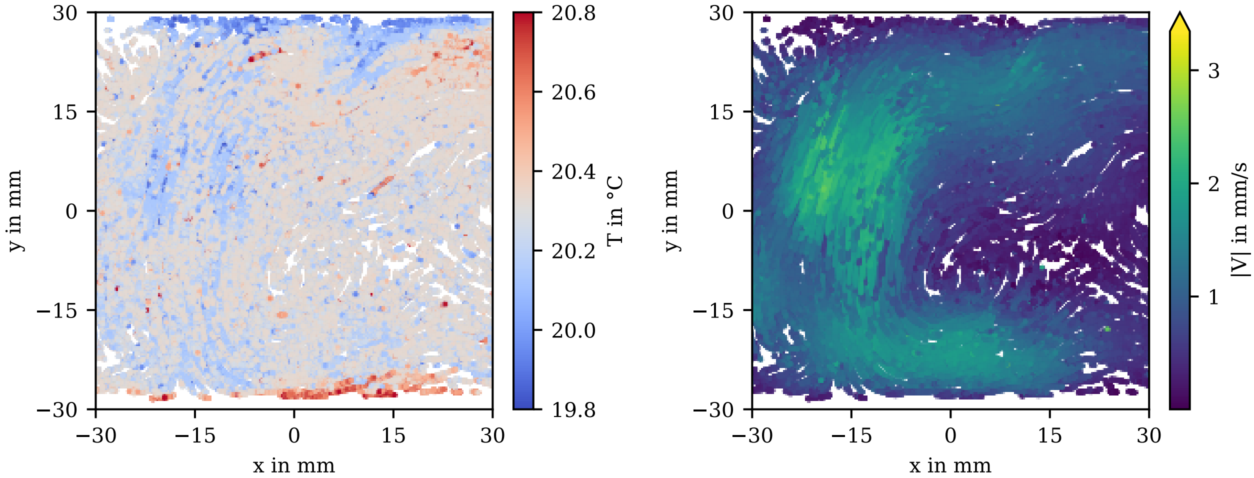

Figure 2: Scatter plot of the particles' temperature (a) and velocity magnitude (b) made from 100 subsequent snapshots.

recorded at a rate of 10 Hz projected into the x-y-plane. Looking at the temperature scatter plot, we observe the lowest and highest temperatures at the boundary layer of the cooling and heating plate, respectively. The dominant large-scale circulation (LSC) common for $\Gamma = O(1)$ can be clearly seen in the scatter plot of $|V|$ even though the LSC is oriented obliquely to the x-y-plane. The particles with the highest $|V|$ at the left side of the plot show a low temperature indicating that the fluid is welling downwards. This shows that the newly developed temperature measurement technique is capable of visualizing the dominant flow features.

During the conference, we want to present details on the implementation, application, challenges and limitations of the technique, which allows unique insights into the flow phenomena by combining temperature and velocity measurements at the same point in 3D space and time.

References

Chillà F and Schumacher J (2012) New perspectives in turbulent Rayleigh-Bénard convection. *Eur Phys J E* 35:1–25

Dabiri D (2009) Digital particle image thermometry/velocimetry: A review. *Exp Fluids* 46:191–241

Malik N, Dracos T, and Papantoniou D (1993) Particle tracking velocimetry in three-dimensional flows: Part II: Particle tracking. *Exp Fluids* 15:279–294

Moller S, Käufer T, Pandey A, Schumacher J, and Cierpka C (2022) Combined particle image velocimetry and thermometry of turbulent superstructures in thermal convection. *J Fluid Mech* 945:A22

Moller S, König J, Resagk C, and Cierpka C (2019) Influence of the illumination spectrum and observation angle on temperature measurements using thermochromic liquid crystals. *Meas Sci Technol* 30:084006

Moller S, Resagk C, and Cierpka C (2020) On the application of neural networks for temperature field measurements using thermochromic liquid crystals. *Exp Fluids* 61:1–21

New Strategies of Overcoming Refractive Interfaces in Lagrangian Particle Tracking

Xin Zeng[1,2], Chuangxin He[1,2*] and Yingzheng Liu[1,2]
1: Shanghai Jiao Tong University, School of Mechanical Engineering, Shanghai, China
2: Shanghai Jiao Tong University, Gas Turbine Research Institute, Shanghai, China
* Correspondent author: chuangxin.he@sjtu.edu.cn

Keywords: Lagrangian particle tracking, Camera calibration, Refractive interfaces, Ray tracing

ABSTRACT The refractive interfaces always exist between the cameras and world points, e.g., a scenario common in experimental fluid mechanics with gas-solid-liquid interfaces at container walls, while it is inaccurate to apply a pinhole model such as pinhole Tsai model (Tsai, 1987) without accounting for the index changes directly for three-dimensional (3D) reconstruction in the Lagrangian particle tracking (LPT) or tomographic PIV (Tomo-PIV) measurements. This work presents some new strategies for overcoming refractive interfaces in LPT, which are built upon the open-source Lagrangian particle tracking (OpenLPT) (Tan, Salibindla, Masuk, & Ni, 2020) and the Shake-the-Box (Schanz, Gesemann, & Schrder, 2016). The camera calibration is performed with the polynomial functions (Elsinga, Scarano, Wieneke, & Oudheusden, 2006) to map the world to image points to account for the nonlinearity introduced by refractive interfaces in lieu of the pinhole Tsai camera model in OpenLPT, meanwhile, all the rays for each pixel is interpolated and saved. The particle triangulation and matching procedure was conducted based on the polynomial calibration with 2 planes, then a new strategy of shaking the sight line (SSL-LPT) in lieu of the "Shake-the-Box" (STB) was applied to improve the accuracy of 3D particle position and utilization rate of high concentration particle images. The accuracy, convergence, and robustness were evaluated using the synthetic particle images dataset with the Johns Hopkins turbulence database for homogeneous isotropic turbulence. The results show that the SSL-LPT strategy can detect up to 99.9% of particles as OpenLPT at the particle image density of 0.05 ppp without any refractive interfaces, meanwhile the efficiency of code is almost as same as OpenLPT. When refractive interfaces exist, the SSL-LPT has better accuracy and a shorter particle tracking time than OpenLPT with a smaller calibration error. The demonstration of flow field reconstruction results with a synthetic dataset shows that the SSL-LPT code is ready to be used for real experiments with refractive interfaces and will be applied to an experimental result on a jet issued from the elliptic nozzle in the soon.

1. Introduction and Method When there is a gas-solid-liquid interface at the container wall, as shown in Figure 1. (a). It is inaccurate to apply the pinhole Tsai model (Tsai, 1987) without accounting for the index changes directly, the projected point position on the image with refractive interfaces is some deviation from that with a direct application of a pinhole Tsai camera model to the exact world and image points for one camera from the array yields the histogram of reprojection errors shown in Figure 1. (b), whose reprojection errors are over 1.0 pixel though the errors are less 5e-6 pixel without interface. The polynomial functions can be utilized to map the world to image points to account for the nonlinearity introduced by refractive interfaces instead of a camera model as

$$u = a_0 + a_1 X + a_2 X^2 + a_3 X^3 + a_4 Y + a_5 Y^2 + a_5 Y^3 + a_6 Y^3 + a_7 XY + a_8 X^2 Y + a_9 XY^2. \tag{1}$$

$$v = b_0 + b_1 X + b_2 X^2 + b_3 X^3 + b_4 Y + b_5 Y^2 + b_5 Y^3 + b_6 Y^3 + b_7 XY + b_8 X^2 Y + b_9 XY^2. \tag{2}$$

Multiple target plane is indispensable to overcoming the refraction interface in Figure 1. (c). The reprojection errors by the polynomial functions are almost consistent with or without refractive interface from Figure 1. (d), which is controlled under 3e-3 pixels and less than that by a pinhole Tsai camera model. For Lagrangian particle tracking with (STB), serval key processes of particle triangulation, matching procedure, STB procedure can be easily performed by the pinhole Tsai camera model, while they cannot be run directly by polynomial functions with 2 calibration plates because the world points outside the plane cannot be calculated by polynomial functions. While the line of sight of each pixel can be determined by two points in calibration plates by polynomial functions, and all the line of sight can be temporarily stored, then the lines of sight are used directly for the particle triangulation and matching procedure based on the volume self-calibration (VSC) algorithm (Wieneke, 2008). Then the 3D particle position with its lines of sight from each camera are temporarily saved for the procedure of shaking the sight line (SSL) to improve the accuracy of the 3D particle position and utilize the residual particle image. The procedure of SSL is to shake the world position in the two 2 calibration plates, replacing the shaking the world position of particles in "Shake-the-Box".

2. Results, Summary and outlook Accuracy, convergence, and robustness of SSL-LPT were evaluated using the synthetic particle images dataset with the Johns Hopkins turbulence database for homogeneous isotropic turbulence. The results show that the SSL-LPT strategy can detect up to 99.9% of particles as OpenLPT at the particle image density of 0.05 ppp without any refractive interfaces, meanwhile the efficiency of code is almost as same as OpenLPT. The position data is processed to obtain the velocity field by applying FlowFit (Gesemann, Huhn, Schanz, & Schröder, 2016), when refractive interfaces exist, as displayed in Figure 2, the SSL-LPT has more tracks and better accuracy than OpenLPT. The demonstration of flow field reconstruction results in Figure 2 with a synthetic dataset shows that the SSL-LPT code is ready to be used for real experiments with refractive interfaces and will be applied to an experimental result on a jet issued from the elliptic nozzle in the soon.

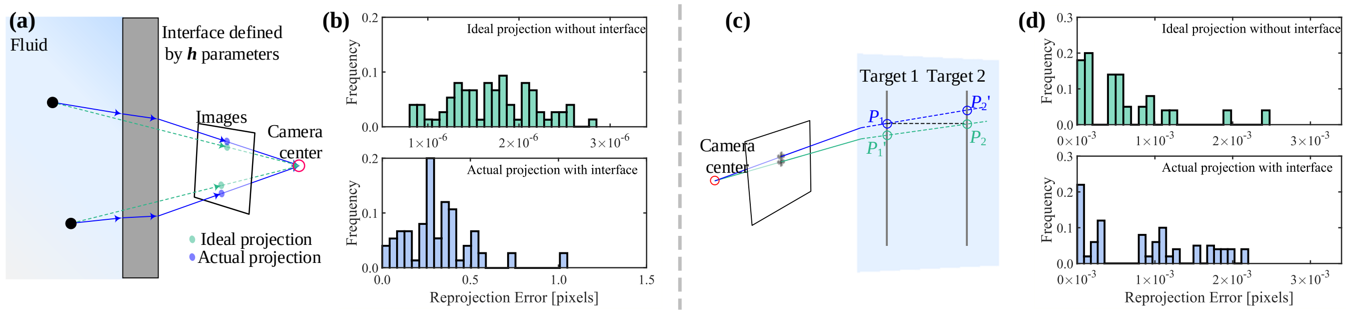

Figure 1. (a) Schematic of imaging through refractive interfaces. (b) Comparison of reprojection errors from application of the pinhole model with/without refractive interface. (c) Schematic of sight lines based on calibration by 2 planes. (d) Comparison of reprojection errors from application of the third-order polynomial with/without refractive interface.

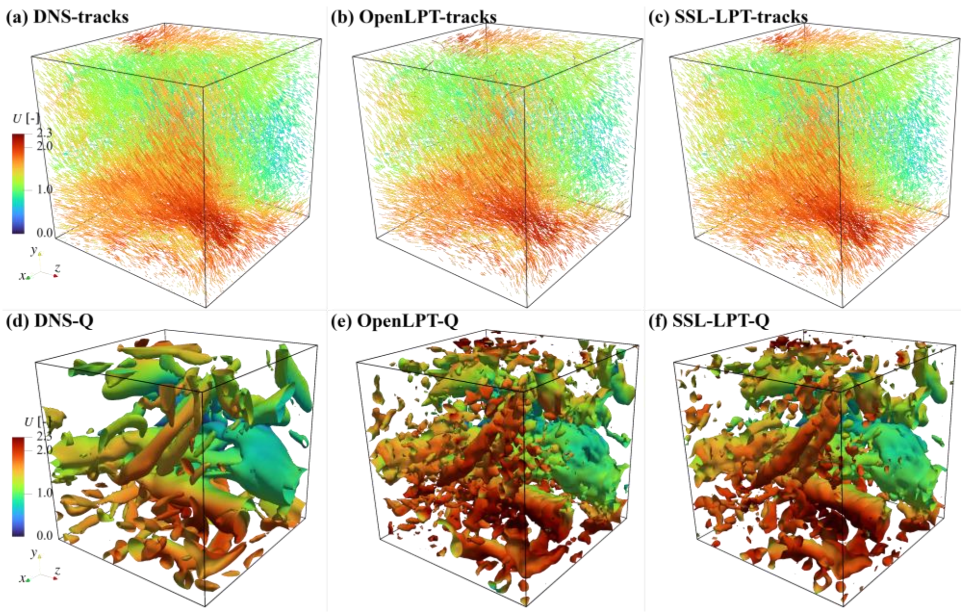

Figure 2. Comparison of flow field reconstruction between OpenLPT and SL-LPT in an octagonal water tanks with refractive interfaces, $\varphi = 2.0°$, h = 20mm.

REFERENCES

- Elsinga, G. E., Scarano, F., Wieneke, B., & Oudheusden, B. W. V. (2006). Tomographic particle image velocimetry. Experiments in Fluids, 41(6), 933-947.
- Gesemann, S., Huhn, F., Schanz, D., & Schröder, A. (2016, 2016). From noisy particle tracks to velocity, acceleration and pressure fields using B-splines and penalties. Paper presented at the 18th International Symposium on the Application of Laser and Imaging Techniques to Fluid Mechanics.
- Schanz, D., Gesemann, S., & Schrder, A. (2016). Shake-The-Box: Lagrangian particle tracking at high particle image densities. Experiments in Fluids, 57(5), 70.
- Tan, S., Salibindla, A., Masuk, A. U. M., & Ni, R. (2020). Introducing OpenLPT: new method of removing ghost particles and high-concentration particle shadow tracking. Experiments in Fluids, 61(2), 1-16.
- Tsai, R. Y. (1987). A versatile camera calibration technique for high-accuracy 3D machine vision metrology using off-the-shelf TV cameras and lenses. IEEE Journal on Robotics & Automation, 3(4), 323-344.
- Wieneke, B. (2008). Volume self-calibration for 3D particle image velocimetry. Experiments in Fluids, 45(4), 549-556.

TECHNICAL SESSION 11
MICRO-NANO FLUIDICS I

Chaired by Kyung Chun Kim

Marangoni driven generation of micro-droplets from water-alcohol mixtures on a substrate liquid

Stefan Puttinger[1,*]

1: Dept. of Particulate Flow Modelling, Johannes Kepler University
Linz, Austria
* Correspondent author: stefan.puttinger@jku.at

Keywords: Marangoni flow, Micro droplet production, Image processing

ABSTRACT The present paper discusses a special type of solutal driven Marangoni flow. It was previously shown that certain combinations of substrate liquids plus alcohol-water mixtures can lead to the production of a large number of micro droplets. The size and spreading radius of the micro-droplets can be manipulated by the concentration of the alcohol. As the experimental setup is very easy to reproduce it can (i) serve as a simple test case for student courses to discuss various aspects of Marangoni flow and (ii) could be elaborated as a convenient way to produce droplets of a certain size in future micro-fluidic applications.

1 INTRODUCTION AND MOTIVATION

Flow patterns driven by capillary and surface tension forces have recently experienced increasing attention since numerous applications in chemistry, biology and life sciences could benefit from controllable and reproducible flow patterns on a microscale. For unbounded two-fluid systems with different surface tension, the Marangoni effect is the main driving force of fluid motion. In previous publications it was shown that the Marangoni effect can be used to produce micro-droplets in such a binary fluid system (Hasegawa & Manzaki, 2021; Keiser et al., 2017). The present paper addresses aspects of such systems that have not been discussed in previous publications like the size and velocity distribution of the satellite droplets along their outward motion.

2 EXPERIMENTS AND IMAGE PROCESSING

Figure 1a shows an example of such a system. A droplet of a solution of water (plus dye) and 35 wt.% of isopropyl alcohol (IPA) is deposited on a 5 mm thick layer of sunflower oil in a petri dish of 90 mm diameter. Since the spreading parameter $S = \gamma_{OA} - (\gamma_{SA} + \gamma_{SO})$ is larger than 0, the necessary condition for total wetting is fulfilled (de Gennes et al., 2004). γ_{OA}, γ_{SA} and γ_{SO} refer to the interfacial tensions between oil and air, solution and air and the solution against oil, respectively. The mother droplet thus forms a thicker core region of radius r_c and then spreads out to a thin wetting layer until it reaches the bursting radius r_b. Between r_c and r_b evaporation of the alcohol changes the driving interfacial tension gradient and the film forms a thicker rim at r_b due to partial dewetting. This rim forms fingers at a certain wavelength λ and from these fingers, droplets are released. These satellite droplets are two to three orders of magnitude smaller than the mother droplet and continue to shrink on their way outwards until they reach the spreading radius r_s. At this position we can assume that the remaining droplets consist mainly of water and dye and most of the alcohol has evaporated.

To analyze the droplet size distribution, we first identify the center position of the mother droplet and then transform the image into a polar coordinate system. This a convenient way to obtain the size distribution of the satellite droplets $d_{SD}(r, \theta)$ and average the results across the angular coordinate. The OpenCV library offers a consistent environment for such conversions and the image processing has been implemented in Python. Figure 1b shows a transformed image after object detection. The mean wavelength λ can be calculated by calculating the fast Fourier transform (FFT) across a vertical line in the area of the fingers.

3 RESULTS AND DISCUSSION

During the first phase of the experiment the spreading radius r_b increases and, as a consequence, also the wavelength λ. Figure 1c demonstrates that λ keeps increasing also in the second phase of the experiment when the mother droplet starts to shrink until it entirely vanishes. Figure 2a and b show the histogram of the droplet size distribution and the size distribution as function of the relative radial position r_{SD}/r_b, respectively. We observe a linear decay of the droplet size with increasing distance to r_b. Since the droplets become very small for higher concentrations of alcohol, the image resolution of the currently available data is not sufficient for a reliable processing of the entire video sequence and for the highest concentration of alcohol it was not possible to identify the total number of droplets. However, the blue dashed lines in Fig. 2b indicate the size distribution for 45 and 55 wt.% of IPA as obtained by manual data extraction. The radial velocity of the droplets was calculated by applying the neural network based optical flow technique proposed by Weinzaepfel et al. (2013). Figure 2c shows the decay of the radial velocities over the temporal evolution of the experiment.

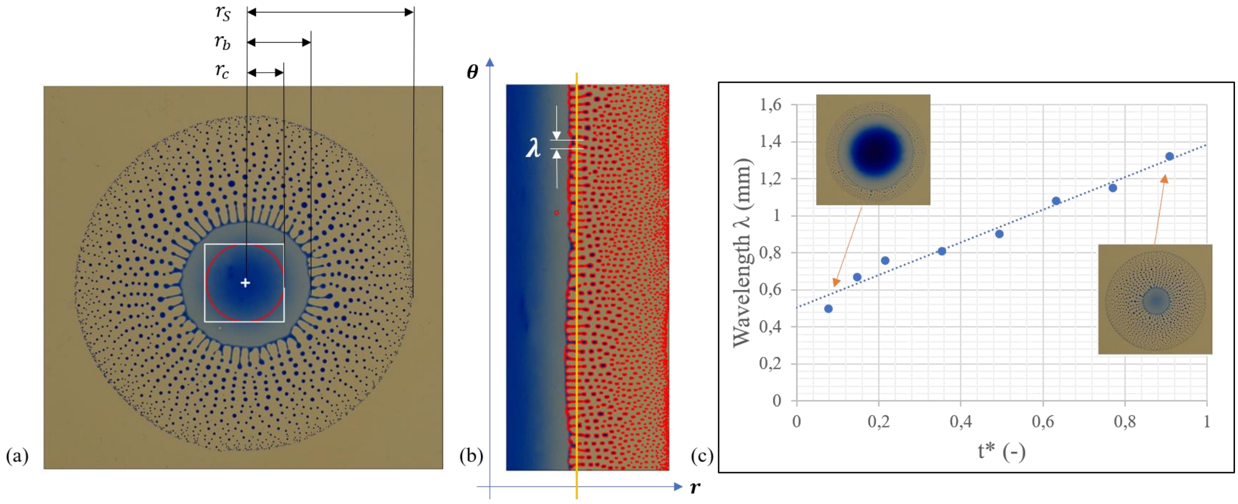

Figure 1. (a) A droplet of water-alcohol mixture (35 wt.% IPA) spreading on sunflower oil. (b) Transformation of the image in (a) to a polar coordinate system. The red areas mark the identified objects. The orange line indicates a position, where the luminosity signal can be analyzed via FFT to obtain the mean wavelength λ. (c) Wavelength λ as a function of relative time $t^* = t/t_{end}$. The inserts show the images for the first and last data point in the graph.

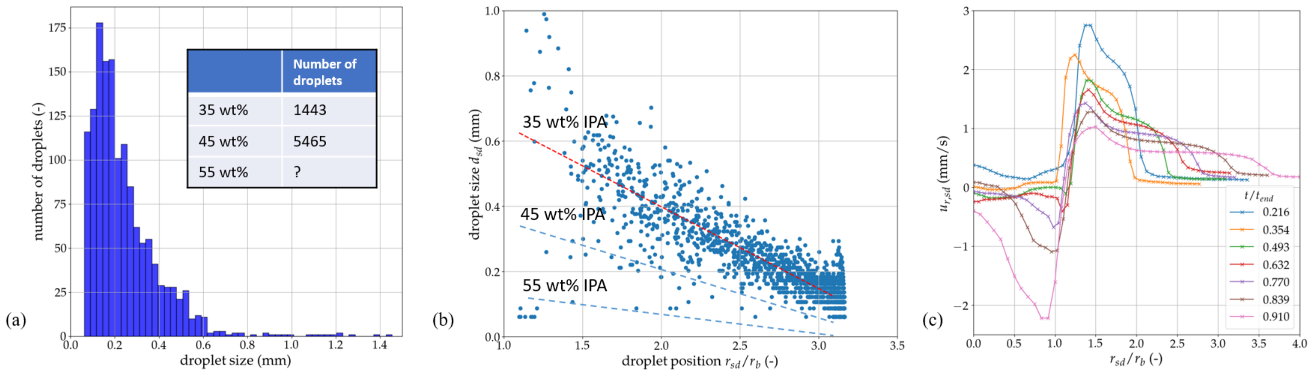

Figure 2. (a) Total number of droplets and size distribution. (b) Droplet size as a function of the relative radial position. (c) radial velocity as a function of the relative radial position for t^*=0.2...0.9.

4 SUMMARY AND OUTLOOK

The present study summarizes a simple but beautiful experiment on a special type of solutal driven Marangoni flow. Certain mixtures of surfactants and water lead to micro droplet production when a millimeter sized mother-droplet is deposited on a substrate liquid. Adding a dye to the mixture allows a simple visualization of the experiment. There is a clear relation of the droplet size to the alcohol concentration. For concentrations above 50 wt.% the generated satellite droplets become very small and the current optical setup lacks of sufficient resolution to obtain reliable data. Future activities will focus on the analysis of such concentration in a microscope setup.

5 REFERENCES

de Gennes, P., Brochard-Wyart, F., & Quere, D. (2004). *Capillarity and wetting phenomena*. Springer.

Hasegawa, K. (長谷川 浩司), & Manzaki, Y. (萬崎 勇貴). (2021). Marangoni fireworks: Atomization dynamics of binary droplets on an oil pool. *Physics of Fluids*, *33*(3), 034124. https://doi.org/10.1063/5.0041346

Keiser, L., Bense, H., Colinet, P., Bico, J., & Reyssat, E. (2017). Marangoni Bursting: Evaporation-Induced Emulsification of Binary Mixtures on a Liquid Layer. *Physical Review Letters*, *118*(7), 074504. https://doi.org/10.1103/PhysRevLett.118.074504

Weinzaepfel, P., Revaud, J., Harchaoui, Z., & Schmid, C. (2013). DeepFlow: Large Displacement Optical Flow with Deep Matching. *2013 IEEE International Conference on Computer Vision*, 1385–1392. https://doi.org/10.1109/ICCV.2013.175

20th International Symposium on Flow Visualization, Delft, the Netherlands ・10 – 13 JULY 2023

Experimental Investigation of the Flow Structure Manipulation in a Micro-hydrocyclones by Applying Particle Image Velocimetry

Yeganeh Saffar[1], David S. Nobes[1,] and Reza Sabbagh[1*]
1: Dept. of Mechanical engineering, University of Alberta, Canada
* Correspondent author: reza.sabbagh@ualberta.ca

Keywords: micro-hydrocyclone, particle separation, microfluidics, particle image velocimetry

ABSTRACT The effect of flow structure manipulation on the locus of zero vertical velocity of a micro-hydrocyclone has been investigated experimentally. Hydrocyclones are widely used for separating particles from liquid suspensions in various industries. The physics inside a micro-scale hydrocyclone, however, is not fully understood due to the complex behavior of particles and fluids and difficulties in performing experiments at the micro-scale. This paper uses particle image velocimetry to investigate the flow behavior inside one of the smallest micro-hydrocyclones reported in the literature. In presentation, we will compare quantified visualized flow in micro-hydrocyclone under different inlet geometries along with a complete description of novel aspects of the experimental procedure.

1 INTRODUCTION

A hydrocyclone is a multi-phase separator widely used in petrochemical, mining and many other industries (Wang et al., 2016). Micro-hydrocyclone technology has been recently introduced to be employed as a high throughput separator without clogging for microfluidics applications (Syed et al., 2021). This device can address the low flow rate issue with microfluidic separators and sorting devices. Instabilites such as Dean, Gortler and Taylor–Couette play an important role in enhancing the performance of a hydrocyclone by increasing the particle residence time (Zhu et al., 2012). However, the low operational range of Reynolds number in micro-hydrocyclone leads to a laminar flow supressing all the effective instabilites (Zhu et al., 2012). Although macroscale hydrocyclones have been studied for their various applications, the physics of the flow in micro-hydrocyclone and the performance efficiency parameters are yet to be known.

In this research, we present an experimental investigation on a micro-hydrocyclone to study the physics of the flow in this device. Particle image velocimetry (PIV) is applied to capture the velocity field. Using the same method, the effect of altering the inlet flow on its performance will be investigated by inducing Dean vortices using a spiral inlet, as shown in Figure 1(a).

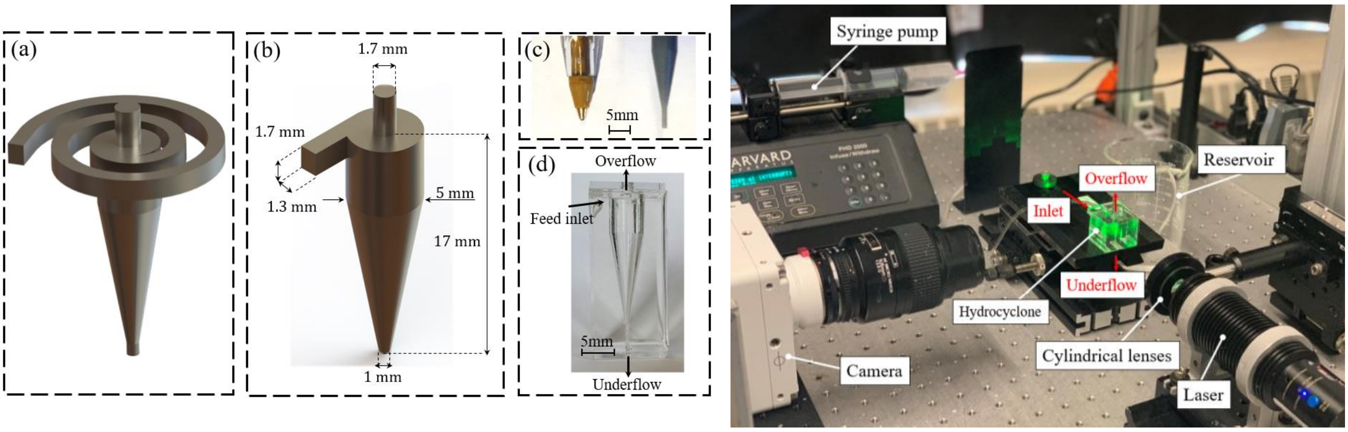

(e)

Figure 1. Solid model of the designed mold with (a) spiral inlet, (b) straight inlet, (c) comparison between the fabricated mold and the tip of a pen, (d) Fabricated microhydrocyclone, (e) experimental PIV setup.

2 METHOD

The designed fluid test cells are micro-hydrocyclones with spiral and straight feed inlets respectively shown in Figure 1(a), (b). These are manufactured using an SLA 3D printer (Form 3, FormLab Inc.) with a 25 µm resolution is used to print the inner part of the mold as shown in Figure 1(c). To increase the surface finishing quality of the cell, the micro-hydrocyclone was coated with a glossy sealing spray. The exterior mold is an acrylic box designed and fabricated to assemble with the 3D printed micro-hydrocyclone. The microfluidic device shown in Figure 1(d) is fabricated by molding using a transparent silicone (Solaris™, Smooth-On, Inc.). Its ultra-transparency provides maximum optical accessibility despite the thick sections. The low viscosity of the silicone allows it to flow in and around complex channel geometries easily. A 50.5% carbamide solution is used to match the refractive index of the working fluid with the device and has a dynamic viscosity of 1.905 mPa.s. A PIV setup as shown in Figure 1(e) is used to apply PIV at the midplane of the micro-hydrocyclone. In this setup a high frame rate camera (Phantom VEO 710, AMETEK Inc.) with a frame rate of 1000 fps was used. A 532 nm laser was used to illuminate the 18 μm hallow glass seeding particles. Commercial software (DaVis 8.4, LaVision GmbH) was also utilized to calculate the velocity vectors from the images obtained from the experiment.

3 RESULTS AND CONCLUSIONS

The in-plane velocity field on the midplane of the micro-hydrocyclone is shown in Figure 2(a) at $Re = 80$, $Re = D_i V_i/\nu$ where D_i is the inlet diameter, V_i is the inlet velocity, and ν is the kinematic viscosity of the working fluid. Flow enters from the inlet and goes toward both underflow and overflow at the bottom and top of the micro-hydrocyclone, respectively. The dual direction motion of the flow leads to formation of a balloon type surface around the overflow with the nondimensional axial velocity, $V_y^* = 0$ where $V_y^* = V_y/V_{y,max}$. This region is known as the locus of zero vertical velocity (LZVV) (Zhu et al., 2012). The axial velocity profile shown in Figure 2(b) indicates the location of the LZVV on the midplane. By investigating the shape of LZVV and correlating it to the performance parameters, an understanding on the effective parameters such as the Reynolds number on the efficiency can be achieved. Figure 2(c) shows the axial velocity along the line $x = 0$ (centerline). This plot indicates the LZVV tip on the midplane and shows its elongation. Figure 2(d) shows the axial velocity profile and the location of LZVV along the $y = 11$ mm line in the cylindrical section of the micro-hydrocyclone. The red dots represent the horizontal location of the LZVV curvature points with respect to the centerline. A detailed visualization of the flow will be discussed in the presentation comparing different boundary conditions of the experiment include the use of a spiral inlet.

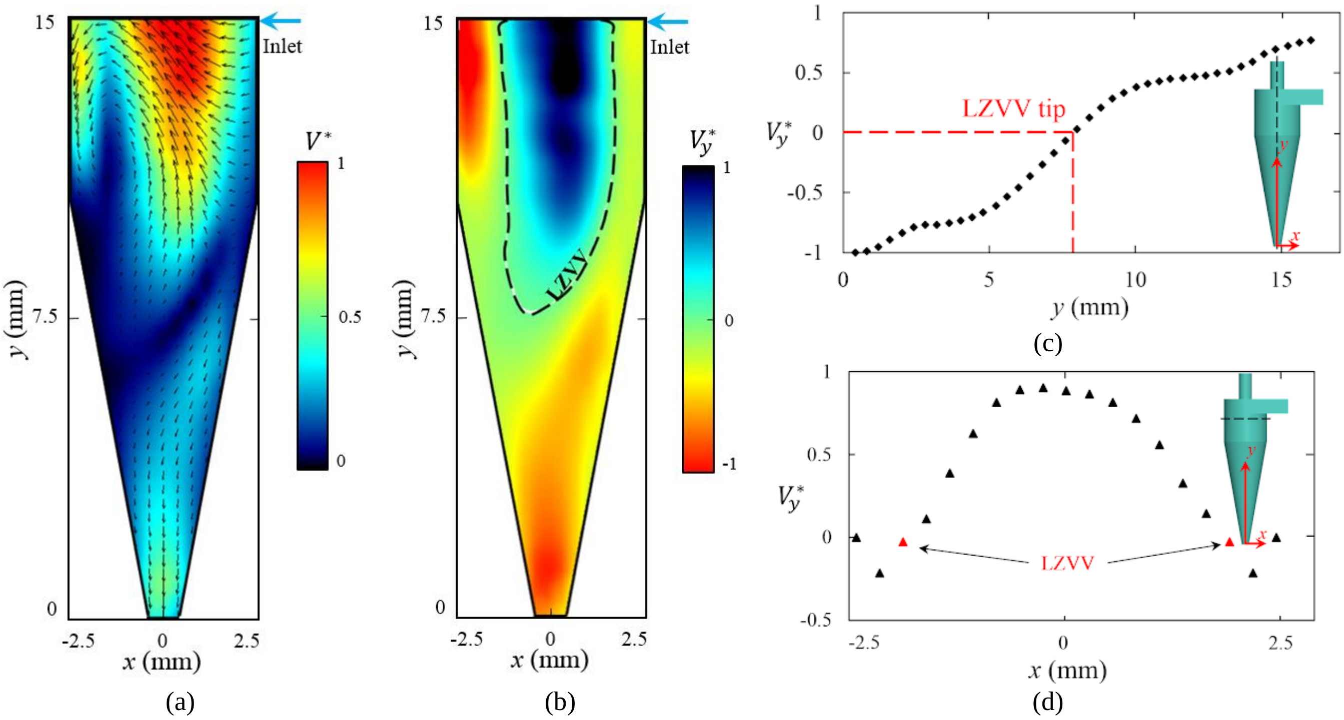

Figure 2. (a) Velocity field, V^* at the midplane of the micro-hydrocyclone, (b) contour of the axial velocity, V_y^* at the center of the micro-hydrocyclone highlighting the LZVV region, (c) axial velocity along the vertical line on the micro-hydrocyclon center line (d) axial velocity along the horizental line at y = 11 mm.

4 REFERENCES

- Syed, M. S., Marquis, C., Taylor, R., & Warkiani, M. E. (2021). A two-step microengineered system for high-density cell retention from bioreactors. *Separation and Purification Technology*, *254*(August 2020), 117610. https://doi.org/10.1016/j.seppur.2020.117610
- Wang, J., Bai, Z., Yang, Q., Fan, Y., & Wang, H. (2016). Investigation of the simultaneous volumetric 3-component flow field inside a hydrocyclone. *Separation and Purification Technology*, *163*, 120–127. https://doi.org/10.1016/j.seppur.2016.02.022
- Zhu, G., Liow, J. L., & Neely, A. (2012). Computational study of the flow characteristics and separation efficiency in a mini-hydrocyclone. *Chemical Engineering Research and Design*, *90*(12), 2135–2147. https://doi.org/10.1016/j.cherd.2012.05.020

Visualization of Polymer Solution-Flow Behavior around Triangle-Shaped Pillar Array in Microchannel

Yoshiyasu Ichikawa[1,*] and Masahiro Motosuke[1]
1: Dept. of Mechanical Engineering, Tokyo University of Science, Japan
* Correspondent author: yos.ichikawa@rs.tus.ac.jp

Keywords:, Microfluidics, Rheology, Dilute polymer flow, Micro PIV/PTV

1 Introduction

When the viscoelastic fluid flows through the porous media, the fluid experiences shear rate changes; the fluid viscosity then changes locally, inducing the complex flow behavior. Understanding this behavior is important for some industrial and biomedical applications. To predict and control this complex behavior, viscoelastic flow measurements have been performed around the micropillar installed in the microchannel where the inertia forces are negligible, mimicking the porous media.

The authors have observed the polymer solutions' behavior around the triangle-shaped pillar array in the microchannel. This geometry can induce intermittent shear-rate changes owing to sudden expansion and contraction flow between the pillar and channel wall. In this study, using the dilute polymer solution, we tried to visualize the rotation behavior inside the low-speed region formed around the pillar due to the flow instability that is reported in some previous studies (Steinberg, 2021). Then, in addition to this rotational behavior, the periodic oscillation of the low-speed region in the spanwise direction of the channel was also observed depending on the experimental conditions. This study aims to understand this periodic oscillation based on the velocity distribution acquisition inside and outside the low-speed region by PIV and PTV.

2 Experimental

Figure 1 shows the schematic of the microchannel used in this study. This microchannel was made from polydimethylsiloxane and had a single array of equilateral triangle-shaped pillars to ensure continuous contraction and expansion flow. The channel had a height (H) and width (W) of 36 µm and 300 µm, respectively. The side length of the triangle-shaped pillar was s = 180 µm. All pillars had the same geometry, and their height was the same as the channel height, H. The bottom of the channel was made of a 1-mm thick glass slide.

As a solution, hydrolyzed polyacrylamide (HPAM, $M_w = 18 \times 10^6$ Da, 30% hydrolysis) in ultrapure water with a concentration of 100 ppm was used. The critical concentration of HPAM with 30% hydrolysis solutions is about 180 ppm (Kawale et al., 2017), thus, the solution in this study was dilute. The rheological property of the solution was investigated by a rheometer and it is confirmed that the solution shows a shear-thinning property.

The HPAM solution containing 1 µm of diameter fluorescent particles was infused into the flow channel using a syringe pump with a flow rate Q varying from 5 to 500 µL/h. A 40× objective lens and a high-speed camera were used to capture the particle images. They were included in an inverted microscope. The imaging domain size was set as 512 µm × 512 µm, and two pillars were placed in this domain. Then, as shown in Fig. 1, The upstream pillar apex was set as the origin O, and the x- and y-axes were set in the streamwise and the spanwise directions, respectively. The velocity components corresponding to the x- and y-axes were also defined as velocity u and v components, respectively.

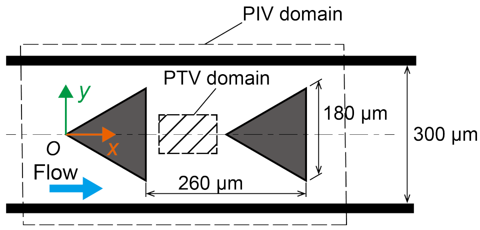

Figure 1. Schematic of the microchannel and pillar shape. The channel height is H = 36 µm.

3 Results and discussion

Figure 2(a) shows an example of the averaged velocity magnitude U (= $(u^2 + v^2)^{0.5}$) distribution in the case of Q = 10 µL/h which was obtained by PIV. The velocity magnitude was normalized U_{ref} (= Q/WH) and the streamline is shown in the figure. From Fig. 2(a), the rotational behavior inside the low-speed region is confirmed. The formation of the low-speed region and the occurrence of the rotational behavior inside it is due to minimization the flow extension stress due to the contraction flow (Qin et al., 2019). It was also observed that the size of the low-speed region changes depending on the flow rate Q.

Subsequently, focusing on the inside low-speed region around the pillar array, the flow velocity inside the region was obtained by PTV using successively obtained 3,000 particle images at 50 fps. The average velocity in the 60 µm × 40 µm ($x \times y$) region between the pillars shown in Fig. 1 was obtained. Note that we focused only on the velocity v component because we had preliminarily confirmed that the low-speed region oscillates mainly in the y-direction. The time series of the v component for Q = 10, 100, and 500 µL/h are shown in Fig. 2(b)–(d). As the flow rate Q increases, we can see that the fluctuation of v increases, and the periodicity of the oscillation becomes strong. The root-mean-square (RMS) value of v (v_{rms}) for each Q was calculated, as shown in Fig. 3. For the viscoelastic fluids, it is well known that elasticity becomes dominant as increasing the shear rate, then the flow shows instability, resulting in increased velocity fluctuation. As shown in Fig. 3, the sudden increase of v_{rms} is shown in $Q > 20$ µL/h. Hence, the transition to the state showing instability could be seen in our experimental conditions. Haward et al. (2021) observed asymmetric flow in the wake of a cylinder and attributed it to the accumulation of elastic stress where the curvature of the streamline increases. When elastic stress exceeds a critical state, the accumulated stress causes the wake to move randomly in a direction perpendicular to the streamline. As shown in Fig. 2(a), in the flow condition of our study, a large curvature area of the streamline was observed outer edge of the low-speed region, and it is considered that the elastic stress acting in this area caused the low-speed region to move and evolve into periodic oscillation behavior.

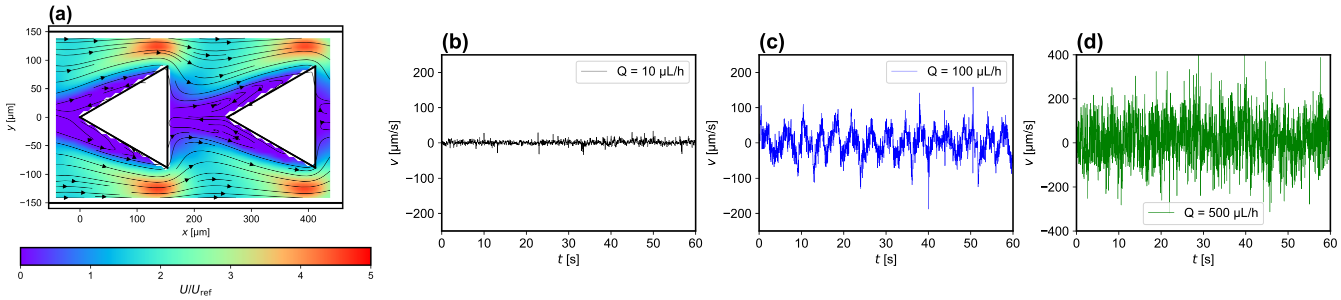

Figure 2. (a) Velocity magnitude around triangle-shaped pillar array for Q = 10 µL/h and the time-series of the velocity v component in the low-speed region for the case of (b) Q = 10 µL/h, (c) 100 µL/h, and (d) 500 µL/h, respectively.

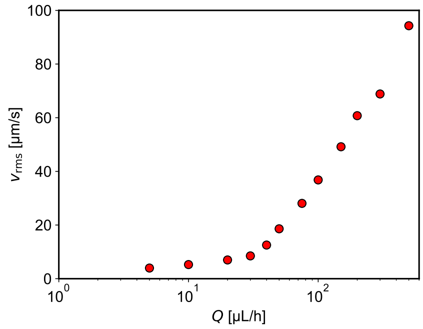

Figure 3. Root-mean-square (RMS) value of the v-component velocity (v_{rms}) depending on flow rate Q.

4 Conclusions

In this study, we investigated the behavior of the low-speed region formed between the triangle-shaped pillar array in the microchannel and its oscillation using the dilute HPAM solution. Focusing on the velocity distribution in the low-speed region, the spanwise component of the velocity shows fluctuation, and the RMS value increases as increasing the flow rate Q. Additionally, it is suggested that the periodic oscillation is due to the curvature of the low-speed region and the accumulation of elastic stress on the curvature.

5 References

Haward, S. J., Hopkins, C. C., Varchanis, S., & Shen, A. Q. (2021). Bifurcation in flows of complex fluids around microfluidic cylinders. Lab on a Chip, 21, 4041–4059.

Kawale, D., Marques, E., Zitha, P. L., Kreutzer, M. T., Rossen W. R., & Boukany, P. E. (2017). Elastic instabilities during flow of hydrolyzed poly-acrylamide solution in porous media: Effect of pore shape and salt. Soft Matter, 13, 765–775.

Qin, B., Salipante, P. F., Hudson, S. D. & Arratia, P. E. (2019). Upstream vortex and elastic wave in viscoelastic flow around cylinder. Journal of Fluid Mechanics, 864, R2.

Steinberg, V. (2021). Elastic turbulence: An experimental view on inertialess random flow. Annual Review of Fluid Mechanics, 53, 27–58.

Evaluation of liquid thickness distribution in micropores on moving elastic surfaces

Rikuto Shinozuka[1], Yoshiyasu Ichikawa[1],
Shinya Sugisawa[2], Tatsuhiko Hatano[2], Yoshio Kaji[2],
Isao Kuwayama[2], and Masahiro Motosuke[1*]
1: Dept. of Mechanical Engineering, Tokyo University of Science, Japan
2: Bridgestone Corporation, Japan
* Correspondent author: mot@rs.tus.ac.jp

Keywords: Solid-liquid interface, Fluorescence observation, Liquid thickness, Micropores

1 INTRODUCTION

The friction coefficient decreases when an object moves on a wet solid surface. To suppress this decrease, some methods have been presented to increase the contact area of boundary lubrication by removing the water film. One of the famous ways to achieve that is by applying an uneven surface with many micropores on the surface of the object . However, the mechanisms of the inflow and outflow of water on the uneven surfaces are still unclear. Visualization of water in the micropores on the moving object would be a key to elucidate the unclear fluid dynamics underneath and to imply an optimized design rule for the appropriate uneven surface to prevent the friction decrease.

We focused on the laser-induced fluorescence (LIF) method to visualize the water dynamics in the micropores. Fluorescence intensity which correlates liquid thickness allows the measurement of liquid thickness in a pore. In this study, we measured the liquid thickness distribution in the micropores on the moving elastic-material surface by LIF to understand the behavior of the liquid film formed in the micropores. For this purpose, we developed visualization and measurement procedures to quantify the liquid thickness distribution in the micropores while changing the pressure acting on the moving object. Then, the liquid thickness in the micropores of the elastic substrate during sliding movement was evaluated under various pressure and velocity conditions.

2 METHODS

An overview of the developed system in this study is shown in Fig. 1(a). This system consists of a moving device that can apply pressure and shear force to an elastic substrate and an observation system based on the inverted microscope. There is a 1-mm thick glass slide at the bottom of the moving device to visualize the fluorescent solution in the pores by microscope. A solution of Rhodamine 6G, a fluorescent dye, mixed with ultrapure water was applied to the glass substrate, and the glass substrate was moved at constant speed while pressing the elastic substrate with constant pressure. The pressure and the shear force between the elastic and glass substrates were measured by load cells. This enables the evaluation of the effects of pressure and shear force on the liquid film thickness in the micropores on the surface of the elastic substrate.

For the liquid film thickness measurement, the elastic substrate having 22.3% of the surface pore rate shown in Fig.1(b) was employed. As a measurement principle for liquid thickness distribution in the pores, the correlation between the fluorescence intensity of the solution and the liquid thickness, which is obtained using the microchannels with various channel heights, as in Fig. 1(c), was used. Since the relationship between fluorescent intensity and liquid thickness is linear in our experimental conditions [1], the fitting line obtained by the least squares was employed as the calibration line.

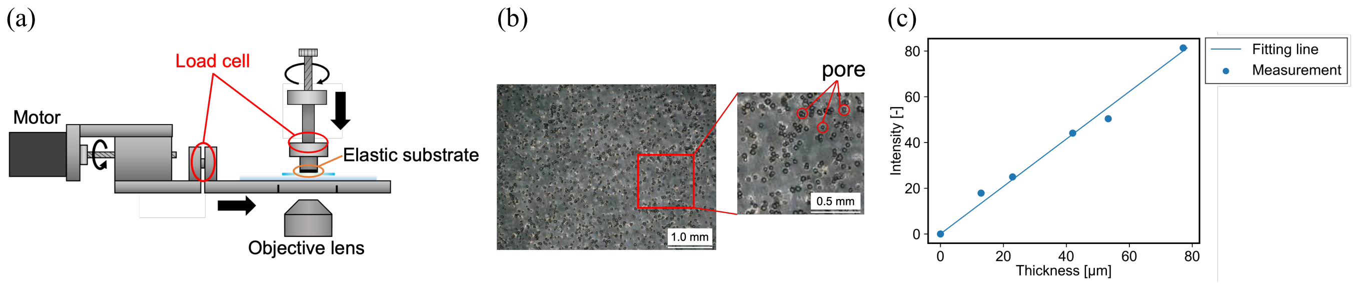

Fig. 1 (a) Schematics of the liquid-film thickness measurement system mimicking the moving object on the wet surface. (b) Surface of the elastic substrate. Enlarged view of each pore is also shown. (c) Calibration line between liquid film thickness and intensity.

3 RESULTS

The liquid thickness in the micropores on the sample surface was measured while changing the moving velocity of the glass substrate and pressure on the substrate. Liquid thickness distribution on the elastic substrate and an example of the cross-sectional shape of the liquid film in a micropore are shown in Fig. 2, which are measured under the condition of 2 mm/s in velocity and 0.3 MPa in pressure. A hemispherical liquid film with a diameter of 88.7 µm and a maximum thickness of 40.5 µm was obtained. It is found that the distortion of the shape due to the movement is small. Also, liquid thickness distributions for a number of pores can be evaluated from the image at the same time. This result exhibits that it is possible to evaluate the liquid film shape in the micropores under moving conditions.

The relationship between the micropore diameter and the maximum liquid thickness in each micropore in the imaging domain was obtained for each experimental condition. The results shown in Fig. 3(a) and (b) shows a positive correlation between the pore diameter and the maximum liquid thickness. The larger the diameter is, the thicker the liquid in the pores. Subsequently, we compared the effect of the moving velocity and the pressure on the substrate on the liquid film thickness distribution. From Fig. 3(a), the slope of the plot increased as the moving velocity increased. As the moving velocity increased, the pore could be filled with the solution due to the increased liquid inflow rate into the pore. Figure 3(b) shows no particular change in relative liquid thickness distribution with the pressure. Focusing on each liquid shape in a pore (Fig. 3(c)), the diameter of the liquid in the pore was slightly enlarged. This trend could be observed in other pores. This would be owing to the increase in the shear force depending on the pressure on the substrate, and it is considered that the deformation of the elastic substrate affected the liquid shape.

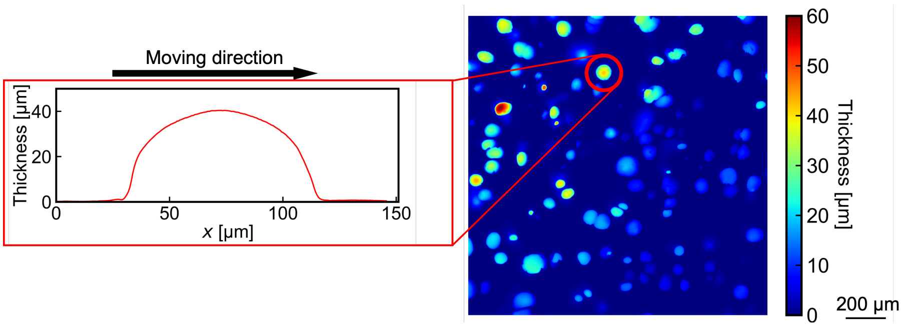

Fig. 2 Liquid thickness distribution and an example of the cross-sectional view of the liquid in a pore obtained under the condition of 1 mm/s in velocity and 0.1 MPa in pressure.

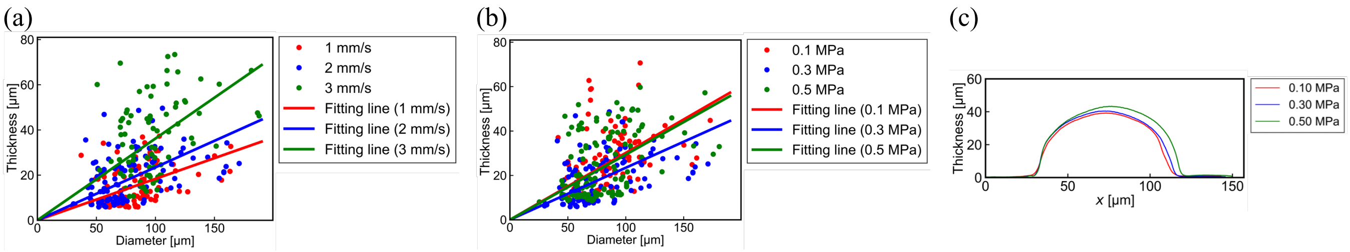

Fig. 3 Liquid thickness distribution for (a) different moving velocities of the glass substrate (0.3 MPa in the pressure) and (b) different pressures on the substrate (2 mm/s in the velocity). (c) Change of liquid shape in the same pore by the pressure (2 mm/s in the velocity).

4 CONCLUSIONS

In this study, we developed an experimental system that can visualize the liquid thickness distribution in micropores on the elastic surface and evaluate the thickness distribution by changing the shear force. From the measurement results, it was confirmed that the liquid thickness in the pores increased with an increase in the moving velocity of the glass substrate, and the diameter of the liquid in the pores was enlarged with an increase in the pressure on the substrate due to the deformation of the elastic substrate.

5 REFERENCES

[1] C. Cadart, E. Zlotek-Zlotkiewic, L. Venkova, O. Thouvenin, V. Racine, M. Le Berre, S. Monnier, M. Piel (2017). Fluorescence eXclusion Measurement of volume in live cells. Methods in Cell Biology, 139, 103-120.

TECHNICAL SESSION 12
HIGH SPEED JETS

Chaired by Friedrich Leopold

High-speed Background Oriented Schlieren imaging of a supersonic reactive jet

Olivier Léon[1,*], David Donjat[1], Juliette Aubrée[1]
1: ONERA/DMPE, Université de Toulouse, France
* Correspondent author: olivier.leon@onera.fr

Keywords: High-speed BOS, Reactive supersonic jet, Tomographic reconstruction

ABSTRACT Imperfectly-expanded reactive supersonic jets are commonly found at the exhaust of space launchers and rockets. Their flow-fields are characterized by shock-cells and chemical reactions inducing high-temperature flames as illustrated in Figure 1. Gaining spatially-extended quantitative insights into the key physical quantities describing these flows is therefore a real challenge. This work demonstrates that high-speed Backgound Oriented Schlieren (BOS) imaging provides a practical approach for the evaluation of instantaneous and average refractive index fields in round jets generated by the combustion of alumina-free propellant. The technical difficulties that were overcome will be discussed, namely background illumination, setup sensitivity and vibration correction.

Figure 1: Photograph of the reactive jet observed by BOS.

The first challenge of this study was to satisfactorily image the observed BOS background pattern through the reactive jet, with the additional constraint of a stabilized regime lasting only about 2 s. To achieve this, we used a high-repetition-rate laser illumination (Litron LDY304, $\lambda = 527\,\mathrm{nm}$) and a matched laser line bandpass interference filter on the camera lens to reject most of the flame emission. High signal-to-noise ratios were additionally achieved by printing the BOS background pattern on a retro-reflective panel. This choice implies that the illumination axis should be close to the optical axis of the camera, with observation angles typically lower than 10°. As shown in Figure 2(a), a convenient solution was found using a liquid laser guide with its end ferrule mounted in a holder housing a spherical lens, placed near the camera. A high-speed 4 MPx camera was used at 800 fps in full-frame (Phantom v341) in synchronization with the laser, providing about 2000 flow snapshots during the useful time window.

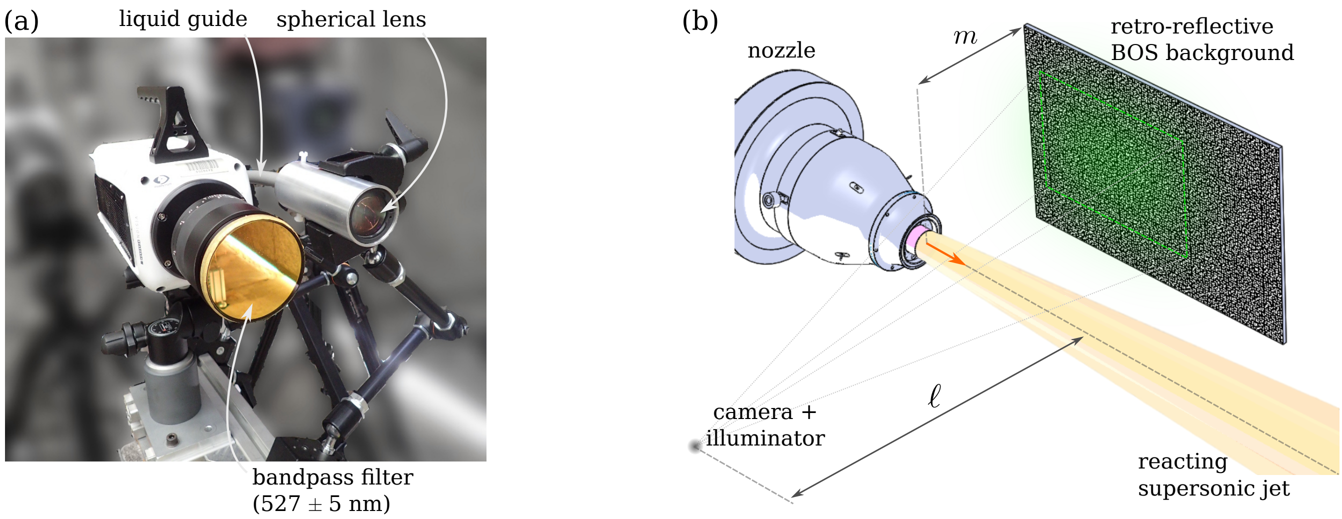

Figure 2: (a) Optical elements for high-speed BOS illumination and imaging; (b) schematic of the BOS setup.

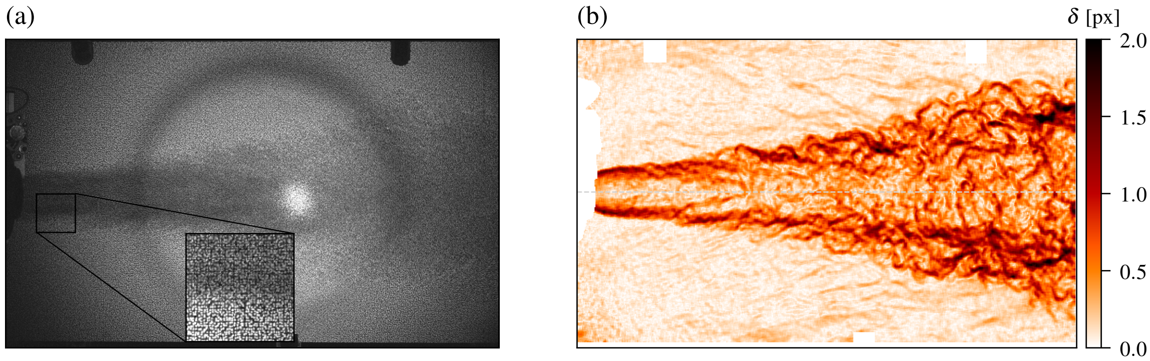

Figure 3: (a) Instantaneous snapshot and (b) norm of the corresponding BOS displacement map.

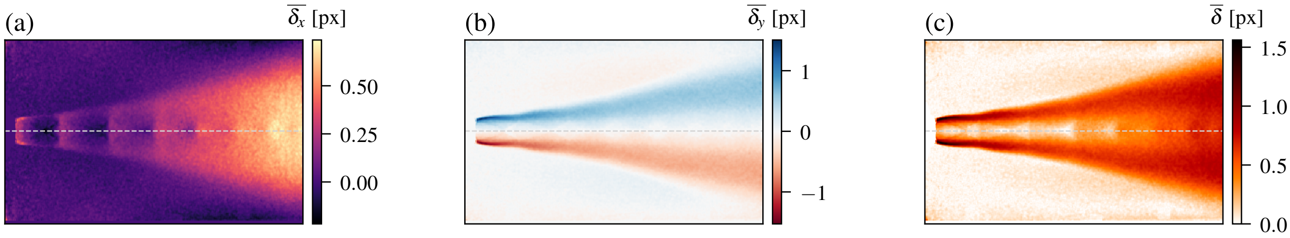

Figure 4: Averaged displacement maps for the stabilized regime: (a) axial displacements; (b) vertical displacements and (c) displacement norm.

A schematic of the BOS experimental setup is depicted in Figure 2(b). Due to the large density gradients encountered in the reactive jet, the distance m between the flow and the background must be relatively short, on the order of 50 cm, to provide adequate BOS imaging sensitivity. Higher values gradually increase astigmatism effects, to the point of severe loss of correlation of the background images with the reference image without flow. A natural drawback of low m values is the increased sensitivity of the setup to vibration. Still, by exploiting measurements in the quiescent regions surrounding the jet, it was found that appropriate post-processing could solve most of the problems induced by background vibrations.

An example of instantaneous acquisition is given in Figure 3(a). The reactive jet clearly induces light attenuation, particularly visible at the nozzle exit. As emphasized in the inset, the background pattern is nevertheless well observed, even in the initial region with maximal density gradients. Dense BOS pattern displacements $\boldsymbol{\delta} = (\delta_x, \delta_y)$ are estimated from this image by cross-correlation with a reference no-flow acquisition using an in-house algorithm (FOLKI, Champagnat et al. (2011)). The displacement norm for this example is given in Figure 3(b). Zero displacements on average are observed outside the jet, showing that the background vibrations have been satisfactorily compensated. For all the tests performed, a 2D linear correction was found to be the most appropriate choice.

Finally, the mean displacement fields obtained for the stabilized jet regime are given in Figure 4. Correct radial symmetry can be observed in these maps. Furthermore, the series of internal shock-cells that one would expect from imperfectly-expanded jets is clearly discernible. Based on these results and a prior calibration of the BOS setup, axisymmetric reconstructions of the mean refractive index field (at wavelength λ) will be presented. Two different reconstruction techniques will be used, namely the direct BOS tomography approach proposed by Nicolas et al. (2015) and the generalized Abel inverse transform for axisymmetric flows presented by Sipkens et al. (2021).

References

Champagnat, F., Plyer, A., Besnerais, G. L., Leclaire, B., Davoust, S., & Sant, Y. L. (2011). Fast and accurate PIV computation using highly parallel iterative correlation maximization. *Experiments in Fluids*, *50*(4), 1169–1182. https://doi.org/10.1007/s00348-011-1054-x

Nicolas, F., Todoroff, V., Plyer, A., Besnerais, G. L., Donjat, D., Micheli, F., Champagnat, F., Cornic, P., & Sant, Y. L. (2015). A direct approach for instantaneous 3d density field reconstruction from background-oriented schlieren (BOS) measurements. *Experiments in Fluids*, *57*(1). https://doi.org/10.1007/s00348-015-2100-x

Sipkens, T. A., Grauer, S. J., Steinberg, A. M., Rogak, S. N., & Kirchen, P. (2021). New transform to project axisymmetric deflection fields along arbitrary rays. *Measurement Science and Technology*, *33*(3), 035201. https://doi.org/10.1088/1361-6501/ac3f83

Particle Image Velocimetry in High Speed Organic Fluid Flows

Theo Michelis[1,*], Adam J. Head[1] ,Matteo Majer[1], Alessio Secchiaroli[1], Carlo De Servi[1], Piero Colonna[1]
1: Faculty of Aerospace Engineering, Delft University of Technology, The Netherlands
* Correspondent author: T.Michelis@tudelft.nl

Keywords: NICFD, PIV, CFD, RANS, De Laval Nozzle

1 INTRODUCTION

Compressible vapour flows involving fluids whose thermodynamic states differ significantly from those of ideal gases occur in several devices that are relevant for propulsion and power applications. The design of these applications' components, especially in the case of turbomachinery, cannot be performed without resorting to accurate equations of state. The result is, otherwise, unreliable, as demonstrated, for instance, by (Guardone *et al*., 2013) for the paradigmatic test case of a supersonic nozzle.
The fluid dynamic design of machinery operating in these conditions necessitates validated CFD codes. Validation can be performed only if accurate experimental information covering a representative range of conditions is available. Particle Image Velocimetry (PIV) is arguably the experimental technique of choice for providing these data. Some initial attempts of using PIV in this type of flows are documented in (Gallarini, 2016; Head *et al*., 2019; Satoshi *et al*., 2015; Valori, 2017).

Typical optical measurement techniques such as PIV have never been successfully attempted in high speed flows of dense organic vapors. The first challenge which needs to be addressed is the selection of the appropriate tracer particles and then the technical challenge of injection of the particles in the fluid loop. A new seeding device must be designed and engineered such that the particles can be delivered to the high temperature and high pressure flow entering the nozzle test section with guaranteeing uniform particle distribution and no flow distortions.

2 APPARATUS AND METHODOLOGY

A schematic overview of the problem is shown in Fig. 1, representing a de Laval nozzle, implemented in the ORCHID (Head, 2021), which has been designed with the method of characteristics. For this work, the working fluid (hexamethyldisiloxane, MM) in the nozzle is subjected to the total inflow conditions of $T_\mathrm{t} = 220 \pm 0.64$ °C and $p_\mathrm{t} = 4 \pm 0.0302$ bara. The corresponding static back pressure is $p_\mathrm{s} = 0.2981$ bara. The aforementioned quantities correspond to experimental measurements and are subsequently used as boundary conditions for numerical simulations.

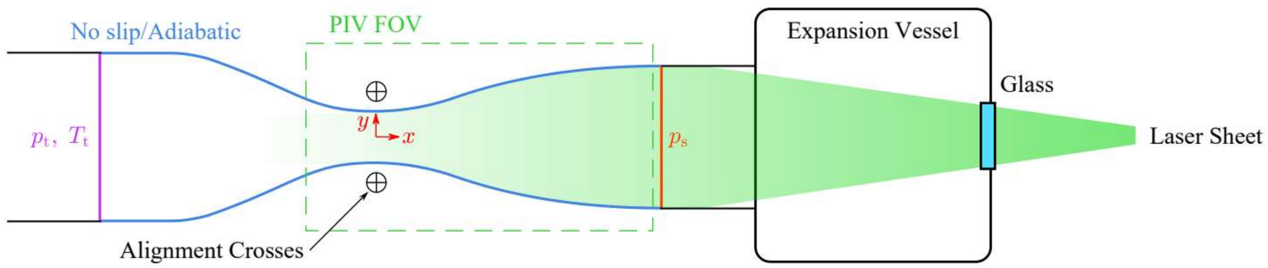

Fig. 1: Schematic of the problem (not to scale), demonstrating the PIV field of view with respect to the computational domain which is indicated in blue on the nozzle walls. The alignment crosses are used to estimate the throat height as the temperature varies.

The nozzle test section's total length and span in ambient conditions are 75 mm and 20 mm, respectively, and the nominal throat height is 7.5 mm. Any changes in throat height due to thermal expansion are optically tracked through two cross indicators machined at $x = 0$ on the nozzle axis. At the experimental conditions previously mentioned the calculated throat is 7.92 mm and is further used for the numerical simulations.

Two-component velocity field measurements are performed on the x-y plane, located at the midspan of the nozzle test section. The spatial calibration gives a resolution of approximately 29 px/mm. Illumination is provided by a dual cavity Quantel Evergreen Nd:YAG laser. The beam is transformed to a sheet of approximately 1mm thickness with a top-hat illumination profile, using a series of spherical and cylindrical lenses as well as two parallel knife edges. The region of interest is imaged with a LaVision Imager LX 2MP camera and a 75 mm Tamron C-mount objective, set an aperture of $f_\# = 8$. The camera sensor is cropped to obtain a field of view of $56 \cdot 27\ \mathrm{mm}^2$, and an ensemble of 5000 image pairs ($\Delta t = 5\ \mu\mathrm{s}$) is recorded. For this preliminary study, a low particle seeding concentration is sought for in order to avoid possible impact of the seeding on the flow. To this end, the natural small-scale debris ($\leq 1\ \mu\mathrm{m}$) circulating in the facility and which consist of iron oxide suffices for the current measurements. Each recording contains on average 48 particle in the field of view, the diffraction pattern of each forms a diameter of approximately 4 pixels on the camera sensor (see Fig. 3b). An important parameter that may affect optical measurements in organic flows is the gradient of refractive index as a consequence of the vapour density gradients. The estimated deviations are $\delta_x = 15$ nm and $\delta_y = 8$ nm, occurring at regions with high reflective index gradient. Since these values are within one camera pixel, deviations due to refractive index cannot be detected, hence, it is concluded that for the current conditions uncertainties in the velocity field are only dependent on the PIV methodology.

3 RESULTS

A comparison of both u and v velocity component fields between RANS and PIV shows that a remarkable agreement between experimental and numerical methodologies is achieved; the obtained departures (within 9 %), mostly in the v component, could be attested to two different factors. First, within the framework of this investigation, the inertia of the particle seeding has not been determined, hence, it is not possible to conclude on how accurately the flow is traced. A second factor is the temporal difference between PIV frames, due to hardware limitations the particle displacement downstream of the throat ranges from 1.5 mm to 2 mm. The behavior of the fluid at the nozzle expansion can be decomposed in three distinct regions, namely the kernel, reflex and uniform regions (Anand *et al.*, 2019). Within the kernel region, flow is accelerated to the desired Mach number (Ma). In turn, the reflex region redirects the expanding flow, ensuring uniform conditions at the nozzle exit. Although the boundary layer is resolved in the RANS simulations, PIV near the wall is unfeasible due to limitations of the current experimental setup, this is visible in Fig. 2.

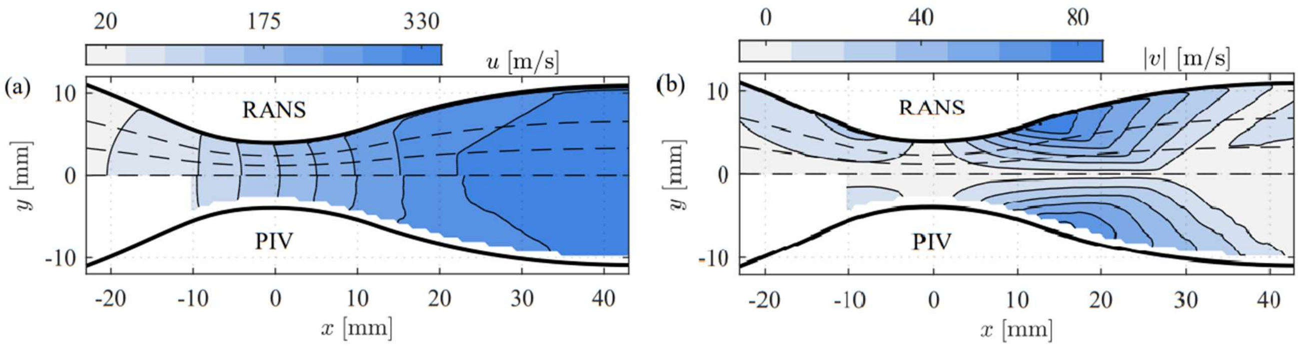

Fig.2 :Velocity components contours estimated from simulations and experiments (a) x direction component, u and (b) y direction component, v. The upper half and lower half of the domain correspond to RANS and PIV data, respectively.

4 REFERENCES

- Anand, N, S. Vitale, M. Pini, G.J. Otero, and R. Pecnik (2019), “Design methodology for supersonic radial vanes operating in nonideal flow conditions,” J. Eng. Gas Turb. Power 141 (2), 022601
- Gallarini, Simone (2016), Design and commissioning of a Laser Dsoppler Velocimetry seeding system for non-ideal fluid flows, Master’s thesis (Politecnico di Milano).
- Guardone, A, A. Spinelli, and V. Dossena (2013), “Influence of molecular complexity on nozzle design for an organic vapor wind tunnel,” J. Eng. Gas Turb. Power 135 (4), 042307
- Head, A.J. (2021), Novel Experiments for the Investigation of Non-ideal Compressible Fluid Dynamics: The ORCHID and First Results of Optical Measurements, Ph.D. thesis (Delft University of Technology)
- Harinck, J, A. Guardone, and P. Colonna (2009), “The influence of molecular complexity on expanding flows of ideal and dense gases,” Phys. Fluids 21 (8), 086101.
- Head, A J, M. Novara, M. Gallo, F. Schrijer, and P. Colonna (2019), “Feasibility of particle image velocimetry for low-speed unconventional vapor flows,” Exp. Therm. Fluid Sci. 102, 589 – 594.
- Satoshi, U, T. Wakana, K. Yoichi, S. Norimasa, and S. Toshiaki (2015), “PIV measurement of carbon dioxide gas-liquid two-phase nozzle flow,” in ASME Proceedings: Symposium on Noninvasive Measurements in Single and Multiphase Flows.

- Valori, V (2017), Rayleigh-Benard convection of a supercritical fluid: (PIV) and heat transfer study, Ph.D. thesis (Delft University of Technology).

Experimental Study of Mixing in a Light Jet

Leo Walter[1,2,*], David Donjat[1], Olivier Léon[1], Gabriele Nastro[2] , Jérôme Fontane[2]
1: ONERA/DMPE, Université de Toulouse, 31055, Toulouse, France
2: ISAE Supaéro, Université de Toulouse, France
[*] Correspondent author: leo.walter@onera.fr

Keywords: Side-jets, Tomographic BOS, Helium-air round jet, Instability

ABSTRACT The challenge of decreasing our reliance on fossil fuels for terrestrial and aerial transportation has spurred an ongoing research effort toward low-carbon energy vectors such as hydrogen. Increased efficiency of mixing downstream of the jet injectors is an important lever toward a new generation of hydrogen internal combustion engines, turbojets, and statoreactors. The study and control of transition mechanisms downstream of the injectors is therefore a key aspect of the increased industrial implementation of hydrogen-based engines.

Light jets experience physical phenomena related to global instability modes which do not appear in the homogeneous counterpart. Under certain conditions of density ratio $S = \rho_{\text{jet}}/\rho_{\text{ambient}}$, Reynolds number Re and aspect ratio $\alpha = \theta/R$ where θ is the momentum-thickness at the jet-nozzle exit and R its radius, light-jets exhibit self-sustained oscillations associated with an absolute Kelvin-Helmholtz instability mode. This instability mode can give rise to remarkable radial ejections of fluid which have a substantial impact on mixing due to an increased interface between the jet and the ambient fluid (Kyle & Sreenivasan, 1993). The physical mechanisms behind the formation of these side-jets is still subject to different conjectures (Monkewitz & Pfizenmaier, 1991; Nastro et al., 2022), and the objective of this study is to underline the physical phenomena responsible for the apparition of side-jets and to provide a better understanding of their structure and effect, as well as to quantify their influence on mixing between the jet and ambient fluids.

To that effect, we use an experimental setup consisting of a helium-air binary mixing jet. First, the jet will be characterized through hot-wire measurements and compared to the existing literature on the subject, notably with the results of Zhu et al. (2017), and the frequency measurements of the primary instability of the light jet performed by Hallberg and Strykowski (2006). Secondly, field measurements will be obtained relying on tomographic Background Oriented Schlieren. For this purpose, a 2D-BOS campaign has been conducted to calibrate and optimize the optical setup for the study of helium-air mixing. An example of the resulting displacement fields are given in Figure 1. We use a helium-air jet due to its similar range of density ratio to hydrogen jets and to circumvent security risks associated with hydrogen gas' explosivity. The light source used in this study is a high-power pulsed laser in order to minimize the temporal blur and maximize the illumination of the optical setup, which reduces the intrinsic circle of confusion.

An important objective of the experimental study is to visualize and analyze the flow structure associated with the side-jets with quantitative 3D density field measurements. This can be achieved by tomographic BOS, which is an optical technique based on the measure of the deviation of a light-ray passing through a refractive medium. The deviation fields are estimated by post-processing of snapshots of the apparent displacement of a background pattern placed behind the flow of interest. The reconstruction of the 3D density field is then performed by directly solving the inverse problem defined by:

$$\varepsilon = \frac{G}{n_0} \int_{\text{ray}\subset\text{flow}} \nabla\rho(s)\mathrm{d}s \tag{1}$$

where ε is the deviation field, ρ the density field, G the Gladstone-Dale constant, n_0 the refractive index of the undisturbed medium, and s the path of the light ray which is modeled by ray-tracing. Considering a discretized problem, this equation for the density field is solved relying on a regularization method to reconstruct the flow from the obtained experimental data. The optimization problem then amounts to minimizing the loss function $\mathscr{J}$:

$$\mathscr{J}(\rho) = \|\mathbf{A}\rho - \varepsilon\|^2 + \lambda\,\|\mathbf{D}\rho\|^2 \tag{2}$$

where λ is the regularization parameter which acts as a weight on the L2-norm of the density gradient, $\mathbf{D}$ the discretized upwinded gradient operator and $\mathbf{A}$ the discretized tomographic operator obtained from equation (1). This method allows to limit the amplification of experimental noise in the inversion and mitigates the artifacts associated with the 3D reconstruction of the flow observed by a limited number of camera points of view (Nicolas et al., 2015).

The use of 3D-BOS to investigate light jets has recently received attention and allowed Amjad et al. (2023) to succesfully reconstruct flow structures classicly associated with variable-density jets. The instantaneous density field measurements resulting from our present study will shed new light on the structure and development of the side-jets as to the authors' knowledge, no quantitative field measurements of the density and mixing induced by side-jets have been published in the literature on the subject.

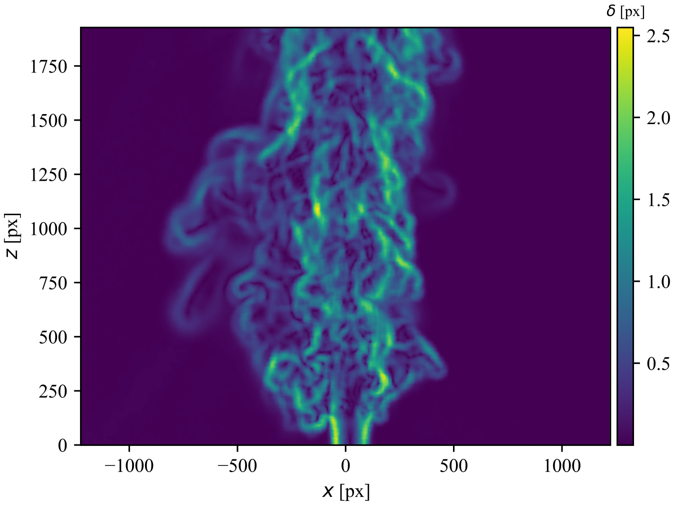

(a)

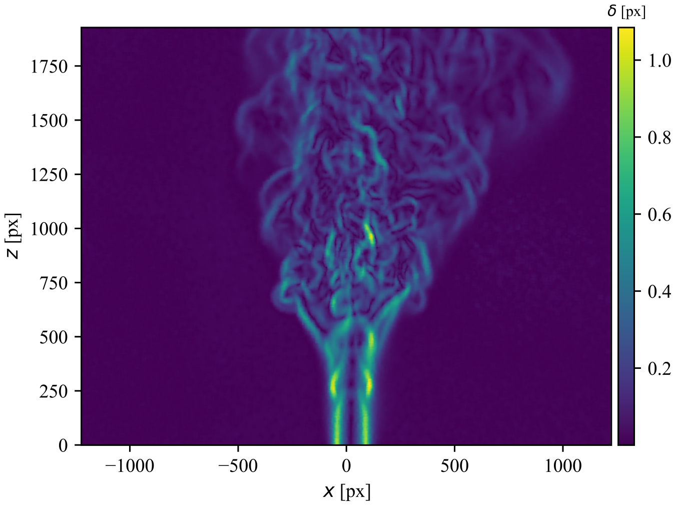

(b)

Figure 1: Instantaneous displacement snapshots of a helium-air jet into quiescent air. (a) $Re = 3000, S = 0.14$. The side-jets present drastic ejection angles and immediately trigger transition to turbulence and the mixing interface between the two fluids is greatly increased (b) $Re = 2000, S = 0.60$. The side-jets ejection angle is smaller than in (a) while still promoting mixing. Kelvin–Helmholtz billows develop on the jet and persist after the apparition of side-jets.

References

Amjad, S., Soria, J., & Atkinson, C. (2023). Three-dimensional density measurements of a heated jet using laser-speckle tomographic background-oriented schlieren. *Experimental Thermal and Fluid Science*, *142*, 110819. https://doi.org/10.1016/j.expthermflusci.2022.110819

Hallberg, M. P., & Strykowski, P. J. (2006). On the universality of global modes in low-density axisymmetric jets. *Journal of Fluid Mechanics*, *569*, 493. https://doi.org/10.1017/s0022112006002357

Kyle, D. M., & Sreenivasan, K. R. (1993). The instability and breakdown of a round variable-density jet. *Journal of Fluid Mechanics*, *249*(-1), 619. https://doi.org/10.1017/s0022112093001314

Monkewitz, P. A., & Pfizenmaier, E. (1991). Mixing by side jets in strongly forced and self-excited round jets. *Physics of Fluids A: Fluid Dynamics*, *3*(5), 1356–1361. https://doi.org/10.1063/1.858065

Nastro, G., Fontane, J., & Joly, L. (2022). Optimal growth over a time-evolving variable-density jet at atwood number. *Journal of Fluid Mechanics*, *936*. https://doi.org/10.1017/jfm.2022.45

Nicolas, F., Todoroff, V., Plyer, A., Le Besnerais, G., Donjat, D., Micheli, F., Champagnat, F., Cornic, P., & Le Sant, Y. (2015). A direct approach for instantaneous 3d density field reconstruction from background-oriented schlieren (BOS) measurements. *Experiments in Fluids*, *57*(1). https://doi.org/10.1007/s00348-015-2100-x

Zhu, Y., Gupta, V., & Li, L. K. B. (2017). Onset of global instability in low-density jets. *Journal of Fluid Mechanics*, *828*. https://doi.org/10.1017/jfm.2017.555

Turbulent shock-induced separation over rigid and flexible walls

Luis Laguarda[1,*], Stefan Hickel[1], Ferry. F. J. Schrijer[1] and Bas W. van Oudheusden[1]
1: Aerodynamics Group, Department of Flow Physics and Technology, Faculty of Aerospace Engineering, TU Delft, The Netherlands
Correspondent author: L.LaguardaSanchez@tudelft.nl

Keywords: high-speed flows, wall-bounded turbulence, flow separation, shock waves, fluid-structure interactions

Interactions between shock waves and turbulent boundary layers (STBLIs) are ubiquitous in high-speed aerodynamics applications (such as air intakes, control surfaces and rocket nozzles). When substantial flow separation occurs, as in figure 1, STBLIs are known to exhibit a very broad range of energetic frequencies (Clemens and Narayanaswamy, 2014). The high-frequency content is associated with small-scale turbulence, and detached shear layer dynamics are a major source of unsteadiness at moderate frequencies (promoting the mass exchange with the reverse-flow region, Piponniau et al. 2009). The lower end of the energetic spectrum, in turn, is related to expansions and contractions of the reverse-flow bubble and longitudinal excursions of the separation shock (Pasquariello et al., 2017). These characteristic low-frequency motions are of particular concern since they lead to intermittent and high-amplitude thermomechanical surface loads, see figure 1. Lightweight skin panels may resonate under such conditions and collapse due to high-cycle fatigue (Eason and Spottswood, 2013). At hypersonic speeds, STBLIs also lead to severe localized heating (Blevins et al., 1993) which can further degrade the mechanical properties of aircraft components (thereby becoming more prone to failure). The accurate characterization of STBLIs is thus necessary, also in the context of dynamic fluid-structure interactions (FSIs), to minimize weight requirements, improve aerodynamic efficiency and expand the operational envelope of current high-speed platforms.

In this study, we perform wall-resolved and long-integrated large-eddy simulations (LES) of impinging STBLI at Mach 2.0 in order to better understand the underlying physics. The resulting LES database includes a high-Reynolds

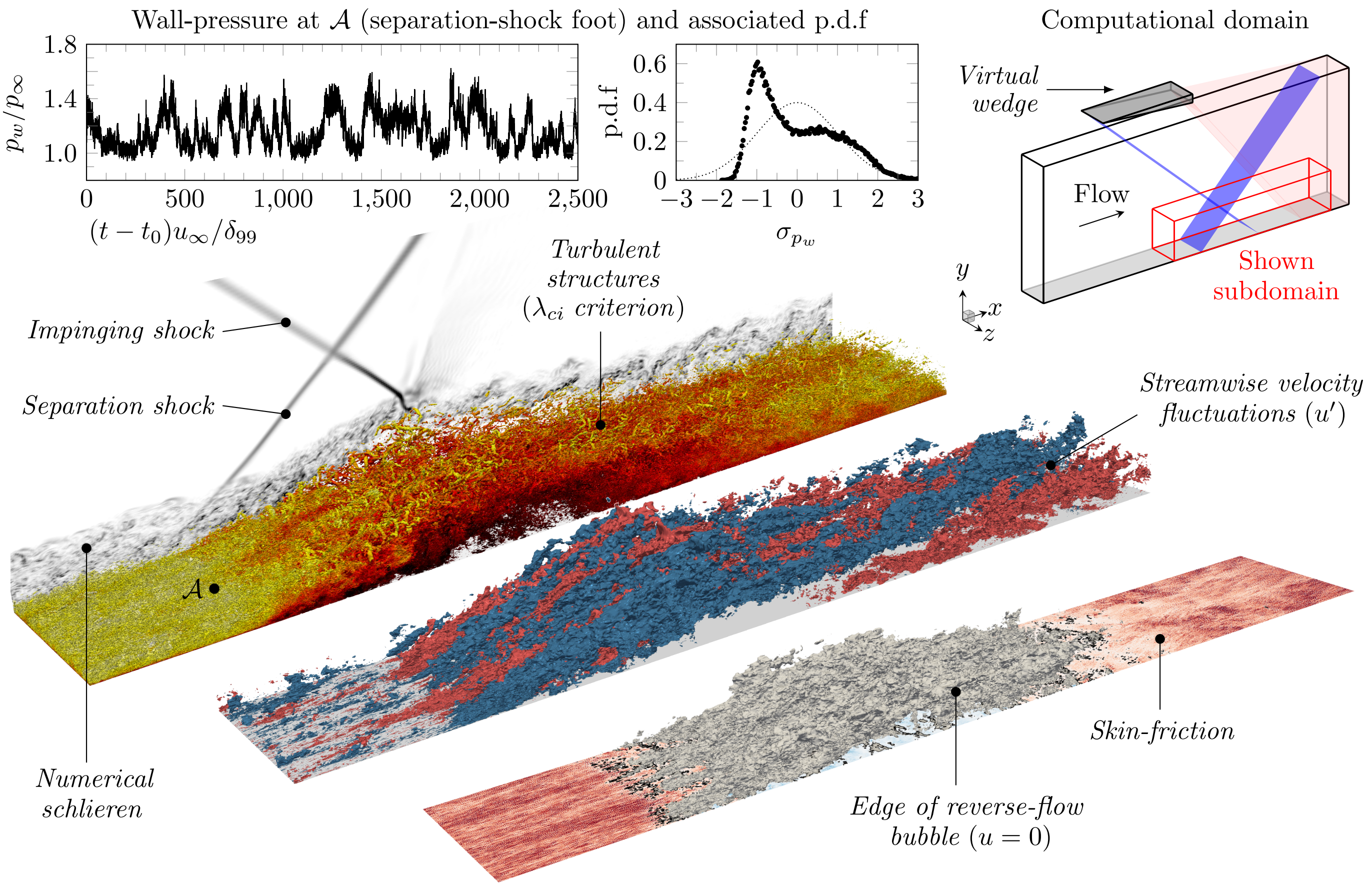

Figure 1: Close-up view of the STBLI region (over a rigid wall). Turbulent structures are colored by the local streamwise velocity, and δ_{99} is the TBL thickness. Free-stream quantities are denoted with the subscript ∞.

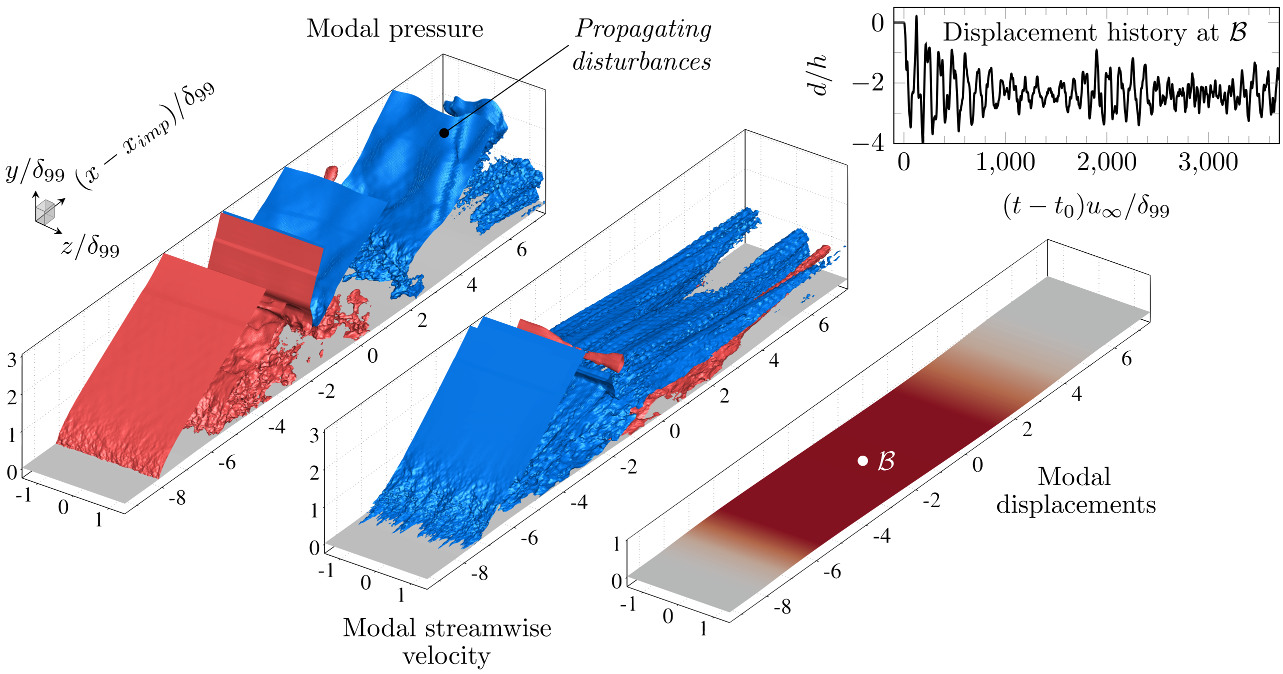

Figure 2: Dynamic mode associated with the first bending frequency of the panel motion (FSI case). Displacement data is normalized by the panel thickness ($h = 0.25$ mm) and x_{imp} is the inviscid impingement point.

interaction (at a friction Reynolds number $Re_\tau = 5118$) that extends the current parameter range of strong STBLI covered with high-fidelity simulations. We also simulated a moderate-Reynolds interaction (at $Re_\tau = 1226$) over a flexible thin-panel that results in a dynamic and complex FSI. The panel exhibits self-sustained oscillatory behavior with varying oscillation amplitude (see figure 2) and the most energetic bending motion corresponds to the first natural frequency of the pre-loaded panel with the mean STBLI wall-pressure. This frequency differs significantly from the first natural frequency of the unloaded flat panel (almost by a factor 4) which highlights the importance of the mean panel deformation and the corresponding stiffening in the resulting FSI dynamics.

The unprecedented resolution of the present simulations enables a unique visualization of the flow that provides valuable insights into the complex three-dimensional nature of STBLI. Incoming streamwise velocity fluctuations, which exert a modulating influence on the separation-shock foot, increase in size as they traverse the interaction (see figure 1). Large arch-shaped structures also develop on the high-speed side of the detaching shear layer, where spanwise inhomogeneity is particularly apparent. Dynamic mode decomposition (DMD, Schmid 2010) of the three-dimensional pressure, streamwise velocity and streamwise vorticity fields (not shown here) reveals that the broadband and most energetic low-frequency dynamics of the separation shock are statistically linked to alternating velocity streaks and large-scale vortices at reattachment. In the presence of the flexible panel, on the other hand, the most energetic dynamics are not broadband; instead, the whole STBLI flow is found to resonate at the first bending frequency of the panel motion. This is confirmed by DMD of the flow and displacement data, which identifies this frequency as the most dominant. Interestingly, streaks are no longer visible in the corresponding modal streamwise velocity field (see figure 2) and the modal pressure reveals downstream propagating disturbances in addition to the characteristic large-amplitude excursions of the separation shock.

References

Blevins, R. D., Holehouse, I., and Wentz, K. R. (1993). Thermoacoustic loads and fatigue of hypersonic vehicle skin panels. *J. Aircraft*, 30(6):971–978.

Clemens, N. T. and Narayanaswamy, V. (2014). Low-frequency unsteadiness of shock wave/turbulent boundary layer interactions. *Annu. Rev. Fluid Mech.*, 46:469–492.

Eason, T. G. and Spottswood, S. (2013). A structures perspective on the challenges associated with analyzing a reusable hypersonic platform. *AIAA Paper*, 2013-1747.

Pasquariello, V., Hickel, S., and Adams, N. A. (2017). Unsteady effects of strong shock-wave/boundary-layer interaction at high reynolds number. *J. of Fluid Mech.*, 823:617–657.

Piponniau, S., Dussauge, J.-P., Debieve, J.-F., and Dupont, P. (2009). A simple model for low-frequency unsteadiness in shock-induced separation. *J. Fluid Mech.*, 629:87–108.

Schmid, P. J. (2010). Dynamic mode decomposition of numerical and experimental data. *J. Fluid Mech.*, 656:5–28.

Day 3

TECHNICAL SESSION 13
FLOW CONTROL

Chaired by Fabio di Felice

Effects of the mixing chamber length and of the nozzle-to-plate distance on the external flow field of impinging sweeping jets

C. D'Angelo[1], C. S. Greco[1], G. Paolillo[1],
T. Astarita [1], G. Cardone[1*]
1: University of Naples "Federico II", Department of Industrial Engineering, Naples, Italy
* Correspondent author: gennaro.cardone@unina.it

Keywords: PIV technique, impinging sweeping jets, flow field

ABSTRACT The external flow field of impinging sweeping jets has been experimentally investigated through the application of the Particle Image Velocimetry (PIV) technique. Three sweeping jet devices, characterized by different mixing chamber lengths (L_f /w = 2.5 , 3.5, 4.5, being w the width of the throat section of the fluidic oscillator), have been investigated and their impinging flow fields have been evaluated for non-dimensional nozzle-to-plate distances H/w ranging between 2 and 10. In order to highlight the influence of the nozzle-to-plate distance and of the mixing chamber length on the impinging flow field of the investigated sweeping jets devices, time-averaged and phase-averaged analyses have been carried out.

1 INTRODUCTION

Due to intrinsic flow instability mechanisms, sweeping jet fluidic oscillators are devices which are able to convert a steady jet into an oscillating jet. Over the last years, the interest in fluidic oscillators has remarkably grown, because of their simplicity, reliability, and low maintenance costs; indeed, the oscillations are entirely self-induced and self-sustained (Bobusch et al.). In the literature several actuator designs have been proposed to generate a sweeping jet. Three main categories are suggested by Woszidlo et al.: feedback-free oscillators, oscillators with one feedback channel and oscillators with two feedback channels (as the one investigated in the current work, illustrated in Figure 1, left).

2 EXPERIMENTAL SETUP

The impinging flow field of the issued sweeping jets has been investigated through the application of the PIV technique. All the experiments have been performed at the same value of the Reynolds number (2.16×10^4). In the employed experimental apparatus (depicted in Figure 1, right) a centrifugal blower is used to collect the air from the ambient; in order to keep the air temperature equal to the ambient one, the air then passes through a heat exchanger. The flow is then directed to the nozzle and comes out in the flow domain, where it impinges on the plate. In order to allow the variation of the nozzle-to-plate spacing H/w, the impinging plate has been mounted on a translation stage. The flow is seeded with olive oil particles generated by a Laskin nozzle. A laser sheet 1 mm thick, provided by a Quantel Evergreen laser, illuminates the region between the nozzle and the impinged plate. The laser sheet passes through the transparent impinging wall and illuminates the entire domain, following the streamwise direction of the flow.

3 RESULTS AND CONCLUSIONS

The effects of the nozzle-to-plate distance and of the mixing chamber length over the flow field of an impinging sweeping jet have been experimentally investigated with the planar PIV technique; the results are presented in terms of the time-averaged and phase-averaged velocity fields and of the distribution of the TKE and of the PKE in the flow domain. Indeed, the phase evolution of the impinging sweeping jet has been effectively reconstructed through the evaluation of the instantaneous signal of the pressure drop across the feedback channel. For each device, values of the non-dimensional nozzle-to-plate distance H/w equal to 2, 4, 6, 8 and 10 have been analyzed. As regards the effect of the nozzle-to-plate distance, for L_f /w = 4.5 the jet sweeps in a rigid way between the two most deflected positions at small impinging distances, while at higher distances there is a phase delay between the motion of the jet in proximity of the exit nozzle and the motion of the jet in proximity of the wall. As regards the influence of the mixing chamber length, in agreement with the numerical work of Seo et al., it has been found that for the devices having L_f /w < 4.5 no sweeping oscillation of the jet can be detected; indeed, a single jet structure has been found in these, while for the device having L_f /w = 4.5 it has been possible to observe that the jet exhibits a typical twin-jet pattern (see Figure 2 (a)). Therefore, the main effect of reducing the length of the mixing chamber is that the twin-jet structure turns into a classical single-jet structure, as can be seen from Figure 2. Moreover, from the analysis of the axial velocity profiles along the direction of the oscillation for the three investigated devices it has been possible to observe that the values of the axial velocity are greater for the devices having L_f /w = 2.5 and L_f /w = 3.5 than the ones obtained for the device having L_f /w = 4.5.

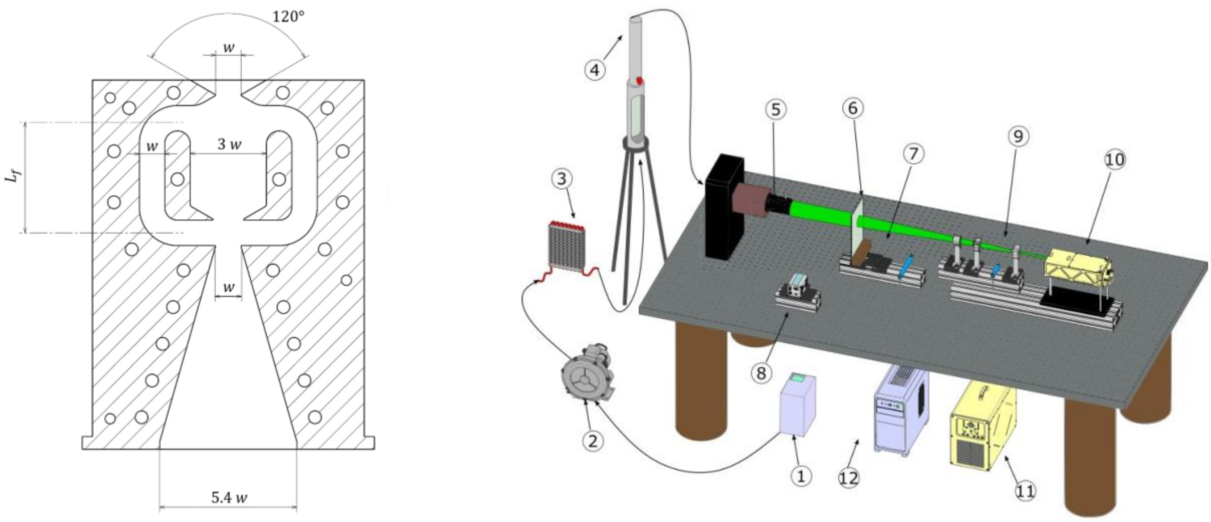

Figure 1. Draft of the employed fluidic oscillator (left) and schematic representation of the experimental setup (right): inverter (1), centrifugal blower (2), heat exchanger (3), flow meter (4), nozzle (5), impinging plate (6), traversing system (7), camera (8), optical lens (9), laser (10), laser power supply (11), computer (12).

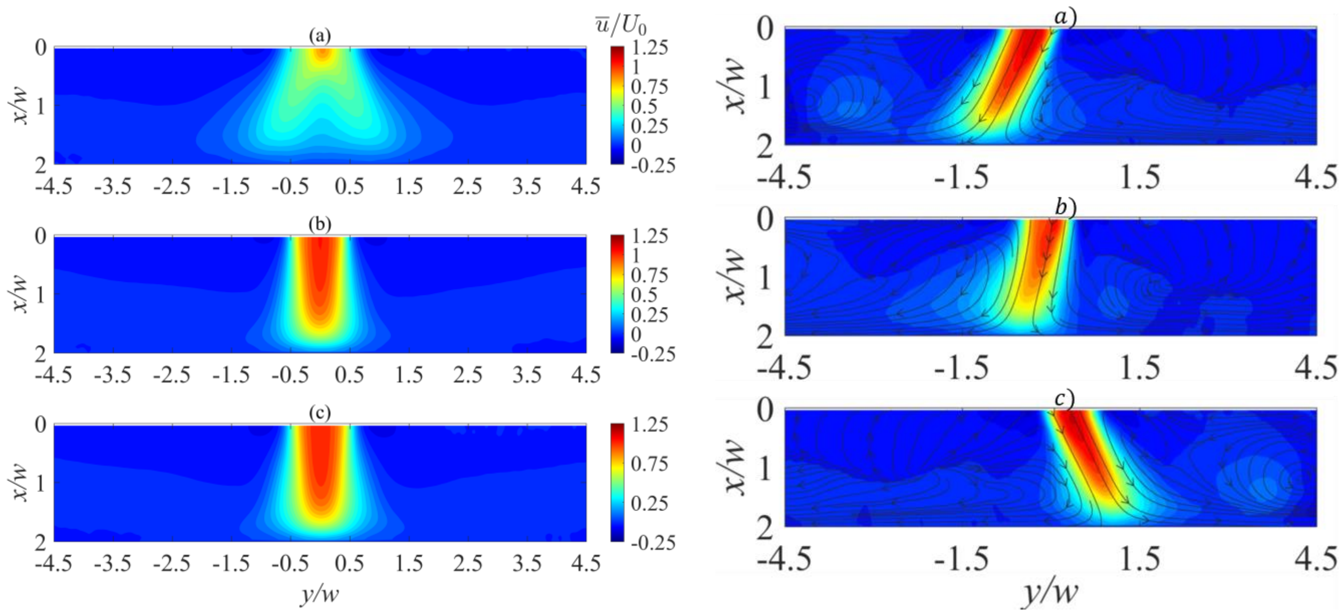

Figure 2. Contours of the time averaged axial velocity field (left) for $L_f/w = 4.5$ (a), $L_f/w = 3.5$ (b), $L_f/w = 2.5$ (c). H/w = 2, Re = 2.6×10^4 and phase-averaged velocity field (right) for (a) $\varphi = 0°$, (b) $\varphi = 90°$ and (c) $\varphi = 180°$ the for L_f/w = 4.5 H/w = 2, Re = 2.6×10^4.

Furthermore, it has been possible to observe that the values assumed by the PKE for the device having $L_f/w = 4.5$ are significantly greater than the ones obtained for the devices having $L_f/w = 2.5$ and $L_f/w = 3.5$, due to the absence of the jet oscillation. The turbulent kinetic energy assumes higher values in proximity of the jet axis for the decive having $L_f/w = 4.5$; instead, for the devices having $L_f/w = 2.5$ and $L_f/w = 3.5$ the highest values of the turbulent kinetic energy are reached in the jet shear layers, which are aligned to the streamwise direction.

4 REFERENCES

- Journal article: Woszidlo, R., Ostermann, F., & Schmidt, H. J. (2019). Fundamental properties of fluidic oscillators for flow control applications. AIAA Journal, 57(3), 978-992.
- Journal article: Seo, J. H., Zhu, C., & Mittal, R. (2018). Flow physics and frequency scaling of sweeping jet fluidic oscillators. AIAA Journal, 56(6), 2208-2219.
- Bobusch, B. C., Woszidlo, R., Bergada, J. M., Nayeri, C. N., & Paschereit, C. O. (2013). Experimental study of the internal flow structures inside a fluidic oscillator. Experiments in fluids, 54, 1-12.

Wake control by a cylinder with oscillatory morphing surface

Lingwei Zeng[1], T.H. New[2,*], Yang Liu[1], and Hui Tang[1,*]
1: Department of Mechanical Engineering, The Hong Kong Polytechnic University, Kowloon, Hong Kong, China
2: School of Mechanical and Aerospace Engineering, Nanyang Technological University, Singapore
* Correspondent authors: dthnew@ntu.edu.sg; h.tang@polyu.edu.hk

Keywords: Active flow control, Oscillatory morphing surface, Fluid-structure interaction

ABSTRACT To control bluff body wakes, various passive and active flow control technologies have been proposed [1], such as surface modifications[2-3] and synthetic jets[4-5]. In this study, a cylinder covered by a flexible latex membrane was tested to study the effects of cylindrical surface oscillations on the wake flow. The experiments were conducted in a closed-loop water channel, where a circular baseline cylinder has a diameter of D = 36 mm and length of H = 420 mm. In contrast, the membrane covered cylinder consisted of a steel skeleton and longitudinally attached ribs (also of 36mm effective working diameter), the latter of which were used to support the latex membrane. An external oscillating piston was used to push/pull water from the steel skeleton and therefore deform the membrane contours. The free stream velocity was fixed at U_∞ = 0.09 m/s with a resulting Reynolds number of Re = $U_\infty D/\nu$ = 3240, where ν is the kinematic viscosity of water. As such, the Strouhal number of the baseline cylinder was determined to be about St = fD/U_∞ = 0.2 and the vortex shedding frequency f was about 0.5 Hz.

To study the effects of membrane surface oscillations on the resulting wake, the membrane surface was excited at four different frequencies of 0.5, 1, 2 and 4 Hz, where they represent different harmonics of the baseline wake frequency. Time-resolved particle image velocimetry (TR-PIV) measurements were used to capture the wake behaviour in the near-field of the tested cylinders temporally.

Results indicate that vortex formation lengths L_f are almost identical for the baseline and passive non-oscillating membrane cases, revealing that they may share similar flow behavior in the near wake, as shown in Figure 1. When surface oscillatory morphing was used, L_f was significantly shortened, especially at optimal frequency perturbations of $\mathrm{St_p}$ = 0.36 (1 Hz) and 0.72 (2 Hz). In particular, vortex formation length is about L_f = 1.22D at $\mathrm{St_p}$ = 0.36, which is approximately 25.2% shorter than the baseline or passive membrane case. This observation implies that the vortex-shedding phenomenon is inhibited for the surface morphing cases. For lower ($\mathrm{St_p}$ = 0.18) or higher frequency ($\mathrm{St_p}$ = 1.44) perturbations, vortex formation lengths will be slightly longer.

Phase-averaged results derived from Proper Orthogonal Decomposition (POD) analysis are presented in Figure 2. For the baseline case, alternative positive- and negative-signed vortices are shed from both sides of the cylinder, forming a classical and highly symmetrical large-scale von Karman vortex street. However, for $\mathrm{St_p}$ = 0.36 surface morphing case, the shear layers will roll up early due to the increased instability caused by the oscillatory surface morphing. As such, the shear layers will transition earlier with a shorter vortex formation length as shown in Figure 2(b). Interestingly, small vortices will form regularly along and superimpose upon the separated shear layers at a higher frequency of $\mathrm{St_p}$ = 1.44 (not shown here for the sake of brevity). More experimental results and analysis will be elaborated during the conference.

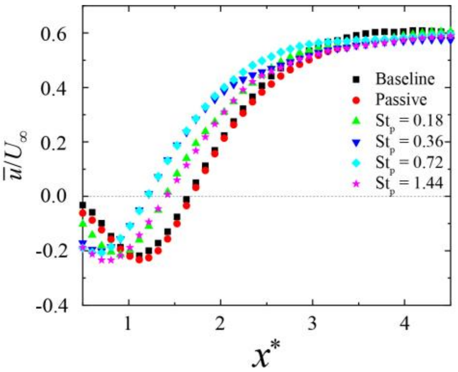

Figure 1. Distributions of time-averaged streamwise velocities $\bar{u}/U_\infty$ in the centerline of cylinders (y^* = 0).

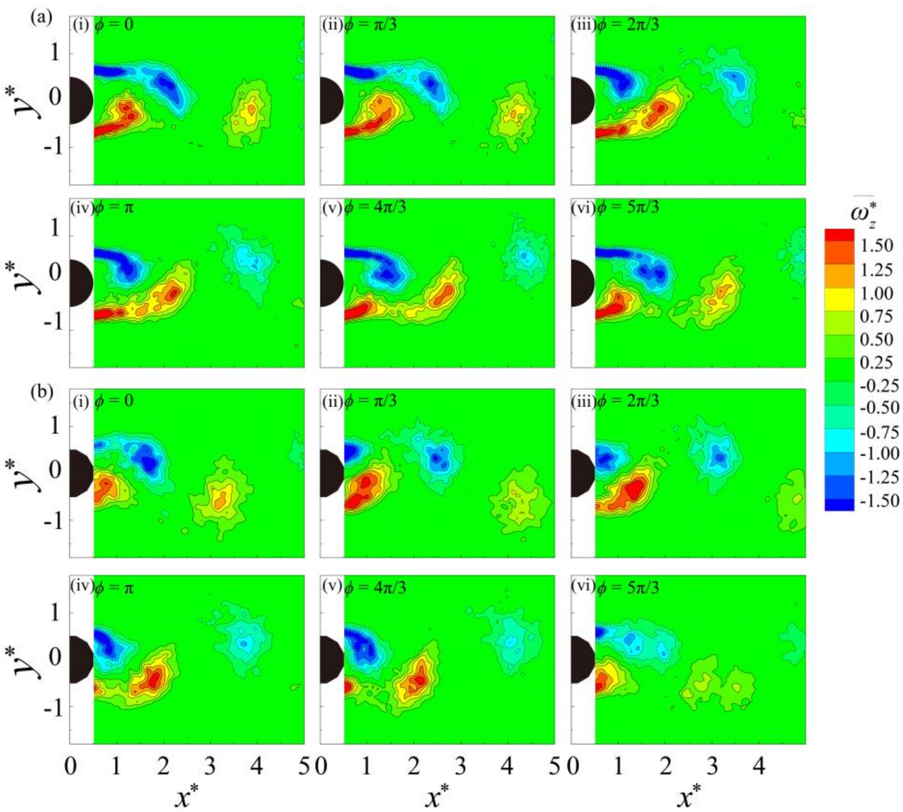

Figure 2. Phase-averaged results for the (a) baseline and (b) $St_p = 0.36$ perturbation cases, where (i) $\phi = 0$, (ii) $\phi = \pi/3$, (iii) $\phi = 2\pi/3$, (iv) $\phi = \pi$, (v) $\phi = 4\pi/3$, and (vi) $\phi = 5\pi/3$ are the different phases of the wake behaviour.

REFERENCES

1. Choi, H., Jeon, W. P., & Kim, J., (2008). Control of flow over a bluff body. Annual Review of Fluid Mechanics, 40, 113–139.
2. Muralidhar, P., Ferrer, N., Daniello, R., & Jonathan, P.R., (2011). Influence of slip on the flow past superhydrophobic circular cylinders. Journal of Fluid Mechanics, 680, 459–476.
3. New, T. H., Shi, S., X. & Liu, Y. Z., (2013). Cylinder-wall interference effects on finite-length wavy cylinders at subcritical Reynolds number flows. Experiments in Fluids, 54(10), 1–24.
4. Tang, H., Salunkhe, P., Zheng, Y. Y., Du, J. X., & Wu, Y. H., (2014). On the use of synthetic jet actuator arrays for active flow separation control. Experimental Thermal and Fluid Science, 57, 1–10.
5. Wang, C. L., Tang, H., Duan, F., Yu, S. C. M., (2016). Control of wakes and vortex-induced vibrations of a single circular cylinder using synthetic jets. Journal of Fluids and Structures, 60, 160–179.

Near wake of the X-Rotor vertical-axis wind turbine with fixed pitch offsets

David Bensason[1,*], Andrea Sciacchitano[1] and Carlos Simão Ferreira[1]
1: Dept. of Flow Physics and Technology, Delft University of Technology, The Netherlands
* Correspondent author: d.y.bensason@tudelft.nl

Keywords: PIV, VAWT, X-Rotor

1 INTRODUCTION

The X-Rotor (Leithead et al., 2019) radically departs from conventional vertical-axis wind turbine (VAWT) designs. The novel geometry relies on an aerodynamic gearbox concept which includes coned blades in the shape of an ”X” with blade-tip mounted horizontal-axis wind turbines (HAWT) responsible for generating electrical power. In contrast to the H-type VAWT, the X-Rotor design includes a coned blade geometry. This three-dimensional aspect will inflict a notable vertical component in the local induction field of the turbine, subsequently affecting the near and far wake dynamics. Furthermore, the X-Rotor design relies on the adjustable pitch of the upper blades to maintain optimum performance. Recent studies have demonstrated the wake recovery benefits of pitched blades in VAWTs, attributed to the inherent counter-rotating vortex pair (CVP) associated with VAWT aerodynamics (Huang et al., 2023). Building on previous work around the X-Rotor, this study aims to experimentally evaluate the impacts of the coned blade geometry and fixed-blade pitch on the near wake. Results will be compared to observations made with traditional H-type VAWTs to draw conclusions and implications on the potential for VAWT technology for farm-level installation and control strategies.

2 METHODOLOGY

Experiments were performed in TU Delft’s Open Jet Facility (OJF), as shown in Figure 1. A scaled X-Rotor with tip radius R = 0.75m is mounted at the centre of the test section and operated at a constant tip-speed ratio $\lambda = \omega R/U_\infty$ of 4. The upper blades of the rotor are adjustable for fixed pitch conditions of $\beta =$ -10°, 0°, and 10°. Stereoscopic particle image velocimetry (PIV) is used to acquire phase-locked measurements at several discrete cross-stream locations of the wake. The measurement system consists of a laser and a set of cameras that illuminate and record fog particles. This setup is rigidly mounted on a traversing bed such that several measurement planes (FOV) can be recorded and stitched together. The recorded wakes focus on the upper half of the rotor and range from cross-stream locations $x/R =$ 0.5 to 3.2, illustrated in Figure 1.

3 RESULTS

The phase-locked normalised streamwise flow component (U_x/U_∞) for the three pitch cases is shown in Figure 2. The measurements are at a streamwise location $x/R\ =$ 1.8, visualised in Figure 1. The frontal area of the rotor is illustrated along with black contour lines indicating the wake shape at $U_x/U_\infty =$ 0.9. A top-view schematic of the upper blade modes of operation is shown along with the results.

As the measurements are still in the near wake, minimal wake expansion is present in the baseline pitch case of $\beta = 0°$. The presence of the CVP at the tips of the blades is notable by the onset of radial expansion and axial contraction in the wake, highlighted by the quivers. The wake shape seems to extend further in the axial direction on the windward side of the rotor ($y/R\ >$ 1.0). The slight asymmetry in the wake can be attributed to the cyclic asymmetric loading of the blades experience by the rotor over its cycle and the subsequent presence of a large-scale tip-vortex on the windward side, which convects upwards. For the pitch case $\beta =$ 10°, a significant axial contraction and radial expansion of the wake is visible, concentrated on the windward side. This is due to the increase in the asymmetry of the rotor loading in favour of the upwind half of the cycle, leading to higher lift forces produced by the blade in the windward section and, subsequently, an increase in radial flow. A large-scale vortex is formed on the windward side of the rotor, inducing a local downwash in the wake. A similar effect is present on the leeward half of the rotor ($y/R\ <$ 1.0), albeit to a lesser degree due to the weaker tip vortex. Finally, the pitch case $\beta =$ -10° exhibits a different mode of operation with respect to the case above. Here, the asymmetry of the rotor loading is increased in favour of the downwind half, where the tip vortices are mirrored with respect to the upwind half. Hence, similarly to the previous pitch case, the lift force in the leeward phase is increased, translating to a significant radial contraction and axial expansion of the wake. The large-scale vortices formed in the leeward and windward halves of the cycle induce a significant local upwash on the upper section of the rotor.

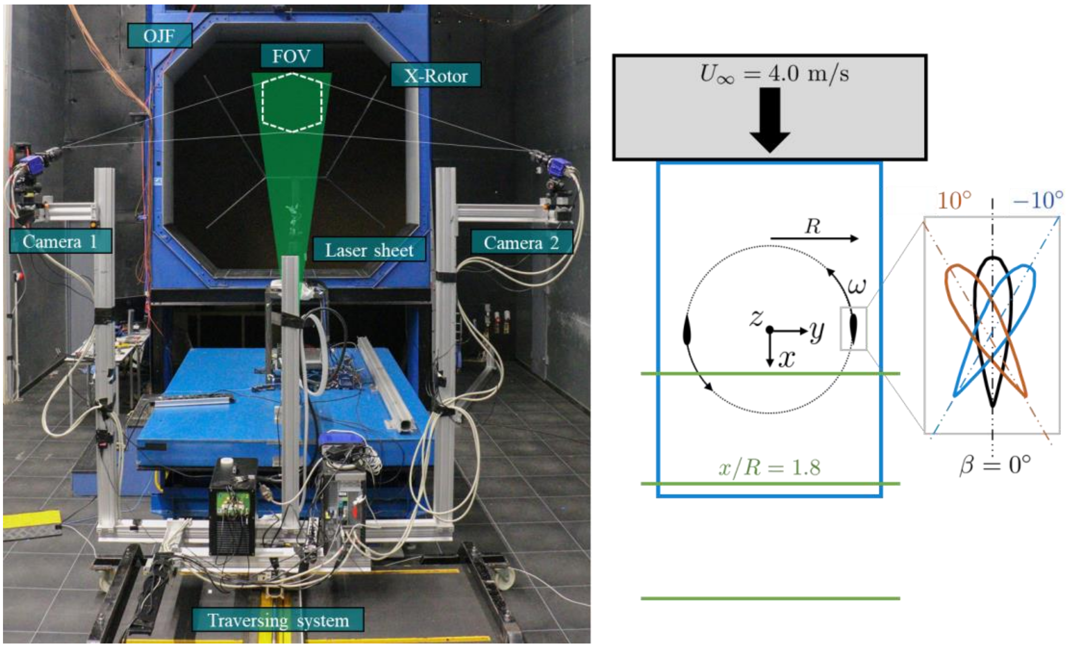

Figure 1. (Left) labelled experimental setup in the OJF, (right) top-view schematic of the measurement domain

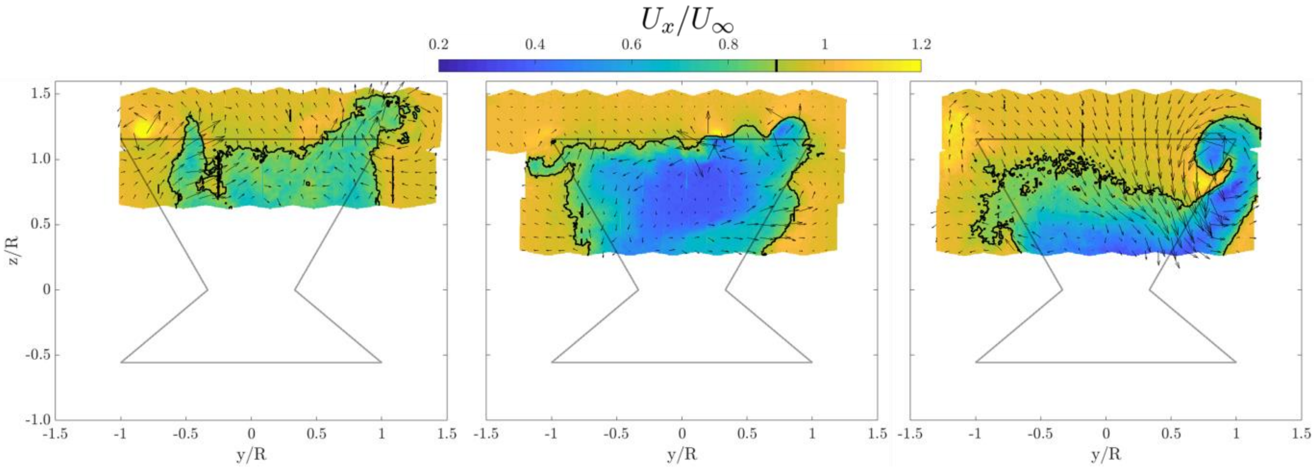

Figure 2. Phase-locked X-Rotor wakes at cross-stream plane $x/R = 1.8$ for fixed pitch cases.

4 CONCLUSIONS

The resulting wakes recorded when using fixed pitch offsets on the upper blades of the X-Rotor exhibit two modes of operation. In the case of a more heavily loaded upwind half of the rotor, the wake is contracted axially and ejected radially outward. In contrast, for the more heavily loaded downwind half, the wake contract radially and ejected axially. Both modes of operation have significant implications for farm-scale VAWT installation, where the simple mechanism of blade pitch shown here already exhibits an increase in momentum transfer and thus an accelerated wake recovery as near as $x/R = 1.8$. Future research will aim to compare the wakes of the studied blade geometries with those of H-type VAWTs, elucidating the impacts of coned blade geometries on the near and far wakes and evaluating the potential of VAWTs for high-density wind farms.

5 REFERENCES

Huang, M., Sciacchitano, A., and Ferreira, C., "On the wake deflection of vertical axis wind turbines by pitched blades," *Wind Energy*, 2023.

Leithead, W., Camciuc, A., Amiri, A. K., and Carroll, J., "The X-rotor offshore wind turbine concept," *Journal of Physics: Conference Series*, Vol. 1356, IOP Publishing, 2019, p. 012031.

Visualization of the flow around two Generic Cyclist Models

Wouter Terra[1,*], Andrea Sciacchitano[1], Siward Vloemans[2], Christopher Brown[3], Toon Huysmans[2]
1: Dept. of Flow Physics and Technology, Delft University of Technology, The Netherlands
2: Dept. of Human-Centered Design, Delft University of Technology, The Netherlands
3: Fluids Laboratory for Aeronautical and Industrial Research (FLAIR), Monash University, Australia
* Correspondent author: w.terra@tudelft.nl

Keywords: PIV, HFSB, Cycling Aerodynamics

1 INTRODUCTION

Cycling aerodynamic investigation in particular focuses on aerodynamic drag reduction of the rider and bike to improve athlete performance. Many of these studies install cyclist mannequins, in contrast to a real person, in a wind tunnel to ensure well-controlled and repeatable measurements (e.g. Crouch et al. 2014, Brown et al. 2020, Terra et al. 2020). The more recent mannequins are typically obtained by scanning individual athletes, resulting in highly realistic models (e.g. Chi et al. 2018, Terra et al. 2020). The consequence of using personal Anthropometric data, however, is that it can not be openly shared, which makes it often difficult to compare results. A cyclist's posture largely determines the large-scale wake flow structures and the aerodynamic drag (Crouch et al. 2014) and, so, a shared, commonly used cyclist model would help to better relate results among the cycling aerodynamic community. Such a model is currently missing; hence, this work aims to introduce two realistic generic cyclist models (GCMs) in two typical cycling postures (time-trial and sprint) and to present a first wake characterization.

2 CONSTRUCTION OF THE CYCLIST MODELS

The method to construct the GCM is based on the DINED mannequin (Huysmans et al. 2020). First, fourteen endurance riders are selected to participate in this work. Each athlete was scanned in the time-trial (TT) and sprint position on their bike using *ARTEC Eva* handheld 3D scanners. The obtained scans were processed (e.g. removing parts of bike and floor) into watertight models, and a set of systematic landmarks were defined on each of them in anatomically meaningful locations. A base mesh, holding the same set of landmarks, then corresponded to each of the individual scans (Vloemans 2022) to finally average these corresponded meshes, resulting in the GCM in TT (Figure 1 top-right) and sprint position (Figure 1 bottom-right). The two digital GCMs were used to produce two physical full-scale models for wind tunnel testing. The wind tunnel models were manufactured by additive manufacturing and a primer was applied. A smooth surface was obtained through polishing with sandpaper (grain 400).

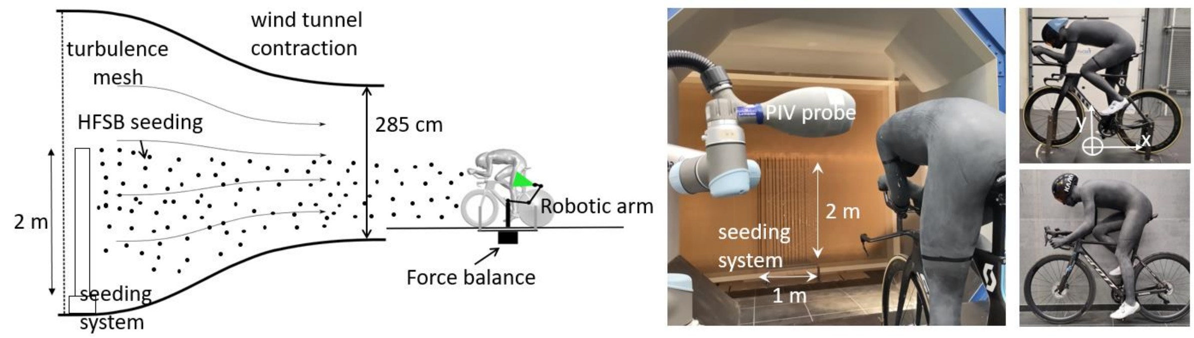

Figure 1: Schematic wind tunnel setup (left), the platform with TT model (middle) and side views of the two GCMs (right).

3 EXPERIMENTAL SETUP

The experiments are conducted in the Open Jet Facility (OJF) of the Aerodynamics Laboratories of the TU Delft. This is a closed-loop, open jet wind tunnel with an octagonal cross-section of 2.85 × 2.85 m, a linear contraction from the settling chamber to the nozzle exit of 1.7:1 and a turbulence intensity in the free-stream <0.5%. The TT model is installed on a TT bike wearing a Kask Minstral helmet (Figure 1-top right). The sprint GCM is installed on a road bike wearing a Kask Bambino helmet (Figure 1-bottom right). The bikes are fixed on both the front and rear axles using a supporting system that is connected to a force balance. The experimental setup and procedures are similar to that of Jux et al. (2018), who measured the flow all around a full-

scale cyclist model using Robotic Volumetric PIV. The air is seeded using a new, in-house developed array of Helium-filled soap bubble generators installed in the OJF's settling chamber (Figure 1-left and middle). The 400 generators are integrated into 15, two-meter long, vertical airfoil shaped staggered wings so that the seeded stream tube spans the entire cyclist model.
At the time of writing this abstract the PIV measurements have not yet been processed. Hence, the measurement equipment and procedures are generally described, and details will be presented during the conference. The Robotic PIV system is used to scan the wake and close to the models, acquiring images for 12 seconds at about 800 kHz at each probe position. The velocity information is obtained, adopting Lagrangian Particle Tracking using Shake-the-Box, and converted onto a Cartesian grid. The measurements are conducted at a typical cycling speed of 14 m/s. To include a first impression of the wake topology in this abstract, we scanned the wake using a 7-hole pitot tube (*ProCap Compact* system, Streamwise GmbH). During the conference, instead, the obtained PIV velocity results are presented together with force balance data.

4 RESULTS

Contours of non-dimensional streamwise velocity, obtained with the ProCap system, in a cross-plane 50 cm downstream of the rear wheel's axis are depicted for the TT and Sprint mannequin. In both cases, a distinct downwash is present in the center of the wake (around z = 0 and 70 cm < y < 120 cm), which is similar to results reported in the literature (Crouch et al. 2014, Jux et al. 2018). The sprint model (right) exhibits a relatively large region of velocity deficit downstream of the head and helmet (around z = 0 and y = 140 cm), which is missing for the TT model. These similarities and differences will be discussed in more detail during the conference.

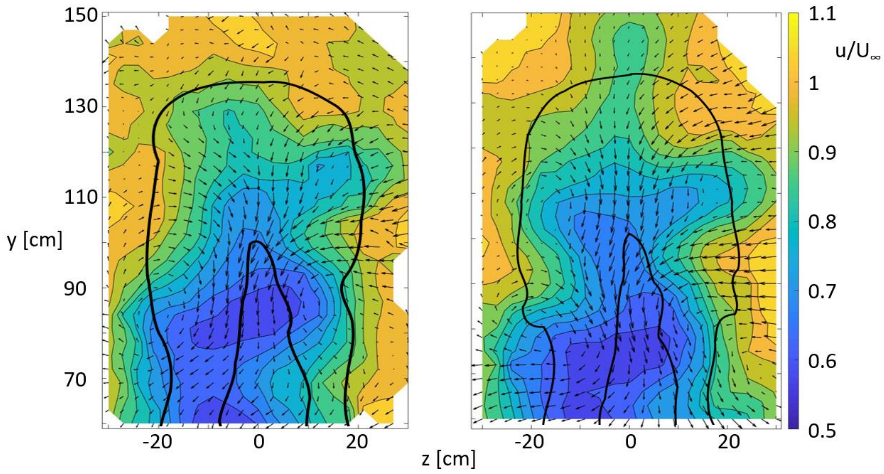

Figure 2: Contours of non-dimensional streamwise velocity downstream of the TT model (left) and the Sprint model (right) including in-plane vectors.

5 ACKNOWLEDGEMENTS

We acknowledge the support Harm Ubbens with scanning the riders and providing equipment for the wind tunnel tests. We also thank Bertus Naagen and Lies Keijser for their contributions in post-processing the scanned data.

6 REFERENCES

Brown, C., Crouch, T., Burton, D., Thompson, M.C. (2020) Understanding the Aerodynamic Benefits of Drafting in the Wake of Cyclists. *Proceedings*, *49*, 32.

Chi, S., Pitman, J., Crouch, T., Burton, D., Thompson, M. (2021). The application of body scanning, numerical simulations and wind tunnel testing for the aerodynamic development of cyclists. *Proceedings of the Institution of Mechanical Engineers. Part P, Journal of Sports Engineering and Technology*, *235*(4), 339–353.

Crouch, T. N., Burton, D., Brown, N. A. T., Thompson, M. C., Sheridan, J. (2014). Flow topology in the wake of a cyclist and its effect on aerodynamic drag. *Journal of Fluid Mechanics*, *748*, 5–35.

Huysmans, T., Goto, L., Molenbroek, J., Goossens, R. (2020) DINED Mannequin. *Tijdschr. voor Hum Factors* 45:4-7.

Jux, C., Sciacchitano, A., Schneiders, J.F.G., Scarano, F. (2018) Robotic volumetric PIV of a full-scale cyclist. *Exp Fluids*, 59:74.

Terra, W, Sciacchitano, A, Scarano, F, Cyclist Reynolds number effects and drag crisis distribution, *Journal of Wind Engineering and Industrial Aerodynamics*, Volume 200, 2020.

Vloemans, S. (2022) Cyclist Mannequin For Aerodynamics Research: Develop a cyclist mannequin from 3D scans for aerodynamics tests. Master's Thesis *TU Delft Repository*.

3D Large Scale Quantitative Flow Visualization around a Thrust Reverser Model

Hysa Ilda [1,2,c], Tuinstra Marthijn [1]; Scarano, Fulvio [2]; Sciacchitano, Andrea [2]; Lammers Karel [1]; Harrison, Charles [4]; Schwartz, Nicolas [4];

[1] Department of Aerospace Vehicles – Vertical Flight and Aeroacoustics, Netherlands Aerospace Center NLR, Marknesse, The Netherlands
[2] Department of Aerospace Engineering, Delft University of Technology, Delft, The Netherlands
[4] Department of Flight Dynamics, Gulfstream Aerospace Corporation, Savannah, GA, USA 31408
[c] Corresponding author : e-mail : Ilda.Hysa@nlr.nl

Keywords: Large- scale PTV, volumetric measurement, aeronautics

ABSTRACT

Aircraft engine thrust can be redirected by thrust reverser (TR) devices to modify the direction of the propulsive force and to rapidly decrease the aircraft speed at landing after touchdown. The flow resulting from angling the thrust vector becomes strongly three-dimensional, it involves large separated regions and exhibits unsteady behaviour. The full characterisation of these complex mechanisms is needed to make accurate predictions leading to design optimisation of TRs. Most previous studies have been conducted with flow visualization techniques, by means of surface tufts and tracing the reversed jet plume by vaporizing liquid nitrogen or by steam injection (van Hengst, 1992). Quantitative measurements are typically performed by pressure probes. Temperature measurements have also been considered for the detection of exhaust fluid re-ingestion (Burgsmueller et al. 1992). Nonintrusive flow field measurements of TR systems at large scales have not been reported yet in literature. Nonetheless, the advancement of studies on TRs by computational fluid dynamics (CFD) requires gathering quantitative data from experiments.

To this end, the present work documents the experimental efforts to realize a large-scale 3D particle image velocimetry (PIV) experiment conducted on a TR system installed in the Low Speed Tunnel of the German-Dutch Wind Tunnels. A model of a nacelle at 1:12-scale in thrust reverser configuration attached to an aircraft is tested in Froude scaled conditions, i.e. for the duplication of the thrust reverser flow, the ratio of the momentum of the nozzle exhaust flow to the tunnel flow is duplicated. Accordingly, the free-stream velocity of the experiment is in the range of 3-5 m/s; and the thrust reverser doors are kept at a fixed angle. The large-scale 3D PIV system comprises helium filled soap bubbles (HFSB) as flow tracers (Scarano et al. 2015), three sCMOS cameras and a double-pulse laser. The PIV analysis is based on the double-pulse Shake-the-Box algorithm (Schanz et al. 2016) yielding sparse particle trajectories, subsequently rendered on a Cartesian mesh with a binning process (Aguera et al. 2016). The measurement domain encompasses approximately a volume of 400 liters and the velocity field is resolved at a scale of 2 cm. The results yield the overall large-scale organization of the flow with the recirculation due to interaction with the ground. Re-ingestion of the flow from the exhaust can be inferred from the fact that the latter is seeded and tracers are observed to travel up to the engine intake. Evidence of flow leakage behind the TR doors is also found. The quantitative visualizations illustrate the effect of the TR forward speed and NPR on the reverse plume direction. The comparison with traditional temperature rake measurement is plotted in Figure 1, and the results show good agreement.

The overall work demonstrates the suitability of large-scale 3D PIV for the investigation of aircraft propulsion integration aerodynamics in industrial wind tunnels.

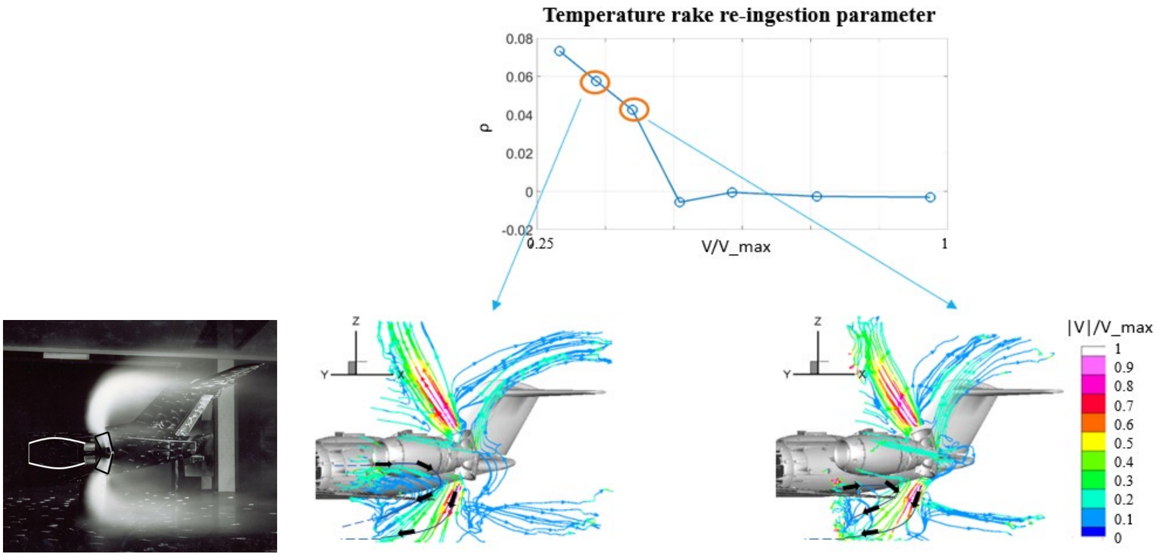

Figure 1 : Comparison of PIV quantitative visualization results with traditional temperature rake measurements for re-ingestion detection.

REFERENCES:

Aguera, N., Cafiero, G., Astarita, T., & Discetti, S. (2016). Ensemble 3D PTV for high resolution turbulent statistics. *Measurement Science and Technology 27:124011*.

Burgsmueller, W., Castan, C., Kooi, J., & Becle, J. (1992). Recent developments in low-Speed TPS-testing for engine integration drag and installed thrust reverser simulation. *AGARD 485*, (pp. 9-1:15). Texas, United States.

Scarano, F., Ghaemi, S., Caridi, G., Bosbach, J., Dierksheide, U., & Schiacchitano, A. (2015). On the use of helium filled soap bubbles for large scale tomographic PIV in wind tunnel experiments. *Experiments in Fluids 56:42*.

Schanz, D., Gesemann, S., & Schroeder, A. (2016). Lagrangian particle tracking at high particle image densities. *Experiments in Fluids 57:70*.

van Hengst, J. (1992). Aerodynamic integration of thrust reverser on the Fokker 100. *AGARD 498*, (pp. 10-1:9). Texas, United States.

TECHNICAL SESSION 14
SCHLIEREN

Chaired by James Heineck

Effect of cryogenic temperature on the flow structure of off-axis under expanded jet impinging on spherical geometry

Alireza Aslani and Kyung Chun Kim*
1: Eco-Friendly Smart Ship Parts Technology Innovation Center,
School of Mechanical Engineering, Pusan National University,
Busan 46241, Republic of Korea
* Correspondent author: kckim@pusan.ac.kr

Keywords: Schlieren, Cryogenic, Under-Expanded, Impinging Jet, Proper Orthogonal Decomposition (POD)

ABSTRACT This study investigates the impact of static inlet temperature (Tin =130, 150, 190, 215 K) on the flow structure of a 5% of the diameter of sphere off-axis supersonic jet exiting a converging-diverging nozzle with an area ratio of 1.277 at a fixed nozzle pressure ratio (NPR=9). The jet impinges on a sphere with a 15 mm diameter located 15 mm away from the nozzle lips. The flow field is visualized on the front face of the sphere using vertical knife edge Z-type schlieren (Settles, 2001), with a pair of Edmond parabolic mirrors having a focal length of 2032 mm and a 2.5 watts white LED. A Phantom VEO 710 high-speed camera record the flow at 67500 frames per second. Furthermore, the proper orthogonal decomposition (POD) technique is employed on the schlieren images to study the dynamic flow system on the shock plate and over the sphere. It showed a significant reduction in the separation and instability over the sphere as the temperature dropped from the refrigerant to the cryogenic state. Also, the recirculation region almost disappeared at cryogenic temperature.

Introduction The rising demand for reducing the carbon footprint of naval and aviation pushed these industries to some radical solutions. Hydrogen combustion is a promising technology to shift toward the zero-emission target in the aviation industry. However, aside from cost, infrastructure, and public perception, the technological challenges must first deal with.

It has been shown that LH2 is almost 250% more ergitec per kilogram than Kerosene (Najjar, 2013). Yet the LH2 can only obtain in very low temperatures, and tanks must deal with very high pressure. That is why any form of crack and linkage will be a supersonic under-expanded jet. Also, because different thin wall shells will surround the tank, the impinging flow in cryogenic temperature must be considered first.

Impinging a supersonic jet is a complex phenomenon mostly studied in idealized conditions of the high or ambient temperature on a flat plate. However, the physics of that needs to be examined on more complex geometries. For example, in manufacturing (Steenkiste, et al., 1999), heat transfer applications (Kim & Lee, 2019), and leakage of hydrogen tanks, the under-expanded supersonic jet impinges on complex geometries mostly curved surfaces. Most currently available studies on impinging supersonic jet have used ambient or hot gas entering the converging-diverging nozzle and then affecting an inclined or horizontal flat plate. However, interest in hydrogen combustion motivates a deeper understanding of impinging cryogenic under-expanded supersonic flow on more complex surfaces. Also, in reality, the axisymmetric case is very rare, and most of the time, the flow will impact the curved surface with a range of deviations from the center line.

In the aviation industry, typical supersonic flows occur at temperatures where gases behave under ideal gas assumptions and experience no changes in chemical composition. That is why the Mach number governs most compressible flow properties, which drives the flow structure. Contrary, there is a lack of knowledge on the flow structures in cryogenic temperature that needs to be studied more in detail.

Discussion The averaged schlieren image compares the flow structure at NPR 9 for different static inlet temperatures from Tin-refrigerant=215K to Tin-Cryogenic 133K, showing deviation in the size of the first shock cell by increasing the height and reducing the width of the first Mach disk (see Fig.1). This deviation is due to the change in the compressibility factor and the speed of sound and the formation of weaker shocks. Also, the difference in the Prandtl Meyer angle at the nozzle exit shows that the cryogenic jet is highly under-expanded due to the heat transfer into the jet at the nozzle exit.

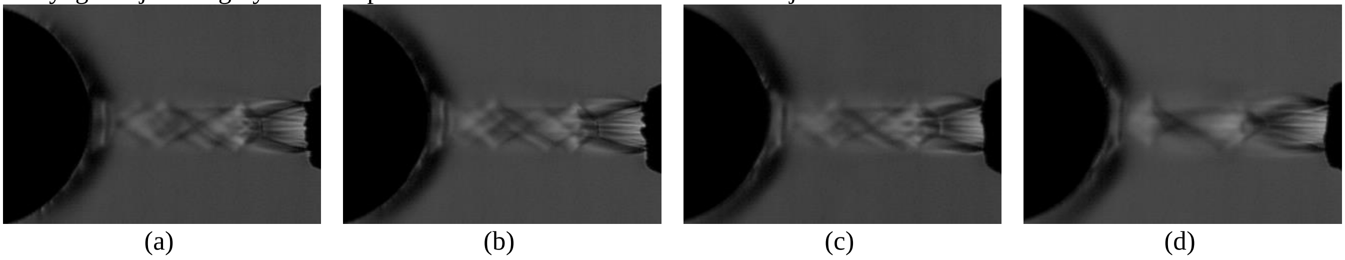

(a) (b) (c) (d)

Figure 1: Average Schlieren image of NPR 9, (a) T_{in}=215K, (b) T_{in}=190K, (c) T_{in}=150K, (d) T_{in}=130K

The principal component known as the proper orthogonal decomposition (POD) denotes the spatial distribution of main flow structures, found by decomposing the pixel values of the schlieren image into a set of orthonormal modes capturing the main vibrational modes of the fluid flow. Consequently, POD modes represent the instability in the flow, so the energy will reduce from the first mode toward the higher modes. Thus POD modes are a valuable tool for visualizing the governing flow feature in complex regimes. In this study, the scaler field is refractive index n, and the mean schlieren image represents the zero modes of the POD. Thus modes are sequenced by the density gradient $(d\rho/dy)2=(kg/m4)2$.

As the schlieren images visualize the density gradient based, applying the pod shows the dominant modes of density variations considering the influence of change in the temperature from cryogenic to the refrigerant zone. Thus the existence of the recirculation region, separation, and acceleration regions in the boundary layer over the sphere could be seen in the first mode of POD.

As expected, due to off-axis impingement, the formation of separation on the sphere's surface varies from the top side to the bottom side sphere. The first mode clearly shows the flow structure containing the separation region and the flow acceleration shrinking as the temperature drops to cryogenic. Also, figure 2 shows the significant reduction in the size and energy of the recirculation region as the Tin increased from the refrigerant state (Tin =215K and 190K) to the cryogenic state (Tin=155K and 130K).

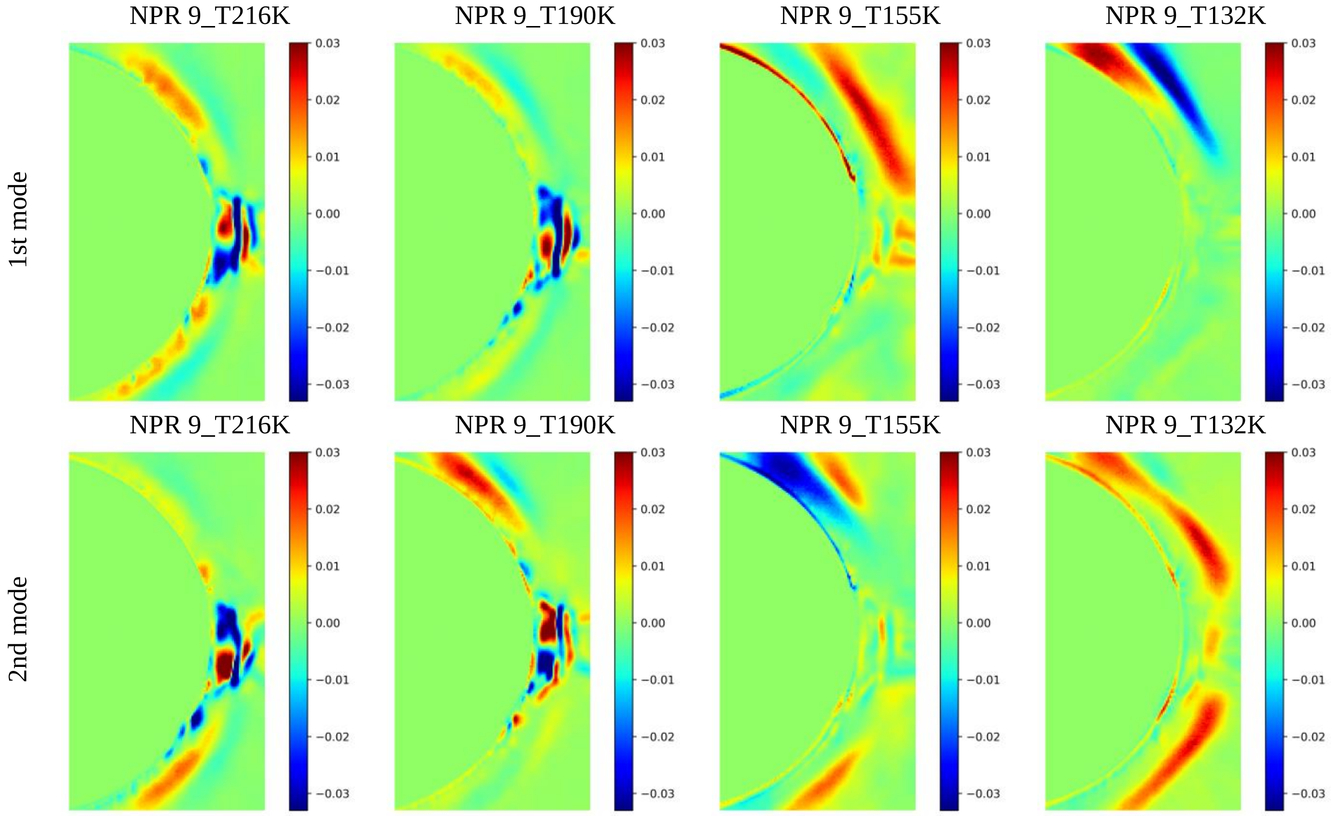

Figure 2: Spatial pattern of first and second POD modes using vertical knife-edge

Acknowledgment This work was supported by the National Research Foundation of Korea (NRF) grant, which is funded by the Korean government (MSIT) (No. 2020R1A5A8018822). This work was also supported by the Korea Institute of Energy Technology Evaluation and Planning (KETEP) and the Ministry of Trade, Industry & Energy (MOTIE) of the Republic of Korea (No. 20223030040120).

REFERENCES

- Kim, D., & Lee, J. (2019). Influence of shock structure on heat transfer characteristics in supersonic under-expanded impinging jets. *International Journal of Thermal Sciences*, 62-71.
- Najjar, Y. (2013). Hydrogen safety: The road toward green technology. *International Journal of Hydrogen Energy*, 10716-10728.
- Settles, G. S. (2001). *Schlieren and Shadowgraph Techniques visualizing Phenomena in Transparent Media.* Berlin: Springer.
- Steenkiste, T., J.R.Smith, R.E.Teets, J.J.Moleski, D.W.Gorkiewicz, R.P.Tison, . . . K.J.Barnett. (1999). Kinetic spray coatings. *Surface and Coatings Technology, 111*(1), 62-71.

Recent Development Work with Self-Aligned Focusing Schlieren

Brett Bathel,[1,*] Joshua Weisberger,[1] Matthew Boyda,[1]
Timothy Fahringer,[1] James Heineck[2]
1: Advanced Measurements & Data Systems Branch, NASA Langley Research Center, United States
2: Experimental Aero-Physics Branch, NASA Ames Research Center, United States
* Correspondent author: brett.f.bathel@nasa.gov

Keywords: Focusing Schlieren, High-Speed Schlieren Imaging, Wind Tunnel Measurements

ABSTRACT A novel compact focusing schlieren instrument has recently been developed that eliminates the need for a separate source and cutoff grid. The technique works by projecting an image of a grid onto a retroreflective surface and then reimaging the projection back onto the original grid. By manipulating the polarization state of the light passing through the instrument, a single Rochon polarizing prism can be used to adjust the schlieren sensitivity by translating it along the instrument's optical axis, which changes the in-plane offset between the reimaged projection and the original grid. This arrangement makes the instrument inherently self-aligned. Relative to conventional focusing schlieren instruments, which require alignment of a separate source grid and cutoff grid to achieve sensitivity, the setup time required in order to obtain high quality focusing schlieren images is significantly reduced. Further, the self-aligned nature of this instrument makes it insensitive to vibrations and allows for on-the-fly adjustments to field-of-view. In this paper we discuss recent work that has been performed to expand the capabilities of this self-aligned focusing schlieren instrument including: schlieren visualization at extreme angles for optically-restricted test facilities, 3D schlieren visualization using a light field camera, acquisition of high quality focusing schlieren images from facilities with low quality windows, and obtaining focusing schlieren images in full-scale ground test facilities.

1 INTRODUCTION

Focusing schlieren, originally developed in the 1940s [Hartmann, Schardin, and Burton] and then modernized in the 1990s [Weinstein], enables visualization of gradients in density in a plane that is orthogonal to the optical axis of the instrument with a narrow depth-of-focus. With a few exceptions, most focusing schlieren systems include a back-illuminated source grid, consisting of a repeating pattern of equal thickness opaque and transparent lines. An image of this source grid is then formed by a field lens on the opposing side of the measurement region onto a separate cutoff grid. This cutoff grid is a scaled copy of the source grid and is offset by a small distance (less than the width of a single line on the cutoff grid) orthogonal to the grid lines and coplanar to the grid itself. By varying the offset distance between the image of the source grid and cutoff grid, the sensitivity of the focusing schlieren can be varied, similar to the amount of knife edge cutoff of an image of a single point-like light source in a conventional schlieren system. However, the numerous transparent lines on the source grid and corresponding opaque lines on the cutoff grid act as independent schlieren systems that form a common schlieren image at the focal plane of the instrument. This, along with the focusing nature of the field lens [Burton], are what enable the instrument to have a narrow depth-of-focus. Further details on focusing schlieren systems can be found in the book by Settles [Settles].

A significant limitation of the focusing schlieren system is that the cutoff grid must essentially be a perfect scaled copy of the source grid so that relatively high-quality focusing schlieren images can be acquired. This requires that a significant amount of time be dedicated to fabricating a source grid, developing a cutoff grid, and aligning the system. Once alignment is achieved, the system cannot be adjusted (e.g., to image a different field-of-view) without repeating this process. Further, any significant vibrations imparted to the system that result in misalignment between the image of the source grid and cutoff grid results in loss of signal. As a result, focusing schlieren has not been widely adopted for flow visualization in wind tunnels and other ground test facilities. Recently, a novel self-aligned focusing schlieren (SAFS) system has been developed at the NASA Langley Research Center that only requires a single grid element to provide a focusing schlieren capability [Bathel & Weisberger, Weisberger & Bathel]. The system works by projecting an image of a grid element onto a reflective or retroreflective surface and then reimaging the projection back onto the original grid element. By manipulating the polarization state of light as it travels through the instrument and making use of a polarizing Rochon prism that only refracts the light returning to the instrument by a small angle (~10s of arc-min), a coplanar offset between the reimaged projection and original grid element is achieved. By translating the polarizing prism along the optical axis of the instrument, the degree of offset can be varied, thereby providing adjustment of sensitivity.

The final paper will highlight recent development work on the SAFS system at NASA Langley Research Center including: schlieren visualization at extreme angles for optically-restricted test facilities, 3D schlieren visualization using a light field camera, acquisition of high quality focusing schlieren images from facilities with low quality windows, and obtaining focusing schlieren images in full-scale ground test facilities. Figure 1 shows some of the results that will be included in the final paper. In Fig. 1a, path-integrated high-speed schlieren of a shockwave/boundary-layer interaction on a flat plate with a ramp is shown and the same flow visualized with SAFS is shown in Fig. 1b. These images demonstrate how SAFS filters out image artifacts that may adversely affect interpretation of flow structures observed in path-integrated schlieren images. Figure 1c shows the setup of a SAFS system in the National Full-Scale Aerodynamics Complex at NASA Ames Research Center. Here, a SAFS system was used to visualize vortices being shed by rotor blades located 60 feet (18.3 m) away, with the full width of the test section being 120 feet (36.6 m).

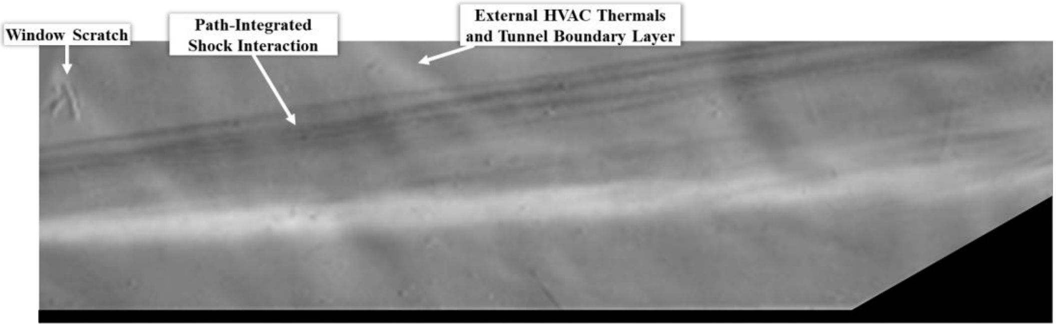

(a)

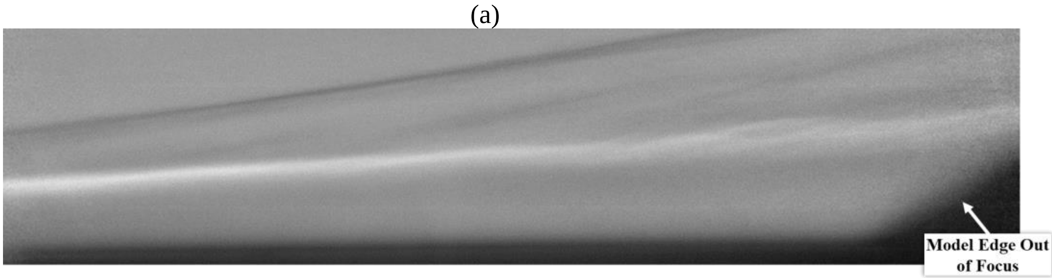

(b)

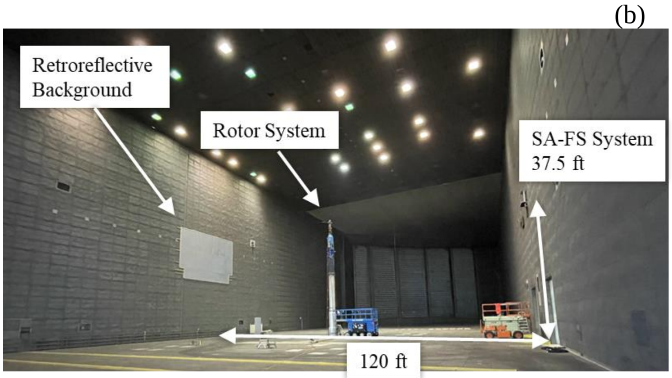

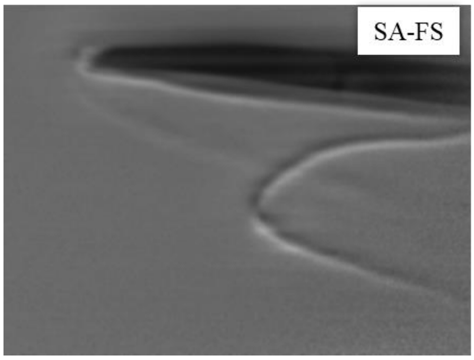

(c) (d)

Figure 1. (a) Path-integrated and (b) SAFS images of a shockwave/boundary-layer interaction in a Mach 10 flow. (c) SAFS setup in the NFAC wind tunnel at NASA Ames Research Center used to visualize (d) rotor blade vortices.

2 REFERENCES

- Bathel, B.F. & Weisberger (2021). Compact, self-aligned focusing schlieren system. Optics Letters, 46(14), 3328–3331.
- Burton, R.A. (1949). A modified schlieren apparatus for large areas of field. Journal of the Optical Society of America. 39(11), 907–908.
- Hartmann, J. (2021). The Acoustic Air-Jet Generator. NASA Technical Translation, TT-20210016495. Translation by Weisberger, J.M. of original article by Hartmann, J. (1940). Fysysk Tidss, 65–113.
- Schardin, H. (1970). Schlieren methods and their applications. NASA Technical Translation, TT F-12731. Original article by Schardin, H. (1942). Ergebnisse der exakten Naturwissenschaften, 20, 303–439.
- Settles, G.S. (2001). Schlieren and shadowgraph techniques. Springer, Berlin Heidelberg.
- Weisberger, J.M. & Bathel, B.F. (2022). Single source/cutoff grid, self-aligned focusing schlieren system. Experiments in Fluids, 63(38).

Art and experiments, how to get closer to flow physics?

Olivier Chazot[1,*] Christoph Oeschger[2], Fabian Gutscher[2] and Florian Dombois[2]
1: Dept. of Aeronautics & Aerospace, Von Karman Institute, Belgium
2: Dept. of Transdisciplinary Studies, Zurich University of the Arts, Switzerland
* Correspondent author: chazot@vki.ac.be

Keywords: Flow visualization, experimental research, flow phenomenology

ABSTRACT

Flow visualization is coming from a long tradition with the practice of making fluid flows visible to aid in a better understanding of their behavior. It is dating back to the earliest observations of fluid motion. It represents a constant effort to describe and understand the physics of the flow to inspect fluid dynamics in more details and/or to optimize specific flow applications.
One of the old and famous examples of flow visualization comes from the work of Leonardo da Vinci, who made sketches of water flowing around obstacles in the 15th century (Fig. 1-a). Analysis on these sketches indicate that they aim to study the behavior of water and to design more efficient water mills (Ackerman, 2002).
Despite these engineering efforts those studies are viewed as piece of art rather than flow investigations. However, the goal of those observations and the corresponding detailed drawing are very similar of today's objectives of research applications. Much more closer to us in the very beginning of the 20th century Etienne-Jules Marey was studying the flow patterns around different objects in a wind tunnel with an original smoke visualization techniques (Fig. 1-b). He obtained very precise and well documented flow pictures that he reported to the science academy in France (Marey, 1900). All those experiments were dedicated to fluid dynamic research and more specifically to the structure of the physics of the flows. However, one have to recognize that all these archives are mostly the interest of artists rather than the one of engineers, even if they were initially dedicated to the latter (Didi-Huberman 2023).

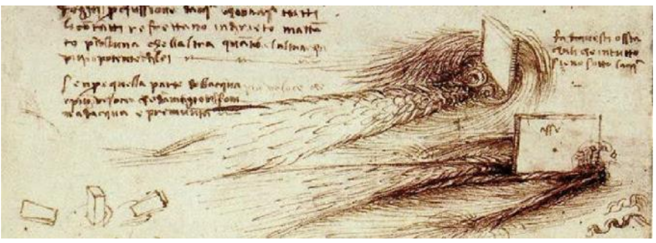

Studies of water flow, percussion, and rivers, c. 1507-09, pen and ink, 290 x 202 mm. Royal Library, Windsor Castle RL 12660 recto. Digital Archive, Biblioteca Leonardiana, Vinci.

Figure 1: a) drawings from Leonardo da Vinci, b) Smoke visualization in wind tunnel, E-J Marey.

Those examples show that flow visualizations have been for quite long at the frontier of art and science. They were at the roots of the development of fluid dynamics. It has always been an important interdisciplinary field for many years, combining aspects of engineering, physics, mathematics, and art. Since several decades this discipline has evolved toward much more technical aspects and has shown impressive capacities and progress in combination with measurement techniques image analysis and numerical developments.
On this route it seems that fluid visualization has separated itself from the artistic approach. As it becomes more independent it is becoming also extremely technical to provide quantitative results and performant flow characterizations. In this development it has certainly had immense success already and many perspectives for improvement. However, it could also face some

limitations, not exclusively technically, but also intrinsic to its methodology and to the framework it has adopted. Setting aside artistic approaches and considering them uniquely for their aesthetic value prevent to benefit from their research process toward the nature of the flows and their reality. Combining flow visualization techniques with artistic research allow to access questions that may not be possible through other methods, and it is an opportunity for further analysis and understanding.

In view of this situation, we would like to reflect on our collaboration with Zurich University of the Arts where a wind tunnel and flow visualizations are being developed associated with transdisciplinary research in art (fig. 2).

Figure 2: Wind tunnel at ZhdK, Zurich University of the Arts (left), Smoke visualization of vortex shedding at ZhdK (right)

In our communication we would like to give a brief overview on the history of flow visualization and expose the importance of experimental work for the description of the flow and its understanding, having a technical and a phenomenological approach. Our main argument should be the discussion of the technical framework in which flow visualizations are performed, the process by which the corresponding images are produced and what its limitations might be (Chazot, 2019). While an articulation with an artistic approach, mainly focus on the phenomenology, raises many questions which are opportunities to stimulate a reflection on the a priori of a strict scientific path and allow for a deeper analysis of the flow physics.

REFERENCES

- Ackerman, James S. “Art and Science in the Drawings of Leonardo Da Vinci.” (2002) In Origins, Imitation, Conventions: Representation in the Visual Arts. Cambridge, MA: MIT Press.
- Chazot, Olivier, (2019): The Roots of Experiments. wind tunnel bulletin n°9. Ed. Florian Dombois, Mario Schulze and Sarine Waltenspül.
- Didi-Huberman, Georges, Laurent Mannoni (2023), Movements of Air, The Photographs from Étienne-Jules Marey’s Wind Tunnels, Edited by: Florian Dombois and Christoph Oeschger, distributed for Diaphanes.
- Marey, Etienne-Jules, Des mouvements de l’air lorsqu’il rencontre des surfaces de différentes formes. (1900), Comptes rendus hebdomadaires des séances de l’Académie des sciences 131, 160–163.

Mach Number Estimation and Pressure Profile Measurements of Expanding Dense Organic Vapors

Fabio Beltrame[1], Adam J. Head[1,*], Theodoros Michelis[1], Carlo De Servi[1], Piero Colonna[1]
1: Faculty of Aerospace Engineering, Delft University of Technology, The Netherlands
* Correspondent author: a.j.head@tudelft.nl

Keywords: NICFD, Schlieren, RANS, De Laval Nozzle

1 INTRODUCTION

Over the past few decades, CFD codes have reached a remarkable level of accuracy because of the extensive availability of accurate experimental data for their verification and validation [11]. However, these experimental data sets are limited to aerodynamic flows or classical and ideal gas dynamics. Although first experimental results on non-ideal compressible effects in supersonic flows of dense organic vapours have been recently published (Conti et al., 2022, Robertson et al. 2020, Zocca et al. 2019), the data in the literature remain insufficient in terms of quantity and quality for the validation of NICFD-capable flow solvers. The Organic Rankine Cycle Hybrid Integrated Device (ORCHID) of the Propulsion and Power laboratory of the Delft University of Technology was built with the aim of producing large quantities of high-quality data for experimental investigations and validation of CFD codes for non-ideal compressible flows of dense organic vapors. The setup is currently equipped with a convergent-divergent nozzle test section with optical access on its sides and seventeen distributed pressure measurement sensors along the flow path. A methodology to extract the midplane Mach distribution in the supersonic flow field from the Schlieren dataset was developed. The extracted Mach number and measured pressure field using a pressure scanner were compared to the SU2 CFD tool numerical predictions.

APPARATUS AND METHODOLOGY

The ORCHID nozzle test section (Head, 2021, App. B) is made from two equal and removable profiles, which are inserted at the top and bottom of the nozzle housing. The side walls of the nozzle are made from transparent windows which provide optical access. Two pressure transmitters Wika UPT 20 are used to characterize the total pressure in the settling chamber and the pressure in the receiver. Both pressure transmitters have an expanded uncertainty of ±0.1 bar. The test section is also equipped with a Scanivalve (SV) DSA3218 pressure scanner which accommodates 16 temperature-compensated piezoresistive pressure transducer and is used in combination with pressure taps to measure the static pressures along the nozzle profile. Figure 2a shows eighteen taps situated along the upper and lower nozzle profiles. Two extra taps are located on the flanges of the settling chamber. The adopted schlieren layout is a two-lens flat mirror z-type configuration. The equipment employed in the experiment is reported by Beltrame et al. (2020). In the experiment described in this paper, an additional camera (BOBCAT IGV-B1610 16bit CCD) is used to image the nozzle profile geometry, allowing to track changes owing to thermal expansion and, hence, determine the nozzle throat size at various operating conditions. The operating conditions targeted in the experiment correspond to the design point of the ORCHID Balance of Plant (BoP) and nozzle test section. After a pre-warming stage (at 180°C for experiments with MM), the TS can be opened, and 20 minutes are necessary to stabilize conditions around the chosen values and evaporate all the liquid which accumulates in the receiver during the startup. Once steady state is achieved, 1,000 schlieren image realizations, which ensure statistical convergence of the measured quantities, are acquired at a frequency of 25 Hz, for a total time of 40 s. Spatial calibration of both cameras is performed by means of a calibration target located at the midspan of the test section, and a pinhole calibration model is employed to account for lens distortion. The DSA3218 pressure scanner is pre-warmed one hour before measuring to ensure thermal stability of the module. The pressure lines are purged with nitrogen to remove any condensate which may have accumulated during the nozzle starting phase, minimizing the risk of damage and maximizing the accuracy of the measurements. The pressures are recorded at an acquisition frequency of 1 Hz. Simultaneous flow visualization can be performed at this stage.

2 RESULTS

The numerical solutions of the flow-field in the ORCHID nozzle are obtained using the open-source flow solver SU2 for MM flowing in an inviscid 2D half-nozzle with symmetry conditions along the midplane (Fuentes Monjas et al. 2022). The total inlet conditions assumed in the CFD model correspond to the average steady values of total pressure and temperature measured at the nozzle inlet during the experimental run. Their values are P^0 (PT011) = 18.36 ± 0.0229 bar, T^0 (TT015) = 253.7 ± 0.66 °C. The pressure measured at the nozzle outlet is P_b (PT004) = 2.21 ± 0.0416 bar. The nozzle profiles considered in the CFD model accounts for the thermal expansion of the nozzle throat, which was measured to be 7.72 mm using a dedicated camera that tracked the position of markers on the lateral surface of the nozzle profiles. The midplane Mach number has been extracted from the Schlieren images according to the line extraction method shown by Beltrame et al. (2020). Figure 1a shows the first schlieren image from the recorded sequence on top, and the moving filter processed version to enhance the flow patterns on the bottom, with the average extracted Mach lines superimposed on the midplane. A shock wave generated by a 5° wedge located at the nozzle outlet can also be observed. Figure 1b shows the comparison between the numerical prediction against the Mach number distribution and its total expanded uncertainty along the nozzle mid-plane obtained experimentally. he extracted Mach number ranges from M = 1.4 ± 0.04 to 1.95 ± 0.05 at positions x/Hth = 1.07 and 7.0, respectively. The Euler simulation predicts higher values for the flow Mach number along the expansion process when compared to the measured Mach number.

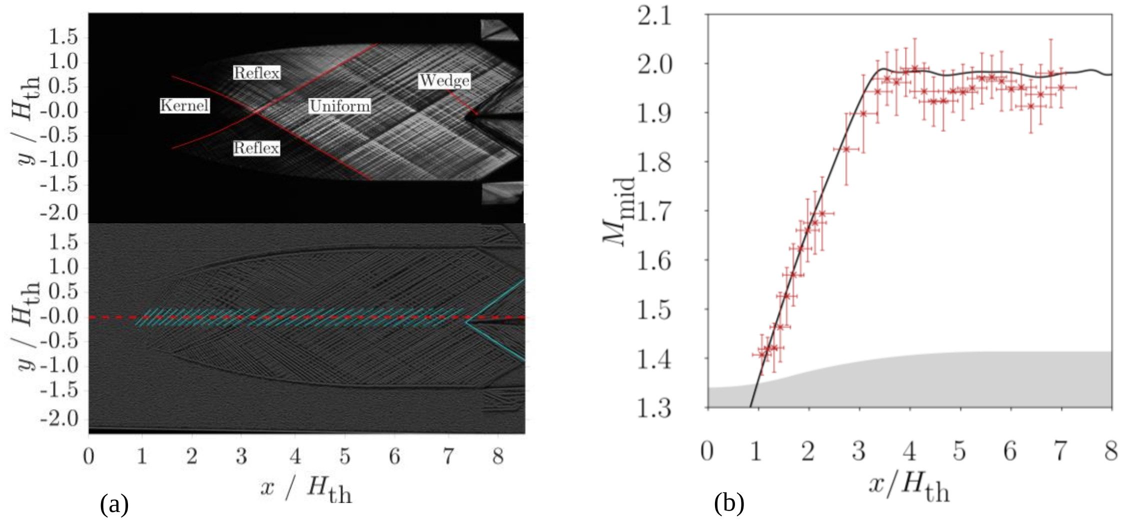

Fig.2: (a). A raw schlieren image showing Mach waves and an oblique shock wave at the nozzle exit at the top. The average extracted Mach lines superimposed on the same post-processed schlieren image is shown below. (b). Comparison between the measured flow Mach number with the corresponding total exp. uncertainty and the Euler solver numerical prediction. Axial coordinate x nondimensionalized with the throat height H_{th}.

Nevertheless, the predicted Mach numbers match reasonably well with the experimental results, where the closest match is located inside the kernel region. The deviation tends to increase towards the nozzle exit, as the Mach number increases. Figure 3 shows the measured static pressure distribution along the top and bottom nozzle profiles complemented with the expanded uncertainty. Sixteen pressure values located at the indicated tap locations are compared against the results of the Euler simulation together with the computed compressibility factor plotted on the Y2 axis. The match is satisfactory with the greatest deviation of 2.2% and 2.7 % inside the kernel and reflex regions.

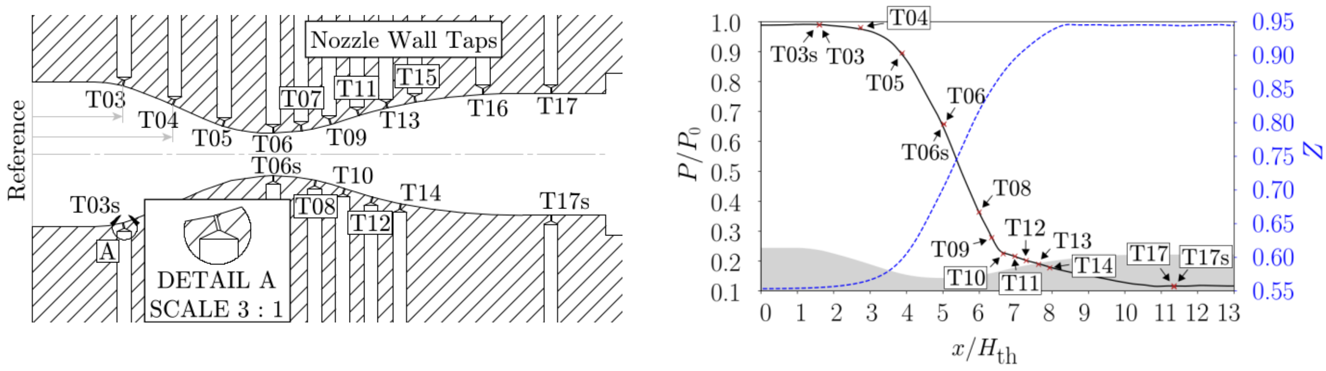

Fig. 2: (a). Cross-section of the planar nozzle showing the positioning of the eighteen pressure taps. Three taps are symmetrically aligned and are indicated by the letter s. Detail A shows that the opening of each tap is perpendicular to the nozzle profile wall. (b)

3 REFERENCES

- Beltrame, F., Head, A. J., De Servi, C., Pini, M., Schrijer, F. & Colonna, P. 2021 First Experiments and Commissioning of the ORCHID Nozzle Test Section. In Pini, M., De Servi, C., Spinelli, A., di Mare, F., Guardone, A. (eds) Proceedings of the 3rd International Seminar on Non-Ideal Compressible Fluid Dynamics for Propulsion and Power. NICFD 2020. ERCOFTAC Series, ERCO, vol. 28, pp. 169–178. Springer International Publishing.
- Fuentes Monjas, B., Head, A J., De Servi, C. & Pini, M. 2022 Validation of the SU2 fluid dynamic solver for isentropic non-ideal compressible flows. In Pini, M., De Servi, C., Spinelli, A., di Mare, F., Guardone, A. (eds) Proceedings of the 4th International Seminar on Non-Ideal Compressible Fluid Dynamics for Propulsion and Power. NICFD 2022. ERCOFTAC Series, ERCO, vol. X, p. X. Springer International Publishing.
- Conti, C. C., Fusetti, A., Spinelli, A. & Guardone, A. 2022 Shock loss measurements in non-ideal supersonic flows of organic vapors. Experiments in Fluids 63 (117), 1432–1114
- Head, A.J. , 2021, Novel Experiments for the Investigation of Non-ideal Compressible Fluid Dynamics: The ORCHID and First Results of Optical Measurements, Ph.D. thesis (Delft University of Technology)
- Robertson, M., Newton, P., Chen, T., Costall, A. & Martinez-Botas, R., 2020 Experimental and numerical study of supersonic non-ideal flows for organic rankine cycle applications. Journal of Engineering for Gas Turbines and Power 142 (8).
- Zocca, M., Guardone, A., Cammi, G., Cozzi, F. & Spinelli, A. 2019 Experimental observation of oblique shock waves in steady non-ideal flows. Experiments in Fluids 60 (6), 101.

Schlieren analysis of the retro-propulsion jet of a reusable launcher's first stage

Francois Nicolas[1], Sylvain Morilhat[1], David Donjat[2,*], Olivier Léon[2], Cedric Illoul[1]
1: ONERA/DAAA, Université de Paris-Saclay, 92190, Meudon, France
2: ONERA/DMPE, Université de Toulouse, 31055, Toulouse, France
* Correspondent author: david.donjat@onera.fr

Keywords: High speed schlieren, Tomographic BOS, retro-propulsion jet, toss back concept, hypersonic wind tunnel

ABSTRACT In the context of future launch vehicle development, the toss back strategy is based on reigniting the rocket's engine to land the reusable first stage. Since a large amount of energy is lost during the return of the vehicle, this simple concept, adopted for SpaceX's Falcon 9, is best suited for very vertical ascent trajectories to minimize fuel consumption during the return flight. Extensive aerodynamic studies of this technology are underway. Indeed, the recovery of the first stage of such a reusable launch vehicle uses controlled deceleration thrusts in low-density atmosphere at very high speeds. These thrusts create an interaction between the retropropulsion jet and the upstream flow, inducing significant mechanical and thermal loads on the stage. This paper presents a Schlieren analysis of the interaction between a supersonic plume exiting a nozzle and a Mach 6 counterflow. Two main flow regimes can be considered depending on the intensity of the thrust, namely the long penetration mode associated with a weak plume and the blunt penetration mode associated with a more significant gas pressure ejection. Figure 1 provides a schematic description of these two modes.

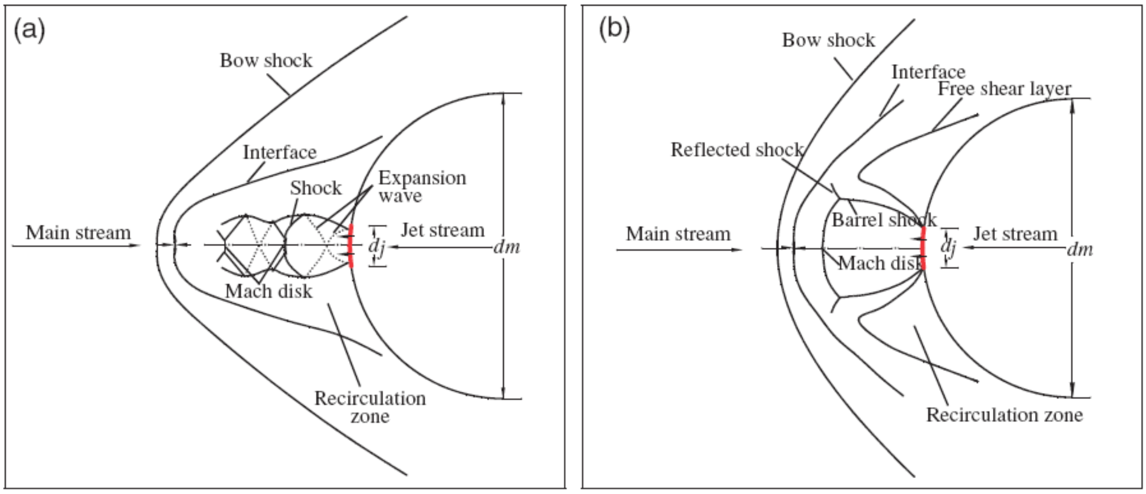

Figure 1: Interaction topologies for a supersonic plume impinging a high speed counter flow - Long (A) and blunt (B) penetration jets (from [3])

The experimental campaign was conducted in the cold hypersonic wind tunnel R2Ch at ONERA, Meudon, France. A uniform flow at Mach 6 was obtained using a contoured axisymmetric nozzle. All tests were performed at a stagnation temperature of 500 K. The stagnation pressure can be selected from a wide range by using a combination of an upstream high pressure tank (190 bar), a downstream vacuum sphere at 100 Pa and a pressure regulator. The model represents the lower part of the first stage of the launcher, 60 mm in diameter, with a tapered divergent nozzle producing a Mach 3.3 flow with an exit diameter of 10 mm. The stagnation pressure ratio between the wind tunnel and the nozzle (called NPR) was varied between 0.2 and 10, resulting in a relevant unsteady database of a retropropulsion jet (see [1]).

First, high-speed schlieren images (at 22 kHz) were taken simultaneously with unsteady pressure measurements (Kulite probes, at 500 kHz rate) at the model base to describe the intense fluctuations induced by these different configurations. An example of snapshots is shown in Figure 2, which illustrates the remarkable evolution of the flow topology with the decrease of the stagnation pressure ratio leading to the stabilization of the flow.

Second, a Background-Oriented Schlieren (BOS) system was implemented to provide an additional quantitative description of these flows. Due to the large density gradients encountered in compressible flows, the distance between the flow and the background must be relatively short to ensure adequate imaging sensitivity, which necessitated installation within the test section. In addition, high signal-to-noise ratios (SNRs) were achieved by printing the background pattern on a retroreflective panel. Illumination was then performed with a low repetition rate Ng:Yag laser (Litron NANO-L-200-1 double pulse $200mJ@15Hz$)

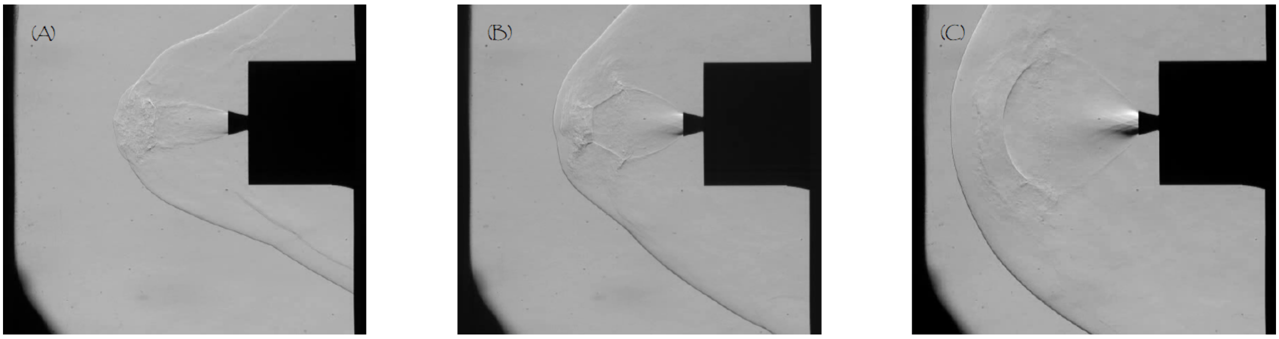

Figure 2: Instantaneous snapshots of high pressure jet flow (wind tunnel stagnation pressure : $P_{i_{WT}} = 5$ bar - NPRs are 1 (A), 0.5 (B) and 0.2 (C) illustrating several blunt penetration jets)

and images were captured with high resolution BASLER camera ($a2A4504-18umPRO$)(at 30 Hz). An example of the instantaneous deflection map obtained for a stabilized regime is shown in Figure 3. Based on these results and a prior calibration of the setup, axisymmetric reconstructions of the density field based on the direct BOS tomography approach proposed by [2] will be presented.

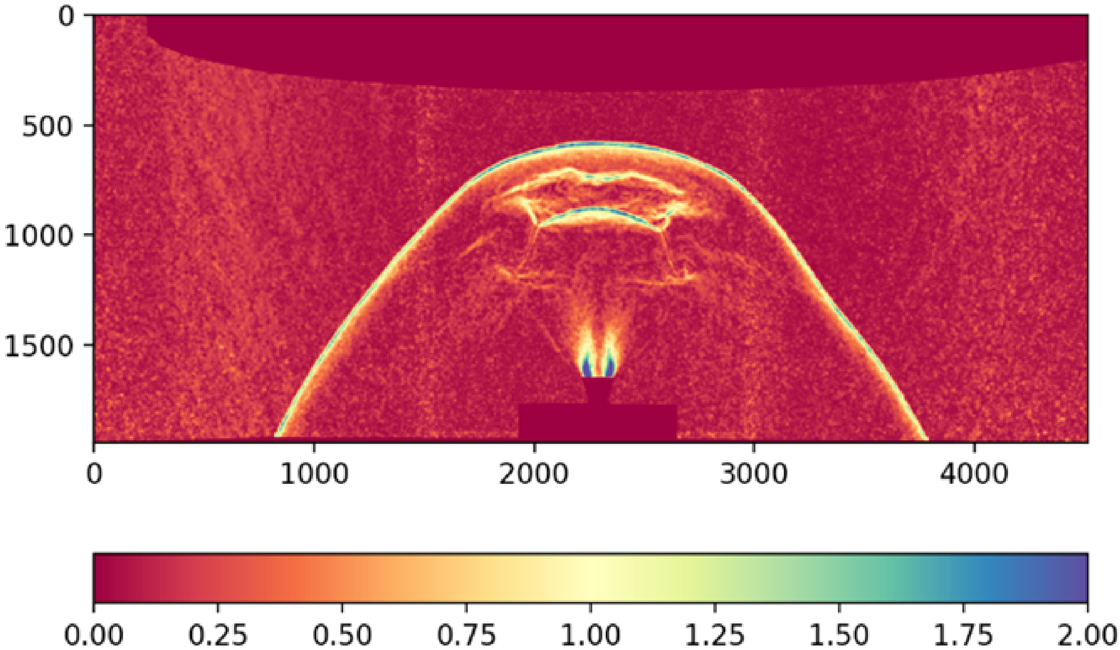

Figure 3: Instantaneous deflection map for the blunt regime (in pixel)

References

[1] Sylvain Morilhat. Experimental analysis of a retro-propulsion jet of a launcher's first stage at mach 6. In *57th 3AF International Conference on Applied Aerodynamics*, 2023.

[2] F. Nicolas, V. Todoroff, A. Plyer, G. Le Besnerais, D. Donjat, F. Micheli, F. Champagnat, P. Cornic, and Y. Le Sant. A direct approach for instantaneous 3d density field reconstruction from background-oriented schlieren (BOS) measurements. *Experiments in Fluids*, 57(1), December 2015.

[3] ChaoYing Zhou and WenYing Ji. A three-dimensional numerical investigation on drag reduction of a supersonic spherical body with an opposing jet. 228(2):163–177, 2014.

TECHNICAL SESSION 15

MEASUREMENT ACCURACY AND UNCERTAINTY

Chaired by Stefano Discetti

Comparison of digital-in-line holography and PIV for the study of turbulent flow

P. Bresson[1], V. Biscay[1], T. Lohez[1], F. Lamadie[2], L. Rossi[1]
1: CEA, DES, IRESNE, DTN, STCP 13108 St Paul lez Durance Cedex, Cadarache, France
2: CEA, DES, ISEC, DMRC, Univ Montpellier, 30207 Bagnols-sur-Ceze, Marcoule, France
* Correspondent author: paul.bresson@cea.fr

Keywords: Digital-in-line holography, PIV processing, Velocimetry

I. INTRODUCTION

DIH, also called lensless imaging, is a very efficient volumetric technique to simultaneously measure 3D positions, trajectories, velocities, shapes and sizes of static or moving particles in diluted media. As it can be used to cover a wide range of particle sizes (typically from the micrometer to the millimeter), it has applications in many fields of research from solid characterization to fluid mechanics and biology. One of the main advantages of DIH is to directly illuminate the sensor, which allows the use of fast cameras and low light sources for high speed particle tracking. This communication compare the performances of DIH for turbulent flow characterization with the widely used PIV, in the presence of obstacles affecting image formation. The final objective is the experimental study of turbulent flows in a mock-up [1] dedicated to the study of the thermal-hydraulic behavior pressurized water reactor fuel assemblies of nuclear reactors by using both technique.

II. EXPERIMENTAL SETUP

The experimental mock up consists of two independent sections. In the first section, an academic axisymmetric round jet flow is established on a 7x10x16 cm observation volume, while in the second section, it is possible to insert different optical obstacles that will more or less disturb the imaging without changing the flow in the first section. This mock-up allows the use of a holographic setup in Gabor configuration [2] with a HeNe laser (632 nm) coupled with a Phantom Miro LAB110 (1280x800 square pixels pixels of 20 µm, frame rate 1600 Hz) and a conventional PIV setup (see Figure 1) with a nanosecond Nd:YAG laser (1064 nm, pulse of 3 ns), generating a 1mm thick laser sheet, coupled with an Imager SX9M (3360x2712 square pixels pixels of 3.69 µm, frame rate 8 Hz).

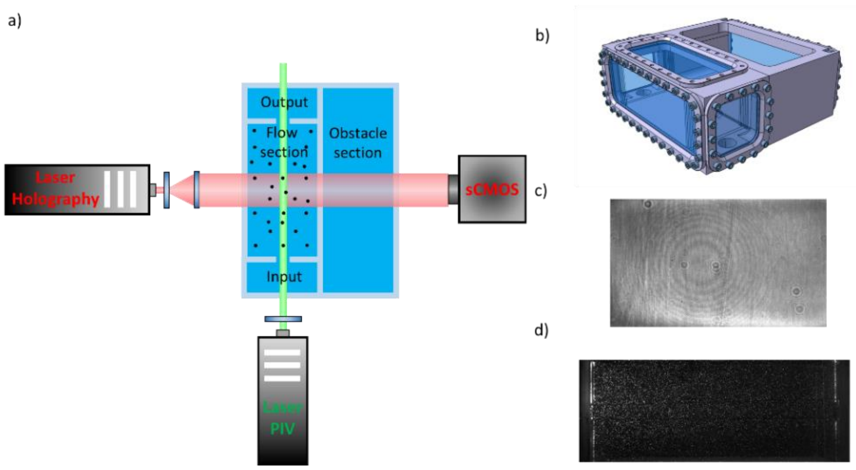

Figure 1. a) Experimental setup b) 3D schematic of the mock-up c) Holography image d) PIV image

III. HOLOGRAMS PROCESSING

Holograms are processed using a back propagation strategy which use the recorded intensity I(x,y) to compute the field at a distance *z* from the sensor. In this goal, the recorded intensity is convoluted with a propagation operator as follow [3]:

$$U_z(u,v) = \frac{e^{ikz}}{i\lambda B_z} e^{i\frac{kC_z}{2A_z}[u^2+v^2]} \left[I\,(x,y) * e^{\frac{jkn_1A_z}{2B_z}(x^2+y^2)} \right] \left(\frac{u}{A_z}, \frac{v}{A_z} \right) \tag{1}$$

The coefficients A, B, C and D refer to the elements of the ray transfer matrix, which is a geometrical description of the optical elements and medium between the sensor *(x,y)* and the particle plane *(u,v)*. λ is the wavelength, n_1 account the refractive index of the medium between the sensor and the first optical.

From the back-propagated holograms, the first step of the processing consists in determining the number of particles and their positions in the detector plane. To do this, an approach inspired by the HYBRID method [4] is used. The second step consists in extracting the position of the particles along the optical axis, to do this a focus function based on the variance of the real part of the intensity of the pixels located on the edges of the particles is calculated. A previous study has checked the numerical processing on a cell flow, while studying the influence of an afocal system on the reconstruction of trajectories (see figure 2).

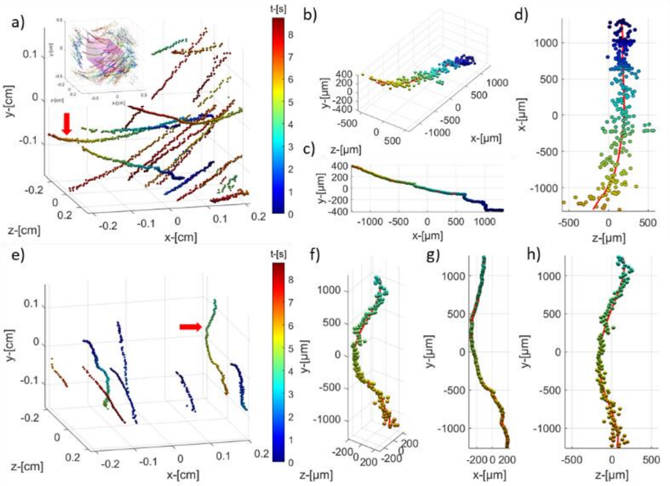

Fig.2 . Particle trajectories in the same measurement volume with a turbulent flow at different times reconstructed holographically using either a) free-space propagation, with b) a single trajectory and its projection on c) x-y and d) x-z, or e) an afocal setup with −3 magnification , with f) a single trajectory and its projection on g) x-y and h) x-z,. The inset in part a) shows the whole measurement volume reconstructed with free-space propagation

IV. PIV

Figure 3 shows the average velocity measured by PIV. The flow rate was adjusted to obtain a Reynolds number around 1000 to minimize turbulence and to simplify comparisons between the different techniques. Each image is processed by a multi-pass processing (64x64 pixels corelation windows then 16x16 pixels corelation windows with a 50% overlap) for a spatial resolution of 60 µm by pixel. Then a post-processing is applied to discard aberant and uncertain speed (corelation peak to peak ratio<1.2). The present jet is slightly bent and is coupled with the outlet at its end. Comparisons between the different techniques can therefore be made at different points in the flow, where its behavior is different.

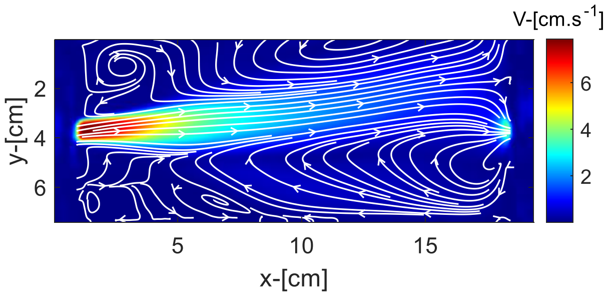

Figure 3. Streamline of the mean velocity field measured by PIV on 5000 images

V. CONCLUSIONS ET PERSPECTIVES

In this communication, a comparison between two particle tracking techniques, DIH and PIV is proposed through the study of an academic jet. The advantages and disadvantages of each technique will be discussed. The next step will be to add obstacles in the second section of the mock-up in oder to study their accounting by the three techniques. In the future, a comparison with a "shake the box"[5] type tracking system will be performed.

VI. REFERENCES

[1] Turankok, N., Moreno, F., Bantiche, S., Bazin, F., Biscay, V., Lohez, T., Picard, D., Testaniere, S.& Rossi, L. (2020). Unsteady pressure and velocity measurements in 5 × 5 rods bundle using grids with and without mixing vanes. Nuclear Engineering and Design. 364. 110687. 10.1016/j.nucengdes.2020.110687

[2] Gabor, D. (2020). A New Microscopic Principle. Nature, 161, 777–778.

[3] Collins, J.& Stuart, A. (1970). Lens-system diffraction integral written in terms of matrix optics. Journal of the Optical Society of America, 60, 1168-1177.

[4] Gao, J., Guildenbecher, D.R., Reu, P.L.& Chen, J. (2013). Uncertainty characterization of particle depth measurement using digital in-line holography and the hybrid method, Optics Express, 21(22):26432-49.

[5] Schanz, D., Gesemann, S., Schröder, A. (2016). Shake-The-Box: Lagrangian particle tracking at high particle image densities, Experiments in Fluids, 57, 70.

Volumetric (Self-)Calibration in the Presence of Obstructing Objects

Bernhard Wieneke
LaVision GmbH, Göttingen, Germany
bwieneke@lavision.de

Keywords: LPT, Shake-the-Box, Calibration, Self-Calibration, 3D-Objects

ABSTRACT Most fluid mechanics problems deal with the interaction of a flow stream with one or multiple objects. Examples are fluid-structure interactions, ground, maritime and air transport, heat exchangers, among many others. The measurement challenge arises when a volumetric flow field is needed around some stationary or moving/flexible object. Illumination produces shadows and the view of cameras is blocked across the objects. In contrast, many volumetric measurements typically only work in illuminated regions with optical access available for all cameras. An additional problem is that the object shape or exact position is not always available. This work presents a method to perform particle track reconstruction by Shake-the-Box (STB) in the presence of obstructions, focusing here on the initial (self-)calibration procedure.

1 OBJECT SHAPE AND POSITION, REQUIRED MODIFICATIONS IN STB

Several techniques are available to determine object shape and position in a fluid flow experiment, among them Stereo-DIC with some (projected) speckle pattern on the object surface, the rough visual hull technique (Adhikari and Longmire, 2012), or knowing the shape beforehand by some CAD-model and fitting the exact position in the measurement volume by added markers of known position or some other methods. The object itself may be rigid and stationary, or flexible and moving in a periodic or non-periodic fashion, in turn making the problem of object mapping increasingly challenging (e.g. in flexible wing experiments, Mertens et al., 2021). Here we assume that the model shape and position is known at all time instances and can be used for STB and volume self-calibration (VSC), see below in fig. 1:

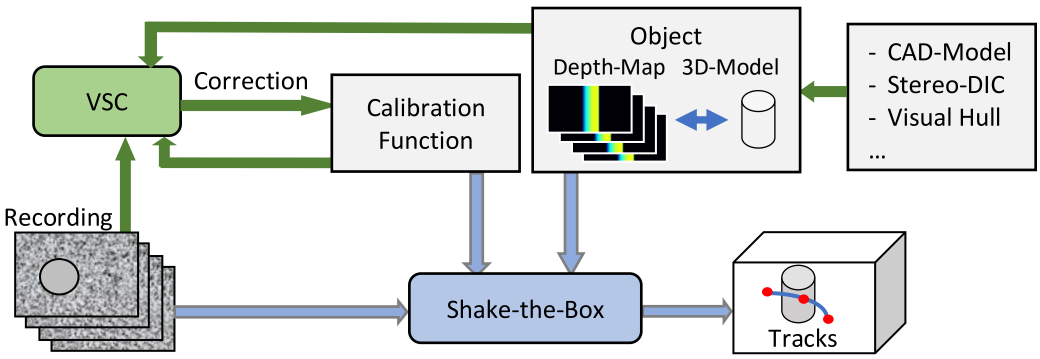

Figure 1: Overview volume self-calibration (VSC) and Shake-the-Box (STB) using an object model

The study here illustrates the fundamental aspects of the problem using the Lagrangian particle tracking (3D-LPT) algorithm Shake-the-Box (STB, Schanz et al., 2016). Modifications are needed for the IPR-part of STB (Wieneke, 2013) to account for partial optical access (i.e. only a fraction of cameras has the particle in view) with respect to particle triangulation, intensity fit and iterative fit of the position (*shaking*) as well as for the particle reprojection to compute the residual images for the next IPR-iteration. The standard reconstruction requires that a particle is viewed by all cameras simultaneously, leading to extensive regions where STB fails (fig. 2 left, flow around a cylinder viewed by 3 front and 3 back cameras, seeding density = 0.05 ppp).

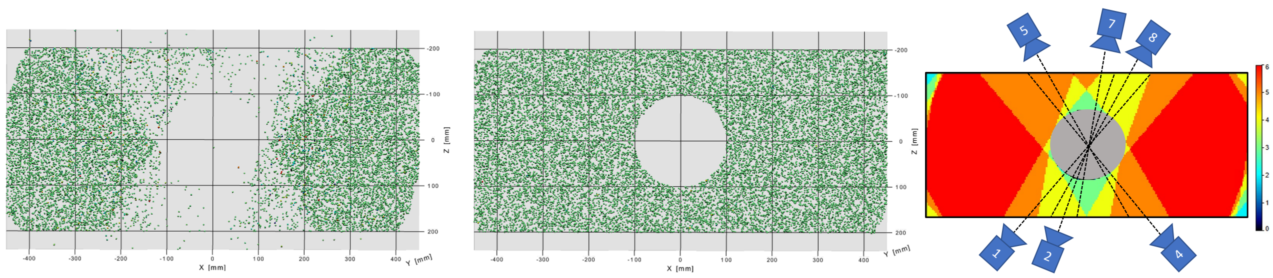

Figure 2: Left: XZ-plane of standard STB, middle: modified IPR-STB using true object information, right: setup with 6 cameras viewing a cylinder along the Y-axis, color = number of cameras viewing a location in the volume.

The object shape and position information can be converted into a depth map for each camera and each pixel, indicating where the line-of-sight (LOS) of some pixel first encounters the object surfaces. STB using this information can fully recover the complete flow around the object (fig. 2 middle). Further details are presented elsewhere (Wieneke, 2023).

2 CALIBRATION AND VOLUME SELF-CALIBRATION

In many cases, the model can be removed for the initial calibration enabling standard procedures like translating a calibration target through the measurement volume. Double-sided plates are required when the object is surrounded by front and back cameras. With the object in place the preferred calibration method is viewing the plate (best double-sided and double-plane) at multiple shifted, rotated, and tilted views in such a way that the front and back cameras can be linked together. Processing is then done by standard bundle adjustment leading to a camera pinhole model.

Volume self-calibration (VSC, Wieneke, 2018) corrects calibration errors due to temporal change in camera position (vibration) or remaining spatial disparities, or even adding an extra correction field for highly localized distortions e.g viewing through curved interfaces. Standard VSC requires that the seeding particles are viewed by all cameras, leading to regions without valid disparity vectors due to obstructions (fig. 3 top). Modifications are needed for VSC again using the object depth maps to provide information which part of the volume is visible by which cameras, recovering valid disparity vectors (fig. 3 middle). Unfortunately, disparity vectors may change significantly according to which set of cameras contribute, requiring an additional correction step at the end of VSC to synchronize neighboring disparity vectors (fig. 3 bottom) after which the correction of the calibration mapping functions can proceed as usual.

Further details and implications for the calibration procedure and volume self-calibration are discussed. Examples with synthetic and real data are provided.

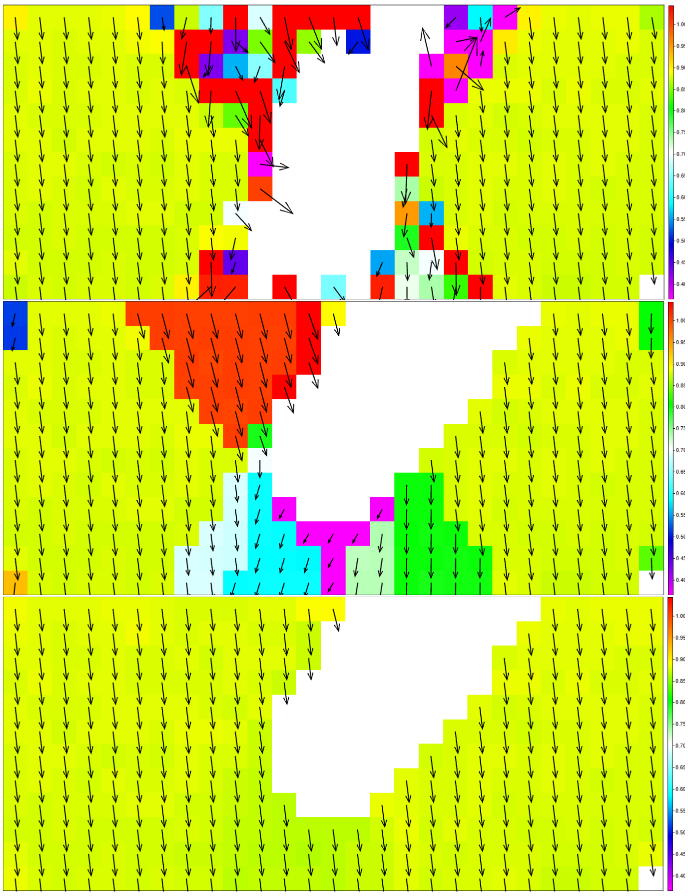

Figure 3. XZ-plane of (dx_1, dy_1)-disparities of camera 1, synthetic data with extra constant image shift, total of 6 cameras, cylinder in the middle along Y-axis, top: standard VSC without any information about obstructing objects, middle: disparity vectors taking care of which subvolumes are visible by which cameras, bottom: with neighborhood correction, iteratively percolating the information from 6-camera subvolumes to neighboring ones. Color = disparity vector component dy_1.

3 REFERENCES

- Adhikari, D., & Longmire, E.K. (2012) Visual hull method for tomographic PIV measurement of flow around moving objects. Experiments in Fluids 53, 943–964
- Mertens, C., de Rojas Cordero, T., Sodja, J., Sciacchitano, A., & Oudheusden, B.W. (2021) Aeroelastic Characterization of a Flexible Wing Using Particle Tracking Velocimetry Measurements. AIAA Journal https://doi.org/10.2514/1.J060713
- Schanz, D., Gesemann, S., & Schröder, A. (2016) Shake-The-Box: Lagrangian particle tracking at high particle image densities. Experiments in Fluids 57:70
- Wieneke, B. (2013) Iterative reconstruction of volumetric particle distribution. Measurement Science and Technology 24:024008
- Wieneke, B. (2018) Improvements for volume self-calibration. Measurement Science and Technology 29(8), DOI: 10.1088/1361-6501/aacd45
- Wieneke, B. (2023) 3D-LPT in the Presence of Obstructing Objects. ISPIV 2023, San Diego, California, USA

On the scalability of helium-filled soap bubbles

Adrian Grille Guerra[1,*], Andrea Sciacchitano[1] and Fulvio Scarano[1]
1: Dept. of Flow Physics and Technology, Delft University of Technology, The Netherlands
* Correspondent author: a.grilleguerra@tudelft.nl

Keywords: PIV, HFSB, shadowgraphy

1 BACKGROUND

Wind tunnel experiments involving the use of particle image velocimetry (PIV) have been upscaled in the last decade with the introduction of helium-filled soap bubbles (HFSB) as tracers (Bosbach et al., 2009). This is particularly relevant to 3D experiments where the illumination needs to be spread over a volume, in turn requiring imaging with a large depth-of-field. This is due to their large diameter (in the order of 300-500 μm) that provides increased light scattering. When used in the neutral buoyant condition, HFSB feature also rather accurate flow tracing (Scarano et al., 2015), as demonstrated by experiments conducted at wind tunnel speed up to 70 m/s (Faleiros et al., 2021). Applications at even larger scale (10 – 100 m) have not been attempted yet and experiments have adopted ad-hoc solutions like using natural tracers (snow flakes, Toloui et al., 2014). The availability of HFSB tracers at a scale that matches the experimental needs relies on the ability to control the tracers' size during production.

A seminal study on the controlled generation of HFSB (Faleiros et al., 2019) has shown that it is possible to vary the size of HFSB, yet maintaining neutral buoyancy, by varying only the fluids flow rates. The study has shown that the bubbles' diameter could be varied between 0.4 and 0.6 mm (max-min ratio, MMR = 1.5). In the present work, methods are discussed that aim at expanding the MMR more significantly. By doing so, one responds to the scaling needs on two sides: at first, smaller tracers will enable volumetric experiments for medium-scale wind tunnel applications; secondly, larger tracers will extend further the range of large-scale PIV for full-scale on-site applications.

2 WORKING PRINCIPLE OF THE HFSB GENERATOR

The geometry of a generic HFSB generator is sketched in Fig. 1. Helium exits from the inner duct, surrounded by a ring-duct for the flow of bubble fluid solution (BFS). On the outer ring, the air flow has two main functions: the flow shear at the lip of the inner tube between air and BFS accelerates the latter and decreases its thickness; furthermore, the convergent duct reduces the cross section of the helium streamtube, which allows producing smaller bubbles and at higher rate. Finally, the size of the helium streamtube can also be controlled by the air to helium relative flow rate.

A fluid supply unit provides the desired helium, BFS and air flow rates (Q_{He}, Q_{BFS} and Q_{air} respectively), while the conditions at the exit are dictated by the orifice diameter, d_o. The released BFS is extruded under the shearing action of the helium and air flows. The work done by the shear stresses at the helium-BFS and air-BFS interfaces accelerates the BFS film. As a result of mass conservation, its thickness is reduced and the surface area is increased. At the end of the nozzle contraction, the BFS flow features a thin annular shape of diameter d_a. The annular BFS film is subject to Plateau-Rayleigh instability, whereby disturbances of varicose mode are amplified eventually leading to the breakdown of the BFS filament into bubbles. The most amplified wavelength, λ, dictates the final bubble diameter, d_b, as well as the production rate.

Past experiments (Faleiros et al., 2019; Gibeau & Ghaemi, 2018) have shown that varying d_b by controlling Q_{air} and Q_{He} is possible. However, for a given generator, only modest variations of the HFSB diameter were obtained. The latter may be ascribed to two factors: 1) the maximum bubble size is limited by the orifice diameter; 2) the lower limit of HFSB size may be determined by the maximum air velocity (viz. shear) that can be tolerated during extrusion of the BFS film. The present work explores the control of HFSB size by altering the orifice diameter d_o, while maintaining unaltered the geometry upstream of the contraction (see Fig. 1).

3 EXPERIMENTAL SETUP

The bubble generator employed is an evolution of the 3D printed HFSB-GEN-V11 generator developed at TU Delft. The SAI 1035 fluid from Sage Action, Inc. is used as BFS. The generator features an exchangeable nozzle cap to easily change the orifice diameter, while maintaining the same internal contraction. The neutrally-buoyant condition in ambient air is maintained by controlling $Q_{He}/Q_{BFS} \cong 1080$ (Faleiros et al., 2019).

Shadow visualizations are performed to observe the production mechanism and infer bubble diameter and production rate. An LED continuous light source illuminates the region of interest (~20 mm at the exit of the generator). Images of the HFSB shadows are taken with a CMOS camera (Photron FASTCAM SA1.1) at a rate of 40 kHz. The digital imaging resolution is approximately 20 px/mm.

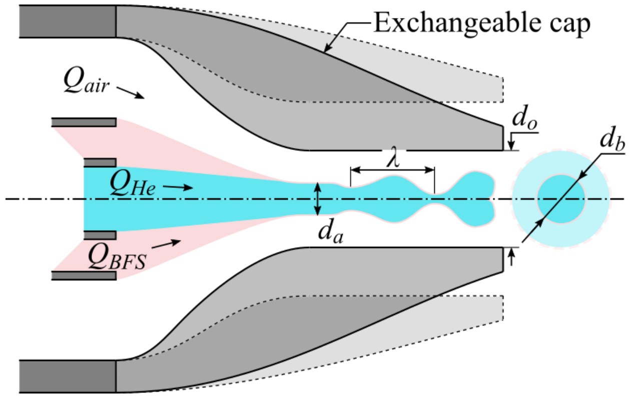

Figure 1. Sketch of a HFSB generator (not to scale).

4 RESULTS

The production of HFSB of different size is explored by considering nozzle caps with orifice diameters from 0.75 mm up to 3 mm. Examples of the bubbles generated are given in Fig. 2 for six different orifice diameters. The shadow images are accompanied by a 1 mm grid to give a clear indication of the bubble size. For every nozzle, the volume flow rates are kept constant at Q_{He}= 10 l/h, Q_{BFS}= 9.3 ml/h and Q_{air}= 100 l/h. From the visualizations, it is apparent that HFSB can be produced within a range of diameters $d_b \in [0.4, 2.5]$ mm simply by changing the orifice diameter of the generator.

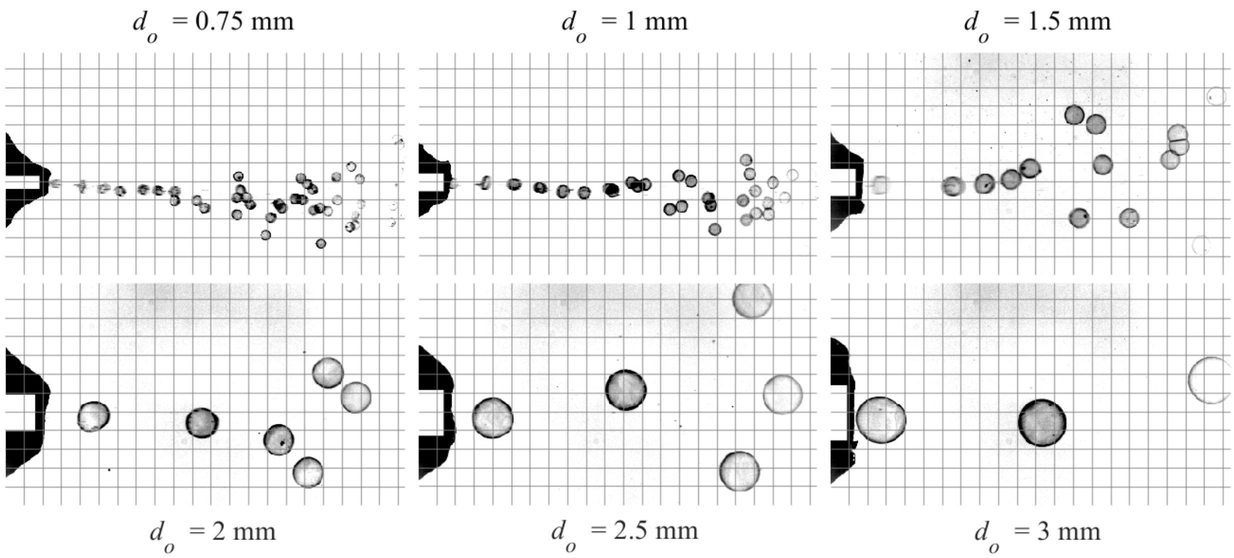

Figure 2. Shadow visualization of HFSB produced varying the orifice diameter of the nozzle. Reference grid with 1 mm pitch.

5 REFERENCES

Bosbach, J., Kühn, M., & Wagner, C. (2009). Large scale particle image velocimetry with helium filled soap bubbles. *Experiments in Fluids*, *46*(3), 539–547. https://doi.org/10.1007/s00348-008-0579-0

Faleiros, D. E., Tuinstra, M., Sciacchitano, A., & Scarano, F. (2019). Generation and control of helium-filled soap bubbles for PIV. *Experiments in Fluids*, *60*(3). https://doi.org/10.1007/s00348-019-2687-4

Faleiros, D. E., Tuinstra, M., Sciacchitano, A., & Scarano, F. (2021). The slip velocity of nearly neutrally buoyant tracers for large-scale PIV. *Experiments in Fluids*, *62*(9), 1–24. https://doi.org/10.1007/s00348-021-03274-9

Gibeau, B., & Ghaemi, S. (2018). A modular, 3D-printed helium-filled soap bubble generator for large-scale volumetric flow measurements. *Experiments in Fluids*, *59*(12), 1–11. https://doi.org/10.1007/s00348-018-2634-9

Scarano, F., Ghaemi, S., Caridi, G. C. A., Bosbach, J., Dierksheide, U., & Sciacchitano, A. (2015). On the use of helium-filled soap bubbles for large-scale tomographic PIV in wind tunnel experiments. *Experiments in Fluids*, *56*(2). https://doi.org/10.1007/s00348-015-1909-7

Toloui, M., Riley, S., Hong, J., Howard, K., Chamorro, L. P., Guala, M., & Tucker, J. (2014). Measurement of atmospheric boundary layer based on super-large-scale particle image velocimetry using natural snowfall. *Experiments in Fluids*, *55*(5), 1–14. https://doi.org/10.1007/s00348-014-1737-1

Experimental Investigation on Flow Characteristics of 3-Dimensional Pitot tubes by PIV Measurements

Woong Kang*, Sunghyuk Im, Doan Trang Nguyen, and Jinwoo Shin
Group for Thermometry and Fluid Flow Metrology, Korea Research Institute of Standards and Science, Republic of Korea
* Correspondent author: woong.kang@kriss.re.kr

Keywords: 3-Dimensional Pitot tubes, Flow Characteristics, PIV Measurements

ABSTRACT 3-Dimensional Pitot tubes are common devices in the turbomachinery field used to measure the components of three-dimensional flows. However, they have recently been considered as a new potential approach for smokestack flow measurements owing to their capability to measure swirl flows (Nguyen et al. 2022). As described in Figure 1, prism (Figure 1b) and sphere (Figure 1c) 3-D Pitot tubes consisting of five sensing holes in the sensing head are numbered from 1 to 5. The central hole is marked as 1, and the other four holes are symmetrically located to the central hole. Holes 2 and 3 are used to measure the yaw-angle velocity component, and holes 4 and 5 are used to measure the pitch-angle velocity component.

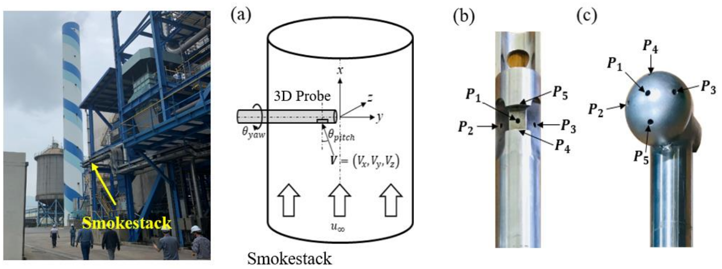

Figure 1. (a) Installation of the 3D Pitot tubes in the stack, (b) Prism 3-D Pitot tube, and (c) Sphere 3-D Pitot tube

In the case of 1-D Pitot tubes, such as a standard Pitot tube or an S-type Pitot tube, the flow velocity can be measured only in one direction from the pressure difference between two pressure holes. The 1-D Pitot tubes measure the flow velocity according to equation (1) which is derived from Bernoulli's equation,

$$V = \frac{\sqrt{2(P_{total} - P_{static})}}{\rho} = C_{Pitot}\frac{\sqrt{2\Delta P_{12}}}{\rho} \tag{1}$$

where C_{Pitot} is the coefficient of the Pitot tube, and $\Delta P_{12}=P_1-P_2$ is the dynamic pressure measured from two pressure holes of the Pitot tube.

US EPA (1971) proposed a yaw nulling method to measure the velocity and direction of the flow using a 3-D Pitot tube. As shown in Figures 1b and 1c, prism 3-D and sphere 3-D Pitot tubes described in EPA Method 2F are studied in this research. Before measuring flow velocity using a 3-D Pitot tube, it should be calibrated (Figure 2a) according to equation (2) under the yaw-nulling condition ($\Delta P_{23}=0$) for each pitch angle θ_p,

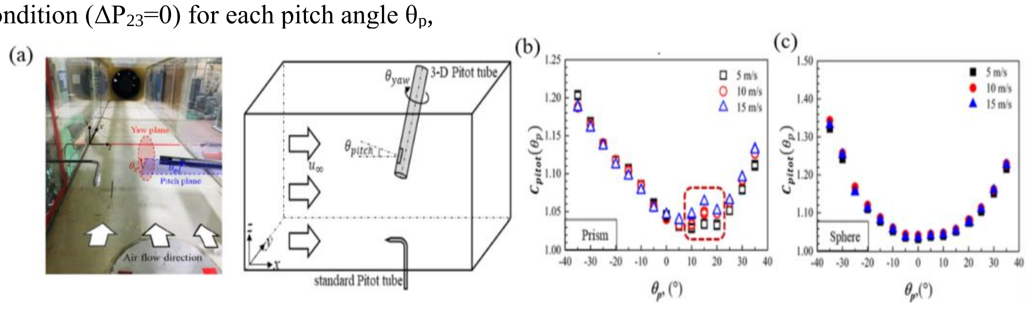

Figure 2. (a) calibration scheme of a 3-D Pitot tube,
(b) coefficient of a prism 3-D Pitot tube and (c) sphere 3-D Pitot tube

$$C_{Pitot}(\theta_p) = \alpha\sqrt{\frac{\Delta P_{std}}{\Delta P_{12}}} \tag{2}$$

where α is the coefficient of a standard Pitot tube, ΔP_{std} is measured pressure difference from the standard Pitot tube. The calibrated coefficient of a 3-D Pitot tube C_{Pitot} (θ_p) should not be changed within the targeted velocity range. In the case of the sphere 3-D pitot tube (Figure 2c), the coefficient is not changed significantly within the flow velocity range of 5 ~ 15 m/s at all pitch angles (-35°< θ_p <35°). In the case of the prism 3-D pitot tube, however, the coefficient varied significantly at a specific pitch angle range (10°< θ_p <20°) as shown in Figure 2b. Crowley et al. (2013) suggested that pressure gradient inside a recirculation zone near a Pitot tube affects the calibration factor of a Pitot tube.

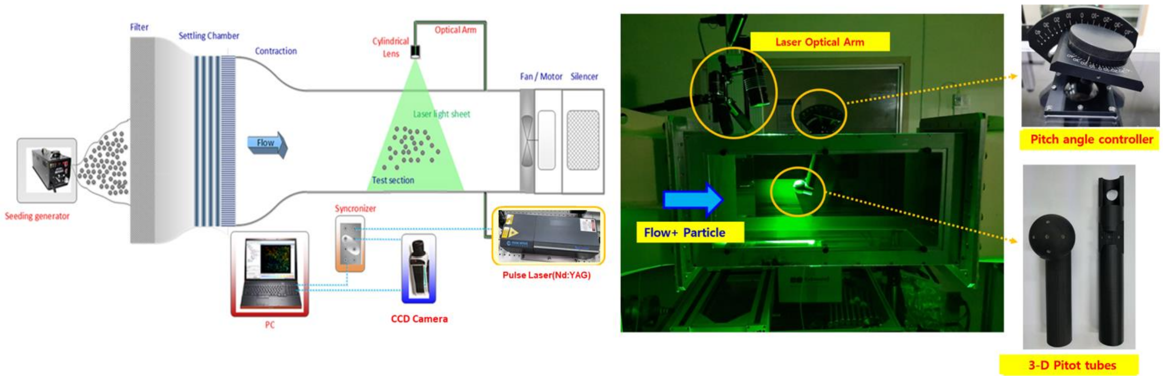

Figure 3. (a) PIV Experimental setup for 3 Dimensional Pitot tubes

In this research, PIV flow visualization measurements were performed around prism and sphere 3-D Pitot tubes (Figure 3). A 5 W continuous laser was used to visualize the flow streak, and a double-pulsed Nd:YAG laser was used for PIV imaging. Particle images were captured by a high-speed camera (PCO1600). Figures 4 show streak lines of flow around 3-D Pitot tubes, and vortices are observed from both Pitot tubes. The vortex around a prism Pitot tube exists near the pressure holes (P5, P1), but the vortex around a sphere Pitot tube exists far behind the pressure hole (P5). The flow separation near the pressure hole causes a pressure gradient and affects the Pitot tube coefficient C_{Pitot}. Figure 4 also show streak lines of flow around a prismatic Pitot tube with different pitch angles from -30 to 30 degree. Further investigation will be performed using particle image velocimetry with different velocity and pitch angles.

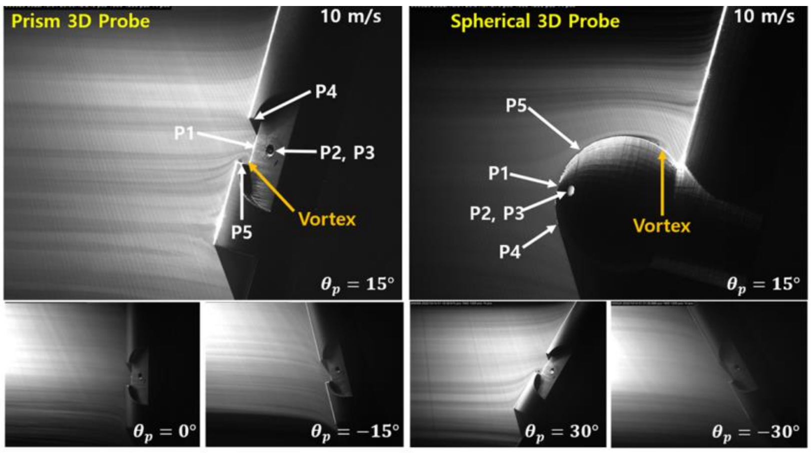

Figure 4. Flow around Prism and Sphere 3-D Pitot tubes with different pitch angles

REFERENCES

- Nguyen, D. T, Choi, Y. M., Im, S, Shin, J., and Kang, W. (2022). Calibration Process and Uncertainty estimation for 3D Pitot tubes to enhance greenhouse gas emission measurements in smokestacks. Metrologia, 59, 1-22.
- US EPA (1971) Determination of Stack Gas Velocity and Volumetric Flow Rate With Three-Dimensional Probes. U.S. Environmental Protection Agency Part60 Appendix A-1 Method 2F
- Crowley, C., Shinder, I. I., & Moldover, M. R. (2013) The effect of turbulence on a multi-hole Pitot calibration. Flow Measurement and Instrumentation, 33, 106-109

High Spatial Resolution Turbulent Channel Flow Measurement Using 2C-2D PIV with 103 MPx Cameras

Bihai Sun[1,*], Callum Atkinson[1] and Julio Soria[1]
1: Laboratory for Turbulence Research in Aerospace and Combustion (LTRAC), Department of Mechanical and Aerospace Engineering, Monash University, Melbourne, Australia
[*] Correspondent author: Bihai.sun@monash.edu

Keywords: 2C-2D PIV, turbulent channel flow, high spatial resolution

ABSTRACT Turbulent channel flow is an important flow configuration because of both its wide application in industrial environments and its canonical flow status in turbulence research. However, few experimental studies exist for turbulent channel flows, especially at high Reynolds number with high spatial resolution velocity field measurements. This paper presents a two-component – two-dimensional particle image velocimetry (2C-2D PIV) of a turbulent channel flow at $\mathrm{Re}_\tau \approx 1{,}600$. Two 103 MPx cameras were used to capture each image of the single-exposed PIV image pair, covering a field of view of the entire channel height and 1.22 channel height in the streamwise direction, while the PIV interrogation window size is less than five viscous lengths in the wall-normal direction.

1 INTRODUCTION

Fully developed turbulent channel flow is a canonical wall-bounded turbulent shear flow that is highly significant to study wall-bounded turbulence. The flow is statistically homogeneous in both the spanwise and streamwise directions, resulting in no spatial growth in the flow direction. Nevertheless, experimental studies of the turbulent channel flow are less common compared to other canonical flow configurations like turbulent boundary layer and fully developed pipe flow, partially due to the required larger footprint of the experimental facility (Monty and Chong, 2009). In order to maintain nominally two-dimensional flow in the channel centreline, the experimental facility requires a high aspect ratio, leading to an order of magnitude larger cross-sectional area in comparison to a turbulent pipe experiment with the same Reynolds number(Schultz and Flack, 2013). The high spatial resolution PIV measurement in the channel centreline also presents some complexities in the experiment. The high spatial resolution measurement necessitates a high magnification more than unity, as well as a long working distance of the lens so the optical system can be placed outside the tunnel. None of the commercially available macro lens offer the ability to meet both criteria, requiring a unique optical setup for this experiment. Also, the tunnel needs to be heavily seeded to ensure enough particles are present in each interrogation window. However, the particles between the measurement plane and the lens scatter the light from the laser sheet, reducing the measurement's signal-to-noise ratio. This paper presents two-component, two-dimensional (2C-2D) particle image velocimetry (PIV) for the turbulent channel flow that overcomes these obstacles for a high spatial resolution measurement.

2 HIGH SPATIAL RESOLUTION PIV OF HIGH REYNOLDS NUMBER CHANNEL FLOW

The experiment was conducted in the LTRAC high-speed water channel. The test section of the water channel is 1.6 m in the streamwise direction, 700 mm in the spanwise direction and 20 mm in the wall-normal direction, corresponding to a channel half-height, h, of 10 mm. Due to the high aspect ratio of the cross-section, the side walls have a negligible effect on the flow at the centreline of the channel flow, and the flow along the centreline of the channel nominally is two-dimensional in the mean (Vinuesa et al., 2014). The water channel is constructed using a stainless steel frame with glass on all four sides, providing full optical access to the channel flow. The water channel is powered by a 5.5 kW motor driving a centrifugal water pump. The water from the pump flows into a settling chamber, which holds 200 litres of water and contains four grids and a honeycomb flow straightener to reduce the turbulence level of the inflow. The flow then goes through a 10-to-1 contraction and a boundary layer trip before entering the channel test section. The PIV measurement domain is 1.5 m (150 h) downstream of the trip to ensure a fully-developed channel flow. At this location, the frictional Reynolds number, Re_τ, is estimated to be 1,600 and the viscous length scale, l^+, is estimated to be 6.3 μm. The field of view of the experiment is in the wall-normal – streamwise direction along the centreline of the channel, which extends the full wall-normal extent of the channel and is 24.5 mm (2.45 h) in the streamwise direction. The field of view is illuminated by an InnoLas Compact 400 PIV lamp pumped Nd:YAG laser, with the flow seeded using hollow glass spheres of 11 μm diameter.

The PIV image pairs were obtained using two Emergent HZ-100-G-M cameras. These cameras have a CMOS sensor measuring 36.1 mm wide and 29.4 mm high, with a total of 103 million (11,276 $\times$ 9,200) pixels. As these cameras do not have a double shutter, a beam splitter is used to match the fields of view of the two cameras which capture each of the single-exposed PIV images. The large image sensor of these cameras presents a challenge for camera position calibration, as the error introduced by lens distortion near the corners of the imaging sensor can be of the order of 10 pixels. To avoid unacceptable uncertainties caused by lens calibration, a lensless imaging registration system based on holographic techniques was developed. Unlike conventional imaging, holography belongs to coherent imaging, where the illumination light is a coherent light with a planar wavefront provided by a laser. When a target is placed in the light path, the interference pattern between the scattered light of the camera and the illumination light is recorded by the camera resulting in the recording of a hologram. Using this technique, it is possible to trace back the incident angle of the imaging light as well as the relative position between the target and each of the two cameras, without distortion introduced by

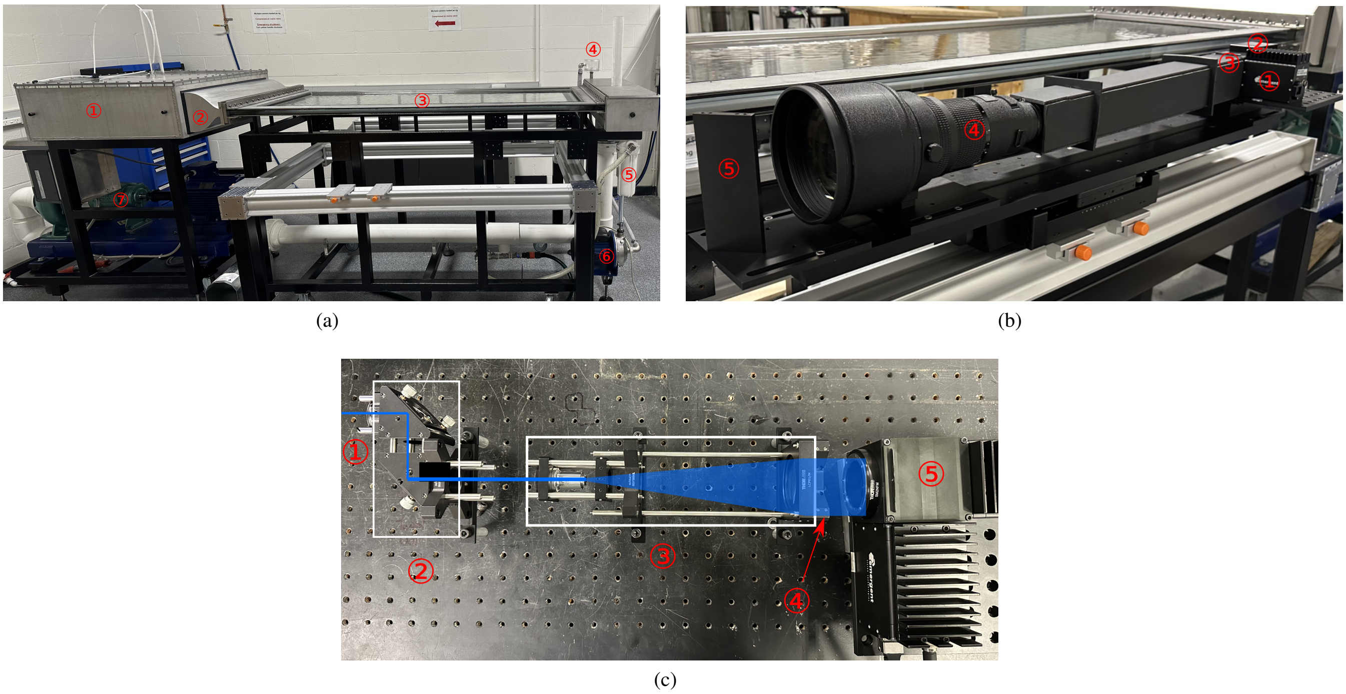

Figure 1: (a) A photo of the LTRAC high speed water channel. 1: settling chamber 2: contraction 3: test section 4: seeding chamber 5: particle filter 6: axillary pump for the filter 7: main pump. (b) A photo of the imaging optical setup. 1: first camera 2: second camera 3: (inside the mount) beam splitter 4: 400mm f/2.8 lens 5: mirror to image inside the channel. (c) Holographic calibration setup for the two cameras behind a beam splitter. Notice that the illumination light incidents directly onto the imaging sensors of the cameras without a lens. 1 (not shown): continous wave solid state laser 2: beam tilting optics 3: beam expanding and collimating optics 4 (in mount): calibration target 5: cameras

a lens. With this method, the relative position in all three translational axes and three rotational axes between the two cameras can be estimated with obtained with low uncertainty and high precision.

The magnification of the imaging system is 1.47 and the object plane is 350 mm away from the side wall of the water channel, which is longer than the working distance of any available macro lens. Therefore, a telephoto lens was used in the experiment, with the lens located just outside the water channel, and the camera positioned about 500 mm away from the lens, as shown in figure 1(b). This optical setup greatly reduces the numerical aperture of the imaging system. Therefore, a large aperture lens, Nikon 400mm f/2.8, is used for the optical PIV imaging system. To increase the signal to noise ratio of the PIV images and at the same time ensure the measurement volume is adequately seeded, a selective seeding device is used so that only the centerline of the tunnel is seeded. The PIV images are analysed using an in-house parallel multigrid/multipass cross-correlation PIV algorithm (Soria, 1996) with a final interrogation window size of 16 viscous lengths in the streamwise direction and 4 viscous lengths in the wall normal direction. The processed PIV velocity fields are corrected for lens distortion using the method described by Sun et al. (2021).

3 RESULTS

More details of the experiment will be presented in the conference paper, including a detailed characterisation of the flow, as well as the first- and second-order statistics of the velocity fields in the channel flow.

4 REFERENCES

Monty JP and Chong MS (2009) Turbulent channel flow: comparison of streamwise velocity data from experiments and direct numerical simulation. *Journal of Fluid Mechanics* 633:461–474

Schultz MP and Flack KA (2013) Reynolds-number scaling of turbulent channel flow. *Physics of Fluids* 25:025104

Soria J (1996) An investigation of the near wake of a circular cylinder using a video-based digital cross-correlation particle image velocimetry technique. *Experimental Thermal and Fluid Science* 12:221–233

Sun B, Shehzad M, Jovic D, Cuvier C, Willert C, Ostovan Y, Foucaut JM, Atkinson C, and Soria J (2021) Distortion correction of two-component two-dimensional piv using a large imaging sensor with application to measurements of a turbulent boundary layer flow at $re_\tau = 2386$. *Experiments in Fluids* 62:183

Vinuesa R, Noorani A, Lozano-Durán A, Khoury GKE, Schlatter P, Fischer PF, and Nagib HM (2014) Aspect ratio effects in turbulent duct flows studied through direct numerical simulation. *Journal of Turbulence* 15:677–706

TECHNICAL SESSION 16
SCALAR MEASUREMENT

Chaired by Di Peng

Post Processing of Fast Response PSP for Blast Wave Testing

Mark K. Quinn*[1], Elliott Nunn[2], John Adams[3], Mike Tanner[3], Steve Goulding[3], Alex Cardy[3], Michael Garrard[3], Neil Stokes[4], David A. Roberts[5], Terry Jewson[6]

1: Senior Lecturer, School of Engineering, University of Manchester, United Kingdom
2: PhD Candidate, Department of Chemistry, University of Manchester, United Kingdom
3: Various roles, Atomic Weapons Establishment, Aldermaston, United Kingdom
4: Optical Systems Manager, Aircraft Research Association, Bedford, United Kingdom
5: Specialist, Aircraft Research Association, Bedford, United Kingdom
6: Instrumentation specialist, Spurpark Ltd.
* Corresponding author: mark.quinn@manchester.ac.uk

Keywords: Pressure-Sensitive Paint, PSP, Shock tube, Unsteady flow

ABSTRACT This paper shows the application of fast response PSP to explosively driven blast wave testing. A sprayable polymer ceramic fast response PSP was applied to an aluminium disc before being coated with PtTFPP as the active luminophore. The disc was then exposed to a blast wave and the response was measured using a high-speed video camera. The PSP measured the transit of the incident shock wave clearly, albeit with a slight response delay following the instantaneous change in pressure. A method for improving the temporal response using pixelwise temporal deconvolution is demonstrated to improve the response to transient blast waves at the expense of increased spatial noise.

In 2001 Winslow et al. [1] demonstrated a dynamic correction technique which highlighted the benefits of correcting PSP non-unity frequency response. Winslow showed that after characterisation of the frequency response using a physics-based model, a transfer function could be derived which corrected the magnitude and phase response of the PSP output. Later work by Funderburk & Narayanaswamy [2] used a similar frequency response correction scheme that relied on modelling the mass diffusion through the PSP substrate. Liu et al. [3] and Numata et al. [4] showed corrections to PSP frequency response by including both the camera exposure time influence and the physical frequency response of the PSP. The dynamic correction of PSP results for non-unity gain and phase lag across a wide range of frequencies is not often performed. In most cases the frequency response is not *actually* known or measuring it is the aim of the experiment. For different substrates, paint solvents, ceramic fillers, paint thicknesses or even different painters, the frequency response characterises may be different.

In this study, the PSP is exposed to an explosively driven blast wave emanating from a shock tube followed by an immediate decay. The PSP response is imaged at 96kHz using a high-speed camera. Rather than trying to evaluate either a frequency response, or estimate a transfer function, a simpler way to consider this transfer is to take a step change and convolve it with a convolution kernel that spreads out a step response.

If, as is the case in this study, a step change is expected, an estimate of the convolution kernel required to turn a step change into a first-order response can be made. The response of the PSP extracted around the pressure taps shown in Figure 1 c) is given in Figure 1 a). The theoretically instantaneous change in pressure is spread out in time in the PSP response across approximately 5 frames. An equivalent exponential response that reaches 95% of its final value within 5 frames would require a time constant of approximately $\tau \approx 5/3$. Deconvolving the PSP pixel time history with the exponential response is applied to every pixel in the PSP video as shown in Figure 1 b, d, and f). This temporal deconvolution has the effect of sharpening discontinuities; however, there is an increase in spatial noise. An increase in spatial noise is not unexpected as the high frequency components in the PSP signal have been significantly amplified; however, the impact of this noise can be mitigated with an edge preserving spatial filter applied on the recovered images.

The deconvolution method shown in this study is not appropriate for studies of quasi-steady flows (such as those in cavities) as the frequency and phase response of the signal will be significant and any dynamic frequency correction scheme will be required to map the attenuation and lag correctly for all frequencies. However, as this study is primarily focused on the shape of the pressure profile for a transient event, the frequency components required to *create* that event are not important, enabling such a simple correction to be effective.

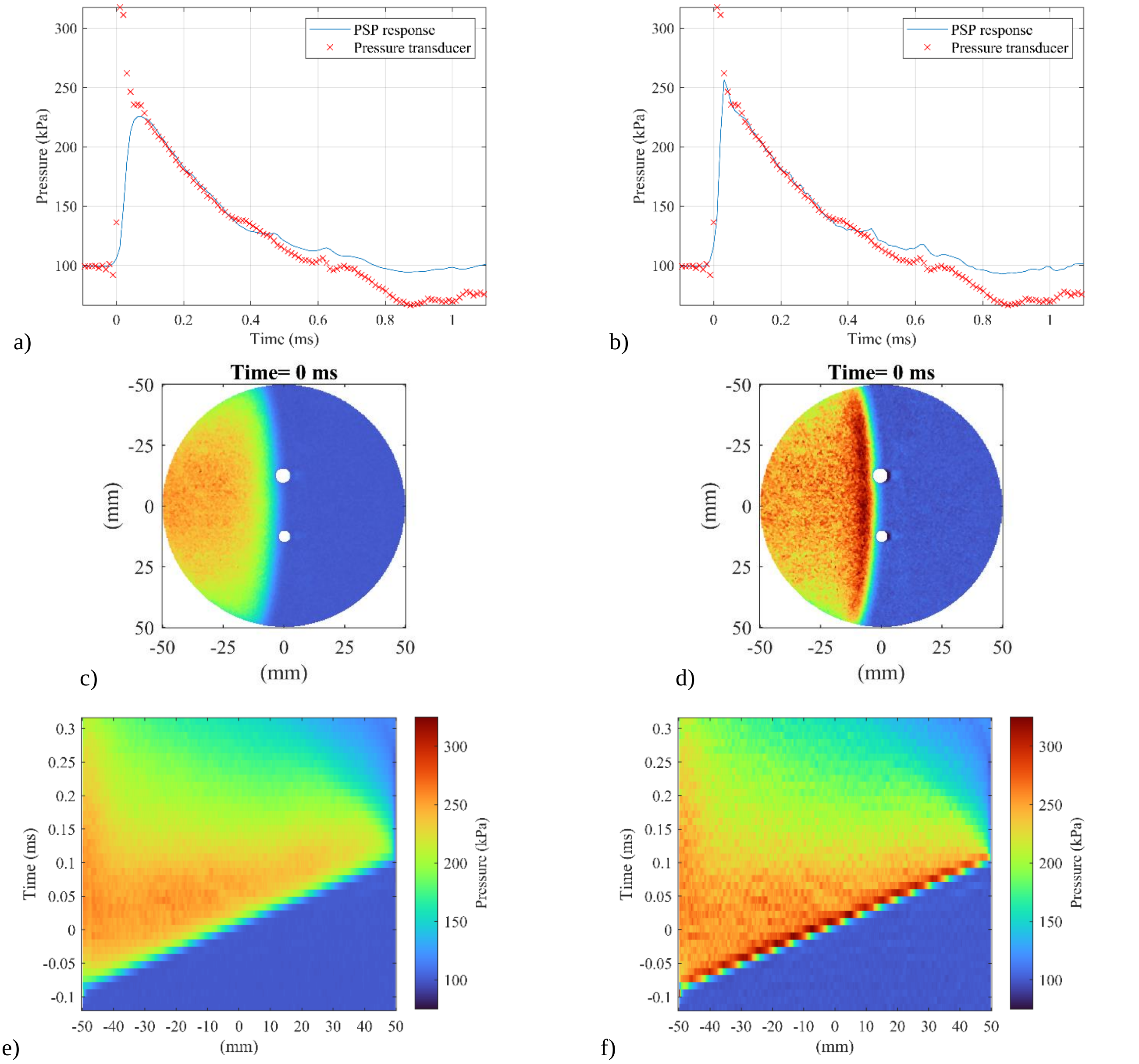

Figure 1. a) standard PSP processing vs pressure transducer, b) temporally deconvolved PSP response vs pressure transducer, c) standard PSP processing image at t_0, temporally deconvolved PSP processing image at t_0, e) standard PSP processing *x-t* diagram, and f) temporally deconvolved *x-t* diagram

REFERENCES

[1] N. A. Winslow, B. F. Carroll, and F. M. Setzer, ‘Frequency response of pressure sensitive paints’, *1996 Fluid Dynamics Conference*, pp. 1–9, 1996, doi: 10.2514/6.1996-1967.

[2] M. L. Funderburk and V. Narayanaswamy, ‘Spectral signal quality of fast pressure sensitive paint measurements in turbulent shock-wave/boundary layer interactions’, *Exp Fluids*, vol. 60, no. 10, pp. 1–20, Oct. 2019, doi: 10.1007/S00348-019-2799-X/FIGURES/17.

[3] X. Liu *et al.*, ‘Resolving dynamic features of kilohertz pressure fluctuations using fast-responding pressure-sensitive paint: measurement of inclined jet impingement’, *Exp Fluids*, vol. 63, no. 4, pp. 1–22, Apr. 2022, doi: 10.1007/S00348-022-03419-4/FIGURES/23.

[4] D. Numata, S. Fujii, H. Nagai, and K. Asai, ‘Ultrafast-Response Anodized-Aluminum Pressure-Sensitive Paints for Unsteady Flow Measurement’, *AIAA Journal*, vol. 55, no. 4, pp. 1118–1125, Jan. 2017, doi: 10.2514/1.J054886.

Velocity and Concentration measurements of a jet submitted to Atmospheric Boundary Layer

Carlo Sanapo[1,*], Sara G. Ruiz[1], Charline Fouchier[1,*], Sebastien Courtiaud[2], and Delphine Laboureur[1]
1: von Karman Institute for Fluid Dynamics, Belgium
2: CEA, DAM, Gramat, France
Correspondent author: carlo.sanapo@vki.ac.be

Keywords: underexpanded jet, dispersion, concentration, light extinction spectroscopy, LS-PIV

1 Abstract

Gas jet dispersion and concentration can pose significant safety hazard if not properly managed. When gas is dispersed from a jet, it can form a flammable or explosive mixture if the concentration of gas in the air is within certain limits. Being able to properly understand the dispersion of such release into atmosphere, submitted or not to cross-flow, is of primarily importance to properly design protection systems and facility layouts. Experimental results of velocity fields have already been obtained in literature [1, 6]. However, these studies focus on a specific set of tank pressure, nozzle geometries and cross flow conditions that are not always representative of an actual leakage from a pressurized reservoir into atmosphere. Therefore, a complete experimental dataset characterizing the dispersion phenomena of such a jet, both in velocity and concentration, when submitted to atmospheric wind conditions is not yet available.

As part of a collaboration with the CEA Gramat, the von Karman Institute is continuing research efforts towards the development of high quality optical measurement techniques for the measurement of the velocity and concentration fields of a supersonic jet submitted to cross-flow, especially far from the release point, in the self-similar region. Such measurements have already been tried on a supersonic jet without cross-flow and with a uniform velocity low speed cross-flow [3], but never when submitted to an atmospheric boundary layer cross-flow. The objective of this work is therefore to fill the gap, as well as to further improve the concentration characterization by comparing two different techniques; Mie Scattering and Light Extinction Spectroscopy (LES).

Measurements are made in the VKI L-1B wind tunnel. This tunnel generates a flow through 4.2 m diameter contra-rotating fans, driven by a variable speed DC motor of 580 kW. As shown in Fig. 1, the rectangular test section ($3 \times 2 \times 20$ m) can be adapted with several types of roughened floors to allow for the growth of a turbulent boundary layer (BL) similar to the lower part of the atmospheric neutral BL. Flow velocity can be varied between 2 and 50 m/s making it one of the most powerful facilities of this type as far as Reynolds simulation is concerned.

Figure 1: Atmospheric boundary layer simulation in L1-B wind tunnel [2]

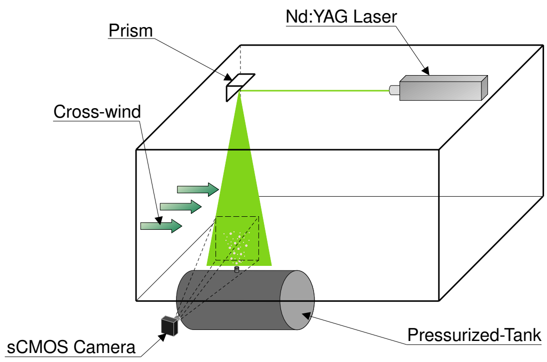

Figure 2: LS-PIV experimental setup within L1-B wind tunnel

Due to the requirements of a large field of view to measure the dispersion in the self-similar region (about $100D \times 100D$ where $D = nozzle\ diameter$, see Fig. 4), LS-PIV (Large-Scale Particle Image Velocimetry) has been successfully applied to measure the velocity field. Fouchier compared standard PIV and LS-PIV measurements of a 7 bar 5 mm under-expanded jet and showed a very good agreement [3]. This technique will therefore be applied to characterize the jet submitted to a BL cross flow. A schematic representation of the experimental setup used is shown in Fig. 2.

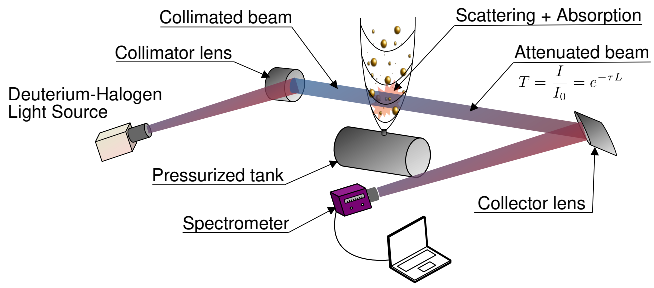

Figure 3: Schematic of LES optical setup and principle

Figure 4: LS-PIV of a jet release from a 2 bar pressurized tank under 5 m/s cross-wind condition

For the concentration, a technique based on the Mie Scattering was adapted and allowed a first experimental assessment of a relative concentration field [3]. The Mie-Scattering technique analyzes images to retried a relative concentration field, assuming that, under certain conditions, the light scattered by particles within a certain volume is proportional to the number of particles within this volume. It is a non-intrusive technique that uses the same set of experimental images produced by the LS-PIV campaign. The image processing allowing to retrieve the concentration was adapted from Naibouglu [5] by Fouchier [3]. However, differences in the evolution of the scaled concentration with different nozzle sizes indicated the need for further improvement of the technique, especially with regards to the correct determination of the reference concentration. Therefore in this work, the relative concentration maps measured by the Mie Scattering technique will be compared to absolute concentration measurements integrated along several lines located at different distances from the jet nozzle exit using LES.

The LES technique relies on the measurement of the transmission spectrum of a collimated light beam passing through the particle laden flow. The intensity of the transmitted spectrum can be converted into volumetric size and concentration distributions. This measurement is possible thanks to a data processing method based on the regularized solution of an ill-conditioned inverse problem [4]. This technique has successfully been applied to several types of flows with similar concentration and particle size as the standard PIV seeding generator used in this study [4]. A schematic of the LES principle and a simplified setup is presented on Fig. 3. It consists of a light source with fibre optics output (OceanOptics DH-2000); at the tip of the fibre an online beam collimator is attached, which decreases the initially very large divergence light beam and deviates it by 90° into the jet. The jet are produced by a pressurized tank equipped by a 5 mm cylindrical nozzle. A seeding generator is connected directly to the tank, as well as the main pressurized air line. Downstream the jet a collector lens ($f = 15$ mm) redirects the beam into a spectrometer. This setup is used to measure the particle size and concentration for different jet exit pressures as well as different heights from the nozzle exit.

The work that will be presented at the conference will focus on a 5 mm nozzle set a 2 bar pressure, and will investigate the effect of a 5 m/s wind on the velocity and concentration profiles. Furthermore, the concentration will be assessed through the two techniques (i.e. Mie Scattering and LES). Discussion on the advantages and drawbacks of each techniques will be proposed.

References

[1] Steven J Beresh, John F Henfling, Rocky J Erven, and Russell W Spillers. Penetration of a transverse supersonic jet into a subsonic compressible crossflow. *AIAA journal*, 43(2):379–389, 2005.

[2] Boris Conan. *Wind resource accessment in complex terrain by wind tunnel modelling.* PhD thesis, Orléans, 2012.

[3] Charline Fouchier. Investigation of the pollutant dispersion driven by a condensed-phase explosion in an urban environment. 2020.

[4] Imre Tamas Horvath. Development and applications of the light extinction spectroscopy technique for characterizing small particles. 2015.

[5] Güneş Nakiboğlu, Catherine Gorlé, István Horváth, Jeroen van Beeck, and Bert Blocken. Stack gas dispersion measurements with large scale-piv, aspiration probes and light scattering techniques and comparison with cfd. *Atmospheric environment*, 43(21):3396–3406, 2009.

[6] TH New, TT Lim, and SC Luo. Effects of jet velocity profiles on a round jet in cross-flow. *Experiments in Fluids*, 40:859–875, 2006.

Evaluation of a temperature response time of a heat resisting TSP film

Satoshi Someya[1*] , Jung Juyong[1], Shimpei Saito[1], Soumei Baba[1] and Naoki Takada[1]
1: National Institute of Advanced Industrial Science and Technology, Japan
* Correspondent author: s.someya@aist.go.jp

Keywords: Temperature sensitive paint, phosphor, Heat transfer

ABSTRACT The temperature sensitive paint method (TSP) is a useful measurement approach to evaluate temperature from a cryogenic temperature to a high temperature over 1000 degrees. An inorganic phosphor TSP was painted on a micro scale ITO heater on a slide glass. The response of TSP to a short pulse heating of the thin micro heater was evaluated. The phosphorescence intensity decreased after the heating power was added to the heater with a certain delay. We assumed the temperature of the heater became maximum when the heating power became maximum. The time discrepancy between the moment at a maximum heating power and the moment at a lowest phosphorescence intensity was defined to the time delay of the TSP. The shortest time delay was 7μs. The fast response TSP for a high temperature measurement was successfully implemented.

1 Introduction

Temperature-sensitive paints (TSP) have been used in many fields in recent years, such as combustors, aircraft, and boiling heat transfer surfaces. Compared to temperature-sensitive liquid crystals, TSP has a wider temperature measurement range and no dependence on the measurement view angle. Infrared cameras have been remarkably developed in recent years, and their range of application has expanded to include the measurement of surface temperature distribution behind a flame, and they have the advantage of being a completely non-contact, non-invasive measurement method that requires no sensor material. However, there are some disadvantages, such as the inability to use TSP at temperatures lower than -40°C, and the influences of presence of a high-temperature heat source in front of the surface to be observed, which may affect measurement accuracy. TSP can be used in a wide range of temperatures from cryogenic temperatures to high temperatures exceeding 1000°C. It has the advantage of being able to measure the temperature of the area where the sensor material is located, regardless of the measurement environment, without being affected by red heat from the surrounding area. However, TSP has also some difficulties, an effect on the flow-field by a coating of the sensor material, the sensor film itself may affect the heat transfer performance, causing a delay in heat transfer and slowing down the temperature distribution(1). In TSP, temperature sensitive metal complex dyes are often applied using a polymer binder. There are reports of sub-micrometer-thick or single-molecule films, and it seems possible to reduce the delay to a relatively small amount. However, these materials have low heat resistance and are not suitable for use at high temperatures exceeding 100°C. Therefore, it is difficult to use them for basic heat transfer research such as boiling of water at ambient pressure. Inorganic phosphors, which are used at temperatures of several hundred degrees Celsius, can be used at temperatures above 100 degrees Celsius because of their high heat resistance. However, the particle size of phosphors is sub-micrometer for small particles and 5 to 8 μm for large ones, so there are certain restrictions on thin-film production. In this study, inorganic phosphors were used as sensor materials to form the thinnest possible TSP films, and their time response was evaluated.

2 Experimental Setup

As shown in Fig. 1, the test apparatus for response evaluation was a heated surface with sputtered ITO film coated with TSP, and temperature changes were measured when the ITO film was heated by applying a short-time high-current pulse to the film. The TSP was excited by a 390-nm LED, and the phosphorescence intensity change was visualized by a high-speed camera. The light source, camera, and a wave generator for heating were synchronized, and the delay was evaluated by analyzing the response of the TSP film on ITO glass during pulse heating. The ITO film was made in a pattern of 20 μm width and 40 μm spacing, with a resistance value of approximately 30 Ω.

The ITO film was heated by applying a current of 80 to 140 V and a maximum of about 5 A. The heating pulse width per pulse was about 100 ms. The heating pulse width was 100 to 200 μs per heating pulse, and the heating repetition frequency was set at 2 Hz to prevent the entire sample from heating up. Fig. 2 shows an example of a timing chart of the system operation control. Following the control pulse, the rectangular wave that controls the timing and length of heating is generated by the wave generator, and power for heating is supplied through the amplifier. Due to the delay in amplifier operation, the heating pulse rises approximately 100 μs after the green colored control pulse in fig.2. Although the control signal is a rectangular wave, the actual applied power has a dull waveform as shown in the yellow line in fig.2. Shortly before the maximum heating power, the motion control pulses for the camera and LED light source were generated; the LEDs emitted light with a pulse width of 200 μs to illuminate the sample, during which time 50 images with a resolution of 256 x 88 pixels were acquired at a capture rate of 200000 images per second. The exposure time per image was 2.1 μs. The spatial resolution of the observed images was 1.05 μm/pixel. Although TSP measurement with such a high spatio-temporal resolution has not been reported in the past, this study realized ultra-high resolution and high-speed sampling in order to evaluate the response delay with high accuracy. The inorganic phosphors are highly heat-resistant and stable, so they do not deteriorate at all even under the strong excitation that makes this high-speed, high-resolution imaging possible. In addition, inorganic phosphors have higher luminescence intensity than metal complexes, etc., enabling the acquisition of images with a high signal-to-noise ratio.

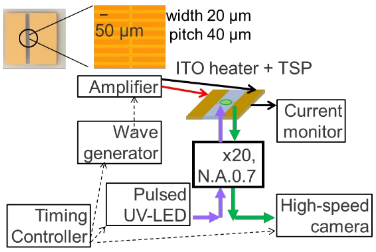

Fig. 1 Schematics of experimental setup

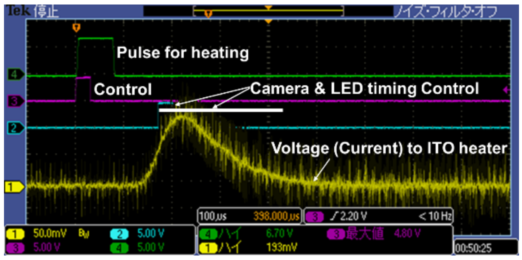

Fig.2 An example of a timing chart

Table.1 TSP layers formed at different conditions

Case	Rotating speed [rpm]	Concentration [relative]	Thickness [μm]	Delay [μs]
A	3500	α	3.5	50.8
B	1500	α	7.0	90.6
C	6000	α	2.0	26.5
D	3500	$1/2\alpha$		7.1
E	3500	$1/4\alpha$		7.5
F	3500	$1/8\ \alpha$		5.6

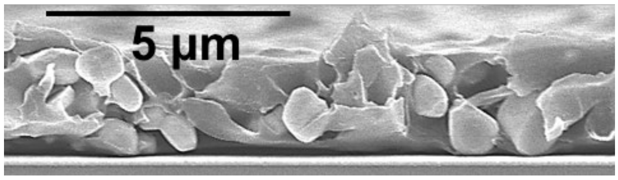

Fig. 3 A SEM image of the TSP layer. (Case C)

3 Results and Discussions

In this study, ZnO:Zn was used as the inorganic phosphor. The spectra and thermosensitivity vary slightly depending on the manufacturer, but this study reports results using ZnO:Zn with an average particle size of 2.5 to 3 μm, manufactured by Phosphor Technology. The brightness of the luminescent particles is proportional to the square of the particle size, so the smaller the particle size, the darker the luminescence. However, when the particle size is large, it is in principle impossible to reduce the thickness of the TSP film. Therefore, in this study, we attempted to reduce the size of ZnO:Zn as much as possible by using a 0.3 mm grinding ball. The milling conditions were the same in all cases. The phosphor particles were uniformly dispersed in the heat-resistant resin binder at the same time as the milling, and the TSP films were formed using a spin coater. The heat-resistant resin binder concentration and spin coater speed were used as parameters for film formation. For the binder concentration, the weight ratio of phosphor, resin diluent, and heat-resistant resin solution under the standard condition (concentration α) was 0.47 : 0.20 : 0.33. The diluent was added to prepare 1/2~1/8 concentration conditions. Fig. 3 shows a cross-sectional SEM image of the deposited TSP film (Case C). The phosphor particle diameter was approximately 1.0 μm, and the thickness of the TSP film in this case was approximately 2.0 μm. A layer of one or two phosphor particles is fixed by resin. The deposition conditions and the thickness of the film measured after deposition are summarized in Table 1. Due to the limitation of space, the details are omitted but will be explained in the presentation.

4 Summary

In this study, a thin film TSP using the inorganic phosphor ZnO:Zn was prepared, and measurement with a high spatio-temporal resolution of 1 μm and a sampling rate of 200,000 samples/second was achieved. The heat transfer delay due to the application of the film to the measurement surface was evaluated. The delay was 7 μs for the film with a reduced amount of binder resin, confirming the fast response.

5 REFERENCES

- Nagai, H., Ohmi, S., Asai, K., Nakakita, K. (2008). Effect of temperature-sensitive-paint thickness on global heat transfer measurement in hypersonic flow. Thermophysics and Heat Transfer, 22-3, 373-381.

Investigation of simultaneous measurement of air temperature and velocity using cold-wire and hot-wire

Hao Wang [1,*] ,Junjie Liu [2] ,Nan Jiang[1]
1: School of Environmental Science and Engineering, Tianjin University, China
2: Tianjin Key Laboratory of Indoor Air Environmental Quality Control, Tianjin University, China
* Correspondent author: wanghao_fm@tju.edu.cn

Keywords: Hot wire, Cold wire, Thermal boundary layer, Simultaneous measurement

ABSTRACT Due to the excellent frequency response of hot-wire anemometer (HWA) ,it is widely used in experimental fluid mechanics.But like all instruments that measure by heat transfer, HWA is easily affected by the ambient temperature fluctuations. In order to minimize the measurement error, accurate and high-frequency ambient temperature measurement and suitable correction methods are necessary. High spatial resolution and high temporal resolution temperature measurements are difficult. Cold-wire is one of the few instruments technique that can provide high frequency, fluctuating temperature measurements. In this study, a calibrator that controls both air temperature and velocity was first built and cold wires of different diameters and aspect ratios were systematically studied to determine the effect of these factors on the measurement of ambient temperature fluctuations. The effects of various factors（hot-wire heat ratio, distance between cold and hot wires, temperature correction methods）on simultaneous instantaneous fluctuating velocity and temperature measurements were also investigated.

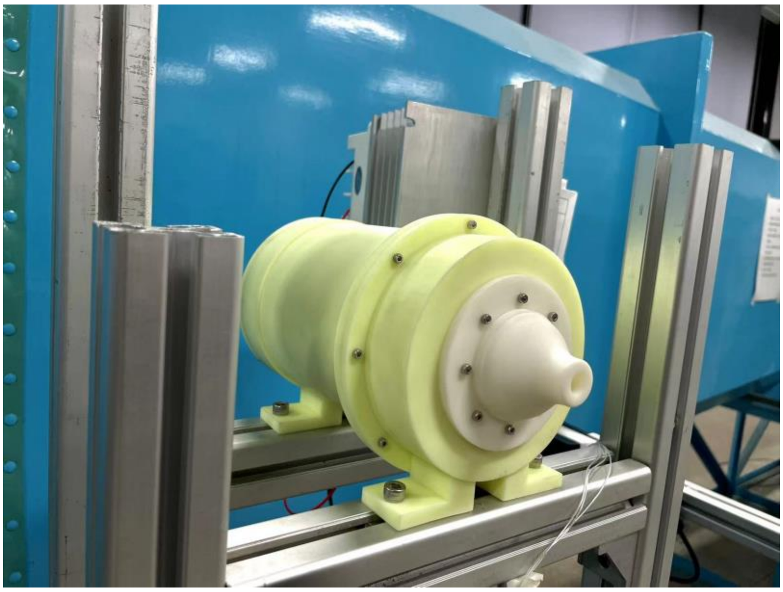

Figure 1. Calibrator

Based on the experimental results of simultaneous measurement of cold wire and hot wire, a correction method for real-time temperature correction of hot wire is proposed. This method is suitable for the strong temperature gradient in the flow field. A 4-meter-long plate is placed in a direct current wind tunnel at Tianjin University. There are a series of proportional–integral–derivative (PID) heating devices at the bottom of the plate, and the temperature of the surface of the plate can be precisely controlled. The PID controller can maintain the temperature fluctuation within ±0.1K. Hot wires and cold wires were used to measure the velocity boundary layer and thermal boundary layer of the plate with friction Reynolds number ranging from 1000 to 1800. Due to the existence of a strong temperature gradient, the measurement results of the hot wire will have a large temperature drift. The temperature fluctuation measured by the cold wire and the temperature correction method can well correct this drift, so as to truly restore the actual velocity fluctuation in the boundary layer.

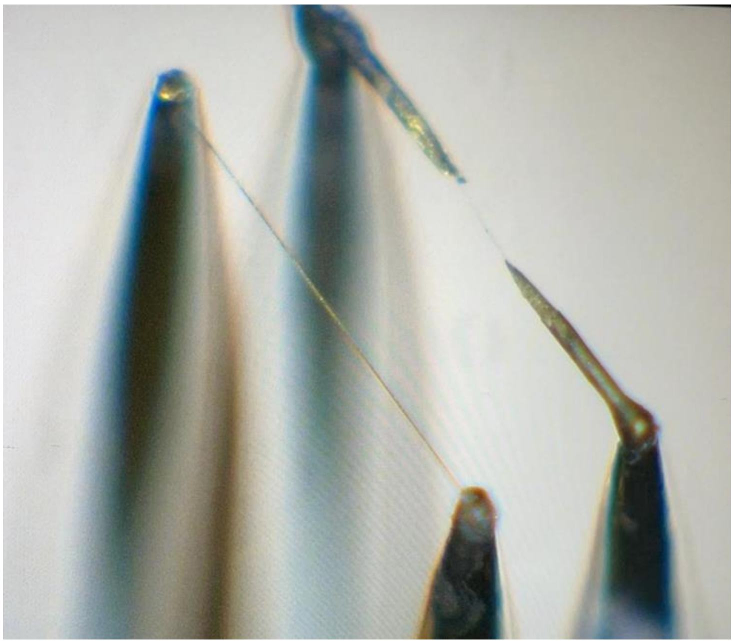

Figure 2. Cold-wire and hot-wire

TECHNICAL SESSION 17
COMPRESSIBLE FLOWS

Chaired by Qingqing Ye

Three-Dimensional Density Measurement around a Hayabusa-type Re-entry Capsule Model

Masato Yamagishi[1*], Yusuke Hirose[2], Masanori Ota[1],
Kiyonobu Ohtani[3], Hiroki Nagai[3]
1: Graduate School of Engineering, Chiba University, Japan
2: Dept. Mechanical & Electronic Engineering,
Tokyo Salesian College of Technology, Japan
3: Institute of Fluid Science, Tohoku University, Japan
* Correspondent author: masa0326yama@chiba-u.jp

Keywords: BOS technique, Three-dimensional measurement, Ballistic range, Hayabusa-type capsule

ABSTRACT Three-dimensional density measurement around a Hayabusa-type re-entry capsule model using the Background Oriented Schlieren (BOS) technique is carried out in the ballistic range at the institute of Fluid Science, Tohoku University. A Hayabusa-type re-entry capsule model with a diameter of 15 mm is used for a projectile, and the Mach number was 1.20. A method of model Position and Pose detection from BOS images was proposed for a capsule model, and unsteady flow field measurement around a free-flight test model was conducted. From the results, we succeeded in measuring the three-dimensional density distribution around a capsule model and visualizing the detailed structure in the wake region.

1 OBJECTIVE

The BOS (Background Oriented Schlieren) technique proposed by Meier [1] enables us to take a quantitative density measurement of a flow field with computer-aided image analysis. In the past study, we succeeded in three-dimensional measurement around a free flight sphere using the Simultaneous multi-angle BOS measurement system in a ballistic range. However, if this method was applied to a re-entry capsule model, it is necessary to obtain the position and pose of free-flight test model at the time of measurement. Therefore, the purpose of this study is to detect the position and pose of the capsule model from the BOS images and to measure the density distribution around the model.

2 METHOD

2.1 BOS technique

When the light ray is bent due to the density gradient in the medium, the background image is captured at the image sensor with displacement Δh. In most cases, Δh is expressed by evaluating its center ray as in Eq. (1)[2]

$$\frac{1}{n_0}\int \frac{\partial n}{\partial r} dl = \frac{l_b + l_c}{l_i l_b}\Delta h \tag{1}$$

In this study, we use the simultaneous multi-angle BOS measurement system to obtain the Δh from different directions and reconstruct the density distribution by ART (Algebraic Reconstruction technique) and SOR method. [2]

2.2 Model Position and Pose detection method

The test model in the BOS image is blurred due to defocus. Therefore, in the proposed method, we use the brightness information in the image to optimize the evaluation function. The proposed method measures the model position and pose from 2 cameras by processing three steps as follows.

(1) The shape of the model is imported by the STL (Standard Triangulated Language) model.
(2) Calculate the simulation image (Eq. (2)) from the camera parameters and initial conditions.

$$Simulation\ image(i,j) = \begin{cases} 0 & \text{model} \\ f(\text{exp.}) & \text{elsewhere} \end{cases}$$
$$f(\text{exp.}) = \sum_{j}^{y}\sum_{i}^{x}\frac{Experimental\ image(\,i,\ j)}{xy} \tag{2}$$

(3) Optimize the model position and pose to maximize the evaluation function (Eq. (3)) while iteratively generating simulation images.

$$G = \sum_{n}^{2} \sum_{j}^{y} \sum_{i}^{x} |Exp.image(i,j)_n - Sim.image(i,j)_n| \tag{3}$$

3 EXPERIMENT

The experiment was conducted using the ballistic range at Institute of Fluid Science (IFS), Tohoku University. Eleven digital cameras were used for the simultaneous multi-angle BOS measurement system (Fig. 1). Hayabusa-type capsule model with a diameter of 15 mm was used for the experiment and its flight speed was Mach 1.20. The temperature and pressure of the atmosphere are 300 K and 101.3 kPa.

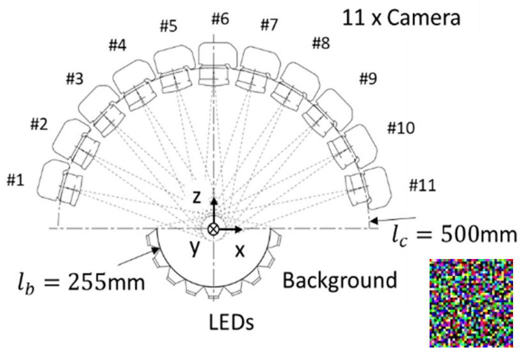

Figure 1. Multi-angle measurement system

4 RESULTS

Fig. 2 shows the reconstructed density distribution around a capsule model. Since the model was out of the measurement area, cam#1 and #11 were excluded from the analysis. Therefore, reconstruction was performed from nine cameras. The model flighted 10 degree down around the x-axis and 2 degree left around the z-axis, however, since the velocity vector of the model is not measured, the angle of attack cannot be calculated. From Fig. 2, we can confirm a symmetrical density distribution in the y-z plane inside the recirculation region.

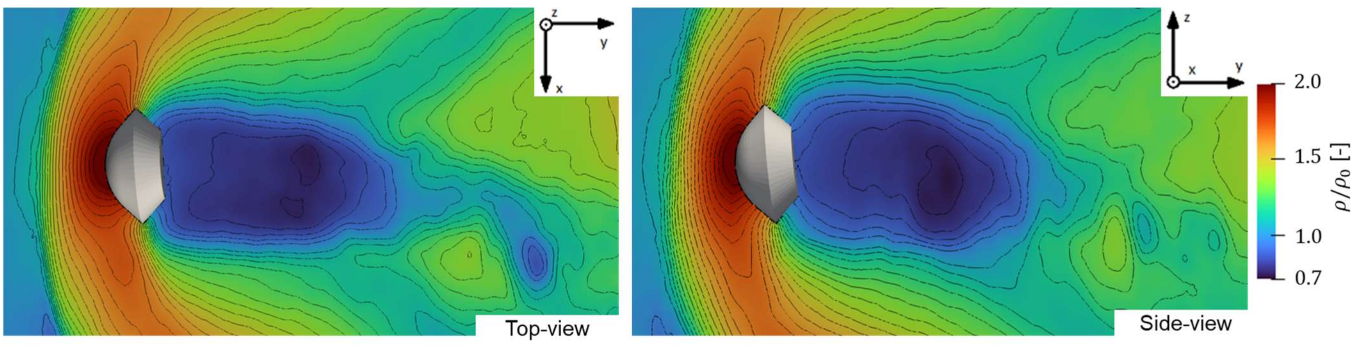

Figure 2. Reconstructed density distribution on x-y plane and y-z plane

CONCLUSION

To capture the flow field around a free-flight test model at high-speed, the simultaneous multi-angle BOS measurement system was constructed in the ballistic range at the Institute of Fluid Science, Tohoku University. We proposed the model position and pose detection method, and the density distribution around the free-flight test model at the speed of Mach 1.20 was successfully visualized.

REFERENCES

[1] G. E. A. Meier (2002). Computerized background-oriented schlieren. Experiments in Fluids, 33, 181-187.

[2] Y. Hirose, K. Ishikawa, Y. Ishimoto, T. Nagashima, M. Ota, S. Udagawa, T. Inage. K. Fujita, H. Kiritani, K. Fujita, K. Ohtani, H. Nagai (2019). The quantitative density measurement of unsteady flow around the projectile. Journal of Flow Control, Measurement & Visualization, 7

Advanced visualizations for transonic buffet understanding

Alessandro D'Aguanno[1,*], Ferry Schrijer[1] and Bas van Oudheusden[1]
1: Dept. of Flow Physics and Technology, TU Delft, The Netherlands
* Correspondent author: a.daguanno@tudelft.nl

Keywords: Transonic buffet, supercritical airfoil, PIV, schlieren, BOS

1 BACKGROUND

The flight envelope of an aircraft operating at high subsonic velocities is bounded by several limitations, one of these consists of the wing experiencing oscillations of a shockwave for a certain range of flow conditions. This phenomenon is referred to as transonic buffet and it may ultimately result in violent structural oscillations of the wing (the so-called buffeting). For Type II buffet (Giannelis et al. 2017), there is a simultaneous oscillation of the shockwave and pulsation of the separated area on the suction side of the airfoil, these flow features are visualized in a schlieren image in Fig. 1 (left). Although there is no univocal explanation of transonic buffet yet, according to several studies the shockwave oscillation results from the propagation of downstream propagating vortices in the separated area and upstream traveling pressure waves (UTWs), generated at the trailing edge to satisfy the Kutta condition (Lee, 1990). From an experimental point of view this phenomenon is generally characterized by using high speed schlieren, laser doppler velocimetry, pressure transducers (Jacquin et al. 2009) and more recently particle image velocimetry (Hartmann et al, 2013). In this study a variety of optical non-intrusive measurement techniques and processing tools will be used to characterize transonic buffet.

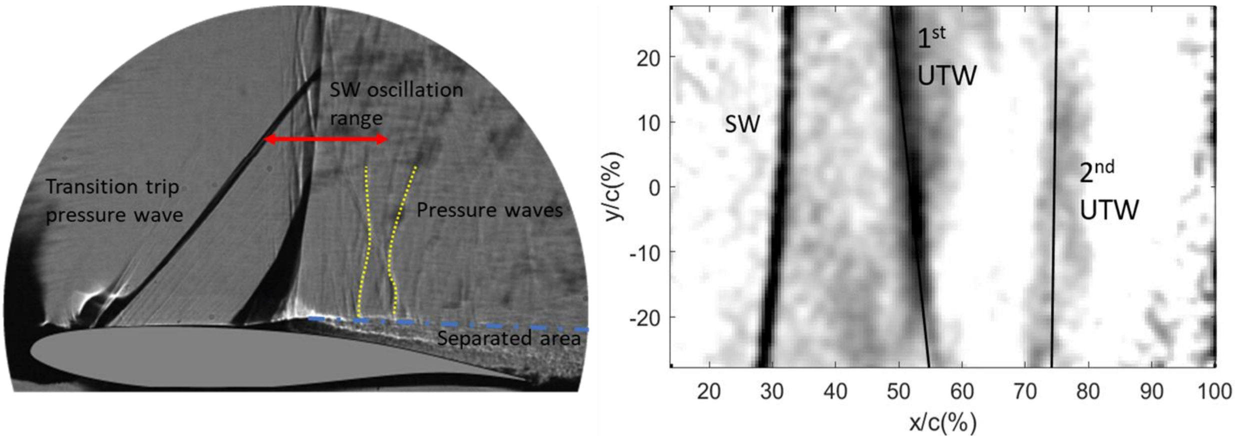

Figure 1. Comparison of a schlieren image in a vertical-chordwise measurement plane (left) and a BOS image in a spanwise-chordwise oriented measurement plane (right).

2 METHODOLOGY

The experiments have been carried out in the transonic-supersonic wind tunnel of TU Delft (TST- 27) for fully developed buffet conditions (Ma=0.7, α=3.5°) on models based on the supercritical airfoil OAT15A. High speed schlieren has been used to characterize the shockwave dynamics and to qualitatively visualize the main flow features. The visualization of UTWs is difficult in view of the spanwise integration of the density gradients. These line-of-sight effects can be reduced by using background oriented schlieren (BOS) by using a spanwise-chordwise oriented view, which allows the clear detection of the shockwave and the UTWs along the span of the airfoil model (see Fig. 1, right). A quantitative visualization of the velocity field has instead been carried out by means of particle image velocimetry acquisitions in various measurement planes. For all the measurement techniques, high speed cameras have been adopted, with an acquisition frequency of 5 kHz, which is high enough to resolve the shock motion (160 Hz for this model) and to capture the propagation of UTWs.

3 SELECTION OF RESULTS

The periodicity of transonic buffet justifies the use of a phase-averaged description of this phenomenon. As an example, two phase-averaged PIV velocity fields are shown in Fig. 2, with the shockwave in its most upstream (left) and downstream position (right). Apart from the shock position, there are important differences in terms of the extent of the separated area, which is wide and originating from the shock foot in the most upstream shockwave position, while being restricted near the trailing edge area in the most downstream shockwave location. A further analysis of the data will also display an inherent asymmetry between the upstream and the downstream travel of the shock motion in terms of shock velocity, with the shockwave dwelling for longer in the most forward position.

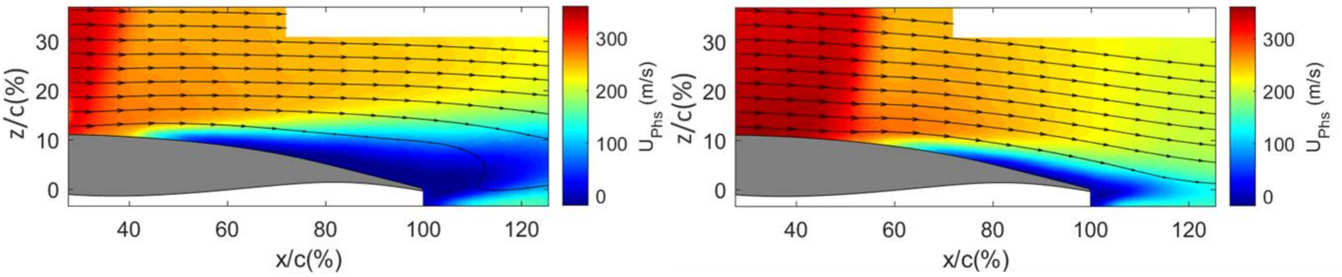

Figure 2. Phase averaged horizontal velocity field in the most upstream (left) and downstream (right) shockwave position.

By means of a proper orthogonal decomposition (POD) of the PIV data and using BOS, the main small-scale flow features considered responsible for the buffet oscillation are scrutinized, namely vortical structures propagating downstream along the suction side and upstream propagating pressure waves. In Fig. 3 the first (left) and the second (right) spatial POD modes (associated with approximately 65% of the total fluctuation energy) are shown for the streamwise velocity component. The first mode is mainly associated with fluctuations in the separated area and shockwave oscillation range, while the second expresses the temporal asymmetry between the behavior of the shear layer and of the separated area. By subtracting a subset of POD modes (11) from the PIV snapshots, the small scale details present in the velocity field are highlighted. The results of this analysis suggest that vortices created at the shock foot, which then convect into the separated region in an area detached from the airfoil, cannot be responsible for the creation of the upstream propagating pressure waves, which are well characterized with the BOS technique.

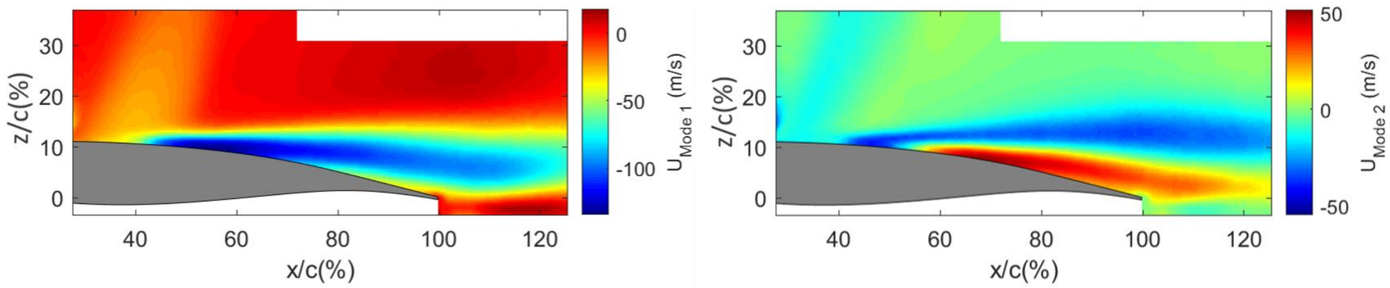

Figure 3. First (left) and second (right) spatial POD modes for horizontal velocity component.

An analysis of the BOS results will show that UTWs are produced at a frequency of about 2000 Hz, with a strength modulated by the buffet frequency (160 Hz), with the stronger waves reaching the SW close to its most downstream position and weaker in proximity of its most upstream position. The spanwise-chordwise oriented field of view will also confirm the coherence of the shockwave position along the span, while it will show that UTWs propagate with a non-zero inclination (see Fig. 1, right).

4 REFERENCES

Giannelis, N. F., Vio, G. A., & Levinski, O. (2017) A review of recent developments in the understanding of transonic shock buffet. *Progress in Aerospace Sciences* 92:39 – 84.

Lee, B. H. K. (1990) Transonic buffet on a supercritical aerofoil. *The Aeronautical Journal* 94:143 – 152.

Jacquin, L., Molton, P., Deck, S., Maury, B., & Soulevant, D. (2009) Experimental study of shock oscillation over a transonic supercritical profile. *AIAA Journal* 47:1985 – 1994.

Hartmann, A., Feldhusen, A., & Schröder, W. (2013) On the interaction of shock waves and sound waves in transonic buffet flow. *Physics of Fluids* 25(2):026101.

Visualization of Transonic Flow around Flapped Busemann Biplane Airfoil by Point Diffraction Interferometer

Masato Taguchi[1,*] Masashi Kashitani[1] and Kohei Tsuji[1]
1: Dept. of Aerospace Engineering, National Defense Academy, Japan
* Correspondent author: taguchi@nda.ac.jp

Keywords: Point Diffraction Interferometer, Transonic flow, Busemann biplane

ABSTRACT Transonic flow around a flapped Busemann biplane airfoil was visualized by means of Point Diffraction Interferometer (PDI). Several flap conditions (leading edge, trailing edge, and both edges with four flap angles for each) were investigated at transonic test flow conditions (M=0.6, 0.7 and 0.8) generated by a shock tube in order to understand the suppression effect on the normal shock wave that forms between the airfoil elements. As a result, it was observed that trailing-edge and both-edge flap configurations were effective for the suppression.

1 INTRODUCTION

Sonic boom is a phenomenon in which shock waves generated by an aircraft during supersonic flight reach the ground surface and produce loud noise. This phenomenon makes it impossible for aircraft to fly over the ground at supersonic speeds due to environmental regulations. The Busemann biplane (Busemann, 1935) is one of the candidates for the next generation of quiet supersonic aircraft that will solve this problem (Kusunose, 2007). This airfoil is designed to cancel the shock waves generated by itself between the biplane airfoil elements at a design Mach number (e.g., M = 1.7) and is expected to reduce the shock waves propagating to the ground surface. In contrast to the excellent characteristics at the design Mach number, it is known that the drag of the biplane would increase significantly at transonic Mach numbers. This is caused by the normal shock wave that forms between the airfoil elements due to choking of the flow between them. To reduce the choking flow, Yamashita et al. (2007) investigated the effect of flaps introduced at each position (leading edge, trailing edge, and both edges) by numerical simulations. They concluded that the use of trailing-edge or both-edge flaps successfully reduced the formation of the normal shock wave between the airfoil elements. Because they applied only a single flap condition, the appropriate flap conditions (i.e., flap angle and configuration) to suppress the normal shock wave for each Mach number condition were not clarified. The flow field associated with the normal shock is considered as a Shockwave/Boundary Layer Interaction (SBLI) problem, where the boundary layer developing on the airfoil surface can have a large influence on the global flow field (e.g., shock wave formation and its locus). Since reasonable prediction of the flow field is difficult using computational fluid dynamics alone, flow visualization that provides quantitative data is required.

In the present study, transonic shock tube experiments were performed with the Busemann biplane airfoil whose design Mach number is 1.7. Several flap conditions are investigated at transonic Mach numbers (M=0.6, 0.7 and 0.8). The flow field was visualized by the Point Diffraction Interferometer (PDI) as interference fringes that are equivalent to isodensity lines.

2 EXPERIMENTAL SETUP

A diaphragmless shock tube is used as an intermittent wind tunnel. The hot gas behind the shock wave generated by the shock tube is used as the test flow. The Mach numbers are set at 0.60, 0.70, and 0.80, and the Reynolds number is Re= 2.85×10^5. The airfoil model is fixed between the windows of the shock tube test section. The model has a chord length of c = 60 mm and a span of 60 mm. Three flap configurations are used: trailing edge, leading edge, and both edge flap as shown in Figure 1. Four flap angles (0.01c, 0.03c, 0.05c, and 0.07c) are used, where they are represented as displacement at the edge.

The PDI optical system is shown in Figure 2. The system consists of a 532 nm CW laser, a beam expander, a 150 mm diameter collimating lens, a concave mirror, a translucent pinhole plate, an imaging lens, and a high-speed camera (FASTCAM NOVA S12, Photron). The pinhole produces an object beam which is transmitted through the plate and a spherical diffracted beam is produced by the pinhole. This diffracted beam acts as a reference beam and produces interference fringes. Except for the pinhole plate, the system is equivalent to a typical schlieren optical system. The frame rate is 30,000 fps and the exposure time is 1/4.8 μs. Since the flow field is considered as a two-dimensional flow, the infinite interference fringes obtained by the PDI are equivalent to isodensity lines.

3 RESULT AND DISCUSSION

The flow fields associated with each flap configuration at Mach number 0.7 for flap displacement 0.05c are shown in Figure 3. For the cases of no flap and leading-edge flap, the fringes are very closely distributed in the region from the throat (i.e., smallest cross section) to the trailing edge. This indicates rapid expansion (i.e., choking) of the flow and normal shock wave formation following the expansion as the local flow velocity exceeds the speed of sound. The leading-edge flap does not suppress the vertical shock wave between the airfoil elements. In contrast, for the trailing-edge flap and both-edge flap, the fringes between the airfoil elements are relatively less, i.e., the flaps in these configurations are effective in reducing the density variation and the normal shock wave formation. This flap effect can also be seen in the other Mach number conditions. The density variation between the airfoil elements is gradually reduced as the flap displacement increases. The normal shock wave is suppressed at flap displacements of 0.05c or greater. At the same time, due to the curvature of the airfoil surface caused by the flaps, the expansion waves and normal shock waves are observed on the outside of the airfoil elements, which were not observed in the no- flap configuration.

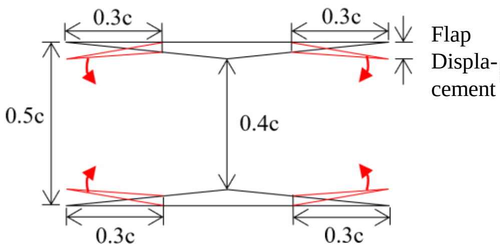

Figure 1. Wind tunnel model

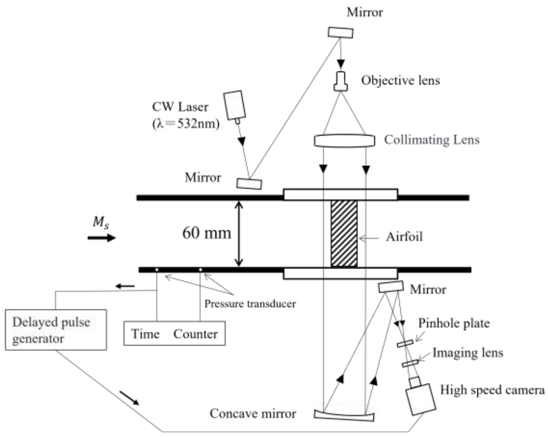

Figure 2. PDI optical system

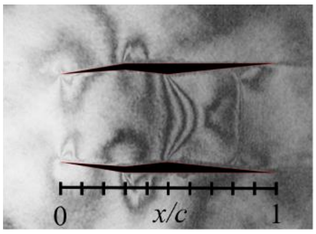

(a) no flap

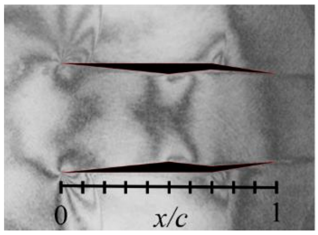

(b) trailing edge flap

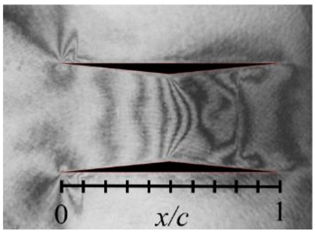

(c) leading edge flap

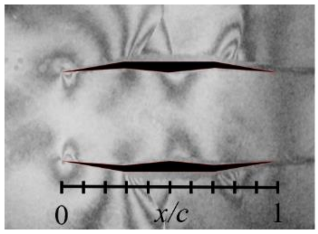

(d) Both edge flap

Figure 3. PDI images for each flap configuration (flap displacement = 0.05c)

4 REFERENCES

- Journal article: Busemann, A. (1935). Aerodynamic lift at supersonic speed. Luftfahrtforschung, 12(6), 210-220.
- Journal article: Kusunose, K., Matsushima, K., Goto, Y., Maruyama, D., Yamashita, H., & Yonezawa, M. (2007). A study in the supersonic biplane utilizing its shock wave cancellation effect. Japan Society of Aeronautical Space Sciences, 55(636), 1-7.
- Conference Proceedings: Yamashita, H., Yonezawa, M., Obayashi, S., & Kusunose, K. (2007). A study of busemann-type biplane for avoiding choked flow. In 45th AIAA Aerospace Sciences Meeting and Exhibit (p. 688).

Investigation of large-scale unsteadiness in a supersonic sidewalls-confined compression ramp flow using fast PSP

Xu Liu[1], Yingzheng Liu[1] and Di Peng[1,*]
1: School of mechanical engineering, Shanghai Jiao Tong University, China
* Correspondent author: idgnep8651@sjtu.edu.cn

Keywords: Compression ramp, Sidewall effect, Large-scale unsteadiness, Fast PSP

ABSTRACT Shock wave boundary layer interactions (SWBLIs) are common flow phenomena in the high-speed vehicles, which have significant impact on the aerodynamic performance, structural safety and start of inlet (Babinsky & Harvey, 2011). Furthermore, the low-frequency, large-scale unsteadiness in the SWBLIs has attracted much attention due to its extra potential influences such as dynamic load/heat transfer and unexpected coupling with flexible panel (Clemens & Narayanaswamy, 2014). Sidewall confinement usually encountered in the internal flow introduces complex 3D effects into the characteristics of SWBLI. Fruitful results have been achieved regarding the sidewall effect on the topology of SWBLI. Comparatively, the sidewall effect on the large-scale unsteadiness of SWBLI is still unclear, which is the main focus of this work. Surface pressure is the crucial knowledge to understand the unsteadiness of SWBLI, but the conventional discrete pressure measurement methods have limited spatial resolution, which is insufficient for investigating 3D flows. Therefore, a global pressure measurement method is demanded. Fast-responding pressure-sensitive paint (fast PSP) is a recently prevalent global pressure measurement technique with high spatial and temporal resolutions in the aerodynamic tests (Gregory et al., 2014; Peng & Liu, 2020). In this work, the SWBLI induced by a sidewalls-confined 28 °compression ramp is investigated in a Ma = 2.84, open, rectangular tunnel using fast PSP, as shown in Fig. 1(a). The floor of the test model is flush-mounted with the floor of tunnel to obtain the naturally-grown turbulent boundary layer with the thickness $\delta_0 \approx 12$ mm and two sidewalls are placed in the main flow region. The sampling rate of fast PSP measurement is set as 8,000 Hz and the spatial resolution is around 0.2 mm/pixel. The global pressure distributions on the floor reveal a dominant primary separation induced by the ramp while no remarkable corner separation, which is expected due to a much thinner boundary layer on the sidewall compared with the floor. More interestingly, separation shock feet are observed to be spanwise non-uniform and vary significantly with time, as indicated in Fig. 1(b). Proper orthogonal decomposition (POD) analysis of the intermittent region successfully extracts multi-scale modes of separation shock feet, as shown in Fig. 2. In addition to the canonical streamwise oscillation mode, many modes with higher orders in both spanwise and streamwise directions are identified, which contribute considerable unsteadiness. Among them, the spanwise high-order modes exhibit the features like the standing wave with two sidewalls acting as the fixed ends. Correspondingly, the streamwise high-order modes exhibit the features like the standing wave within the streamwise intermittent region but show less energy contributions. The pre-multiplied power spectral densities of POD coefficients show that the multi-scale modes exhibit broadband low-frequency characteristics centered at hundreds of hertz. The center frequency shifts towards higher frequencies as the spanwise and streamwise orders increase, and this trend is more notable for the increasing streamwise order.

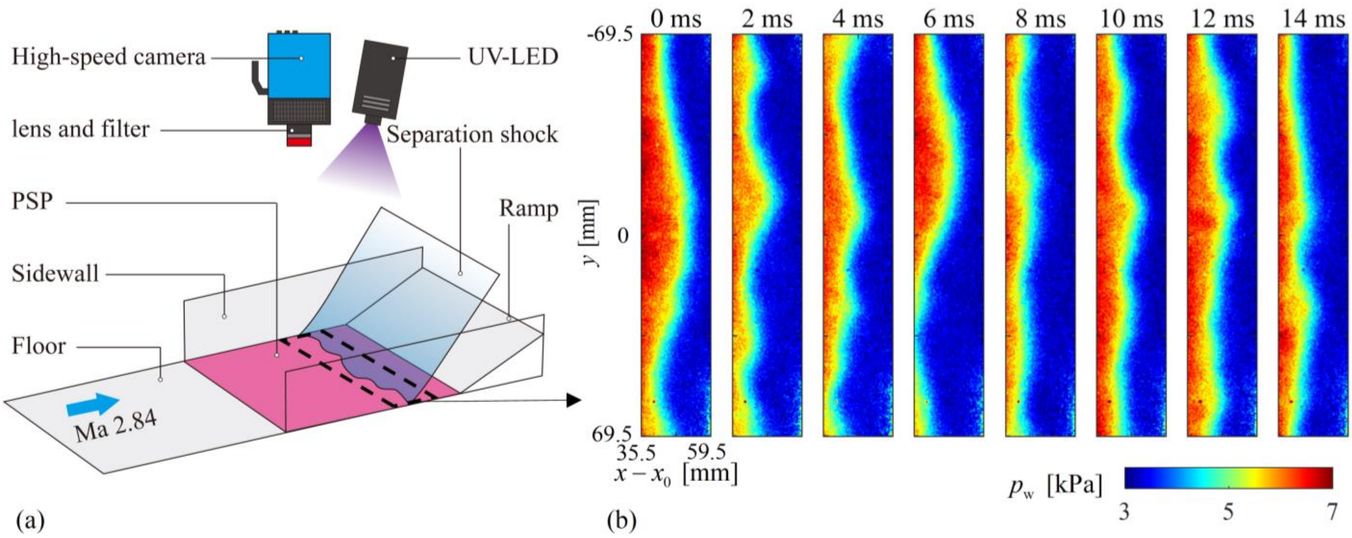

Fig. 1 (a) Schematic of fast PSP measurement system and (b) instantaneous pressure distributions in the intermittent region

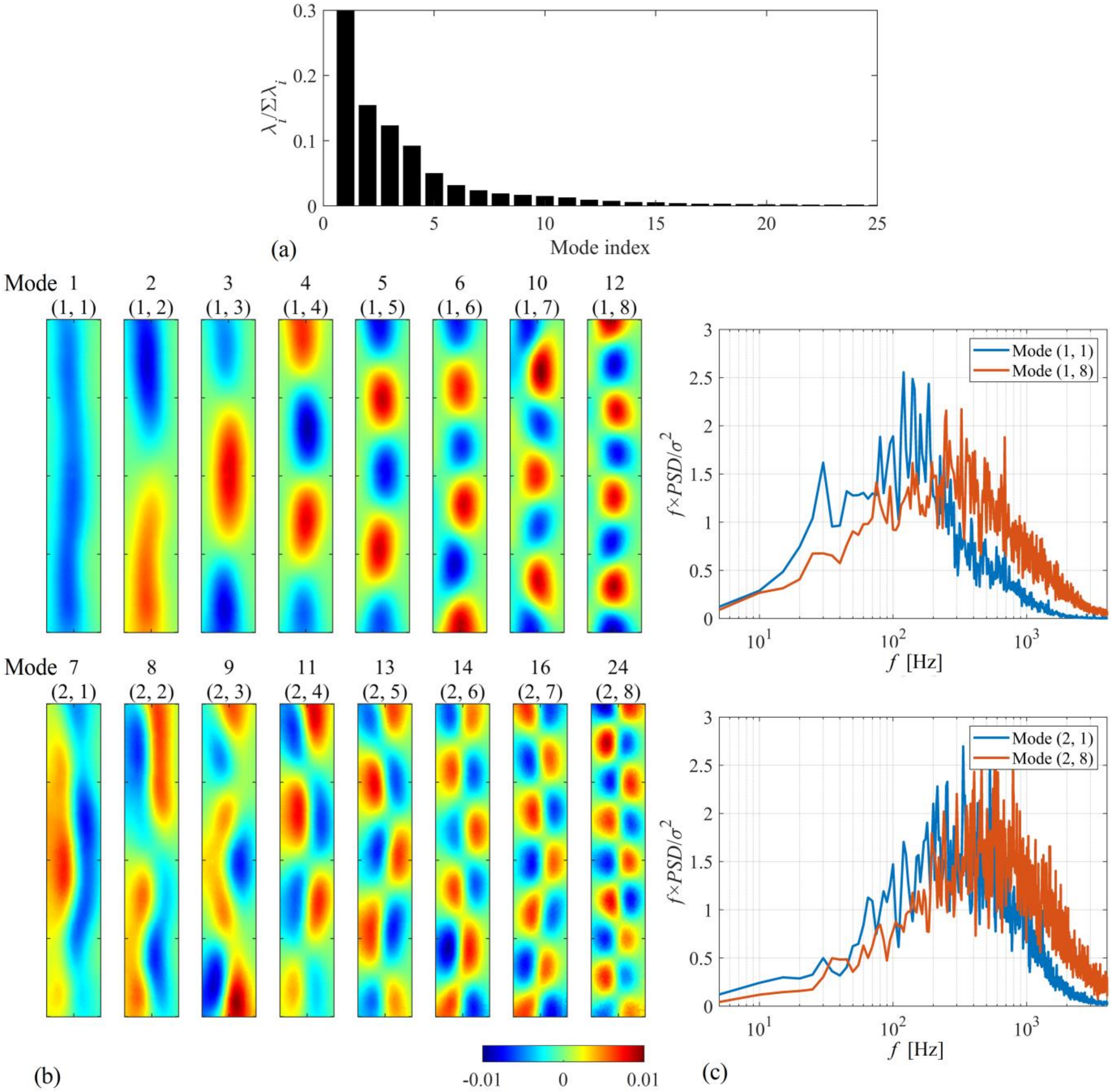

Fig. 2 POD results: (a) POD mode energy distribution, (b) contours of PSP modes and (b) pre-multiplied power spectral densities of POD coefficients

REFERENCES

- Babinsky, H., & Harvey, J. K. (2011). Shock Wave–Boundary-Layer Interactions, Cambridge University Press.
- Clemens, N. T., & Narayanaswamy, V. (2014). Low-Frequency Unsteadiness of Shock Wave/Turbulent Boundary Layer Interactions. Annual Review of Fluid Mechanics, 46(1), 469-492.
- Gregory, J. W., Sakaue, H., Liu, T., & Sullivan, J. P. (2014). Fast Pressure-Sensitive Paint for Flow and Acoustic Diagnostics. Annual Review of Fluid Mechanics, 46(1), 303-330.
- Peng, D., & Liu, Y. Z. (2020). Fast pressure-sensitive paint for understanding complex flows: from regular to harsh environments. Experiments in Fluids, 61(1).

TECHNICAL SESSION 18
BIO-MEDICAL FLOWS

Chaired by Filippo Coletti

Stenosis influence on the flow patterns across a 180-degree curved artery model: A Defocusing PTV study

Gonçalo Coutinho[1,*] Ana Moita[1,3], Massimiliano Rossi[2] and António Moreira[1]
1: IN+ Center for Innovation, Technology and Policy Research, IST, University of Lisbon, Portugal
2: Dept. of Industrial Engineering, Alma Mater Studiorum University of Bologna, Italy
3: CINAMIL - Military Academy Research Center, Portugal
* Correspondent author: goncalo.coutinho@tecnico.ulisboa.pt

Keywords: Defocusing PTV, Cardiovascular flow, Artery model, Stenosis

ABSTRACT

It is well-established that atherosclerosis which occurs due to plaque accumulation on the walls of the arteries is predominantly found in curved and branching sections of the blood vessels, where the combination of wall-shear stress (WSS) and the multidirectionality of the flow can contribute to their progression (Glagov et al., 1988). In the context of curved arteries, a typical benchmark experiment is the measurement of the flow across a 180-degree curved artery model. This phenomenon is well-documented, with several studies correlating the evolution of the vortical flow patterns across the 180-degree curved artery with the regions where atherosclerosis is prone to progress (Cox et al., 2019). Such studies however addressed the problem from the perspective of healthy (normal) human vascular system i.e., without the presence of arterial diseases which are well-known for creating abnormal flow patterns.

A common example of an arterial disease is the arterial blockage, also known as stenosis. From a fluid mechanics point of view, the reduction of the blood vessel area creates sudden pressure changes as well as variations in WSS and flow patterns, and “jet-like” flow will dominate the flow downstream the stenosis. Such phenomena will accordingly play a role in the progression of atherosclerosis in the region downstream the stenosis (Freidoonimehr et al., 2021). Although this problem has been considered for straight arteries, the studies in curved arteries are still scarce and limited to numerical simulations (Zhou et al., 2018). Additionally, in a curved artery, the problem becomes more complex as it is expected that the “jet-like” flow from the stenosis will disturb typical vortical flow patterns found around the curve and therefore alter the regions where atherosclerosis is most likely to progress.

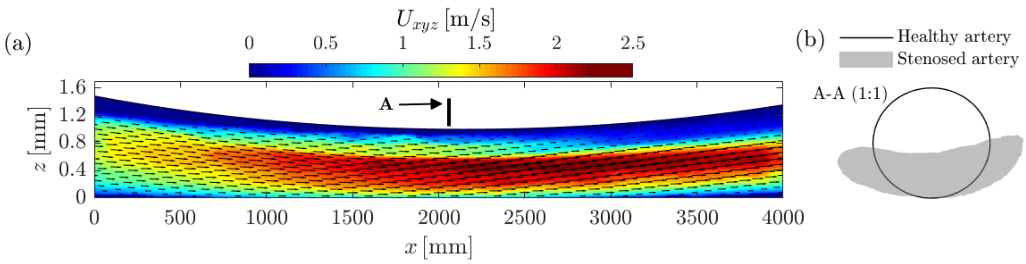

Figure 1. (a) Total velocity magnitude (U_{xyz}) at the stenosed region upstream the 180-degree curved of our artery (b) Comparison between the shape and location of a healthy artery and our model of a stenosed artery with an eccentric stenosis and an area stenosis ratio of AS = 33%.

In the present work, we aim to experimentally characterize the three-dimensional (3D) flow field across a 180-degree curved artery model with an eccentric stenosis located upstream the curve entrance and hence contribute to a better understanding of the impact of the stenosis on the flow patterns across the curve. To create the 180-degree curved artery model, a commercially available silicone tube ($D = 1.6\ mm$) was placed inside a U-shaped 3D-printed to mould with a 2-mm acrylic plate underneath, yielding a curvature ratio of $r/R = 1/21$. To minimize the optical distortions due to the curved wall of the tube and to hold the tube in place, polydimethylsiloxane (PDMS) was cast over the tube and into the 3D-printed mould. The stenosis was created by using a metallic wire (D=1.2mm) actuated vertically on top of the silicone tube using a micrometer stage. The severity of the stenosis was calculated from our measurements, considering the area stenosis ratio (AS): The area reduction caused by the stenosis and it yielded AS = 33%. To measure the 3D flow field, we used a defocus particle tracking method referred to as general defocusing particle tracking (GDPT) (Barnkob and Rossi, 2020). We used standard micro particle image velocimetry system, including a high-speed laser in double-pulse mode as backlight. The optical system consisted of a x4 magnification lens, with an additional cylindrical lens placed in front of the camera sensor to produce astigmatic particle images. A constant flow rate of Q = 120 mL/min was imposed using a standard syringe pump, yielding a Reynolds number of $Re = 523$ and Dean number of $De = 114$. As working fluid, we used a Newtonian blood analogue based on distilled water, urea, and glycerol with the same refractive index as the PDMS/silicone (Brindise et al., 2018). As post-processing step, the data from the GDPT evaluation was corrected for the refractive index and it was also rotated to account for misalignments of the measurement volume (cp. Coutinho et al., 2022).

The flow field was first measured at the location of the stenosis to characterize the shape of the stenosis and the "jet-like" flow immediately downstream the stenosis. Figure 1(a) shows the measured total velocity magnitude $U_{xyz}= \sqrt{v_x^2 + v_y^2 + v_z^2}$ at the stenosis, where we can observe the "jet-like" flow appearing just downstream the stenotic region. Additionally, Fig. 1(b) shows the shape and location of the imposed stenosis (AS = 33%) obtained from the DPT measurements when compared to a healthy artery. Subsequently, the flow was measured at three different radial positions across the curve (45º, 90º, 135º). To provide comparison between a healthy artery and the stenosed artery, we also measured the flow in a similar model without the stenosis and in the same radial positions, as shown by the schematic in Fig.2. The secondary velocity magnitude $U_{xz}= \sqrt{v_x^2 + v_z^2}$ is shown in Fig. 2(a)-(c) for the healthy artery and in Fig. 2(d)-(f) for the stenosed artery. Whereas for the healthy artery we observe the so-typical pair of counter-rotating, symmetric vortices (Cox et al., 2019), in the stenosed artery an additional flow structure appears breaking the horizontal symmetry of the flow as shown in Fig. 2(d)-(f).

The current measurements are expected therefore to provide an experimental perspective on the impact of an eccentric stenosis located upstream the curve entrance of an 180-degree curved artery model on the flow patterns across turn and serve as prequel for experimental setups able to reproduce realistic, clinically-relevant conditions. We will discuss velocity fields from a fluid mechanical point-of-view, while correlating it with the progression of arterial diseases such as atherosclerosis. Additionally, guidelines and recommendations for the application of the GDPT method for this type of flows will be provided.

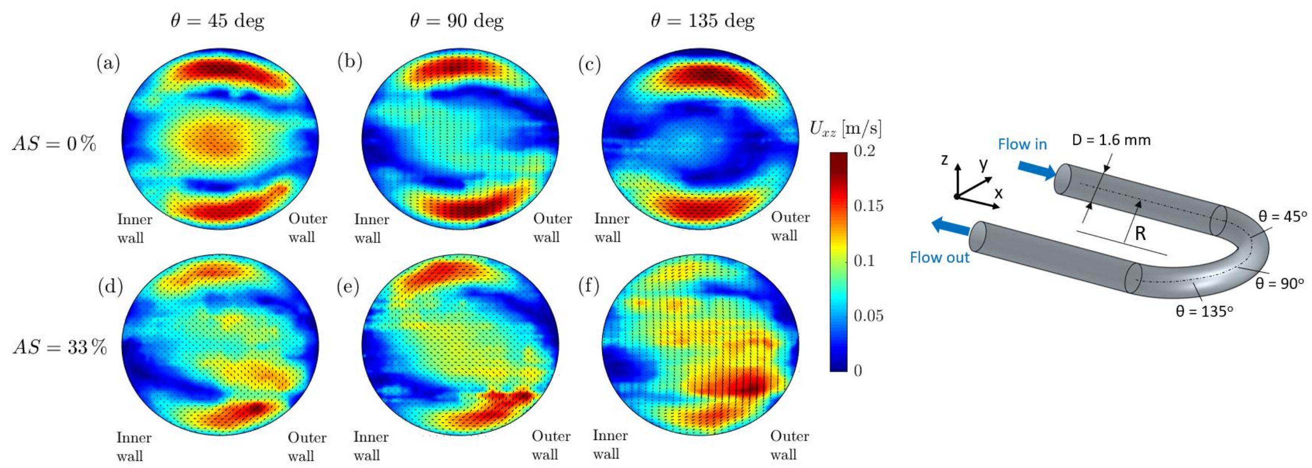

Figure 2. Different secondary flow patterns (Uxz) across the 180-degree curved artery model (θ = 45º, 90º, 135º), including a schematic of the measured positions in the normal artery (AS=0%). (a) – (c) Normal artery model. (d) – (f) Stenosed artery model with an area stenosis ratio AS = 33%.

REFERENCES

- Barnkob, R., & Rossi, M. (2020). General defocusing particle tracking: fundamentals and uncertainty assessment. Experiments in Fluids, vol. 61.
- Brindise, M., Busse, M., & Vlachos, P. (2018). Density and Viscosity Matched Newtonian and non-Newtonian Blood-Analog Solutions with PDMS Refractive Index. Experiments in Fluids, vol. 59.
- Coutinho, G., Moita, A., Ribeiro, A., Moreira, A., & Rossi, M. (2022). On the characterization of bias errors in defocusing-based 3D particle tracking velocimetry for microfluidics. Under review.
- Cox, C., Najjari, M.R., & Plesniak, M. (2019). Three-dimensional vortical structures and wall shear stress in a curved artery model. Physics of Fluids, 31:121903.
- Freidoonimehr, N., Chin, R., Zander, A., & Arjomandi, M. (2021). Effects of shape of the stenosis on the hemodynamics of a stenosed coronary artery. Physics of Fluids, 33:081914.
- Glagov, S., Zarins, C., Giddens, D. P., & Ku, D. (1988). Hemodynamics and atherosclerosis. Insights and perspectives gained from studies of human arteries. Archives of pathology & laboratory medicine, vol .112.
- Zhu, C., Seo, J., & Mittal, R. (2018). Computational modelling and analysis of haemodynamics in a simple model of aortic stenosis. Journal of Fluid Mechanics, vol. 85 pp. 23-49.

Advantages of a Topological Anomaly on Blood Flow in a Fly's Wing Vein Network

Kazuki Sugiyama[1*], Yoshihiro Kubota[2], and Osamu Mochizuki[1]
1: Graduate School of Science and Engineering, Toyo University, Japan
2: Dept. of Mechanical Engineering, Toyo University, Japan
* Correspondent author: s46a02200012@toyo.jp

Keywords: Wing veins, Insect, Blood flow, Pipe network

ABSTRACT The wing veins of insects are known for their versatility. However, the impact of their network structure on blood circulation remains poorly understood. Our topological analysis revealed an anomalous vein on a fruit fly's forewing, the function of which was unknown. We demonstrate that this single vein has the potential to contribute to energy-efficient blood transportation in the wing, by visualizing the flow patterns in the wing utilizing a pipe network analysis. Our findings suggest that the venous network on insect wings has potential biomimetic applications in the design of efficient transportation networks.

1 INTRODUCTION

The wing veins play several vital roles in insect wing; e.g., improvement of the toughness (Dirks & Taylor, 2012) and resistance against defection (Rajabi et al., 2020). Transportation of insect blood, hemolymph is one of them (Salcedo & Socha, 2020). Pulsatile organs in the thorax achieve hemolymph flow in the venous network (Salcedo & Socha, 2020). The network structure of the veins should influence the hemolymph flow and the pressure requirement for the pumping organs, considered as a pipe network. However, its effect on hemolymph circulation had not been studied. Our topological analysis revealed that the fruit fly has an irregular vein component on its wing as shown in Figure 1. This vein is called the posterior cross vein (PCV) whose functions or advantages have not been appreciated. The purpose of our study is to reveal the advantages of this anomalous vein in wing circulation. It would help reveal the contribution of the venous structure to circulation on insect wings.

2 METHODS

We visualized hemolymph flow in the venous network by a pipe network analysis leveraging the analogy with a pipe network. We determined the volume flow rate and pressure drop in the vein components using the Hardy-Cross method (Cross, 1936). It can solve the simultaneously established Darcy-Weisbach equations for all loops of the pipe network with unknown flow rate and pressure loss in the pipe components. The hydraulic diameters and lengths of the veins are given via measurement on the forewing of the fruit fly. The inflow rate at the inlet was assumed to be constant at 5.2×10^2 $\mu m^3/s$, and the outflow rate is the same as it under the mass conservation law. The hemolymph flow is considered as fully developed laminar with Reynolds number around 10^{-5} order in the steady state; thus we considered the pressure loss that occurs due to the frictional loss. Utilizing this numerical method, we could demonstrate effect of the PCV on hemolymph circulation by virtually removing or repositioning it.

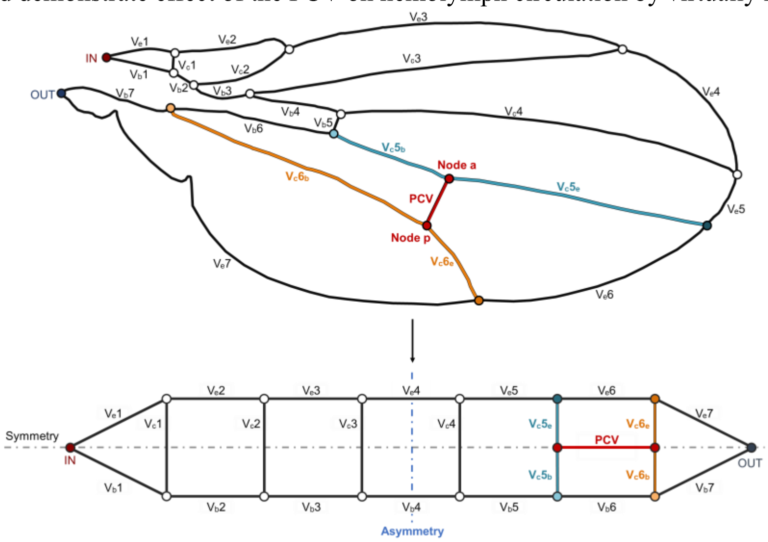

Figure 1. Characterization of the wing vein network through topological transformation.

3 RESULTS

We determined the flow rate distribution in the PCV-lost wing and actual wing. Figure 2a shows the hemolymph flow rate in each wing vein in the wing without the PCV. The dark-colored vein has much flow rate, and the light-colored vein has less. The white triangles show flow directions. Hemolymph one-directedly flows along the wing edge (V_e) and base (V_b) from the inlet to the outlet. Hemolymph in the edge veins flows into the base veins through the connecting veins (V_c). Figure 2b shows the change rate in the hemolymph flow rate due to addition of the PCV. In the red and blue color respectively express an increase and decrease in the value, and changed flow directions are emphasized by orange triangles. Flow towards the edge occurs in parts of connecting veins that are adjacent to the vein. They are anteriorly adjacent on the edge side and posteriorly adjacent on the base side (V_c5_e and V_c6_b). These changes result in the overall pressure loss in the through the network. The pressure loss in the PCV-lost wing and complete wing are 6.7×10^2[Pa] and 6.5×10^2[Pa], respectively; the vein reduces 4.1% of the pressure loss. This effect potentially reduces energy consumption by the pulsatile organ because pump power is proportional to pumping pressure. The single vein probably improves energy efficiency of wing vein circulation.

4 CONCLUSION

We demonstrated previously unexplained functions of the single anomalous vein, PCV. Our calculation demonstrated addition of this vein reduces the pressure loss in the entire network implying its potential to improve energy efficiency of circulation. Our findings highlight the potential for the addition of similar paths to improve energy efficiency in existent transportation systems.

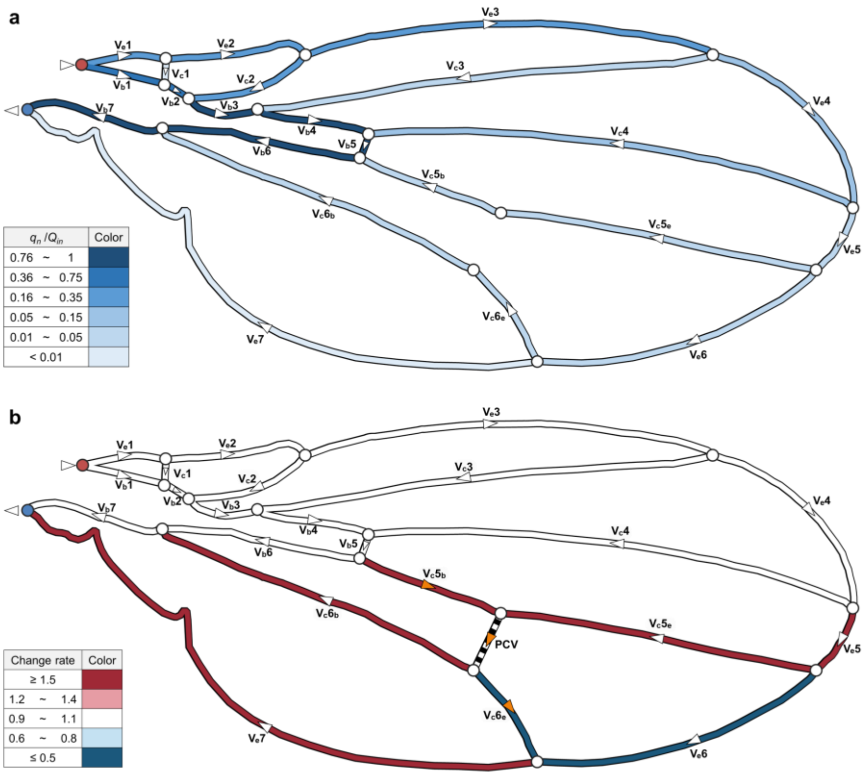

Figure 2. a:Distribution of hemolymph flow rates in the PCV-lost network. b: Change in hemolymph flow rates due to the existence of the PCV.

5 REFERENCES

- Cross, H. (1936). *Analysis of flow in networks of conduits or conductors /*. University of Illinois. Engineering Experiment Station. Bulletin.
- Dirks, J.-H., & Taylor, D. (2012). Veins Improve Fracture Toughness of Insect Wings. PLoS ONE, 7(8), e43411. https://doi.org/10.1371/journal.pone.0043411
- Rajabi, H., Dirks, J.-H., & Gorb, S. N. (2020). Insect wing damage: Causes, consequences and compensatory mechanisms. Journal of Experimental Biology, 223(9), jeb215194. https://doi.org/10.1242/jeb.215194
- Salcedo, M. K., & Socha, J. J. (2020). Circulation in Insect Wings. Integrative and Comparative Biology, 60(5), 1208–1220. https://doi.org/10.1093/icb/icaa124

Video Analysis of the Glimmer Synchronization of *Luciola Parvula* Fireflies

Nao Ninomiya[1,*], Shiro Kobayashi[1], Kotaro Yamazaki[1]
and Masayuki Iigo[2]
1: Dept. of Opt. Eng., Utsunomiya Univ., Japan
2: Center for Bioscience Res. and Edu., Utsunomiya Univ., Japan
* Correspondent author: nino@utmu.jp

Keywords: Video Analysis, Firefly, Synchronization, Body Clock

ABSTRACT It is known that the *Luciola parvula* fireflies clearly emit the lights at regular time intervals and synchronize between multiple males are observed, but the details of synchronization have not yet been clarified. Presently, we took videos of the luminescence phenomenon of multiple male *Luciola parvula* fireflies and performed a correlation analysis on the details of the time change of the luminescence brightness of each male *Luciola parvula* fireflies. The 12 *Luciola parvula* fireflies are kept in glass wells so that each *Luciola parvula* fireflies can only moves in restricted areas and their luminescence is recorded by a digital movie camera at the video rate of 30 fps. According to the preliminary study, each glimmer lasts about 3 frames and thus the time series brightness is fitted by a parabolic function in order to give a precise timing of maximum brightness. First of all, time intervals between glimmers of each *Luciola parvula* fireflies are evaluated. Secondly, the glimmer correlation between different *Luciola parvula* fireflies are investigated. As a result, it was clarified that the light emission cycle of *Luciola parvula* fireflies is almost constant at 0.54 seconds, more than 70% of all light emissions are synchronized and the order of synchronization is almost fixed with very small delay. Consequently, it has been shown quantitatively that the glimmers of male *Luciola parvula* fireflies are well synchronized.

1 INTRODUCTION

Fireflies emit the lights as they are named but the patterns of light emission are different with species and sex. They have a lot of meanings in their light emission and if we can evaluate the difference in the pattern of light emission of fireflies, it may be possible to make some insight into the communication mechanism. (Nakagawa and Tanaka (2019), Hanson et al. (1971))

It is known that both sex of the *Luciola parvula* fireflies clearly emit the lights at regular time intervals and synchronizations between multiple males are observed, but the details of synchronization have not yet been clarified. The quantitative evaluation of the synchronization of the light emission by multiple males may help understanding the communication between fireflies and serve as a clue to assist their breeding and to understand the body clock mechanism.

Presently, we took videos of the luminescence phenomenon of multiple male *Luciola parvula* fireflies and performed a correlation analysis on the details of the time change of the luminescence brightness of each male *Luciola parvula* fireflies.

2 MEASUREMENT

The *Luciola parvula* fireflies were captured in Takanosu area of Niigata in July of 2020 and 2021. They are kept in the test room which had the light period from 5:00 AM through 19:00 PM and a dark period from 19:00 thorough 5:00 AM. The test room temperature was maintained at 20°C.

The video cameras used in this study were Canon PowerShot G7 X and GoPro HERO9. The 12 male *Luciola parvula* fireflies were kept in glass wells so that each *Luciola parvula* fireflies could only moves in restricted areas and their luminescence is recorded by a digital movie camera from above at the video rate of 30 fps in 2020 as shown in Figure 1 left and by the camera in the bottom of acrylic case at 240 fps in 2021 as shown in Figure 1 right. The image resolution of the videos is 1920 x 1080 pixels.

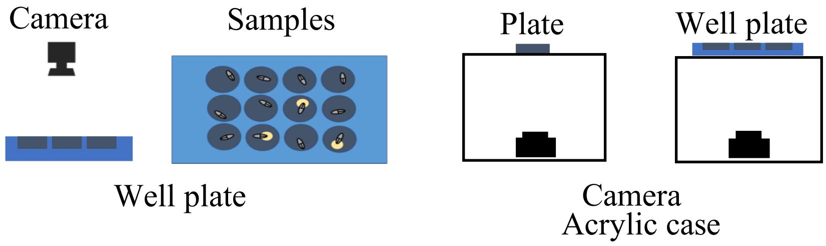

Figure 1. Experimental Setup.

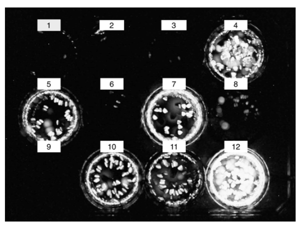

Figure 2. Superposition image

The movie file of the recorded video was processed and saved as a series of still images. The colored images are converted into greyscale images. As the fireflies move around in each cell of well plate, first the brightness of each pixel has been accumulated throughout the video and thus we obtained the superposition image as shown in Figure 2, which gives us the positions of each firefly. The fireflies are named as series #1 through #12. In order to separate the noise from the signal, the brightnesses of 9x9 pixels are averaged around the brightest pixel of each image and then the average of higher than 15 is recognized as the glow of firefly. According to the preliminary study, each glimmer lasts about 3 frames of 30 fps and thus the time series brightness is fitted by a parabolic function in order to give a precise timing of maximum brightness.

3 RESULTS

3.1 Time Interval

A time series plot of lights emission of 12 fireflies shows that the light emissions of the *Luciola parvula* fireflies are very sharp and intermittent and thus the time intervals between flashes of each firefly are evaluated. As the average intervals of each firefly are almost the same and the standard deviations of each interval are very small compared to the average, it can be said that the cycle of the flashing by the *Luciola parvula* fireflies is quite constant with an average interval of 0.54 sec.

3.2 Synchronization

As we have recorded the flashing of fireflies for a long time period, we can also evaluate the relative relationship of flashing by each firefly. It can be seen from the timing chart that there is obvious synchronization of flashing between fireflies and the rate of synchronization is higher than 75% for all fireflies and almost 85% of all flashing are synchronized. This is a clear evidence that the flashing of the male *Luciola parvula* fireflies is synchronized.

Table 1 shows the mean of the time differences of the emission peak between two fireflies of all possible combinations when they show the synchronization. Negative values in Table 1 indicate that the fireflies in the horizontal series glow later relative to the fireflies in the vertical series, while positive values indicate that they glow ahead of time.

Table 2. The light emission lag time.

Average (sec)						
	No.12	No.11	No.7	No.4	No.5	No.10
No.12		-0.0210	-0.0177	-0.0334	-0.0290	-0.0558
No.11	0.0210		-0.0024	-0.0171	-0.0156	-0.0413
No.7	0.0177	0.0024		-0.0145	-0.0081	-0.0371
No.4	0.0334	0.0171	0.0145		-0.0055	-0.0256
No.5	0.0290	0.0156	0.0081	0.0055		-0.0218
No.10	0.0558	0.0413	0.0371	0.0256	0.0218	

The time difference between # 7 and # 11 and that between # 4 and # 5 are very small, indicating that these 2 pairs glow at almost the same timing when they are synchronized. Comparing the time differences between 6 fireflies, it can be said that there is a luminance ranking when looking at the average over the entire video, although the ranking fluctuates momentarily within 20 min. of the video.

4 CONCLUSIONS

According to the observation of light emission by multiple male *Luciola parvula* fireflies, following conclusions are obtained.

1. The light emitting of fireflies were found to be synchronized, with mostly in multiples of about 0.54 seconds each.

2. The number of times fireflies synchronize is more than 70% of the total number of firefly emissions, and it can be said that they synchronize most of their emissions.

3.The time of the emission peaks during synchronization varied, and the order of the emission peaks sometimes changed momentarily, but from the overall average, it appeared that the order of the synchronization was fixed.

4. When multiple fireflies are emitting light, the emission cycle tends to be shorter than when a single firefly is emitting the light, and the blinking rate seems to be faster.

The synchronization to the artificial external stimulus and many other aspects will be introduced at the symposium.

5 REFERENCES

- Nakagawa, M. and Tanaka, H. (2019), A Plausible Model of Synchrony in *Pteroptyx effulgens* and Its Occurrence Condition for Traveling Waves, J. Jpn. Soc. Indust. and Appl. Math., Vol. 29, No. 3, pp. 250-293.
- Hanson, F. E., Case, J. F, Buck, E. and Buck, J. (1971), Synchrony and flash entrainment in a New Guinea firefly, Science, 174, 161-164.

Day 4

TECHNICAL SESSION 19
CONVECTION

Chaired by Bas van Oudheusden

Three-dimensional visualization of Rayleigh-Bénard convection using Contactless Inductive Flow Tomography

Rahul Mitra*, Max Sieger, Felix Schindler, Tobias Vogt, Sven Eckert, Frank Stefani, Thomas Wondrak.
Dept. of Magnetohydrodynamics, Institute of Fluid Dynamics, Helmholtz-Zentrum Dresden-Rossendorf, Bautzner Landstr. 400, 01328 Dresden, Germany.
* Correspondent author: r.mitra@hzdr.de

Keywords: Inductive flow measurement, 3D velocity reconstruction, Rayleigh-Bénard convection, Liquid metal flow

ABSTRACT

Rayleigh-Bénard convection (RBC) is a complex and dynamic fluid flow phenomenon that arises from the interplay between buoyancy and viscosity in a fluid that is heated from below and cooled from above. A three-dimensional (3D) flow visualization of Rayleigh-Bénard convection can give deeper understanding of its flow dynamics and heat transfer mechanism. While there has been extensive research on the flow dynamics of fluids with a Prandtl number Pr (ratio of momentum diffusivity to thermal diffusivity) close to or higher than one, like water (Paolillo et al. 2021), experimental investigations of fluids with a low Prandtl number in the order of 10^{-2} like liquid metals are still rare. Such kind of fluids are opaque preventing the use of optical methods like particle image velocimetry. Ultrasound Doppler Velocimetry (UDV) can be utilised which measures one velocity component along the ultrasound beam line of one transducer (1D1C). However, a large number of probes, which need to be in contact with the melt, are required to measure several velocity components or velocity distributions in larger fluid volumes, which is often impractical and expensive.

The novel Contactless Inductive Flow Tomography (CIFT) (Stefani et al. 2004), in contrast, is able to visualise the global 3D velocity field (3D3C) in conducting liquids. The procedure comprises two stages: the first stage entails the generation of electric currents within the electrically conductive fluid under the influence of one or more applied excitation magnetic field(s). The flow-induced perturbations of the applied magnetic field(s) are measured by appropriate magnetic field sensors positioned outside the fluid volume. The second stage involves the subsequent determination of the velocity field by solving the associated linear inverse problem using the measured values of the induced magnetic field. Due to contactless nature of CIFT, it has the potential to be applied for measurement of velocity of very hot and chemically aggressive fluids, e.g. liquid steel in continuous casting process (Glavinić et al. 2022).

Figure 1a shows the Rayleigh-Bénard cylindrical vessel with the height of 640 mm and the diameter of 320 mm filled with the eutectic alloy GaInSn and the mounted CIFT excitation coils. Forty-two Fluxgate probes are arranged in 7 rings with 6 sensors each around the vessel as depicted in Figure 2b. Exemplarily, Figure 1a shows one sensor mounted on an aluminium bar. Stability measurements indicate that the magnetic field can be measured over 12 hours with a deviation of less than ±5nT in the whole time of experiment, if appropriate measures are taken to compensate thermal expansion and the effects of the changes of the earth magnetic field (Sieger et al. 2022). Simultaneous flow measurements were performed using CIFT, UDV and temperature probes at three different Rayleigh numbers (Ra = 9.33×10^{6}, 5.31×10^{7} and 6.02×10^{8}) and the three-dimensional time-dependent velocity field was reconstructed using CIFT for every second.

In our presentation, we will show a comparison of CIFT and UDV to investigate the accuracy of reconstructed velocity field. We will then concentrate on a detailed analysis of the measured flow for the highest Rayleigh number (Ra = 6.02×10^{8}). It turned out that the flow is highly volatile. Figure 2 shows exemplarily the reconstructed velocity field for four different moments in a time interval of 37 free-fall times (tff). In this time period the structure of the velocity changes from a triple-roll (Figure 2a) over a double-roll (Figure 2b) to a nearly single-roll (Figure 2c) and back to a double-roll (Figure 2d) with a different orientation. Finally, such complex velocity fields can be further analysed by means of advanced mathematical methods like Proper Orthogonal Decomposition similar to Paolillo et al. 2022, as we will show in our presentation.

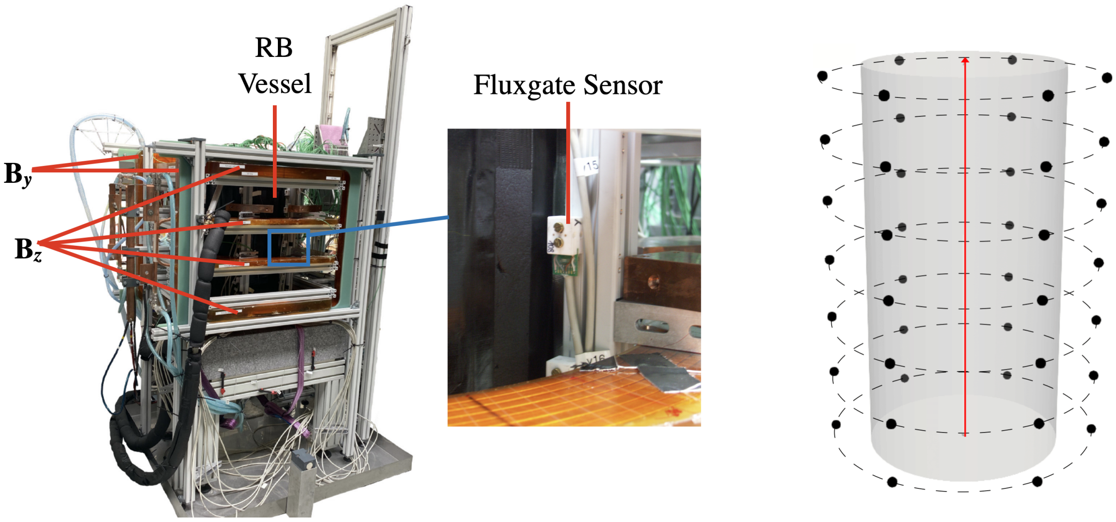

(b) (a)

Figure 1: (a) CIFT measurement system mounted on a Rayleigh-Bénard convection cell. (b) Schematic of the 7×6 sensor configuration used for measurements.

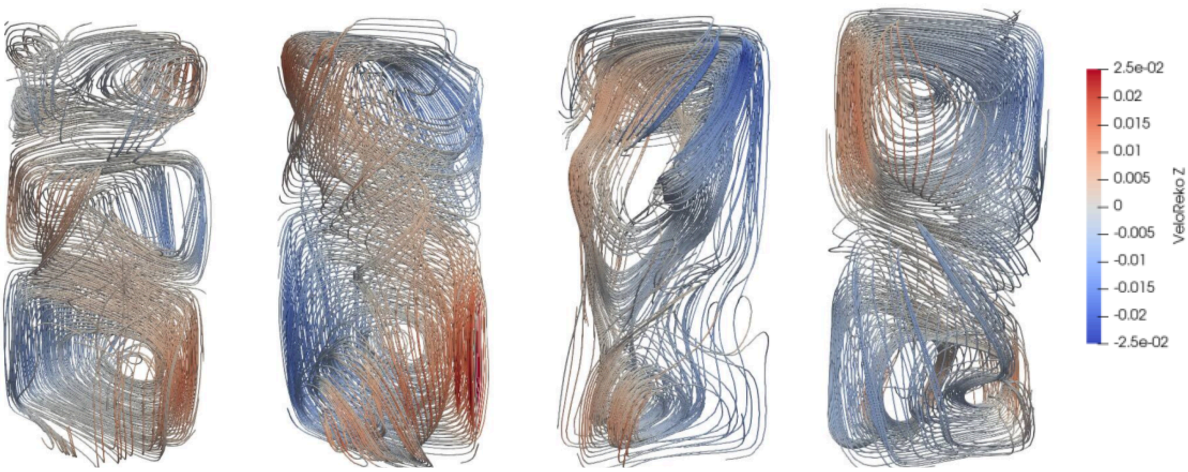

(a) (b) (c) (d)

Figure 2: Snapshots of the three-dimensional flow pattern at Ra = 6.02×10^8: streamlines for (a) t/tff = 1195, (b) t/tff =1209, (c) t/tff=1233 and (d) t/tff =1242, the colour represents the amplitude of the vertical velocity component in m/s.

REFERENCES

- Paolillo, G., Greco, C., Astarita, T., & Cardone, G. (2021). Experimental determination of the 3-D characteristic modes of turbulent Rayleigh–Bénard convection in a cylinder. *Journal of Fluid Mechanics, 922*, A35.
- Stefani, F., Gundrum, T., & Gerbeth, G. (2004). Contactless inductive flow tomography. *Physical Review E*, *70*(5), 056306.
- Glavinić, I., Galindo, V., Stefani, F., Eckert, S., & Wondrak, T. (2022). Contactless Inductive Flow Tomography for Real-Time Control of Electromagnetic Actuators in Metal Casting. *Sensors*, *22*(11), 4155.
- Sieger, M., Mitra, R., Schindler, F., Vogt, T., Stefani, F., Eckert, S., & Wondrak, T. (2022). Measurement challenges in contactless inductive flow tomography for Rayleigh-Bénard convection cells. Magnetohydrodynamics, 58(1-2), 25-32.

Application of 3D LIF and PIV in studying Poiseuille-Rayleigh-Bénard convection

Sina Kashanj[1] and David S. Nobes[1,*]
1: Dept. of Mechanical Engineering, University of Alberta, Canada
* Correspondent author: dnobes@ualberta.ca

Keywords: 3D PIV, 3D LIF, Natural convection, Mixed convection, Poiseuille-Rayleigh-Bénard

ABSTRACT An experimental investigation of the flow of Poiseuille-Rayleigh-Bénard convection (PRBC) in mixed convection regimes, both for continuous and reciprocating flows is presented. A 3D scanning particle image velocimetry and 3D scanning two-color laser-induced fluorescence technique is used to measure the velocity and temperature of the flow field. The study aims to explore the flow structures of PRBC and measure the heat transfer properties. The study highlights the spatiotemporal nature of the formation of the large-scale circulating structure and its impact on heat and momentum transport.

1 Introduction

Large-scale circulating structures (LSC) have a significant role in heat and momentum transfer in wall bounded turbulent buoyancy-driven flows (Zwirner et al., 2020). In the natural convection in an enclosure heated from below and cooled from above, known as Rayleigh-Bénard convection (RBC), formation of LSC leads to an enhancement in heat and momentum transport properties (Zwirner et al., 2020). Turbulent RBC is significantly unsteady and the number and scale of the circulating structures varies temporally affecting the state of the flow (Zwirner et al., 2020). Mixed convection in a wall bounded flow heated from below is known as Poiseuille-Rayleigh-Benard convection (PRBC) (Maughan & Incropera, 1987). In PRBC, it is shown that formation of LSC is a spatiotemporal phenomena which is a function of the length of the heated channel as well as the development time (Maughan & Incropera, 1987). Although the formation of LSC in PRBC can enhance the heat transfer, in real applications it is suppressed due to the short length of the heated channel and temporal unsteadiness (Maughan & Incropera, 1987). An important case with temporal unsteadiness is a reciprocating flow in which the formation of the LSC could be suppressed due to the acceleration and deceleration of the flow (Maughan & Incropera, 1987).

The role of LSC in RBC flow has been a focus of interest in the last decade, yet there is not a coherent understanding of the effect of LSC in mixed convection. This work is an experimental investigation on the flow of Poiseuille-Rayleigh-Bénard flow in mixed convection regime. This experimental study is undertaken for both continues and reciprocating flows. To explore the flow structures of PRBC and measure the velocity of the flow field, a 3D scanning particle image velocimetry (PIV) is employed. To measure the temperature of the flow field and the heat transfer properties, a 3D scanning two-colour laser-induced fluorescence (LIF) system is also used.

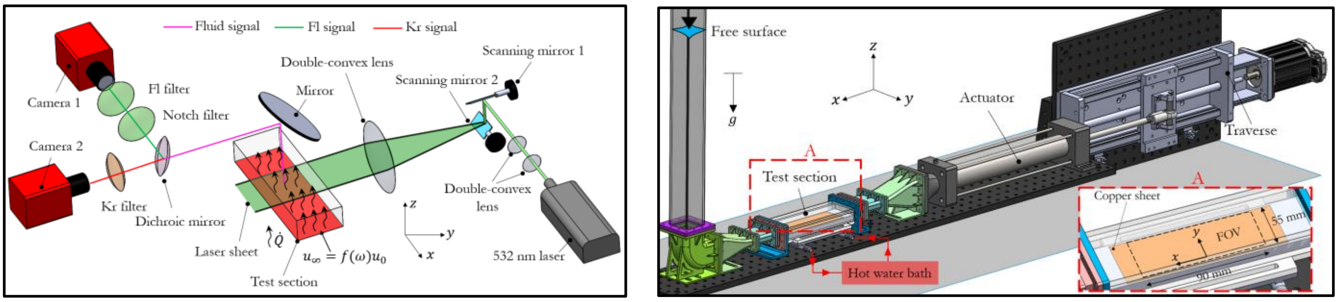

(a) (b)

Figure 1. (a) Schematic of the optical measuement system used to apply 3D LIF and PIV. (b) Rendering of the solid model of the fluid test rig designed and fabricated to generate continuse and reciprocating flows. Zoomed area, A, depicts the test section properties.

2 Methodology

A schematic of the optical measurement system used to apply 3D PIV and 3D two-colour LIF is illustrated in Figure 1(a). To apply 3D two-colour LIF a 532 nm laser was used. Two scanning mirrors were also used to generate the laser sheet and to scan the volume of the test section, z-direction. Two fluorescent dyes of Fluorescein (Fl) and Kiton red (Kr) were used to apply two-colour LIF. For each fluorescent dye a camera with a set of optical filters were used to collect the temperature sensitive signal of each dye. More details of the applied technique for the thermometry can be found in (Kashanj & Nobes, 2023). By eliminating camera 1 in Figure 1(a), and using camera 2 with a long-pass filter with the cut-on wavelength of λ=600 nm, the 3D scanning PIV were applied using the same scanning system as used for LIF. Fluorescent seeding particles with the size of 3.2 μm and with the maximum absorption and emission wavelength of λ=520 nm and λ=580 nm was used to capture the flow field. Using a first face mirror as is shown in Figure 1(a), the field of view in $x - y$ direction was captured for both PIV and LIF. The rendering of the solid model of the fluid test rig designed and fabricated for the experiment can be seen in Figure 1(b). An actuator was connected to a traverse to generate the reciprocating flow in x-direction. The test section is also fabricated with the half-height of h=5 mm, using acrylic sheet and the bottom of it is featured by a thin copper sheet, 3 mm. The copper sheet is connected to a flow chamber below recirculating the hot water from a water bath. The flow channel is mainly fabricated using an SLA 3D printer with the precision of 25 μm.

3 Results and Outlook

The velocity map of the flow at the mid-height of the test section, z=5 mm can be seen in the Figure 2(a) for four different phases of $\omega = \pi/2\,, \pi, 3\pi/2$, and 2π where $\omega = 2\pi/T$ and T is the period of oscillation. Results shown in Figure 2 are also in the peak Reynolds number of $Re_p = 80$, and Womersly number of $\alpha = 8.4$, where $\alpha \equiv h\sqrt{\omega/\nu}$ and $Re_p \equiv 2u_m h/\nu$. In these two definitions, u_m is the maximum velocity, h is the half-height of the channel, and ν is the kinematic viscosity of the working fluid. As can be observed in $\omega = \pi/2$ and $\omega = 3\pi/2$, flow is in the peak of the acceleration phase at two different directions which occurs before the start of the deceleration. Two other phases of $\omega = 0$ and $\omega = \pi$ in Figure 2(a) are showing the start of the acceleration in two different directions. The stagnation line at $y^* = 0.35$ can be observed for both phases, $\omega = \pi$ and $\omega = 2\pi$. In the presentation, full results of this work including the 3D results of the velocity and temperature measurement of the both continues and reciprocating flow will be disucssed. The velcoity profile of u_x along the width of the channle, y-direction is shown in Figure 2(b) for a single cuycle of reciprocation, $0 \leq \omega < 2\pi$. The red colour plots depicts the velocity profile of the four velocity contours shown in Figure 2(a). The stagnation line also can be seen in this figure for $\omega = 0$ and $\omega = \pi$ showing the start of the reverse flow direction.

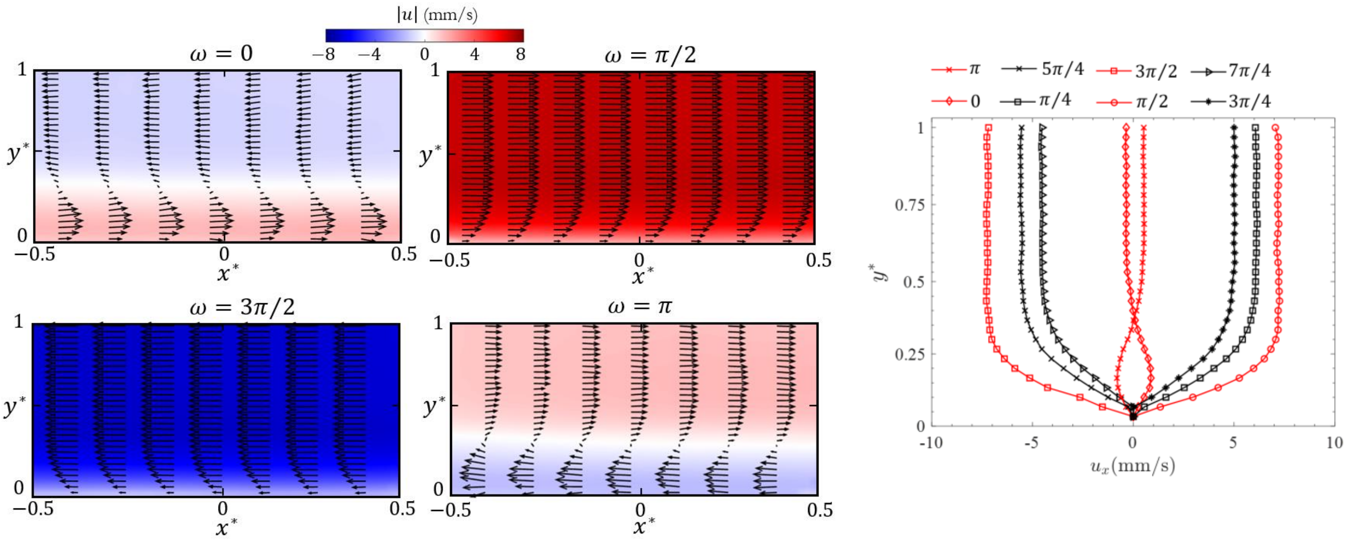

(a) (b)

Figure 2. (a) Contour of the velocity magnitude in $x - y$ plane at the midheight of the test section, z=5 mm at the four different phases of $\omega = \pi/2$, $\omega = \pi$, $\omega = 3\pi/2$, and $\omega = 2\pi$. (b) Velocity profile, u_x along the width of the channle, y for different phases of reciprocating flow; red colour denotes the phases that are shown as velcoity contours in (a).

4 REFERENCES

- Kashanj, S., & Nobes, D. S. (2023). Application of 4D two-colour LIF to explore the temperature field of laterally confined turbulent Rayleigh–Bénard convection. *Experiments in Fluids*, *64*(3). https://doi.org/10.1007/s00348-023-03589-9.
- Maughan, J. R., & Incropera, F. P. (1987). Experiments on mixed convection heat transfer for airflow in a horizontal and inclined channel. In *International Journal of Heat and Mass Transfer, 30(7)*.
- Zwirner, L., Tilgner, A., & Shishkina, O. (2020). Elliptical Instability and Multiple-Roll Flow Modes of the Large-Scale Circulation in Confined Turbulent Rayleigh-Bénard Convection. *Physical Review Letters*, *125*(5). https://doi.org/10.1103/PhysRevLett.125.054502.

Particle Transportation by Convective Flow around a Photothermal Bubble under CW and Frequency-Modulated Laser Irradiation

Koki Okada[1], Yoshiyasu Ichikawa[1,2],
Masahiro Motosuke[1,2,*]
1: Dept. of Mechanical Engineering, Tokyo University of Science, Japan
2: Water Frontier Research Center (WaTUS), Tokyo University of Science, Japan
* Correspondent author: mot@rs.tus.ac.jp

Keywords: Particle manipulation, Microbubble, Photothermal effect, Marangoni effect, Plasmon

1 INTRODUCTION

The technique of accumulating particles that are dispersed in a liquid is promising for microfabrication and analysis of biochemicals[(1)]. A photothermal bubble, a bubble with a diameter of 1–50 µm generated on a solid-liquid interface by photothermal conversion of a laser beam, is one of the tools for the accumulation. The liquid-gas interface of the photothermal bubble has a surface tension difference due to the temperature gradient because of the higher temperature near the heat source (e.g., metal nanostructure) on the solid surface. This interfacial flow is called the Marangoni effect and results in the transportation of the suspended particles from the bulk toward the three-phase contact line. Particles are eventually deposited on the solid surface. However, the transport velocity, pathways of particles, and deposition process are still unclear. Therefore, we visualized the transportation and accumulation processes of particles under laser irradiation with continuous and frequency-modulated conditions to vary the temperature gradient that induces the convection flow.

2 EXPERIMENTAL SETUP

Gold nanoparticles (GNPs) substrate, which can absorb laser beam by localized surface plasmon resonance, was prepared to generate photothermal bubbles. It was fabricated by adsorbing gold nanoparticles synthesized by the citric acid reduction method onto the surface of a 0.15-mm-thick cover glass positively charged with pDADMAC.

Fluorescent polystyrene spheres with diameters of 500 nm were used as the transport target. They were diluted to 0.1 vol% with ultrapure water to be used as the sample solution. The solution was sealed in a chamber that consisted of a 1-mm-thick silicone sheet, a GNPs substrate on the bottom, and a cover glass on the top. The chamber was set on the stage of an inverted microscope, and a focused beam from a diode laser with the wavelength of 637 nm was irradiated from the bottom through an objective lens (100×, NA = 1.49) to generate a bubble on the GNPs substrate. The calculated beam spot diameter was 1.8 µm. Output laser power was 50 mW, and the laser beam was modulated by a square wave signal (frequency: 100 kHz, duty cycle: 0.5) from a function generator. Excitation light for the fluorescent particles was continuously irradiated through the objective lens, and a high-speed CMOS camera captured fluorescence from the particles with a shutter speed of 5000 fps.

3 RESULTS AND DISCUSSION

Figure 1(a) shows composited images in the time range of 1 ms or 20 ms under continuous and modulated irradiation conditions. The irradiation started at $t = 0$. Particles and the bubble were observed from the bottom (i.e., through the GNPs substrate), and the solid-liquid interface on the substrate was on the focal plane of the observation. In 0–1 ms of continuous irradiation, particles are transported toward the bottom of the bubble, and some particles are deposited in rings along the contact line. Flow velocity near the bubble was estimated at more than 1 mm/s because the particles moved more than 10 µm within 1 ms. This flow structure was maintained until $t = 5$ ms. After that, the flow velocity rapidly decreases, and most particles have velocities of less than 0.01 mm/s, as seen in the image of $t = 10$–30 ms. The fog-like region around the bubble is a circulating flow perpendicular to the observed plane[(2)], and attracted particles are trapped in the flow. In 490–510 ms, particles are deposited only on the left side of the bubble. This results from the collective deposition of trapped particles by the interfacial flow created by particle adsorption at the liquid-gas interface[(3)].

In $t = 0$–1 ms of the modulated condition, the motion of the particles is similar to that of continuous irradiation, except that the high-velocity region is smaller, probably because the averaged beam power is half of the continuous irradiation case. However, in $t = 10$–30 ms, particles are transported faster than in the continuous case, with maximum velocities of more than 0.1 mm/s. In addition, the deposited particles surrounded the bottom surface. In $t = 490$-510 ms, the deposited particles might replace the liquid-gas interface near the bottom of the bubble and decrease the driving force of convection, resulting in a decreased flow velocity.

We investigated the detail of the accumulation process under the modulation conditions. Figure 1(b) shows the process of the deposition of the particles. Two particles were transported toward the contact line and adsorbed outside the deposited particles. This behavior differs from that under the continuous irradiation, which collectively deposits after being trapped in circulating flow. We also compared the relative intensity, the ratio between the average intensity before and after the irradiation. The relative intensity under the modulated condition was larger and increased more sharply than in the continuous irradiation condition, as shown in Figure 1(c). Although the intensity increases continuously even under the continuous irradiation, the slope of the increase is low because the trapped particles are not immediately deposited. That may be attributed to the magnitude of the temperature gradient at the liquid-gas interface, which depends on the temperature field and the bubble size. From these results, laser modulation changes not only the flow velocity but also the flow structure and the accumulation process of particles.

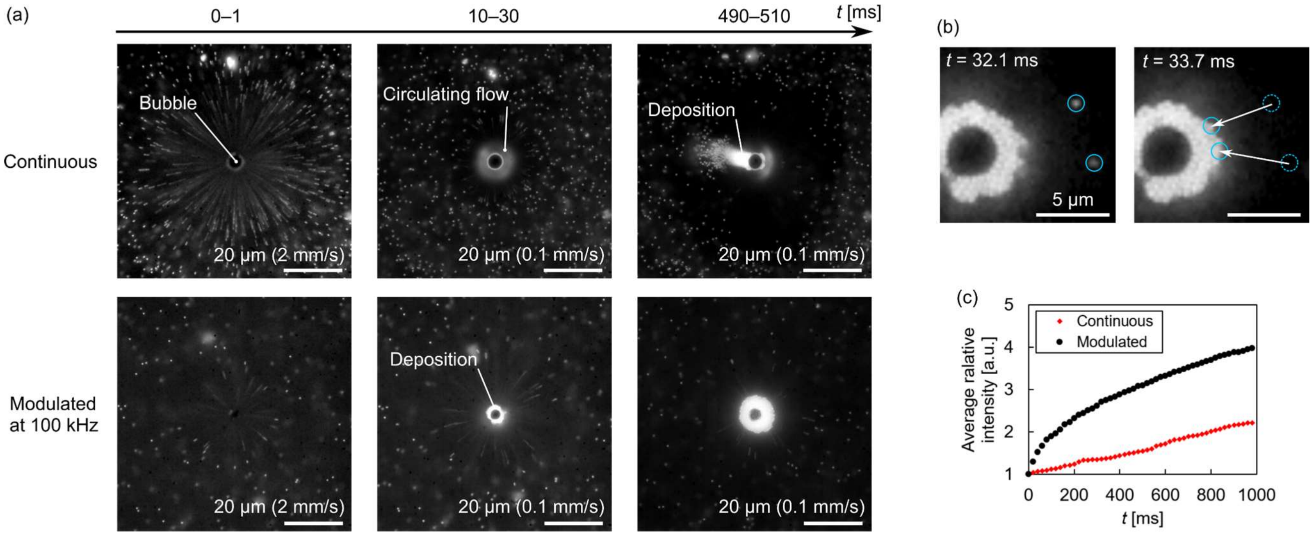

Figure 1. (a) Time-dependent particle accumulation process in continuous irradiation (upper) and 100 kHz modulation (lower). Scale bars also show the velocity determined from the length of the particle path. The laser irradiation was started at t = 0. The contrast of each image is adjusted for better visibility. (b) Particle deposition process on the modulated condition. Blue circles indicate the positions of particles. (c) Time evolution of the averaged relative intensity in the region within 30 µm from the center of the bottom of the bubble.

4 CONCLUSIONS

We visualized the transportation of 500-nm-sized polystyrene particles by the convective flow around a photothermal bubble. In continuous and modulated irradiation conditions, particles migrated to the three-phase contact line with a velocity of more than 1 mm/s for the first few milliseconds. After 10 ms from the heating, although the dominant flow velocity reduced to less than 0.01 mm/s under the continuous irradiation condition, flow velocities reaching 0.1 mm/s were observed under the modulated conditions. Moreover, the attracted particles were directly deposited under the modulated case, resulting in more rapid and larger amounts of accumulation than in the continuous case. These results mean the laser modulation alters the convection structure around a photothermal bubble.

5 REFERENCES

(1) Li, J., Hill, E. H., Lin, L., & Zheng, Y. (2019). Optical nanoprinting of colloidal particles and functional structures. ACS nano, 13(4), 3783–3795.

(2) Okada, K., Ichikawa, Y. & Motosuke, M. (2023). Convective flow in nanoparticle suspension generated around a photothermal bubble. Japanese J. Multiphase Flow, 37(1), 46–54.

(3) Okada, K., Kodama, K., Yamamoto, K., & Motosuke, M. (2021). Accumulation mechanism of nanoparticles around photothermally generated surface bubbles. Journal of Nanoparticle Research, 23(8), 188.

PIV measurements of tornado like ventilation flows

Jong Hoon Kang[1,*] and Sung Yong Jung[2]
1: Iron Steel Process Engineering Research Group, POSCO Technical Research Lab, Republic of Korea
2: Dept. of Mechanical Engineering, Chosun University, Republic of Korea
* Correspondent author: engdr@posco.com

Keywords: PIV processing, Tornado-like flow, Ventilation flow, Vortex flow

ABSTRACT The effects of the exhaust flow rate and jet velocity and, which significantly influence the vortex flow characteristics, on the vortex characteristics are investigated by using a particle image velocimetry (PIV) technique. The increase of side jet velocity leads to the widened vortex core and the increase of vortex strength. When the induced swirling force is high enough, a higher exhaust flow can make more stable vortex flows. To investigate the effectiveness of the vortex ventilation system, the concentration of ultra-fine particulate matters is monitored. The ventilation performance has a similar trend with size, circulation and swirl ratio over core region of vortex structures. This study propose a useful analysis method based on PIV to characterize tornado-like flows in vortex ventilation systems. In addition, these PIV results can be employed as basic data in the design and operation of vortex ventilation systems.

1 INTRODUCTION

The ventilation system is one of the most important components in indoor environments to ensure air quality and contaminant capture from small residents to large factories Kang and Lee (2008). Local ventilation systems, where the ventilation device is located near the contaminant generation, are used for enhancing contaminant removal efficiency. A simple exhaust hood is typically used for local ventilation, the exhaust hood is placed near the pollutant sources because the removal efficiency decreases with increasing distance due to the decrease of suction velocity Dallavalle (1933). However, a close placement limits the flow of the worker's traffic and equipment arrangement. To overcome this limitation, new local ventilation systems that employ vortex flows resembling a tornado have been developed Cao et al. (2018). Although it is important to understand the dynamic behavior of vortex flows in this ventilation system, the effect of operating conditions on flow characteristics has not been well understood. The present study proposed an innovative small-scale vortex generating system for controlling effective ventilation height by introducing the vorticity at all heights was employed. This system could overcome the limitation of vortex ventilation systems employed in previous researches having a device only at a single height for providing vorticity. Vortex characteristics in the proposed vortex ventilation system, such as the vortex core region, vortex intensity, and stability of vortex structures were investigated in terms of the operating parameters (side jet velocity and flow rate of the exhaust hood) using a particle image velocimetry (PIV) technique. PIV can provide instantaneous velocity field information over large planar regions and is suitable for investigating the flow structures and velocity fluctuations of large-scale vortex flows. The ventilation performance of the vortex ventilation system was investigated by monitoring the concentration of ultra-fine particulate matters ($PM_{2.5}$).

2 METHOD AND RESULT

Figure 1(left) shows a schematic diagram of PIV measurement for a vortex ventilation model simulating a ventilation system installed in a POSCO steel factory. An updraft flow was generated by an exhaust fan, and multiple side jets were used to supply the angular momentum for generating vortex flows. A two-head 200mJ Nd:YAG pulse laser (New Wave Research, Inc., USA) emitting a 532 nm wavelength laser was used to make a laser sheet with an optical lens. A CCD camera (VH-16MC, IMAGEOPS, USA) having a spatial resolution of 4,872 × 3,248 was employed to capture particle images and the corresponding field of view size was 0.35 m × 0.23 m. 1–3 μm olive oil droplets were seeded as tracer particles. To supply sufficient tracer particles, the system was placed inside an enclosed chamber of 1.3 (height, H) m × 1.2 (width, W) m, and the chamber wall and bottom were made of transparent acrylic for laser incidence and image capturing. More detailed information has been described in our published paper Kang et al. (2022).

The mean velocity vectors and turbulent kinetic energy (TKE) contours for various side jet velocities are shown in Fig. 1(right). The turbulent kinetic energy (TKE) was analyzed to compare the stability of formed flow structures. The TKE was small with no side flows because the velocity magnitude was small having small corresponding fluctuation component. Symmetrical TKE distributions occurred when induced swirl strength existed. When V_s is higher than 0.58 m/s, TKE was almost zero at the vortex center, and TKE had a peak around the vortex core boundary. The high TKE regions were widen as V_s increased, and this represented the decrease of vortex structure stability.

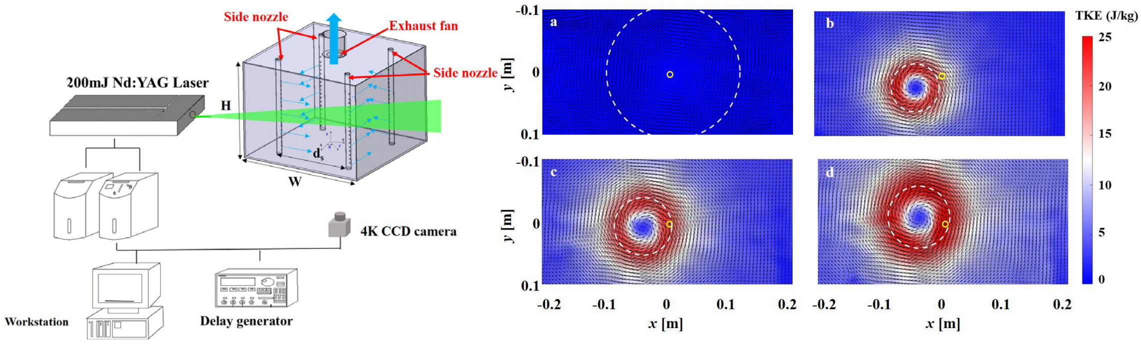

Figure 1. Schematic diagram of PIV experimental set-up(left) and Mean velocity vectors and turbulent kinetic energy contours for V_s of a: 0, b: 1.15, c: 1.73, d: 2.30 with Q_{ex} = 0.129 m^3/s (right)

3 CONCLUSIONS

In the present study, the characteristics of tornado-like flows in a simulated vortex ventilation system were measured using PIV. The effects of major operating parameters, including the side jet velocity and exhaust flow rate on the vortex core region, vortex strength, and stability of the vortex structures were analyzed. The vortex flow exhibited a helical upward motion. As V_s increased, the vortex core size and circulation increased, but the effective energy loss increased as well. The ventilation performance has same dependency with vortex size, circulation and swirl ratio over core region. A useful analysis method using PIV data was proposed to evaluate the vortex characteristics in vortex ventilation systems. In addition, this study can be used as basic data for the design and operation of a vortex ventilation system and relevant CFD analyses for large-scale factory ventilation systems.

4 REFERENCES

- Cao, Z., Wang, Y., Zhai. C., & Wang, M. (2018). Performance evaluation of different air distribution systems for removal of concentrated emission contaminants by using vortex flow ventilation system. Building and Environment, 142, 211–220.
- Dallavalle, J. (1933). The importance of velocity characteristics in the design of local exhaust hoods. The Journal of Industrial Hygiene, 15, 18–26.
- Kang, J. H., Kim, J. J., Park, H. W., & Jung, S. Y. (2022). Characterization of tornado like flows for improving vortex ventilation performance. Journal of Building Engineering, 46, 103726.
- Kang, J. H., & Lee, S. J. (2008). Improvement of natural ventilation in a large factory building using a louver ventilator. Building and Environment, 43, 2132–2141.

TECHNICAL SESSION 20
MICRO-NANO FLUIDICS II

Chaired by Morgan Li

20th International Symposium on Flow Visualization, Delft, the Netherlands ・10 – 13 JULY 2023

Photoelastic Measurement of Finger Growth in Saffman-Taylor Instability

Misa Kawaguchi[1], Ryuta X. Suzuki[2], Yuichiro Nagatsu[3], and Yoshiyuki Tagawa[1,2,*]

1: Dept. of Mech. Sys. Eng., Tokyo University of Agriculture and Technology, Japan

2: Institute of Global Innovation Research, Tokyo University of Agriculture and Technology, Japan

3: Dept. of Appl. Phys. Chem. Eng., Tokyo University of Agriculture and Technology, Japan

* Correspondent author: tagawayo@cc.tuat.ac.jp

Keywords: Instability, Viscous fingering, Flow birefringence, Photoelastic measurement, Hele-Shaw flow

ABSTRACT Photoelastic measurement around viscous fingering (VF) in radial Hele-Shaw cell were performed to visualize stress field. As a result, characteristic phase retardation distributions were obtained, and these results were interpreted using velocity profile in the gap. In particular, the lower phase difference at the fingertip may be due to the blunted velocity profile.

1 INTRODUCTION

Flow instability is ubiquitous in nature and industry. When a less viscous fluid displaces a more viscous one in small area, such as porous media or Hele-Shaw cells, the interface forms a finger-like pattern due to flow instability caused by the viscosity difference. This is known as Saffman-Taylor instability (Saffman&Taylor, 1958) or viscous fingering (VF) (Homsy, 1987).

The previous theoretical, experimental, and numerical approaches all pointed out that the three-dimensional (3D) structure inside the gap plays an important role in the onset and suppression of VF (Bischofberger *et al*., 2014; Oliveira&Meiburg, 2011). Yang & Yortsos (1997) theoretically showed that the initiation of VF in miscible systems is directly related to the transition of the interface structure from smooth to sharp shock front formation.

In the context of the importance of the 3D structure by previous studies, we focused on the flow-induced birefringence, which is related to the flow stress through the stress-optical law (Janeschitz-Kriegl, H., 2012) to evaluate the stress field around VF. The phase difference Δ caused by birefringence is proportional to the principal stress difference σ_d.

$$\Delta = C\sigma_d b \tag{1}$$

where b is the thickness of the object to be measured, and C is the stress-optic coefficient. This technique can perform unsteady measurement thanks to the high-speed polarization camera. In addition, 3D information can be taken into account based on the integrated photoelasticity (Yokoyama *et al*, 2023).

2 EXPERIMENTAL METHOD

Figure 1 shows the experimental setup: a radial Hele-Shaw cell has gap of 0.3 mm with metal plate. The less viscous fluid was injected into the Hele-Shaw cell filled with the more viscous one by a syringe pump (PUMP 11 ELITE, Harvard Apparatus) with constant flow rate of 1 ml/min. A light source (SOLIS-565C (λ=543 nm), Thorlabs) and a high-speed polarization camera (CRYSTA PI-5WP, Photron) with a lens (Z16 APO, Leica) were used. The measurement area was 1/4 region of Hele-Shaw cell. The frame rate was 250 fps. The spatial resolution was 55.6 μm /pixel. The results were obtained using CRYSTA Stress Viewer software (Photron), ImageJ and MATLAB. The more viscous fluid was mixture of glycerol (85%) and aqueous cellulose nano crystal (CNC) (CNC-HS-FD, CelluloseLab) (1.33 wt%) suspension. The less viscous fluid was water. The more viscous fluid, a mixture of glycerol and CNC solution, showed a slightly shear-thinning property due to CNC.

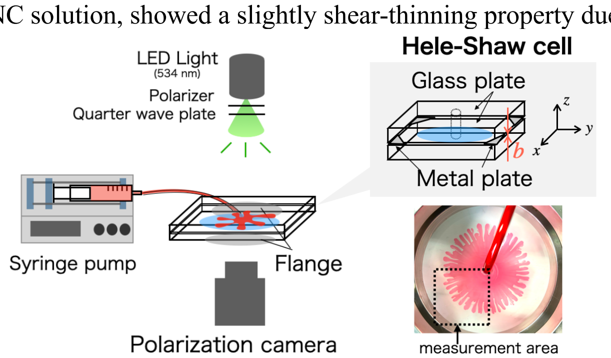

Figure 1. Experimental setup.

3 RESULTS & DISCUSSIONS

Figure 2 shows image sequences of phase retardation distribution in more viscous fluid. Note that the phase retardation is including not only shear stress contribution in *x-y* plane but also that in *x-z* plane. For phase retardation far away from the fingers, the phase retardation initially increased then decreased. This time evolution can be interpreted to corresponding to the velocity profile development. Initially, the velocity profile is assumed to be close to uniform, then it developed with boundary layer.

For the phase retardation around finger, the three characteristics were observed: (i) higher region between the fingers near the tip end, and (ii) lower region at the base of the finger, (iii) lower region at the tip of the finger. In the region of (i) and (ii), shear stress in *x-y* plane is relatively dominant compared to the shear stress in the gap because azimuthal angle was near ±45° in those regions (results are not shown here). In the region of (iii), normal stress in *x-y* plane is dominant because azimuthal angle was almost zero. In this region, we hypothesized that the shear stress in cross-section (*x-z* plane) is dominantly reflected to the magnitude of phase retardation. According to the previous research, the concentration profile in the gap was like shock front and this shape is maintained during finger growth (Bischofberger *et al*., 2014). From that result, the velocity profile is expected to be blunted at the center of gap. When the velocity profile becomes blunted, the sum of velocity gradient in *z*-direction decreases. Therefore, one possible reason lower region of Δ at the fingertip is blunt structures in the cross-section.

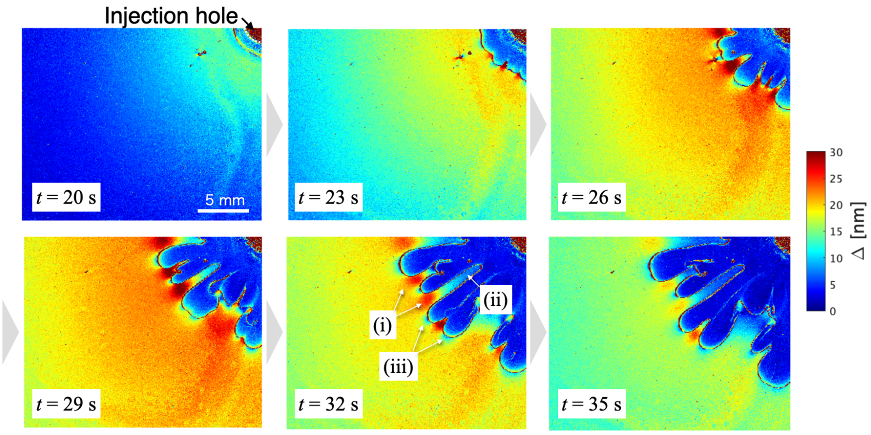

Figure 2. Image sequences of phase retardation distribution in *x-y* plane. Stress filed is visualized in outer (more viscous) fluid.

4 CONCLUSION

Photoelastic measurement around VF in radial Hele-Shaw cell were performed. As a result, the evolution of phase retardation in penetrated fluid (more viscous fluid) was changed with instability onset and finger growth. It may be related to the velocity profile development. In particular, lower region of phase retardation at the tip of the finger may be related to the blunted velocity profile. It will be qualitatively evaluated in the future works.

5 ACKNOWLEDGEMENT

This research was funded in part by JSPS KAKENHI Grant Number JP20H00223, JP23K13252, and JST PRESTO Grant Number JPMJPR21O5.

6 REFERENCES

- Bischofberger, I., Ramachandran, R., & Nagel, S. R. (2014). Fingering versus stability in the limit of zero interfacial tension. Nature communications, 5(1), 5265.
- Homsy, G. M. (1987). Viscous fingering in porous media. Annual review of fluid mechanics, 19(1), 271–311.
- Janeschitz-Kriegl, H. Polymer melt rheology and flow birefringence (Vol. 6). Springer Science & Business Media (2012).
- Oliveira, R. M., & Meiburg, E. (2011). Miscible displacements in Hele-Shaw cells: three-dimensional Navier–Stokes simulations. Journal of fluid mechanics, 687, 431–460.
- Saffman, P. G., & Taylor, G. I. (1958). The penetration of a fluid into a porous medium or Hele-Shaw cell containing a more viscous liquid. Proceedings of the Royal Society of London. Series A. Mathematical and Physical Sciences, 245(1242), 312–329.
- Yang, Z., & Yortsos, Y. C. (1997). Asymptotic solutions of miscible displacements in geometries of large aspect ratio. Physics of Fluids, 9(2), 286–298.
- Yokoyama, Y., Mitchell, B. R., Nassiri, A., Kinsey, B. L., Korkolis, Y. P., & Tagawa, Y. (2023). Integrated photoelasticity in a soft material: phase retardation, azimuthal angle, and stress-optic coefficient. Optics and Lasers in Engineering, 161, 107335.

Study on quantum dots' diffusion inside silica monolith

Yusaku Abe[1,*] Naoki Tomioka[1] and Yu Matsuda[1]
1: Dept. of Modern Mechanical Engineering, Waseda university, Japan
* Correspondent author: ya-jupiter0309@toki.waseda.jp

Keywords: Single-Particle Tracking, SPT, Diffusion

ABSTRACT Porous media have many pores inside. Particles' diffusion inside porous media seems to heterogeneous behavior because of their collision to pore-wall, adsorption to pore-surface, and the like. Then ensemble mean of particles is not enough for discovering particles' behavior, but an approach that aims to understand particle's behavior from the trajectories of individual particles is more suitable. However, it is difficult to measure trajectories of individual particles by conventional methods. In this study, we visualized trajectories of individual particles moving inside porous media using single-particle tracking (SPT), which enables direct observation of the motion of individual particles.

1 INTRODUCTION

Porous media are widely used because they have some unique properties, and these properties caused by many pores inside it. For example, silica monolith that have an integral porous body made from quartz silica are used as a filter and an adsorption column. Thus, we need to visualize how particles diffuse inside porous media to utilize porous media effectively. However, conventional measurement methods evaluate porous media properties in bulk scale. For example, mercury porosimeter[1] measure pore size distribution in bulk scale. Here we report the results of the measurement of individual particles' motion using single-particle tracking (SPT). SPT is the measurement method of tracking probe particles inside measuring object. By analyzing probe particles' trajectories, we visualize particle's behavior and understand the underlying physics governing particle motion. For example, SPT has been utilized to uncover the dynamics in soft matter systems[2,3] and particle's motion in cell[4].

2 METHODS

In this study, single-particle tracking images were obtained using a fluorescence microscope (IX-73, Olympus, Japan). Quantum dots in the region of interest were excited by a 488 nm continuous wave (CW) laser source (OBIS488LS, Coherent, USA). Reflected emission from quantum dots passes through confocal scanner unit (CSU-X1, Yokogawa Electric, Japan) to pass through to an EM-CCD camera (C9100-23B, ImagEM X2, Hamamatsu Photonics, Japan). The images had an area of about 1678 μm^2 (262,144 pixels). Videos were recorded at 30 ms exposure time and consisted of 500 frames.

3 RESULTS

Fig. 1 shows a histogram of the measured diffusion coefficient as obtained by mean squared displacements (MSD) analysis per each probe. This histogram has two peaks; one peak is about $10^{-15}\ m^2/s$, and the other peak is about $10^{-13}\ m^2/s$. In this experimental condition, the diffusion coefficient of the probe diffusing freely in the solvent is $4.57 \times 10^{-13}\ m^2/s$. Here it can be seen that while some probes diffuse like freely, some probes diffuse slower than probes diffusing freely. Fig. 2 shows a histogram of the measured moment scaling spectrum (MSS) as obtained by analysis of each probe. MSS is used to characterize probe's motion[5]. MSS make use of higher order moments, while MSD analysis use of the second moment. For details of the MSS, please see this article[6]. $\text{MSS slope} = 0.5$ represents Brownian diffusion, $0 < \text{MSS slope} < 0.5$ represents confined diffusion, and $0.5 < \text{MSS slope} < 1.0$ represents super diffusion. Then, the result in Fig. 2 indicates that most probes were confined inside pores.

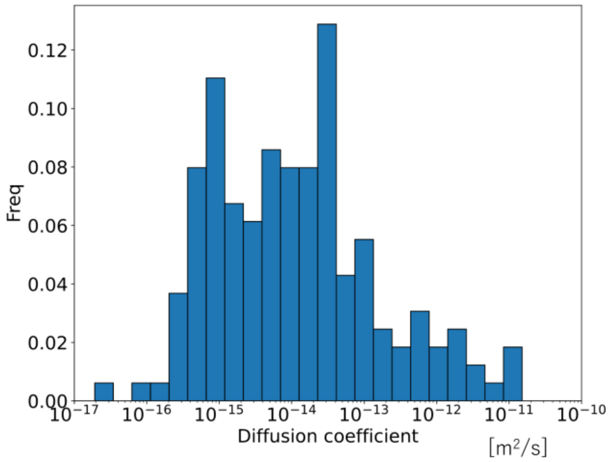

Figure 1. Histogram of diffusion coefficient.

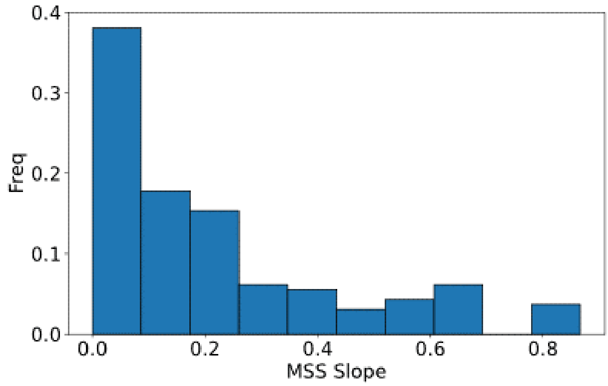

Figure 2. Histogram of MSS Slope.

4 CONCLUSIONS

In this study, we realize visualization of trajectories of individual particles inside porous media. Statical analysis of diffusion coefficient and MSS, it is obvious that some particle is confined inside pore. Importantly, particle diffusion is very different for each particle.

5 ACKNOWLEDGEMENTS

This study partially supported by a JSPS, Japan Grant-in-Aid for Scientific Research (B), No. 19H02086, 22H01421.

6 REFERENCES

1) Giesche, H. (2006). A general (practical) overview. Part Part Syst Charact, 23, 9-19.

2) Rose KA, Molaei M, Boyle MJ, Lee D, Crocker JC, Composto RJ. (2021). Particle tracking of nanoparticles in soft matter. J Appl Phys, 127, 191101.

3) Iwao R, Yamaguchi H, Niimi T, Matsuda Y. (2021). Single-molecule tracking measurement of PDMS layer during curing process. Physica A: Statistical Mechanics and its Applications, 565, 125576.

4) Jaqaman K, Loerke D, Mettlen M, Kuwata H, Grinstein S, Schmid SL. (2008). Robust single-particle tracking in live-cell time-lapse sequences. Nat Methods, 5, 695-702.

5) Arts M, Smal I, Paul MW, Wyman C, Meijering E. (2019). Particle Mobility Analysis Using Deep Learning and the Moment Scaling Spectrum. Sci Rep, 9, 17160.

6) Sbalzarini IF, Koumoutsakos P. (2005). Feature point tracking and trajectory analysis for video imaging in cell biology. J Struct Biol, 151, 182-195.

Microbubble size measurements in impure water from Interferometric Particle Imaging

Rens Stigter[1,*] Gert Dekkers[2], Daniele Fiscaletti[1], Gerrit Elsinga[1], Tom van Terwisga[1,2], Jerry Westerweel[1]
1: Dept. of Process and Energy, Technical University of Delft, Netherlands
2: Dept. of Maritime and Transport Technology, Technical University of Delft, Netherlands
* Correspondent author: m.stigter@tudelft.nl

Keywords: IPI, Shadowgraphy, Microbubble concentration, Cavitation inception

Introduction Underwater radiated noise has been shown to seriously affect the behaviour of marine life in hunting, communicating and resting, and to have an impact on their demography (Duarte et al, 2021). Sound levels have drastically increased over the last decades, and the IMO has introduced regulations to keep noise pollution under control. Propeller cavitation is the main source of shipping noise. To reduce these sound levels, it is necessary to predict the cavitation inception of ship propellers accurately, which has a severe dependence on water quality. At Delft, in the new Multi-Phase Flow Tunnel (MPFT), we intend to monitor the water quality during cavitation inception experiments by measuring the microbubble size distribution and concentration. Several optical techniques have been applied to measure the size distribution of microbubbles (Mees et al., 2010, Russell et al. 2020), but their sensitivity to water impurities mimicking the sea water conditions, such as particles, salt and surfactants, have never been investigated to the knowledge of the authors. In this study, we firstly cross-validate Interferometric Particle Imaging (IPI) and shadowgraphy by comparing the measured size of the microbubbles. Moreover, we assess the capability of IPI to identify impurities that have been added to fresh water.

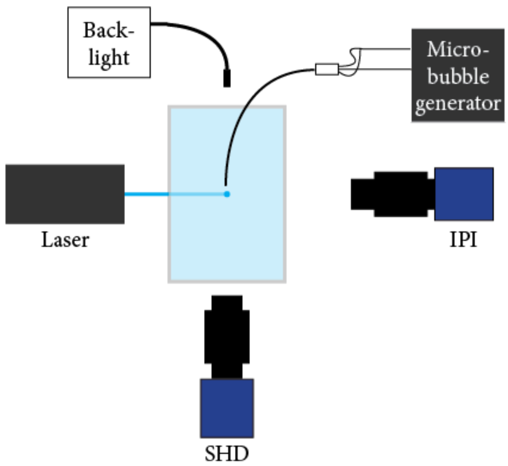

Figure 1. Schematic of the top-view of the experimental setup.

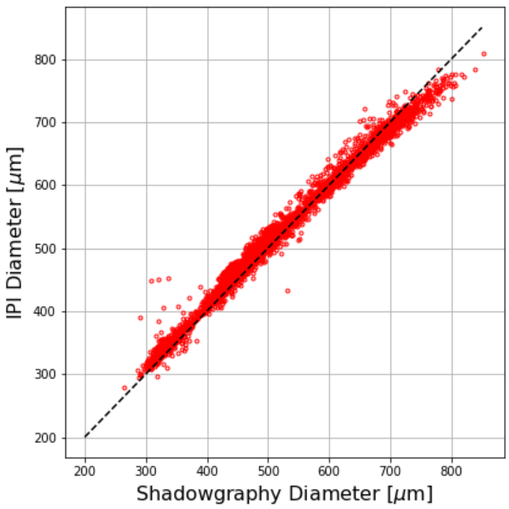

Figure 2. Comparison between the size measurements of the microbubbles from Shadowgraphy and IPI

Method IPI exploits the Mie-scattering pattern from a spherical droplet or bubble that is illuminated by a coherent laser source to determine its diameter. When the bubble is out of focus, the Mie-scattering pattern appears as a parallel fringe pattern onto the bubble disk (Maeda et al. 2000). The relation between the bubble diameter D and the fringe wavelength λ is:

$$D = \frac{K}{C\,\lambda} \tag{1}$$

Where K is a calibration constant found from evaluating the Mie-scattering theory and C a calibration constant depending on the experimental setup. We want to validate the IPI measurements using a comparison with Shadowgraphy (SHD). The measurements were done in a small container filled with water (10 L), with a 488 nm continuous-wave laser emitting a laser beam, which entered the container at the bottom. The IPI camera was oriented on the side window of the container, at a 90 degree scattering angle and parallel polarization. SHD was oriented perpendicular to IPI. A stream of bubbles was generated using the bubble generator device ElveFlow OB1. Optical filters were exploited to enable simultaneous measurements of IPI and SHD in the same region of the flow. The optical setup was aligned such that the same bubble was captured in both IPI and SHD in the same timeframe at approximately the same height in the image. Both techniques used a 105 mm Nikkon lens, resulting in a magnification of approximately 1 at the focal plane. Demineralized water was used in all measurements. Figure 1 shows a schematic of the experimental setup.

Results The bubble size as estimated by SHD and IPI is shown in Figure 2. The different techniques agree well, having a relative error $(D_{IPI} - D_{SHD}) / D_{IPI} * 100\ \%$ ranging from + 3% for the smallest bubble sizes to -5% for the largest. A typical bubble image for both techniques is shown in Figure 3. The left hand side shows the shadowgraphy image of a bubble, with a bright spot in the middle caused by refracted backlight. The shadow above the bubble is caused by reflections in the container. The right hand side shows a bubble image from IPI, which is relatively large because the bubble is strongly out of focus. The fringes are clearly visible in the image, they have a small wavelength, of approximately five pixels. While the bubble size estimation of both techniques have good agreement, several factors are found that will have an influence on the bubble concentration estimated by IPI. First, overlapping bubbles are well-known to be a shortcoming of IPI. The overlap can be modelled using a Poisson distribution (Damaschke et al, 2002). Another well-known shortcoming are tilted fringe patterns. From our results, these patterns originate from light scattering from nearby bubbles. When the distance between these bubbles changes, the tilted fringe pattern changes both orientation and wavelength. Furthermore, for some bubbles, a relatively low signal-to-noise ratio is observed for the fringe pattern. This can also explain part of the observed discrepancies between the techniques.

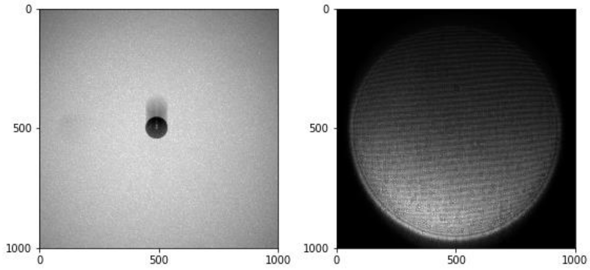

Figure 3. Typical bubble image of Shadowgraphy (left) and IPI (right).

After validating the microbubble size measurements, we examine as follows their sensitivity to water impurities. This has the aim of assessing whether Shadowgraphy and IPI can be applied in experiments where sea water conditions are reproduced. In the same apparatus as described before, tests were conducted after adding salt, surfactants and (spherical) particles to the water, in different rounds. Figure 4 shows the images of an (almost) spherical particle for both techniques. The spherical particle shows a fringe pattern that is very similar to that of bubbles. In this case, the particle and the bubble can no longer be distinguished. A potential source of error in the IPI measurements arises when the particle is in the line of the bubble and the lens, and close to the bubble. In this case a hologram appears on the bubble image (Figure 5).

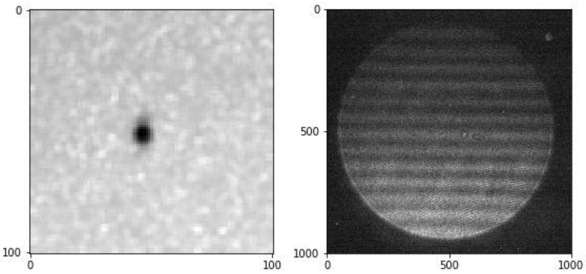

Figure 4. Image of spherical particle from Shadowgraphy (left) and IPI (right).

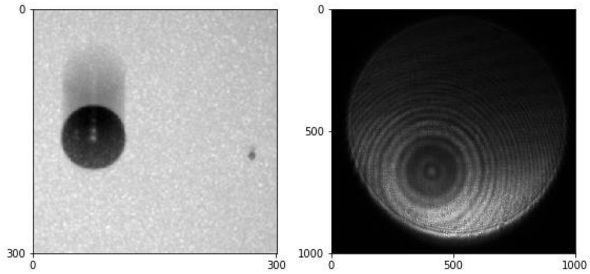

Figure 5. Hologram on IPI bubble (right) due to a particle between the bubble and IPI lens, as seen at the Shadowgraphy image (left).

Further research Future research involves the application of IPI to assess the concentrations of microbubbles. Preliminary tests were performed, which revealed some discrepancies between SHD and IPI, with IPI underestimating the bubble concentration. By comparing the concentration measurements of SHD and IPI, we are able to determine the different error sources in the concentration estimate of IPI. This will help us develop a method to monitor the bubble sizes and concentrations in the MPFT in Delft during cavitation experiments.

References

Damaschke, N., Nobach, H. & Tropea, C. (2002) Optical limits of particle concentration for multi-dimensional particle sizing techniques in fluid mechanics. Experiments in Fluids, 32:143-152

Duarte, C.M., Chapuis, L., Collin, S.P., Costa, D.P., Devassy, R.P., Eguiluz, V.M. et al (2021). The soundscape of the Anthropocene ocean. Science, 371 (6529).

Maeda, M., Kawaguchi, T. & Hishida, K. (2000). Novel interferometric measurement of size and velocity distributions of spherical particles in fluid flows. Meas. Sci. Technol. 11:L13-L18

Méès, L., Lebrun, D., Allano, D., Walle, F., Lecoffre, Y., Boucheron, R. & Fréchou, D. (2010). Development of interferometric techniques for nuclei size measurement in cavitation tunnel. 28th Symposium of Naval Hydrodynamics. Pasadena, United States. Hal-02414550

Russell, P., Venning, J., Pearce, B.W. & Brandner, P.A. (2020). Calibration of Mie scattering imaging for microbubble measurement in hydrodynamic test facilities. Experiments in Fluids, 61:93

Numerical Study on Ionic Wind from Pin to Mesh with Hole Configuration

Tae Sung Ahn[1], Ji Hong Chung[2], Dong Kee Sohn[2] and Han Seo Ko[2,3*]
1: Dept. of Semiconductor and Display Engineering, Sungkyunkwan University, Republic of Korea
2: School of Mechanical Engineering, Sungkyunkwan University, Republic of Korea
3: Dept. of Smart Fab. Technology, Sungkyunkwan University, Republic of Korea
* Correspondent author: hanseoko@skku.edu

Keywords: Electrohydrodynamic (EHD), Negative Corona Discharge, Trichel pulse, Plasma, Ionic wind

ABSTRACT Ionic wind is generated by corona discharge and collision between ions and neutron particles, which is a promising technology for gas pumping application. The purpose of this study is to enhance the velocity of ionic wind by negative corona discharge in a needle-mesh system. By making a central hole in a mesh, the pressure drop across the mesh electrode could be reduced and the velocity of the ionic wind increased accordingly. Using plasma and fluid simulation, an optimal point based on the diameter and distance of the hole was determined. It was found that the hole diameter of 5 mm at the distance of 5 mm resulted in the maximum velocity. The calculated model was verified with 3 % compared to the experimental results.

1 INTRODUCTION

It has been shown that the corona discharge induces an EHD force which results in an ionic wind. In a certain case, a Trichel pulse is generated in corona discharge environment. By making a central hole in the mesh electrode, the pressure drop can be reduced. When the distance between the needle and the mesh electrode increases, the ionization rate and EHD force are reduced. This study aims to analyze the velocity of the ionic wind using numerical simulations of ionic wind with the Trichel pulse, and to evaluate the effect of the hole diameter in the mesh electrode with the distance. The results were compared with the particle image velocimetry (PIV) experiments.

2 MODEL DESCRIPTION

The drift-diffusion plasma fluid model was used to simulate negative corona discharge. Although there are many species (N_2, O_2, O and so on) and reactions in air discharge, a simplified model was used with 3 species (positive ion, negative ion, and electron) and solved for 3 sets of continuity equation (1)~(3) for electron, positive ion and negative ion density as well as a Poisson equation (4) for electric field.

$$\frac{\partial n_e}{\partial t} + \nabla \cdot \left(-\mu_e \vec{E} n_e - D_e \nabla \mathrm{n_e}\right) = \alpha n_e \left|\mu_e \vec{E}\right| - \eta n_e \left|\mu_e \vec{E}\right| - k_{ep} n_e n_p, \tag{1}$$

$$\frac{\partial n_p}{\partial t} + \nabla \cdot \left(\mu_p \vec{E} n_p - D_p \nabla \mathrm{n_p}\right) = \alpha n_e \left|\mu_e \vec{E}\right| - k_{ep} n_e n_p - k_{np} n_n n_p, \tag{2}$$

$$\frac{\partial n_n}{\partial t} + \nabla \cdot \left(-\mu_n \vec{E} n_n - D_n \nabla \mathrm{n_n}\right) = \eta n_n \left|\mu_n \vec{E}\right| - k_{np} n_n n_p, \tag{3}$$

$$\nabla \cdot \vec{E} = -\nabla^2 V = \frac{e\left(n_p - n_e - n_n\right)}{\varepsilon_0 \varepsilon_r}. \tag{4}$$

where n_e, n_p and n_n are number density for electron, positive ion, and negative ion, respectively. μ_e, μ_p, μ_n, D_e, D_p and D_n are mobility and Diffusion corefficients for electron, positive ion, and negative ion, respectively. α, η, k_{ep}, and $k_{np}$are townsend coeffient, attachment with 2 body and 3 body collision, recombination coefficients of positive ions with electron and negative ions, respectively. The swam parameter was obtained from previous reserch (Kulikovsky, 1997). The current was calculated using Sato's equation (Sato, 1980) and secondary electron emission coeffiecient was assumed to be 0.01, and boundary conditions were found based on the referance (Dordizadeh et al., 2015). The Navier-Stokes equation was sovled using k- ε model for tulbulance and Non-Darcian flow model for porouse media. The EHD force was defined by $F_{ehd} = e(n_p - n_e - n_n)\vec{E}$. Since it was calculated as 2D-axisymmetry, an electrode of mesh-type was assumed to be a plate in plasma model and porous media in fluid model. Porosity and permeability were determined by CFD to be 0.4204 and 1.49×10^{-9}, respectively, with an error of about 3 %. The minimum mesh size was 0.15 μm near the needle tip, and total number of meshes was approximately 300,000.

3 SIMULATION RESULTS

There are differences in the timescales between the plasma and fluid models, as the frequency of the Trichel pulse is more than 100 kHz. As a result, the plasma model was simulated in the nanosecond timescale, while the fluid model was simulated in the microsecond timescale.

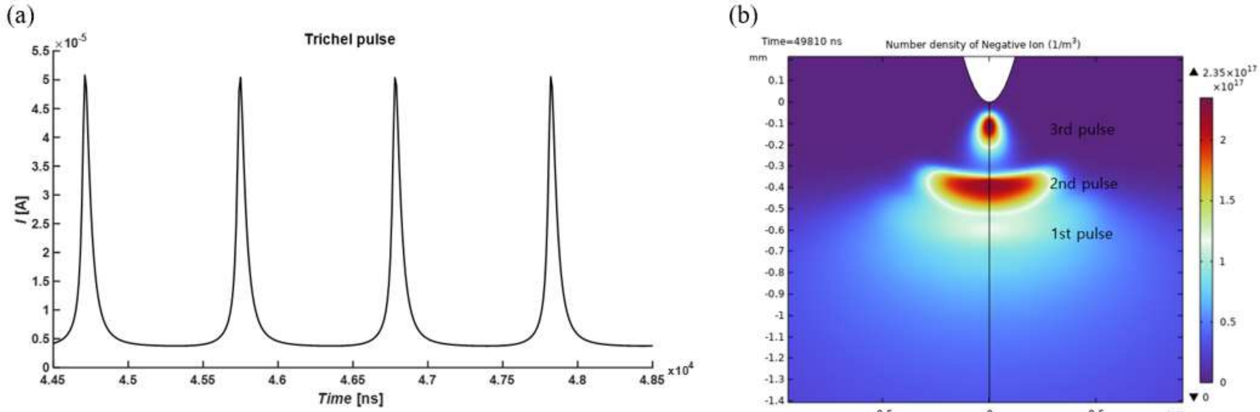

Figure 1. (a) Current of negative corona discharge with Trichel pulse and (b) Number density of negative ion.

In the plasma model, the Trichel pulse was obtained with a time-average current of 8 μA and a frequency of 952 kHz under the condition of -5 kV and 10 mm with the needle-mesh distance. In the fluid model, it was observed that the maximum velocity near the needle was greater without a central hole compared to the case with a central hole. However, at a measuring point 25 mm from the electrode, the velocity was much higher for the case with a central hole than that for the case without the hole. By comparison with the experiment, the velocity error was observed to be about 3 %. Additionally, the maximum velocity varied according to the distance and diameter of the central hole.

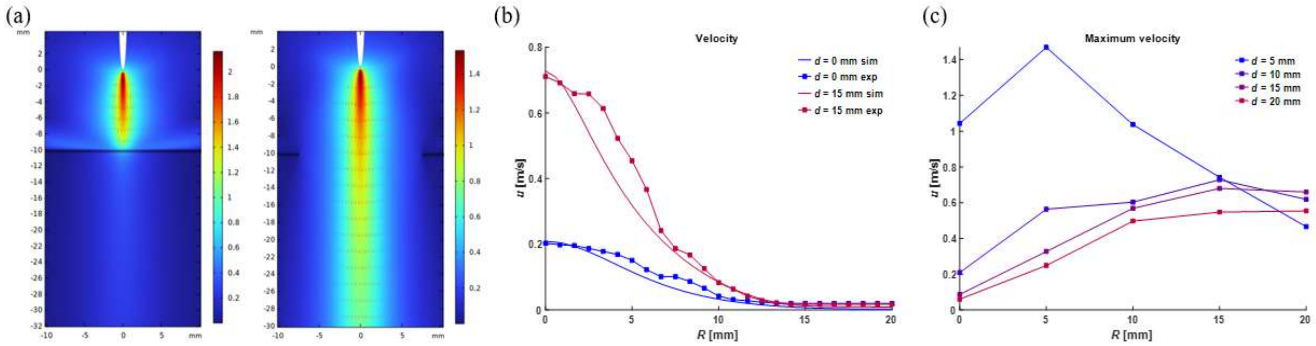

Figure 2. (a) Velocity without and with a central hole [m/s], (b) Comparison of velocity between experiment and simulation, and (c) Maximum velocity depending on distance between electrodes and diameter of hole (x-axis)

4 CONCLUSION

This study investigated the ionic wind using numerical simulation of plasma and fluid models. The results showed the optimal diameter of the central hole in the mesh-type electrode which causes a pressure drop. The dependency on the distance between pin and mesh electrode was also analyzed. Specifically, the maximum velocity was observed at the 5 mm distance with 5 mm diameter, 10 mm distance with 15 mm diameter, and 15 to 20 mm distance with 20 mm diameter cases. These findings can provide useful information for the design and optimization of the ionic wind-based devices.

5 REFERENCE

- Kulikovsky, A. A. (1997). Positive streamer between parallel plate electrodes in atmospheric pressure air. Journal of Physics D: Applied Physics, 30(3), 441–450.
- Sato, N. (1980). Discharge current induced by the motion of charged particles. Journal of Physics D: Applied Physics, 13(1), 3–7.
- Dordizadeh, P., Adamiak, K., & Peter Castle, G. S. (2015). Numerical investigation of the formation of Trichel pulses in a needle-plane geometry. Journal of Physics D: Applied Physics, 48(41).

Experimental analysis of the capillary rise in divergent tubes in microgravity

Domenico Fiorini[1,2*], Alessia Simonini[1], Johan Steelant[3], David Seveno[2], Miguel A. Mendez[1]
1: Environmental and Applied Fluid Dynamics, von Karman Institute, Rhode-Saint-Genese, Belgium
2: KU Leuven, Dept. of Materials Engineering, Leuven 3001, Belgium
3: ESTEC-ESA, Keplerlaan 1, Noordwijk, The Netherlands
* Correspondent author: domenico.fiorini@vki.ac.be

Keywords: Capillary flows in microgravity, interface detection, PIV

Modelling the dynamics of a gas-liquid interface along a solid surface is fundamental in coating and capillary-driven flows. These applications have often been characterized using semi-empirical or theoretical correlations that link the contact angle at the wall to the contact line dynamics. However, [1] recently showed that classic quasi-stationary models fail in situations where inertia plays a significant role. This is the case in many applications in microgravity, such as the sloshing of space propellants and the cryogenic propellant management. A critical case study for analysing the fundamentals for these is the capillary rise experiments. These experiments in [2] show that the modelling of surface tension strongly impacts the prediction of liquid displacement. Moreover, they assessed that the interface dynamics results as a competition between viscous and inertial effects. It is therefore essential to analyse parallel to the dynamic contact angle the role of the flow field beneath the interface on the capillary rise.

In this work, we experimentally analyse the capillary rise and the interface dynamics of highly wetting fluids (HFE7200) in microgravity. The experiments were carried out during the 78th ESA parabolic flight campaign. The experimental conditions reproduced through the flights provide a larger duration of the capillary-dominated phase compared to previous studies and allow for characterizing the relationship between the interface shape, its motion and the underlying flow field at different gravity levels. The investigated configuration consists of a diverging U-tube (DUT) with the fluid confined in a closed environment. The configuration and a picture of the experimental set up is shown in Fig. 1a and Fig1b. This configuration ensures a saturated gas environment, and the capillary forces have a double effect on the motion of the liquid since both ends of the liquid column create a capillary pressure drop that pulls the interface in opposite directions. We acquire high speed visualizations of the gas liquid interface in backlighting configuration using a LED screen (D in Fig1a) behind the DUTs (C in Fig1a). These are post-processed using standard image processing routines to retrieve the meniscus interface and contact angle. PIV was used to characterize the velocity field beneath the interface using the configuration shown in Fig. 1c.

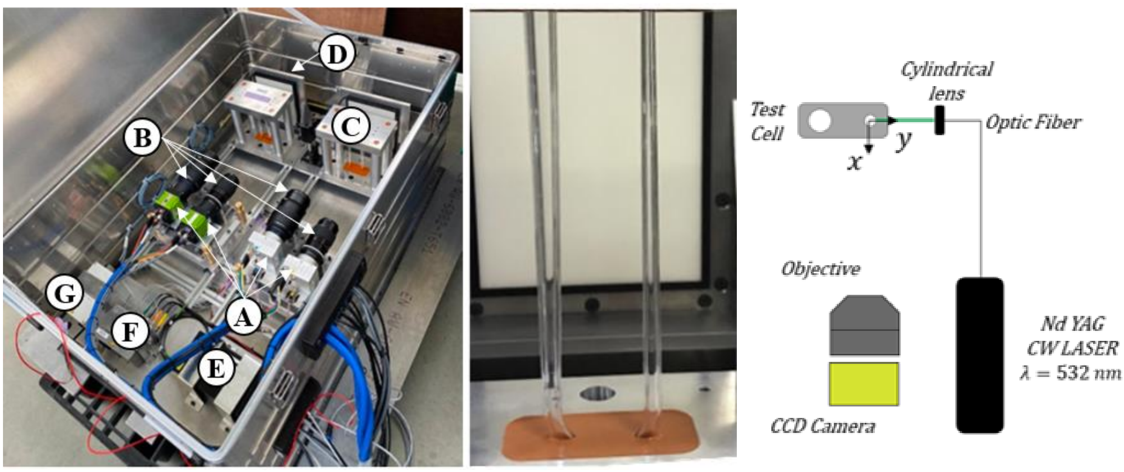

(a) (b) (c)

Figure 1 - Divergent U-tube facility (a) Picture of the setup with (b) Backlight configuration (c) PIV configuration

Two experiments were performed in parallel, with a camera acquiring images on each side of the two tubes. The motion of each interface is recorded with a high-speed camera (model JAY SP-12000-CXP4), acquiring grey-scale images at 300 fps. All cameras (A in Fig1a) mount objectives with 105mm focal lenses (B in Fig1a) and are positioned to acquire the full motion of the interface while spanning the largest possible tube length. The final pixel size corresponds to 0.013μm.
The PIV is carried out using a planar laser sheet produced on one side of the tube as shown in Fig1 c. The fluid was seeded with FMR-1.3 1-5 μm Red Fluorescent Miscospheres from Cospheric. The particles were illuminated with a continuous laser source (LMX-532 from Oxxius, E in Fig.a) with a wavelength of 532 nm and a maximum power of 800 mW. The PIV images are pre-processed using the Proper Orthogonal Decomposition (POD)-based background removal introduced by [3].

The PIV pre-processed images as in Fig. 2b and are processed using adaptive iterative multigrid interrogation [4] to retrieve the velocity fields. The PIV interrogation is carried out using OpenPIV processing tool [5] and windows with a 2:1 aspect ratio. We use a Dynamic Region of Interest (DROI) to follow the gas-liquid interface across the available Field of View (FOV). This allows focusing the analysis always in the region below the interface. The results are interpolated with Radial Basis Functions to achieve super-resolution [6].

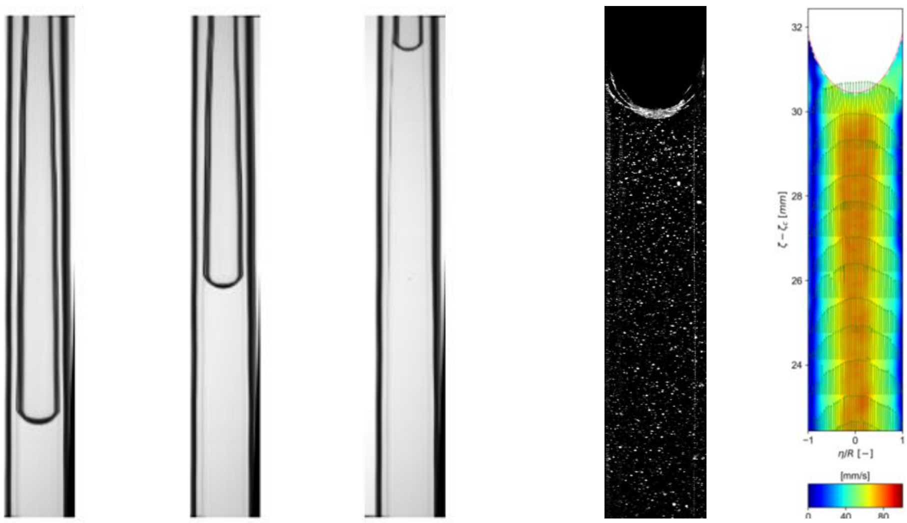

(a) (b) (c)

Figure 2 – Backlight visualization at different stages of the capillary rise (a) and PIV measurements (b) POD pre-processed (c) Velocity contour and velocity profile at selected locations.

The experiments start with the announcement of the plane being at 40 degrees inclination. Shortly after the announcement, the gravity levels drop from approximately 1.8g to approximately 0g and the two liquid interfaces begin moving along the axis of the tube due to the unbalanced capillary action of the interfaces. Concerning the stream-wise variation of the velocity profile, at a distance of approximately 3 mm, the velocity profile appears nearly parabolic in all snapshots. Fig. 2c shows the case of larger acceleration where the flow inertia appears to push the validity of the parabolic profile closer towards the interface (up to nearly 1 mm from it). Near the interface, the liquid accelerates towards the contact line in order to match the inner parabolic velocity profile with the outer interface shape. Combining the two measurement techniques, the full paper will present the impact of the flow field on the contact line region and on the capillary motion of the interface.

[1] Fiorini, D., Mendez, M.A., Simonini, A., Steelant, J., and Seveno, D., Effect of inertia on the dynamic contact angle in oscillating menisci, Physics of Fluids, vol. 34, no. 10, p. 102116, 2022.
[2] Stange, M., Dreyer, M.E., and Rath, H.J., Capillary driven flow in circular cylindrical tubes, Physics of fluids, vol. 15, no. 9, pp. 2587–2601, 2003.
[3] Mendez, M., Raiola, M., Masullo, A., Discetti, S., Ianiro, A., Theunissen, R., and Buchlin, J.M., Pod-based background removal for particle image velocimetry, Experimental Thermal and Fluid Science, vol. 80, pp. 181–192, 2017.
[4] Scarano, F. and Riethmuller, M.L., Advances in iterative multigrid piv image processing, Experiments in fluids, vol. 29, no. 1, pp. S051–S060, 2000.
[5] Liberzon, A., Lasagna, D., Aubert, M., Bachant, P., Kaufer, T., Jakirkham, Andreas, B., Boyko, V., Cameron, D., Joe, B., Tomerast, and Ranleu, Openpiv/openpiv-python: Open-piv-python (v0. 22.2) with a new extended search piv grid option, 2020
[6] Ratz, M., Fiorini, D., Simonini, A., Cierpka, C., and Mendez, M.A., Analysis of an unsteady quasi-capillary channel flow with time-resolved piv and rbf-based super-resolution, Journal of Coatings Technology and Research, pp. 1–14, 2022.